NASA/CP–1998–206960

Life and Microgravity Spacelab (LMS) Final Report

J.P. Downey, Compiler
Marshall Space Flight Center, Marshall Space Flight Center, Alabama

February 1998

The NASA STI Program Office...in Profile

Since its founding, NASA has been dedicated to the advancement of aeronautics and space science. The NASA Scientific and Technical Information (STI) Program Office plays a key part in helping NASA maintain this important role.

The NASA STI Program Office is operated by Langley Research Center, the lead center for NASA's scientific and technical information. The NASA STI Program Office provides access to the NASA STI Database, the largest collection of aeronautical and space science STI in the world. The Program Office is also NASA's institutional mechanism for disseminating the results of its research and development activities. These results are published by NASA in the NASA STI Report Series, which includes the following report types:

- TECHNICAL PUBLICATION. Reports of completed research or a major significant phase of research that present the results of NASA programs and include extensive data or theoretical analysis. Includes compilations of significant scientific and technical data and information deemed to be of continuing reference value. NASA's counterpart of peer-reviewed formal professional papers but has less stringent limitations on manuscript length and extent of graphic presentations.

- TECHNICAL MEMORANDUM. Scientific and technical findings that are preliminary or of specialized interest, e.g., quick release reports, working papers, and bibliographies that contain minimal annotation. Does not contain extensive analysis.

- CONTRACTOR REPORT. Scientific and technical findings by NASA-sponsored contractors and grantees.

- CONFERENCE PUBLICATION. Collected papers from scientific and technical conferences, symposia, seminars, or other meetings sponsored or cosponsored by NASA.

- SPECIAL PUBLICATION. Scientific, technical, or historical information from NASA programs, projects, and mission, often concerned with subjects having substantial public interest.

- TECHNICAL TRANSLATION. English-language translations of foreign scientific and technical material pertinent to NASA's mission.

Specialized services that complement the STI Program Office's diverse offerings include creating custom thesauri, building customized databases, organizing and publishing research results...even providing videos.

For more information about the NASA STI Program Office, see the following:

- Access the NASA STI Program Home Page at ***http://www.sti.nasa.gov***

- E-mail your question via the Internet to help@sti.nasa.gov

- Fax your question to the NASA Access Help Desk at (301) 621–0134

- Telephone the NASA Access Help Desk at (301) 621–0390

- Write to:
  NASA Access Help Desk
  NASA Center for AeroSpace Information
  800 Elkridge Landing Road
  Linthicum Heights, MD 21090–2934

Preface

The Life and Microgravity Spacelab (LMS) was an ambitious scientific mission with the goal to plan, integrate, and perform a number of spaceflight experiments and to do so in half the time normally required. Due to the diversity of the experiments, the international participation, and the shortened template for performing the mission, LMS provided an opportunity for NASA to obtain lessons learned for scientific operations upcoming on the International Space Station. That the mission was successful in performing the experiments with few compromises in the investigators' desires is a tribute to the investigators' teams and the support they received from the international space agencies involved.

LMS was manifested in September of 1994 and flew abroad the shuttle Columbia from June 20 through July 7, 1996. The planning and integration of the mission was performed in 21 months. This was the shortest planning period for any such mission, far shorter than the 3 to 4 years typical for other Spacelab missions. As a result, the payload costs were approximately half those of other Spacelab missions. At the time, the flight was the longest duration space shuttle flight in the history of the program. The mission was planned for 16 days but was extended to 17 days in flight to increase the scientific return of the mission.

There were 40 scientific investigations associated with LMS involving research sponsored by NASA's Office of Life and Microgravity Sciences and Applications (OLMSA). Unlike most Spacelab missions, there was a roughly equal split of the laboratory experiments between the life sciences and the microgravity science divisions of OLMSA. There were 16 life sciences and 24 microgravity science investigations, supported by data from three accelerometers.

The mission was international in scope. Five space agencies took part. In addition to NASA, investigators from the European, French, Italian, and Canadian space agencies were involved. The payload included principal investigators from ten countries. The payload crew of LMS was also international. Payload Specialists Robert Thirsk and Jean-Jacques Favier and their alternates Luca Urbani and Pedro Duque were from Canada, France, Italy, and Spain respectively. They were joined by NASA astronauts Susan Helms, Richard Linnehan, Charles Brady, Kevin Kregel, and Tom Henricks.

The LMS payload experiments were monitored and commanded by investigator teams from sites all over the world. The US sites included Marshall Space Flight Center in Huntsville, Alabama, Lewis Research Center in Cleveland, Ohio, Johnson Space Center in Houston, Texas, and Kennedy Space Center in Florida. European sites in Toulouse, France, Milan and Naples, Italy, and Brussels, Belgium were also active during the flight. This distribution of payload experiment teams was without precedence and provided lessons for such operations in the future.

The material following describes the initial results of the varied experiments which flew on LMS. In microgravity science these included interfacial fluid physics studies of thermocapillary flow and electrohydrodynamics performed in the Bubble, Drop and Particle Unit. Also the most extensive set of microgravity experiments to date regarding the morphology of semi-conductors and metal alloys was performed in the Advanced Gradient Heating Facility. These materials were formed under different processing conditions to achieve a spectrum of morphologies including single crystals, equiaxed dendrites, and columnar dendrites. The final group of microgravity experiments was protein crystal growth investigations performed in the Advanced Protein Crystallization Facility, which included in-flight, in situ observations of growth and post-flight crystallography studies.

The various life sciences investigations included studies on lignin formation in the Plant Growth Facility, the role of corticosteroids in bone loss performed on rats in the Animal Enclosure Module, and the development of medaka fish eggs performed in the Space Tissue Loss Module. In addition a number of human physiology experiments involving musculoskeletal studies were performed on the Torque Velocity Dynamometer (TVD). Other human physiology investigations included neuroscience studies of torso rotation and canal and otolith function, metabolic experiments on calcium and caloric balance, behavior and performance studies of circadian rhythms and cognitive performance, and a study on pulmonary function. Taken together these investigations gave the most complete characterization and understanding of human response and adaptation to spaceflight performed to date.

The results reported in this document reflect the presentations that were made at the LMS One Year Science Review hosted by the Canadian Space Agency in St. Hubert, Canada, on August 20 and 21, 1997. Also included in this document are the written reports of investigators who could not attend this meeting. The analysis of the data gathered before, during, and after flight is on-going for most of the investigations and therefore the reports should be regarded as preliminary. It is presumed that when appropriate the principal investigators will submit their findings to refereed journals. With this in mind, the following material should not be regarded as appropriate for scientific reference.

On a personal note, I would like to mention my gratitude to those with whom I worked who made the LMS mission so successful. The list is much too long to specify everyone and in fact, given the complexities of spaceflight, there are surely a large number of people deserving my thanks of whom I am not even aware. Since LMS was an example of teamwork, I think it is best to simply thank the teams. These would include mission management, their contractors McDonnell Douglas and Teledyne Brown Engineering, Spacelab operations laboratory, the flight director's team, the international agencies involved, particularly ESA who provided the microgravity hardware and the TVD, and of course the astronauts, particularly the alternates who did not get to fly but worked as hard as anyone. I would like especially to thank the people who worked the mission scientist team as they made my job remarkably easy. Finally, I would like to extend my appreciation to the investigators and their teams. The efforts of all those taking part in this mission were dedicated to giving these investigations an opportunity to succeed but ultimately it is the effort of the science teams which determines the success of a mission. The following pages are a testament to the quality of the investigators and investigations involved in this mission.

James Patton Downey

James Patton Downey
LMS Mission Scientist
NASA Marshall Space Flight Center
Huntsville, Alabama

Note: Reports on the following JSC Human Life Sciences Project experiments are not included in this document because they were not available at press time:

- E036 - "Relationship of Long-term Electromyographic Activity and Hormonal Function to Muscle Atrophy and Performance"
- E073 - "Canal and Otolith Interaction Studies"
- E409 - "An Approach to Counteract Impairment of Musculoskeletal Function in Space"

Table of Contents

Preface iii

Microgravity Science Experiments

Advanced Gradient Heating Facility (AGHF)

Coupled Growth in Hypermonotectics 1

Directional Solidification of Refined Al - 4 wt.% Cu Alloys 15

Effects of Convection on Interface Curvature during Growth of Concentrated Ternary Compounds 27

Directional Solidification of Al - 1.5 wt.% Ni Alloys 51

Interactive Response of Advancing Phase Boundaries to Particles 61

Particle Engulfment and Pushing by Solidifying Interfaces 75

Advanced Protein Crystallization Facility (APCF)

Crystallization of EGFR-EGF 89

Crystallization of Apocrustacyanin C1 93

Crystallization and X-ray Analysis of 5S rRNA and the 5S rRNA Domain A 101

Growth of Lysozyme Crystals at Low Nucleation Density 113

Comparative Analysis of Aspartyl tRNA-synthetase and Thaumatin Crystals Grown on Earth and In Microgravity 129

Lysosome Crystal Growth in the Advanced Protein Crystallization Facility Monitored via Mach-Zehnder Interferometry and CCD Video 151

Analysis of Thaumatin Crystals Grown on Earth and in Microgravity 165

Crystallization of the Nucleosome Core Particle 179

Crystallization of Photosystem I 187

Mechanism of Membrane Protein Crystal Growth: Bacteriorhodopsin-mixed Micelle Packing at the Consolution Boundary, Stabilized in Microgravity 197

Crystallization in a Microgravity Environment of CcdB, a Protein Involved in the Control of Cell Death 205

Crystallization of Sulfolobus Solfataricus 223

Bubble, Drop and Particle Unit (BDPU)

Oscillatory Thermocapillary Instability 237

Thermocapillary Convection in Multilayer Systems 249

Bubble and Drop Interaction with Solidification Front 265

Table of Contents (cont'd)

A Liquid Electrohydrodynamics Experiment 275

Boiling on Small Plate Heaters under Microgravity and a Comparison with Earth Gravity 293

Thermocapillary Migration and Interactions of Bubbles and Drops 303

Nonlinear Surface Tension Driven Bubble Migration 317

Space Acceleration Measurement System (SAMS) / Orbital Acceleration Research Experiment (OARE) 319

Life Sciences Experiments

Animal Enclosure Module (AEM)

Role of Corticosteroids in Bone Loss During Space Flight 337

JSC Human Life Sciences Project

E029 - Magnetic Resonance Imaging after Exposure to Microgravity 361

E030 - Extended Studies of Pulmonary Function in Weightlessness 397

E074 - Direct Measurement of the Initial Bone Response to Spaceflight in Humans 437

E401 - The Effects of Microgravity on Skeletal Muscle Contractile Properties 451

E407 - Effects of Microgravity on the Biochemical and Bioenergetic Characteristics of Human Skeletal Muscle 463

E410 - Torso Rotation Experiment 501

E920 - Effect of Weightlessness on Human Single Muscle Fiber Function 517

E948 - Human Sleep, Circadian Rhythms and Performance in Space 533

E963 - Microgravity Effects on Standardized Cognitive Performance Measures 567

E971 - Measurement of Energy Expenditures During Spaceflight Using the Doubly Labeled Water Method 581

Plant Growth Facility (PGF)

Compression Wood Formation in a Microgravity Environment 589

Space Tissue Loss Configuration B (STL-B)

Development of the Fish Medaka in Microgravity 607

Advanced Gradient Heating Facility (AGHF)

Coupled Growth in Hypermonotectics

Principal Investigator:

Dr. J. Barry Andrews
University of Alabama at Birmingham
Birmingham, Alabama

Coupled Growth in Hypermonotectics

J. Barry Andrews* and Sam R. Coriell**
***University of Alabama at Birmingham**
Birmingham, AL 35294
****National Institute of Standards and Technology**
Gaithersburg, MD 20899

OBJECTIVE

The primary objective of this project is to obtain a better understanding of solidification processes in immiscible alloy systems. While many alloys in these systems show great potential for use in engineering applications (in particular for superconductors, bearings, catalysts, electrical contacts, and magnetic materials) control of the solidification process is difficult due to gravitationally imposed flows and sedimentation. This project makes use of the low-g environment available during low-Earth orbit to obtain samples solidified without the deleterious influence of gravity. The experimental results are compared to those obtained from modeling the solidification process and are used to help enhance the models developed. Success in this effort will eventually lead to an improved knowledge of ways in which to control microstructures developed in these intriguing alloys.

BACKGROUND

Two-liquid immiscibility is usually associated with a monotectic alloy system, an example of which is represented by the phase diagram in Figure 1. One of the most prominent features of this phase diagram is the miscibility gap in which two separate liquids co-exist over a temperature and composition range. It is also apparent that a transformation can occur in this system which involves the decomposition of one liquid phase to form a solid and another liquid phase (i.e. the monotectic reaction $L_1 \rightarrow S_1 + L_2$).

The monotectic reaction is similar to another type of reaction, called the eutectic reaction, which occurs in many alloy systems ($L \rightarrow S_1 + S_2$). As a result, some of the theoretical work carried out on eutectics can provide a starting point for the development of a model for monotectics. However, the fact that one of the product phases in a monotectic is a liquid can lead to substantially different behavior than that observed in eutectic systems where both product phases are solids.

One of the useful features of eutectic alloy systems is that by directionally solidifying the alloys under the proper conditions, a structure can be obtained which consists of aligned fibers of one phase in a matrix of the other. This fibrous composite structure forms as a result of the unmixing of the liquid phase to form the two product phases. In this reaction the solute rejected during the formation of one of the solid phases is consumed in the formation of the other solid phase. This "coupled growth" process has also been observed in some immiscible alloy systems for alloys of monotectic composition.

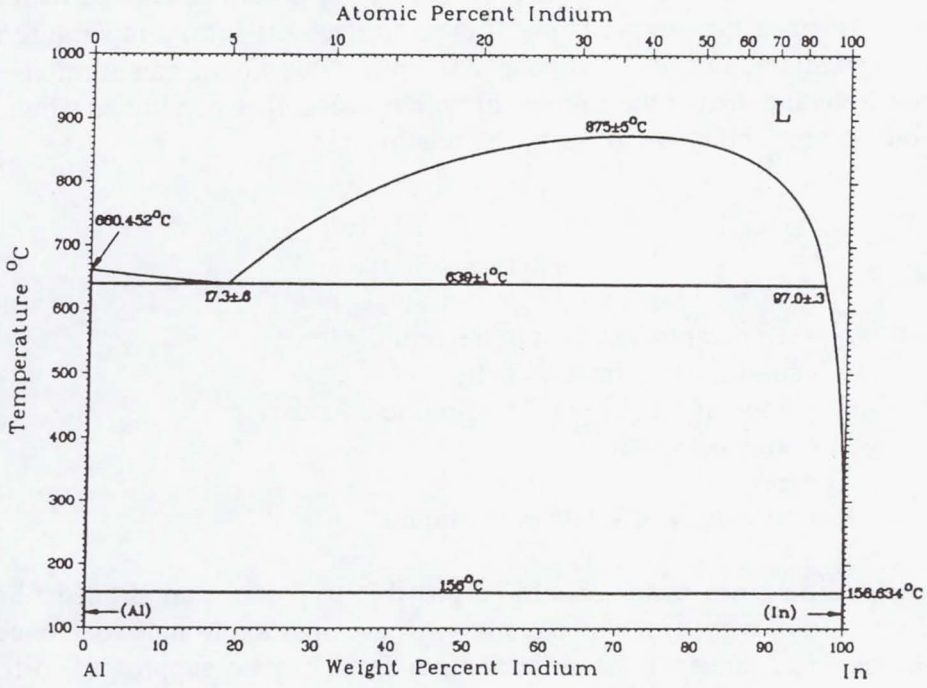

Figure 1. Phase diagram for the aluminum-indium alloy system

It is well known that in eutectic alloy systems, alloys which are off of eutectic composition can also be directionally solidified to produce fibrous microstructures. In fact, the use of off-eutectic compositions provides a means of controlling the volume fraction of the fibrous phase. However, there has been some controversy whether off- monotectic alloys, especially those with solute contents higher than the monotectic (i.e. hypermonotectic alloys) can be directionally solidified under conditions which would lead to a stable coupled growth process and the development of a fibrous microstructure.

As seen in an off-eutectic alloy, steady state coupled growth in an off-monotectic alloy should involve two diffusion fields. One of these fields would be associated with the "unmixing" process, which is part of coupled growth. This diffusion field should only extend into the liquid a short distance, approximately one half the interfiber spacing. The other diffusion field would arise due to the alloy being off of monotectic composition. The composition of the liquid far removed from the solidification front would be equal to the alloy composition, while the composition at the front would be held at the monotectic composition. This composition variation, which would occur primarily close to the solidification front, is called the solute boundary layer.

The presence of a solute boundary layer in the liquid in advance of the solidification front gives rise to the possibility of interfacial instability. The composition variation with position in the liquid results in a variation in the temperature at which the miscibility gap would be entered. Just adjacent to the interface, a temperature as low as the montectic temperature can be tolerated without entering the miscibility gap. However, as the composition increases with distance from

the interface the temperature at which the miscibility gap would be entered increases as well. If the thermal gradient in the sample is insufficient to keep the local temperature above the local miscibility gap temperature, the second phase immiscible liquid can form in advance of the solidification front and disrupt the coupled growth process. The conditions which must be met in order to avoid this instability are given by the relationship

$$\frac{G_L}{V} > \frac{m_L (C_o - C_m)}{D_L}$$

where G_L = temperature gradient in the liquid
V = solidification front velocity
m_L = slope of the $(L_1 + L_2)$ two-phase boundary
C_O = alloy composition
C_M = monotectic composition
D_L = diffusivity of solute in the liquid

If the above conditions are met it should be possible to produce an aligned fibrous composite microstructure even in a hypermonotectic alloy. It is important to note that since the formation of the L_2 phase in advance of the solidification front can be suppressed, difficulties due to sedimentation of the L_2 phase during directional solidification can be avoided. However, there are other gravity driven phenomena that make ground based experimentation difficult.

While the solute depleted boundary layer in advance of a solidification front should make it possible to achieve steady state coupled growth by using the proper growth conditions, this boundary layer may give rise to undesirable fluid flow in the sample. In almost every known immiscible alloy system the solute has a higher density than the solvent. This implies that for vertical solidification, the solute depleted boundary layer in advance of the solidification front will have a lower density than the liquid above it. This density variation is expected to result in convective flows which can lead to difficulties during solidification. In most cases the resulting convective flow can cause compositional variations that are sufficient to prevent coupled growth over a substantial portion of the sample.

In order to obtain steady state coupled growth conditions in immiscible alloys both interfacial stability and convective stability will be required. It should be possible to obtain interfacial stability by directionally solidifying alloys using a high thermal gradient to growth rate ratio. This requirement can best be met by using a furnace that can produce a high thermal gradient in the sample during solidification. Convective stability presents more of a problem. Analysis implies that the only way to reduce convective flows to the level required for this study is by carrying out directional solidification under microgravity conditions.

DATA ACQUISITION AND ANALYSIS

The Coupled Growth in Hypermonotectics project involves the directional solidification of a range of alloy compositions over a range of growth rates. For the Life and Microgravity Spacelab (LMS) mission, three alloy compositions in the aluminum-indium immiscible system

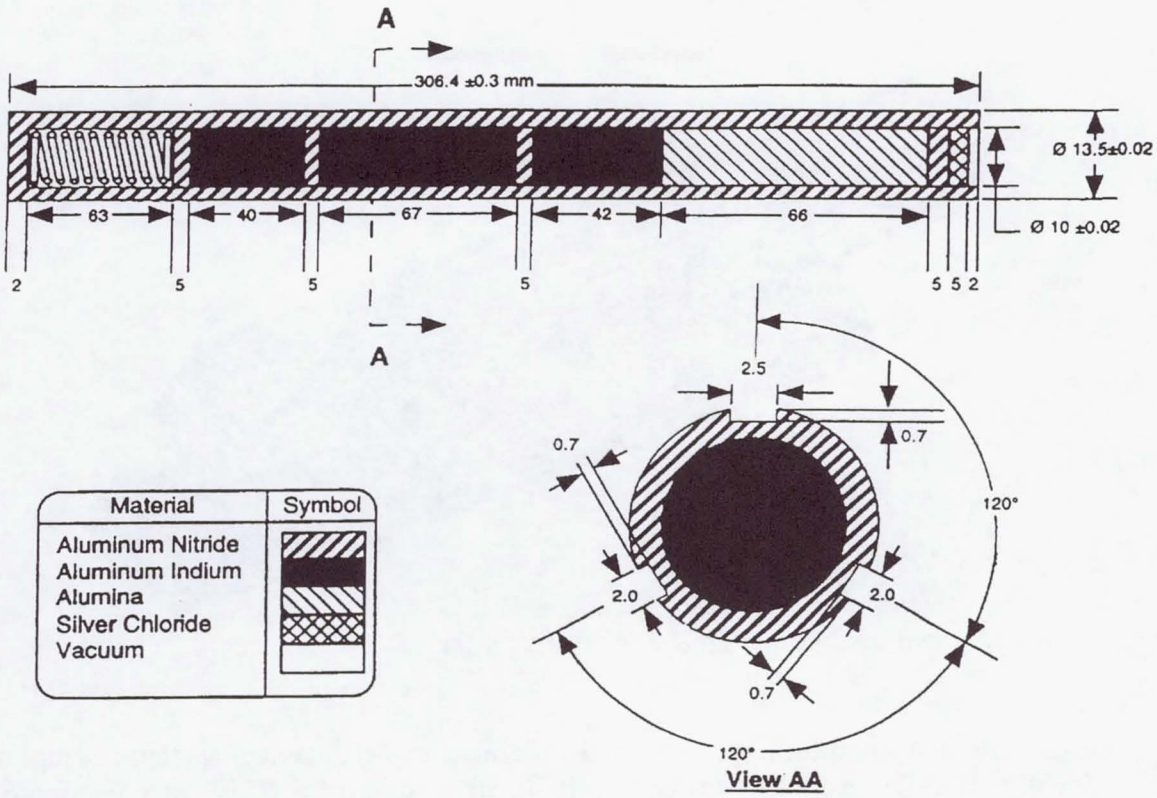

Figure 2. Schematic of the ampoule assembly utilized to process aluminum-indium immiscible alloys during the LMS mission.

were directionally solidified. The Advanced Gradient Heating Facility (AGHF) was used to directionally solidify these samples and all samples were solidified at the same rate of 1.0 μm/s. The samples were sealed under vacuum in aluminum nitride ampoules which contained several sample segments, pistons and a spring in order to maintain the desired growth conditions during processing (See Figure 2). Thermocouples were embedded into the wall of the ampoule and were used to monitor temperatures and determine thermal gradients and growth rates. Alloys were produced from five-nines pruity components and were vacuum induction melted.

A great deal of effort was used in the preparation of the alloy and ampoule assemblies in order to avoid the presence of any free surfaces or voids in the samples during processing. Free surfaces were undesirable because the surface tension driven flow at those surfaces could result in undesirable mixing within the sample. In order to avoid free surfaces generated due to contraction of the sample prior to and during solidification, a piston and high temperature carbon spring were utilized. In an attempt to reduce any residual gasses, which could have led to bubble formation, the alloys were vacuum induction melted. In addition, the ampoule components were all vacuum degassed at 1250° C for more than 6 hours. Samples were loaded and sealed under a vacuum of at least 1×10^{-4} Torr.

During processing, data was collected on furnace position, acceleration (3 axes), furnace translation rate, sample thermocouple outputs, and hot and cold zone temperatures.

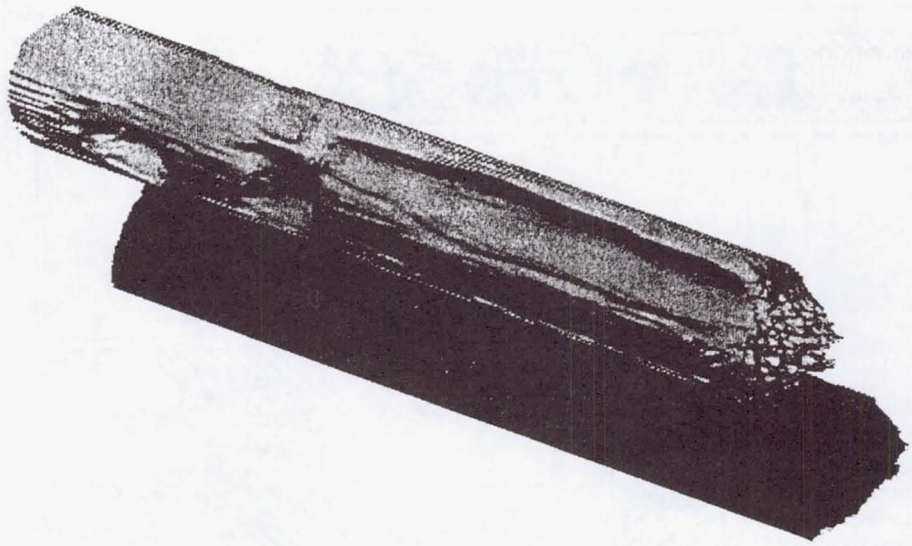

Figure 3. Computed tomography image obtained for the 18.5wt% In sample, FM 1.

Metallographic and compositional information is also to be obtained on these samples. The directionally solidified samples will be longitudinally sectioned and one of the sample halves mounted for metallographic analysis. The other half of the sample will be transversely sectioned and these sections used for compositional analysis (using precision density measurements) and then metallographic analysis. Analysis of the transverse sections will permit determination of interfiber spacings and the volume fractions of the phases along the length of the sample.

RESULTS AND DISCUSSION

Several difficulties were encountered during processing of the CGH samples aboard LMS. The first difficulty concerned a thermal gradient in the flight furnace that was substantially lower than that obtained using the engineering model of the furnace. This reduced thermal gradient is expected to have a detrimental influence on the ability to maintain a stable solidification front, especially for the highest composition alloy. Another difficulty involved the loss of data telemetry from the AGHF during processing of the 18.5%. In alloy. Several attempts were made to reestablish the data link without success. Unfortunately, there was no data recording capability within the AGHF facility so all data on furnace position and sample temperatures were lost for this sample.

Radiographic analysis and computed tomography of the samples while still in their ampoules revealed the presence of several significant sized voids in in two of the flight samples (See Figures 3, 4 and 5). These unexpected voids give rise to several difficulties. First, the voids provide free surfaces, which, with the high thermal gradients in this experiment can allow surface tension induced flow and undesirable mixing in the sample. However, perhaps an even worse problem is the inconsistency in growth conditions that will exist along the sample. The voids will obviously change the local cross sectional area of the sample and result in local variations in both thermal gradient and growth rate. These variations in local conditions will make analysis of the results much more difficult.

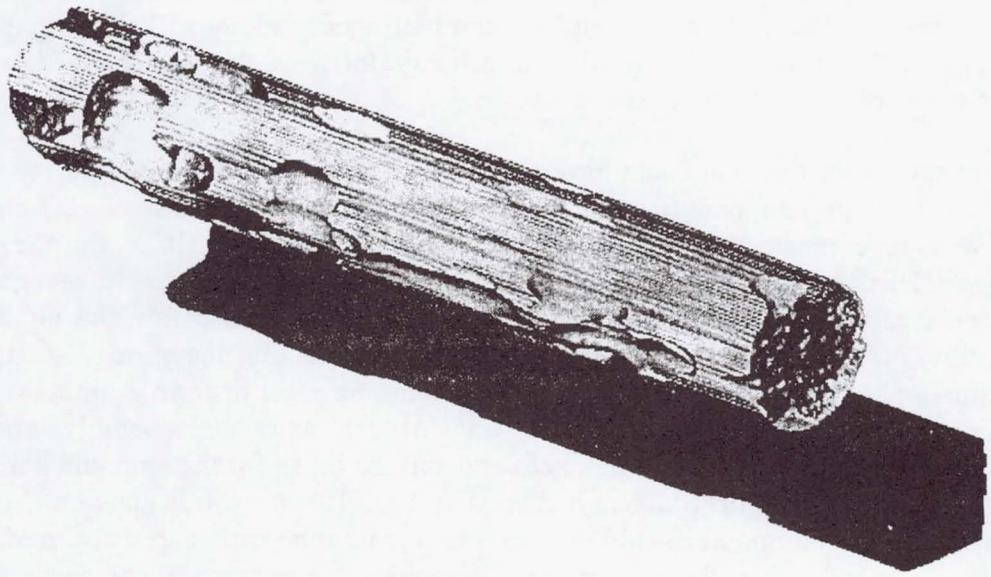

Figure 4. Computed tomography image of the 19.7wt% In, FM 2 sample.

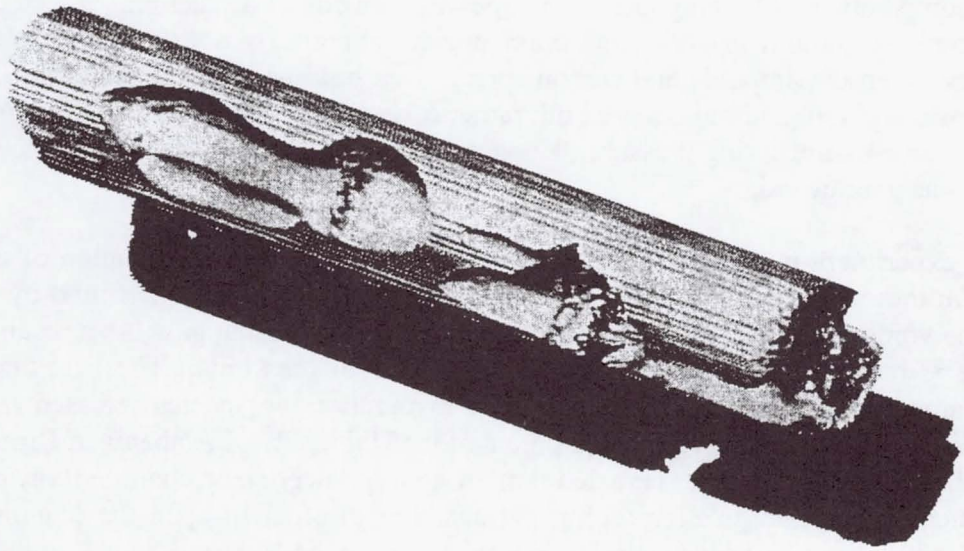

Figure 5. Computed tomography image obtained for the 17.3wt% In, monotectic composition sample, FM 3.

One of the first questions which must be answered in this study concerns the source of these voids. This information is especially important since additional flight experiments are anticipated in this study. As a result, the primary focus of this project to date has been to determine the source of these unexpected voids.

There are several factors that could have led to the development of voids in these samples. For example, if the high temperature spring failed or if one of the pistons stuck, the ampoule would not be able to compensate for the thermal contraction in the melt or for the solidification shrinkage. This type of failure could result in the formation of voids. In several of the early experiments carried out during development of the ampoule assembly the aluminum-indium alloy leaked past the uppermost piston into the area containing the spring. At these elevated temperatures (1110° C) the carbon spring and aluminum react to form aluminum carbide, thus destroying the spring. After initial testing of the ampoule assembly, more stringent specifications were placed on the tolerances and surface finish for the ampoule bore and pistons. Further testing indicated this problem had been solved. However, it is apparent from post flight x-ray analysis of the ampoule assemblies that leakage into the spring area occurred in two of the flight ampoules and one of the ground based ampoules. Once this leakage occurred is assumed the spring would have become ineffective.

Another factor that could lead to the development of voids in the samples is leakage of gas past the silver chloride seal at the bottom of the ampoule. Gas that entered the ampoule could result in bubble formation in the melt if the gas pressure within the bubble could not be overcome by the spring assembly. Each ampoule was helium leak tested after assembly in order to avoid this possibility. However, it is conceivable that changes in the integrity of the seal occurred during subsequent handling or during heating for processing.

Another possibility for gas bubble formation involves gas release from within the ampoule either due to decomposition of a component at temperature or due to a reaction. A reaction between the aluminum or indium and the aluminum nitride ampoule is not anticipated. In addition, reactions between the ampoule and carbon spring were not observed during testing. The vapor pressures of aluminum and indium are both rather low at the temperatures utilized and should be easily overcome by the spring pressure. However, it is still possible that some reaction is taking place that was overlooked.

Since this experiment is to fly on future missions, it was felt that identification of the source of the voids in these samples was a critical factor. Much insight could be gained by determining whether the voids contained a gas, and if so, the composition of that gas. As a result most of our recent efforts have focused on identifying the contents of the voids. The first thought was to open the ampoules in a vacuum chamber and to monitor the species released using a mass spectrometer. However, a survey of equipment at the University of Alabama at Birmingham and at Marshall Space Flight Center revealed that an appropriately sized chamber was not available and that mechanical manipulation within the chamber in order to open the ampoule was very limited. Further discussions led us to Dr. Witold Palosz at the Marshall Space Flight Center who has been using a specifically designed apparatus to determine residual gas content in fused silica ampoules used in semiconductor processing. Dr. Palosz's approach has been to break open an ampoule in a small vacuum chamber and determine the gas content by slowly lowering the

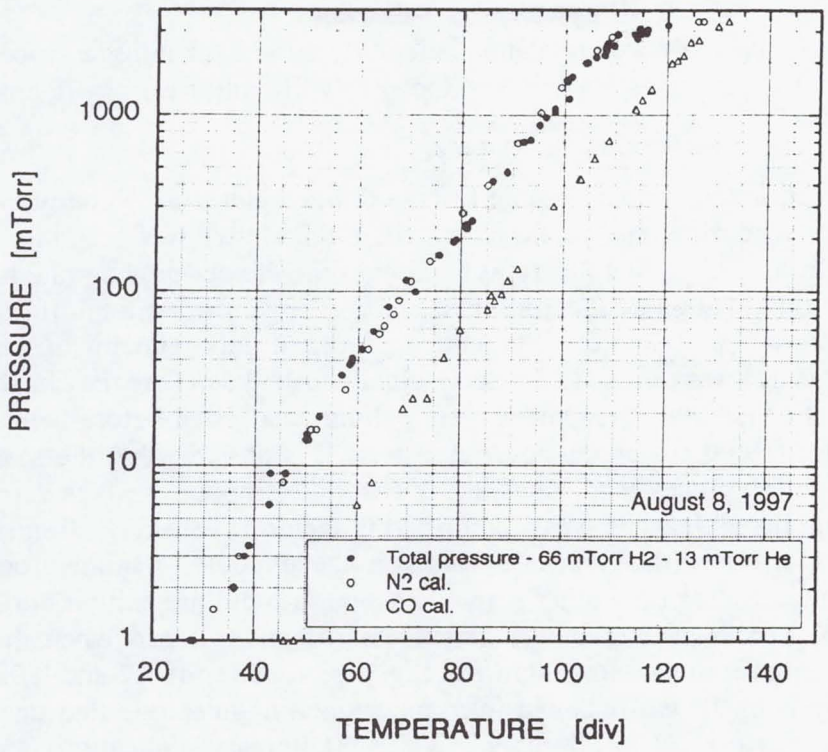

Figure 6. Pressure vs. temperature variations during a typical residual gas analysis. The open circles represent a nitrogen calibration curve while the open triangles represent a carbon monoxide calibration curve. The temperature scale covers a range of roughly 20K to 120K.

temperature and monitoring pressure changes. By noting the temperatures at which pressure drops occur (due to condensation) it is possible to identify the gases present. Significant modifications, including the construction of a new vacuum chamber, were necessary before this apparatus could be used to open the aluminum-nitride ampoules. Before the final configuration was obtained, several versions were tested, and the apparatus was redesigned and reconstructed. As a result, the apparatus was only recently available for use and a limited amount of time has been available for the analysis of data. The findings, while preliminary, are quite interesting and are discussed below.

Preliminary Findings

In order to facilitate opening of an ampoule in the vacuum chamber, a shallow groove was cut around the perimeter of the ampoule at the desired location. The ampoule was then placed in the vacuum chamber such that the groove location was within with a bellows in the system. After evacuating the system, the ampoule could be fractured simply by bending the system at the bellows.

A typical test procedure involved evacuation of the chamber for a sufficient time to allow the ampoule to out-gas. After out-gassing had dropped to a reasonable value, the ampoule was cracked and the gas collected. The temperature was then lowered and pressure changes monitored in order to determine the gas content. A typical Pressure vs. Temperature plot is

shown in Figure 6. This figure also contains calibration curves for nitrogen (open circles) and carbon monoxide (open triangles) which are the most difficult gases to distinguish by this technique.

The first sample tested in the system, sample FM1, exhibited behavior which was later found to be nontypical. After evacuating the system for one hour the sample was found to be out-gassing at a rate of 400mTorr/hr. After 20 hours total pumping time the out-gassing rate had dropped to 150m Torr/hr. The outgassing rate then dropped to 40mTorr/hr after a total of 46 hours and to 13 mTorr/hr after 66 hours. When the ampoule was opened only $0.06cm^3$ of gas (at standard temperature and pressure) was released. These results indicate that a leak may have been present in this ampoule. All of the sealed ampoules were helium leak tested before being incorporated into the cartridge assemblies for processing. However, it is possible that the seal failed either during handling or during processing. Retesting of all of the ampoule seals is currently planned in order to determine if seal leakage was a contributing factor to void formation in some cases. Another possibility is that a hairline crack developed in the ampoule when the groove was cut to serve as a fracture site. Most of the other ampoule assemblies did not exhibit outgassing to this extent. In addition, as shown in Table 1, the volume of gas released when the other flight ampoules were opened was much more significant, giving volumes of 1.7 and 0.92 cm^3 at STP. Compositional analysis of the gas obtained from the flight ampoules revealed that a significant amount of nitrogen was present in all cases. While preliminary, indications are that carbon monoxide was also present in two of the ampoules. It is tempting to speculate on the source of this carbon monoxide, especially since this gas was found in the two ampoules in which the alloy leaked past the piston and came in contact with the carbon spring. However, additional calibration runs are necessary to verify the presence of carbon monoxide. These calibration runs are the next order of business.

The nitrogen found in these flight ampoules may have come from several sources. Of course, one possibility is from air which was either trapped in, or leaked into, the ampoule. Since the ampoules were sealed in a vacuum after an elevated temperature bakeout there should have been very little air initially present in the ampoules. Another possibility is due to breakdown of the aluminum nitride ampoule material at the elevated temperatures used during processing. While there is very little information available pertaining to this possibility, tests are currently being carried out to collect gases released by aluminum nitride during extended duration elevated temperature exposure.

Two ground based control samples were also processed as a part of this investigation. One of these samples, GM1, contained a rather large void in the cold load segment of the ampoule. Unfortunately, this ampoule was apparently cracked when the groove was cut to facilitate opening and a gas analysis could not be obtained. The remaining ground based ampoule, GM2, exhibited almost ideal behavior. The sample was essentially void free and no leakage occurred past the piston into the spring assembly. Analysis of the residual gas present in this ampoule revealed 0.34 cm^3 of almost pure hydrogen (at standard temperature and pressure) was present. Obviously this result is quite different than that observed in the other ampoules. We currently have no explanation for the source of this gas.

Table 1: Preliminary Results from Residual Gas Analysis

SAMPLE NUMBER	COMPOSITION (wt % In)	PRELIMINARY GAS COMPOSITION	GAS VOLUME AT STP(cm^3)	COMMENTS
FM1	18.5	Nitrogen + some CO_2	0.06	May have leaked
FM2	19.7	Nitrogen	1.73	
FM3	17.3	Mostly nitrogen some CO & H_2	0.92	
GM1	18.5			Ampoule cracked
GM2	19.7	Almost all hydrogen	0.34	Essentially void free

SUMMARY AND FUTURE PLANS

To summarize our findings to date, three immiscible aluminum indium samples were directionally solidified during the LMS mission. Two of these samples contained voids that were sufficient in size to modify the solidification parameters locally during processing. In addition, the aluminum-indium alloy leaked past the uppermost piston in two of the flight ampoules and one of the ground based ampoules and destroyed the carbon spring. Most work to date has concentrated on identifying the gas present in the voids in order to help determine their source.

Residual gas analysis revealed that the voids contained primarily nitrogen with some ampoules also containing smaller amounts of a gas, which, at this stage is thought to be carbon monoxide. Additional testing must be carried out to verify this finding. Analysis of one of the ground based ampoules revealed a residual gas composed almost entirely of hydrogen. This ground-based sample was essentially void free.

Much remains to be done in the analysis of these samples. Part of this work involves a continuation of the investigation of void formation. This will include collection and testing of any gases released during extended duration high temperature exposure of an ampoule. The seals for each ampoule will also be helium leak tested. Additional testing will be carried out to determine if the ampoules all met surface finish and tolerance specifications as well.

In addition to the work described above, an extensive amount of metallographic analysis remains to be done on these samples. This work will involve determination of the interfiber spacings and volume fractions of phases as a function of position along the samples. The findings from the metallographic analysis will be used to first determine if interface stability and coupled growth were obtained. The specific microstructural details will then be used to test the monotectic solidification model developed as part of this investigation.

Bibliographic Citations of Articles/Presentations Resulting from the Flight for the Project:
Coupled Growth in Hypermonotectics

"Coupled Growth in Immiscible Alloys," J. B. Andrews, L. Hayes, Y. Arikawa, S. O'Dell, and A. Cheney, Space Processing of Materials, Proceedings SPIE - The International Society for Optical Engineering, ed. N. Ramachandran, Vol. 2809, pp. 12-22, 1996.

"Microgravity Processing of Immiscible Aluminum-Indium Alloys," J. B. Andrews, L. J. Hayes, Y. Arikawa, S. R. Coriell, accepted for publication in Advances in Space Research, 1997.

"Analysis of Monotectic Growth: Infinite Diffusion in the L_2 Phase," S. R. Coriell, W. F. Mitchell, B. Murray, J. B. Andrews, Y. Arikawa, Journal of Crystal Growth, 1997.

"Directional Solidification of Immiscible Aluminum-Indium Alloys under Microgravity Conditions," J. B. Andrews, L. J. Hayes, Y. Arikawa and S. R. Coriell, Proceedings - Spacebound '97 and Proceedings of the 9th International Symposium on Experimental Methods for Microgravity Materials Science, accepted for publication in both.

"The Influence of Convection in Directionally Solidified Hypermonotectic Alloys," L. J. Hayes and J. B. Andrews, Proceedings - Spacebound '97 and Proceedings of the 9th International Symposium on Experimental Methods for Microgravity Materials Science, accepted for publication in both.

"Numerical Simulation of a Monotectic Solidification Front with Marangoni Flow," Y. Arikawa, J. B. Andrews, S. R. Coriell, W. F. Mitchell, B. Murray, Proceedings - Spacebound '97 and Proceedings of the 9th International Symposium on Experimental Methods for Microgravity Materials Science, accepted for publication in both.

"An Evaluation of Ceramic Ampule Materials for Processing of Immiscible Aluminum-Indium Alloys under Microgravity Conditions," A. B. Cheney and J. B. Andrews, Proceedings - Spacebound '97 and Proceedings of the 9th International Symposium on Experimental Methods for Microgravity Materials Science, accepted for publication in both.

Coupled Growth in Hypermonotectics

J. Barry Andrews* and Sam R. Coriell**
***University of Alabama at Birmingham**
Birmingham, AL 35294
****National Institute of Standards and Technology**
Gaithersburg, ME 20899

NON-TECHNICAL SUMMARY

Well over 1000 alloy systems exhibit immiscible behavior in the liquid state, where, like oil and water, two liquids form that do not mix. Many of these alloy systems show promise for use in engineering applications such as superconductors, high performance permanent magnets, electrical contact materials and catalysts. However, controlling the solidification process in order to produce desirable structures in these alloys is very difficult. An improved understanding of solidification processes is needed, but study of the solidification process on Earth is hindered by the inherent flows which occur in these systems and by the possibility of the heavier of the two liquid phases sinking to the bottom of the container during processing.

The objective of this investigation is to gain an improved understanding of solidification processes in immiscible alloy systems. A portion of the study involves the development of experimental techniques which will permit solidification of immiscible alloys to produce aligned microstructures. A parallel effort is underway to develop a model for the solidification process in these alloy systems. This analysis avoids many of the simplifying assumptions often utilized in similar analyses. Results from experimentation will be compared to those predicted from the model and utilized to improve the model. In order to permit solidification under the conditions necessary to form fibrous structures in these immiscible alloys, experimentation must be carried out under low-gravity conditions.

This experiment used the Advanced Gradient Heating Facility (AGHF) and low-gravity conditions to help remove the complications of sedimentation and buoyancy driven convective flow during directional solidification of immiscible alloys. Alloys in the aluminum indium system were solidified using specialized aluminum nitride ampoules in order to control several undesirable effects that are sometimes observed during low gravity processing. Three alloy compositions were processed in order to permit comparison with the model over a composition range. Two ground based control samples were processed under conditions identical to those of two of the flight samples in order to allow a direct comparison of the results.

Upon analysis several voids were found in two of the flight ampoules. The presence of these voids will present problems in the analysis of the samples since the voids can influence the solidification conditions locally. Most work to date has focused on identifying the gas present in these voids in an attempt to identify their source. Preliminary data has been collected and several experiments are underway in this area. The next step in the project will involve a detailed structural analysis of the samples.

Advanced Gradient Heating Facility (AGHF)

Directional Solidification of Refined Al - 4 wt.% Cu Alloys

Principal Investigator:

Dr. Denis Camel
DEM/SES
Grenoble, France

LMS-AGHF-ESA2b EXPERIMENT DIRECTIONAL SOLIDIFICATION OF REFINED Al-4wt.%Cu ALLOYS

M.D. DUPOUY, D. CAMEL, F. BOTALLA, J. ABADIE and J.J. FAVIER

Commissariat à l'Énergie Atomique - CEREM - Département d'Étude des Matériaux
17 Rue des Martyrs, 38054 Grenoble Cédex 9, France

(1) OBJECTIVES

In the case of directional solidification of inoculated alloys under diffusive transport conditions, the transition from columnar to equiaxed grain structure is predicted to occur continuously through intermediate mixed structures, as a function of the nuclei density N_0, temperature gradient G and solidification rate R [1]. The Hunt's model could not be verified experimentally [2, 3] because, in practice, gravity driven convection affects these three parameters. For this reason, more recent models [4, 5] try to include convective effects. However, in order to assess the models, experiments able to separate convection from the other mechanisms involved are still needed. The purpose of the LMS-AGHF-ESA2b experiment was to examine the columnar to equiaxed transition (CET) in a refined Al-4wt.%Cu alloy under conditions in which convection is minimized and diffusive phenomena are dominant, and in which the nuclei density N_0 is controlled through the refiner content. From these experimental results, we expected to check Hunt's model, and in a more general way, to better understand the underlying physical mechanisms associated with equiaxed dendritic solidification of alloys, and the influence of convection on this type of growth.

(2) BACKGROUND

Metal alloys normally solidify with dendritic structures. In constrained growth, arrays of columnar dendrites are commonly observed and grow parallel and in a direction opposite to that of heat flow. However, with aluminium alloys used for engineering applications it is frequently desirable to ensure that the cast microstructure has an equiaxed dendritic as opposed to a columnar dendritic morphology. In aluminium the columnar to equiaxed transition is promoted by the addition of inoculants which are termed grain refining master alloys (or grain refiners) [6]. Grain refiners are most commonly Al-Ti-B master alloys. Over the last two decades much work has been done to understand the factors which influence the columnar to equiaxed transition. Hunt [1] proposed to model steady state equiaxed growth in the constitutional undercooled region in front of a columnar array, in order to predict the transition from columnar to equiaxed grain structure as a function of the nuclei density N_0, and local temperature gradient G and solidification rate R. Weinberg and co-workers [2, 3] undertook unidirectional solidification experiments vertically upwards in Sn-Pb and Al-Cu systems, in non steady state conditions, so that G and R varied continuously during solidification, to track the CET and check Hunt's model. But they could not verify the Hunt's prediction for inoculated samples, partly due to the low thermal gradients involved. In fact, gravity driven convection may strongly affect both the nuclei distribution and the undercooled region. For this reason, more recent models [4,5,7] try to include these last effects. However, well controlled equiaxed dendritic solidification experiments are needed to provide benchmark data for the testing and refinement equiaxed microstructure evolution models, both in the pure diffusion limit as well as with convection.

With this aim in view, we performed a series of experiments under reduced gravity (EUROMIR 95 and LMS 96) where Al-4wt.%Cu alloys refined at different levels (2 to 50 ppm B, and 10 to 250 ppm Ti) with Al-5Ti-1B master alloys, were unidirectionally solidified with continuously decreasing temperature gradient G and increasing rate R. Nearly isothermal samples from the same batch were also solidified in parallel, to give the reference purely equiaxed microstructure. Reference ground based experiments were also performed in identical thermal conditions with different orientations relative to gravity. In this paper we only present the results of the LMS-AGHF-ESA2b experiments.

(3) EXPERIMENTAL PROCEDURE

3.1 Materials

Two ingots were prepared from super purity Al (99.995 wt%) and electrolytic Cu, at the nominal composition of 4 wt.%Cu and with the respective refiner contents given in Table 1, according to the following procedure. The Al-4wt.%Cu master alloy was melted in a 42 mm diameter graphite mould coated with boron nitride. The required quantity of grain refiner, cut from an Al-5wt.%Ti-1wt.%B master alloy in rod-form, and Ti in excess if needed, was stirred into the melt for 3 minutes, and the alloy was then solidified at a cooling rate of 5°C/min, in a thermal gradient of about 16°C/cm. For the unidirectional solidification experiments, four equivalent rods were extracted from each ingot by spark erosion, and then machined to the diameter of 12 mm. Ground reference and space samples were taken from equivalent rods.

Experiments	Al-5Ti-1B rate (kg/T)	Ti content (ppm)	B content (ppm)	Microgravity samples	ground based samples
AGHF 1	0.2+excess Ti	100	2	FM1	GM2
AGHF 2	0.2	10	2	FM2	GM1

Table 1 : Refining contents of the experiments

3.2 LMS-AGHF-ESA2b experiments : unidirectional solidification

During the LMS mission in June 1996, two Al-4wt.%Cu alloys refined at the different levels given in table 1, were solidified in the Advanced Gradient Heating Facility (AGHF) of ESA which is a Bridgman type furnace.

Each tantalum cartridge contained two samples as illustrated in Fig.1, with the same refining content, inserted in a boron nitride crucible. The longer sample (95 mm) was solidified under varying G and R, and the shorter one (45 mm) was solidified in nearly isothermal conditions, and used as a reference case for equiaxed growth. To measure local temperature gradients and solidification rates during the whole experiment, the cartridges were equipped with 19 thermocouples (12 for the gradient sample and 7 for the isothermal one), glued on the outer surface of the crucible or inserted in a central multibore capillary Al_2O_3 tube (8 of them).

Heaters were programmed to cool down at a given cooling rate, i.e. 1°C/min. The processing parameters were predetermined by experiments performed in the breadboard and engineering models of the AGHF in the Centre National d'Études Spatiales (CNES) in Toulouse (France).

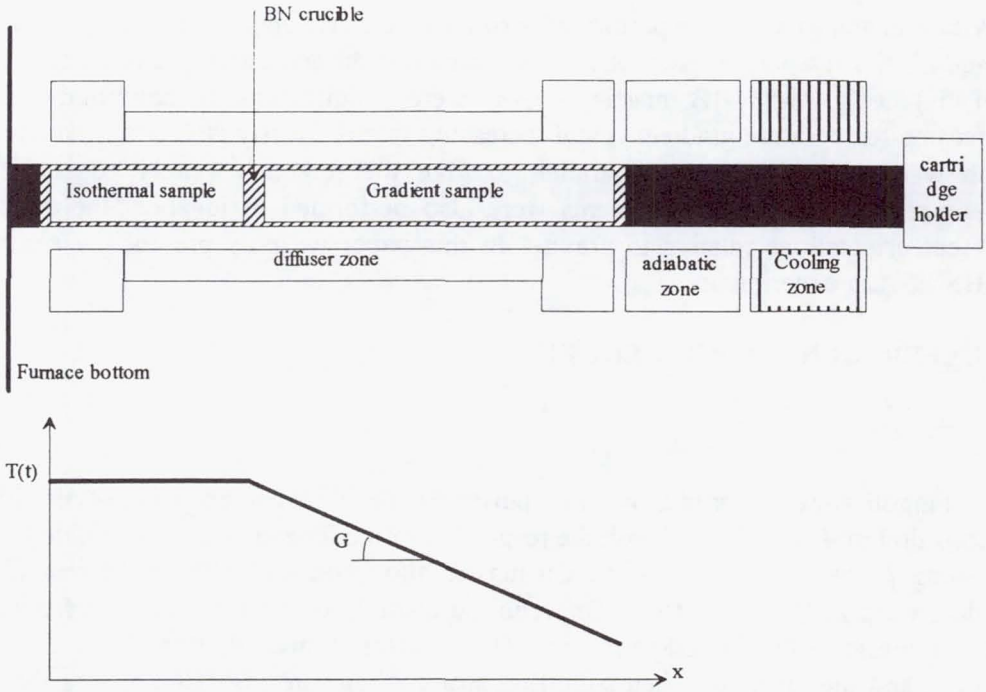

Figure 1 : Schematic representation of LMS-AGHF-ESA 2b experiment.

Thermal data

Thermal conditions in the gradient samples are analysed by recording time variations of the temperature differences between neighbouring thermocouples of the central capillary. Times corresponding to the passing of the solidification front at the level of each thermocouple are then determined from the breaks appearing on these curves, and the average velocity between thermocouples i and i+1 is evaluated as :

$$R_i = \frac{x_{i+1} - x_i}{t_{i+1} - t_i}$$

where x_i is the position of thermocouple i, and t_i the passing time of the front at thermocouple i. The temperature gradient in the liquid ahead the front is then calculated as :

$$G_{Li} = \frac{T_{i+1}(t_i - 2mn) - T_i(t_i - 2mn)}{x_{i+1} - x_i}$$

Values of G and R at the beginning and end of solidification are given on Table 2. An example of the overall solidification paths in a logR vs logG diagram is shown on Fig.5.

Microstructural examination

Longitudinal sections of solidified rods, taken parallel to the growth direction, were prepared by conventional metallographic procedures. In order to reveal grain morphologies, and to enable equiaxed grain densities to be measured, metallographic sections were anodized with HBF4 aqueous solution (34% HBF4 acid in water) at 30 V DC for between 2 and 3 minutes at room temperature. When viewed with crossed polarizers in an optical microscope, grains of different orientations were clearly delineated. Grain density measurements were performed only on those parts of samples that were found to have a fully equiaxed grain morphology. The grain density was evaluated by means of image processing softwares and grains counting methods based on stereology [8, 9].

(4) EXPERIMENTAL RESULTS

4.1 Isothermal samples

Typical grain structures formed in isothermal samples under microgravity and on the ground are shown in the longitudinal sections of Fig.2a and b. Average grain densities measured on the different isothermal samples are given on Table 2.

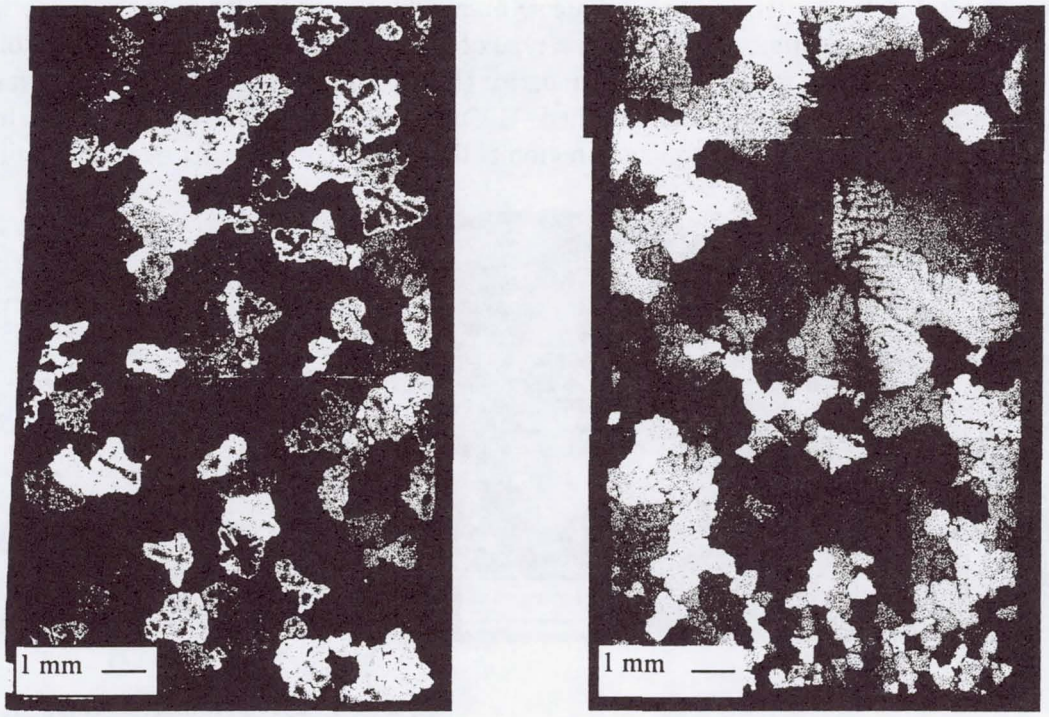

a b

Figure 2 : Optical micrograph of an anodized microstructure viewed under polarized light showing a longitudinal section of : a) FM1 microgravity isothermal sample, with a regular equiaxed structure, b) GM2 ground based isothermal sample, with a strong settling effect.

Sample	N_0 (part./mm^3)	Initial thermal conditions G(K/cm) - R(cm/s)		Final thermal conditions G(K/cm) - R(cm/s)	
FM1	5.1	17.0	$6.82\ 10^{-4}$	5.3	$2.58\ 10^{-3}$
FM2	1.37	12.7	$1.10\ 10^{-3}$	5.6	$1.20\ 10^{-3}$
GM1	0.35	19.2	$1.70\ 10^{-3}$	5.4	$1.93\ 10^{-2}$
GM2	0.92	12.7	$1.28\ 10^{-3}$	8.8	$1.50\ 10^{-3}$

Table 2 :Averaged N_0 measurements for isothermal samples :
initial and final thermal conditions (G, R) at the growth front, for gradient samples.

In microgravity isothermal FM2 sample, the equiaxed grain structure is very regular with homogeneous grain size. In presence of excess Ti (FM1 sample) grain sizes are smaller (nearly a factor 2). A slight variation of grain size can be observed for this sample, probably due to a bad distribution of excess Ti. All the grains have a dendritic microstructure. In ground based samples GM1 and GM2, grain sizes are much less uniform than in microgravity, as shown in Fig.2b : a thin region with very small grains is present at the bottom of the samples, but grains are much larger in the central part, so that the average grain density is larger than in microgravity (Table 2).

4.2 Gradient samples

Microgravity gradient samples FM1 and FM2 show a continuous transition from an anisotropic structure at the beginning of solidification (Fig.3) towards a fully equiaxed microstructure at the end of solidification (Fig.4a). Indeed, the interdendritic segregated regions are found to be elongated and preferentially oriented in the direction of the temperature gradient in the first part of the sample (Fig.3a), and this effect progressively disappears along the solidification direction. This anisotropy is however not reflected in the grain structure itself, which shows no elongation in the solidification direction (Fig.3b). One can only remark a tendency for the grain boundaries to be either parallel to the temperature gradient, or nearly perpendicular to it. Eutectic inclusions are preferentially concentrated along the first type of boundaries. These inclusions form dihedral angles at the intersection of perpendicular boundaries (Fig.3c). In the regions where the grain boundaries are not filled with eutectic, small aligned Al_2Cu platelets are observable (Fig.3d). In presence of excess Ti (FM1 sample), the equiaxed region at the end exhibits smaller dendritic grains.

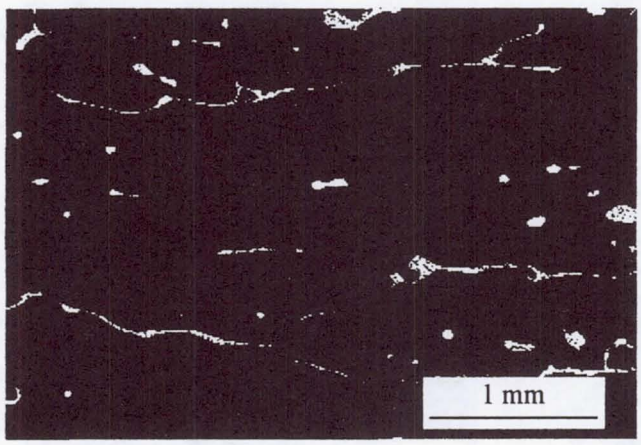

a

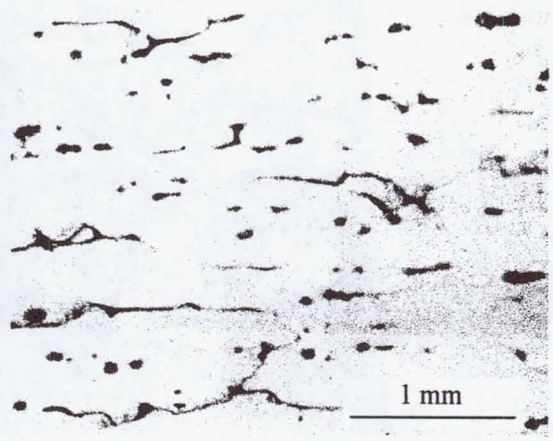

b

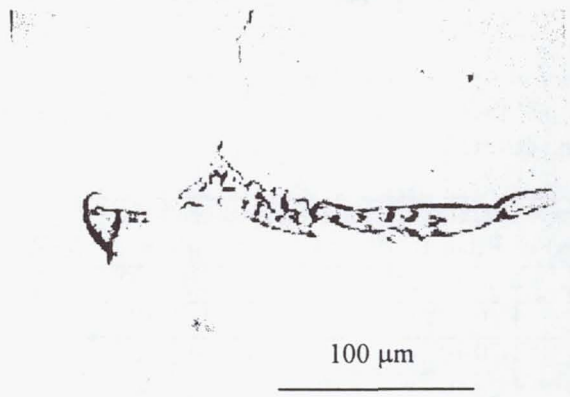

c

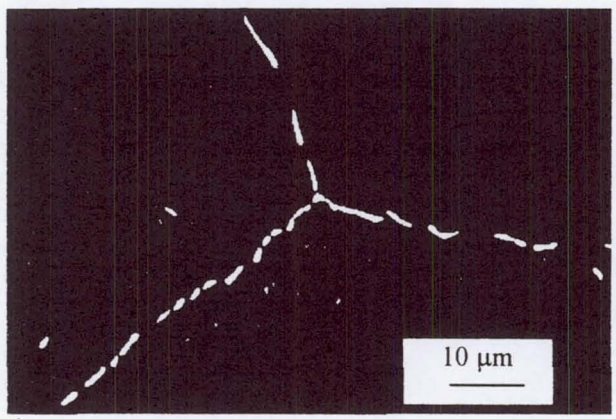

d

Figure 3 : Microstructures obtained in the first solidified part of FM1 gradient sample : a) SEM picture showing the elongation of interdendritic segregated regions in the solidification direction, b) optical metallography of anodized sample showing no elongation of the grains, c)dihedral angle formed at the junction between a eutectic inclusion and a grain boundary perpendicular to the solidification direction, d) aligned Al_2Cu precipitates formed at a grain boundary containing no eutectic.

Ground based GM1 and GM2 samples exhibit slightly different grain structures, due to their different Ti level. The GM1 sample (without excess Ti) is fully columnar, except at the end, where few equiaxed grains appear, mainly on the periphery of the sample (Fig. 4b). In presence of excess Ti (GM2 sample), a sharp transition from purely columnar to equiaxed structure is observed.

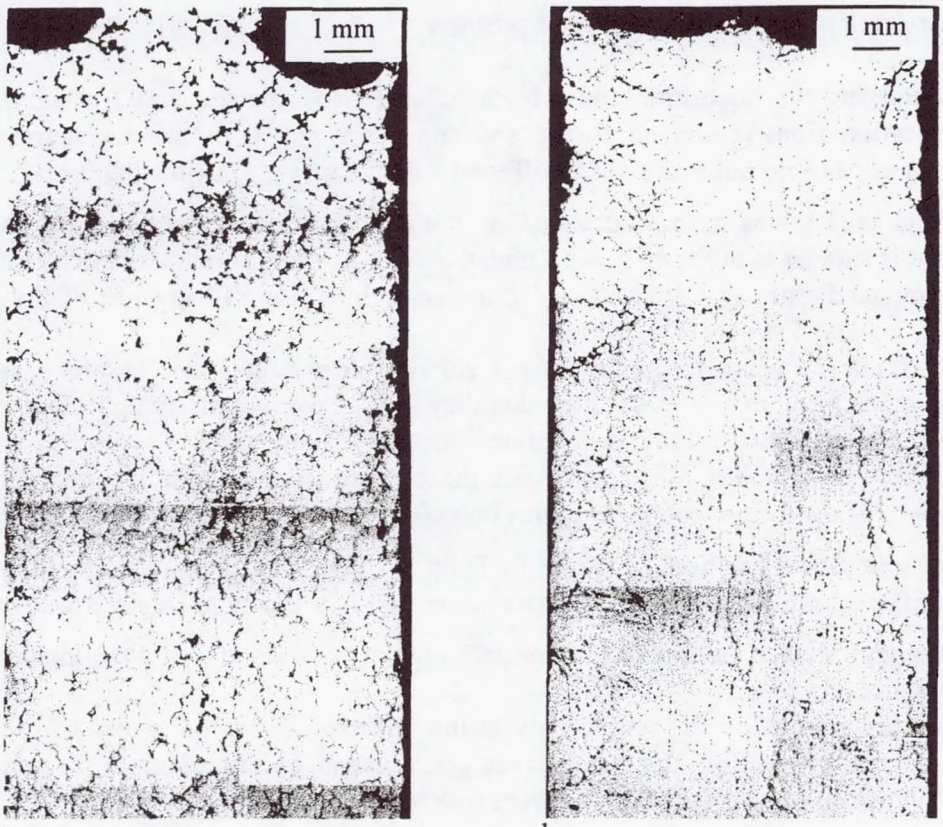

Figure 4 : grain structure of the last solidified part of gradient samples : a) equiaxed structure of the microgravity sample FM1, b) mixed columnar-equiaxed structure of the ground sample GM1

(5) DISCUSSION

The mechanisms controlling the equiaxed grain sizes in the isothermal samples and the grain structure transition in the gradient samples are discussed below. In each case, one first consider space samples where convective effects are minimized. Then, the influence of convection is discussed by comparing ground and space macrostructures.

5.1. Isothermal samples

In space samples, the refiner is found to operate, even for the case of the low Ti content (10ppm). This result shows that there is no significant fading of the efficiency of the refiner particles during their long stay into the liquid (4 hours), and that, if a lower limit of excess Ti necessary for heterogeneous nucleation on the TiB_2 particles exists, it should be very low. However, the grain size is significantly smaller in the sample with 100ppm Ti. This may be due to an increase of the number of efficient nucleation sites and/ or a contribution of the Ti content in the liquid to slow down the growth of the equiaxed grains. Comparatively, the grain structure in the ground samples is strongly influenced by the settling of refiner particles towards the bottom. This settling is however not complete due to the slight mixing by natural convection.

5.2 Gradient samples

In order to interpret the microstructures observed in the microgravity and ground gradient samples, we will first briefly recall the accepted description of the columnar-equiaxed transition.

The model of the columnar-equiaxed transition :

Considering the nucleation and growth of crystals inside the liquid ahead an already formed solidification front (columnar front), and supposing that both the nucleating particles and the growing crystals do not move, three different situations have to be distinguished :

- if equiaxed grains cannot nucleate, i.e. if the constitutional undercooling ahead the columnar front is smaller than the nucleation undercooling, a purely columnar structure is expected ;
- if equiaxed gains can nucleate and grow enough to stop the advance of the columnar front, a fully equiaxed structure will result ;
- at last, if the equiaxed grains do not fill completely the space before being reached by the columnar front, then it is admitted that they will be overgrown by it, so that a mixed columnar-equiaxed structure should be obtained. Let us remark that this presupposes that, due to a selection mechanism associated with the relative cristallographic orientation of the grains, growth of the former columnar grains is preferred to that of the new impinged grains.

A simple model has been proposed by Hunt [1] to predict the conditions for transition between these different microstructures. The main assumptions of the model are the following :

- stationary state is considered, corresponding to the situation of directional solidification in a Bridgman furnace ;
- equiaxed nucleation is possible only in the undercooled region, ahead of the columnar front ; there is no convection, and the equiaxed grains cannot be shifted out of the undercooled region.
- columnar undercooling ΔT_C is given as follows :

$$\Delta T_C = \left(\frac{R C_0}{A} \right)^{1/2}$$

R is the columnar dendrite tip velocity, C_0 is the wt.% alloy composition. A = -[D/8m (1-k)Γ] where D is the diffusion coefficient of solute in the liquid, m is the liquidus slope of the phase diagram, k is the equilibrium distribution coefficient and Γ is the Gibbs-Thomson coefficient. In this expression, the DG/R contribution is neglected.
Briefly, a transition from a mixed to a fully equiaxed microstructure is predicted when :

$$G_L < 0.617\, N_0^{1/3} \left[1 - \left(\frac{\Delta T_N}{\Delta T_C} \right)^3 \right] \Delta T_C$$

where G_L is the temperature gradient in the melt, N_0 the number of nucleating sites per unit volume, and ΔT_N is the nucleation undercooling. Hunt also considers that the structure becomes practically fully columnar if the volume fraction of equiaxed grains becomes lower than an arbitrary limit. The corresponding transition occurs when :

$$G_L > 0.617 (100\, N_0)^{1/3} \left[1 - \left(\frac{\Delta T_N}{\Delta T_C} \right)^3 \right] \Delta T_C$$

If ΔT_N can be neglected compared to ΔT_C , the above relations simplify as follows :

$$G < 0.617\, N_0^{1/3} \left(\frac{V C_0}{A}\right)^{1/2} \quad \text{and} \quad G > 0.617\,(100\, N_0)^{1/3} \left(\frac{V C_0}{A}\right)^{1/2}$$

Comparison with our space results :

In our experiment, a preferential growth of the grains in the direction opposite to the heat flux is evidenced by the elongation of the interdendritic segregated regions. But, contrarily to the theoretical expectations, one cannot distinguish two different categories among the grains and none of them appears elongated. A similar trend was observed in the previous MIR experiment with a higher refiner content. But, in the present case, the elongation length of the segregated regions appears even larger than the characteristic dimension of the grains. This can only be explained by a motion of the grain boundaries behind the front. Such a motion of the transverse grain boundaries is possible since they generally did not contain residual liquid (as evidenced by the absence of a eutectic layer). On another hand, the presence of fine Al_2Cu precipitates along all the boundaries attests that this motion occurred above the eutectic temperature. Finally, a consistent description of the formation of the observed grain structure would be as follows : A large density of more or less elongated grains would initially be formed because, due to the absence of a sharp selection mechanism, new impinged grains would grow as well as the older ones. Then, grain boundaries which become free of residual liquid might start moving, thus leading to a more stable isotropic arrangement of the grain structure. Thus, the above microstructure will be referred to as "recristallized" in the following.

According to our interpretation, the transition between our recristallized microstructure and the fully equiaxed one should correspond to the equiaxed-mixed transition of Hunt's model. In order to compare the observed conditions of the transition with the ones predicted by the model, we proceeded in the following way. Due to the low Ti levels of interest, viz 0.001-0.01 wt.%, we have neglected the growth restriction effect (the product m(1-k) is large for Ti in molten Al [10]), and we have considered our alloys were strictly binary. Thus, we have taken for A the experimental value given by Hunt [1], A = 300 $\mu m.s^{-1}.wt.\%.K^{-2}$. As Ziv and Weinberg did [3], we have neglected the ΔT_N term before ΔT_C.

The isothermal samples were expected to solidify in an equiaxed way, to give us the number of grains per unit volume, and thus the nuclei density N_0, with the Hunt's assumption where each equiaxed grain is associated with a nucleation event. Grains counting methods based on stereology give more accurate value for the grain density, than estimation from grain size measurements, due to the dendritic form of the grains, and the polydisperse grain distribution. This density, considering the Hunt's model, leads to the construction of equiaxed, mixed and columnar fields on a log(G)-log(R) diagram. Thanks to thermal data, the construction of the « solidification paths » of each experiment was made possible, as illustrated on Fig.5.

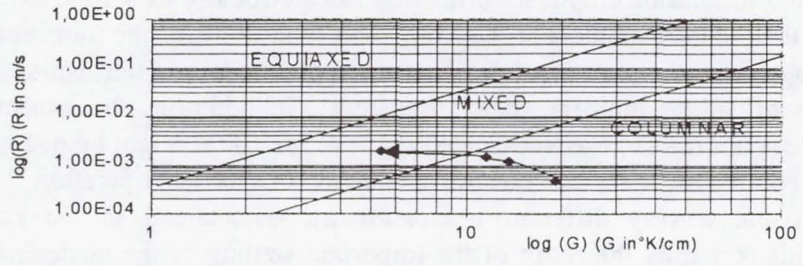

Figure 5 : Plot of growth velocity, R, against temperature gradient, G, showing the predicted columnar and equiaxed regions for GM1 sample, with the experimental solidification path.

It permitted to establish the structures expected by Hunt and compare with our experimental results. This comparison is summarized in Table 3.

Sample	observed grain structure	predicted grain structure
FM1	recristallised-equiaxed	columnar-mixed
FM2	recristallised-equiaxed	columnar-mixed
GM1	columnar-equiaxed	columnar-mixed
GM2	columnar	columnar-mixed

Table 3 : Comparison between the observed and predicted grain structures

It appears that our microgravity samples are more equiaxed than predicted. Several hypothesis can be made to explain this departure :

- in Hunt's model, the contribution of solute boundary layer built-up ahead the columnar front to decrease its temperature (by around DG/V) is neglected. This effect, which is not negligible in the first part of our solidification path, does not change the local undercooling, but increases the extent of the undercooled region, and thus gives more time for the equiaxed crystals to grow ;
- taking into account the growth restriction effect of Ti should slightly decrease the A value, and thus shift the predicted transition towards lower velocities and higher gradients. On another hand, no significant difference is observed in this respect between the samples with and without excess Ti.

Ground samples / the effect of convection on the columnar-equiaxed transition :

Qualitatively, different complementary factors can be invoked to explain the observed shift of the columnar-equiaxed transition under the effect of convection :

- as already evidenced on isothermal samples, the settling of nucleating particles causes an accumulation in the lower stagnant parts and a depletion of N_0 elsewhere ;
- in addition, part of the growing equiaxed crystals may be swept away from the front ;
- at last, the solute built-up ahead the front, and thus the corresponding contribution to the front undercooling, are reduced, which leads to a decrease of the extent of the undercooled region.

The first factor can be taken into account at first order in the frame of Hunt's model by deriving N_0 from the average grain density measured in isothermal samples (Table 2). In this way, a rough agreement is found with our ground experiments, which might be explained by the fact that negligence of solute built-up is better justified in this case.

(6) CONCLUSIONS

The present microgravity experiment has for the first time shown a continuous transition from a purely equiaxed to an anisotropic solidification microstructure as a function of solidification rate and the local temperature gradient at the front. The conditions for the transition have been found to somehow depart from the ones predicted by the simple model of Hunt which in particular neglects the influence of solute built-up ahead the front. In addition, the aspect of the anisotropic microstructure is not the same as anticipated in the model. This might be due to the fact that for our experimental conditions, there was no strong selection mechanism operating.

By comparison, a very different microstructure is obtained in the corresponding ground references. This is mainly the result of the important settling of the nucleating particles occurring during the long stay in the liquid state inherent to the thermal profile presently applied. However this single effect can hardly explain the abrupt character of the transition between zones with very

large columnar grains and purely equiaxed zones. A possible other factor is the motion of the growing equiaxed crystals relative to the advancing columnar front. This last point is a topic for our next proposed experiment in AGHF, which will focus on the morphology of the equiaxed grains themselves.

ACKNOWLEDGEDMENTS

The authors are greatly indebted to the European Space Agency and specially to J. Stroede. The financial and technical support of the Centre d'Etudes Spatiales is also gratefully acknowledged. Special thanks are given to H. N'guyen Thi for his support at the LMS mission, as well as to D. Buscoz and J.E. Mazille for the Image Analysis.

REFERENCES

[1] J.D. Hunt, Mater. Sci. and Eng. **65**, 75 (1984).
[2] R. B. Mahapatra and F. Weinberg, Metall. Trans. **B18**, 425 (1987).
[3] I. Ziv and F. Weinberg, Metall. Trans. **B20**, 731 (1989).
[4] C. Beckermann and C.Y. Wang, Annual Rev. Heat transfer, vol. VI, ed. C.L. Tien (1995).
[5] M. Rappaz et al., Materials Science Forum vols. **217-222**, 7 (1996).
[6] D.G. Mc Cartney, Int. Mater. Rev. **34**, 247 (1989).
[7] C.Y. Wang and C. Beckermann, Met. and Mat. Trans., Part I to III (1996)
[8] F. Botalla, DEM internal Report n° 09/97, CEA Grenoble, 1997
[9] D. Buscoz DEM internal Report n° 10/97, CEA Grenoble, 1997
[10] M. Johnsson, L. Backerud and G.K. Sigworth, Metall. Trans. **A24**, 481 (1993).

SUMMARY OF THE LMS-AGHF-ESA 2b EXPERIMENT

In the case of directional solidification of inoculated alloys under diffusive transport conditions, the transition from columnar to equiaxed grain structure is predicted to occur continuously through intermediate mixed structures, as a function of the nuclei density N_0, temperature gradient G and solidification rate R. On the ground, gravity driven convection affects these three parameters. For this reason, recent models try to include convective effects. However, in order to assess the models, experiments able to separate convection from the other mechanisms involved are still needed.

With this aim in view, we performed a series of experiments under reduced gravity (EUROMIR 95 and LMS 96) where Al-4wt.%Cu alloys refined at different levels (2 to 50 ppm B, and 10 to 250 ppm Ti) with Al-5Ti-1B master alloys, were unidirectionally solidified with continuously decreasing temperature gradient G and increasing rate R. Nearly isothermal samples from the same batch were also solidified in parallel, to give the reference purely equiaxed microstructure. Reference ground based experiments were also performed in identical thermal conditions with different orientations relative to gravity.In the present work, the results of the LMS experiments are analysed.

In the samples solidified in microgavity under nearly isothermal conditions, the refiner is found to operate, even for the case of the low Ti content (10ppm). This result shows that there is no significant fading of the efficiency of the refiner particles during their long stay into the liquid (4 hours), and that, if a lower limit of excess Ti necessary for heterogeneous nucleation on the TiB_2 particles exists, it should be very low. However, the grain size is significantly smaller in the sample with 100ppm Ti. This may be due to an increase of the number of efficient nucleation sites and/ or a contribution of the Ti content in the liquid to slow down the growth of the equiaxed grains.

Comparatively, the grain structure in the ground samples is strongly influenced by the settling of refiner particles towards the bottom. This settling is howver not complete due to the slight mixing by natural convection.

Samples solidified under varying G and R in microgravity show for the first time a continuous transition from a purely equiaxed to an anisotropic solidification microstructure as a function of solidification rate and the local temperature gradient at the front. The conditions for the transition are found to somehow depart from the ones predicted by the simple model of Hunt which in particular negects the influence of solute built-up ahead the front.. In addition, the aspect of the anisotropic microstructure is not the same as anticipated in the model. This might be due to the fact that for our experimental conditions, there was no strong selection mechanism operating.

By comparison, a very different microstructure is obtained in the corresponding ground references. This is mainly the result of the important settling of the nucleating particles occurring during the long stay in the liquid state inherent to the thermal profile presently applied. However this single effect can hardly explain the abrupt character of the transition between zones with very large columnar grains and purely equiaxed zones. A possible other factor is the motion of the growing equiaxed crystals relative to the advancing columnar front. This last point is a topic for our next proposed experiment in AGHF, which will focus on the morphology of the equiaxed grains themselves.

Advanced Gradient Heating Facility (AGHF)

Effects of Convection on Interface Curvature during Growth of Concentrated Ternary Compounds

Principal Investigator:

Dr. Thierry Duffar
DEM/SES
Grenoble, France

DTA - CEREM
DÉPARTEMENT D'ÉTUDES DES MATÉRIAUX

Service de Physico Chimie des Matériaux

Fiche d'Action GRAMME

Grenoble, le 25 juillet 1997

COMPTE RENDU SPCM n° 15/97

LMS One year science review

PRELIMINARY RESULTS OF THE AGHF ESA-8 EXPERIMENT

N. DUHANIAN, T. DUFFAR (Principal Investigator), J. ABADIE

C. MARIN*, E. DIEGUEZ* (Co-Investigator)

* DFM/LCC, Universidad Autonoma de Madrid, SPAIN

Sera soumis pour publication dans « International Journal of Microgravity Science and Technology »

Liste de diffusion du CR. SPCM n° 15/97 du 25 juillet 1997

Conseiller Scientifique M2RI	M. FAVIER
M2RI/DEM/Dir (1 seul ex.)	MM. LEMOINE AUBERT
DOC/DEM	
M2RI/DEM/SPCM	MM. ABADIE CAMEL DUFFAR Mlle DUHANIAN Mme DUPOUY M. GARANDET Mme KERNEVEZ MM. NABOT PRAIZEY SANTAILLER WARIN
Conseiller Scientifique	M. DESRE
C.N.E.S./Paris	MM. BONNEVILLE ZAPPOLI Mme LEON
NASA-MSFC, Huntsville	M. DOWNEY
Univ. Autonoma Madrid	M. DIEGUEZ
ESA/ESTEC	M. STRÖDE MM WALTER, MINSTER
CNES Toulouse/CADMOS	M. DESROCHES

Page de garde + Résumé + Liste de diffusion

M2RI/DEM/SGM	MM. MORET DANROC
M2RI/DEM/SPCM/DIR	ROBERT
M2RI/DEM/SPCM/LSE	BLOCH
M2RI/DEM/SPCM/LSC	Mme MERMILLIOD
M2RI/DEM/SPCM	Tous A1 et Thésards

RESUME

L'expérience spatiale LMS-AGHF-ESA8 est dévolue à l'étude de la solidification des alliages concentrés. C'est un domaine qui souffre simultanément de l'absence de description théorique rigoureuse des phénomènes physiques mis en jeux et d'un manque d'expériences soignées pour les valider.

Nous décrivons le dispositif expérimental et les paramètres de l'expérience, choisis pour en optimiser les résultats. L'alliage retenu est le pseudo-binaire semiconducteur GaSb-InSb, pris comme matériau modèle.

Les premiers résultats expérimentaux, qui restent à compléter par des mesures plus approfondies, permettent de tirer des conclusions dans deux domaines :

- Du point de vue ségrégations chimiques, on a mis en évidence dans l'échantillon spatial une homogénéisation inattendue du liquide tout au long de la solidification. Ce phénomène ne rentre pas du tout dans le cadre de notre compréhension actuelle de la solidification des alliages concentrés.
- Sur le plan des interactions cristal-creuset, le phénomène de démouillage, consistant en un décollement de l'échantillon par rapport au creuset, a été quantifié pour la première fois. Les résultats obtenus sont en bon accord avec nos derniers développement théoriques sur le sujet.

ABSTRACT

The space experiment LMS-AGHF-ESA8 was devoted to studies on the solidification of concentrated alloys. Indeed, the knowledge in this field suffers simultaneously of a lack of theoretical description of the physical phenomena involved and of clear experiments to validate them.

We describe the experimental set-up and the experimental parameters chosen in order to optimize the results. The alloy used is the pseudo-binary semiconductor GaSb-InSb, taken as model material.

The first results, still to be confirmed by more in depth measurements, lead to conclusions in two domains :

- The chemical segregations in the flight sample have shown an unexpected homogenization of the liquid all along the solidification. This phenomenon does not agree with the present understanding of the solidification of concentrated alloys.
- The crystal-crucible interactions, leading to detachment under microgravity conditions, have been quantified for the first time. The results are in good agreement with our theory on the subject.

ACKNOWLEDGMENTS

This experiment has been supported by the ESA, the GRAMME agreement between CEA and CNES and the Spanish Ministry of Research. The development and exploitation of this experiment have only be possible due to the great efforts of a number of people involved at various stages. The PI's would like to thank all of them for their efforts :

C. Marin and P. Dutta for the preparation of the feed and seed materials.

J. Abadie for taking care of the cartridges' development, design and integration.

J.P. Pissard, S. Cantaloup and the teams in SOTEREM and CNES for the industrial integration of the cartridges.

A. Desroches, G. Begnini, and the whole CADMOS team for their help during the flight and ground experiments.

B. Desaunettes and P. Vedrenne, EPSILON, for their help in numerical simulation of the thermal field in the cartridges.

The ESA team at the POCC, with a special mention for J. Ströede , head of the AGHF project at ESA.

N. Duhanian for taking care of the ground reference experiments, for the processing of the samples and analysis of the experimental results.

But our best regards will be for H. Ben Aïm, for her constant help and support, and Adèle ...

1 SCIENTIFIC OBJECTIVES

The ESA8 experiment is essentially devoted to the study of the solidification of concentrated alloys. When an alloy is melted then solidified back, a number of phenomena are occurring, which has an impact on the quality of the resulting solid. For example, there are several growth regimes during solidification that lead to very different structures of the sample: the first stage is characterized by a smooth solid/liquid interface; when the growth rate is increased, the interface becomes wavy and, at highest rate, totally disturbed. We have restrained our experiment to the first stage.

The shape of the solid/liquid interface and the chemical segregations of the components of the alloy have a large influence on the final quality of the sample. These phenomena are now rather well understood in the case of diluted alloys (i.e. when the chemical composition has no sensitive effect on the physical parameters of the sample, such as density or melting temperature) but there is a lack of both theory and experiments in the case of highly concentrated alloys [1].

Indeed, the large number of physical phenomena involved make the problem very complicated:
- Heat transfer in the liquid and solid phase, including release of latent heat at the interface.
- Hydrodynamical movements in the liquid that are due to differences in temperature or in chemical composition. The resulting variations of density interact with the gravity field and generate movements.
- Chemical segregations during solidification due to the fact that the solidified solid has not the same composition than the liquid: some components of the alloys stay in the remaining liquid rather than being incorporated in the solid.

In diluted alloys, these three phenomena are well decoupled (the thermal field induces movements that induce chemical species transport) and the problem is rather simple (but it took more than thirty years to get a satisfactory model!). In concentrated alloys, there is feedback between the phenomena (chemical field induces movements and modifies thermal properties, especially melting temperature) which makes the problem much more complicated.

The purpose of the experiment is to quantify the effect on solidification of variations in the external thermal field (by varying the crucible material) and in the gravity level (by comparison between space and ground experiments) by measuring:
- The temperature distribution around the sample.
- The interface shape along the growth process.
- The chemical segregations in the resulting solid.

Another, totally independent, objective of the experiment is to study the phenomena of dewetting. This denotes a detachment of the sample from the crucible, which is commonly observed when semiconductor materials are solidified under microgravity conditions [2, 3] even though it is never observed on earth.

2 EXPERIMENT PARAMETERS, DEVELOPMENT AND PROGRESS

The alloy is a mixing of 20% (molar) of InSb and 80% of GaSb. These two compounds are semiconductors that can be mixed in any proportion in the solid and liquid states and then the system can be considered as binary. Antimonides are the less toxic semiconductor compounds and furthermore they melt at the lowest temperature (530°C for InSb and 710°C for GaSb). This makes them good candidates for a space experiment where safety concerns are mandatory and thermal energy restricted. They are well known to show the dewetting phenomenon.

The InSb is heavier than GaSb and is rejected in the liquid. It is then expected that it stabilizes the convective motion of the liquid close to the interface when the alloy is solidified vertically on earth and that is why it has been chosen as the « solute ». The concentration of 20% corresponds to the maximum difference between the solidus and liquidus lines of the pseudo-binary phase diagram. The physical properties of these materials are very well known, including wetting properties on the crucibles (wetting is of importance in the detachment matter).

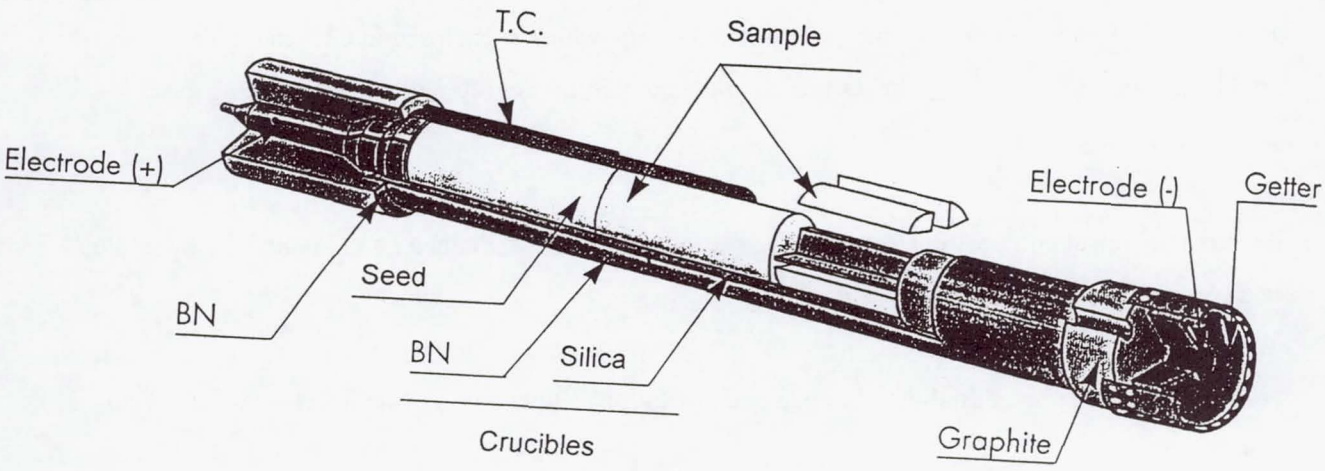

Fig 1: Sketch of the experimental set-up.

To avoid undercooling of the sample, a « seed », which is not melted and is used as initiator of the growth, is placed at the cold side of the sample. Because the experiment is not focused on structural quality, the seed is not a single crystal. Seeds and feed materials have been prepared from pure (6N) In, Ga, Sb and Te. The preparation by itself is a complicated task that led to a specific publication [7].

In order to act on the interface curvature during the growth, two crucibles are used. One is made in quartz, with a very low thermal conductivity that gives interfaces with a very low curvature. The second one is in boron nitride (BN) which gives strong interface curvatures. The inner diameters of the crucibles were measured with a precision of a few micrometers, for subsequent comparison with the external diameter of the solidified samples. Both crucibles don't conduct electricity. This is of importance because the investigation on the interface curvature is made by applying electrical pulses to the sample at regular intervals. By this way the Joule effect and the Peltier effect generate heat close to the interface and disturb the growth. This disturbance can be revealed by subsequent cutting, polishing and etching of the sample : the shape of the interface at the moment of the pulse is materialised by a thin line visible on the polished, etched surface. By measuring the distance between two lines, and knowing the time between the two electrical pulses, it is also possible to calculate the growth rate. The parameters of the Peltier pulse marking are: duration 800 ms, amplitude 18 A and they are sent every ½ hour. It is necessary to dope the alloy with Te (10^{19} to 10^{20} at/cm^3) in order to get a good etching and demarcation of the interfaces. The electrical current enters the sample by the hot (liquid) side, via a graphite piece and is collected at the cold part by a bronze pincer around the seed. Nine thermocouples are placed all along the crucibles in order to measure in real time the thermal field around the sample.

To avoid pollution of the sample, the experimental set up, which is enclosed in a standard Ta cartridge, is under vacuum. A getter is placed at the hot part in order to pump the remaining gases during the heating of the cartridge.

Given the chemical composition, the growth rate, thermal gradient, diameter and length of the sample are a compromise between several constraints:

- Allocated time for the experiment.
- Avoidance of interface destabilization due to constitutional supercooling (the interface must remain smooth).
- Avoidance of thermal convection due to residual gravity fluctuations during the space experiment.
- Interface curvature must be high enough so that fluctuations are detectable.
- Border effects at the beginning and end of the sample must be avoided.

Taking into account the available theoretical literature on these effects [4-6], the optimal parameters were found:

- Growth rate 1.1 μm/s. This will be the value chosen for the furnace pulling.
- Thermal gradient in the liquid: 60 K/cm.
- Sample diameter 12 mm.
- Sample length: 152 mm plus 63 mm of seed. At least 95 mm of the sample will be solidified under controlled conditions.
- Experiment duration (controlled growth): 24 hours.

In order to optimise the experimental design and the thermal profile, two prototype tests have been performed. A qualification test, including vibrations, has then been performed in order to fix the flight design and parameters. Only minor modifications have been implemented after these tests. The most important was due to the fact that it has been found impossible to identify the Peltier pulse marks when they are sent with a perfect periodicity. A few pulses with an interval of ten minutes have then been put among the ½ h spaced pulses.

The scientific observations performed on the samples during these preliminary tests have been communicated [8]. They will be emphasized in a most quantitative way for the ground reference test.

During the first attempt to perform the experiment during the flight, a fault corresponding to an open circuit in the Peltier pulse marking electrical circuit was detected by the furnace. The electrical resistance of the Peltier circuit was measured by the crew in the flight model (infinite value, open circuit) and in the spare model (0.6 Ohms). It was then decided to process the spare model for the second attempt. The cartridge has been inserted without problem and the processing (pulling of the furnace) phase began at MET 9/14:02 for 26 hours and 40 minutes: the experiment gained the advantage of been processed during the 11th day of the mission that was a rest day for the crew. Then the gravity disturbances were supposed lower than for a busy day. Figure 2 gives the process parameters of the furnace versus time, as programed in real time during the flight experiment.

The thermocouples' measurements were analysed directly during the flight. (Excepted TC1 which failed after 2h at high temperature). The interface position versus time, extrapolated from the melting temperature and TC readings, showed a very constant nominal growth rate. The thermal gradients in the liquid were 60°C/cm or higher, as expected.

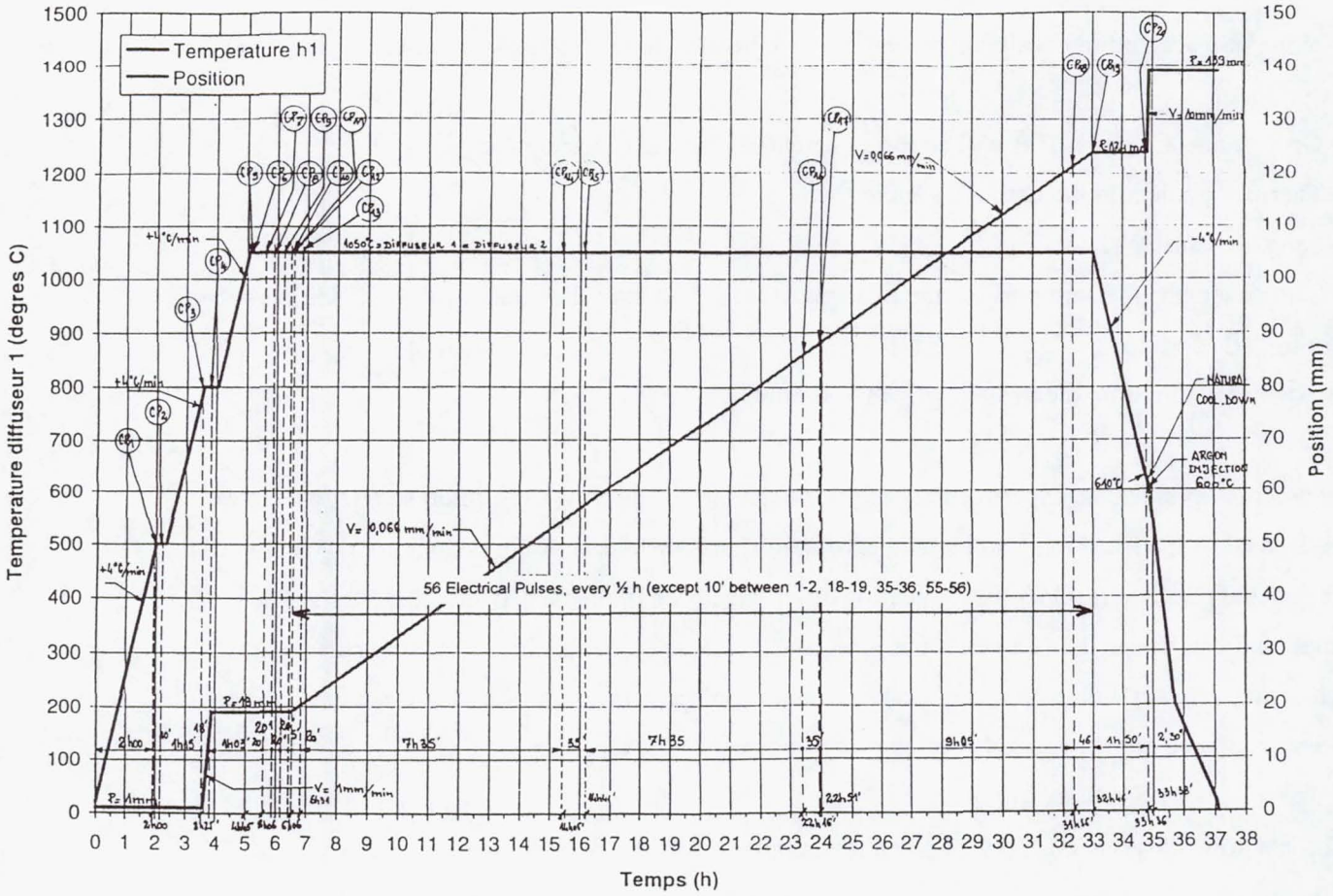

Fig 2: Process parameters of the flight experiment.

During opening of the cartridge and extraction of the sample, a bubble at the hot part was observed, taking the whole diameter of the crucible. It was then supposed that the electrical current has not passed through the sample and that the interface demarcation was not efficient. Indeed, subsequent polishing and etching attempt never gave any trace of interface marking. This bubble is probably the consequence of the presence of a fissure in the feed material right in front of the hottest part of the heating element of the furnace. It is supposed that the melting process began at the fissure and that the fissure gap increased more and more, because this semiconductor contracts during melting, leading finally to a big bubble. Careful analysis of TC readings at the beginning of the processing phase showed an anomaly (not detected during the flight) of heat transfer in the region of the bubble. This insures that the bubble didn't move during the solidification process and remained at the same position from the beginning to the end. Figure 3 shows a picture of the flight sample.

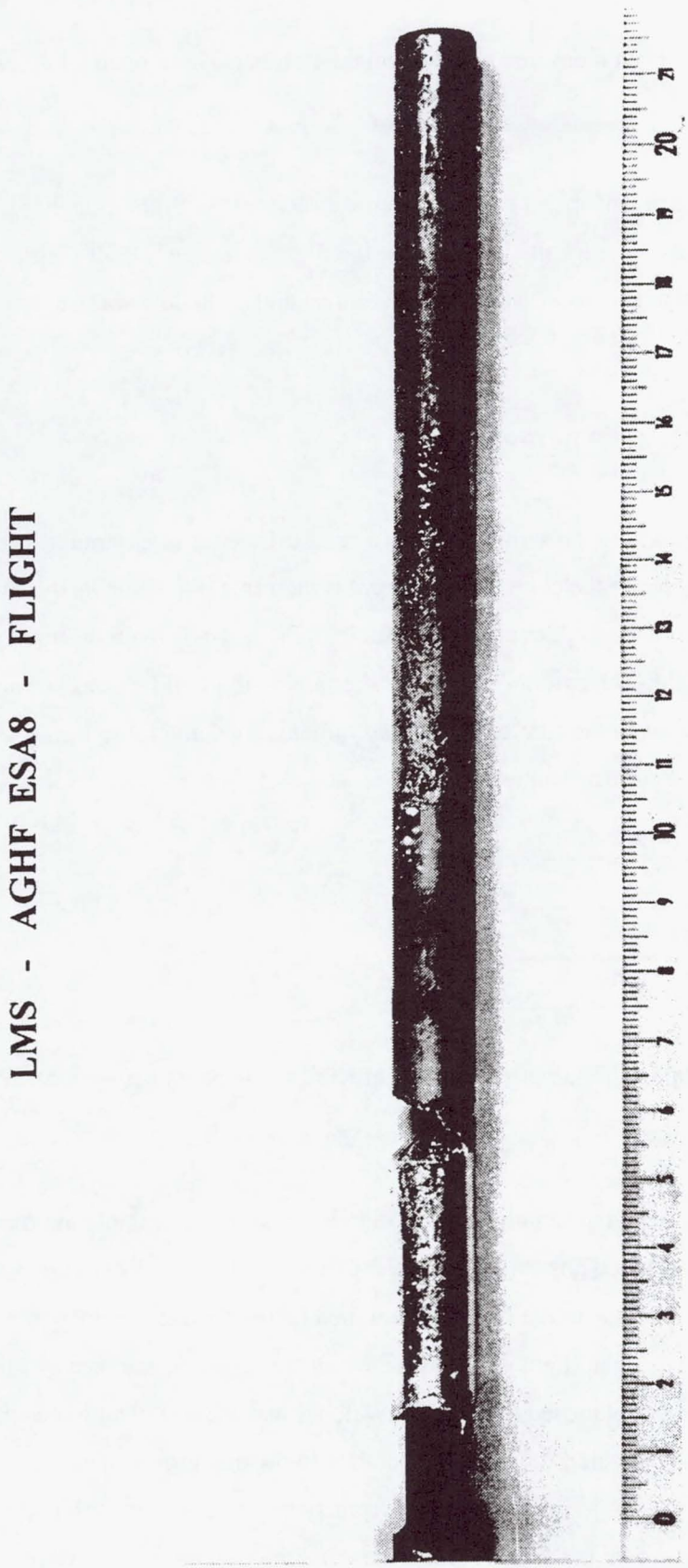

Fig 3: External view of the flight sample. The seed is on the right (between 16 and 21 cm), the BN/SiO_2 junction at 10.5 cm and the bubble can be seen on the left (between 5 and 6 cm).

Vacuum inside the cartridge has been measured at the opening: 10 mbar. These residual gases were not analysed.

The ground reference test has been performed end of November 1996 in the flight model of the furnace, with the same parameters than for the flight, using the flight cartridge initially rejected by the furnace. Every process parameters and observations were nominal and no bubble was observed.

3 RESULTS ON CRUCIBLE-SAMPLE INTERACTION

Visual observation of the flight and ground samples shows a clear difference of external aspect in the BN crucible. In the quartz crucible, on the contrary, the aspect is the same. Fig 4 shows the surface morphology of the flight sample in the middle of the BN crucible. Fig 5 shows the morphology at the BN/SiO_2 junction. On the SiO_2 side, the external surface of the sample is a molding of the roughness of the machined crucible, as well as in the case of the ground sample. Fig 6 and table 1 give a profilometer quantification of the surface roughness.

	SiO_2	BN
Ground	3 µm	7 µm
Flight	3 µm	25 µm

Table 1: Apparent roughness (Ra) of the sample in the two crucibles, compared between earth and space.

Fig 7 and Fig 8 show the variations of the sample external diameter and of the crucible internal diameter (as measured before and, when possible, after the experiment). The results are practically the same for ground and space samples. Due to the measurement method (electronic vernier), the measured diameter for the BN part of the flight sample is taken on the ridges. It can then be inferred that the outer top surface of the ridges touched the crucible wall because there is clear evidence that the ground sample, with the same diameter, touched the crucible. In the part grown in silica, it can be noticed a close contact between the sample and the crucible (practically no gap) on earth and a narrow (10 to 20 µm) gap for the sample grown in space. It seems then that the sticking of the sample on the quartz was stronger on earth than in space where some differential contraction occurred between the sample and the crucible. It seems that both samples grown in BN were allowed to contract freely.

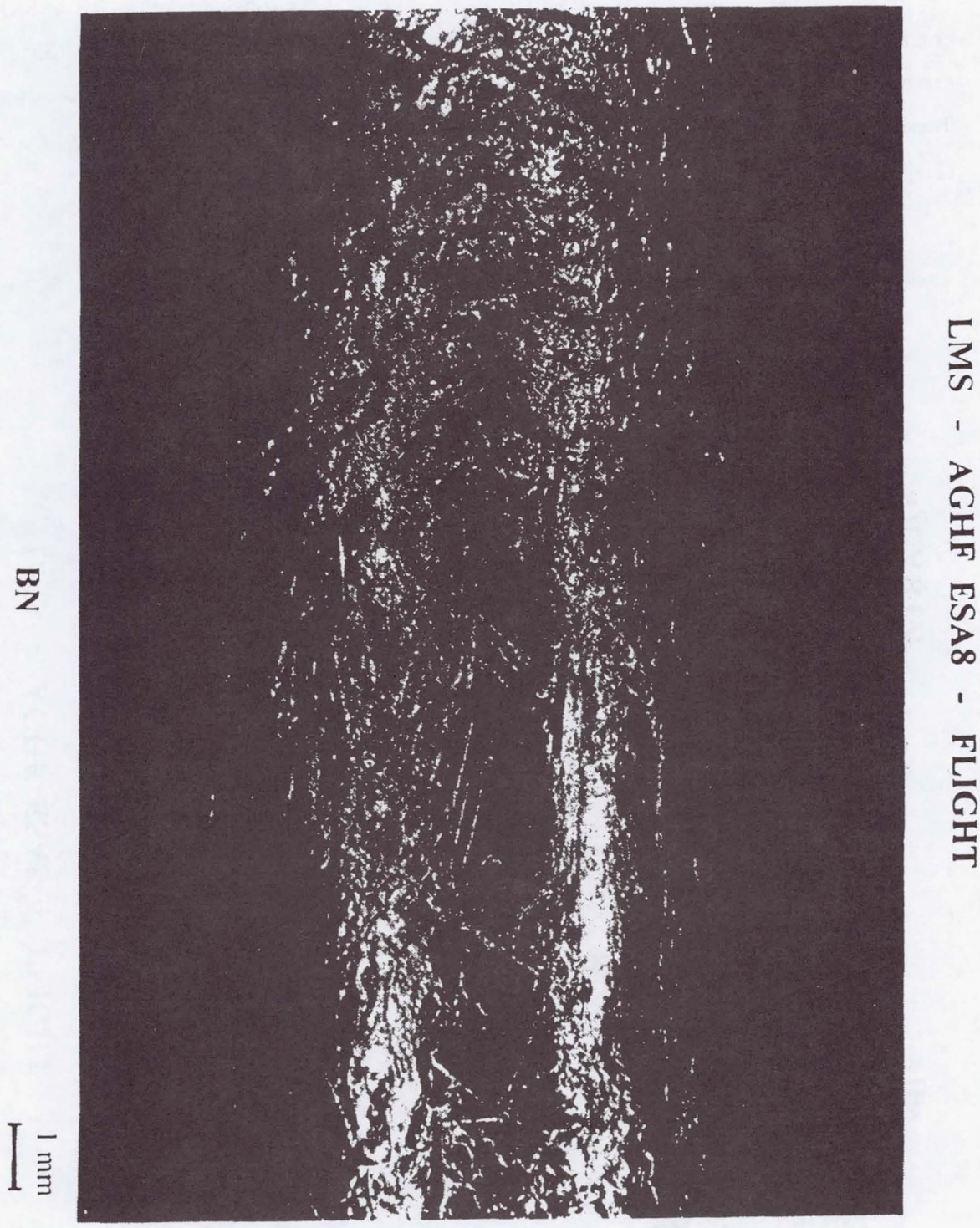

Fig 4: External aspect of the flight sample from the BN crucible

The conclusions of these observations are that the dewetting of the sample occurred only in space for the BN crucible. The sample shows the classical « ridges » on it surface. From the profilometers, the depths of the valleys between the ridges have a mean value of 25 µm with maximum values of 40 µm.

For the three other configurations, the sample was a molding of the roughness of the BN or SiO_2 crucibles. Considering that the contact angle of antimonides on silica is 120° and on BN 135° [9], it can be concluded that the largest contact angle causes de-wetting and the lowest causes sticking. These results are in good qualitative and quantitative agreement with our understanding of de-wetting [2,3].

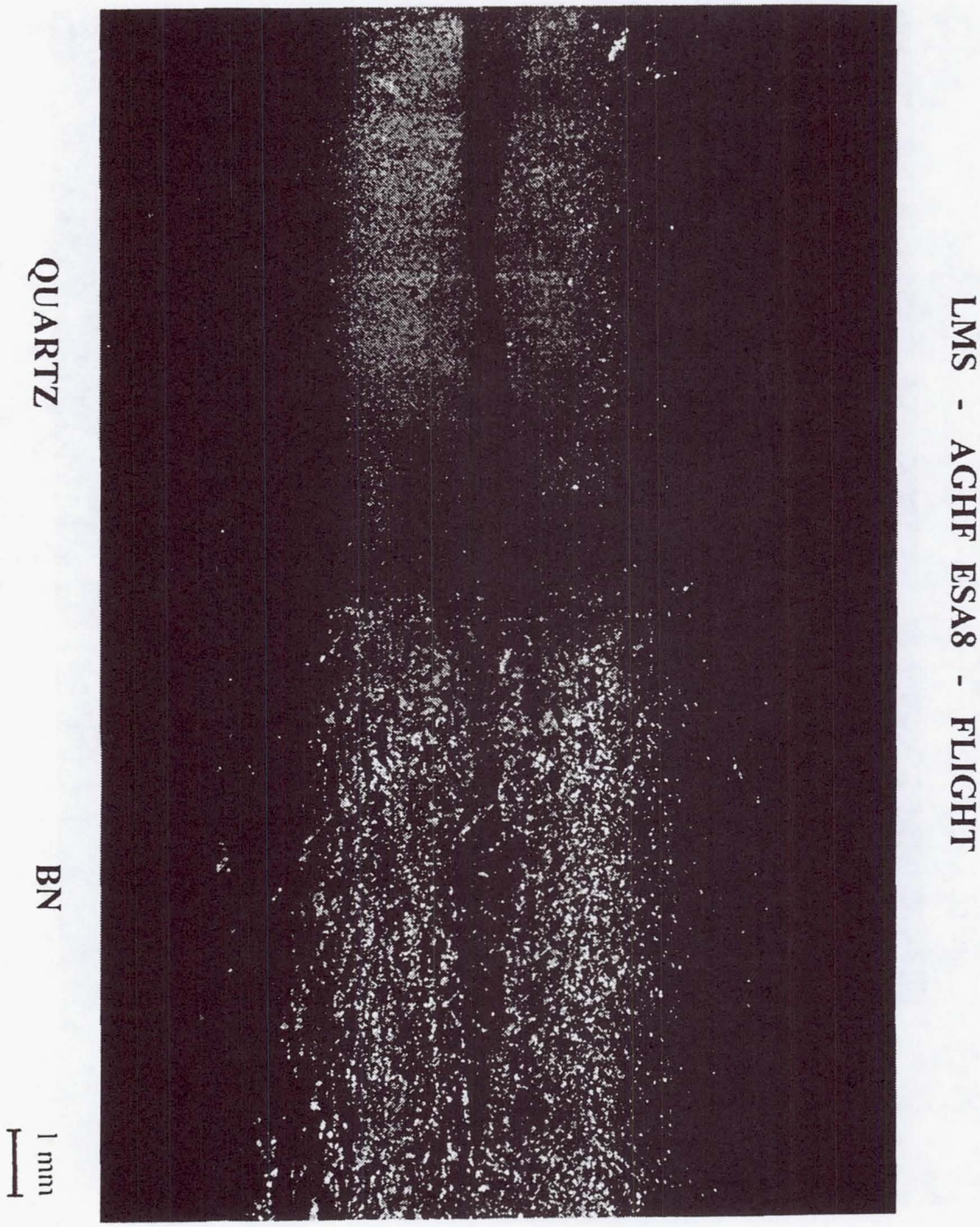

Fig 5: Surface morphology of the flight sample at the BN/SiO_2 junction

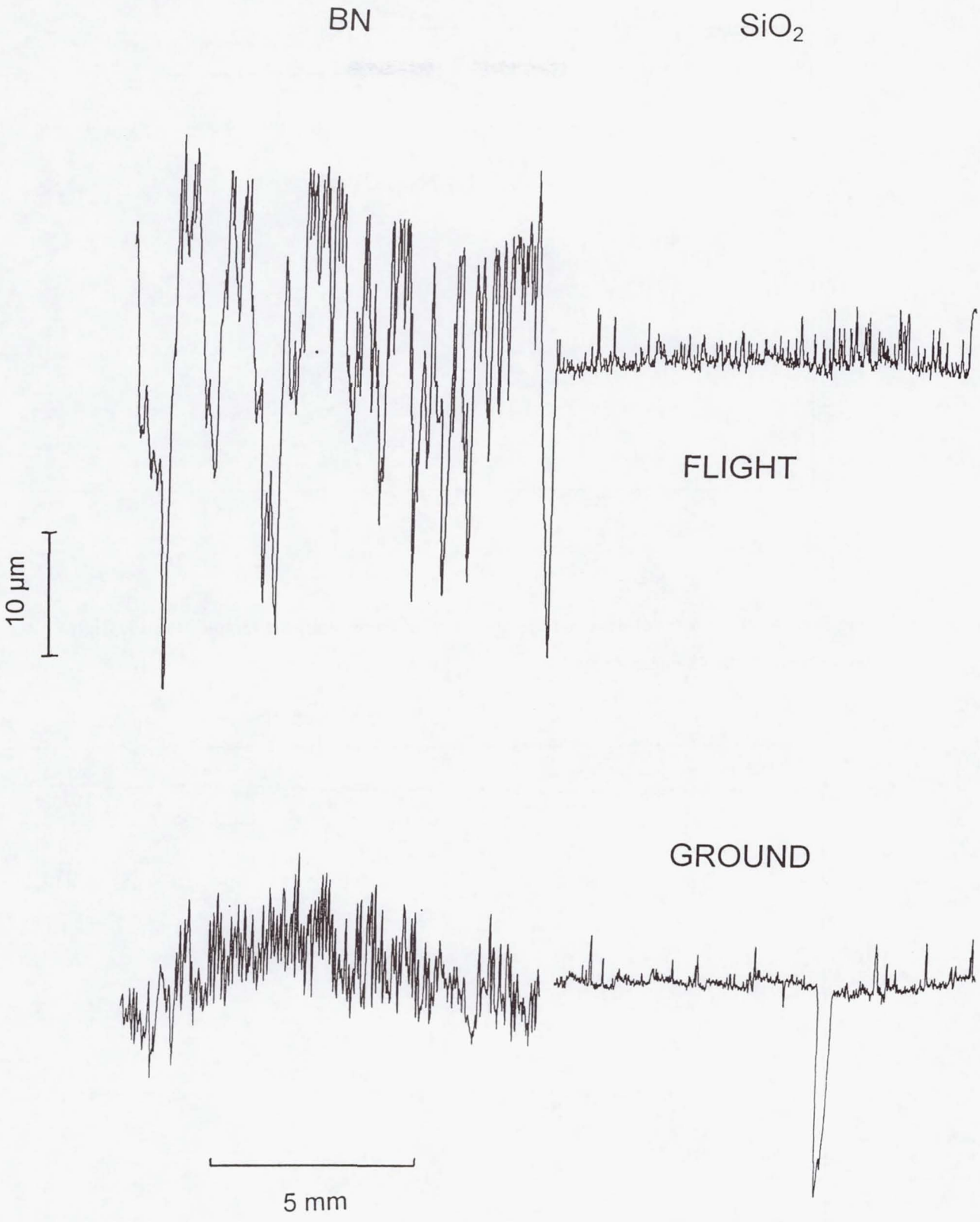

Fig 6: Surface roughness of the flight and ground samples in the BN and SiO_2 crucibles.

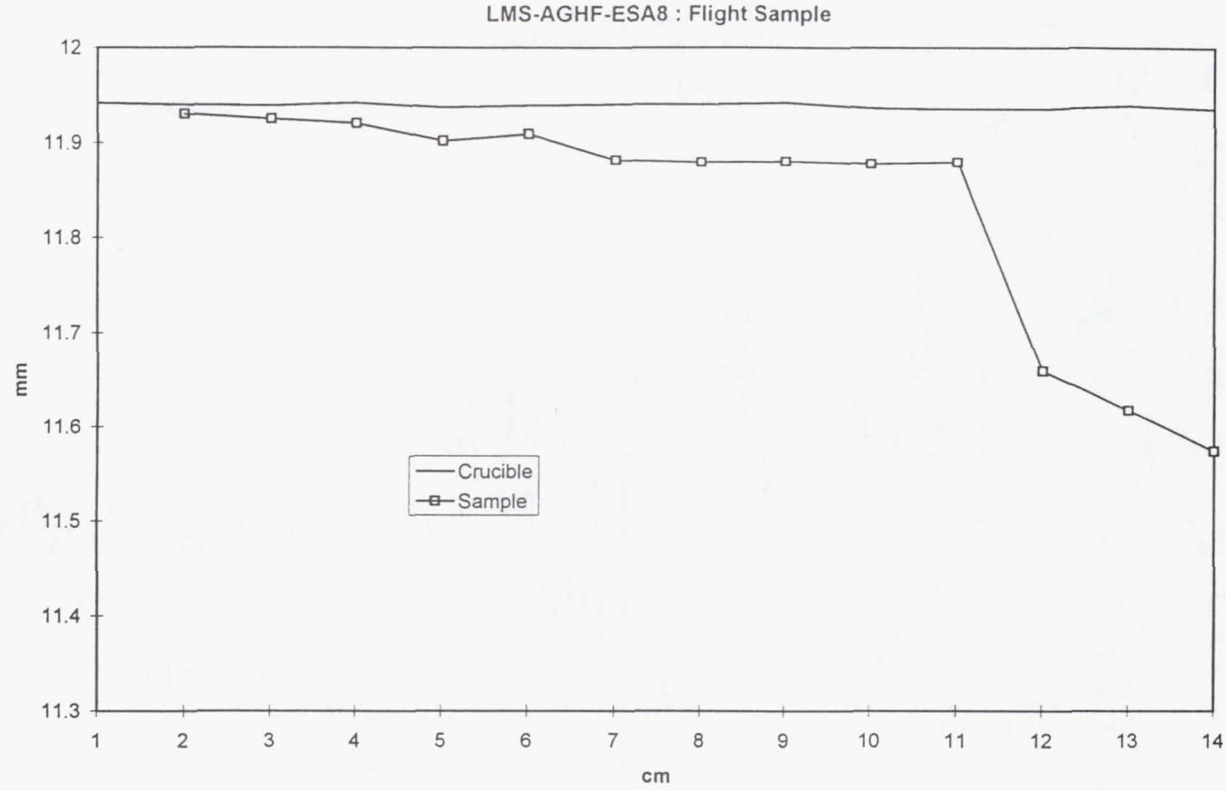

Fig 7: Internal diameter of the crucibles and external diameter of the sample after the flight experiment, versus sample length.

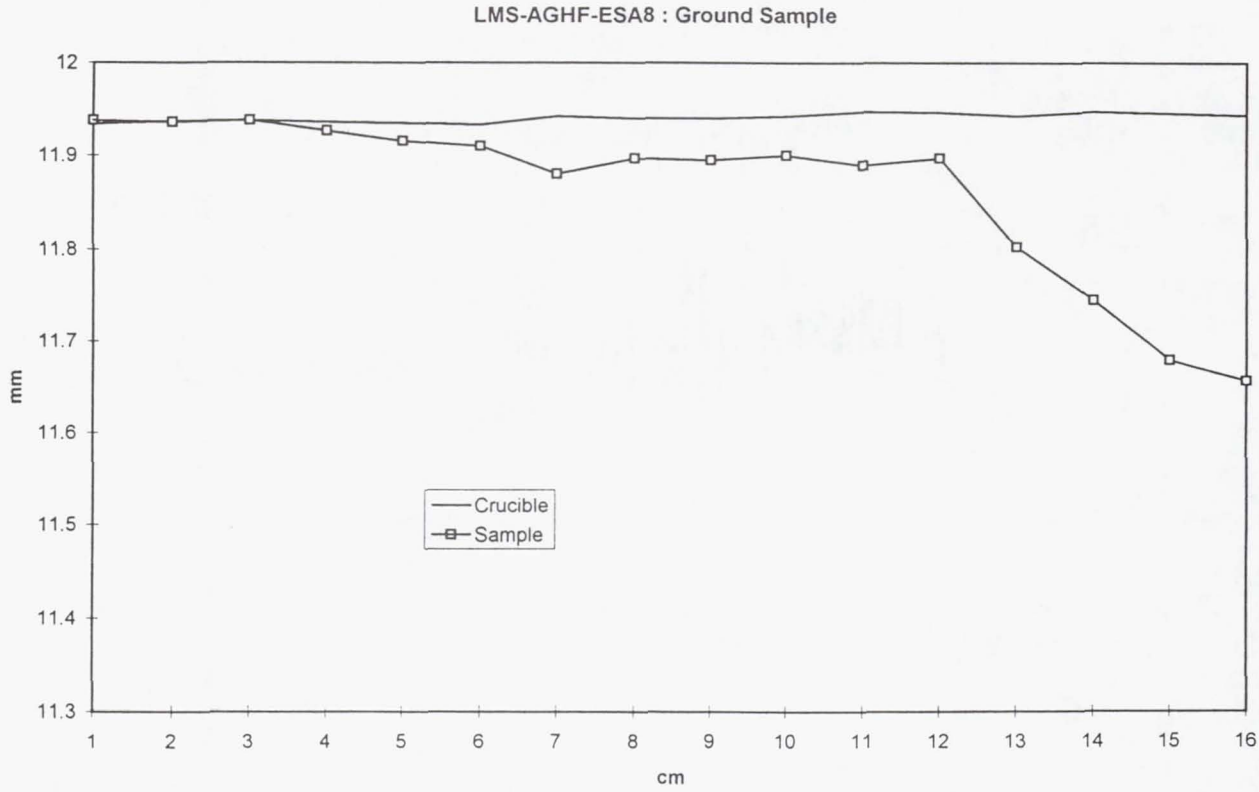

Fig 8: Internal diameter of the crucibles and external diameter of the sample after the ground experiment, versus sample length.

4 RESULTS ON CHEMICAL SEGREGATION

After cutting longitudinally in two parts, the samples were polished and the chemical concentration of InSb was measured by the electron microprobe method. These analyses are not totally completed. Especially, chemical analysis of the Te distribution is lacking.

Figure 9 shows the longitudinal composition of the flight sample on its axis. Fig 10 A and B give the radial segregation curves, respectively in the BN and in the SiO_2 parts.

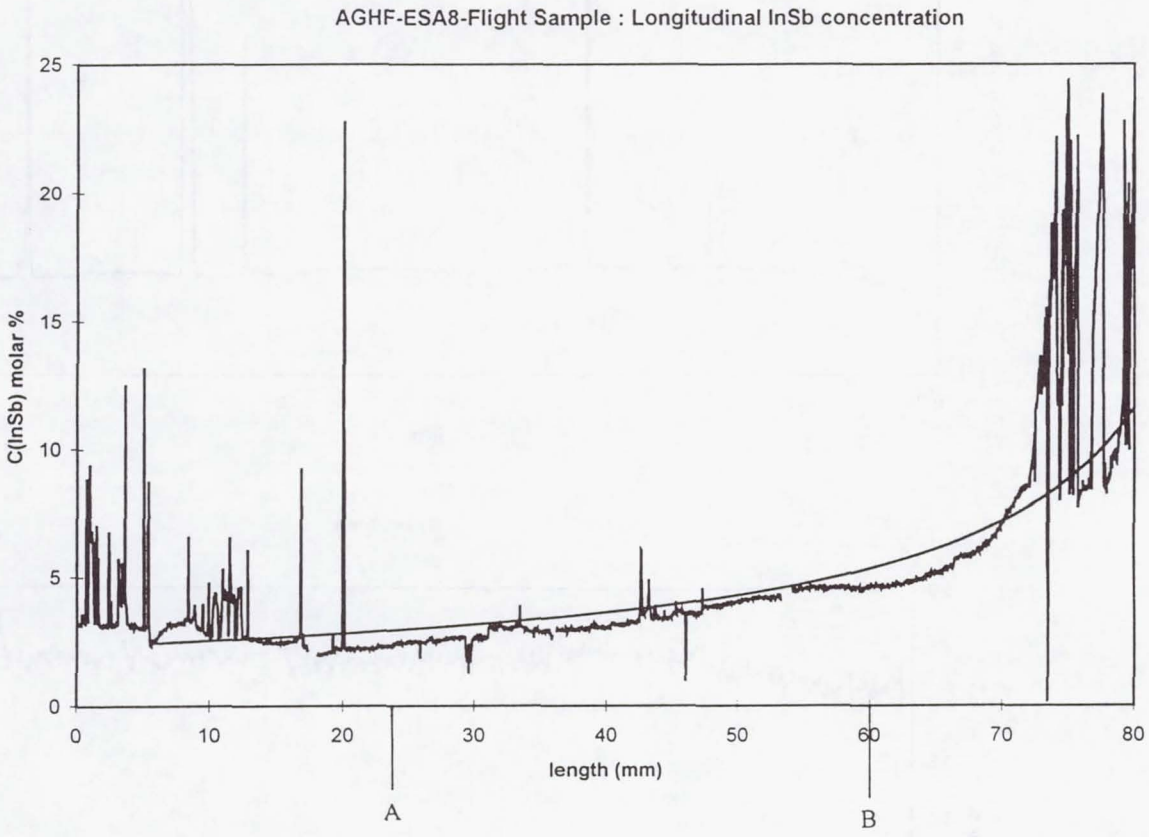

Fig 9: Longitudinal InSb concentration along the flight sample axis. Solid line represents the theoretical Scheil's law with full mixing in the liquid.

The solid line on figure 9 corresponds to the theoretical Sheil equation of full mixing. It appears clearly that the solidification occurred under strong mixing of the rejected InSb in the bulk liquid, whatever the mechanism of mixing. This result is totally supported by the radial segregation curves of fig 10: the sample is practically homogeneous radially, which is characteristic of a very strong mixing at the immediate vicinity of the solid/liquid interface. Only at the very beginning of the growth, a relatively fast increase of concentration occurred, followed by a kind of destabilization that can be seen on the etched sample. Nevertheless, this destabilization does not correspond to the classical

Mullins-Sekerka criteria, because of a too low concentration at this point. The classical destabilisation can be seen at the 10% level, at the end of the sample. Further in depth chemical analysis, especially close to the BN/SiO_2 junction, are needed to have a better insight on the results.

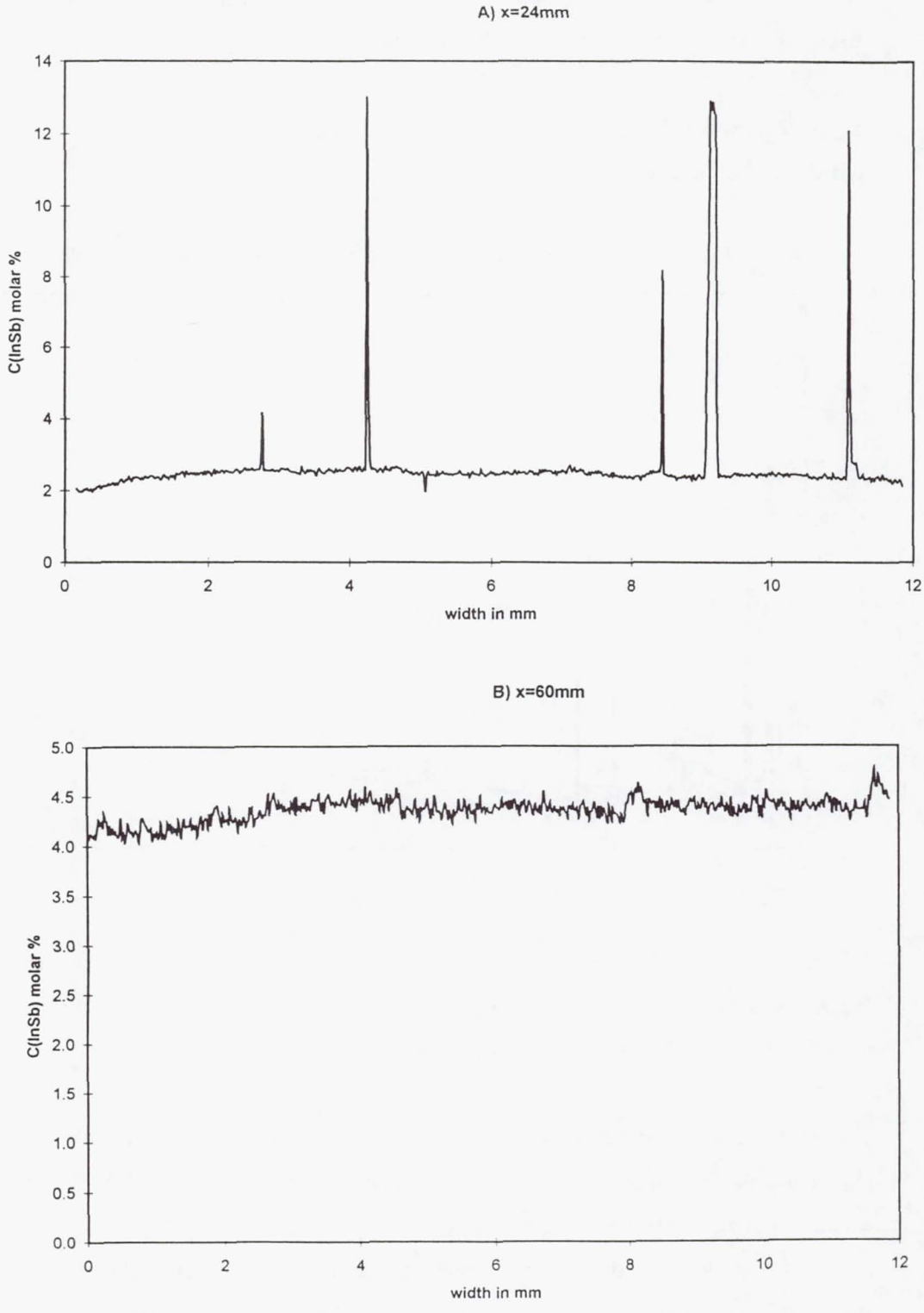

Fig 10: Radial InSb concentration along sample diameter, at the positions A and B.

From the radial segregation curves, it can be expected that the solid/liquid interfaces were practically flat (only curved due to the effect of the crucible on the thermal field) and that its speed didn't experience strong variations. This is in good agreement with the very stable growth rate deduced from the thermocouples' measurements and attenuates the disappointing lack of interface marks for the flight sample.

Because the mixing was very strong close to the interface, it is not believed that some Marangoni convection, associated to the bubble 10 cm away, could be responsible of such a result. From quick estimation of the thermal and solutal Grashoff numbers, it can be concluded that, at the very good gravity level measured during the experiment (better than 10^{-5} g_0 in the frequencies under interest) the residual thermal convection cannot mix the liquid and that solutal convection was always of a lower magnitude than the thermal one.

Then this very surprising result is still to be explained. It should be pointed out that similar results have recently been reported in the case of microgravity growth of concentrated semiconductor alloys: see for example [10 and 11].

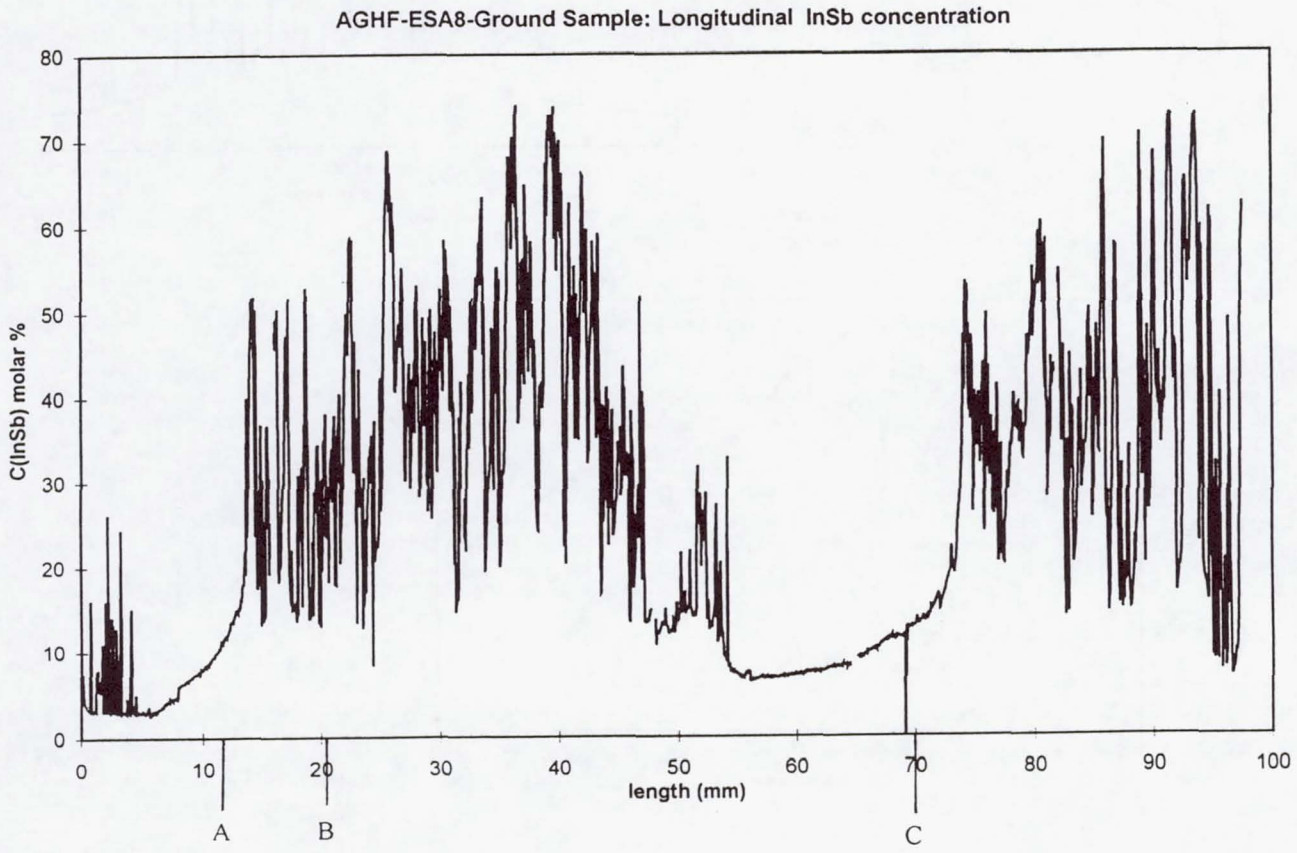

Fig 11: Longitudinal InSb concentration along the ground sample axis.

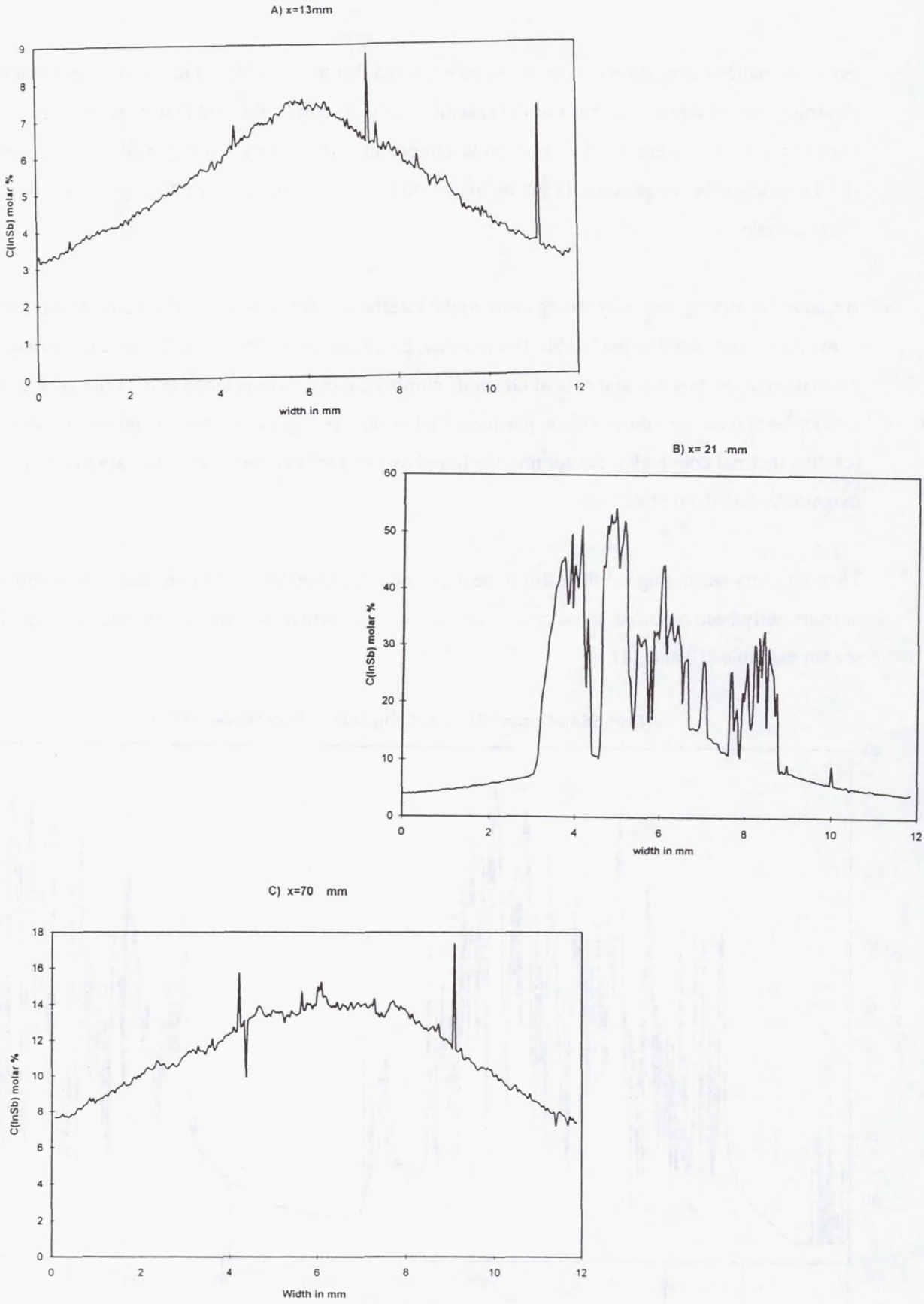

Fig 12: Radial InSb concentration along diameter of the ground sample, at the positions A, B and C.

For the ground sample, Fig 11 and 12 give the longitudinal (on the axis) and radial segregations. Fig 13 shows the structure of the sample and the marked interfaces, as revealed by chemical etching. It can be seen that the middle of the sample is destabilized after some distance of growth in the BN and SiO_2. In between, the quality is rather good. A very qualitative explanation of these observations can be given:

- The initial solid liquid interface is curved, concave when seen from the liquid, due to thermal field.
- When growth proceeds, the InSb is rejected, especially toward the center of the sample (due to the curvature), where the concentration increases (see fig 12-A) and then the melting point decreases.
- This leads to a more curved interface (fig 13) and the process goes ahead with a greater and greater amount of InSb toward the axis.
- Destabilisation occurs (Fig 12-B) when the axial and radial thermal gradients are no more sufficient to stabilise the interface.
- At the junction between the two crucibles, the thermal field in the liquid is highly distorted and this gives a strong thermal convection that mixes the liquid.
- Then the process is repeated in the silica.

Of course, this is only a very hypothetical explanation and it is necessary to quantify the relative magnitude of thermal convection, solutal damping, increase of interface curvature, etc., in the transient process in order to validate it. Because of the very complicated, highly coupled non linear nature of the problem, only a full numerical simulation taking into account all the thermal, hydrodynamical and chemical phenomena can be used for this purpose.

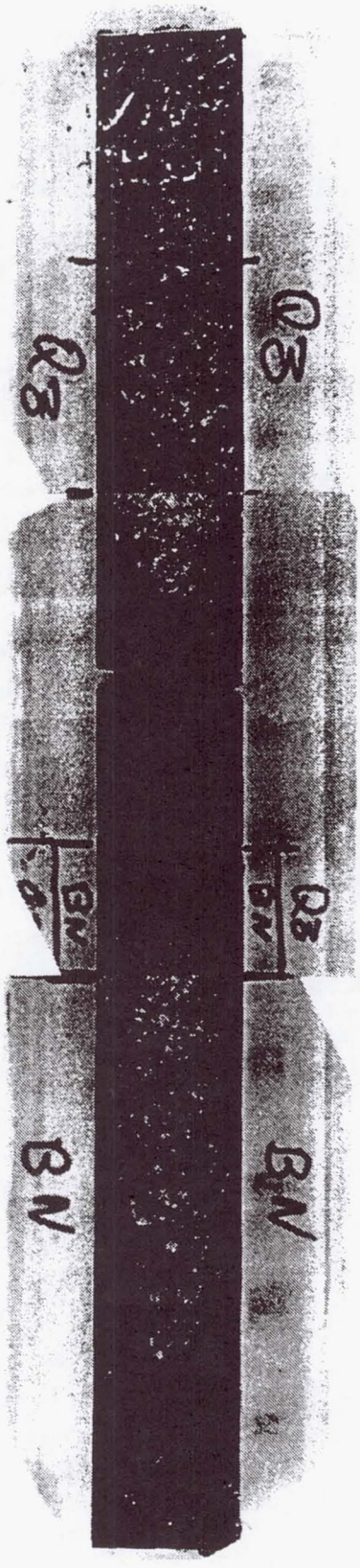

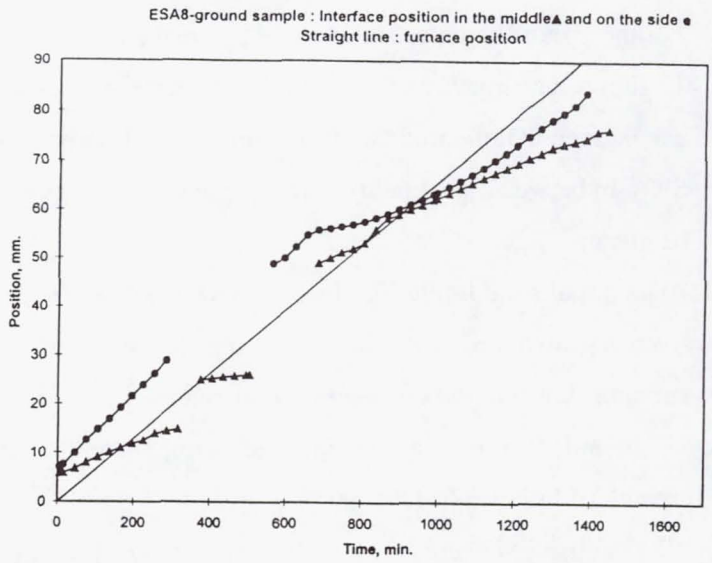

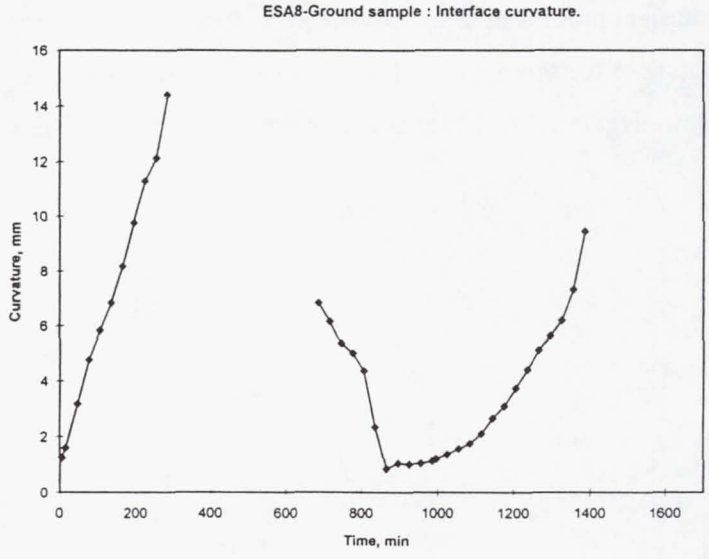

Fig 13: Metallography of the ground sample showing the destabilized central zones and some interface markings. Position and curvature of the viewed interfaces.

5 CONCLUSION

This experiment has given important results concerning two major effects of microgravity in semiconductor growth:

- The de-wetting phenomenon has been quantified in terms of sample roughness and diameter. It has been shown that the contact angle of the liquid on the crucible gives de-wetting when it is high and sticking when it is lower. The measurements and observations are in good agreement with our understanding of the phenomena.
- Chemical segregation analyses have shown that, under less than 10^{-5} g_0 residual accelerations, a full mixing of the rejected solute in the remaining liquid is observed close to the interface. This result cannot be explained with a simple estimation of the leading convective forces.
- Segregations observed on earth show complicated behavior which will necessitate a detailed global numerical simulation to assess our qualitative description. It is hoped that the quality of the experimental results is good enough to validate, or invalidate, the results of the simulation.

Further work on this experiment concerns full analysis of the thermal data, taking into account the effect of the measured chemical analysis on the melting point, in order to get good estimates of the growth rate and thermal gradients. Then results will be compared to detailed numerical simulations. Also, analysis of ground samples at different, lower, compositions are in progress.

Due to the very surprising strong mixing obtained in space, a ground experiment in the horizontal configuration would be of interest in order to solidify under well-known highly convective conditions.

BIBLIOGRAPHY (ref. 7, 8 and 12 are directly related to the ESA8 experiment)

[1] « Handbook of crystal growth », D.T.J. Hurle Editor, North Holland, 1993

[2] T.Duffar, I.Harter, P.Dusserre Journal of Crystal Growth, Vol 100 (1990) pp 171-184

[3] T. Duffar, P. Boiton, P. Dusserre, J. Abadie, J. Crystal Growth, under press.

[4] S. Corriel, F. Sekerka, J. Crystal Growth, 46(1979) 479-482

[5] J.P. Garandet, J. Crystal Growth, 125 (1992) 112-120

[6] C. Barat, Ph-D Thesis, Univ. de Rennes, 1995

[7] C. Marin, P. Dutta, E. Dieguez, P. Dusserre, T. Duffar, J. Crystal Growth, 173 (1997) 271-276

[8] N. Duhanian, T. Duffar, J. Abadie, C. Marin, E. Dieguez, M. Chaudet, 5èmes journées de la matière condensée, Soc. Fr. Physique, Orléans, 28-30 Aout 1996

[9] I. Harter, P. Dusserre, T. Duffar, J.P. Nabot, N. Eusthatopoulos, Journal of Crystal Growth, Vol 131 (1993) pp 157-164

[10] S. Lehoczky, F.R. Szofran, D.C. Gillies, D.A. Watring, NASA μg Materials Science Conf. Huntsville, 10-11 June 1996, NASA conf. Publi. 3342, 345-350.

[11] K. Kinoshita, H. Kato, S. Yoda, Xth European Symp. Physical Sciences in Microgravity, St Petersburg, 15-20 June 1997.

[12] N. Duhanian, T. Duffar, C. Marin, J. Abadie, M. Chaudet, E. Dieguez Xth European Symp. Physical Sciences in Microgravity, St Petersburg, 15-20 June 1997.

Advanced Gradient Heating Facility (AGHF)

Directional Solidification of Al - 1.5 wt.% Ni Alloys

Principal Investigator:

Dr. Henri Nguyen Thi
Université d'Aix-Marseille III
Marseille, France

DIRECTIONAL SOLIDIFICATION OF Al - 1.5 wt% Ni ALLOYS DURING THE LMS - AGHF - ESA7 EXPERIMENTS

H. Nguyen Thi, B. Billia, Y. Dabo
Laboratoire MATOP, Associé au CNRS, Université d'Aix-Marseille III
Faculté des Sciences St-Jérôme, Case 151,
13397 Marseille Cedex 20, France
and
D. Camel, B. Drevet, M.D. Dupouy, J.J. Favier
DTA/CEREM/DEM/SE, CENG, 17 Rue des Martyrs,
38054 Grenoble Cedex 9, France

(1) OBJECTIVES

The final properties of alloys depend strongly on the microstructures formed at the solid - liquid interface during the solidification process. Thus, a precise understanding of this pattern formation is essential to produce high quality materials. In ground-based experiments, even when solidification is performed in a both thermal and solutal stabilizing configuration, strong convective flows remain present due to residual radial thermal gradients. The purpose of the LMS - AGHF - ESA7 experiment is to examine cellular and dendritic arrays under conditions in which convection is minimized and diffusive phenomena are dominant. From these experimental results, scientists will better understand the dynamics of the microstructures and also enlighten the influence of convection on the solidification.

(2) BACKGROUND

During the directional solidification of a binary alloy, three experimental parameters control the morphology of the solid - liquid interface, namely the initial solute concentration, the temperature gradient at the solid - liquid interface and the growth rate. If the first two factors are maintain constant, at slow growth velocities, the solidification front is planar; as the rate is increased, above a critical value, the interface forms a cellular microstructure which becomes dendritic at higher growth velocities. This pattern formation is associated to the Mullins - Sekerka instability [1] and much effort has been devoted to predict the characteristics of the cell or dendritic arrays as a function of the solidification control parameters [2].

However, convection in the melt is well known to be the source of various perturbative effects which can modify or mask some important physical mechanisms [3]. Attempts are often made in directional studies to eliminate buoyancy convective motion in the liquid phase. A simple way of doing this is to ensure that the density gradient is everywhere vertical, the heaviest material being at the bottom. This occurs when growth takes place upwards in an alloy system in which the rejected solute is denser than the solvent. Nevertheless, even in this experimental configuration, it is well known that strong convective flow can exist owing to radial effects, especially in the cellular growth regime [4-6].

As shown in previous experiments [7, 8], a comparative study between samples solidified at 1g and under microgravity is worth to provide critical information concerning the influence of convection upon the directional solidification. Al - 1.5 wt% Ni is well adapted for such a study as the distribution coefficient is much lower than one (i.e. the solute is almost completely rejected at the front during the solidification process) and the solute (nickel) is denser than the solvent (aluminum).

(3) EXPERIMENT

LMS - AGHF - ESA7 experiments

During the LMS mission in June 1996, two Al - 1.5 wt% Ni alloys were solidified in the Advanced Gradient Heating Facility (AGHF) of ESA which is a Bridgman type furnace. After being machined into rods of 8 mm in diameter and 218 mm in length, the samples were elaborated in a boron nitride crucible. To measure temperature gradient and solidification rate during the whole experiment, the cartridges were equipped with 12 thermocouples, glued on the outer surface of the crucible. The processing parameters were predetermined by experiments performed in the breadboard and engineering models of the AGHF in the Centre National d'Etudes Spatiales (CNES) in Toulouse (France).

For both experiments, the thermal gradient was about (35±2) K/cm but two different pulling rate profiles were used. In one experiment, a single low solidification velocity was imposed (V = 0.05 mm/min) whereas in the second run, two growth rates were successively applied (V = 0.2 mm/min and 0.1 mm/min). After a solidified length of typically three centimeters, the residual liquid was quenched by a rapid furnace displacement (V = 10 mm/min). This stopped the solidification and froze the interface microstructure.

Determination of longitudinal concentration profile

The axial concentration profiles are obtained by analyzing in grey levels the X - Ray picture of each sample. This technique presents the great advantage to be non destructive and also enable us to precisely determine the successive steps of the experiment, namely the initial position of the interface and final position of the solidification front just before the quench. The solute concentration is then given in arbitrary unit and will be calibrated with chemical or microprobe analysis in future.

Metallographic procedure

Since metallic alloys are opaque, a somewhat tedious procedure has to be used to obtain the morphology of the solid - liquid interface. During the solidification, after stationary conditions are reached, the shape of the solidification front is fixed by quenching the residual liquid phase. After the experiment, the morphology of the solidification front is revealed by polishing on a longitudinal section of the sample, containing the quenched interface. Transverse sections of the samples are also obtained by the same metallographic procedure.

(4) RESULTS

Concentration profiles

The solute distribution in a directionally solidified alloy depends strongly on the type of transport in the liquid phase [9]. In μg experiments, the absence of convection leads to a diffusive mass transport in the melt as opposed to 1g-experiments where convecto-diffusive transport is dominant. Nevertheless, for the considered convection, namely upwards solidification with a solutal stabilizing effect, a weak longitudinal macrosegregation is expected with a large radial macrosegregation [6]. This point is confirmed by the concentration measurements on 1g-samples as shown in Fig.1. After an initial transient, the average solute composition is quite constant at a value slightly lower than the nominal value. This clearly shows that the convective roll formed weakly mixes with the bulk liquid.

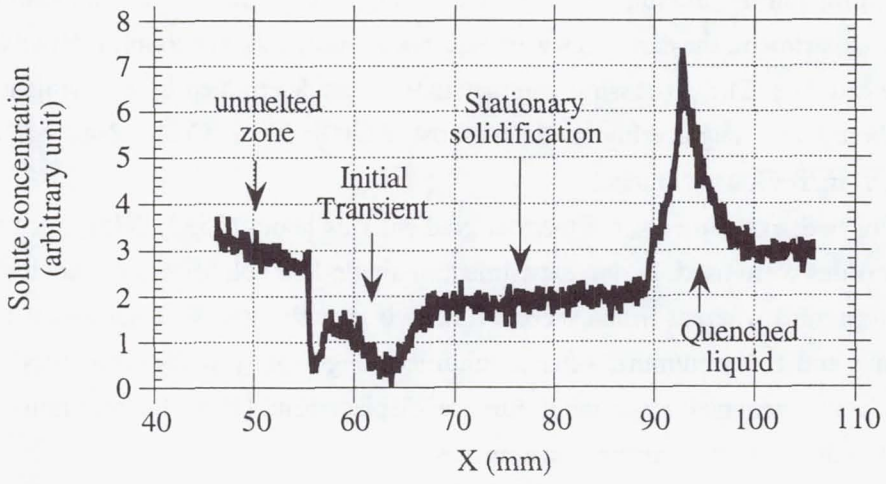

Figure 1: *Longitudinal segregation in Al - 1.5 wt % Ni sample solidified at 1g (G = 33 K/cm and V = 0.06 mm/min)*

Macroscopic shapes of the solidification front

Fig.2 shows typical solidification fronts for sample elaborated at 1g (Fig.2a and 2b) and in μg (Fig.2c). The effect of convection results in a severe distortion of the solidification front which could be divided in a cellular region and eutectic borders. The microstructure is obviously not

uniform across the specimen cross section and therefore a large radial macrosegregation is expected.

The explanation for this effect is that fluid flow occurs as a consequence of gravity. The flow is as described in [4, 6]: the interdendritic liquid which is solute richer, therefore denser than the bulk liquid, moves towards any depressed region of the solidification front and further retards solidification there. When the local solute concentration reaches the eutectic composition, eutectic growth occurs and the lighter liquid moves upwards away from the solidification front. Therefore, if the interface is not completely horizontal, convection inevitably occurs.

In real experimental conditions, this may happen because of the differences in thermal conductivities of the solid, the liquid and the crucible material. This may also be produced by microconvection in the tip zone [4]: when one cell in the cellular array lags behind its neighbors, the denser liquid flows down, further eliminating other neighboring cells and producing the distorted solid - liquid interface.

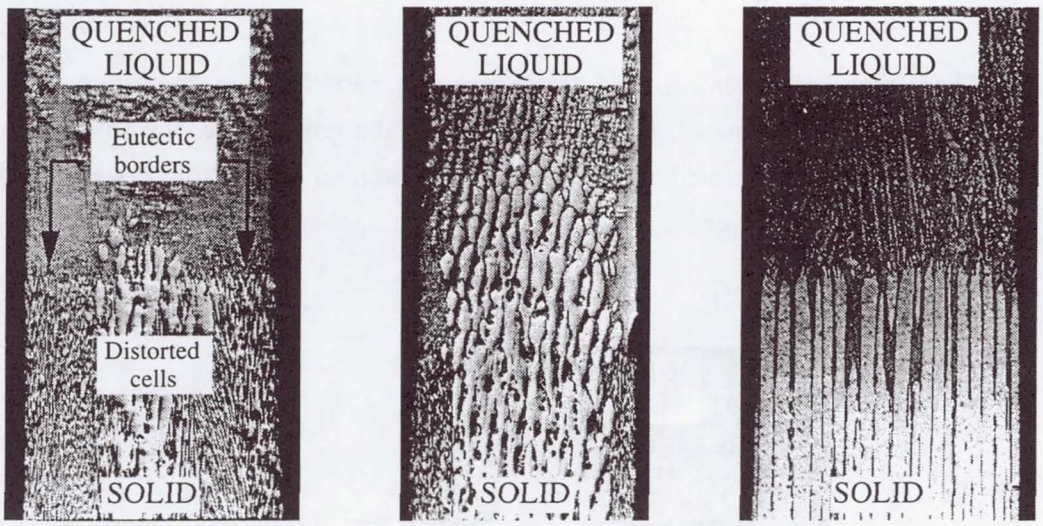

- a- *- b -* *- c -*

Figure 2: *Longitudinal sections of Al - 1.5 wt% Ni samples solidified :*
at 1g: - a - V = 0.060 mm/min, G = 33 K/cm and - b - V = 0.107 mm/min, G = 37 K/cm
in μg: - c - V = 0.053 mm/min, G = 34 K/cm

Microstructures of the solid - liquid interface

Typical cross sections, four millimeters under the quenched interface, are presented in Figure 3. In 1g-specimen (Fig.3a), the microstructure is not uniform across the sample section: in the core of the sample, the microstructure is cellular but becomes more and more dendritic close to the eutectic border. A strong tendency for these dendrites to grow towards the eutectic region is also observed. Moreover, the location where these eutectic regions take birth is not correlated with the symmetry of the thermal conditions applied by the furnace to the sample. As for the AGHF samples grown at 1g, this feature is always obtained and, in most of experiments carried out in our laboratory, the solidification front could be described as consisting of two parts: a cellular or dendritic array and an eutectic zone (Fig.3b). In that case, the cells are said "clustered". On the

contrary, in µg-sample (Fig.3c), the cellular array is rather uniform and covers the whole section.

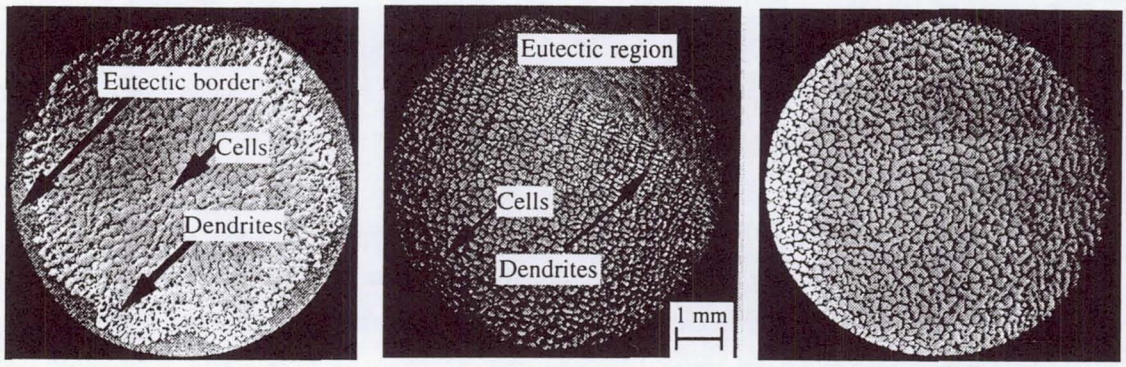

- *a* - - *b* - - *c* -

Figure 3: *Transverse sections of Al - 1.5 wt% Ni samples solidified :*
at 1g: - b - V = 0.06 mm/min, G = 33 K/cm and - c - V = 0.20 mm/min, G = 24 K/cm
in µg: - a - V = 0.23 mm/min, G = 33 K/cm

These conclusions remain valid for experiments carried out at the Laboratory, in the same range of solidification rates. For a higher value of the growth rate, the solid - liquid interface becomes obviously dendritic but the macroscopic distortion of the front does not occur (Fig.4). The influence of the convection is thus more important in the range of low velocities, for cellular or weakly dendritic growth.

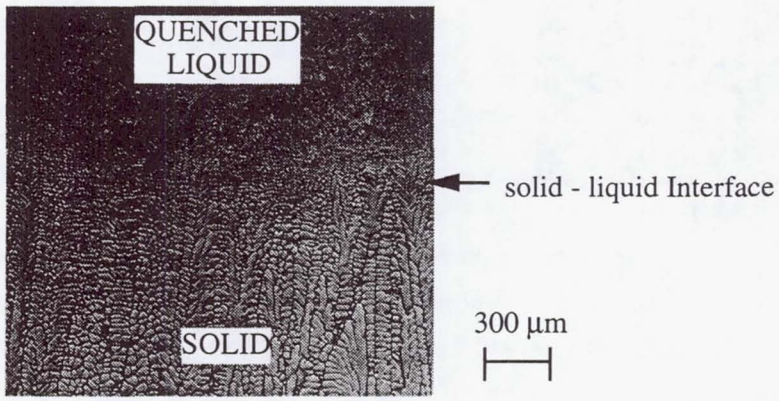

Figure 4: *Longitudinal section of Al - 1.5 wt% Ni samples solidified at 1g: V = 1.7 mm/min, G = 24 K/cm*

All these results are in very good agreement with the model of Dupouy et al, for dendritic growth [6]. Assuming that convection will have a significant effect on the solidification as soon as the ratio Γ of the characteristic velocity of the convective flow U* to the solidification rate V is greater than unity, it is possible to draw the theoretical curve of the transition between the convective and the purely diffusive regimes (Fig.5). Experimental data are also reported in this figure. Circles symbols correspond to cellular microstructures which are strongly perturbed by convection and square symbol to one experiment where the solidification front is dendritic but with no visible influence of the convection.

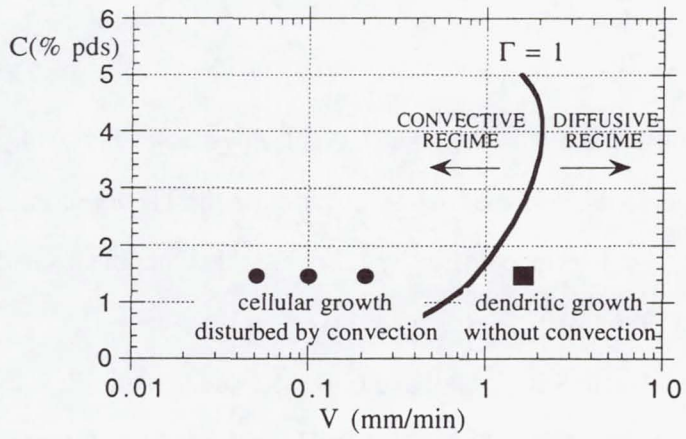

***Figure 5**: Transition curve between convective and diffusive regimes for Al - Ni alloy in the composition - growth rate diagram*

(5) CONCLUSIONS

This comparative experimental study has shown that the coupling between the natural convection and the morphological microstructures can be strong even when solidification is performed in a both thermal and solutal stabilizing configuration. In that case, ground based experiments are invariably perturbed by the thermosolutal convection and, consequently are totally unsuitable for a study of cellular or dendritic arrays. For this alloy, only μg environment with a dominant diffusive transport can provide reliable data.

(6) ARTICLES/PRESENTATIONS RESULTING FROM THE FLIGHT

1) Proceeding of the « *Joint Xth European and VIth Russian Symposium on Physical Sciences in Microgravity* », St-Petersburg (Russia), 15-21 June 1997
2) Proceeding of the « *5èmes Journées Européennes de la Thermodynamique Contemporaine* », Toulouse (France), 16-19 September 1997

(7) ACKNOWLEDGMENTS

The authors are greatly indebted to the Europeen Space Agency and specially to J. Stroede. The financial and technical support of the Centre National d'Etudes Spatiales is also gratefully acknowledged.

(8) REFERENCES

[1] W.W. Mullins and R.F. Sekerka, J. Appl. Phys. 35 (1964) 444

[2] J.S. Langer in Chance and Matter, Lectures on the Theory of Pattern Formation, Les Houches Summer School (Eds by J. Souletie, J. Vannimenus and R. Stora, North Holland (1986), 689)

[3] M.E. Glicksman, S.R. Coriell and G.B. McFadden, Ann. Rev. Fluid Mech. 18 (1986) 307

[4] M.H. Burden, D.J. Hebditch and J.D. Hunt, J. of Cryst. Growth 20 (1973) 121

[5] J.D. Verhoeven, J.T. Mason and R. Trivedi, Metall. Trans. A 17A (1986) 991

[6] M.D. Dupouy, D. Camel and J.J. Favier, Acta Metall. Vol.37, N°4 (1989) 1143

[7] D. Camel, J.J. Favier, M.D. Dupouy and R. Le Maguet, Proceedings of Vith European Symposium on Material Sciences under Microgravity, ESA - SP 256 (1987) 317

[8] B. Drevet, D. Camel, C. Malmejac, J.J. Favier and H. Nguyen Thi, Q. Li, B. Billia, Adv. Space Res. Vol.16, n°7 (1995) 173

[9] J.P. Garandet, J.J. Favier and D. Camel, Handbook of Crystal Growth, Vol.2B (1994) 659

SUMMARY OF THE LMS - AGHF - ESA7 EXPERIMENT

The final properties of alloys depend strongly on the microstructures (cells and dendrites) formed at the solid - liquid interface during the solidification process. Thus, a precise understanding of this pattern formation is essential to produce high quality materials. In ground-based experiments, even when solidification is performed in a both thermal and solutal stabilizing configuration, strong convective flows remain present due to residual radial thermal gradients. The purpose of the LMS - AGHF - ESA7 experiment is to examine cellular and dendritic arrays under conditions in which convection is minimized and diffusive phenomena are dominant. In addition, a comparative study between samples solidified at 1g and under microgravity is worth to provide critical information concerning the influence of convection upon the directional solidification.From these experimental results, scientists will better understand the dynamics of the microstructures and also enlighten the influence of convection on the solidification.

Advanced Gradient Heating Facility (AGHF)

Interactive Response of Advancing Phase Boundaries to Particles

Principal Investigator:

Dr. Ulrike Hecht
ACCESS
Aachen, Germany

INTERACTIVE RESPONSE OF ADVANCING PHASE BOUNDARIES TO PARTICLES

U. Hecht and S. Rex, ACCESS e.V., Intzestr. 5, D-52072 Aachen, Germany

MISSION: LIFE AND MATERIALS SCIENCE - **LMS** / JUNE 1996
EXPERIMENT: **INTRAPP** (ESA5)
FACILITY: ADVANCED GRADIENT HEATING FACILITY (AGHF)
DOCUMENT: PROGRESS REPORT / JUNE 1997

1. INTRODUCTION

The high strength/density ratio makes particle reinforced aluminum alloys with precipitation-hardenable matrices e.g. 2XXX attractive for use in aircraft and automobile structural parts. The most effective way to achieve high quality - low cost PRMMC products is via casting processes. Development and application might be improved by understanding of the microstructural evolution during solidification, especially with respect to the distribution of the reinforcing particles.

The microgravity experiment INTRAPP, performed in the Advanced Gradient Heating Facility (AGHF) during the Spacelab Mission-LMS in June '96, aimed to investigate specific transient and morphological aspects of the interaction between inert particles and solidification interfaces in the aluminum based commercial composite material 2014 + 10 vol% Al_2O_3. Actually, it is not evident if and how particle pushing criteria developed for planar interface in steady state motion can be transfered to transient and/or non-planar solidification. The experiment was completed in November 1996 with the realization of flight identical ground reference tests in the Flight Model (FM) of the AGHF. The samples and the corresponding processing data sets are since available for evaluation.

The experimental results, summarized in appendix 1, show that several specific interaction patterns between particles and solid/liquid interfaces have been successfully generated in the different sample regions as corresponding to the selected processing parameters:

1. particle pushing at coarsening grains in the mushy zone of the fusion interface during stabilization
2. particle pushing and the transition from pushing to engulfment in directional solidification with planar interface within the initial transient
3. interdendritic entrapment of the particles during directional solidification with dendritic interface
4. interdendritic entrapment of particles at columnar and equiaxed dendrites during solidification at constant cooling rate

This report addresses the evaluation of the thermosolutal history and of the related particle distributions in the different sample regions, with focus on the phenomenon of particle pushing in the initial transient. The results will be discussed in comparison with theoretical model predictions.

2. EXPERIMENTS

The microgravity experiment INTRAPP comprised the experiment development in the BBM and the EM of the AGHF, as well as processing of two cartridges in orbit and in 1g reference runs, correspondingly. The cartridge design, schematically represented in figure 1, shows the core parts containing two cylindrical samples, one sample subjected to directional solidification with planar and dendritic interface and the second one to solidification at constant cooling rate with columnar and equiaxed dendritic morphology.

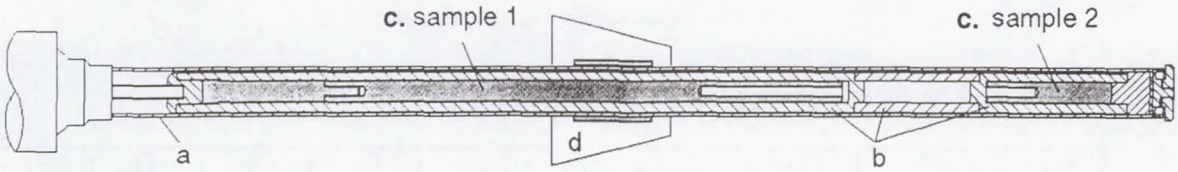

Figure 1. Cartridge design
a. cartidge tube (Ta-W 2.5 wt%), **b.** crucibles and isolating ring (BN-ZrO_2 composite), **c.** samples (2014 + 10 vol% Al_2O_3), ∅ 8 *206 mm and ∅ 8 *39 mm **d.** liquid metal ring
A number of 14 Inconel-sheethed thermocouples (typ N ∅ 0.5) were placed in individual grooves at the outer circumference of the crucibles at different longitudinal position.

2.1. Sample material

The sample material consisted of the commercial composite 2014 + 10 vol% Al_2O_3 (DURALCAN), the particles being of nominally 13 µm mean size and of angular morphology with an elongation factor close to unity. Figure 2 shows the solidification characteristics (2a.) and the microstructure (2.b) of the sample material in the as extruded condition. Table 1. contains the standard composition of the matrix alloy.

For the investigation of particle / interface interactions in this composite, knowledge about the segregation behavior of the matrix, as well as a reasonable estimation of the magnitude of repulsive forces is required. Qualitatively, the segregation behavior and the invariant reactions in 2014 correspond to the quaternary system (Al-Cu-Mn-Si) as assessed by Mondolfo [1]. The magnitude of repulsive forces is related to interfacial energies in the three phase system: particle / liquid / solid, or else to constants of molecular interaction like the Hamaker constant [2] or the London-van der Waals constant [3]. For Al_2O_3 in 2014 the interfacial energies σ_{ps}, σ_{pl} and σ_{sl} are taken from literature data refering to aluminum or aluminum alloys [4,5]. The interfacial energy difference, calculated according to [6], gives $\Delta\sigma$ = 0,68 [N/m], the accuracy being estimated to ± 0,2 [N/m].

2.2. Processing parameters

The parameters, heater temperature and furnace velocity, were defined such as to obtain directional melting of the two samples, followed by directional solidification of sample 1 at two different furnace velocities and subsequent solidification of sample 2 at a constant cooling rate of 4 [K/min], the furnace being immobile.

For sample 1 the parameters were selected as to obtain an interface position (isotherm 620°C) close to the middle of the adiabatic zone and moreover, to obtain the transition from particle pushing to engulfment prior to the morphological destabilization of the planar interface.

Figure 3 summarizes the processing parameters applied in the two µg- and the corresponding 1g-reference runs. Figure 4 shows typical gradient profiles along the directionally solidified sample 1.

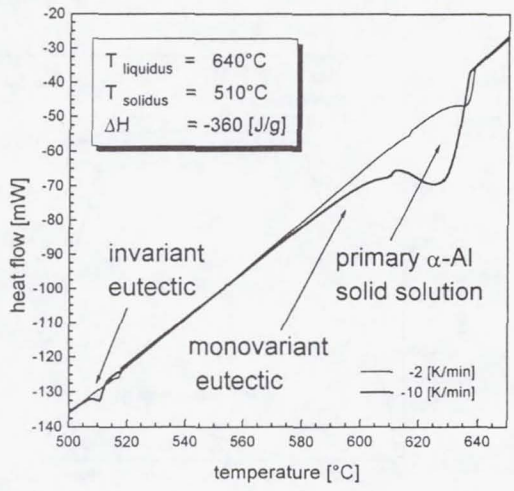

Figure 2a.
Solidification characteristics of the matrix alloy determined by differential scanning calorimetry (typ Perkin-Elmer DSC 7)

Table 1. Chemical composition of the matrix alloy 2014

Element [wt%]	Cu	Si	Mn	Mg	Fe	Cr	Ti	Zr	Al
min.	3.90	0.50	0.40	0.40	-	-	-	-	bal.
max.	5.00	1.20	1.20	0.80	0.10	0.15	0.15	0.25	bal.

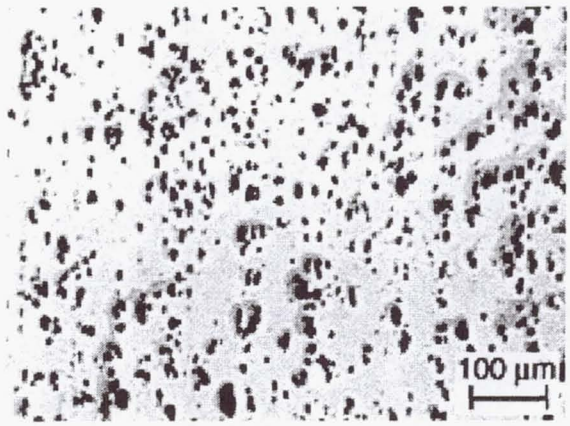

Figure 2 b. Microstructure in the as extruded condition. The alignement of the alumina particles along the direction of extrusion (vertical) can be observed.

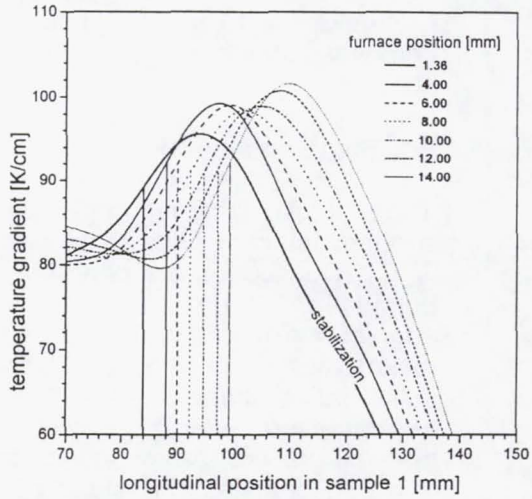

Figure 4. Gradient profiles
Axial profiles of the thermal gradient for consecutive furnace positions in FM2 and the corresponding positions of the interfance (v = 0.03 mm/min)

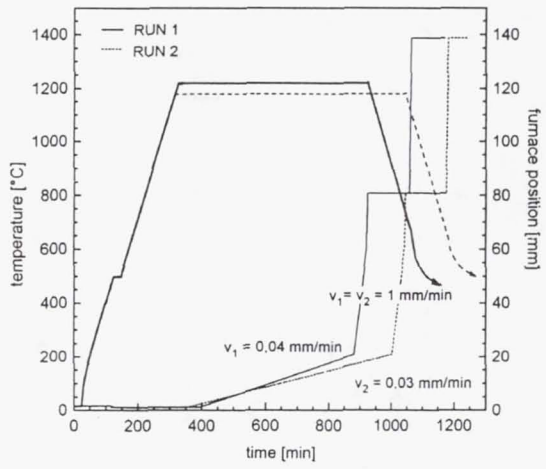

Figure 3. Processing parameters
Diffuser temperature and furnace velocity profiles applied during run 1 (FM1, GM1) and run 2 (FM2, GM2). The two "quenching" operations were ment for rapide furnace positioning, rather than for structural conservation of the interface.

2.3. Evaluation techniques

The evaluation is based on the analysis of the particle distribution and its correlation with the thermosolutal conditions during solidification. For this purpos the samples were cut along their longitudinal axis by using a diamond wire saw of 170 µm wire diameter, one sample half being dedicated to longitudinal analysis, the second to the preparation of transversal metallographic sections.

The analytical techniques that have been employed are: microscopy (LM and SEM), interactive automated image analysis and EDX / WDX for measurement of solutal profiles in line scans and area mappings. The thermal history is based on as-registered thermocouple data, while ongoing work is dedicated to a more detailed simulation of the thermal field.

3. EXPERIMENTAL RESULTS

3.1 Transition from particle pushing to engulfment at planar interface in the initial transient

Solidification with planar interface in the initial transient is associated with the increase of concentration for alloying elements with subunitary partition coefficient, of volume fraction of pushed particles and of the interface velocity. Under these conditions the particle / interface interaction reveals two aspects: First, because more evident to observe, the transition from pushing to engulfment occuring when a critical pushing configuration is reached. Second, the evolution of the pushing configuration prior to particle engulfment, which is suspected to occur in subcritical force equilibrium with continuous adjustment of the liquid gap width.

In the given experimental conditions the transition from pushing to engulfment was observed after 2.5 mm (run 1) and 5.5 mm (run 2) of particle pushing. The critical velocity model of Pötschke and Rogge [7], transcribed into a more general form gives:

(1)
$$v^2\eta^2[\alpha + \beta(c/G\eta) + \gamma(c/G\eta)^2] = 1.69\,\Delta\sigma^2$$

$$\alpha = 240(R/a_0)^2\mu^2$$
$$\beta = 16\,(R/a_0)^2\mu\,(|m_l|\Delta\sigma / kD)$$
$$\gamma = (|m_l|\Delta\sigma / kD)^2$$

For the experimental verification of this model the evaluation of the thermal gradient and of the solute concentration at the transition to engulfment is required. Moreover, knowledge of the effective interface velocity and of the effective melt viscosity can be attempted via the models of Coriell et al. [8] and Stefanescu et al. [9].

Figure 5 shows the critical thermal gradients at the transition to engulfment, as extracted from thermocouple data.

Figure 6 exemplarily shows the solutal profiles measured along one scan line in sample FM2.

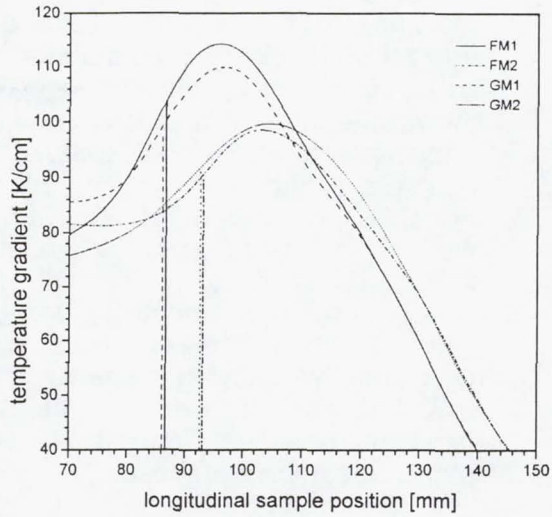

Figure 5. Temperature gradient profiles at the transition pushing / engulfment. From the axial gradient profiles at the moment of engulfment, the critical gradient is determined as corresponding to the respective position of the interface at the onset of engulfment.

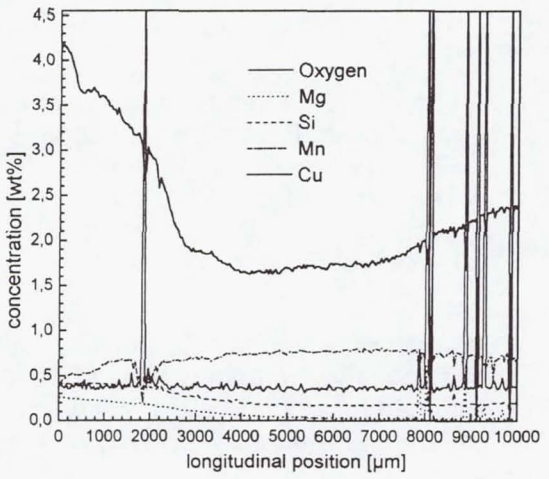

Figure 6. Axial concentration profile along the initial transient of FM 2.
Three parallel WDX-line scans were measured per sample as follows:
scan length 10 mm, step width 40 µm and beam defocus 5 µm.
The oxygen peaks correspond to Al_2O_3-particles and roughly indicate the beginning of pushing and the transition from pushing to engulfment.

In addition, stage mapping of the elements Cu, Mn, Mg and O was performed for the samples FM2 and GM2 in order to check if the longitudinal scans are indeed representative. Figure 7 shows one longitudinal scan through the mapping area in FM 2 in comparison to the lateral scatter. From the line scans the critical concentration of the individual alloying elements was extracted as corresponding to the respective position of beginning engulfment. Figure 8 and figure 9 show the evolution of two representative alloying elements, copper and manganese, along the initial transient of the flight and ground reference samples respectively.

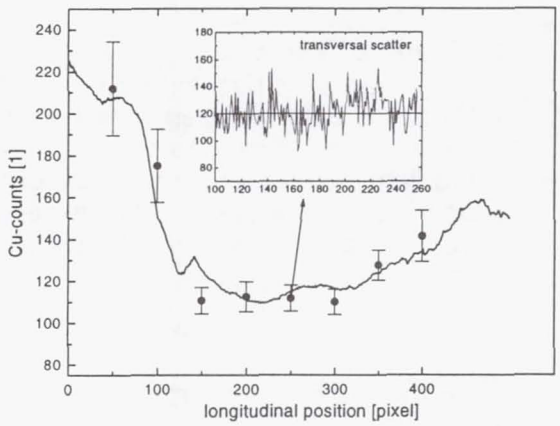

Figure 7. Sections through the area mapping of the copper concentration in FM 2. Area size: 5 *10mm
The error bars indicated at selected positions of the longitudinal scan represent the transversal scatter.

In order to define the "critical concentration", the multiply alloyed matrix is reduced to an equivalent binary matrix via the transformations [10,11]:

$$(2)\quad ce = \Sigma ci, \qquad \text{for } i = 1 \text{ to } 5$$
$$m_l e = (\Sigma ci \cdot m_l i) / ce$$
$$ke = (\Sigma ci \cdot m_l i \cdot ki) / ce \cdot m_l e$$

Here, the indices "i" are related to the individual binary systems between Al and the alloying elements, while "e" represent the equivalent binary data.
These transformations are rather simple. A more refined analysis of the segregation behavior based on thermodynamics of the multiply alloyed matrix will further enhance the evaluation.

This is especially true with respect to the partition coefficients and the liquidus slopes. In ternary or higher alloyed systems the sign of the liquidus slope changes for certain elements (e.g. Mn in Al-Cu-Si-Mn) from negative to positive, as the system passes into the binary eutectic region, although the partition coefficient remains subunitary. It depends on the sign of m_l, wether the solutal distortion induced by a particle leads concave or convex deformation of the interface.

A check of the matrix segregation has been made by solidifying the particle free alloy 2014 at constant cooling rate and measuring the solute profile across a dendrite arm via EDX. The segregation pattern, represented in figure 10, shows a change from increasing ($m_{lMn} < 0$) to decreasing Mn-concentration ($m_{lMn} > 0$) related to intermetallic phase nucleation in the system Al-Cu-Mn-Si-Mg [1].

A detailed investigation of the segregation profiles obtained during directional solidification of the INTRAPP-samples will address this behavior of Mn, which is representative for specific elements in higher alloyed systems.

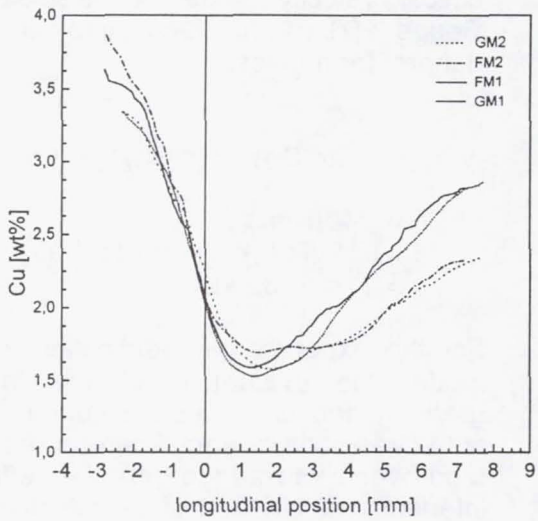

Figure 8. Axial concentration profiles for the main alloying element Cu.
The sample position "0" corresponds to the initial position of the liquidus temperature + 10°C, being the position at which the string-like particle agglomerates, originating from coarsening grains in the mushy zone, cease to exist.

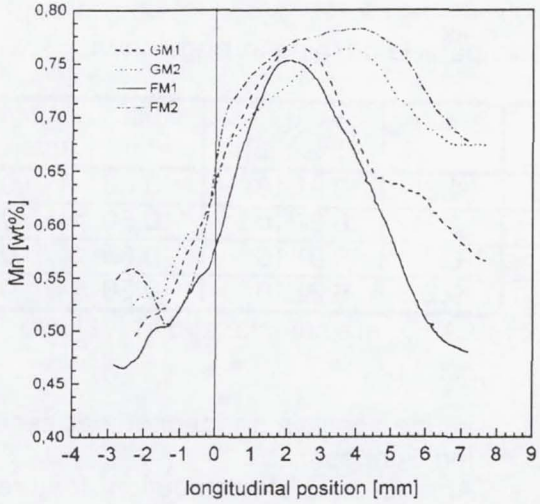

Figure 9. Axial concentration profiles for the alloying element Mn.
The position "0" corresponds to the initial position of the liquidus temperature + 10°C, e.g. to the position at which the string-like particle agglomerates, originating from coarsening grains in the mushy zone, cease to exist.

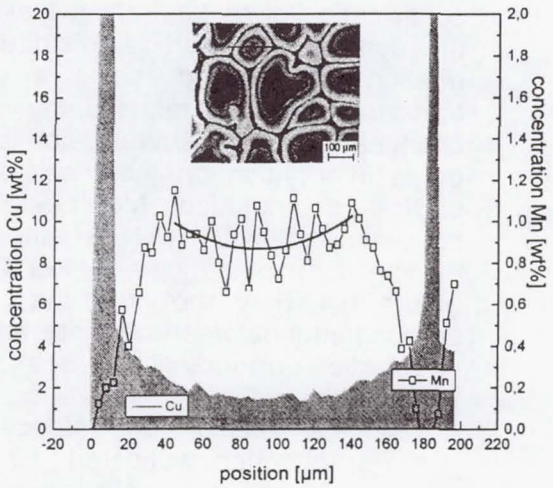

Figure 10. Solute profile across a globulitic dendrite obtained during unconstained solidification of the particle-free matrix alloy 2014 at 2 [K/min]. Colour etching with Weck's reagent gives an optically accessible view of the segregation . The EDX scan line is indicated in the inserted image.

To date, the critical conditions for the transition from particle pushing to engulfment should be regarded as an order of magnitude analysis only. They are summarized in Table 2.

Here, the effective melt viscosity is calculated according to:

(3) $\eta = \eta_0 \cdot (1+2.5\ f_p+10.05\ f_p^2)$ [8]
(4) $f_p = (\pi R^2 z) \cdot f_{p0} / (\pi R^2 z')$,

where z represents the pushing length, z' the width of a boundary layer where the pushed particles accumulate e.g. z'=1.2 [mm], R the sample radius, and f_{p0} the initial volume fraction of particles in the MMC.
Based on these data, the critical velocity is calculated according to Pötschke and Rogge [7] and included in table 2. It results that the experimental data are in good agreement with the model predictions, especially when taking into account that the interface velocity is lower than the furnace translation velocity. This correction will be included during further work. An analysis of errors associated with the critical velocity values will be addressed together with a more rigouros treatment of the segregation in the matrix.

Beside the transition from pushing to engulfment, a quite challenging question arises with respect to the evolution of the pushing configurations along the initial transient. We expect these configurations to be subcritical force equilibria, continuously adjusting to the change of governing variables (c, η, v, G). The adjustment process is realized through changes of the local curvature and of the liquid gap width. Subcritical force equilibria are consistent with the concept of the critical velocity, or more general of the "critical conditions", as being the maximum velocity - or the maximum concentration etc. - for which force equilibrium can be established.

Transfering the model of Pötschke and Rogge to transient pushing along the initial transient predicts, that with increasing concentration of the alloying element both forces increase, with the viscous drag force increasing more rapidly than the molecular repulsive force. Consequently, force equilibrium is established at gradually decreasing width of the liquid gap. Figure 11 principally shows the evolution of subcritical force equilibria with changing curvature of the interface according to [7]. The analysis of the experimental data on transient pushing is in progress.

Table 2. Critical conditions for the transition from particle pushing to engulfment

Run	G [K/cm]	c [wt%]	$\|m_l\|$ [K/ %]	k	η [Ns/m2]	vexp.	vcrit. [7] [µm/s]
Flight 1	109	2.93	3.20	0.2	$3.9E10^{-3}$	0.66	0.60
Flight 2	87	3.04	2.98	0.2	$6.3E10^{-3}$	0.50	0.43
Reference 1	101	2.74	3.10	0.2	$3.9E10^{-3}$	0.66	0.61
Reference 2	88	2.98	3.03	0.2	$6.3E10^{-3}$	0.50	0.44

Data for calculation of the critical velocity in 2014 / Al_2O_3 are summarized in [12]

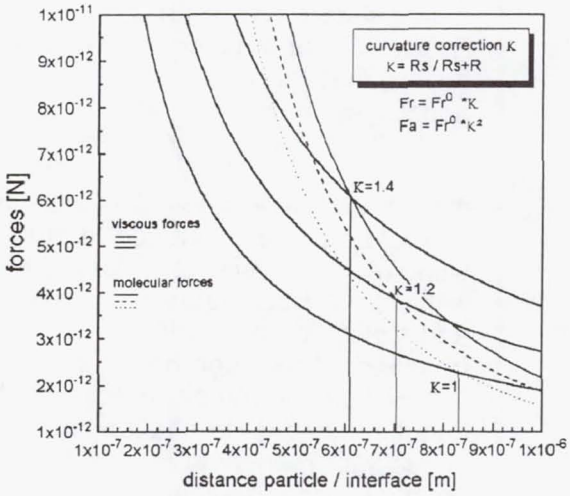

Figure 11. Subcritical force equilibria configurations calculated according to [7] for a 20 µm-sized Al_2O_3 particle in the equivalent binary matrix Al-X, as function of the particle induced interface curvature (e.g. concentration).

3.2 Particles at dendritic solid/liquid interface in constrained and unconstrained growth

The INTRAPP samples contain two regions with dendritic morphology: In samples 1 constrained dendritic growth was generated over a length of 40 mm, at v=1.0 [mm/min] and a thermal gradient of 85 to 105 [K/cm]. The samples 2 were designated to unconstrained dendritic growth at constant cooling rate, but due to residual axial temperature gradients the dendritic structure is columnar with a transition to equiaxed growth in the region of the cartridge hot end only. In the dendritic regions particle distributions were measured by interactive automated image analysis on longitudinal sections of the flight samples.

Among several distribution features, the mean choard length (MCL) has been selected for evaluation. The MCL is measured perpendicular to the sample axis, thus representig a means to quantify the spacing between stringlike particle agglomerates that occur in columnar dendritic structures. Figures 12 and 13 show the evolution of the MCL in the flight samples, for solidification at a furnace velocity of 1 mm/min and at constant cooling rate of 4 [K/min], respectively. The evolution of MCL with proceeding solidification gives interesting insight into the dynamics of particle distribution in relation to spacing selection during transients that are induced by velocity changes etc.. Its absolute value scarcely bears information on the mechanism of particle incorporation. More details can be visualized in LM with an appropriate etching technique (figure 14) or by SEM (figure 15). They show that the particles are located inbetween dendrite arms e.g. in eutectic surroundings, for both, ground and flight samples.

Models based on steady state pushing, although validated for planar interface [7], fail to explain the observed interdendritic particle distribution e.g. the critical velocity for unconstrained growth configuration calculated according to [7] ranges from 10^{-13} to 10^{-14} [m/s] depending on the concentration. This extreme reduction of the critical velocity compared to the constrained planar growth is due to the fact, that a particle of lower thermal conductivity than the melt depresses the interface via both, thermal and solutal distortion. This order of magnitude analysis suggests, that interdendritic particle incorporation is based on entrapment mechanisms, rather than on "pushing in force equilibrium".

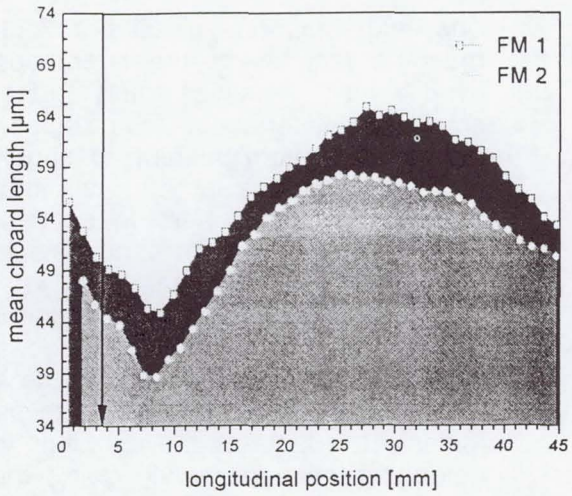

Figure 12. Particle distribution in the *flight samples, directionally solidified* at v=1.0 mm/min, G = 85-105 K/cm. The evolution of the mean choard length shows the response of the particle distribution to the velocity transient at the steplike increase of the furnace translation velocity from 0.03 (0.04) to 1 mm/min (arrow).

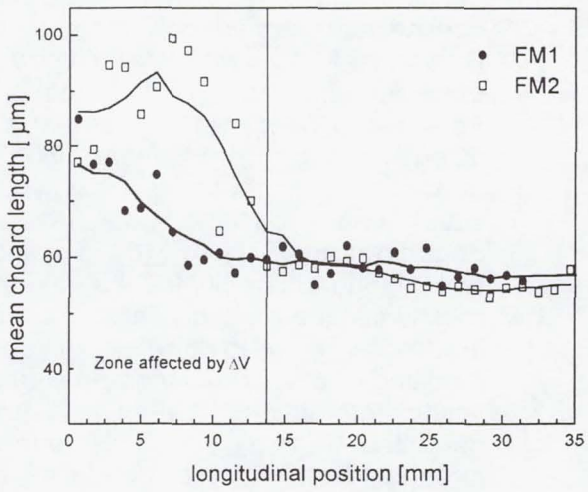

Figure 13. Particle distribution in the *flight samples, solidified at a constant* cooling rate of 4 K/min.
The high values of the MCL in the left region are due to the fact that filling of the free volume is accomplished by flow of particle free matrix melt.

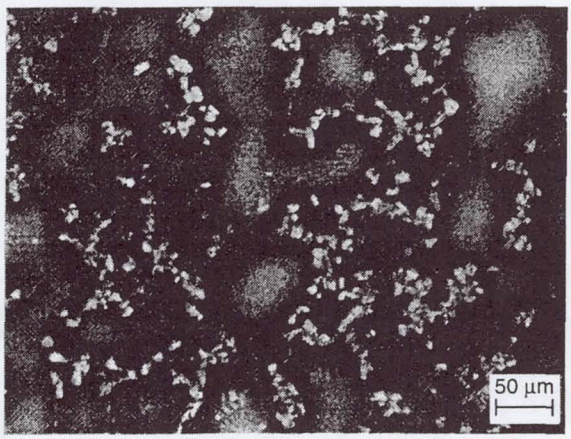

Figure 14. Interdendritic location of particles in FM 1, solidified at a constant cooling rate of 4 K/min. Colour etching with Keller's reagent reveals the segregation pattern of the matrix.

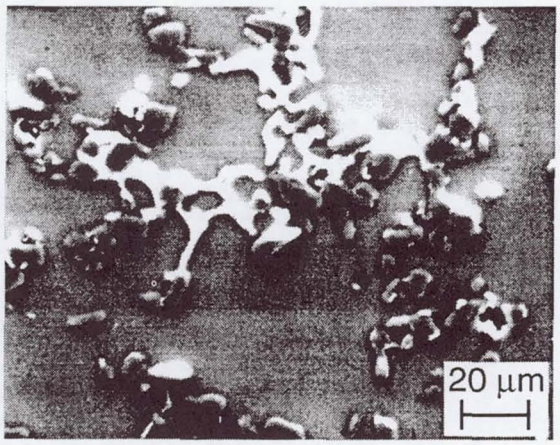

Figure 15. Interdendritic location of particles in FM 2, solidified at a constant cooling rate of 4 K/min. The Al_2O_3 particles (dark) are surrounded by eutectic (white).

Complementary experiments on particle behavior during solidification at constant cooling rate, carried out in 1g-gravity via Differencial Scanning Calorimetry point towards following specific mechanisms: For cooling rates ranging from 0.2 to 50 [K/min] particle entrapment inbetween dendritic branches is followed by subsequent pushing at coarsening dendrite arms (figure 16). For cooling rates higher than 50 [K/min] entrapment mechanisms are mainly related to particle induced morphological instabilities, resulting from the longrange thermosolutal interaction between particles and dendrites (figure 17). This interaction strongly disturbs the dendritic microstructure compared to the unreinforced matrix.

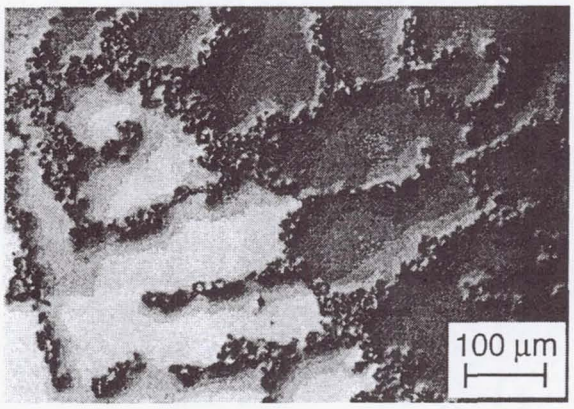

Figure 16. Coarsening controlled interdendritic particle distribution
dT/dt = -2 [K/min]

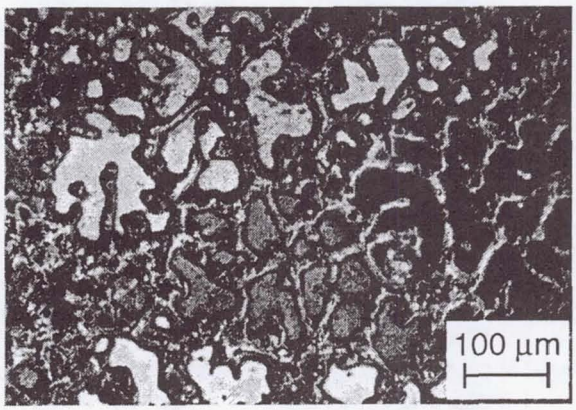

Figure 17. Entrapment controlled interdendritic particle distribution
dT/dt = -100 [K/min]

4. CONCLUSIONS AND OUTLOOK

The experimental results reflect the manifold facettes of the interaction between inert particles and advancing solid/liquid interfaces. From these, only the transition from pushing to engulfment at planar interface in the initial transient has been reported here in some detail, showing that the critical conditions for the transition to engulfment are in good agreement with predictions according to the model of Pötschke and Rogge. Moreover, particle pushing along the initial transient indicates that the system particle / interface adapts to the evolution of the governing variables, while going through a series of subcritical pushing configurations. The evaluation of these pushing configurations is in progress.

These results show, how sensitively particle pushing depends on processing conditions and more, how complex it is to transfer physical models (binary systems, individual particle etc.) to real systems, even in the rather simple case of a planar interface. The situation gets more complex - and more interesting - for dendritic morphologies of the solidifying matrix in constrained or unconstrained growth.

Here, critical velocity models fail to predict the observed interdendritic particle incorporation by several orders of magnitude, meaning they are non-applicable as such. More general, the phenomenon of pushing in force equilibrium is probably irrelevant for particles at morphologically structured interfaces, being covered by thermosolutal interaction mechanisms. Detailed understanding of the interaction, therefor requires numerical simulation to resolve the timedependent thermosolutal and force interaction at high spacial resolution.

So far, the dependence of the critical conditions for the transition from pushing to engulfment on the gravity level, is not evident. This is expected to be more pronounced for pushing during the initial stages of the initial transient. Here, for low concentration of alloying elements the magnitude of the buoyancy force, ranging at about 10^{-11} [N], is comparable to that of the repulsive and drag forces, meaning that force equilibria are g-sensitive. This aspect will be treated during further evaluation.

REFERENCES

1. L.F. Mondolfo: Aluminum Alloys. Structure and Properties, Butterworth and Co. Publishers Ltd., London, 1976, pp. 656

2. H.C. Hamaker: Physica IV. No 10, 1937, pp. 1058-1072

3. D.E. Temkin et al.: Sov. Phys. Crystallogr., 1977, vol. 22, pp. 13-17

4. L.E. Murr: Interfacial Phenomena in Metals and Alloys, Addison Wesley Publishing Co., Reading, MA, 1975, pp. 101-131

5. J.G. Li: Ceramics Int., 1994, vol. 20, pp. 391-412

6. G. Kaptay: Mat. Scie. Forum, 1996, vol. 215-216, pp. 467-474

7. J. Pötschke and V. Rogge: J. Cryst. Growth, 1989, vol. 94, pp. 726-738

8. S.R. Coriell et al.: J. Cryst. Growth, 1994, vol. 140, pp. 139-147

9. D.M. Stefanescu and F. Rana: in Metallurgical Development and Control in Materials Processing, D.R. Durham and A. Saigal, eds., 1989, vol. 14, pp. 95-100

10. M. Bobadilla et al.: J. Cryst. Growth, 1988, vol. 89, pp. 531-544

11. M. Rappaz et al.: Metall. Trans A, 1990, vol. 21A, pp. 1767-1782

12. U. Hecht and S. Rex: Met. Trans., 1997, vol. 28 A, , pp. 867-874

List of symbols

η	effective viscosity of the melt	Ns/m^2
η_0	viscosity of the pure melt	Ns/m^2
f_p	effective volume fraction of particles	
f_{p0}	initial volume fraction of particles	
v	inerface velocity (furnace velocity)	m/s
c	concentration of alloying elements	wt%
G	temperature gradient	K/m
$\Delta\sigma$	interfacial energy difference	N/m
R	particle radius	m
a_0	atomic distance in the melt	m
μ	ratio of thermal conductivity particle /melt	
$\lvert m_l \rvert$	slope of the liquidus line	K/wt%
k	equilibrium partition coefficient	
D	diffusion coefficient	m^2/s

Acknowledgment

This work was financially supported by the German Agency for Space Affairs DARA GmbH under grant FKZ 50WM9565.

OVERVIEW OF RESULTS

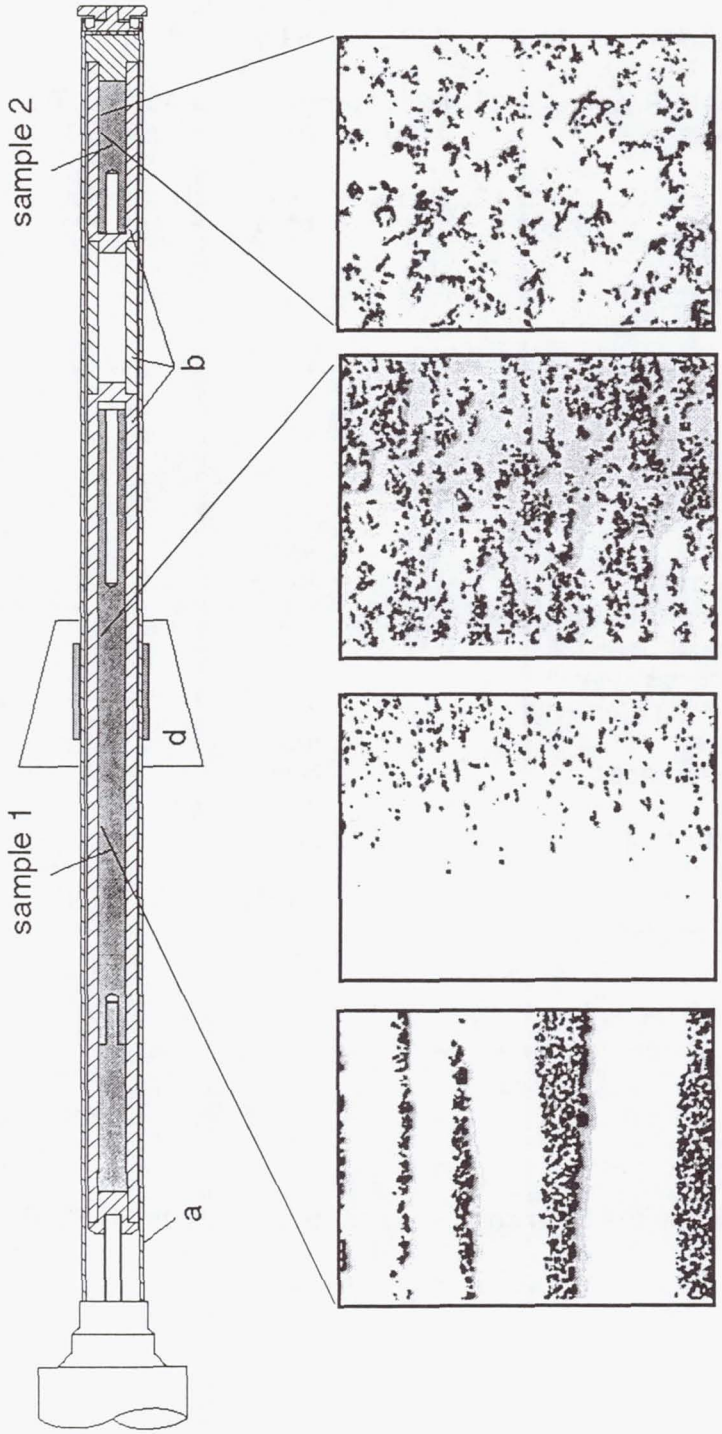

particle entrapment and pushing at columnar and equiaxed dendrites during solidification at constant cooling rate of 4 K/min

particle entrapment and pushing at columnar dendrites during directional solidification:
v = 1.00 [mm/min]
G = 85 ÷100 [K/cm]

transition from pushing to engulfment at planar interface in the initial transient:
v = 0.03 (0.04) [mm/min]
G = 85 ÷110 [K/cm]

particle pushing at coarsening grains in the mushy zone of the fusion front during thermal stabilization

INTERACTIVE RESPONSE OF ADVANCING PHASE BOUNDARIES TO PARTICLES

INTRAPP

U. Hecht and S. Rex, ACCESS e.V., Intzestr. 5, D-52072 Aachen, Germany

Many natural and artificial composite materials offer unique properties that cannot be obtained with a single material. Small ceramic particles for instance, when mixed into aluminum alloy, lead to an increase of the overall strength and abrasive resistance, making the material attractive for use in aircraft and automobile components. It is well known, that the properties of the composite material do not only result from the rule of mixture, but that they are highly sensitive to newly created characteristics of the material. Such characteristics are the structure of the interface between particles and the base alloy and the distribution of particles inside the base alloy. It is also known that particles are preferentially located in specific regions of the base alloy, for instance inbetween the tiny tree-like structures called dendrites, that grow from the molten alloy during solidification. Here, the particles form net-like agglomerates and can lateron act as crack-paths. A reason for this behavior might be the very small forces, some 10^{-8} [N] small, that act between the growing solid and the ceramic particle, pushing the particle further into the liquid as growth proceeds. The forces originate from fluctuations of the electric charge inside the atoms, much like the forces that hold liquid atoms together in the condensed state.

The microgravity experiment INTRAPP, performed in the Advanced Gradient Heating Facility (AGHF) during the Spacelab Mission-LMS in June '96, investigated the behavior of alumina particles (mean size 13 µm) in interaction with advancing solid / liquid interfaces. The samples consisted of the aluminum based commercial composite material 2014 + 10 vol% Al_2O_3. The microgravity results show a large variety of particle behavior: at plane solidification front particles were pushed over several mm like being swept away by a snow-plough, before getting engulfed into the solid. At non-planar front, particles were found to be located inbetween the dendrite arms. Moreover, the large solidification interval of the alloy allowed to show particles being pushed at coarsening grains in the mushy zone.

From the manifold data, particle pushing at plane front was evaluated first and shows good agreement with the theoretical model of Pötschke and Rogge. It also shows the complexity of transfering theoretical models to real commercial materials. This becomes more evident when processing conditions come closer to application, e.g. when dendritic growth is generated in the base alloy: For these situations further modeling activities are necessary when more than a qualitative prediction of the particle distribution is desired. The microgravity experiment gave new impulse to our modeling activities, as it suggests two overlapped mechanisms of particle incorporation at dendritic interface: particle induced entrapment and pushing at coarsening dendrite arms.

The numerical simulation of this dynamic interaction will improve the understanding of the microstructural evolution during solidification and might enhance development and application of particle reinforced composites.

Advanced Gradient Heating Facility (AGHF)

Particle Engulfment and Pushing by Solidifying Interfaces

Principal Investigator:

Dr. Doru Stefanescu
University of Alabama
Tuscaloosa, Alabama

Particle Engulfment and Pushing by Solidifying Interfaces

- *PEP* -

One Year Report

D.M. Stefanescu, PI, B.K. Dhindaw, CoPI, F.R. Juretzko, Gr. Res. Asst.
The University of Alabama

P.A. Curreri, CoPI, S. Sen, CoPI
NASA - Marshall Space Flight Center

S. Breeding, R. Spivey
TEC-Master

During the LMS Mission on the space shuttle Columbia (between June 22 and July 6, 1996), three experiments were conducted to evaluate the effect of liquid metal convection on the phenomenon of particle engulfment and pushing by solidifying interfaces (*PEP*). This report includes the results obtained after one year of analysis of flight results. In addition, a succinct account of ground pre-flight results is included, so that an appropriate comparison can be made. Ground post-flight experiments were also performed, but their analysis is not complete at this time.

1. Objectives

During solidification of metal matrix composites the ceramic particles interact with the solidification front. This interaction is responsible for the final microstructure. The solutal and thermal field, as well as fluid motion at the liquid/solid interface influence both interface morphology and the particle/interface interaction itself. It is thus imperative to fully understand the solidification science and transport phenomena aspects associated with the process in order to control it.

The scientific objectives of this work include: 1) to enhance the fundamental understanding of the physics of interaction between inert particles and the solidification interface, and 2) to investigate aspects of melt processing of particulate metal matrix composites in the unique microgravity environment that will yield some vital information for terrestrial applications. The proposal itself calls for a long term effort on the Space Station. The LMS was a flight opportunity with limited scope. Its main objectives were as follows:

- to evaluate the experimental method including thermal regime, velocity regime, analysis procedures;
- to obtain preliminary data on the critical velocity of particle engulfment.

2. Background

The phenomenon of interaction of particles with melt interfaces has been studied since the mid 1960's. While the original interest in the subject was mostly theoretical, researchers soon came to the realization that understanding particle behavior at solidifying interfaces may yield practical benefits. The experimental evidence demonstrates that there exist a *critical velocity* of the planar solid/liquid (SL) interface below which particles are *pushed* ahead of the advancing interface, and above which particle *engulfment* occurs.

While the problem is relevant to many fields of work such as cryobiology, frost heave in soils, ceramic superconductors, etc., the majority of research work involving *PEP* is aimed at metal matrix composites. Here the driving force is to obtain a homogenous particle distribution. To achieve this goal one has to control the cooling conditions of cast composites in such a way that the

solidification velocity is higher than the critical velocity. Only with a homogeneous distribution of the reinforcement phase the improved mechanical properties of these materials can be fully exploited.

While numerous models have been proposed over the years in an attempt to explain particle behavior at the SL interface, a paucity of data exist in particular for ceramic particles dispersed in metal matrices. The basic assumptions of all models include spherical and inert particles, and macroscopically planar SL interface. Existing literature data on this subject are rather limited. With a few exceptions the SL interface, for which the data have been reported, is not planar. Thus, the results do not refer to the pushing / engulfment transition, but rather to pushing / entrapment. The particles used in most studies were not spherical but had an irregular shape, which runs against one of the basic model assumptions. These and other constrains of presently available experimental data make the task of model validation for metallic systems an impossible one. Accordingly, the main goal of the flight program is to provide reliable experimental data that can be used for validation of models describing particle behavior at the solidifying interface in metal matrix composite materials.

3. Methods of Data Acquisition and Analysis

3.1 Selection of metal matrix - ceramic particle system

The metal matrix - ceramic particle system to be used for evaluation of the critical velocity for the pushing / engulfment transition (*PET*) must satisfy the requirements imposed by the major assumptions in existing particle pushing models. These assumptions include: pure metal matrix, planar SL interface, spherical particle, particle is chemically inert with respect to the metal, minimum liquid convection at the SL interface, no flotation or sedimentation of particles.

Based on these restrictions the experimental system chosen consisted of zirconia particles dispersed in a pure aluminum matrix. Aluminum (99.999% Al) was selected in spite of obvious difficulties resulting from its high affinity for oxygen, because it is the basis for the most promising cast metal matrix composites for mass production. In addition, an Al-4.5% Ni alloy was also prepared, to explore the implications of low solutal levels, and of change in wettablity.

Zirconia particle were selected because they do not react with aluminum up to temperatures of 900 °C. While both zirconia and silicon carbide are non-wetting at 700 °C, as the temperature is raised to 1100 °C the SiC becomes wetting, indicating an interface reaction. Zirconia remains non-wetting. Additionally, ZrO_2 is thermodynamically more stable than Al_2O_3. Thus no reducing reaction is expected below 900 °C. Finally, spherical zirconia particles are available, while it was impossible to find spherical SiC particles.

The general shape of the zirconia particles is presented in **Fig. 3-1**. The nominal particle diameter was 500 μm. A size distribution of the particles is given in **Fig. 3-2**.

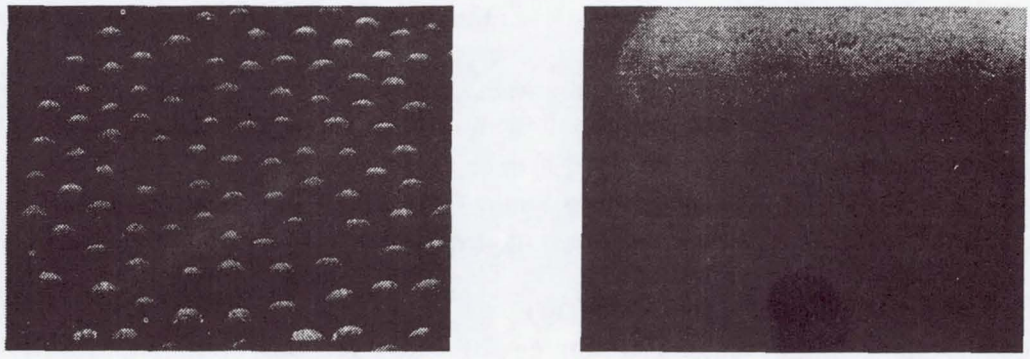

Fig. 3-1 SEM images of zirconia particles

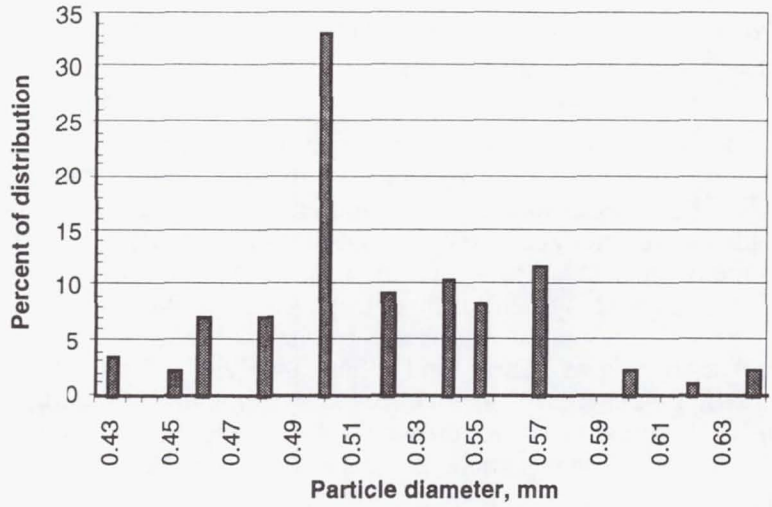

Fig. 3-2 Zirconia particle size distribution

3.2 Sample preparation

The same method was used for ground and flight sample preparation. The samples to be used for directional solidification were prepared by melt processing in a resistance furnace under high purity argon atmosphere and casting into a graphite mold to produce cylindrical specimens of 9 mm diameter and 100 mm length. Two to three vol.% zirconia particles were added to the liquid and mechanically mixed before pouring.

3.3 Evaluation of particle position

The zirconia particle distribution in the aluminum samples after casting and after DS was evaluated through real time X-ray Transmission Microscopy (*RXTM*). Magnifications of up to 20x were used. A three dimensional distribution of the particles was obtained by rotating the sample under the X-ray beam and recording the transmitted image on a video recording device.

In addition to *RXTM* all ground samples were examined by optical metallography. The samples were grounded layer by layer to map the volumetric particle location. About 200 μm of material were removed each time. As the particles were 500 μm in diameter it was possible to locate all of them. The flight samples will also be examined by optical metallography.

A number of criteria for interpretation of experimental results were established to obtain "clean" data for the evaluation of the *PET*, as follows:

- Particles were assumed to be *pushed* if:
  for ground (quenched) samples: particles were found at or very near the quench interface;
  for all samples: there were no particles in the middle of the sample in the DS region.
- Particles were assumed to be *engulfed* if:
  for ground (quenched) samples: there were no particles at the quench interface.
  for all samples: there were particles in the middle of the sample in the DS region;
- Clusters of particles were ignored.
- Particles at the following locations were ignored: the first 3 mm from the initial melt interface; the walls of the sample; particles attached to gas bubbles.

3.4 Ground pre-flight methodology

The ground samples (9 mm dia. x 100 mm length) were directional solidified in a Bridgman-type furnace. A total of 28 experiments were run with Al-ZrO_2 and 22 experiments were run with AlNi-

ZrO_2. The gradients at the SL interface, as measured with the main heater temperature set at 800 °C and the trim heater temperature set at 850 °C, were 100 K/cm. For each sample only one translation velocity was used. After enough solid was produced through DS the crucibles containing the samples were quenched in water.

In DS experiments it is well known that the furnace translation velocity is not the same as the solidification velocity. To evaluate an *average solidification velocity*, the distance between the initial melt interface and the SL interface after quenching was measured and divided by the furnace translation time.

3.5 Flight methodology

During the LMS Mission three samples were directionally solidified in the AGHF facility. They will be referred here as flight samples FM1, FM2, and FM3. The main characteristics of the samples are summarized in **Table 1**. The ampoule-sample assembly for the three flight samples is shown in **Fig. 3-3**. Each ampoule-sample assembly was instrumented with 12 thermocouples. Three of these were placed into a ceramic sheath and incorporated into the sample by casting. The remaining eight were positioned in grooves on the outside of the crucible. Different furnace velocity regimes were used during the DS of the samples. For FM1 a step-wise decreasing regime was used, while for the other two a step-wise increasing regime was chosen. The exact numbers used for furnace translation velocity are given in **Table 1**. The flight data were recorded on a spreadsheet and included furnace position, furnace velocity, thermocouple position, and temperature for each thermocouple versus time. The SL interface velocity resulting from the different furnace translation velocities was calculated based on thermocouple data.

Table 1 Characteristics of flight samples

Flight sample	Material	Ampoule-sample	Velocity regime, μm/s
FM1	Al - ZrO_2	spring-piston	20 - 5 - 0.5
FM2	AlNi- ZrO_2	expansion reservoir	1 - 3 - 9
FM3	Al - ZrO_2	expansion reservoir	1 - 3 - 9

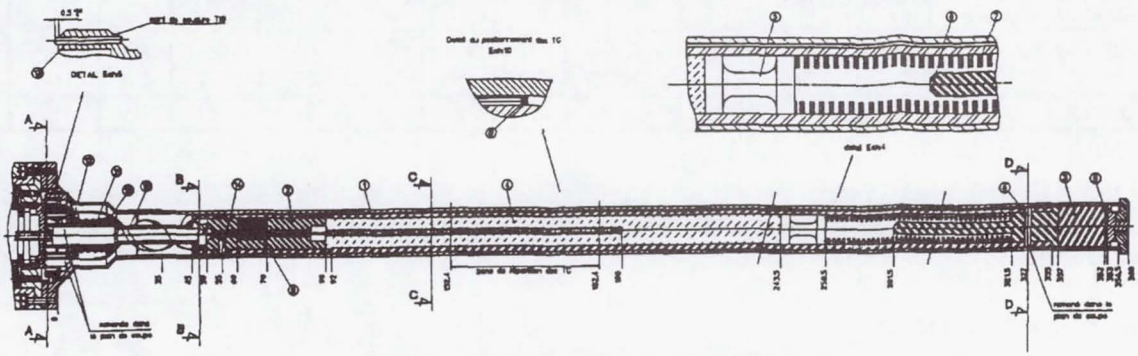

a) spring-piston design: sample FM1

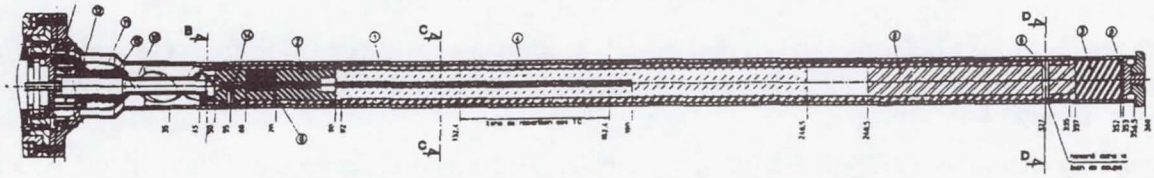

b) expansion reservoir design: samples FM2 and FM3

Fig. 3-3 Design of ampoule-sample assembly.

Each flight sample was examined after micro-g processing by X-ray computer tomography (*CT*) to asses its integrity.

4. Flight Results Compared with Ground Results

4.1 Ground results

From the 28 experiments run only 13 experiments were considered "clean" and were used for the evaluation of the *PET*. Some typical examples of particle distribution after DS are shown in **Fig. 4-1**. Note that on sample Al-14 two particles present in the DS region were not considered as engulfed because they were engulfed during the initial transient when the solidification velocity is not steady.

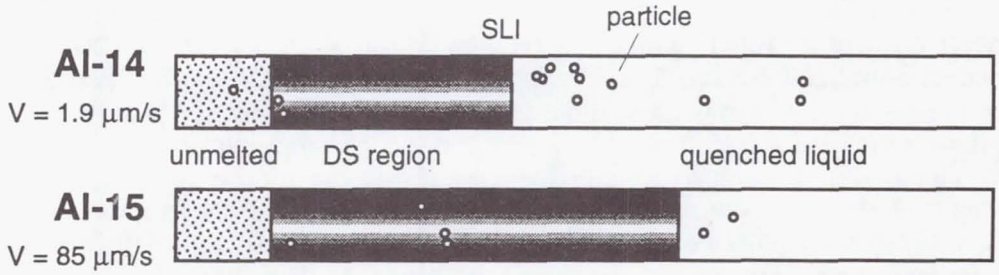

Fig. 4-1 Schematic representation of particle distribution in DS aluminum - zirconia samples: top - pushing; bottom - engulfment.

The results of the directional solidification experiments for the aluminum-zirconia system are summarized in **Table 2**. For ease of interpretation the data have been listed in increasing order of the solidification velocity at which they have been processed. From these data it is obvious that a clear *PET* exists at a solidification velocity between 1.9 and 2.4 μm/s. However, a notable exception is seen for sample Al-18.

Table 2 Experimental results for aluminum - zirconia samples

Solidification velocity, μm/s	1.3	1.3	1.5	1.9	2.4	2.6	5.8	6.5	10.9	11.9	15	44.8	85
Sample no.	Al-22	Al-27	Al-28	Al-14	Al-23	Al-21	Al-29	Al-30	Al-17	Al-18	Al-24	Al-16	Al-15
Result*	P	P	P	P	E	E	E	E	E	P	E	E	E

* P: pushing, E: engulfment

For the AlNi-zirconia system particles were engulfed at all velocities used, that is from 1.2 to 80 μm/s. Thus, it is apparent that the PET should occur at velocities smaller than 1.2 μm/s. This lower range of velocities is beyond the present capabilities of the UA furnace.

4.2 Flight results

4.2.1 Engineering report

Both the cartridge containing the ampoule, and the ampoule after extraction from the cartridge were examined by X-ray and computer tomography (*CT*). The results of the cartridge *CT* evaluation are shown in **Fig. 4-2**.

The spring-piston assembly used for sample FM1 functioned as expected. Some liquid Al leak is seen past the fore side of the piston. This leak does not seem to be significant, since no Al is seen in the 90° position of the *CT* (lower picture on **Fig. 4-2a**). No metal has leaked past the aft side of

the piston, and the nominal operation of the spring-piston assembly was not affected. As a result of this no void is seen between the piston and the sample and the sample itself was sound.

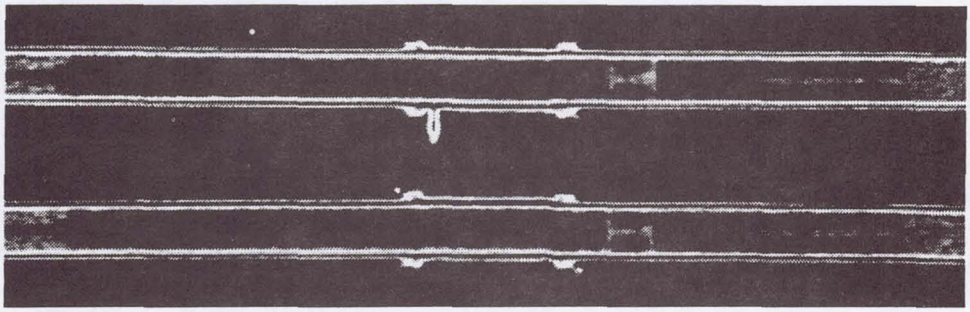

a) sample FM1

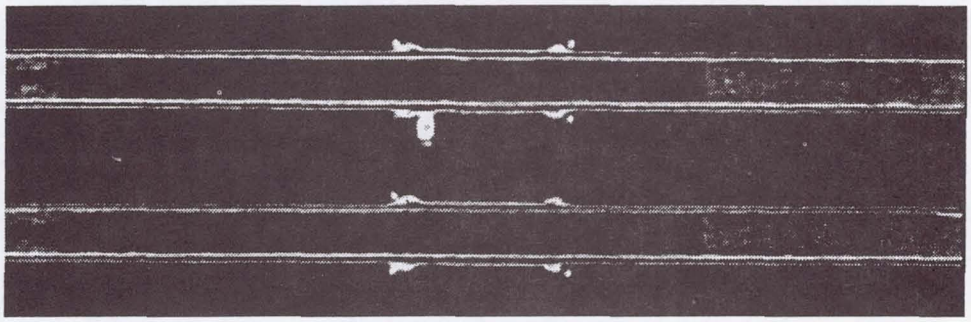

b) sample FM2

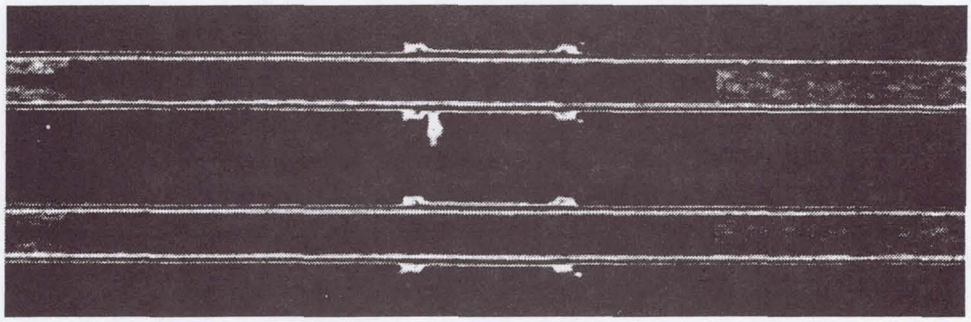

c) sample FM3

Fig. 4-2 *CT* images of the flight cartridge - ampoule assembly.

Sample FM2 was less successful. On **Fig. 4-2b** it is seen that several voids have formed along the sample. It appears that the liquid metal has fractured in that region resulting in a two-part solid sample: an upper part that is in contact with the alumina plug, and a lower part.

Sample FM3 behaved as expected. On **Fig. 4-2c** it is seen that the shrinkage cavity was positioned between the metal and the alumina plug. The sample itself appears to have no significant shrinkage porosity or voids.

4.2.2 Science report

Samples FM1 and FM3 which consisted of Al-ZrO_2 will be discussed first. A summary of *RXTM* particles positions in the FM1 sample before and after flight is given in **Fig. 4-3**. To identify the particles positions with respect to velocity zones, a velocity-distance graph was associated with the *RXTM* images. It is quite clear that at velocities of 5 μm/s and above all particles were engulfed. A more detailed analysis is necessary for the region solidified at 0.5 μm/s. To this effect the region of

interest was enlarged in **Fig. 4-4**. It is seen that as the SL interface velocity decreases from 5 to 0.5 μm/s particles are still engulfed (no.1, 2 and 3). In the region of 0.5 μm/s all particles have been pushed by the interface, with the exception of particle no. 4. However, upon rotating the sample during *RXTM* examination it was found that this particle is very close to the crucible wall, which means it should be removed from consideration. As soon as the velocity increases due to rapid furnace translation at the end of the experiment particles are engulfed (no. 5). A detailed *RXTM* image of the region of interest is presented in **Fig. 4-5**.

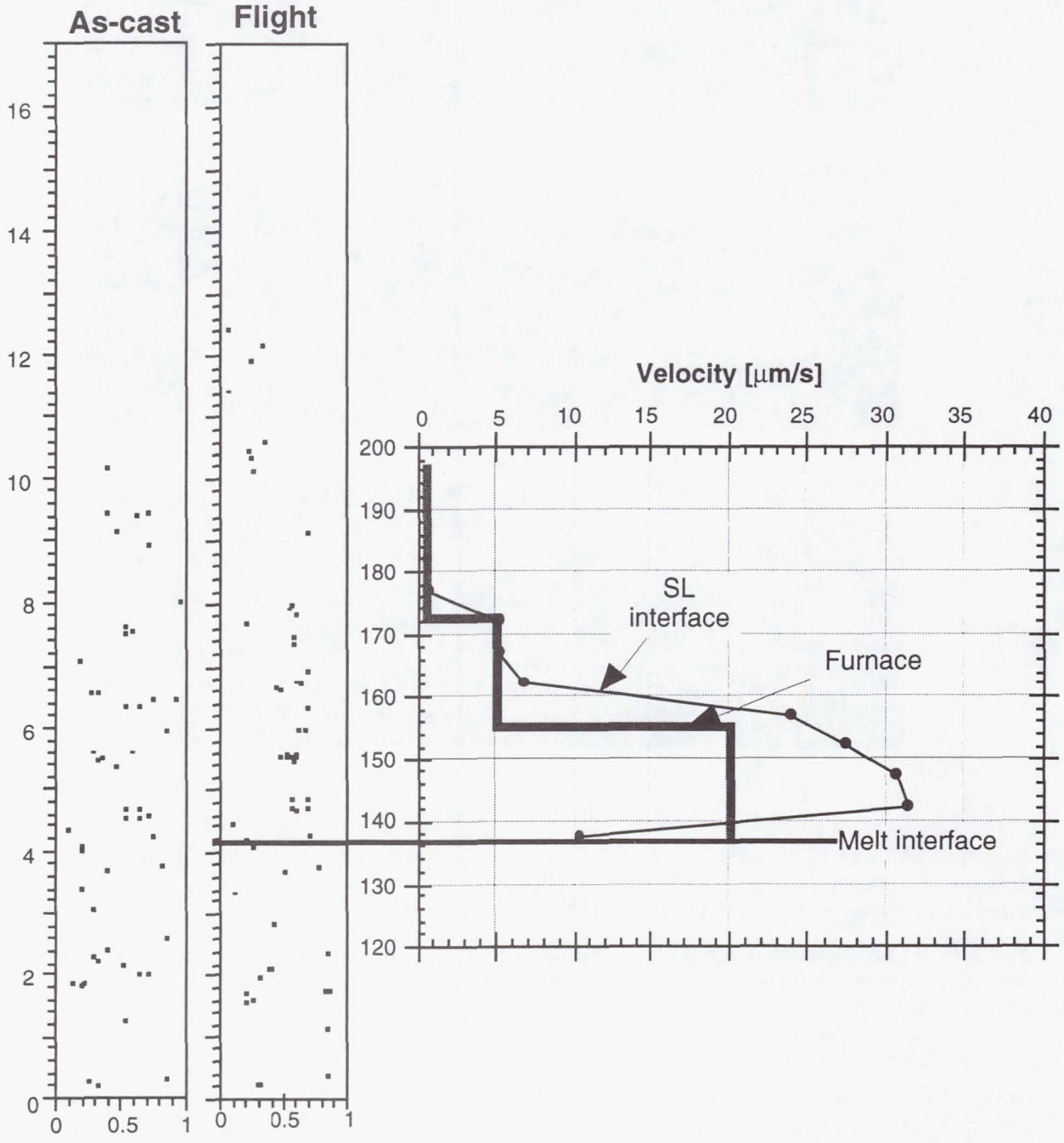

Fig. 4-3 Summary of *RXTM* evaluation of particles positions correlated to furnace and solid/liquid interface velocity for sample FM1.

It must be noted that the interface velocity could be accurately determined only as long as thermocouple information was available. Then, since in the 0.5 μm/s regime our calculations indicated that furnace velocity and interface velocity were linear and had approximately the same slope, the position of the SL interface was extrapolated as shown in **Fig. 4-4**.

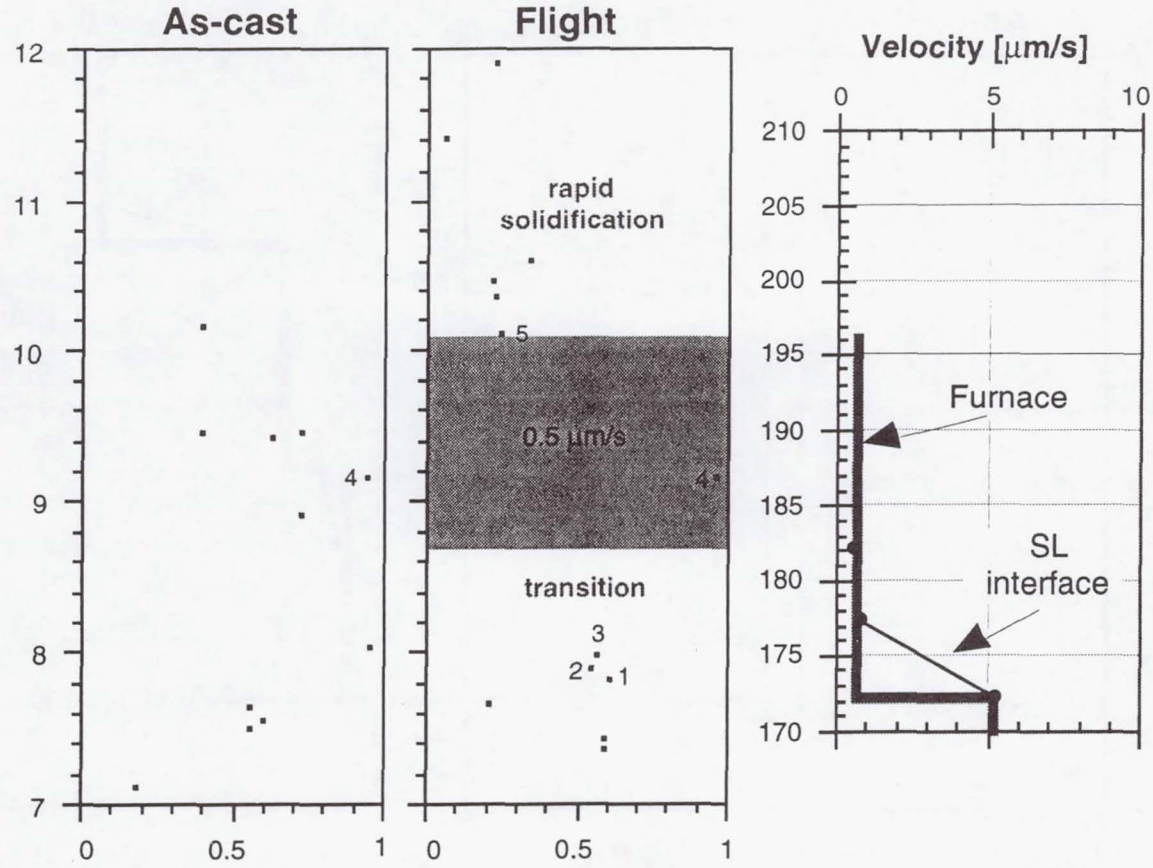

Fig. 4-4 Summary of *RXTM* evaluation of particles positions in sample FM1 in the region of furnace translation rate of 0.5 μm/s.

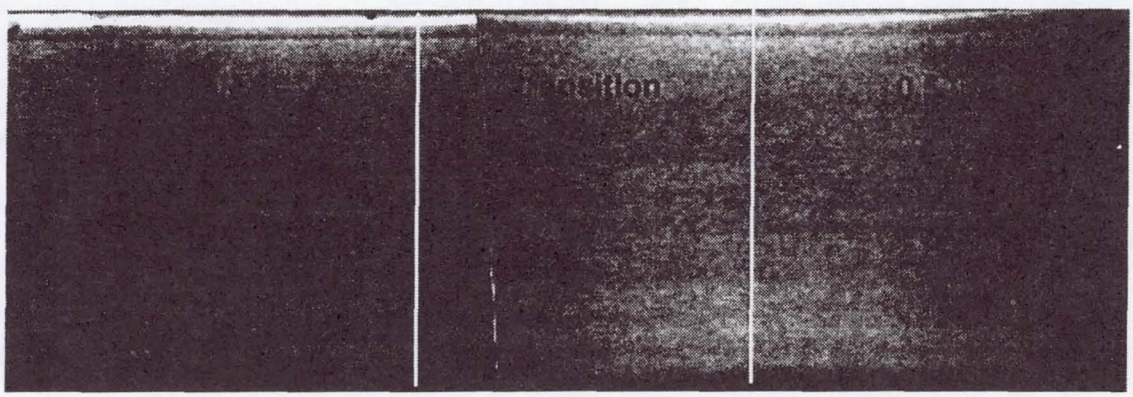

Fig. 4-5 *RXTM* image of flight sample FM1. Particles are engulfed at 5 μm/s and in the transient region. No valid engulfed particles are present in the 0.5 μm/s region.

From the analysis of *RXTM* particles position in the FM3 sample before and after flight (**Fig. 4-6**) it is concluded that, since particles are found in all three velocity regions, engulfment occurred even at the lowest velocity regime used in this sample, which was of 1 μm/s.

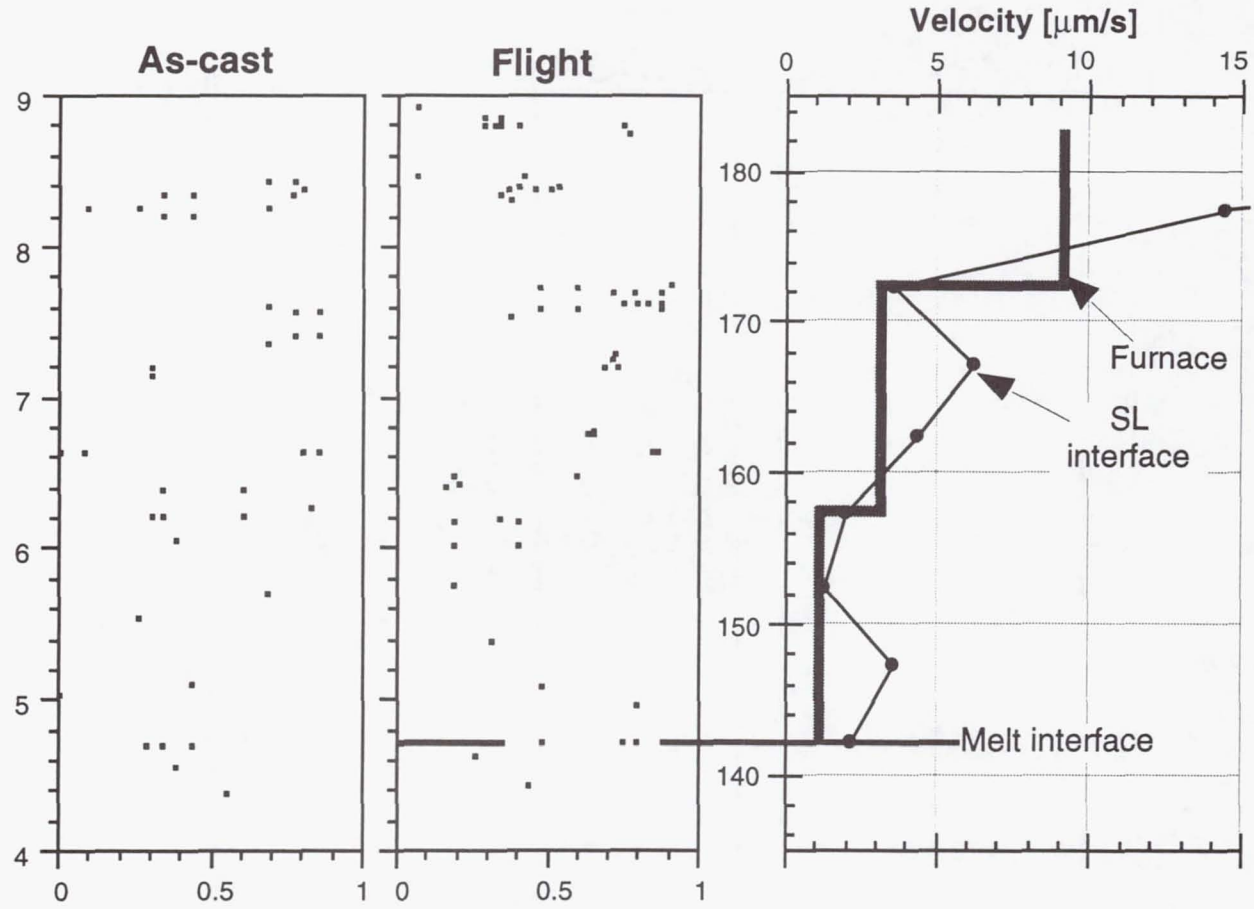

Fig. 4-6 Summary of *RXTM* evaluation of particles positions in sample FM3 in the region of furnace translation rate of 1 and 3 μm/s.

The material used for sample FM2 was AlNi-ZrO_2. The *RXTM* particles position in this sample is presented in **Fig. 4-7**. From the analysis of these data it is apparent that the target interface velocity of 1 μm/s has been achieved only on a very narrow region of the sample. It is not clear if pushing occurred in that region. It was also observed, even by *RXTM*, that many particles have reacted, in particular toward the end of the sample. Clearly, metallographic analysis and additional experiments are required to allow for any definitive conclusions.

4.3 Discussion

One of the basic criteria for acceptability of *PEP* experimental results is an *inert particle / matrix* system. Thus, before any definitive conclusions could be reached on any of the flight samples, it must be documented that no reaction occurred at the particle / matrix interface. At this time only some preliminary results are available on sample FM3. They are illustrated in **Fig. 4-8**. It is seen that as long as moderate temperatures were reached during processing a clean particle / matrix interface is obtained. The white borders on **Fig. 4-8a** are only shadows. However, at temperatures higher than 900 °C, EDAX analysis confirmed that zirconia particles reacted with the matrix, producing an oxidized interface (**Fig. 4-8b**). The oxidized region is Al_2O_3. It is thus clear that a complete analysis of particle /matrix interface must be conducted for the regions of interest.

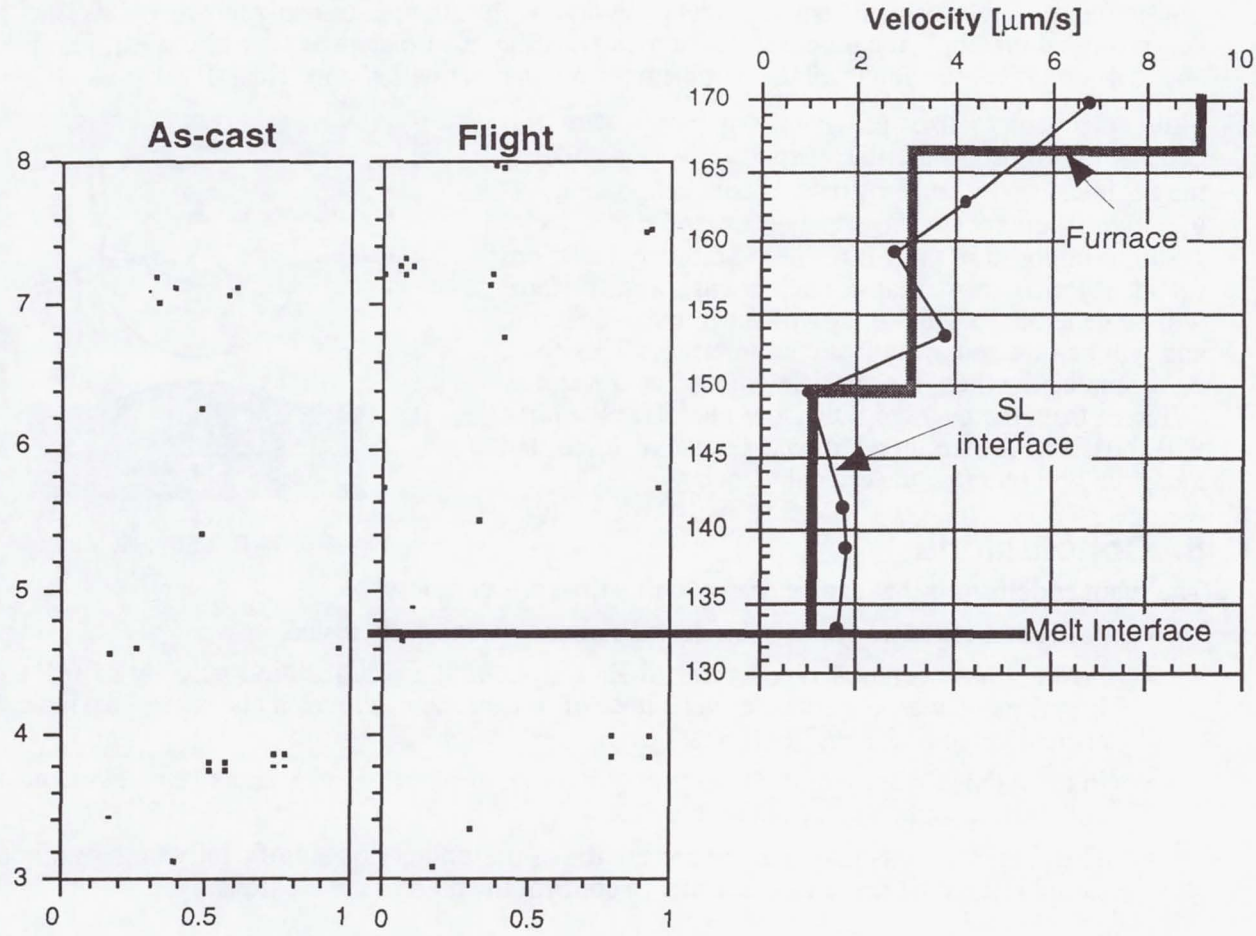

Fig. 4-7 Summary of *RXTM* evaluation of particles positions in sample FM2 in the region of furnace translation rate of 1 and 3 μm/s.

Assuming for the time being that in the controlled DS regions of the samples zirconia particles did not react, it seems to be possible to conclude that the absence of convection resulted in a decreased critical velocity. Indeed, for the Al-ZrO_2 system flight results seem to indicate a critical velocity between 0.5 and 1 μm/s, while ground experiments suggest a critical velocity between 1.9 and 2.4 μm/s.

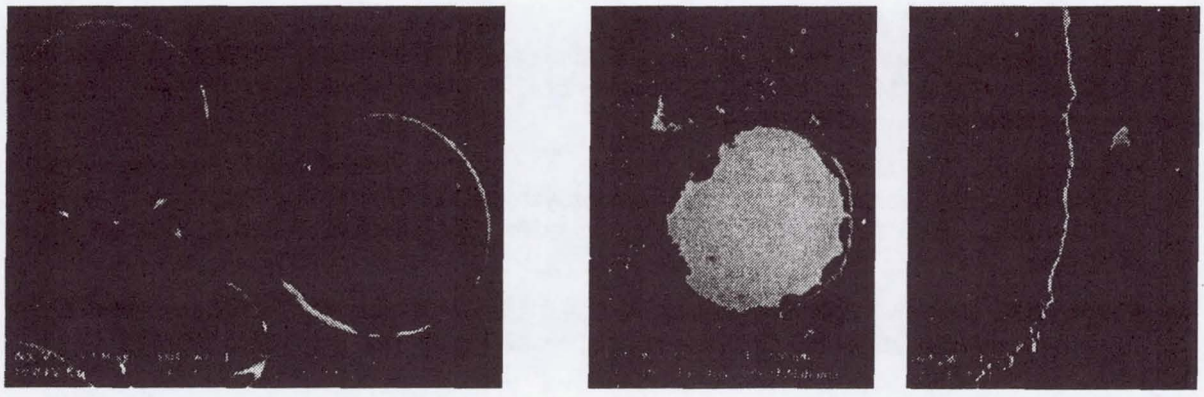

a) good interface in the DS region at 710 °C

b) oxidized interface in DS region at 950 °C

Fig. 4-8 SEM evaluation of particle (zirconia) - matrix (Al) interface

These results are not surprising. Indeed, work with organic transparent materials has also demonstrated that the critical velocity increases with the level of convection in the liquid, and that above a certain convection level the particle does not interact with the interface at all[1].

Fluid mechanics also provides arguments for this behavior. Assuming that the particle moves parallel to the SL interface because of natural convection (**Fig. 4-9**), it can be expected to roll because of the velocity gradient imposed in the *y*-direction. Simple calculations for ideal fluids show that in such a case a "lift" force will be generated[2]. This force will act in the *y*-direction and will be directed away from the interface. This force is accentuated when the particle moves at a velocity different from the average fluid flow rate[3].The lift force will thus behave like an additional repulsive force and therefore will increase the critical velocity.

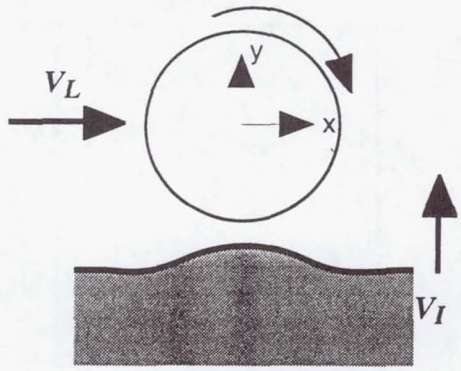

Fig. 4-9 Origin of the lift force.

5. Conclusions

The main conclusions that can be drawn at this time are as follows:

- A flight methodology has been developed and successfully tested.
- Pushing has been observed in the Al-ZrO_2 system at a solidification velocity of 0.5 μm/s. Engulfment was observed at velocities of 1 μm/s and above. This seems to indicate a critical velocity for *PET* of 0.5 to 1 μm/s.
- In the AlNi- ZrO_2 system pushing may have been observed at 1 μm/s. However, no firm conclusion could be reached at this time.
- The present results may only be considered as preliminary. A significantly larger number of samples must be processed in order to confirm the present conclusions.

6. Bibliographic Citations

H. T. Pang, D. M. Stefanescu and B. K. Dhindaw, "Influence of Interface Morphology on the Pushing/Engulfment Transition of Polystyrene Particles in Succinonitrile + Water Matrices," in *Cast Metal Matrix Composites*, Proceedings of the 2nd International Conference, D. M. Stefanescu and S. Sen editors, AFS, Des Plaines, Illinois (1994) 57-69

H. Pang and D. M. Stefanescu, "Influence of Interface Morphology on the Pushing/Engulfment Transition of Polystyrene Particles in Succinonitrile + Water Systems," in *Experimental Methods for Microgravity Materials Science Research*, R. A. Schiffman and B. Andrews editors, TMS Warrendale. Pa (1994),209-213

D. M. Stefanescu, R. V. Phalnikar, H. Pang, S. Ahuja and B. K. Dhindaw, "A Coupled Force Field-Thermal Field Analytical Model for the Evaluation of the Critical Velocity for Particle Engulfment", ISIJ International 35, 6 (1995) 700-707

F.R. Juretzko, D.M. Stefanescu, B.K. Dhindaw and S. Sen, " Interfacial Energy $\Delta\gamma$ - Theoretical and Experimental Evaluation For Metal-Ceramic Systems," in *Processing, Properties and Applications of Cast Metal Matrix Composites*, P.K. Rohatgi editor, The Minerals, Metals & Materials Society (1996) 21-31

S. Sen, B.K. Dhindaw, D.M. Stefanescu, A. Catalina and P.A. Curreri, "Melt Convection Effects on the Critical Velocity of Particle Engulfment", J. Crystal Growth **173**, 3-4 (1997) 574-584

7. Non-technical Summary

In this experiment zirconium oxide particles dispersed in liquid aluminum were used to model what happens to inert, nonreactive particles at the solid-liquid interface in different systems. Convection, and thus movement in the liquid, complicates the physics of the material interaction on Earth. By conducting this investigation in microgravity these difficulties could be overcome. When discrete particles are present in a liquid matrix, directional solidification of the liquid will either cause the particles to become engulfed in or pushed out of the solid. Whether particles are engulfed or pushed depends on the speed of solidification. If the solidification velocity is higher than a certain critical velocity, the particles are engulfed by the advancing solid; if it is lower, they are pushed ahead of the solid.

Modeling these systems has future applications in fields ranging from superconductor and metal matrix composites to frost heaving and cryobiology. For example, particle engulfment is beneficial when creating metal matrix composites, which are metals that incorporate strengthening particles, usually of a ceramic material, for reinforcement. Engulfment of these particles results in their being uniformly distributed, giving the composite material better properties than if the particles were pushed during solidification. In addition, understanding the physics behind particle engulfment and pushing can lead to solutions to problems like frost heaving. Frost heaving occurs when water that has seeped around soil begins to freeze. Because the solidification velocity of the water is slower than the critical velocity for engulfment, the soil particles are pushed out of the solid water (ice), causing the combination of ice and soil to take up as much as 300 percent of the volume of the original soil and water mixture. The increase in volume can displace road surfaces and foundations, causing a great deal of damage. The exploration of these physical phenomena may provide a stepping stone for those who wish to conquer such earthly problems.

References

[1] S. Sen, B.K. Dhindaw, D.M. Stefanescu, A. Catalina and P.A. Curreri, J. Crystal Growth, **173**, 3-4 (1997) 574-584

[2] R.H. Nunn, *Intermediate Fluid Mechanics*, Hemisphere Publishing Co., New York (1989) 51-55

[3] P.G. Saffman, J. Fluid Mechanics, **31** (1968) 624

Advanced Protein Crystallization Facility (APCF)

Crystallization of EGFR-EGF

Principal Investigator:

Dr. Christian Betzel
European Molecular Biology Lab
Hamburg, Germany

subject: LMS One Year Science Review

protein crystal growth experiment / APCF

The EGF receptor is the prototype of a family of tyrosine kinase receptors involved in cell growth control. Many human malignancies are characterized by its overexpression. The solution of the EGF receptor structure would pave the way for drug design and novel concepts of therapeutical treatment of tumors. However, the crystal structure of none of the growth factor receptors has been solved so far. - The difficulty of crystallizing a membrane protein has been overcome by purifying only the hydrophilic external domain of the EGF receptor. Using this ectodomain the co-crystallization with the ligand EGF was achieved; diffraction of these crystals had been poor, probably due to the high amount (30% of molecular mass) of heterogenous carbohydrate. Microgravity conditions have been tested which seemed to favour crystal growth. However, results have been variable so far.

On LMS different batches of EGF receptor preparations were flown all of which have proved to crystallize in the laboratory, however after non-predictable time spans. Four hanging drop reactors and one dialysis reactor were used; comparable set-ups in APCF reactors served as laboratory controls.

Results:

Two hanging drop reactors yielded showers of non-usable micro-crystals (lab controls also). Crystals of 0.25 mm length grew in another hanging drop reactor (Fig. 1) whereas the corresponding lab control contained just amorphous precipitate. The fourth hanging drop reactor provided small lancet-like crystals (Fig. 2), with similar crystals in the lab controls. Fig. 3 shows the fragment of a larger crystal which grew in the dialysis reactor and broke during removal from the chamber; if in these reactors crystals grow sticking to the dialysis membrane, cracking during harvest is almost inevitable. The corresponding lab control did not yield crystals.

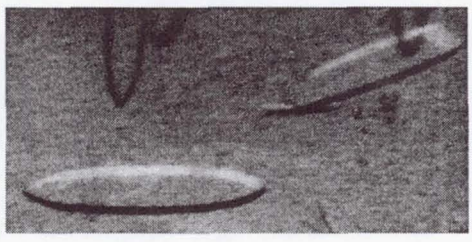

Fig. 1

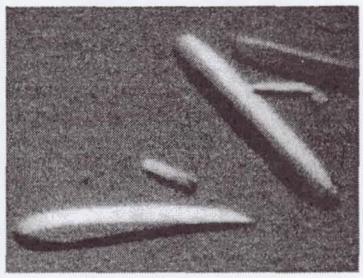

Fig. 2

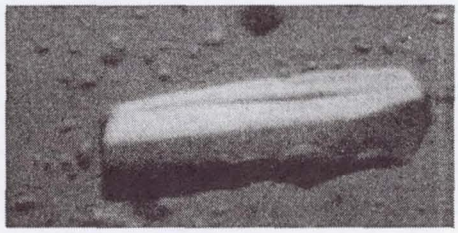

Fig. 3

Ten crystals from two reactors were analyzed using synchrotron radiation. However, the diffraction was poor, and collection of data was impossible. From previous experiments a high solvent content (65%) of EGF receptor crystals is known; therefore a larger crystal size is required for diffraction. This was e.g. achieved in a former microgravity experiment (STS-47) when a crystal of 0.5 x 0.3 mm was obtained.

Summarized, the growth of EGF receptor crystals seems to be favoured by microgravity conditions, since the results of 2 out of 5 set-ups were superiour to the corresponding lab controls, at least in terms of crystal growth. It emerges also that for a difficult protein like the EGF receptor the small number of 5 trials may be not sufficient to achieve satisfying results.

Dr. Wolfgang Weber

Institut für Physiologische Chemie

Universitätskrankenhaus Eppendorf, Hamburg

Advanced Protein Crystallization Facility (APCF)

Crystallization of Apocrustacyanin C1

Principal Investigator:

Dr. Naomi Chayen
Imperial College
London, England

Crystallization of Apocrustacyanin C1 on the LMS Mission

PI Naomi Chayen, Imperial College London

The results of the mission were obtained jointly with Prof Helliwell's group in Manchester University and P. Zagalsky of Royal Holloway College, U of London

Introduction

Apocrustacyanin C1 had previously been crystallised on the IML-2 and USML-2 and >Shuttle missions. On IML-2 the crystals grown in space were mostly better diffractors compared to the Earth grown crystals.CCD video was used to follow the crystallisation. The crystals, which grew in the vapour diffusion droplet moved in a circular way,consistent with that of Marangoni convection (Chayen et al. 1997). The images also display a ``halo'' effect around the growing crystals which is attributed to the presence of a depletion zone (i.e., solution regions which are depleted of this coloured protein).

>The crystals from the USML-2 mission (which were not monitored by CCD video) >underwent an X-ray mosaicity analysis.The quality enhancement between earth grown and microgravity grown crystals was not as marked as for the lysozyme crystals grown in dialysis geometry nor was it consistent between the two populations, although the best crystal was microgravity grown (Snell et al. >1997).

Objectives of experiment

The crystallisations on LMS aimed to complement, and expand upon the X-ray analyses obtained from the USML-2 crystals (as CCD video was not available to >monitor the crystallisations on the LMS mission).

Experimental

>Apocrustacyanin C1 was crystallised on the LMS Shuttle mission. Four >crystallisations were carried out on the flight, and four identical experiments >were conducted as ground controls during the period of the mission. These >ground controls were set up at the same time, and used the same solutions as >those of the mission.

>Synchrotron X-ray analysis of the LMS apocrustacyanin crystals was carried out
>at two facilities. Firstly at the NSLS using beamline X26C. Here, protein crystal mosaic spread measurements by use of rocking curves is an indicator of the internal physical perfection present (Helliwell 1988). The addition of an analyser crystal between the sample and detector enables reciprocal space mapping of omega, the sample axis,and omega ', the analyser axis (Snell 1997). Reciprocal space maps, along one axis provide a measure of pure mosaicity effects (volume and orientation), and along the other axis strain effects.
>Combination of the use of this technique with X-ray topography (Stojanoff et
>al. 1996),can produce a finely detailed picture of a single reflection, and an in-depth knowledge of the internal order of the crystal.The analysis of this data is still in progress, however an example topograph,and reciprocal space map are shown in figures 1 and 2.
>
>Secondly, at the bending magnet source beamline, BL19 at the ESRF, where two
>complete datasets,one of an LMS crystal, and one of an LMS ground control crystal were obtained.
>The resolution limits of apocrustacyanin C1 crystals grown onboard the LMS
>missions in a vapour diffusion reactor and earth grown controls were
>determined from 1 degree oscillation images. Operating parameters during data
>collection were lambda = 0.7513 Angstroms ; CCD detector
> (image intensifier type), exposure times 30 secs, rotation angles 1 degree,
>delta lambda / lambda = 10-4. Overall I/Sigma I for LMS = 30.4,
>and for ground control = 9.5. LMS crystal volume = 0.0432 mm3, ground control
>crystal volume = 0.0034 mm3.
>The full data merge for both LMS and ground control is shown in table 1.
>Obviously the LMS crystal is diffracting
>off the edge of the detector, since the Rmerge at 2 A is 10.4%, by contrast,
>the earth control Rmerge at 2 A is 40 %. But the crystal volume for the earth
>is 12 times smaller, and for ground control = 9.5. LMS crystal volume = 0.0432
>mm3, ground control crystal volume = 0.0034 mm3.
>When compared to earlier data collections on earth and microgravity grown
>apocrustacyanin crystals, these results show that resolution limits are
>dependent on the data collection source and measuring conditions. The full
>exploitation of the crystal perfection
>available is very difficult if step widths of 10-4 degrees are required.
>Nevertheless, new area detectors like the pixel detector could exploit such
>quality (for a discussion see Helliwell (1992) and
>Chayen \et (1996)) when used in conjunction with X-ray undulator sources, which
>have extremely fine collimation inhorizontal and vertical directions.

>References
>
>Snell, E.H. 1997 Quality evaluation of macromolecular crystals using X-ray
>mosaicity measurements. Canadian Space Agency, in press
>
>Snell, E.H., Cassetta, A., Helliwell, J.R., Boggon, T.J., Chayen, N.E.,
>Weckert, E., H\"olzer, K., Schroer, K., Gordon, E.J. & Zagalsky, P.F. 1997
>Partial improvement of crystal quality for microgravity grown apocrustacyanin
>C1. Acta Cryst D 53 , 231-239.
>
>Chayen, N.E., Boggon, T.J., Cassetta, A., Deacon, A., Gleichmann, T., Habash,
>J., Harrop, S.J., Helliwell, J.R.,
>Neih, Y.P., Peterson, M.R., Raftery, J., Snell, E.H., H\"adener, A., Niemann,
>A.C., Siddons, D.P., Stojanoff, V.,
>Thompson, A.W., Ursby T. & Wulff, M. 1996
>Trends and challenges in experimental macromolecular crystallography.
> Quarterly Rev. Biophysics 29, 227-278.
>
>Chayen, N.E., Snell, E.H., Helliwell J.R. & Zagalsky, P.F. 1997 CCD video
>observation of
>microgravity: apocrustacyanin C1. J. Cryst. Growth, 171, 219-225.
>
>Stojanoff, V., Siddons, D.P., Snell E.H. & Helliwell, J.R., 1996 X-ray
>topography: An old technique with a new application. Synchrotron Radiation
>News, 9, 25-26.
>
>Helliwell, J.R. 1988 Protein crystal perfection and the nature of radiation
>damage. J. Cryst. Growth, 90, 259-272.
>
>Helliwell, J.R. 1992 Macromolecular Crystallography with Synchrotron Radiation.
>Cambridge University Press, UK
>
>Figure 1:
>Protein crystal quality assessment via topographic images of an LMS ground
>control apocrustacyanin C1 grown as an example.
>
>Figure 2:
>Protein crystal quality assessment via reciprocal space mapping of the same LMS
>ground control apocrustacyanin C1 crystal. The reciprocal space map shows omega
>verses omega ', with intensity on the z axis.

Table 1

Resolution (Angstroms)	LMS Rmerge	LMS Completeness %	Rmerge	Completeness %	LMS Ground Control
25.00 -- 4.92	0.048	86.5		0.045	97.2
4.92 -- 3.91	0.048	91.0		0.047	99.0
3.91 -- 3.42	0.050	92.6		0.070	99.5
3.42 -- 3.11	0.051	94.2		0.089	99.8
3.11 -- 2.88	0.058	94.7		0.130	99.9
2.88 -- 2.71	0.064	95.0		0.172	99.7
2.71 -- 2.58	0.070	95.3		0.203	99.8
2.58 -- 2.47	0.074	96.6		0.230	99.6
2.47 -- 2.37	0.075	96.1		0.239	99.9
2.37 -- 2.29	0.084	95.2		0.266	99.5
2.29 -- 2.22	0.084	97.9		0.265	99.7
2.22 -- 2.15	0.085	95.7		0.275	99.1
2.15 -- 2.10	0.086	98.1		0.317	98.6
2.10 -- 2.05	0.094	95.3		0.358	98.9
2.05 -- 2.00	0.104	98.2		0.403	98.2
Overall	0.056	94.7		0.110	99.2

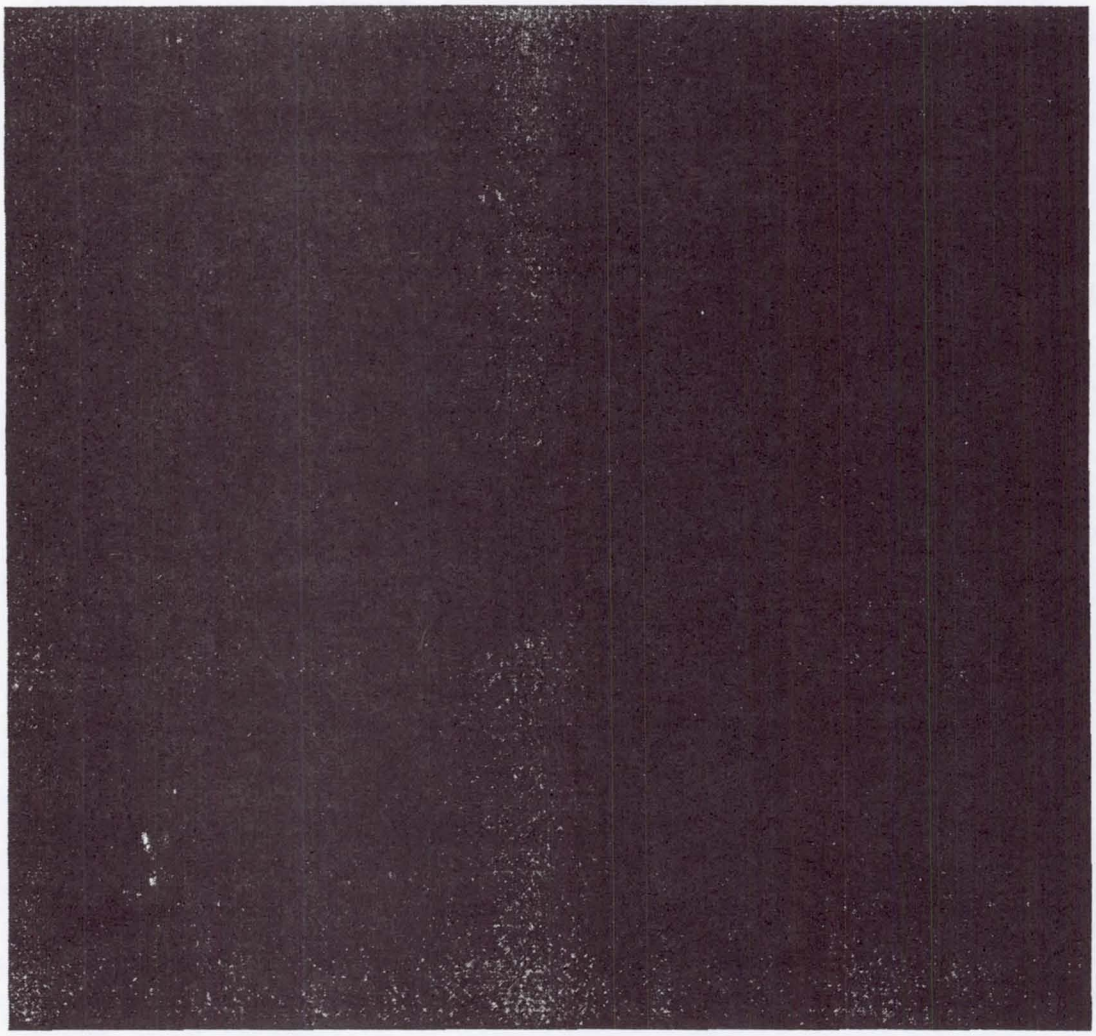

Figure 1

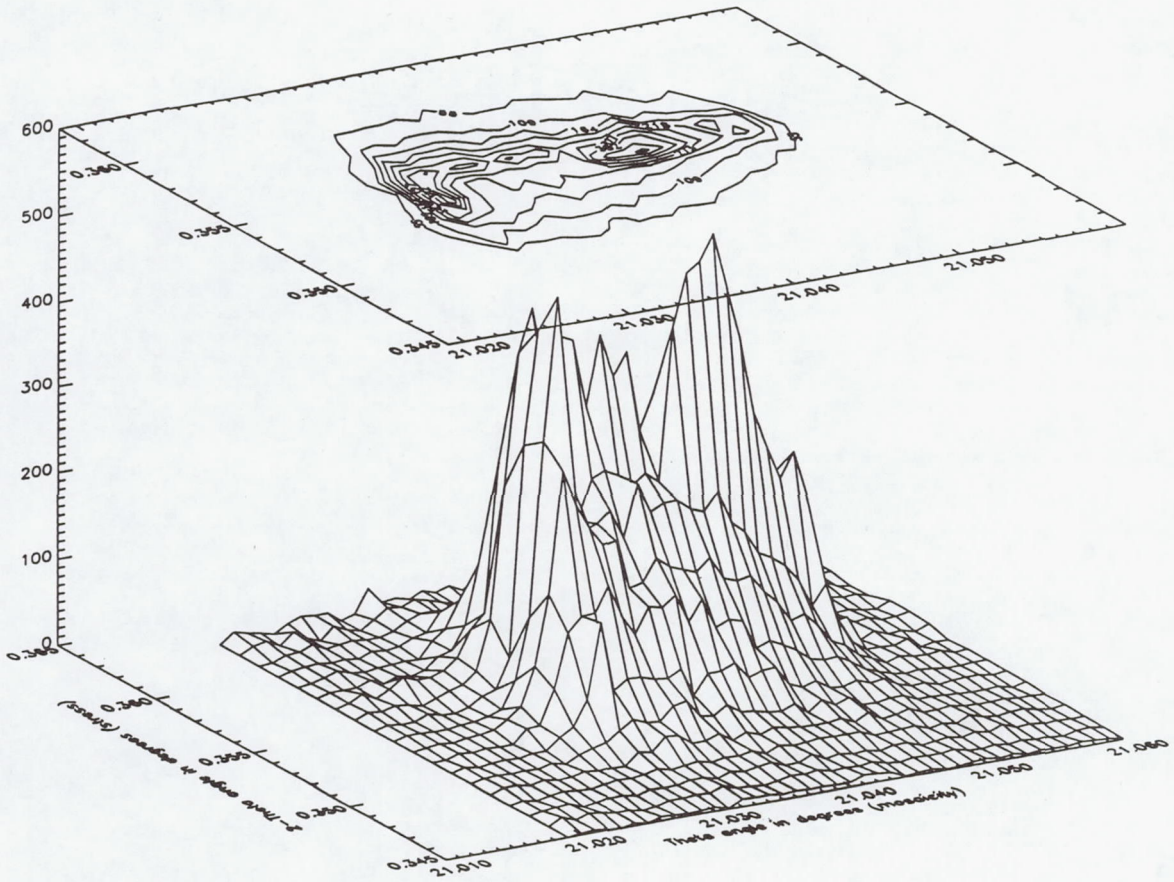
600
500
400
300
200
100
0.360
0.355
0.350
0.345
21.010
21.020
21.030
21.040
21.050
21.060
Theta angle in degrees (resistivity)

Figure 2

Advanced Protein Crystallization Facility (APCF)

Crystallization and X-ray Analysis of 5S rRNA and the 5S rRNA Domain A

Principal Investigator:

Dr. Volker Erdmann
Free University of Berlin
Berlin, Germany

Final science report of the experimental results from the LMS space mission in 1996.

Crystallization and x-ray analysis of 5S rRNA and the 5S rRNA domain A.

Prof. Dr. Volker A. Erdmann and Siegfried Lorenz

Freie Universität Berlin, Institut für Biochemie, Thielalle 63, D-14195 Berlin-Dahlem, Germany.

Introduction

The ribosomal 5S rRNA is an essential component of the ribosomes. Ribosomal particles lacking 5S rRNA have a greatly reduced peptidyltransferase activity. Because of its functional importance and the fact, that the 5S rRNA interacts specifically with several ribosomal proteins, it is of great interest to know its three dimensional structure at atomic resolution. Based upon chemical and enzymatic structural characterization and the comparison of more than 750 different 5S rRNA sequences a secondary structure for this class of RNA molecules has been derived, which is generally accepted. (**Figure 1**). The size of the 5S rRNA, 120 nucleotides in length, limits its structural determination to that by x-ray analysis. With this goal in mind we have tried for more than ten years the crystallization of about 20 different 5S rRNA species **(Figure 2)**. The best results obtained so far are those for the 5S rRNA from *Thermus flavus*, whose crystals diffract up to a resolution of 8 Å **(1).**

Since crystal structure analysis of whole 5S rRNA molecules could provide so far only low resolution data at 8 Å, we turned to the chemical synthesis and structural determinations of the individual 5S rRNA domains.

Figure 3 shows as example the structure of the domain A from *Thermus flavus* 5S rRNA and the fact that a large number of solvent molecules are associated with this molecule. **(2, 3).**

Currently we are continueing our crystallization experiments with engineered *Thermus flavus* 5S rRNA molecules. Internal breathing of the structure on one hand and small differences in the primary structure of the 5S rRNA molecules on the other hand can significantly influence the ability to produce well ordered crystals. For example, crystals from the *Thermus aquatics* 5S rRNA gave a resolution up to 25 Å, while crystals from the *Thermus flavus* 5S rRNA gave a resolution up to 8 Å. The difference in the primary structure are only the exchange of 9 nucleotides. These nucleotides differing in the two structures are labeled by solid circles in **Figure 1.** With this observation in mind, we used engineered variants of *Thermus flavus* 5S RNA in such a fashion that an improved crystallization was anticipated. First results of the purified 5S rRNA variants show crystals in dimensions up to 0.6 mm. One of the engineered variants was used in the APCF (Advanced Protein Crystallography) microgravity experiment on the USML-2 space mission in November 1995 and one in the LMS space mission in June 1997.

Material and Methods

1. About 20 different 5S rRNAs were prepared from isolated ribosomes or ribosomal subunits by extraction with phenol and purified by two chromatographic procedures on Sephadex G 100 gelfiltration or by hydrophobic interaction chromatography with Phenylsuperose **(1).** Having tested various crystallization methods we found, that the best crystals were obtained by the microdialysis method.

2. The 5S rRNA domain A from *Thermus flavus* was prepared by solid phase chemical synthesis **(3).** Crystals of the dodecamer suitable for x-ray analysis were obtained by vapor diffusion in Linbro plates followed by repeated seeding of the crystals.

3. The engineered variants of *Thermus flavus* 5S rRNA were synthesized on the DNA level and then transcribed in large amounts *in vitro*. The chromatographically purified RNA was crystallized in Linbro plates by the hanging drop method and also in the APCF microdialysis reactors during the ESA and NASA USML 2 and LMS space mission. The crystals were analysed by using the

image plate detector at the EMBL Synchrotron beam line X 11 at DORIS / DESY, Hamburg, Germany and also at the ELETTRA Sincrotrone Trieste in Italy

Results and Discussion

The preliminary assignment of the wild type *Thermus flavus* 5S rRNA crystal lattice is monoclinic, space group C2, with units cell dimensions a = 190 Å, b = 110 Å, c = 138 Å and ß = 117 Å. The unit cell volume is 2.69 x 10^6 Å and the packing volume 4.3 Å / dalton. The solvent content for the crystals is about 70%. The resolution was up to 8 Å **(1).** The reason for this low diffraction could be the internal breathing of the structure and the large size of the RNA molecule.

To overcome the problems associated with the crystallization of whole 5S rRNA molecules we tried to crystallize chemical synthesized structural domains of this RNA from *Thermus flavus* and *E.coli* **(Figure 1)**. It is anticipated that the knowledge of all domain structures of the 5S rRNA molecule will eventually permit the determination of the whole RNA structure. In this report we show for example the structure of the domain A from *Thermus flavus* 5S rRNA. Two crystals were used to collect data up to 2.3 Å resolution. The final structure of the dodecamer presented in **Figure 3** is a right handed A type double helix with two strands defined as A and B according to Figure 1. Strand A consists of 245 non-hydrogen atoms and strand B of 263. The structure includes a total of 159 solvent molecules. 49 water molecules were located (blue label) in the interior of the duplex and 68 externally involved in the first hydration shell around the surface of the duplex.

The remaining 42 represent crystal water filling the spaces between the domains. In conclusion it is quite apparent, that with the recent developments of the methodology to synthesize defined RNA molecules it will be possible to determine their atomic structures by x-ray analysis.

In addition to the crystallization experiments of the domain A from *Thermus flavus* 5S rRNA we crystallized the chemically synthesized domain E from the same RNA **(5).** The crystals are trigonal with unit cell dimensions a = b = 42.8 Å, c = 162 Å. The resolution of the crystals reached a value of 2.8 Å. The chemically synthesized domain E from *E.coli* 5S rRNA was also crystallized. Data sets were collected (S. Klußmann et. al, unpublished results). In addition 11 other chemically synthesized RNA fragments have been crystallized (V.A. Erdmann et. al, unpublished results).

First results of the purified *Thermus flavus* 5S rRNA variants, isolated on the DNA level by *in vitro* transcription, in which the 3`and 5`ends were stabilized, yielded crystals up to 0.6 mm length. Although the crystals obtained so far did not show an improved resolution (10 Å), we are currently continuing these studies with different structural variants and by variations of crystallization conditions. The variations of crytallization conditions include also crystallization experiments under microgravity conditions. In November 1995 we initiated these studies with engineered *Thermus flavus* 5S rRNAs in the USML-2 Mission (ESA/NASA) in APCF (Advanced Crystallography Protein Facility) microdialysis reactors. Of five reactors three yielded crystals. The crystals obtained were larger in size than those obtained simultaneously from ground control experiments **(Figure 4)**. In the LMS mission in June 1996, we continued these experiments also in the APCF system. Of seven reactors all yielded crystals. The crystals obtained were larger in size than those obtained in silmultaneous ground control experiments. The largest space grown crystals in the LMS Mission exhibited a length of 0.45mm. In the ground-control experiment 5 chambers yielded crystals. These were smaller in size than those grown in space.**(Figure 5)**. The crystals were analyzed by synchrotron radiation at DESY in Hamburg, and at the ELETTRA Sincrotrone Trieste, Italy. In the LMS mission space crystals exhibited a resolution of about 8 Å. We were not able to determine the resolution of the simultaneously obtained ground crystals, because they were to small in size. The resolution of the best crystals of the engineered *Thermus flavus* 5S rRNA grown in the laboratory yielded until now a resolution of 8 Å.

Summary

1. 19 different 5S rRNAs were isolated from ribosomes and tested for their ability to crystallize. The best results gave the 5S rRNA from the thermophilic bacterial strain *Thermus flavus AT62.* The resolution of the crystals was up to 8 Å **(1).**

2. The chemical synthesized domain A from *Thermus flavus* 5S rRNA was crystallized. The diffractions of the crystals were 2.3 Å. The structure has been solved **(2).** Chemically synthesized domain A from *Thermus flavus* has been also crystallized **(5).** Data sets from domain E from *E. coli* are collected.

3. Engineered variants of 5S rRNA are produced on the DNA level by *in vitro* transcription. It is anticipated that stabilizing elements at the 3` and 5´ends in the primary structure will reduce the flexibilities of these RNA molecules in order to yield crystals for x-ray analysis.

4. The influence of microgravity on the crystal growth was tested with one engineered 5S rRNA variants in the ESA and NASA APCF/USML-2 and LMS space missions. The results obtained show clearly that the space grown crystals were larger in size than those in the ground controls.The diffraction of engineered *Thermus flavus* 5S rRNA crystals grown in space is nearly the same then the crystals in the best laboratory experiments. The crystals from the simultaneous ground control experiments were to small for diffraction studies.

References:

1) Lorenz, S., Betzel, Ch., Raderschall, E., Dauter, Z., Wilson, K.S. and Erdmann, V.A. (1991) J. Mol. Biol. 219, 399-402.

2) Lorenz, S. Betzel, Ch., Fürste, J.P., Bald, R., Zhang, M., Raderschall, E., Dauter, Z.,Wilson, K.S. and Erdmann, V.A. (1993) Acta Crystallogr. D 49, 418-420.

3) Betzel, Ch., Lorenz, S., Fürste, J.P., Bald, R., Zhang,M., Schneider, T.R., Wilson, K.S. and Erdmann, V.A. (1994) FEBS Letters 351, 159-164.

4) Bald, R., Brumm, K., Buchholz, B., Fürste, J.P., Hartmann, R.K., Jäschke, A., Kretschmer-Kazemi, R., Lorenz, S., Raderschall, E., Schlegl, J., Specht, T., Zhang, M., Cech, D. and Erdmann, V.A. (1992) in: (Lilley, D.J. Heumann, H. and Suck, D., eds.) pp. 449-466, Basel-Birkhäuser-Verlag.

5) Nolte, A., Klußmmann, S., Lorenz, S., Bald, R., Betzel, Ch., Dauter, Z., Wilson, K.S., Fürste, J.P. and Erdmann, V.A. (1995) FEBS Letters 374, 292-294.

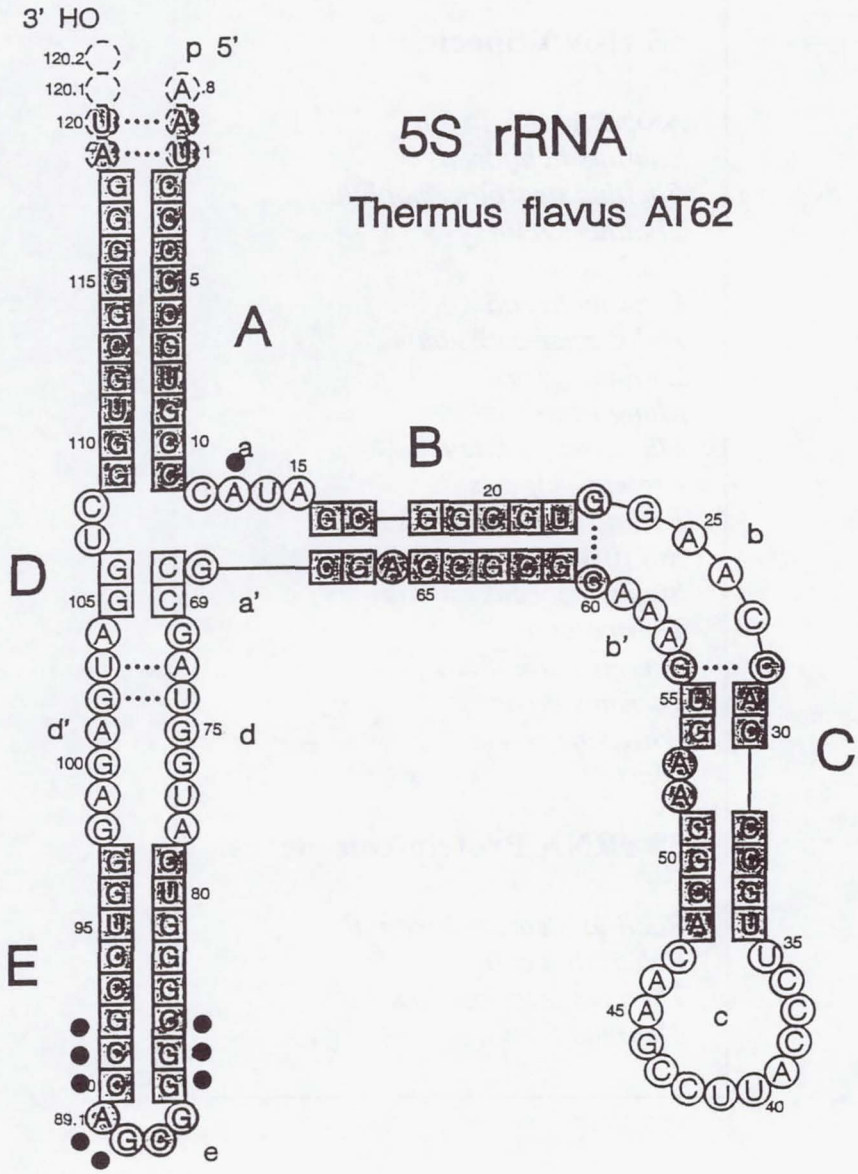

Figure 1
Secundary structure model of 5S rRNA.

5S rRNA Species:

Azobacter vinelandii
Bacillus lichiformis
Bacillus stearothermophilus
Bacillus subtilis
Caulobacter
Echerichia coli
Halobacter cutirubum
Lupinus luteus
Mung bean
Micrococcus luteus
Proteus vulgaris
Pseudomonas fluorescens
Rat (liver)
Staphylococcus aureus
Thermotoga
Thermus aquaticus
Thermus flavus
Wheat germ
Yeast

5S rRNA Protein-complexes:

Bacillus stearothermophilus
Echerichia coli
Thermus thermophilus
Thermus flavus

Figure 2
5S rRNA species for crystallization experiments.

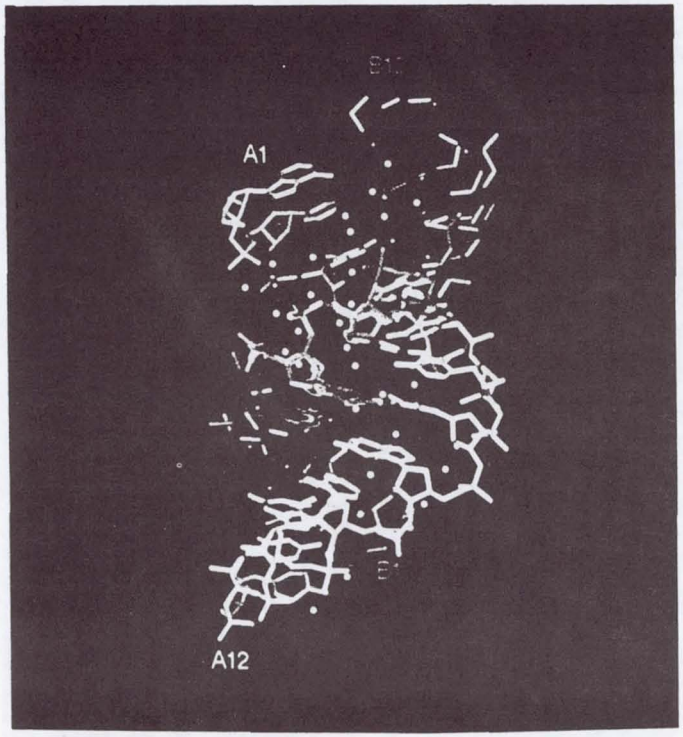

Figure 3

Crystal structure of the dodecamer 5S rRNA domain Helix A with 117 water molecules.

(Left side: 49 water molecules in the interior of the duplex).

(Right side: 49 internal plus 68 external water molecules).

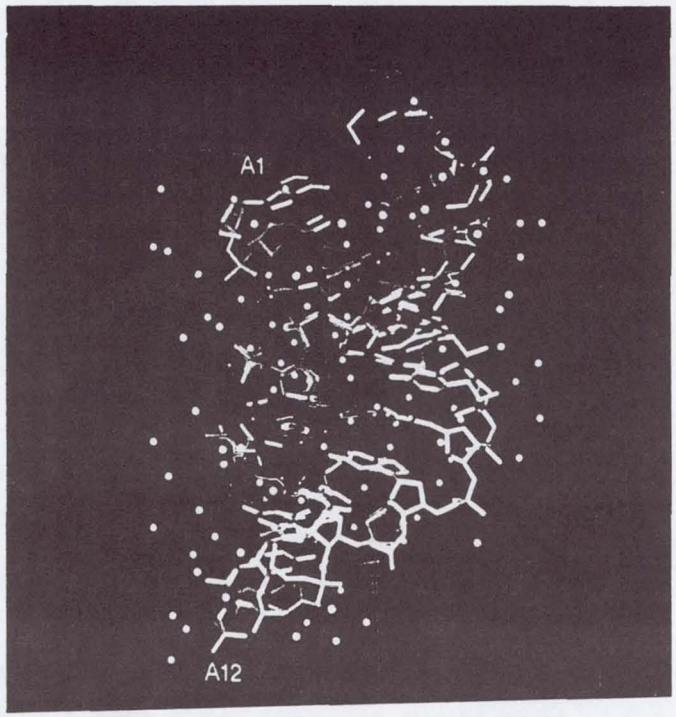

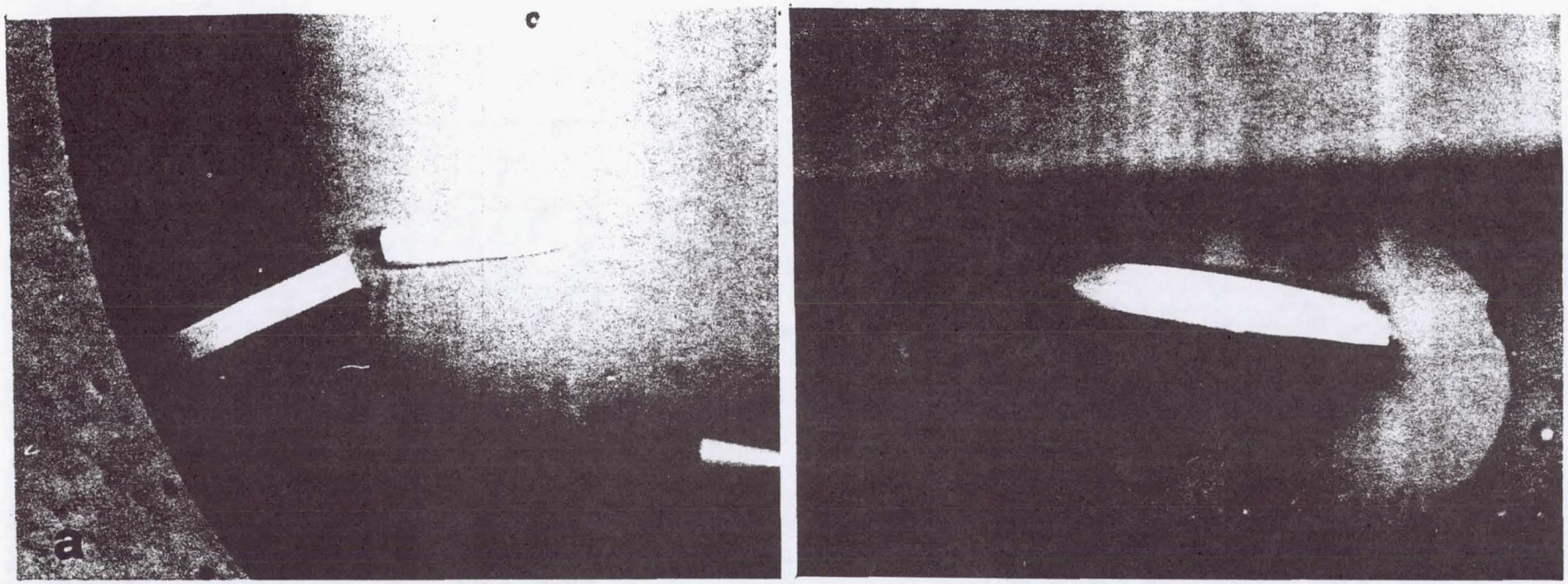

Figure 4

Crystals of engineered *Thermus flavus* 5S rRNA

a) grown on earth, (0.4 mm length),

b) grown in APCF reactor under microgravity, (0.7 mm length).

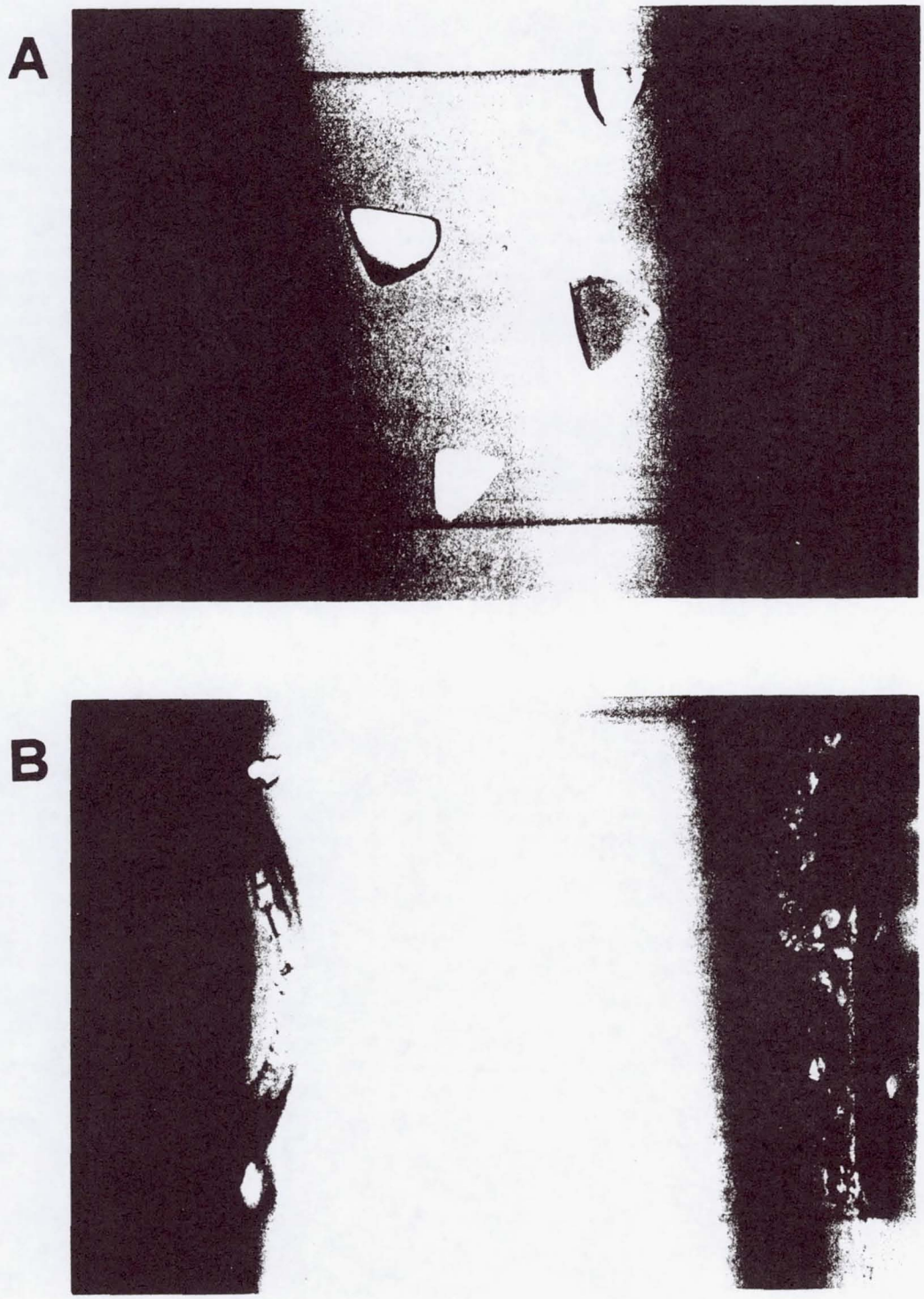

Figure 5

Crystals of the bacterial 5S rRNA *Thermus flavus* under microgravity conditions crystallize better in size, shape and quality (A) than the ground control crystals (B). The crystals were obtained in the ESA / NASA mission LMS, 1996

Advanced Protein Crystallization Facility (APCF)

Growth of Lysozyme Crystals at Low Nucleation Density

Principal Investigator:

Dr. Juan Garcia-Ruiz
University of Granada
Granada, Spain

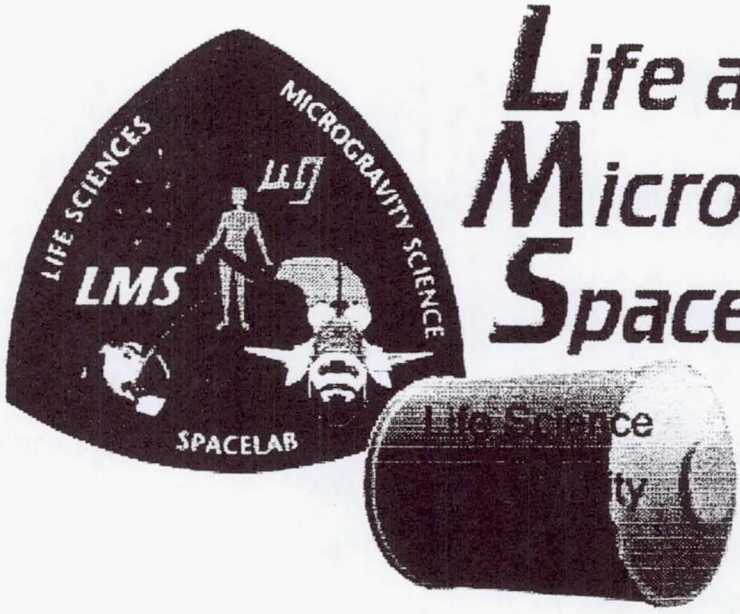

Life and Microgravity Spacelab

Growth of Lysozyme Crystals at Low Nucleation Density. Experimental Report.

Mission Data	
Facility	APCF
Mission Number	STS-78
Shuttle	Columbia
Launch Date	10:49 am EDT on June 20, 1996 at KSC
Landing Date	08:37 am EDT on July 7, 1996 at KSC
Activation of APCF	05:19 pm EDT on June 20, 1996
Deactivation of APCF	03:49 am EDT on July 6, 1996
Process Phase Duration	15 days, 10 hours, 30 min.

Research Team	
Principal Investigator	**Juan Manuel García Ruiz**
Participants	**Fermín Otálora** **Deyanira Rondón** **M. Luisa Novella**
Report Prepared by	F. Otálora & J.M. García-Ruiz

1. OBJECTIVES **2**

2. RESULTS **3**

2.1. NUCLEATION 3
2.2 GROWTH RATE 4
2.3. CRYSTAL MOVEMENT 5
2.4 INTERFEROMETRY 6
2.5. X RAY STUDIES 9

CONCLUSIONS **12**

ARTICLES/PRESENTATIONS RESULTING FROM THE FLIGHT **13**

SUMMARY OF THE EXPERIMENT AND THE ACCOMPLISHMENTS **14**

Laboratorio de Estudios Cristalográficos
IACT, Campus Fuentenueva (Fac. Ciencias)
18002, Granada Spain

Tel: +34-58-243360 Fax: +34-58-243384 Email: otalora@goliat.ugr.es jmgruiz@goliat.ugr.es

This Report is available on-line at http://gazpacho.ugr.es/wwwbook/apcf_rep.htm

1. Objectives

Five experiments were prepared for this flight in the same reactor type (FID200) and with the same initial concentrations (10% Sodium Chloride and 100 mg/ml Lysozyme). The experiments were prepared with the following objectives:

- **Test of the new Mach-Zehnder interferometer installed in the APCF facility**. During mission STS-78, the APCF has flown equipped for the first time with a Mach-Zehnder interferometer to study the concentration of reactants inside the protein chamber. The experiment at position 1L3 was designed to test this feature.

- **Crystal growth rate and movement studies**. Three of the five reactors were accessible by the APCF video camera. Time series of images during crystal growth can be used to study growth rate and crystal movement due to residual acceleration in the microgravity environment.

- **Precipitation of Lysozyme at high concentration**. Non equilibrium one-dimensional techniques for crystal growth has shown their potential for crystal growth. The space-time self organisation of supersaturation provokes inhomogeneous distributions of nucleation density, growth rate and crystal size[1]. Our experience from on-ground experiments shows that long growth chambers and high protein concentration are the optimum conditions to explore the properties of these systems. This is the reason to use 100 mg/ml lysozyme solutions and to fill with this solution the plug channel in experiments (1R2 and 2R2).

- **Testing the use of capillaries inside the protein chamber**. In soft materials like proteins, handling of crystals is supposed to create defects that can potentially lower the crystal quality. Very good quality crystals are obtained routinely on ground by growing the crystals inside X-ray capillaries, which allows its use in diffraction experiments without further handling of crystals and mother liquor. Shocks during manoeuvres of the spaceship (specilly during landing) are also avoided. A pack of flat capillaries is introducing filling the protein chamber in two of the experiments (1R1 and 1R2) to check the usefulness of this technique in the APCF.

The following table summarises the configuration and initial conditions of the five experiments:

Flight Configuration						Initial Conditions		
Stack	Type	Pos.	S/N	Video	Interf.	Salt Res.	Rot. Plug	Prot. Ch.
1	FID200	1L3	324/B	5	5	10 % ClNa	Agarose 0.5%	100 mg/ml Lysozyme
1	FID200	1R2	316/B	-	-	10 % ClNa	100 mg/ml Lysozyme	100 mg/ml Lys. Cap.
1	FID200	1R1	207/B	-	-	10 % ClNa	Acetate buffer	100 mg/ml Lys. Cap.
2	FID200	2R3	208/B	6	-	10 % ClNa	Acetate buffer	100 mg/ml Lysozyme
2	FID200	2R2	322/B	4	-	10 % ClNa	100 mg/ml Lysozyme	100 mg/ml Lysozyme

Initial conditions for the experiments were selected based on our experience in protein crystal growth into capillaries[2] after test experiments performed on ground using APCF reactors with the protein chamber filled with a gelled protein solution to mimic microgravity conditions.

---

[1] J.M. García-Ruiz, F. Otálora (1997) ESTEC contract 11629/95/NL//JS final report. J.M. García-Ruiz, A. Moreno, F. Otálora, C. Viedma, D. Rondón and F. Zautscher (1997) *J. Chem. Education*. In Press. F. Otálora & J.M. García-Ruiz. *J. Crystal Growth* 169 (1996) 361-367. F.Otálora and J.M. García-Ruiz *J. Crystal Growth* 169 (1997) In Press.

[2] J.M. García-Ruiz, A. Moreno, C. Viedma & M. Coll. *Res. Bull.* 28 (1993) 541-546. J.M. García-Ruiz and A. Moreno. *Acta Crystal. D50 (1994) 483-490.* J.M. García-Ruiz, A. Moreno, A. Parraga & M. Coll. *Acta Crystal. D* 51 (1995) 278-281. J.M. García-Ruiz, A. Moreno, F. Otálora, C. Viedma, D. Rondón and F. Zautscher, *J. Chem. Education.* (1997) (In press). J.M. García-Ruiz and A. Moreno, *J. Crystal Growth. 169 (1996) 361-367. A.* Moreno, D. Rondón & J.M. García-Ruiz. *J. Crystal Growth* 166 (1996) 919-924. F. Otálora & J.M. García-Ruiz. *J. Crystal Growth* 169 (1996) 361-367. F. Otálora, J.M. García-Ruiz y A. Moreno, *J. Crystal Growth* 168 (1996) 93-98.

2. Results

2.1. Nucleation

Experiments in which the plug channel contains lysozyme solution produced a larger number of smaller crystals than experiments in which buffer solution is used inside the plug. In the first case, nucleation flux is very large at the plug channel, where concentrated salt and protein solutions meet. In general, even for the experiments containing buffer solution in the plug channel, nucleation flux was higher than expected. This fact is due to the short length of the protein chamber in the APCF. In counterdiffusion experiments in which long enough growth chambers are used (as in the Gel Acupuncture method[2]), the incoming of one reactant is expected to produce a supersaturation gradient along the growth chamber resulting in a spatio-temporal structuration of the supersaturation field. As a result, crystals nucleate at different supersaturation in different parts of the systems and growth at different rates to different final sizes. If the growth chamber is too short for a given waiting time for nucleation, precipitation takes place after the homogenisation of the system that, therefore, loss its spatio-temporal structuration. Although FID200 reactors are the APCF reactors with longer protein chambers (this was the reason for selecting these reactors), they proven to be short for the kind of experiment proposed. Induction times for lysozyme (figure 1) are long enough to provoke nucleation after the almost complete homogenisation of the salt concentration inside the protein chamber, giving rise to a large number of crystals evenly distributed over the chamber (figure 2). The expected spatial structuration of the nucleation flux is therefore masked by the apparently homogeneous precipitation over the protein chamber due to salt homogeneisation. Even in this case, the effect is still observable, specially when only the early formed nucleus (after 47 hours) are taken into account. Figure 3 shows the spatial distribution of these first nucleation events into the protein chamber. Nucleation flux in the direction of the salt gradient is structured, displaying a maximum approximately at the centre of the chamber. Some structure is also shown in the perpendicular (y) direction, but this is probably due to the presence of bubbles at the entry of the protein chamber close to the corners (see figure 2).

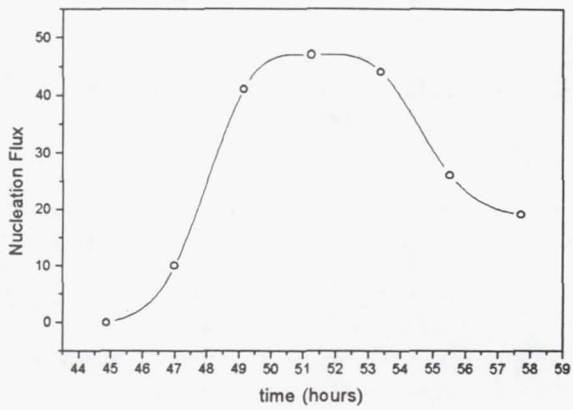

Figure 1. Nucleation flux versus time plot for Experiment 1L3. The number of new crystals observed in each image acquired at the given time is plotted versus the acquisition time. Maximum nucleation flux is observed after 51'5 hours, The shape of the peak is asymmetric. The tail of the peak cannot be explored to later times due to the large number of crystals already in the field of view that avoids clear recognition of new nucleation events.

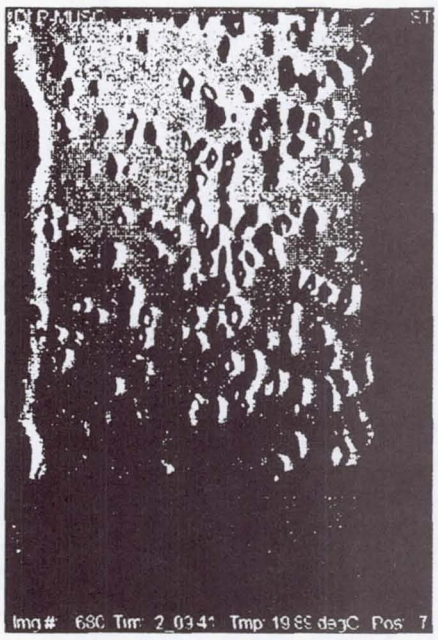

Figure 2: View of the experiment 1L3 57 hours after activation.

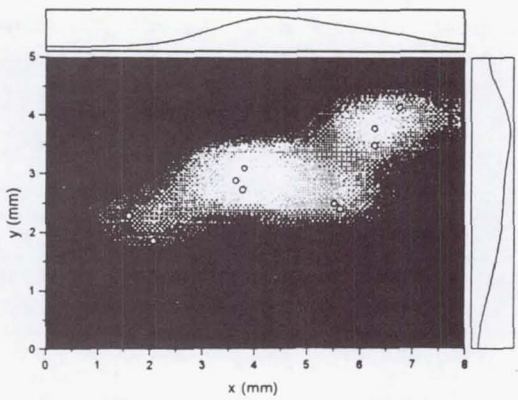

Figure 3: Spatial distribution of the first nucleated crystals (circles) inside the protein chamber. Cumulative nucleatio probability curves are projected in the direction of both axis.

2.2 Growth Rate

Image analysis methods has been used to study the growth rate of crystals. These methods has been discussed in detail elsewhere[3], therefore only a brief description of the methodology is included here. Six crystals has been selected from reactor 1L3. Crystals in reactors 2R2 and 2R3 cannot be used for this study because the first image is acquired after 91 hours, late after the nucleation in these reactors. Time series for the growth history of the crystals selected are automatically cut and pasted to have a single image displaying their growth history. From this image, shown in figure 4, the projected area after form factor correction is obtained at each step. The square root of this projected area is used as a representative lengthscale to be used in the absence of the crystal length perpendicular to a crystal face, a figure not directly obtainable from the APCF image recording system.

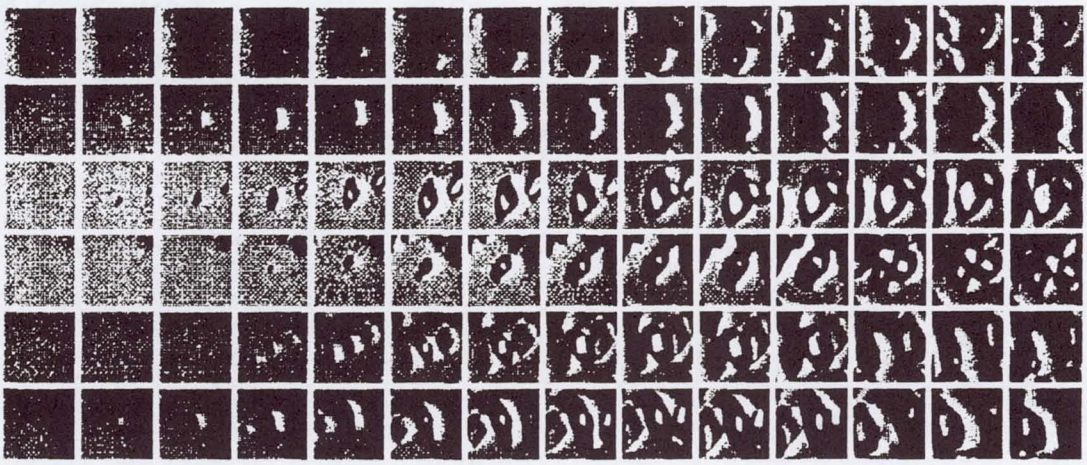

Figure 4: Collage of subimages displaying the growth history of the six crystals analysed. Frames are time aligned and start at the image where the first nucleation is detected. Time series ends at a time where the number and size of crystals makes unreliable the detecion of projected areas.

Figure 5 shows the square root of projected area (length) of the crystals versus the square root of time plots for these crystals. These plots display large linear areas consistent with the dynamics of diffusive transport. These linear regions are limited by an initial non-linear region in which growth rate is controlled by the nucleation kinetics and a second non-linear region at late times due to the exhaustion of protein concentration by the coalescence of the protein depletion zones around the growing crystals.

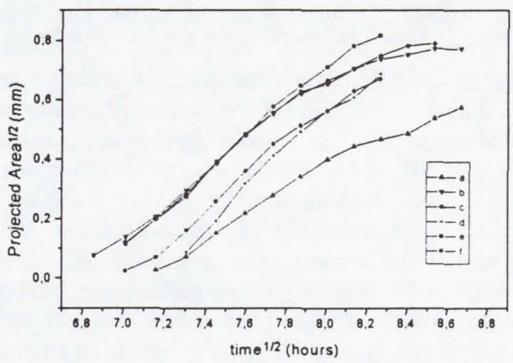

Figure 5: Time evolution of the crystal size for the six crystals analysed. The central part of most of the curves are clearly straight.

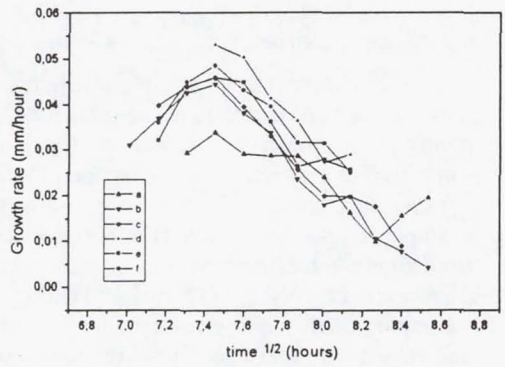

Figure 6: Growth rate of the crystals analysed. A maximum growth rate exists at the end of the kinetics regime.

[3] J.M. Garcia-Ruiz, F. Otálora (1997) ESTEC contract 11629/95/NL//JS final report. F.Otálora and J.M. Garcia-Ruiz *J. Crystal Growth* 169 (1997) In Press.

Figure 6 shows the growth rate of the six crystals analysed. Maximum growth rates up to 140 Å/sec are observed slightly after nucleation. These growth rates then slowly decrease towards zero. The measured maximum growth rates, the initial regime of increasing growth rate and the time lapse between maximum and close to zero growth rate are consistent with previous observation of flight experiments[3] as well as with on-ground observations.

2.3. Crystal movement

Crystals move during their growth. This movement has been studied by computing the centre of mass of the projected area computed for growth rate measurements. Figure 7 shows the position of each of the six crystals at equivalent times and a path interpolated between these positions. Average displacement during the 28 hours period represented is 0.1 mm although displacements as large as 0.6 mm are observed.

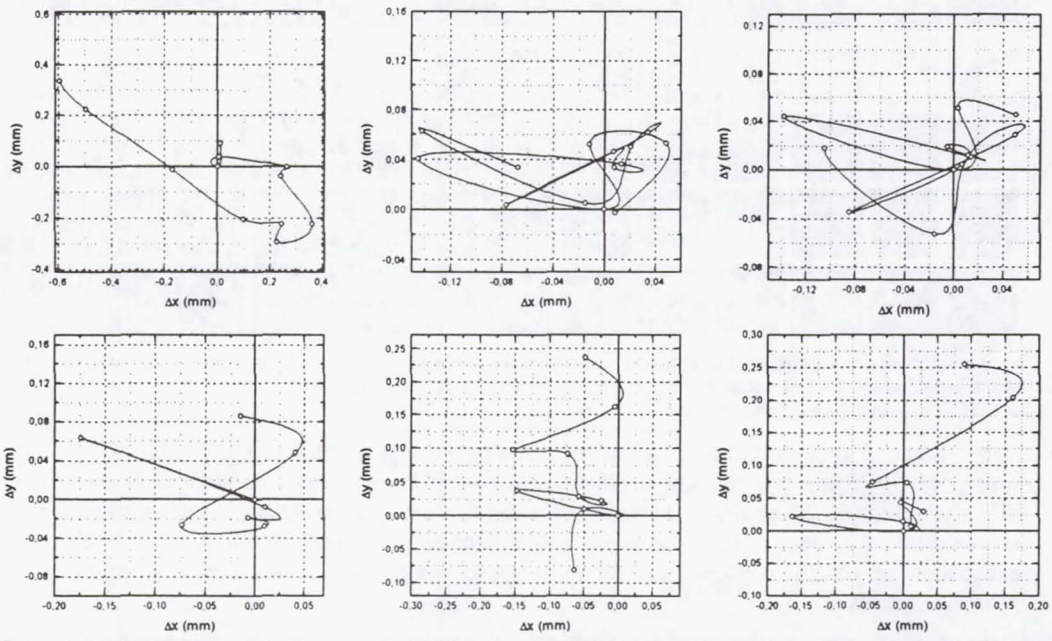

Figure 7: Crystal movements during the first 28 hours of crystal growth. The paths has been represented in such a way that they are comparable: all plots contains a data point at x=y=0. This point corresponds to the same time in all paths.

To understand the origin of these displacements, the first important question is: Do all crystals move in the same direction at the same time? This question addresses the lengthscale of the mechanism giving rise to the crystal movement. If this mechanism is at the sub-reactor lengthscale (for example some kind of convection), the direction of movement of different crystals is expected to be uncorrelated. On the other hand, if the motion is related to mechanisms working at a suprareactor lengthscale (for example residual accelerations of the spaceship) crystals would move in the same direction. Although from figure 7 the movement of crystals seems uncorrelated, a more systematic study undercover the correlation of crystal movements. Taking the position of crystals in two consecutive images and subtracting their x and y co-ordinates in each image, we get a displacement representing the direction and velocity of movement during the period between images. Representing these vectors in a polar plot, the head of the vectors corresponding to different crystals during the same time period must be grouped if the movement of crystals is correlated, else they must be scattered. Such a plot is shown in figure 8, each symbol represents a different time period. This plot shows a collective movement of the crystals, the heads of the displacement vectors are close to each other, and this clustering of the data points seems proportional to the net displacement: data points are more grouped for larger displacements (distance from origin) than for smaller ones. This can be due to random errors during the measurement of the crystal position or to the coexistence of two processes producing crystal movements, one at a subreactor lengthscale and of roughly constant strength and other of suprareactor lengthscale and of varying strength.

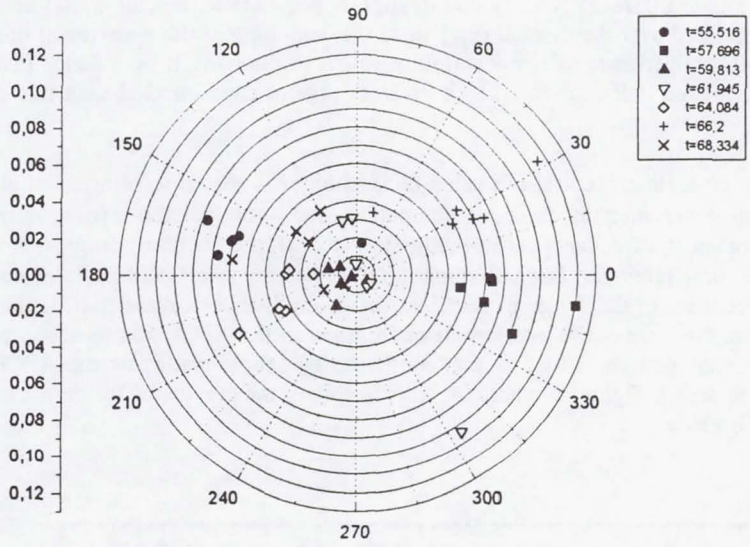

Figure 8: Movement of crystals inside the 1L3 reactor. Data points represented in the polar plot indicate the head of the displacement vectors. Each symbol correspond to a different time period starting at the time indicated in the symbol caption. Radial axis is net displacement in millimetres.

We have tried to correlate these movements with acceleration data. To this aim, we contacted colleges managing the ASTRE accelerometer measurements who kindly supplied us their data. Unfortunately, when we start processing these records, no information was found for the time period we were interested in. Later, it was confirmed that, from 174/16:00 to 175/00 the ASTRE data have been lost. We are contacting now teams managing other accelerometers onboard STS-78 to get new acceleration data.

2.4 Interferometry

Experiment 1L3 was selected to test the new Mach-Zehnder interferometer installed in the APCF and flown for the first time during the STS-78 mission. During the first 15 hours, the average grey intensity inside five image windows was recorded at a rate of 12 samples per hour (The position of these windows is shown in figure 9). Then the whole interference pattern is recorded at a rate starting at 5 samples per hour and decreasing until the end of the experiment.

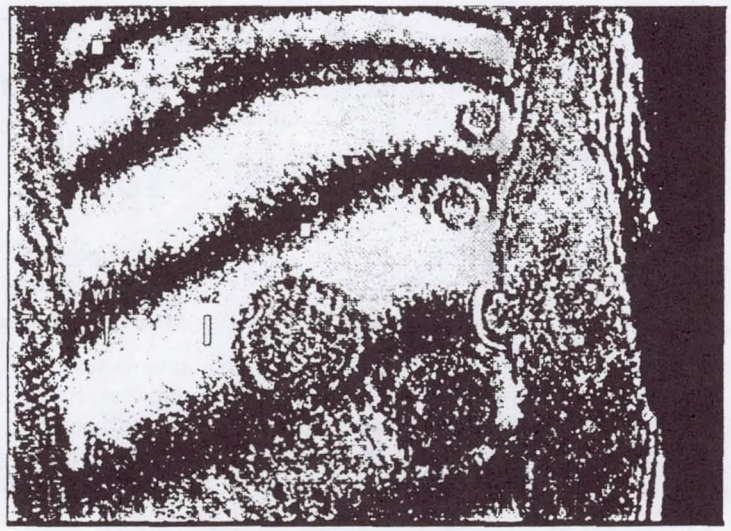

Figure 9: Reference fringe pattern and position of grey value measurement windows in experiment 1L3.

Each interferogram carries only information on relative phase along the image. This phase must be corrected subtracting an initial phase (derived from the pattern in figure 9) and followed during time to record phase increments of 2π each time a new fringe crosses over a given pixel or window. This phase is

$$\varphi(x,y,t) = \varphi_0(x,y) + 2\pi F(x,y,t)$$

where φ_0 is the initial phase difference (mostly due to slightly non-parallel reactor walls) and F is the number of fringes that crossed over the pixel at (x,y) since the beginning of the experiment until time t. This phase can be finally converted to salt concentration values multiplying it by a factor that linearly relates the change in refraction index produced by a given change of concentration with this change in concentration.

It is clear that, to evaluate concentrations using this technique, a spatial reference (initial status of the system before inhomogeneisation) is needed to compute φ_0 and a time reference (time series of grey values at each pixel sampled at a frequency large enough to detect all the travelling fringes) is needed to compute F. To have this time reference, laser illumination must be very stable because laser instabilities produce random displacements of the fringe pattern that make impossible to evaluate F. Unfortunately, during the LMS mission, the laser of the interferometer installed in the APCF was unstable, producing frequent jumps of the fringe pattern. This fact was confirmed by people managing the APCF project. This erratic jumps can be seen in figure 10 where the time history of the grey value inside three different windows (see figure 9) is plotted.

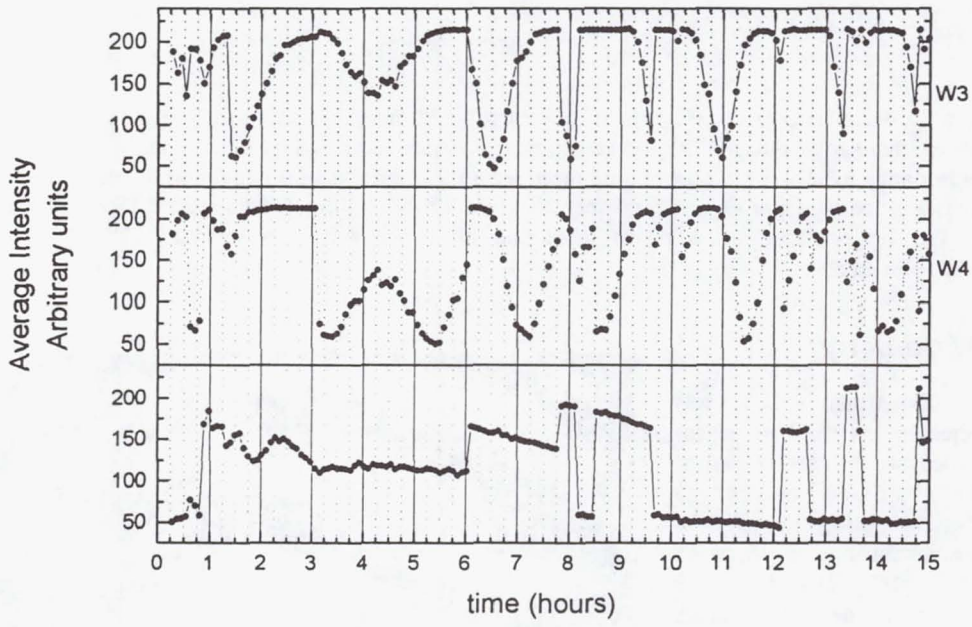

Figure 10: Time evolution for the first 15 hours of the average grey value inside three of the windows defined in figure 9.

The bottom plot show the grey value time evolution for the w5 window. This window is located on the quartz glass of the reactor body. Therefore no change in grey value is expected in this window during the experiment because the optical path at this position is constant. It can be clearly seen that this grey value, related with the local phase, randomly jumps with time in an unpredictable way. This instability destroys the information on the number of fringes that travels over a given window. The two top plots show the grey value evolution in windows w3 and w4, inside the protein chamber. This curves should be sinusoidal-like waves (as can be seen in w3 and w4 from 3 to 6 hours) of variable frequency related to the time derivative of salt concentration allowing the evaluation of the F function. This lack of stability continues during the whole experiment as can be seen in figure 11, where the grey value at a window on the glass body (obtained from the full interferograms recorded after 15 hours) is plotted from t=15 hours to the end of the mission.

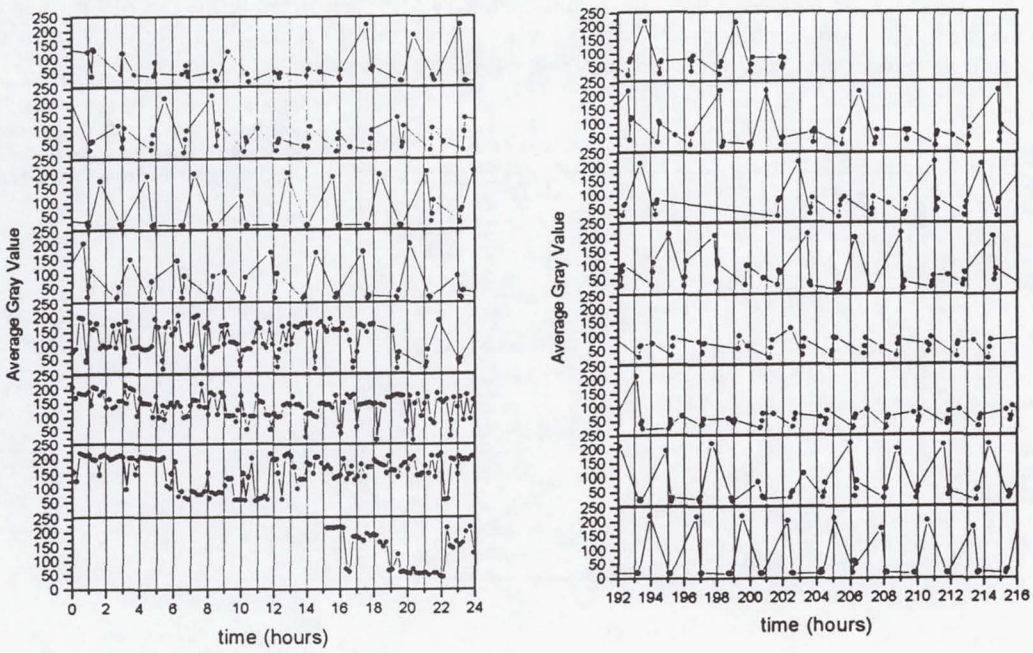

Figure 11: Average grey value inside a window positioned on the glass body of the reactor for times covering the whole experiment. First day is at left bottom and last day at right top.

With these data, only relative information is available, that is: we only know the spatial concentration gradient for each image without any knowledge of the time gradient (the concentration change at a given point between two consecutive images). Therefore, we cannot reconstruct absolute concentration maps inside the protein chamber. Only relative concentration maps, i.e. maps of concentration where an unknown offset is uniformly added to all concentration values can be computed. Two of such maps for the experiment 1L3 are shown in figure 12 for one time before nucleation and a time after nucleation of crystals in the protein chamber.

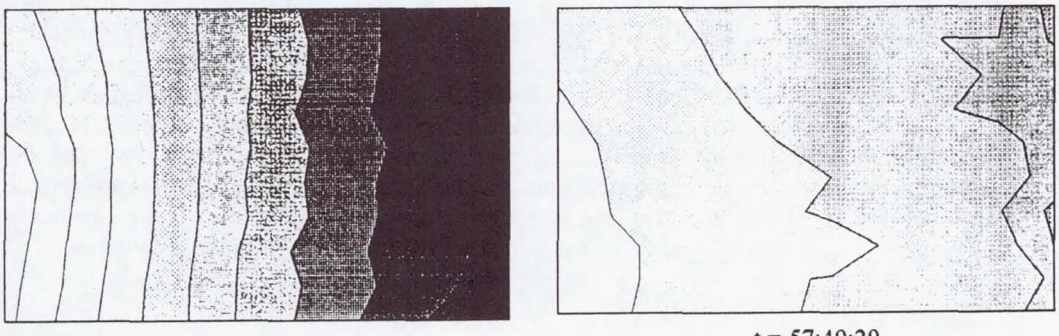

Figure 12: Relative concentration maps inside the protein chamber. Concentration difference between consecutive lines is 0.2 % w/v.

To improve the usefulness of these data we are currently trying to use external extra information in order to recovery the lost time derivative information. Our approach consist in using simulation data for this task. Simulations of diffusion-reactions systems have been developed in our laboratory during

the last years[4]. These simulations include one and three dimensional simulations of the APCF. Fitting the experimental gradients to the simulated profiles for the same time, an estimation of the unknown offset can be calculated. Figure 13 shows our preliminary data fitting for the interferometric data obtained from an on-ground preliminary interferometry study performed inside the APCF flight model[5] to the salt diffusion profiles computed using a three dimensional simulation of the APCF. Although the fit is very good, the use of this technique deserve further discussion in our laboratory.

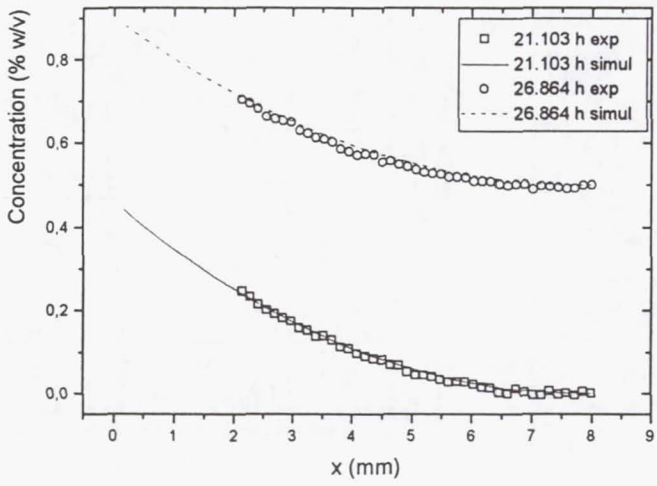

Figure 13: Experimental (from interferometry) and simulated salt concentration profiles inside the FID200 APCF reactor for two different times.

2.5. X Ray studies

Limit of resolution for these crystals has been measured at station W32 at LURE (Orsay, France), the average resolution limit for the crystals analysed being about 1.25Å. The use of flat capillaries inside the protein chamber simplify the handling of crystals although some problems related to the sealing of capillaries must be solved. One crystal grown inside them produced a diffraction pattern of higher resolution than those grown without capillaries (1.15 Å), but this result was not reproducible, therefore there is no clear evidence of limit of resolution improvement using these capillaries.

Line profiles for diffraction spots at 3Å resolution were measured in station D25b installed at the positron storage ring DCI at LURE. This station is optimised for mosaicity measurement using extremely low vertical divergence and bandwidth as well as a very high resolution goniometer. During the experiments reported here, we used a four reflections (three of them symmetric) Si 111 monochromator (d=3.1353 Å) oriented to reflect in the vertical plane. The wavelength was adjusted to 1.2 Å (11.033°). The NaI scintillation detector was set at 2θ=22.07° (symmetrical setting) to record diffraction spots having the same spacing than the monochromator. Using this combination of monochromator and recording geometry, a total experimental width of only 0.8'' is superimposed to the measured peaks. All widths in this work are reported without correction for this experimental width. Line profiles acquired were fitted as the addition of several (from 2 to 4) gaussian functions

$$y = y_0 + \frac{A}{w\sqrt{\pi/2}} Exp\left(-2\left(\frac{(x - x_c)}{w}\right)^2\right)$$

[4] F. Otálora (1995) PhD Thesis, Univ. Granada. F. Otálora & J.M. García-Ruiz. J. Crystal Growth 169 (1996) 361-367. F. Otálora and J.M. García-Ruiz. (1997) J. Crystal Growth. In Press. J.M. García-Ruiz, F. Otálora (1997) ESTEC contract 11629/95/NL//JS final report

[5] We are testing this technique using on-ground data rather than data from the LMS mission because laser was stable during the experiment performed on-ground in the same conditions that the flight experiments and therefore we know the absolute concentration profiles.

where y_0 is an offset (background noise level), A is the area (integrated intensity) of the peak, w is its width and x_c is the co-ordinate of the maximum. Lorentzian functions has been also tested, but they produce fits of lower quality.

Very small mosaicity values has been found. All peaks show non-corrected FWHM ranging from 10'' to 20''. All these peaks are fitted to the addition of 2 to 4 domain peaks. The width of these components ranges from 4.5 to 15 arc seconds. Figure 14a shows a very narrow peak (FWHM = 10.5''). This crystal peak is composed of only two domain peaks, having widths of 6.1'' and 12.3''. The integrated intensity of these domain peaks is 17165 for the narrow peak and 26311 for the wide one (a ratio of 0.65). Figure 14b shows the profile of the same peak after closing the beam by adjusting the slits while controlling the beam size and position using an X-ray camera in the path of the direct beam

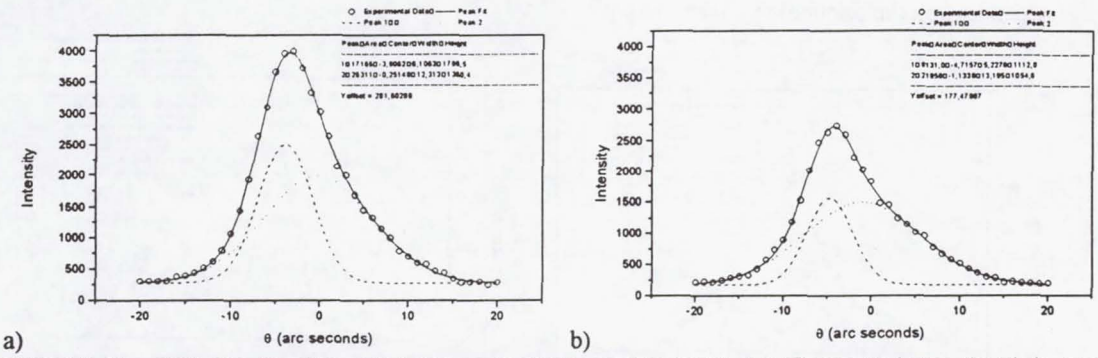

Figure 14:. Line profile of a diffraction peak from a space-grown lysozyme crystal. a) profile recorded when the whole crystal is exposed. B) profile recorded exposing only the central part of the crystal.

through the crystal. This peak, records the contribution of the central part of the crystal. The position and width of the two domain peaks is very similar (5.2'' and 13.2''), but their relative intensity has changed to 9131 for the narrow peak and 21858 for the wide one (a ratio of 0.42).

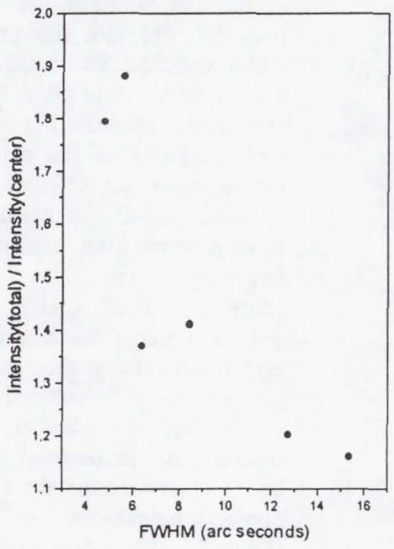

Figure 15: Ratio of the integrated intensity recorded exposing the whole crystal and only the central part versus the width of the corresponding domain peak.

The volume of the crystal is composed of two mosaic blocks although no conclusions can be derived in terms on their nature and defect structure except that they are not perfect mosaic domains and they are not homogeneously distributed over the crystal, the parts of lower quality being concentrated at the centre of the crystal. This is reasonable since the growth rate of these crystals changes with time as shown in chapter 2.2, being faster at the beginning of the experiment (while the centre of the crystal is growing). It has been previously shown that the domains of different quality making up a lysozyme single crystal are not homogeneously distributed and that this inhomogenity can be caused by differences in growth rates[6]. Figure 15 shows the ratio between the intensity of different domain peaks when exposing the whole crystal and the intensity when only the centre of the crystal is exposed versus the width of the domain peak. This figure clearly shows that the intensity reduction is larger for narrow peaks than for wider ones and therefore that the average quality of he central zones of the crystals is lower that that of peripheral zones.

Different crystals in the same experiment show different number of domain peaks although the average width of these components is in the same range. Figure 16a shows the line profile of a crystal from the

[6] F. Otálora, J.M. García-Ruiz and A. Moreno, *J. Crystal Growth* 168 (1996) 93-98.

same experiment as that illustrated in figure 14. This profile has a FWHM of 13.8'' and is composed of four gaussians of widths 14.5'', 8.13'', 6.4'' and 4.6''. After acquiring this profile we rotated the crystal by 80 degrees (the limit of the goniometer) and recorded another spot at the same resolution (3 Å). This peak is illustrated in figure 16b. Large differences are observed between both crystal peaks. At first sight, it is clear than the peak illustrated in figure 16b is wider (27.0''). This means that the mosaicity (mean misalignment between mosaic blocks) and probably also the internal defect structure of each block are anisotropic properties. The same domain peak, seen from different directions can show different widths and therefore different heights (though the same amplitude) and the relative position of these domain peaks change depending on the crystallographic directions, producing crystal peaks of different width. Anisotropy in the width of domain peaks can be due to the accumulation of one of two-dimensional crystal defects in a given direction, or by differences in the mechanic properties of the crystal lattice giving rise to microbending (at the scale of several unit cells) of different amplitudes depending on the orientation.

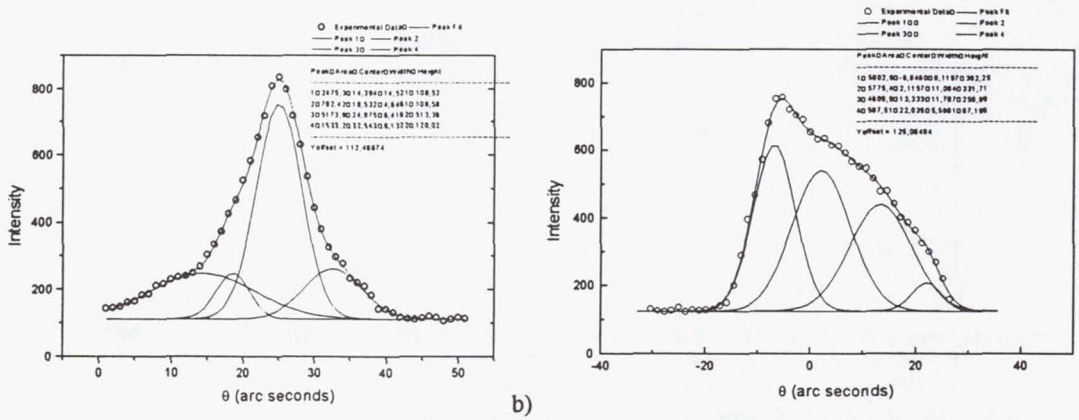

Figure 16: Profile of two spots from the same crystal. Both spots are recorded at θ angles differing in 80°.

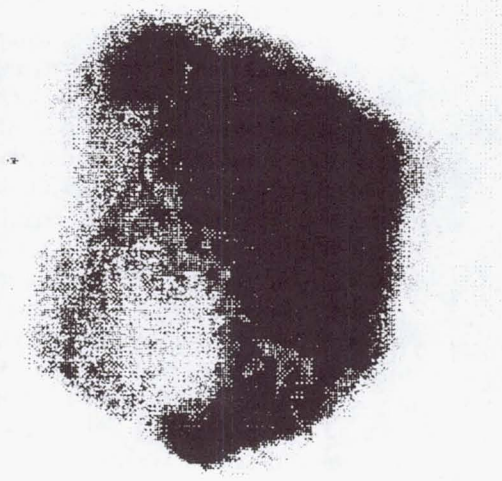

Figure 17. Topography recorder from the spot whose profile is illustrated in figure 14. As faces and edges are observed, this spot is a very clear projection of the crystal.

Taking into account that the intrinsic width of a perfect lysozyme crystal can be estimated[7] to be less than 1'' and that the experimental width with the set-up used is about 0.8'', a width of, at most, 1.8'' can be attributed to factors other than the real mosaic spread of the samples. The best domain peaks found (having a width of about 5'') must, therefore, contain some kind of further defect structure such as a given concentration of discrete crystalline defects or a continuous bending of the crystal structure at the scale of a few arc seconds. This second possibility seems to be coherent with the mechanical properties of protein crystals and with the absence of sharp domain boundaries in topography (figure 17).

[7] J.R. Helliwell. J. Crystal Growth 90 (1988) 259

Conclusions

Nucleation in the experiments was higher than expected. Studies performed after the flight and the results presented here on time and space distribution of the nucleation flux support indicate that this fact is due to a early homogenization of the salt concentration inside the protein chamber because of the shortness of that chamber. Although the final result is an almost equal probability of nucleation over the whole chamber, taking into account only the first nucleation events, a spatial structure similar to that observed in one dimensional counterdiffusion experiments is observed. This control on the spatio-temporal distribution of non-constant nucleation flux inside APCF reactors has never been attempted before this experiment Further experiments with lower protein concentration and, if possible, longer protein chambers are necessary to continue advancing in this direction.

Crystal size (length) versus square root of time for the crystals studied show linear zones during most of the experimental time with two crossovers, the first one at the beginning of the experiment and another close to he homogenization. This behaviour is interpreted as a result of the diffusion control of the growth rate during the experiment after a first short stage controlled by nucleation kinetics. This trend is broken when the protein exhaustion zones around growing crystals display important overlapping. Maximum growth rates up to 0.05 mm/hour are observed slightly after nucleation.

Crystal movement has been observed at average rates of 3.6 μ/h (maximum rate of 20 μ/h). The movements of different crystals are correlated, for a given time all crystals move in the same direction, suggesting that they are produced by a mechanism operating at a lengthscale larger than the growth cell such as residual accelerations of the spaceship. Another mechanism producing uncorrelated movements of crystals at lower rates seems to be superimposed to the previous one. These random displacements can be due to random errors in the determination of the crystal position or to a short lengthscale mechanism (such as some kind of convection) operating inside the protein chamber. More measurements of crystal movements are being performed to confirm the existence of this second mechanism.

Progresses with interferometric data have been difficult (and continue to be) because of technical problems. The laser installed in the Mach-Zehnder interferometer was unstable during the mission, cluttering the interferograms with random phase jumps. These data, as supplied, are unsuitable for absolute concentration calculations inside the reactor, and our work is being concentrated in recovering this reference information by using simulation of transport dynamics inside APCF reactors. Our first results seems promising, with a good agreement between simulation and experiments, but they are still under active development and discussion.

X-ray diffraction showed the very good quality of crystals, an average limit of resolution of 1.25 Å has been observed. The use of flat capillaries reduces the crystal handling by getting rid of the mounting step. Most of our work using X-rays has been devoted to an exhaustive study of mosaicity.

At a larger scale, very good lysozyme crystals seem to be composed of several slightly defective mosaic domains, in a number ranging from two to four for the samples examined. Very small mosaicity values has been found. All peaks show FWHM ranging from 10'' to 20'' and are composed by at least two domains having FWHM as low as 5'' (without correction). These values are comparable with those found for crystals grown on-ground by the gel acupuncture method. Therefore, in this case no advantages seem to be derived from the microgravity growth of lysozyme in terms of mosaicity. Since mosaicity is mainly controlled by the density and nature of crystalline defects in the crystal and this concentration is mainly a function of the growth rate, this result is consistent with the large initial growth rates measured in crystal lysozyme crystal growth experiments in the APCF and with the mixed regime for lysozyme growth kinetics[8] that provokes large fluctuations in growth rate. This conclusion cannot be interpreted, as a claim against microgravity experiments because no relation has yet been demonstrated between mosaicity and limit of resolution and, from our results, it may even not exist. More experimentation in microgravity crystal growth is needed to complete our present knowledge on this problem, including the systematic determination of accurate limit of resolution and mosaicity values for different macromolecules growing under different kinetic regimes.

[8] P.G. Vekilov, J.I.D. Alexander, F. Rosenberger. Phys. Rev. E 54 (1996) 6650-6660.

Mosaicity is an inhomogeneous and anisotropic property. Domains of different quality are not homogeneously distributed. The central part of crystals analysed, that has grown at a faster rate, accumulates the domains having higher mosaicity. We found large FWHM differences for peaks at the same resolution in the same crystal observed from different orientations. This proves that mosaicity can be anisotropic. This anisotropy must be due to differences in the width of domain peaks contributing to the shape of the whole peak or to differences in the relative position of these domain peaks. Further enhancement in the mosaicity values is expected by using protein of very high purity. Our experiments in microgravity (as well as those on-ground) has been performed using lysozyme from Sigma without further purification. The influence of impurities will be tested and compared with that of other physicochemical parameters.

Articles/presentations resulting from the flight

Our results on X-ray studies have been presented at the Spacebound 97 held in Montreal (May 1997) and will be published in the conference proceedings. Nucleation, growth rate and crystal movements will be presented at the ECM-17 to be held in Lisbon (August, 1997) and are the subject of an article in preparation to be submitted to Journal of Crystal Growth. Crystal movement result are being used as part of an article on this topic to be submitted to Microgravity Sci.Technol. References are collected in the following list:

- F. Otálora, B. Capelle, A. Ducruix and J.M. García-Ruiz (1997) "Characterisation of tetragonal lysozyme single crystals grown in the sts-78 mission" oral communication presented in the Spacebound97 Montreal, Mayo 1997.

- F. Otálora, B. Capelle, A. Ducruix and J.M. García-Ruiz (1997) "The mosaicity of protein crystals grown in normal and reduced gravity environments". Accepted for publication into the conference Proceedings.

- Otálora, F., Rondón, D., Novella, M.L. and García-Ruiz, J.M. (1997) "Lysozyme crystal growth in microgravity. X-ray, image analysis and interferometric results from the APCF during LMS mission." oral communication presented in the ECM-17 to be held in Lisbon, August 1997.

- Otálora, F., Rondón, D., Novella, M.L. and García-Ruiz, J.M. (1997) "Lysozyme crystal growth in microgravity. X-ray, image analysis and interferometric results from the apcf during lms mission." In preparation, to be submitted to Journal of Crystal Growth.

- J.M. García-Ruiz and F. Otálora (1997) "Crystal movements during microgravity crystal growth experiments" In preparation, to be submitted to Microgravity Sci.Technol.

Summary of the experiment and the accomplishments

The objectives of this set of experiments were concentrated on the technical and phenomenological aspects of protein crystal growth in the APCF. Therefore, a well known protein, lysozyme, was selected. Technical topics investigated were the new APCF Mach-Zehnder interferometer available for the first time during this mission and new experimental settings for APCF reactors such as the use of gelled solutions, the filling of the rotatory plug with protein solution and the use of a pack of flat capillaries filling the protein chamber. Phenomenological studies include investigations on the growth kinetics of lysozyme under counterdiffusion conditions in microgravity and the movement of crystals during growth. Additionally, an in-depth study on the mosaicity of these microgravity crystals has been performed including the comparison of these results with on-ground observations.

The underlying idea of this set of experiments was to get information on how the APCF performs as a device for purely diffusive counterdiffusion experiments. In this framework, interferometry is useful to control the dynamics of diffusive transport, gelled solutions can be used to control the time and space gradients of supersaturation and the use of the rotatory plug as part of the growth chamber makes it longer reinforcing the one-dimensional nature of the experiment. Nucleation flux and growth rate are a function of the rich spatio-temporal behaviour of the system due to its out of equilibrium nature. The movement of crystals during growth acts, in principle, as a limiting factor for the ideal diffusive experiment and, therefore, must be studied and understood, but it can be used even as a beneficial feature for crystal growth if it its predictable and manageable. The final output of the whole process are the, hopefully, good protein crystals for structural analysis; here we tried the use of flat capillaries to have pre-mounted crystals free of further mounting and handling and performed a exhaustive study on the mosaicity of the crystals obtained, comparing the results from this mission with that from on-ground experiments using one-dimensional counterdiffusion techniques and assessing the usefulness of this value in terms of crystal quality meassure.

Lysozyme crystals grown in a diffusive regime, although the out of equilibrium counterdiffusive nature of the experiments was not fully exploited due to the shortness of the reactors that causes the almost complete homogenisation of the protein chamber before nucleation. Crystals move during crystal growth due mainly to small residual accelerations of the spaceship. The use of capillaries inside the protein chamber is a beneficial feature that eliminates the need of further crystal handling. The usefulness of interferometric data was compromised by laser instabilities. Mosaicity of the crystals obtained is very good, although no significantly better than that of crystals grown on-ground by the Gel Acupuncture method. In any case, mosaicity seems not to be directly correlated with the resolution limit in diffraction studies.

Advanced Protein Crystallization Facility (APCF)

Comparative Analysis of Aspartyl tRNA-synthetase and Thaumatin Crystals Grown on Earth and In Microgravity

Principal Investigator:

Dr. Richard Giegé
CNRS
Strasbourg, France

Comparative analysis of Aspartyl tRNA-synthetase and Thaumatin crystals grown on earth and in microgravity

LMS (STS-78) L+1 Report

by

Joseph D. Ng, Bernard Lorber, and ‡Richard Giegé

UPR 'Structure des Macromolécules Biologiques et Mécanismes de Reconnaissance ' Institut de Biologie Moléculaire et Cellulaire du CNRS, 15 rue René Descartes, F-67084 Strasbourg Cedex, France

‡Corresponding Author

Introduction

Evidence has accumulated in the past years from a variety of experiments performed in microgravity, that suggest reduced gravity conditions can diminish the deleterious factors and consequently improve the quality and increase order for protein crystals (DeLucas *et al.*, 1986; 1989; 1991; DeLucas & Bugg, 1987; Erdmann *et al.*, 1989; McPherson *et al.*, 1991). Macromolecular crystal growth experiments, using the *T. thermophilus* AspRS expressed in *E. coli* (ttAspRS) and the plant sweetening protein, Thaumatin, were conducted on a US Space Shuttle mission designated Life Microgravity Spacelab (LMS) mission STS-78, flown June 20-July 7, 1996. The studies were carried out using dialysis reactors of the Advanced Protein Crystallization Facility (APCF) provided by Dornier Deustche Aerospace. The experiments in each device were performed at a constant temperature during a complete mission elapsed time of 16 days. The fundamental objectives of this study was to obtain crystals of protein in microgravity, to determine if the influence of microgravity affects crystal growth and to observe any anomalies or enhancement in growth that may implicate a gravity effect.

Model Proteins

Thaumatin

Thaumatin is a monomeric protein from the African Serendipity Berry *(Thaumatococcus daniellii)* valued for its intensely sweet taste and its use as a non caloric sweetener. It has a molecular weight of 21,500, contains four disulfide bridges, and possesses a high degree of stability. It consists primarily of beta structure organized in two associated domains. The structure was first determined in an orthorhombic crystal at 1.7 Å resolution (Ogata *et al.* , 1992), and later in a second orthorhombic, a monoclinic, and a tetragonal crystal form (Ko *et al.*, 1994). The tetragonal crystal form, grown from tartrate, and refined to 1.7 Å resolution (Ko *et al.*, 1994) was that studied in these experiments. The mechanisms and kinetics of growth at the molecular level for thaumatin crystals are among the most thoroughly characterized of any protein crystal (Malkin *et al.*, 1996a; Malkin *et al.*, 1996b). Crystals can be grown in a conventional laboratory in 12 to 48 hours at room temperature by a variety of methods. The crystals are of space group $P4_12_12$ with a = b= 59 Å and c = 158 Å having a single molecule as the asymmetric unit. The habit is that of a tetragonal bipyramid, often reaching linear dimensions in the conventional laboratory greater than 1 mm. The crystals, which contain about 45% solvent, are mechanically robust. Their growth has been studied by a variety of physical techniques including interferometry (Kuznetsov *et al.*, 1995) and atomic force microscopy (Malkin *et al.*, 1996a; Malkin *et al.*, 1996b).

Aspartyl-tRNA synthetase

The vital and key step in the process of translating genetic information is the aminoacylation of tRNA (Giegé *et al,* 1993). The enzymes that mediate this action are the aminoacyl-tRNA synthetases which catalyze the addition of an amino acid to their cognate tRNAs (*e.g.* Schimmel & Söll, 1979; Schimmel, 1987; Giegé *et al,* 1993). Structurally, aaRS's exhibit a wide divergence shown by differences in their molecular size, oligomeric state, modular and three-dimensional structures (Moras, 1992). Sequence analyses of all known aaRS's have led to the categorization of these enzymes into two classes having each ten members (Eriani *et al,* 1990). The class distribution is correlated to the functional property of aaRS's and to their capacity to charge the amino acid at either the 2'- or the 3'-hydroxyl group of the 3' end ribose (Fraser *et al,* 1975; Sprinzl & Cramer, 1975).

Two of the most well characterized class II synthetases are the aspartyl-tRNA synthetases from yeast and *Thermus theromophilus*. Structural information have been obtained for both of these enzymes and have found to share common structural motifs (Ruff *et al,* 1991; Delarue *et al,* 1994). In particular, the aspartyl-tRNA synthetase from *T. thermophilus* (ttAspRS) has been cloned, overexpressed in *Escherichia coli*, crystallized and its structure determined to 2.5 Å resolution (Poterszman *et al,* 1993; Delarue *et al,* 1994). Orthorhombic crystals of the ttAspRS can be grown out of precipitation with the space group $P2_12_12_1$ with cell dimensions a = 61.4Å, b = 156.1 Å and c = 177.3 Å (Ng, *et al.*, 1996) . ttAspRS is a homodimer with each subunit having a molecular weight of 66 kD and a polypeptide composed of 580 amino acids (Poterszman *et al,* 1993). This enzyme has sequence and structural features that can be related to other AspRS's and class II aaRS's. A comparison among seven known sequences of AspRS's has revealed a clear partition between eucaryotes and prokaryotes having molecular features that are uniquely exhibited in the thermophilic enzyme which are not found in any of the other known AspRS's (Poterszman *et al.,* 1993). The crystallographic structure of ttAspRS revealed the first atomic description of a prokaryotic AspRS and showed structural motifs that are specific to prokaryotes (Delarue *et al.,* 1994).

The most striking biochemical property of ttAspRS, as with most other thermophilic enzymes, is its resistance to denaturation under high temperatures. It is relatively very stable in that it can sustain biological activity at temperatures up to 80°C and is able to charge aspartate to its cognate tRNA at a wide range of temperatures. This property makes ttAspRS a favorable model protein for crystal growth studies, in particular for explaining effects of temperature. This is most interesting for studies on synthetases which are relatively unstable molecules in contrast to other proteins like lysozyme that are often studied under microgravity.

Materials and Methods

Proteins and chemicals

Preparation of Thaumatin

Thaumatin was purchased from Sigma (St Louis, MO). A single batch (Cat. N° T-7638, lot 108F0299) of dry protein powder was used. The protein was dissolved either in a buffer prepared with 0.1 M N-[2-acetamido]-2 iminodiacetic acid (ADA) (Cat. N° A-9883, lot 92H5635, Sigma) adjusted at pH 6.5 with NaOH or in water (see Table 1). For crystallization, the precipitant stock solution was 1.6 M sodium DL-tartaric acid (Cat. N°T-5259, lot 101H0695, Sigma) in 0.1 M ADA titrated with NaOH to pH 6.5. All solutions were prepared with ultrapure sterile water (Fresenius, Louviers, France) and sterilized by filtration through 0.22 µm pore size membranes (Millex, Millipore).

A concentrated stock solution of thaumatin was freshly prepared by adding 1 ml of ADA buffer pH 6.5 to 100 mg protein powder. After dissolution, the solution was centrifuged for 20 min at 15,000 g. The supernatant was filtered through 0.22 µm Ultrafree low binding membranes (Cat. N°UFC3 0GV 00, Millipore). The protein concentration was calculated from the UV absorbance of a 1/250 dilution using a molar extinction coefficient of 28,270 (based on the tryptophan and tyrosine content).

Isolation and purification of ttAspRS

The ttAspRS expressed in *E. coli* was purified with two chromatographic steps as described by Poterszman *et al* (1993) with slight modifications. An attractive property of recombinant ttAspRS is that it is heat tolerant. Crude bacterial cell extract can be exposed to elevated temperature, thus denaturing contaminant proteins. The ttAspRS thus can be found exclusively in the soluble portion of the cell extract and use of denaturants is not required for recovery at any stage. The ttAspRS enzyme can essentially be purified to more than 90% homogeneity.

Crystallization apparatus and conditions used

We have utilized dialysis liquid diffusion reactors (DIA) for crystallization within the Advanced Protein Crystallization Facility (APCF) developed by Dornier Deutsch Aerospace (Snyder *et al*, 1991; Bosch *et al.*, 1992) aboard the NASA Space Shuttle, Columbia (STS-78, mission LMS). The dialysis reactor consists of two quartz glass blocks separated by a dialysis membrane. The upper block contains the protein solution (67 µl or 188 µl), the lower block, the salt solution. A cylindrical quartz glass plug containing also the salt solution separates the salt and buffer chamber. Upon activation, the glass plug is rotated by 90°C so that all chambers become open and all volumes then come into contact. Likewise, the plug is rotated back during deactivation before returning to earth. Reactors for space and ground controls were prepared in exactly the same manner and had undergone the exact same transport and pre-launch conditions (this included any delay launch time as well). The DIA ground control reactors were activated for the same period of time as the ones that were launched in space in parallel with the time of flight. Two 67 µl reactors were used for the crystallization of ttAspRS and two 188 µl reactors were used for thaumatin. The contents of the reactors and the crystallization conditions are described in Table 1.

The APCF was activated several hours after a microgravity environment was achieved, and deactivated (the stopcocks rotated in reverse) a few hours before reentry. Duration of activation of the crystallization reactors under the microgravity environment was 16 days for this mission. Following the mission the dialysis cells were immediately examined, photographed, and X-ray diffraction analysis initiated.

Crystallographic methods

Three dimensional X-ray data were collected at the EMBL Outstation DESY, Hamburg, Germany on beam line X11 using a MAR Research image plate. Complete data sets of the protein crystals grown on LMS and the corresponding earth controls were obtained using crystals of same size and volume. Data were collected at 20°C with crystal-to-detector distance of 250 mm. Oscillation angles of 0.5° were used with an X-ray wavelength of approximately 0.91Å with exposure time varying from 20 to 30 sec. Data collection was evaluated on line with the programs DENZO and SCALEPACK (Otwinowski & Minor, 1996) at the DESY synchrotron station. Both earth and microgravity grown crystals were collected to 2.0 Å with $R_{sym's}$ ranging from 0.023 to 0.435 for ttAspRS. Similarly, earth and microgravity grown crystals of thaumatin were collected to 1.6 Å with $R_{sym's}$ ranging from 0.021 to 0.175 for reflections having an I/σ greater than 3.

The mosaicities of ttAspRS and the thaumatin crystals, obtained under both ground and space growth conditions, were evaluated by measuring the rocking widths for selected reflections presented as the full width at half maxima (FWHM) (Helliwell, 1988). Crystal mosaicity yields the angular dispersion of the crystal blocks characterizing the crystals and in turn reflects the intrinsic crystal order (Weisgerber & Helliwell, 1993). Space and earth grown crystals of the same volumes were mounted in standard glass capillaries. Data for mosaicity measurements were recorded by using a CCD detector on beamline CRG BM2 (D2AM) at ESRF, Grenoble, France. This particular synchrotron beamline produces a highly collimated, intense radiation of very low divergence and minimal $\delta\lambda/\lambda$. The critical energy was 19.5 keV with a focused beam of 0.3 mm diameter at the sample with a maximum vertical divergence of 0.15 mrad and a maximum horizontal divergence of 9.0 mrad (Ferrer *et al.*, 1996; personal communication). The intensity of the full beam was about 10^{11} ph/sec at 0.98 Å wavelength with an energy resolution, $\delta\lambda/\lambda$, of approximately 10^{-4}. Direct monochromatic measurements were obtained by recording data over oscillation ranges of 0.5 degree for indexing of reflections and subsequently an oscillation angle of 0.003 degrees with 0.2 degrees of crystal rotation at 10 seconds exposure per frame. The data for mosaicity analysis were processed with XDS and images of the intensities visually observed and quantitated with MARVIEW (Kabsch, 1988a, 1988b).

Reflections were measured in the vertical plane with respect to the direct beam so that a fully recorded reflection can be expressed as:

$$\varphi_r = \gamma + \eta + (\delta\lambda/\lambda)\tan\theta$$

where φ is the reflecting range, γ is the mean divergence in the plane defined by the direct and the diffracted beams, η is the crystal sample mosaicity, λ is the average wavelength of the X-ray beam and θ is the Bragg angle of the reflection (Snell et al., 1995; Ferrer et al., 1996). The values of γ and $\delta\lambda/\lambda$ were minimized in this study by considering only reflections located in the vertical plane including the incident beam and those at low resolution. The measured FWHM value has the instrument resolution function value IRF (0.15 mrad or 0.009°) deconvoluted out. The profiles presented here were not corrected for Lorentz broadening.

Results and Discussion

Visual and microscopic observations

Crystals were observed in the two dialysis reactors containing thaumatin and only in one reactor containing the ttAspRS for microgravity. All of the corresponding dialysis reactors activated as ground controls for both proteins contained crystals . There was a clear increase in average and largest sizes of crystals grown by dialysis in microgravity compared with ground controls. For thaumatin the number and sizes of crystals from the dialysis reactors were assessed with an optical microscope and are summarized in Table 2. Each of the space flight reactors contained more than 1000 crystals having an average size range of 0.4 (Fig 1) The corresponding ground control reactors contained about twice the number of crystals having an average size range of 0.3 mm.

In the space reactor containing ttAspRS, three huge crystals were found in the protein chamber in the midst of precipitation measuring over 3 mm in its longest dimensions in size accompanied with some very small crystals. However, the corresponding ground controls contained only very few crystals also with no more than

two to three in each reactor having the largest size of about 2mm in length. Even though ttAspRS crystals obtained from both space and earth grown environments were relatively large, the crystals grown in microgravity were exceptionally large (Fig 2).

Visually, the quality of the crystals of both proteins obtained from space, particularly those growing free of any surfaces, and including the largest, was very high. They appeared virtually flawless, with no observable imperfections, striations, or habit anomalies. Crystals attached to the cell walls (and which presumably nucleated there) did show defects near the sites of growth initiation but became flawless as growth proceeded into the bulk solution.

X-ray intensity measurements

X-ray diffraction data were collected from a total of three thaumatin crystals grown in microgravity. The data were merged to form a single data set. We have compared individual crystals grown in space and on earth in similar APCF cells. In all measurements, the amount of data greater than 3σ (the average I/σ in all resolution ranges) was better for the microgravity crystals than for the earth controls. Both earth and space crystals diffract easily beyond 1.6 Å with the inclination of the space grown crystal to extend to higher resolution. A quantitative comparison in the high resolution range 2.1-1.6 Å of a representative crystal from space and earth having the same size and volume is shown in Fig. 3. The data show reproducibly a significant increase of the I/σ ratio for the space grown crystals over all the resolution range investigated (Ng, *et al.*, 1997).

In the same manner three-dimensional intensity data were collected from two ttAspRS crystals grown in space (one of these is shown in figure 2). Figure 4 shows the distribution of observable data, I/σ greater than 3 compared to its corresponding earth-grown crystals. For the resolution range studied, space grown crystals yield as much as 93% more diffraction intensities than the control crystals grown on earth. However, at the resolution limits, the diffraction intensities of the earth and space grown crystals were only marginally different.

Mosaicity measurements

Fig. 5 and 6 presents typical mosaicity profiles of representative reflections from both space and earth grown crystals of thaumatin and ttAspRS respectively. The reflection profiles lie in the vertical plane of diffraction at approximately 4 Å resolution and their intensities were normalized for direct comparison. In the case of thaumatin, the curves appear coarse, displaying numerous shoulders, particularly in the latter portions of the profiles (Fig. 5). For all reflections, such irregularities were present, suggesting that the local features of the profile could be reflective of intrinsic properties of the crystal.

Each set of reflection profiles of the space and earth grown crystals were averaged and Gaussian fits of the sets of profiles were calculated (solid lines). Full widths at half maxima (FWHM) of the Gaussian curves were measured and in the case of thaumatin, the FWHM was 47 millidegrees (0.047 deg) for a crystal grown on earth (panel A) compared to 18 millidegrees for the space crystal (panel B). The difference in mosaicity between space and earth grown ttAspRS were much more dramatic showing the ttAspRS crystal from space to be about 8 times less mosaic than its corresponding earth control (Fig 6).

Notably, in all the reflections of all the space thaumatin grown crystal mosaicity profiles analyzed, a principle shoulder is observed in the beginning of the profiles while the end of the profiles remain very smooth and the curve diminishes sharply. We have no clear explanation for this observation. It may be possible that

these shoulders are indicative of some degree of twinning in the crystal or due to other defects not detected by low-magnification visual microscopy produced during storage or transport on the ground. This phenomenon contributes to the non-symmetrical fit of the Gaussian curves. In our measurements, the Gaussian plots are fitted to the principle peaks in which the FWHMs were evaluated. We have only considered the principle peak at this instant to represent the actual mosaicity profile for the space grown crystals. Even if the shoulder widths were included in the measurement of the FWHM, the value would still be significantly less than that of the earth grown crystals.

Consistently, reflections from crystals grown in microgravity from both space missions displayed narrower peaks of greater amplitude. This is likely a consequence of reduced discrete defects and dislocations compared to crystals grown on earth. The relative intensity and peak width differences of averaged profiles measured from reflections derived from space and earth grown crystals presented in Fig. 5 and 6 typify the mosaicity of thaumatin and ttAspRS crystals obtained on earth and in space. Tables 3 and 4 summarize the mosaicity evaluations of the space and earth grown crystals.

Conclusion

The results presented here for thaumatin and ttAspRS crystals grown in microgravity reinforce the conclusions of other reports based on different macromolecules that a microgravity environment can provide unique advantages (Giegé *et al.*, 1995). In these experiments the microgravity grown crystals were consistently and significantly larger, and substantially more defect free as judged by direct visual inspection. The resolution limit of the diffraction pattern, the I/σ ratio as a function of the Bragg angle, and the mosaic spread of crystals are generally agreed to reflect both the degree of internal order and the long range defect structure and its distribution within the crystal. That is, they serve as measures of the average statistical disorder of the molecules about the lattice points, as well as the extent of local but severe disorder introduced by defects such as dislocations, stacking faults, point defects or incorporated foreign material (Malkin *et al.* , 1996a). All of the data presented here, both intensity distributions and mosaic spread measurements, imply a higher degree of internal order, a lower defect density, and a reduction of severe faults for crystals grown in the absence of gravity.

Similar results, based on intensity data for microgravity grown crystals of several proteins, have been reported previously (DeLucas *et al.*, 1989; Day & McPherson, 1992; Koszelak *et al.*,1996), and comparable results based on mosaicity measurements have been presented for others (Snell, Weisgerber & Helliwell, 1996). Our conclusion is that they are mutually supportive and complementary, and both suggest the same conclusion, that crystals grown in microgravity can be significantly improved in their diffraction properties when compared with those grown on earth.

Acknowlegement

This research was supported by grants from the National Aeronautics and Space Administration (NASA), the Centre National d'Etudes Spatiales (CNES), and the Centre National de la Recherche Scientifique (CNRS). We acknowledge the help of Philippe Dumas, A. Théobald-Dietrich and C. Sauter at various steps of this project in Strasbourg. We thank J.R. Helliwell and J. Hirschler for discussions on mosaicity. We are grateful to R. Bosch and P. Lautenschlager at Dornier GmbH for their technical support. We thank DESY at Hamburg, and ESRF at Grenoble, for the provision of synchrotron facilities. We acknowledge M. Roth from Grenoble for

his assistance. Our appreciation also extends out to the European Space Agency (ESA) for flight opportunities in Europe on the NASA Space Shuttle, to the astronauts of the LMS mission for their participation and K. Fuhrmann and O. Minster of ESA for their administrative support. Finally, we thank CNES for a fellowship to J.D. Ng.

References

1 Bosch, R., Lautenschlager, P., Potthast, L. and Stapelmann, J. (1992) *J. Cryst. Growth* **122**, 310-316

2 Day, J. and McPherson, A. (1992). *Protein Science* **1**, 1254-1268.

3 Delarue, M., Poterszman, A., Nikonov, S., Garver, M., Moras, D. and Thierry, J. C. (1994) *EMBO J.* **13**, 3219-3229

4 DeLucas, L. J., Suddath, F. L., Snyder, R., Naumann, R., Broom, M. B., Pusey, M., Yost, V., Herren, B., Carter, D., Nelson, B., Meehan, E. J., McPherson, A. and Bugg, C. E. (1986) J. *Crystal Growth* **76**, 681-693

5 DeLucas, L. J. and Bugg, C. E. (1987) *Trends in Biotech.* **5**, 188-192

6 DeLucas, L. J., Smith, C. D., Smith, C. D., Smith, H. W., Senadhi, V. K., Senadhi, S. E., Ealick, S. E., Bugg, C. E., Carter, D. C., Snyder, R. S., Weber, P. C., Salemme, F. R., Ohlendorf, D. H., Einspahr, H. J., Clancy, L., Navia, M. A., McKeever, B. M., Hagabhushan, T. L., Nelson, G., Babu, Y. S., McPherson, A., Koszelak, S., Stammers, D., Powell, K. and Darby, G. (1989) *Science* **246**, 651-654

7 DeLucas, L. J., Smith, C. D., Smith, W., Senadhi, V.-K., Senadhi, S. E., Ealick, S. E., Carter, D. C., Snyder, R. S., Weber, P. D., Salemme, R. R., Ohlendor, D. H., Einsphar, H. M., Clancey, L. L., Navia, M. A., McKeever, B. M., Nagabhushan, T. L., Nelson, G. and Bugg, C. E. (1991) *J. Crystal Growth* **110**, 302-311

8 Erdmann, V. A., Lippmann, C., Betzel, C., Dauter, Z., Wilson, K., Hilgenfeld, R., Hoven, J., Liesum, A., Sainger, W., Muller-Fahrnow, A., Weber, G., Stegen, K. and Plaas-Link, A. (1989) *FEBS Lett.* **259**, 194-198

9 Eriani, G., Delarue, M., Poch, O., Gangloff, J. and Moras, D. (1990) *Nature* **347**, 203-206

10 Ferrer, J.-L., Hirschler, J., Roth, J. and Fontecilla-Camps, J. C. *ESRF Synchrotron Report* (1996) , 27-28

11 Fraser, T. H. and Rich, A. (1975) *Proc. Natl. Acad. Sci. USA* **72**, 3044-3048

12 Giegé, R., Puglisi, J. D. and Florentz, C. (1993) *Progr. Nucleic Acid Res. Mol. Biol.* **15**, 129-206

13 Giegé, R., Drenth, J., Ducruix, A., McPherson, A. and Saenger, W. (1995) *Prog. Crystal Growth and Charact.* **30**, 237-281.

14 Helliwell, J. R. (1988) *J. Cryst. Growth* **90**, 259-272

15 Kabsch, W. (1988a) *J. Applied Crystallography* **21**, 67-71

16 Kabsch, W. (1988b) *J. Applied Crystallography* **21**, 916-924

17 Ko, T.-P., Day, J., Greenwood, A. and McPherson, A. (1994) *Acta Cryst. D* **50**, 813-825

18 Koszelak, S., Leja, C. and McPherson, A. (1996) *Biotech. And Bioengin.* 52, 449-458.

19 Malkin, A. J., Kuznetsov, Y. G., Glantz, W. and McPherson, A. (1996a) *J. Struct. Biol.* **117**, 124-137

20 Malkin, A. J., Kuznetsov, Y. G., Glantz, W. and McPherson, A. (1996b) *J. Phys. Chem.* **100**, 11736-11743

21 McPherson, A. (1976) *Crystallography Reviews* **6**, 157-308.

22 Moras, D. (1992) *Current Opinion Struct. Biol.* **2**, 138-142

23 Ng, J. D., Lorber, B., Witz, J., Théobald-Dietrich, A., Kern, D. and Giegé, R. (1996) *J. Crystal Growth* **168**, 50-62

24 Ng, J. D., Lorber, B., Giegé, R., Koszelak, S., Day, J., Greenwood, A. and McPherson, A. (1997) *Acta Cryst. D*, In press

25 Ogata, C. M., Gordon, P. F., de Vos, A. M. and Kim, S. H. (1992) *J. Mol. Biol.* **3**, 893-908

26 Otwinowski, Z. and Minor, W. (1996) *Meth. in Enzymology* **276**, 307-326

27 Poterszman, A., Plateau, P., Moras, D., Blanquet, S., Mazauric, M.-H., Kreuzer, R. and Kern, D. (1993) *FEBS Lett.* **325**, 183-186

28 Ruff, M., Krishnaswarny, S., Boeglin, M., Poterszman, A., Mitschler, A., Podjarny, A., Rees, B., Thierry, J.-C. and Moras, D. (1991) *Science* **252**, 1682-1689
29 Schimmel, P. R. and Söll, D. (1979) *Annu. Rev. Biochem* **48**, 601-648
30 Schimmel, P. (1987) *Annu Rev. Biochem* **56**, 125-158
31 Snell, E. H., Weisgerber, S., Helliwell, J. R., Wechert, E., Hölzer, K. and Schroer, K. (1995) *Acta Cryst. D* **51**, 1099-1102
32 Snyder, R. S., Fuhrmann, K. and Walter, H. U. (1991) *J. Cryst. Growth* **110**, 333-338
33 Sprinzl, M. and Cramer, F. (1975) *Proc. Natl. Acad. Sci. USA* **72**, 3049-3053
34 Weisgerber, S. and Helliwell, J. R. (1993) Joint CCP4 & ESF-EACBM newsletter on Protein Crystallography **29**, 10-13

FIGURE LEGENDS

Figure 1. Crystals of thaumatin grown in microgravity. The average size of the crystals were approximately 0.4 mm in the longest direction seen directly in the protein chamber of the APCF reactor

Figure 2. Crystals of the ttDRS grown in microgravity (upper panel, A) and on earth (lower panel, B). a) d) A) The biggest crystal measured to be 3.3 mm x 2.5 . This crystal was carefully removed from the APCF reactor chamber, washed with a sodium formate wash buffer and placed on a glass cover slip for visual evaluation before the x-ray analysis. B) The control crystals grown on earth measured up to 2.0 mm x 1.1 mm. One of the crystals was transferred into a glass cover slip and carefully rinsed with a sodium formate wash buffer to remove the precipitated debris for observation before mounting into a capillary glass tube for x-ray analysis.

Figure 3. Graphs of the intensity (I) *versus* estimated error (σ) ratio as a function of resolution ($\sin^2\theta/\lambda^2$) for thaumatin earth and space grown crystals analyzed by synchrotron sources. The graphs are presented as modified I/σ over resolution where the value of I/σ 's are the effective "signal-to-noise" for the diffraction pattern at the resolution corresponding to the respective ($\sin^2\theta/\lambda^2$) values.

Figure 4. Graph of the intensity (I) versus estimated error (σ) ratio as a function of as a function of resolution ($4\sin^2\theta/\lambda^2$) for ttDRS earth and space grown crystals analyzed by synchrotron source. For the resolution range shown, space grown crystals yield as much as 93% more diffraction intensities ($>3\sigma$) than the control crystals grown on earth. However, at the maximum resolution limit, the diffraction intensities of the earth and space grown crystals were only marginally different.

Figure 5. Profiles of three representative reflections (17 -1 23), (-2 12 12), and (16 -10 5) at 4 Å were each evaluated from an earth (A) and space grown thaumatin crystal (B) studied for LMS. Reflections were obtained in the vertical diffraction plane such that the rotation axis was horizontal and perpendicular to the X-ray beam. Each set of reflection profiles for space and earth grown crystals were averaged and Gaussian fits of the sets of profiles were calculated (solid lines). The Gaussian plots were fitted to the principle peaks in which the FWHMs were evaluated. Only the principle peak is considered to represent the actual mosaicity profile for the space grown crystals. The full width at half maximum (FWHM) of a Gaussian fit for each profile was measured and its value deconvoluted out by the instrument resolution function value, IRF (0.15 mrad or 0.009°). FWHM values are indicated by short horizontal lines in the profiles and they show that the space grown crystal are about 2.5 times less mosaic than that of the earth grown. The intensities shown are normalized and the actual peak intensities measured to 250,000 counts per 0.1 seconds for the space crystal. In contrary, the spot intensities corresponding to the same reflections for the earth crystal were approximately two times less. Panel C shows a relative comparison of the averaged mosaicity profiles from an earth to a space grown crystal for the same reflections.

Figure 6. Profiles of three representative reflections (14 8 9), (4 33 -13), and (-14 5 -7) at 4 Å were each evaluated from an earth (left panel) and space grown ttDRS crystal (right panel). Reflections were obtained in the vertical diffraction plane such that the rotation axis was horizontal and perpendicular to the X-ray beam. Each set of reflection profiles for space and earth grown crystals were averaged and Gaussian fits of the sets of profiles were calculated (solid lines). Only the principle peak is considered to represent the actual mosaicity profile for the space groan crystals. The full width at half maximum (FWHM) of a Gaussian fit for each profile was measured and its value deconvoluted out by the instruments resolution function value, IRF (0.15 mrad or 0.009°). The intensities shown are normalized and the actual peak intensities measured to 570,000 counts per 0.1 seconds for the space crystal. In contrast, the spot intensities corresponding to the same reflections for the earth crystal were approximately 19 times less.

TABLES

Table. 1. Content of APCF Reactors

Table 2. Number and Size of Space and Earth Grown Crystals in APCF Dialysis Reactors

Table 3. Mosaicity Characteristic of Ground and Space Grown Thaumatin Crystals

Table 4. Mosaicity Characteristic of Ground and Space Grown ttAspRS Crystals

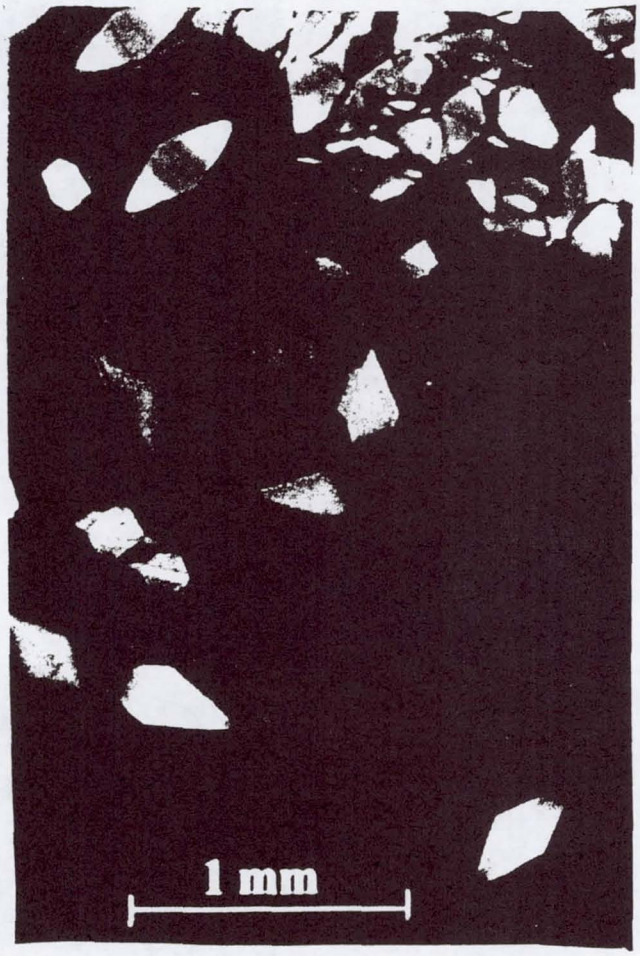

Figure 1

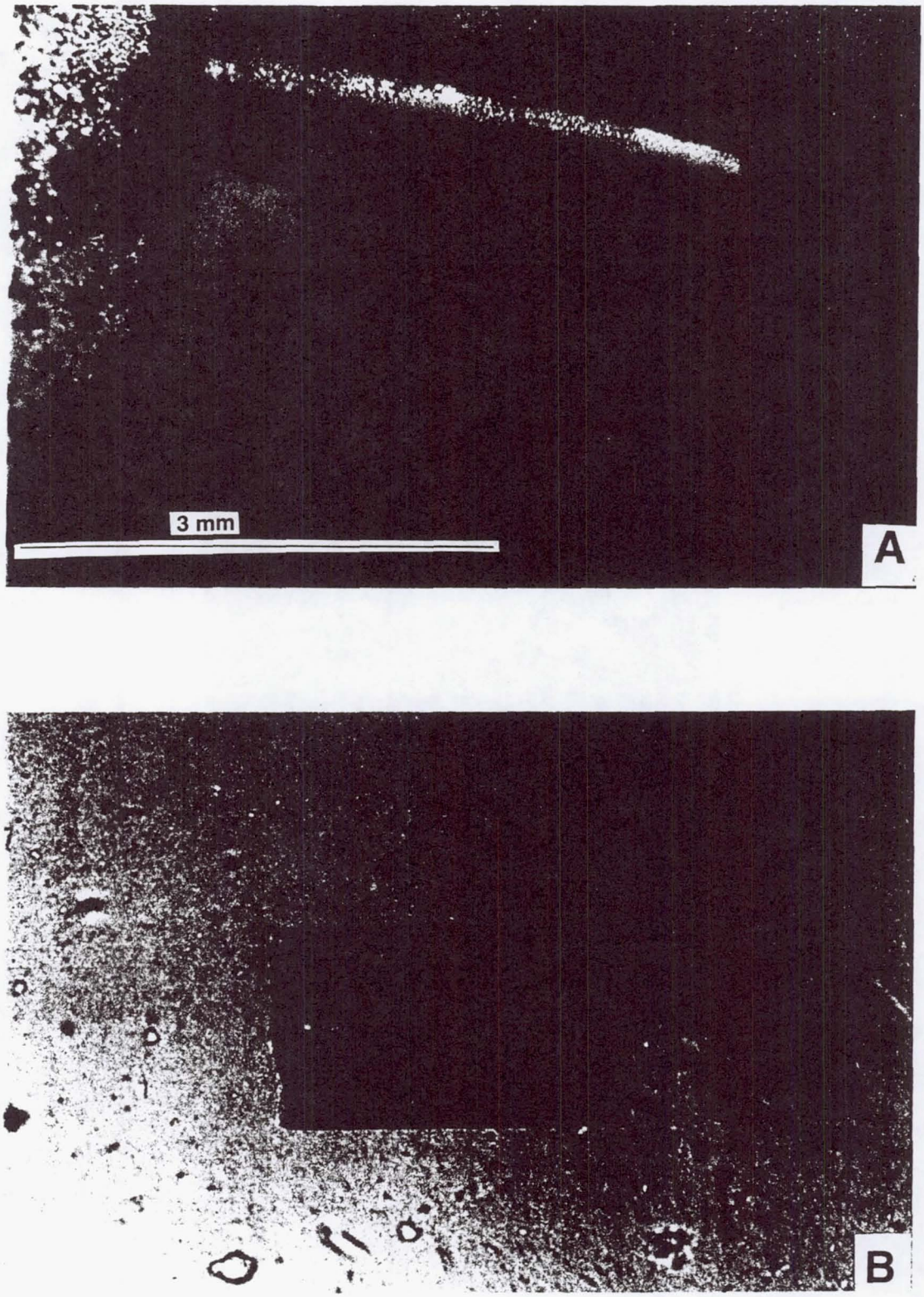

Figure 2

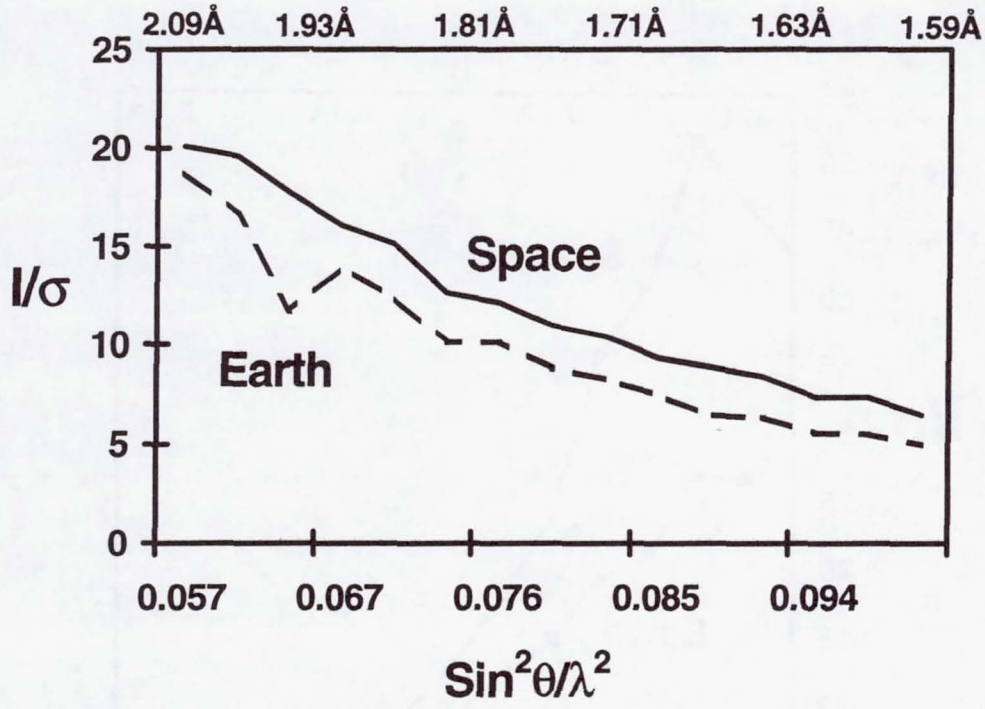
2.09Å
1.93Å
1.81Å
1.71Å
1.63Å
1.59Å
25
20
15
10
5
0
I/σ
Space
Earth
0.057
0.067
0.076
0.085
0.094
Sin²θ/λ²

Figure 3

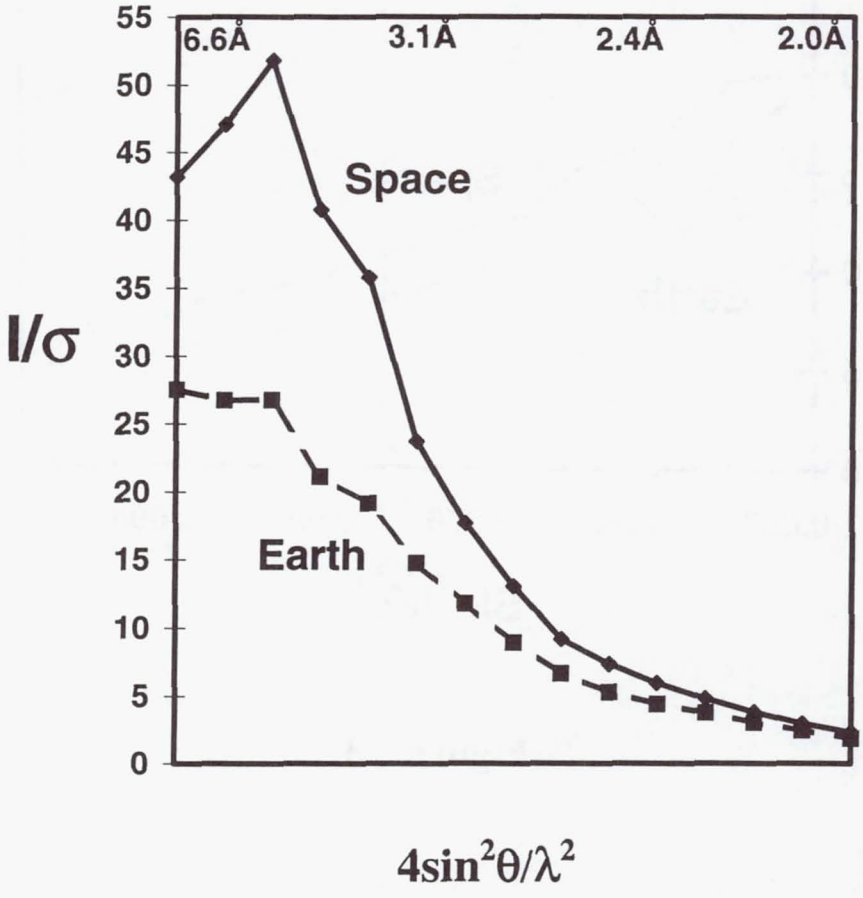
55
50
45
40
35
30
25
20
15
10
5
0
6.6Å
3.1Å
2.4Å
2.0Å
Space
Earth
I/σ
4sin²θ/λ²

Figure 4

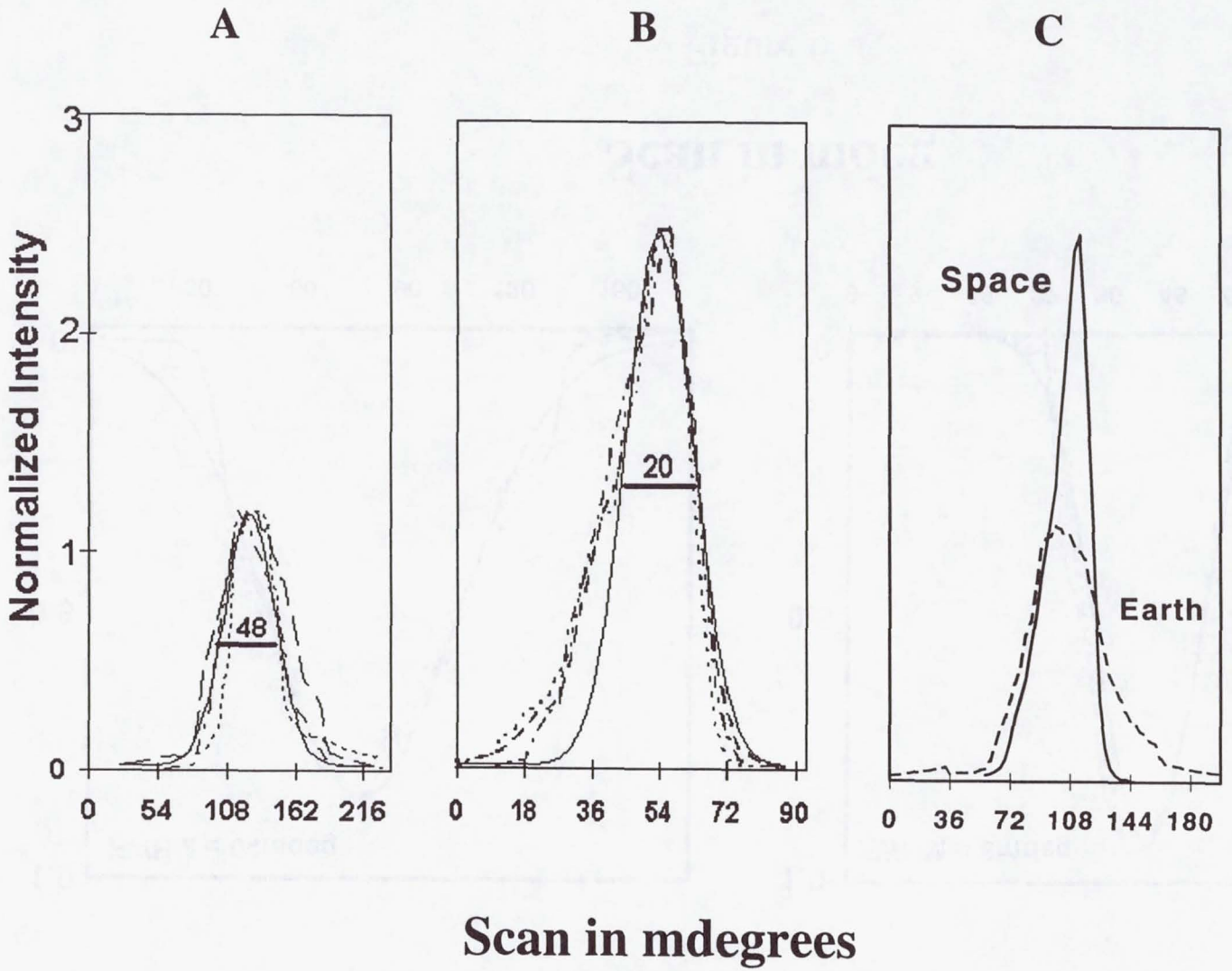
A
B
C
Normalized Intensity
3
2
1
0
48
20
Space
Earth
0 54 108 162 216
0 18 36 54 72 90
0 36 72 108 144 180
Scan in mdegrees

Figure 5

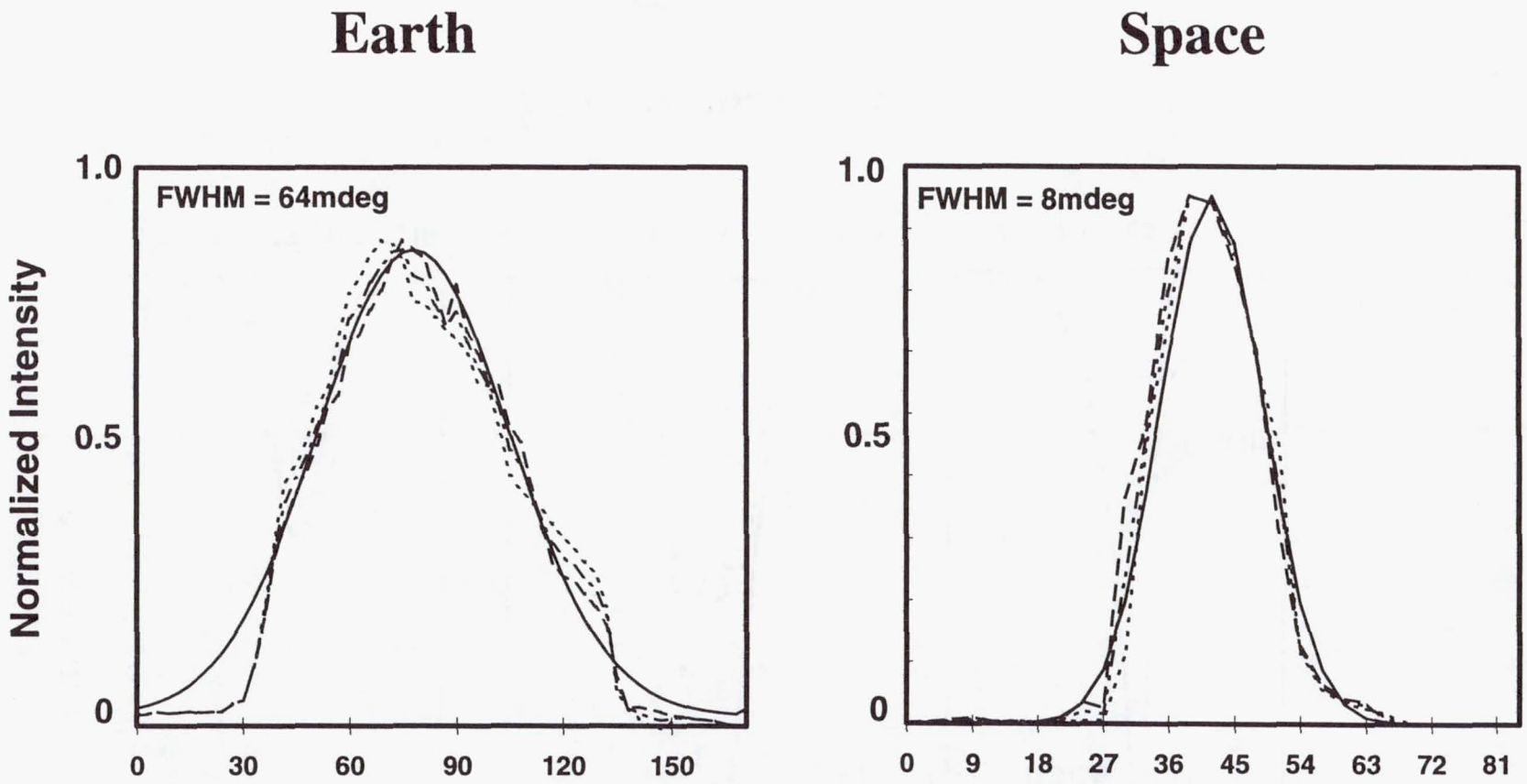
Earth
Space
FWHM = 64mdeg
FWHM = 8mdeg
Normalized Intensity
1.0
0.5
0
0
30
60
90
120
150
1.0
0.5
0
0
9
18
27
36
45
54
63
72
81
Scan in mdeg

Figure 6

Table 1. Content of APCF Reactors

Reactor no.	Protein	Reactor Chambers								
		Protein			Buffer		Piston		Salt	
		Protein conc. (mg/ml)	Buffer	Volume (µl)	Buffer	Volume (µl)	Buffer	Volume (µl)	Buffer	Volume (µl)
1	Thaumatin	20	A	188	B	59	B	246	B	295
2	Thaumatin	20	A	188	B	59	B	246	B	295
3	ttAspRS	20	C	67	D	59	D	246	D	295
4	ttAspRS	20	C	67	E	59	E	246	E	295

Solution A: 0.1 M ADA buffer and 0.20 M sodium tartrate pH 6.5.
Solution B: 0.1 M ADA buffer and 0.95 M sodium tartrate pH 6.5.
Solution C: 25 mM Tris-HCL buffer, 1 mM $MgCl_2$, 1 mM DTT pH 7.5.
Solution D: 40% saturated ammonium sulfate in 25 mM Tris-HCL buffer, 1 mM $MgCl_2$, 1 mM DTT pH 7.5.
Solution E: 50% saturated ammonium sulfate in 25 mM Tris-HCL buffer, 1 mM $MgCl_2$, 1 mM DTT pH 7.5.

Table 2. Number and Size of Space and Earth Grown Crystals in APCF Dialysis Reactors

	Space		Corresponding Earth Controls	
Reactor (Protein chamber size)	No. of crystals	Average Size(mm) (longest dimensions)	No. of crystals	Average Size(mm) (longest dimensions)
1 (188µl)	1250	0.4	2000 +	0.3
2 (188µl)	1150	0.4	2000 +	0.3

Reactors containing more than 2000 crystals are noted as 2000+. (Number of crystals exceeding 2000 could not be counted with high accuracy; therefore, a more precise number was not indicated in these reactors).

*Even though reactors flown on LMS contained many crystals from space as well as on the ground, it was qualitatively observed that there were less and bigger crystals grown in the space reactors than those that grew on earth.

Table 3. Mosaicity Characteristic of Ground and Space Grown Thaumatin Crystals.

Crystal	*Earth 1*	*Earth 2*	*Space 1*	*Space 2*
FWHM (mdeg)	54	47	21	18
Deviation (mdeg)	5	5	3	5
Number of spots	5	3	5	3

The presented FWHM values have the instrument resolution function value deconvoluted out.

Table 4. Mosaicity Characteristic of Ground and Space Grown ttAspRS Crystals.

Crystal	Earth 1	Earth 2	Space 1	Space 2
FWHM (mdeg)	68	64	12	8
Deviation (mdeg)	5	5	3	2
Number of spots	5	3	4	3

The presented FWHM values have the instrument resolution function value deconvoluted out.

Advanced Protein Crystallization Facility (APCF)

Lysosome Crystal Growth in the Advanced Protein Crystallization Facility Monitored via Mach-Zehnder Interferometry and CCD Video

Principal Investigator:

Dr. John Helliwell
University of Manchester
Manchester, England

Final Written Report

Prof. John R. Helliwell[1] (P.I.) and Titus J. Boggon[1]

Co-workers:
Interferometry : Peter Lautenschlager[2], Lothar Potthast[2]
X-ray Evaluation : Edward H. Snell[3], D. Peter Siddons[4], Vivian Stojanoff[5]

Lysozyme Crystal Growth In The Advanced Protein Crystallization Facility Monitored Via Mach-Zehnder Interferometry And CCD Video

1. Structural Chemistry Section, Department of Chemistry, University of Manchester, Oxford Road, Manchester, M13 9PL UK.
E-mails: John.Helliwell@man.ac.uk and titus@spec.ch.man.ac.uk
2. Domier GmbH, Raumfahrt-Infrastructruktur, 88039 Friedrichshafen, Germany
3. NASA, Laboratory for Structural Biology, Code ES76, Bldg 4464, MSFC, Huntsville, Al 35812. USA
4. NSLS, Brookhaven National Laboratory, Upton, NY 11973, USA
5. ESRF, Ave. des Martyrs - B.P. 220, 38043 Grenoble Cedex, France

Aims of the Experiment

The complex system of crystallisation is the major bottle-neck to obtaining high quality X-ray diffracting protein crystals. It is hypothesised that by reducing the number of parameters which influence the crystal growth system it would be easier to understand, and therefore adapt and control the system to produce better quality crystals. In particular that microgravity might well reduce mosaicity indicative of a longer range 'coherence length' or domain size, over earth grown counterparts, thus realising the perfect protein crystal limit[1]. Microgravity protein crystal growth negates the buoyancy effects of convection and sedimentation, leaving undisturbed diffusion kinetics to dominate solutal fluid flows. Microgravity protein crystal growth is therefore a method of reducing the number of parameters which can adversely influence the growth of highly perfect protein crystals. With this in mind, the two main aims of the experiments we performed on the LMS mission were to conduct analyses of both the protein crystal growth medium in microgravity and of the quality of the resulting crystals.

It has been shown that in the near ideal crystal growth environment of microgravity, lysozyme crystals grow to give the most perfect internal order yet observed in a protein crystal[2,3], whereby the microgravity crystals were significantly better than earth grown controls. This result has been confirmed with other proteins, although not to such a degree of perfection[4]. The aim then of this work is to understand to a better degree the crystallisation process in microgravity and in future to apply the lessons learnt, about e.g. crystallisation geometry, g-jitter stability[5] or crystallisation conditions, to future missions.

Our investigation firstly centred on crystallisation solutal kinetics, using Mach-Zehnder interferometry. The aim of which was to monitor the solutal movements via correlation with changes in the gradient of refractive index in the observed area. Charge Coupled Device (CCD) video was also used to verify the positional stability of the crystals during growth, whereby a comparison of the growth rates and movements of crystals could be made with previous microgravity experiments [5-8].

Secondly, an X-ray analysis investigating mosaicity (rocking curve), reciprocal space mapping, and topography of the resulting crystals was undertaken. The perfection of the crystals is being compared between microgravity grown, and earth grown, and also with crystals obtained from previous missions [2,3,6,9].

Ground trials and preparation experiments

Ground control experiments were conducted during the mission. The crystallisations were set up at the same time, and using the same solutions, as those of the mission. All parameters were kept as identical as possible to the microgravity case, although a temperature stability during growth of 20±0.1 °C was not possible, and ±1 °C was used.

Interferometric ground control crystallisations were carried out at Dornier GmbH using the APCF-Engineering Model. These experiments were prepared using exactly the same protocol as the microgravity mission.

The mission

Four lysozyme crystallisations were carried out in microgravity, and four identical experiments were conducted as ground controls during the period of the mission. Two crystallisation conditions were used, one with a higher precipitant concentration, and one with a 7 % lower precipitant concentration. The crystallisations used dialysis geometry, containing 541 µl of precipitant, 59 µl of buffer and 188 µl of protein solutions. Two microgravity reactors (reactors 7 and 9) were monitored using Mach-Zehnder interferometry and CCD video, the

other two microgravity reactors were not visually monitored during the mission. All reactors produced crystals, some of which were subsequently analysed using various X-ray sources.

Evaluation of Mach-Zehnder Interferometer images

Of the two reactors monitored using Mach-Zehnder interferometry, one (reactor 7) contained the slightly higher precipitant concentration so it was monitored at a slightly faster rate. Due to time constraints on digitally recording the images (about 4 minutes per whole image), whole interferograms were not able to be collected for the first 15 hours after APCF activation. Instead 2 windows were defined (w1 and w2 in figure 1), which monitored the average grey value at 4 and 6 minute intervals for reactors 7 and 9 respectively. After 15 hours, interferograms recording the whole reactor were collected at 11 minute intervals for both reactors (figure 1).

Unfortunately the laser was unsteady, and a combination of mode switching and loss of intensity occurred throughout the mission. This was problematic, especially in the first 15 hours, when average grey values were the only method of analysis. Consequently, fringes were probably missed in that period. However, a more complete analysis is possible with the whole interferograms collected after the 15 hour point, although, these also have been affected by the problematic laser (figure 2).

There was, however, enough data to suggest some very interesting results. Firstly, the direction of fringe movement reversed at about the 8 hour point in both reactors, and then again at the point that crystals become visible in the CCD video monitoring, between 25 and 31 hours (depending on the position within the protein chamber)(figure 2). Compared to the solitary reversal in fringe movement direction present in the ground control experiments[10], this is a surprising result which should be looked at more closely. It suggests that a different pre- and post- nucleation process occurs in microgravity compared to the earth grown case. We are at present also modelling the effects of a diffusion dominated crystallisation experiment.

Finally, the whole protein chamber interferograms demonstrated the stability of fluid within microgravity crystallisation by showing an effect that is rarely seen using Mach-Zehnder interferometry on earth. Depletion zones are visible around growing crystals (figure 3).

Evaluation of CCD video images

The two reactors that were monitored using interferometry were also monitored using CCD video. Images of the whole protein chamber were taken at one focal length position every 2 hours beginning 15 hours after activation of the APCF (MET 0/21:17) for reactor 7. In reactor 9 the first image was taken after 90 hours of APCF activation. In our two previous missions, we had not yet had such a chance before to analyse such a high frequency of CCD video images, and covering the whole protein chamber. This is a major step forward in capability and was important (see below).

Previously, in our CCD video monitored experiment on Spacehab-1 a bulk movement of crystals was noted at the time that the EURECA satellite was retrieved (unpublished results). In the IML-2 mission, we tracked 3 crystals moving over 40 minute periods[5], but due to the narrow field of view, and 8 hour time delay between groups of images, our analysis of these crystal movements was restricted.

It was exciting therefore to analyse images from LMS that viewed the whole protein chamber and at a much higher frequency. Crystals became visible at varying times throughout the reactor, with the first crystals visible 25 hours 37 minutes after APCF activation. We noted significant crystal movements (figures 4 and 5) throughout the mission, whereby nucleation events occurred throughout the chamber but were very quickly followed by a global sedimentation drift towards the top of the reactor. The only crystals that remained in their

nucleation positions were those that grew on the chamber walls. By following 20 different crystals for the periods that they could be accurately tracked (figure 5), sudden global movements could be seen, in addition to the steady drift, at the 76, 102 and 145 hour points, as well as many other times. The total drift distance, for all 20 crystals analysed, over time periods ranging from 24 to 260 hours, ranged between 0.42 and 3.38 mm with an average speed of ~0.004 microns / second (i.e., 40 Å / second). The sudden movements were much larger; total distances travelled being ~0.2 mm in ~2 hours, i.e., ~0.03 microns / second, 300 Å / second).

We have also previously described the monitoring of crystal growth rates[5,6] and correlation of spurts and lulls in these growth rates with astronaut exercise periods. It is possible to perform this analysis from the images we have, and we will do this in the future.

Relation to earlier work and the aims

CCD video of 3 previous protein crystal growth microgravity missions, Spacehab-1, IML-2 and the EURECA satellite, clearly shows that crystal movements are affected by the geometry of crystal growth apparatus, and the quality of the microgravity. Dr N.E. Chayen[i] grew Apocrustacyanin C_1 crystals on the IML-2 (STS-65) Shuttle mission using a vapour diffusion geometry. The crystals clearly showed cyclic motion at a speed of 2 microns / second throughout their growth, akin to that expected from Marangoni convection[8]. This work, agreeing with the theory[11], highlighted major anxieties with protein crystal growth in microgravity using the 'hanging drop' technique (which incorporates a liquid - vapour phase boundary). Lysozyme crystal growth using the dialysis membrane technique on board the Spacehab-1 (STS-57) and IML-2 Shuttle missions showed relatively small, but significant, crystal movements as described above. However, these results clearly show that the dialysis technique (which has no liquid - vapour phase boundary) produces a much more stable environment for protein crystal growth than the vapour diffusion technique. We have also analysed protein crystal growth onboard an unmanned platform. α-Crustacyanin was grown on the ESA's EURECA satellite using a liquid-liquid free interface diffusion geometry (again incorporating no liquid - vapour phase boundary) by Dr P.F. Zagalsky[ii]. We noted that for long periods of time the free floating crystals grew without moving[7], and were only disturbed by failures of the temperature control system. The results obtained from the LMS mission reinforce, and expand upon, the results obtained previously. We are attempting, at present, to link crystal movements observed during the LMS mission to gravitational accelerations affecting the mission. This is overall within the context of trying to consistently achieve protein crystal quality improvements through the harnessing of microgravity[9].

X-ray analysis of crystal perfection

Synchrotron X-ray analyses were carried out at the NSLS using beamline X26C. A variety of methods were used to analyse a number of crystals. Crystal mosaic spread measurements by use of rocking curves is an indicator of the internal physical perfection present[1]. The addition of an analyser crystal between the sample and detector enables reciprocal space mapping of ω, the sample axis, and ω′, the analyser axis[12]. Reciprocal space maps in one axis provide a measure of pure mosaicity effects (volume and orientation), and in the other axis strain effects. In combination with the technique of X-ray topography[13], a very finely detailed picture of a single reflection can be obtained to produce an in-depth knowledge of the overall internal order of the crystal. We conducted such data collections on a number of crystals at the NSLS, the analysis of which is still in progress, although two examples are shown here (figure 6).

[i] Biophysics Section, Blackett laboratory, Imperial College of Science, Technology and Medicine, London. SW7 2BZ UK
[ii] Royal Holloway, University of London, Egham, Surrey TW20 0EX UK.

Using the Manchester X-ray source, R-AXIS area detector and a variety of processing packages, two similar crystals, one grown on the LMS mission, and one using the same conditions, but on earth, were analysed. The data merging statistics are shown in Table 1. Under these experimental conditions, it is clear that the intrinsic crystal perfection is not harnessed (e.g., via an ultra-fine step scan technique ~0.0001°, see ref 3 for details reflection signal to noise optimisation especially figures 3c and 4) and hence, the data quality (R_{merge}, I/σ) are essentially identical. For the LMS microgravity grown lysozyme crystal the data collection protocol was as follows: 60° of 0.75° oscillations at a distance of 250 mm using 30 minute exposures, followed by 60° of 0.50° oscillations at a distance of 300 mm using 20 minute exposures. For the earth grown crystal the data collection protocol was identical, and then in addition 60° of 1.5° oscillations at a distance of 450 mm using 4 minute exposures were recorded. The LMS crystal was 0.50 x 0.50 x 0.35 mm (0.0875 mm^3) and the earth control crystal was 0.70 x 0.50 x 0.45 mm (0.1575 mm^3).

	LMS		LMS Ground Control	
Resolution	Rmerge	Completeness %	R merge	Completeness %
99.00 - 4.19	0.054	95.1	0.056	98.8
4.19 - 3.33	0.064	98.8	0.064	99.2
3.33 - 2.91	0.075	99.2	0.07	97.1
2.91 - 2.64	0.085	99.6	0.08	97.5
2.64 - 2.45	0.093	99.9	0.09	96.6
2.45 - 2.31	0.093	99.6	0.09	97.7
2.31 - 2.19	0.099	99.3	0.097	96.9
2.19 - 2.10	0.105	98.1	0.105	96.1
2.10 - 2.02	0.12	94.3	0.116	94.9
2.02 - 1.95	0.135	88.8	0.139	92.1
1.95 - 1.89	0.165	77.3	0.163	88.7
1.89 - 1.83	0.186	66.5	0.187	81.4
1.83 - 1.78	0.239	62.1	0.249	70.9
1,78 - 1.74	0.271	54.5	0.255	64.3
1.74 - 1.70	0.393	45.1	0.344	56.1
Overall	0.072	85.5	0.069	88.8

Table 1. X-ray data sets collected on LMS and LMS ground control lysozyme crystals on the Manchester R-AXIS area detector using a MoKα anode (λ = 0.71 Å wavelength). Overall I/σ for the LMS crystal = 15.7 and for the ground control crystal = 16.5. Identical X-ray generator (RU 200 rotating anode) power settings were used).

Lessons for future missions from LMS

There were problems experienced with the interferometry side of the experiment and which fell under two categories. Firstly, an unstable laser overheated many times whereby wavelength shifts (and changes in the interferometric pattern) and intensity losses were experienced. The grey-scale data collection (before 15 hours) and many of the whole interferograms were rendered much more complicated for analysis. Secondly, the lack of whole interferograms collecting data over the important, and unusual, period before 15 hours should be addressed in a future mission.

The CCD video analysis of the LMS crystallisations show a significant crystal drift within the Shuttle (also seen on the IML-2 mission[5]). This is in contrast with protein crystal growth experiments that took place onboard the EURECA satellite where completely stationary crystal growth was observed for long periods of time[7]. The comparison of these sets of CCD video results points towards protein crystallisations conducted onboard

unmanned platforms as a more stable environment. Nevertheless the overall drift speed of 40 Å / second presumably is tolerable but will be of interest to those investigators modelling the physical chemistry of protein crystal growth. However, the sudden jumps of ~0.2 mm over 2 hour periods (i.e., 0.03 microns / second, 300 Å / second) due presumably to sudden g-jitter disturbances, is a more serious anxiety for realising the best quality protein crystals.

Overall conclusions

As well as the dynamics of the fringe reversal, more microgravity crystals were made available and allowed the X-ray analyses, thus considerably extending our earlier work.

References

1. J.R. Helliwell, 1988, *J. Cryst. Growth*, **90**, 259-272.

2. J.R. Helliwell, E.H. Snell and S. Weisgerber, 1996, *Proceedings of the 1995 Berlin Microgravity Conference* edited by L. Ratke, H. Walter and B. Feuerbacher, *Springer Verlag*, 155-170.

3. E.H. Snell, S. Weisgerber, and J.R. Helliwell, E. Weckert, K Hölzer and K Schroer, 1995, *Acta Cryst. D* **51**, 1099-1102.

4. J. Ng and R. Giegé, *To be published.*

5. E.H. Snell, T.J. Boggon, J.R. Helliwell, M.E. Moskowitz and A. Nadarajah, *Acta Cryst. D, in press.*

6. N.E. Chayen, T.J. Boggon, A. Cassetta, A. Deacon, T. Gleichmann, J. Habash, S.J. Harrop, J.R. Helliwell, Y.P. Nieh, M.R. Peterson, J. Rafery, E.H. Snell, A. Hädener, A.C. Niemann, D.P Siddons, V. Stojanoff, A.W. Thompson, T. Ursby and M. Wulff, 1996, *Quarterly Rev. Biophysics*. **29**, 227-278.

7. T.J. Boggon, N.E. Chayen, P.F. Zagalsky, E.H. Snell and J.R. Helliwell, *Faraday Transactions, submitted.*

8. N.E. Chayen, E.H. Snell, J.R. Helliwell and P.F. Zagalsky, 1997, *J. Cryst. Growth*, **171**, 219-225.

9. E.H. Snell, A. Cassetta, J.R. Helliwell, T.J. Boggon, N.E. Chayen, E. Weckert, K. Hölzer, K. Schroer, E.J. Gordon, and P.F. Zagalsky, 1997, *Acta Cryst D* **53**, 231-239.

10. E.H. Snell, J.R. Helliwell, T.J. Boggon, P. Lautenschlager, and L. Potthast, 1996, *Acta Cryst. D* **52**, 529-533.

11. R. Savino and R. Monti, 1996, *J. Cryst. Growth*, **165**, 308-318.

12. E.H. Snell, 1997, *Canadian Space Agency, In press.*

13. V. Stojanoff, D.P. Siddons, E.H. Snell and J.R. Helliwell, 1996, *Synchrotron Radiation News*, **9**, 25-26.

Figure captions

Figure 1 : An example of a whole interferogram with interference fringes clearly visible. The two grey value measuring windows are marked as w1 and w2, and the white strip indicates the area analysed in figure 2.

Figure 2 : Analysis of the movement of fringes within the white strip shown in figure 1. The average grey value of pixels in x within the white strip has been obtained and shown here as a single pixel. The height (y) is unchanged for both sets of pixels. This figure shows an overview of the movements of fringes within the white strip over 34 hours. Direction of finge movement reversal occurs between 25 (R) and 31 (R') hours (depending on latitude within the chamber) correlating with the first crystals becoming visible (at which time there is a loss of definition in the finge pattern experienced). The effect of laser instability is clearly seen as large jumps in the finge pattern, and also as pale strips.

Figure 3 : Shows the merging of an interferogram and a CCD video image taken with a 3½ minute interval between the images. A protein depleted zone is visible.

Figure 4 : Sequence of 4 CCD video images taken at a) 1d 18h 32m, b) 2d 18h 4m, c) 4d 8h 25m and d) 15d 15h 32m (these timings are MET). The images show the movement of crystals over the whole LMS mission. It is significant to note that while many crystals nucleate throughout the protein chamber, all sediment to the top of the reactor (right hand side of the pictures). Crystals that do not move throughout the whole mission have grown attached to the chamber wall.

Figure 5 : Three graphs showing the movements of 20 crystals. Graph a) shows X versus Y, b) X versus Time and c) Y versus Time. The units are pixels and hours (MET). Sudden crystal movements are visible at 76, 102 and 145 hours, especially in figure 5b, in addition to the gradual global drift.

Figure 6 : Example of a reciprocal space map a) and an X-ray topograph b) of microgravity grown LMS lysozyme crystals. The reciprocal space map shows ω versus ω', with intensity on the z axis.

Acknowledgements

Dr J. Stapelmann, R. Bosch, W. Fritzsch, and W. Scheller of Dornier GmbH are thanked for their continuing help and support with this work. Drs K. Fuhrmann, H. Walter and O. Minster at ESA are acknowledged for their support of these experiments. The NSLS is acknowledged for providing beam time for this work.

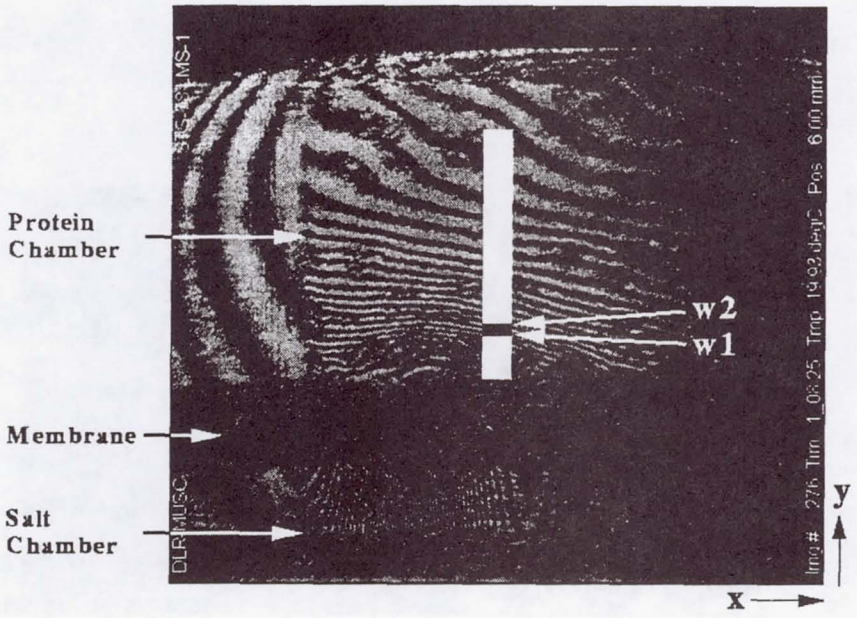

Figure 1

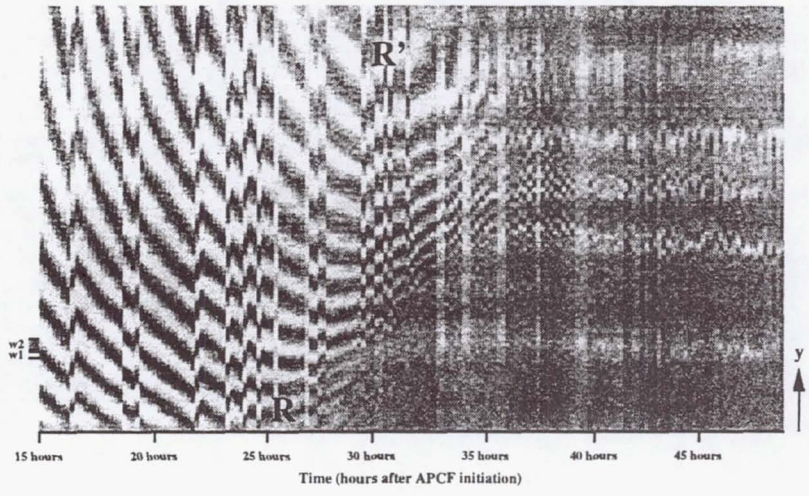
R'
R
w2
w1
y
15 hours
20 hours
25 hours
30 hours
35 hours
40 hours
45 hours
Time (hours after APCF initiation)

Figure 2

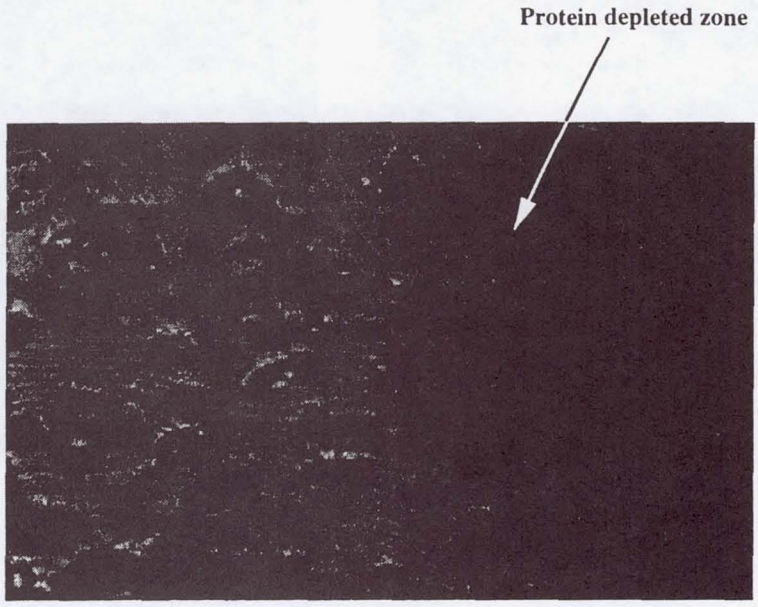

Figure 3

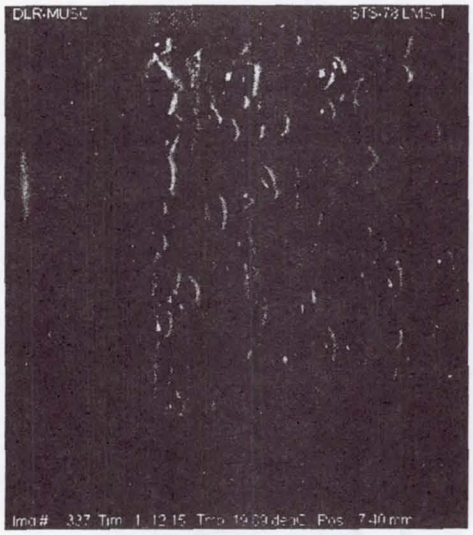

(a) MET
01/18:32

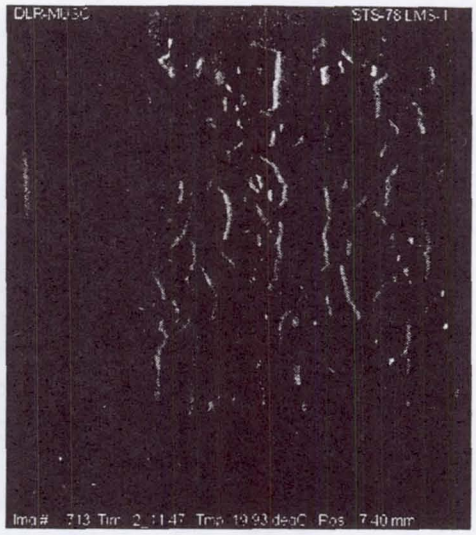

(b) MET
02/18:04

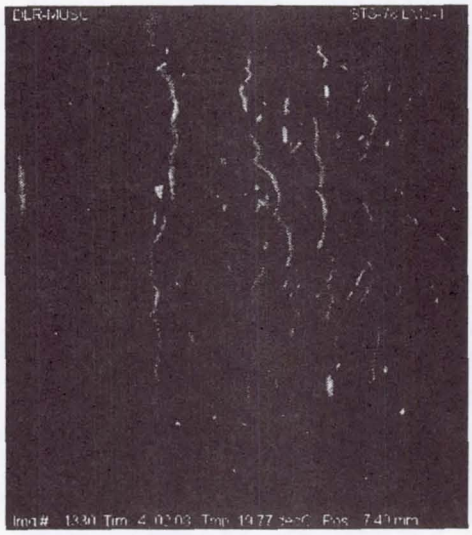

(c) MET
04/08:25

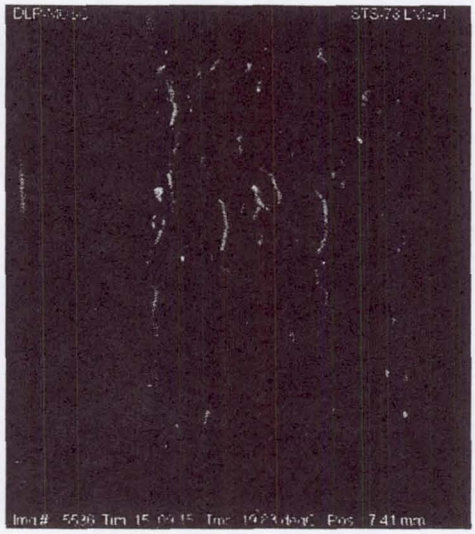

(d) MET
15/15:32

Figure 4

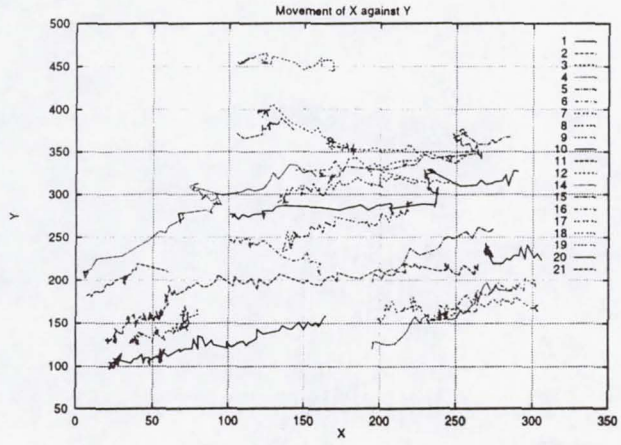
Movement of X against Y
Y
X

(a)

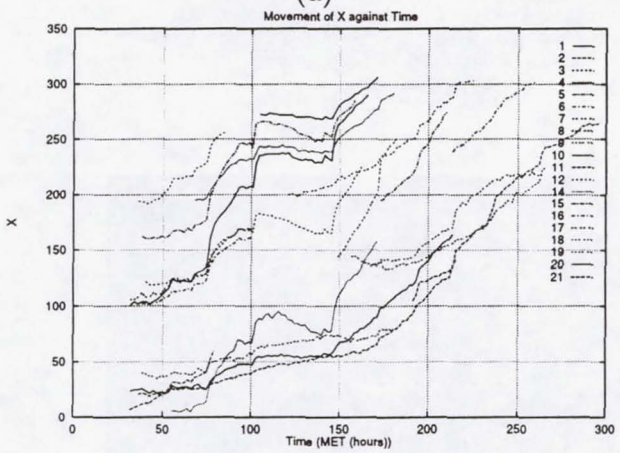
Movement of X against Time
X
Time (MET (hours))

(b)

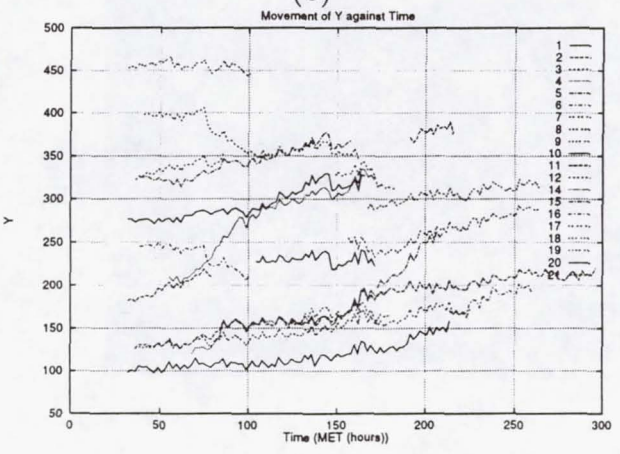
Movement of Y against Time
Y
Time (MET (hours))

(c)

Figure 5

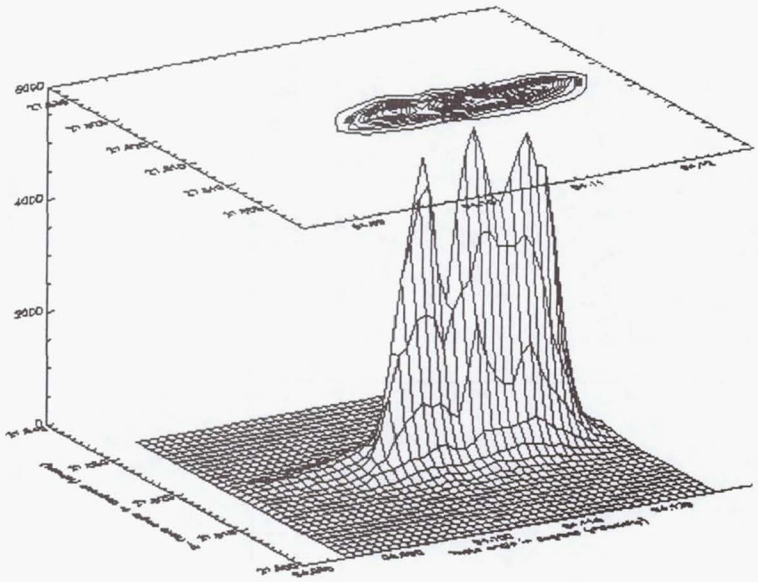

(a)

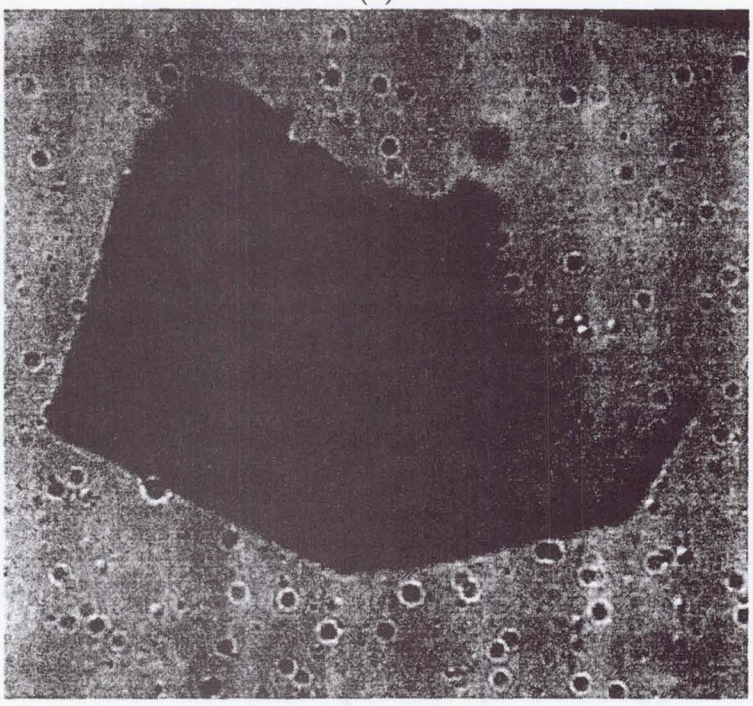

(b)

Figure 6

Advanced Protein Crystallization Facility (APCF)

Analysis of Thaumatin Crystals Grown on Earth and in Microgravity

Principal Investigator:

Dr. Alexander McPherson
University of California, Irvine
Irvine, California

Final Report of Advanced Protein Crystallization Facility on LMS:

Analysis of Thaumatin Crystals Grown on Earth and in Microgravity

by

Stanley Koszelak, John Day, Aaron Greenwood and Alexander McPherson

University of California, Irvine, Department of Molecular Biology & Biochemistry
Irvine, CA 92697-3900

Previous experiments have demonstrated that, in at least some cases, macromolecular crystals of improved quality can be grown in a microgravity environment as is obtained, for example, on the U.S. Space Shuttle or the Russian Space Station Mir (DeLucas, *et al.*, 1989; Day & McPherson, 1992; Koszelak, *et al.* 1995; Long, *et al.*, 1996). Presently, the most extensively used facility for such experiments is the European Space Agency (ESA) designed Advanced Protein Crystallization Facility or APCF (Snyder, *et al.* 1991; Bosch, *et al.* 1992). This system allows crystallization to proceed by vapor diffusion, batch, dialysis, and free interface diffusion methods and it provides limited video recording of some experiments as they actually appear in space.

On Space Shuttle missions designated United States Microgravity Laboratory-2 (USML-2, October, 1995) and Life and Microgravity Sciences (LMS, June, 1996), joint experiments were carried out by our French (Strasbourg) and American (Riverside) groups based on the crystallization of the protein thaumatin. Using common protein, buffer, and precipitant solutions, thaumatin was crystallized at a variety of protein concentrations using two different approaches, dialysis and liquid-liquid diffusion. Following retrieval of the samples, post flight microscopy and X-ray analyses were carried out on the crystals grown in microgravity. Of particular interest to us were (1) relevance of the choice of methodology, (2) the influence of protein concentration on crystal size, and (3) quantitative comparison of the microgravity grown crystals with those produced on earth.

Materials and Methods

Thaumatin was purchased from Sigma Biochemicals, St. Louis, Mo. and dissolved in 0.1 M ADA buffer at pH 6.5. The precipitant solution was 1.6 M sodium tartrate in 0.1 M ADA at

pH 6.5 All solutions were sterilized by microfiltration before loading of flight samples. Solution used by both laboratories were made in Strasbourg and divided between investigators.

Thaumatin is a monomeric protein from the African Serendipity Berry valued for its intensely sweet taste and its use as a non caloric sweetener. It has a molecular weight of 21,500 contains four disulfide bridges, and possesses a high degree of stability. It consists primarily of beta structure organized in two associated domains. The structure was first determined in an orthorhombic crystal at 1.7 Å resolution (Ogata, *et al.* 1992), and later in a second orthorhombic, a monoclinic, and a tetragonal crystal form (Ko, *et al.* 1994). The tetragonal crystal form, grown from tartrate, was also refined to 1.7 Å resolution, and was that studied in these experiments. Tetragonal thaumatin crystals can be grown in a conventional laboratory in 12 to 48 hours at room temperature by a variety of methods. The crystals are of space group $P4_12_12$ with a=b=59Å and c=158Å having a single molecule as the asymmetric unit. The habit is that of a tetragonal bipyramid, often reaching linear dimensions greater than 1mm. The crystals, which contain about 45% solvent, are mechanically robust. Their growth has been studied by a variety of physical techniques including interferometry (Kuznetsov, *et al.* 1995) and atomic force microscopy (Malkin, *et al.* 1996a and b).

The APCF has been previously described (Giegé, *et al.* 1995) and, indeed, successful experiments with other proteins and viruses have been reported (McPherson, 1996; Koszelak, *et al.* 1995). An APCF unit provides for a total of 48 individual crystallization cells maintained at constant temperature (22°C ≠ 0.1° in this case) from the time of loading, the duration of the mission, to analysis. Both dialysis and free interface diffusion cell types are activated by 90° rotation of a stopcock valve that establishes continuity between protein and precipitant chambers.

For dialysis, a semi permeable membrane separates the two chambers. In experiments conducted on USML-2 the Strasbourg group used five dialysis crystallization reactors and the Riverside group three free interface diffusion reactors. For LMS, the Strasbourg group used two reactors of the dialysis type and the Riverside group eight of the liquid-liquid diffusion type.

The APCF was activated on both missions several hours after a microgravity environment was achieved, and deactivated (the stopcocks rotated in reverse) a few hours before reentry. Several cells were observed during the mission at fixed intervals and recorded by video microscopy. In the case of the dialysis cells, parallel experiments were carried out in Strasbourg, France in identical cells during the periods of both missions. No parallel ground controls were carried out for the free interface diffusion cells since the method functions quite differently in a one g environment. Following the missions the dialysis cells were returned to Strasbourg for analysis and the free interface diffusion cells to Riverside. They were, in both cases, immediately examined, photographed, and X-ray diffraction analysis initiated.

At the University of California at Riverside, complete three dimensional X-ray diffraction data were collected at 17°C on the crystals grown on USML-2 by free interface diffusion as described previously (Ko, *et al.*, 1993a, b; Larson *et al.*, 1993) from capillary-mounted crystals using a San Diego Multiwire Systems (SDMS) double multiwire detector system (Xuong *et al.*, 1985) with crystal-to-detector distances of 535 mm. Frame sizes were 0.14° with 2-3 min/frame. The x-rays were generated by a Rigaku RU-200 rotating anode generator operated at 45 kV and 145 mA with a Supper monochromator to give 1.54Å radiation. Crystals were exposed for 24-48 h. Data collection procedures and experimental parameters were identical for both earth and space grown crystals. Redundancy of recordings ranged from four to eight. Data correction,

reduction, merging, and statistical analysis used the programs supplied by SDMS. For both earth and microgravity grown crystals the $R_{sym's}$ varied from 0.035 to 0.06 to the limits of resolution of the data sets.

Results

Visual and Microscopic Observations: For both missions crystals were observed in all of the cells, both dialysis and free interface diffusion, for microgravity and for ground controls. There was a clear increase in average and largest sizes of crystals grown by the French group by dialysis in μg compared with ground controls, an example, that of lysozyme is shown in Figure 1. In the best of the three free interface diffusion cells, the largest crystals were three to five times the volume of the best crystals produced in either laboratory on earth. In both types of cells some of the largest thaumatin crystals measured more than 2 mm from apex to apex of the tetragonal bipyramids.

The number and sizes of crystals from the dialysis reactors were assessed under an optical microscope. Each of the flight reactors contained 30 to 250 crystals having a size range of 0.4 mm to 1.8 mm. The corresponding ground control reactors contained approximately 550 to 30,000 crystals having a size range of 0.100 mm to 0.9 mm (see report by Ng, *et al.* for details).

A notable observation originating independently from both the Strasbourg group (using dialysis) and the Riverside group (using free interface diffusion) was the dependence of average and largest size on protein concentration, a major experimental variable. Independent of approach, the largest crystals clearly grew at highest protein concentration and the smallest crystals at lowest protein concentration. This is shown in Figure 2 for crystals grown at three

different protein concentrations (35, 17 and 7 mg/ml) by free interface diffusion under otherwise identical conditions.

Visually, the quality of the crystals, particularly those growing free of any surfaces, and including the largest, was very high. They appeared virtually flawless, with no observable imperfections, striations, or habit anomalies. Those attached to the cell walls (which presumably nucleated there) did show defects near the sites of growth initiation but became flawless as growth proceeded into the bulk solution.

X-ray Intensity Measurements: X-ray diffraction data were collected from a total of four thaumatin crystals grown in microgravity by free interface diffusion in microgravity. All were from a cell which was under video observation. The data were merged to form a single data set. This microgravity set was then compared with the best data ever previously obtained from crystals grown in a conventional laboratory, data which was, in fact, used to solve and refine the reported structure of the tetragonal thaumatin crystals (Ko, *et al.*, 1993a). This comparison is shown as a modified Wilson plot (Wilson, 1949 and 1970) in Figure 3 in which the average intensity divided by its estimated error is plotted as a function of $\sin^2\theta/\lambda^2$.

As with several previously reported investigations of macromolecular crystal growth in microgravity, two features of the comparison emerged. First, the I/σ ratio of reflections obtained for crystals grown in microgravity was substantially higher (approximately double) that for ground grown crystals, and over the entire resolution range analyzed. Second, the limit of resolution of the diffraction pattern was somewhat higher for microgravity grown crystals compared to those grown on earth, 1.5 Å vs. 1.7 Å resolution respectively. While 0.2 Å may appear only a marginal increase, in this portion of the resolution range it is significant and,

combined with the improved I/σ over the entire resolution range, yields nearly 30% more diffraction intensities (> 3σ) for the microgravity grown crystals. We would like to point out that the true limit of resolution for the microgravity crystals was never measured in this analysis because technical constraints prevented collection of data beyond 1.5 Å. The continued strength of the diffraction pattern at the 1.5 Å mark suggested to us that the actual resolution limit of the microgravity grown crystals was beyond this point.

Conclusions

The results presented here for thaumatin crystals grown in microgravity in the APCF by two different techniques are consistent. They reinforce the conclusions of other reports based on different macromolecules that a microgravity environment provides distinct advantages. In the best of only a few thaumatin crystals grown in microgravity, compared with several orders of magnitude more trials conducted on earth, the microgravity grown crystals were consistently and significantly larger, and substantially more defect free as judged by direct visual inspection. In this investigation this appears to be independent of the choice of crystallization method and the loading and handling of the APCF cells.

An interesting observation was that there was a clear correlation between ultimate crystal size and protein concentration. This suggests that in future experiments, the optimal results may be obtained by even further increasing macromolecule concentration over that utilized in the conventional laboratory. This is contrary to what one would do generally in the conventional laboratory where the best results are usually achieved at the lowest levels of supersaturation.

The resolution limit of the diffraction pattern, the I/σ ratio as a function of the Bragg angle, and the mosaic spread of crystals are generally agreed to reflect both the degree of internal

order and the long range defect structure and its distribution within the crystal. That is, they serve as measures of the average statistical disorder of the molecules about the lattice points, as well as the extent of local but severe disorder introduced by defects such as dislocations, stacking faults, point defects or incorporated foreign material (Malkin, *et al.* 1996). All of the data presented here, both intensity distributions and mosaic spread measurements imply a higher degree of internal order, a lower defect density, and a reduction of severe faults for crystals grown in the absence of gravity.

While similar results, based on intensity data for microgravity grown crystals of several proteins, have been reported previously (McPherson, 1997; Koszelak, 1995, 1996, DeLucas, *et al.* 1989), and comparable results based on mosaicity measurements have been presented for others (Helliwell, *et al.* 1996; Ferrer, *et al.* 1996; Snell, *et al.* 1995), this is the first experiment to produce crystals grown by multiple methods and analyzed by both approaches. Indeed, our conclusion is that they are mutually supportive and complementary, and both suggest the same conclusion, that crystals grown in microgravity can be significantly improved in their diffraction properties when compared with those grown on earth.

Apart from lysozyme, no other protein crystal has been used to investigate mosaicity differences between earth-grown and space-grown crystals. The data presented here indicates that the mosaic spread of reflections from microgravity grown thaumatin are reduced by more than a factor of two over earth grown crystals. This is comparable to what was observed for tetragonal lysozyme where space-grown crystals were observed to be improved by a factor of three over corresponding earth controls (Helliwell, *et al.* 1996; Ferrer, *et al.* 1996; Snell, *et al.* 1995).

References

Day, J. and McPherson, A. Macromolecular crystal growth experiments on International Microgravity Laboratory-1. *Protein Science* 1, 1254-1268, (1992).

DeLucas, L. J., C. D. Smith, H. W. Smith, V. K. Senagdi, S. E. Senadhi, S. E. Ealick, C. E. Bugg, D. C. Carter, R. S. Snyder, P. C. Weber, F. R. Salemme, D. H. Ohlendorf, H. M. Einspahr, L. Clancy, M. A. Navia, B. M. Mckeever, T. L. Nagabhushan, G. Nelson, Y. S. Babu, McPherson, A., S. Koszelak, D. Stammers, K. Powell and G. Darby. Protein Crystal Growth in Microgravity. *Science* 246, 651-654 (1989).

Ferrer, L. J., Hirschler, J., Roth, M. and Fontecilla-Camps, J. C. (1996) ESRF Experiments Reports. Pg. 27-28.

Giegé, R., Drenth, J., Ducruix, A., McPherson, A. and Saenger, W. (1995) Prog. Cryst. Growth and Charact. 30, 237-281.

Helliwell, J. R., Snell, E. and Weisgerber, S. (1996) In Materials and Fluids Under Low Gravity, Lecture Notes in Physics (L. Ratke, H. Walter and Feuerbacher B., eds.), pp. 155-170, Springer.

Ko, T.-P., Ng, J. D., Day, J, Greenwood, A. and McPherson, A. X-ray structure determination of three crystal forms of canavalin by molecular replacement. *Acta. Cryst.* D49, 478-489 (1993).

Ko, T.-P., Day, J., Greenwood, A. and McPherson, A. The Structures of Three Crystal Forms of the Sweet Protein Thaumatin. *Acta Cryst.,* D50, 813-825, (1994).

Koszelak, S., Day, J., Leja, C., Cudney, R. And McPherson, A. Protein and Virus Crystal Growth on International Microgravity Laboratory-2. *Biophysical Journal* 69, 13-19 (1995).

Larson, S. B., Koszelak, S., Day, J., Greenwood, A., Dodds, J. A. and McPherson, A. The three dimensional structure of satellite tobacco mosaic virus at 2.9 Å resolution. *J. Mol. Biol.*, 231, 375-391 (1993).

Long, M. M., Bishop, J. B., Nagabhushan, T. L., Reichert, P., Smith, G. D. and DeLucas, L. J. (1996) *J. Cryst. Growth* 168, 233-243.

Malkin, A. J., Kuznetsov, Y. G., Glantz, W. and McPherson. Atomic force microscopy studies of surface morphology and growth kinetics in thaumatin crystallization. *J. Phys. Chem.* 100, 11736-11743 (1996).

Malkin, A. J., Kuznetsov, Y. G. and McPherson, A. Defect Structure of Macromolecular Crystals. *J. Struc. Biol.* 117, 124-137 (1996).

McPherson, A. Macromolecular crystal growth in microgravity. *Crystallography Reviews*, 6(2) 157-308 (1996).

Ogata, C.M., Gordon, P.F., de Vos AM, and Kim, S.H. (1992). *J. Mol. Biol.* 3, 893-908.

Snell, E. H., Weisgerber, S., Helliwell, J. R., Weckert, E., Hölzer, K. and Schroer, K. (1995) *Acta Cryst.* D51, 1099-1102.

Snyder, R. S., Fuhrmann, K. and Walter, H. U. (1991) *J. Cryst. Growth* 110, 333-338.

Xuong, N.-H., Nielson, C., Hamlin, R. and Anderson, D. (1985) *J. Appl. Cryst.* 18, 342-360.

Figure 1

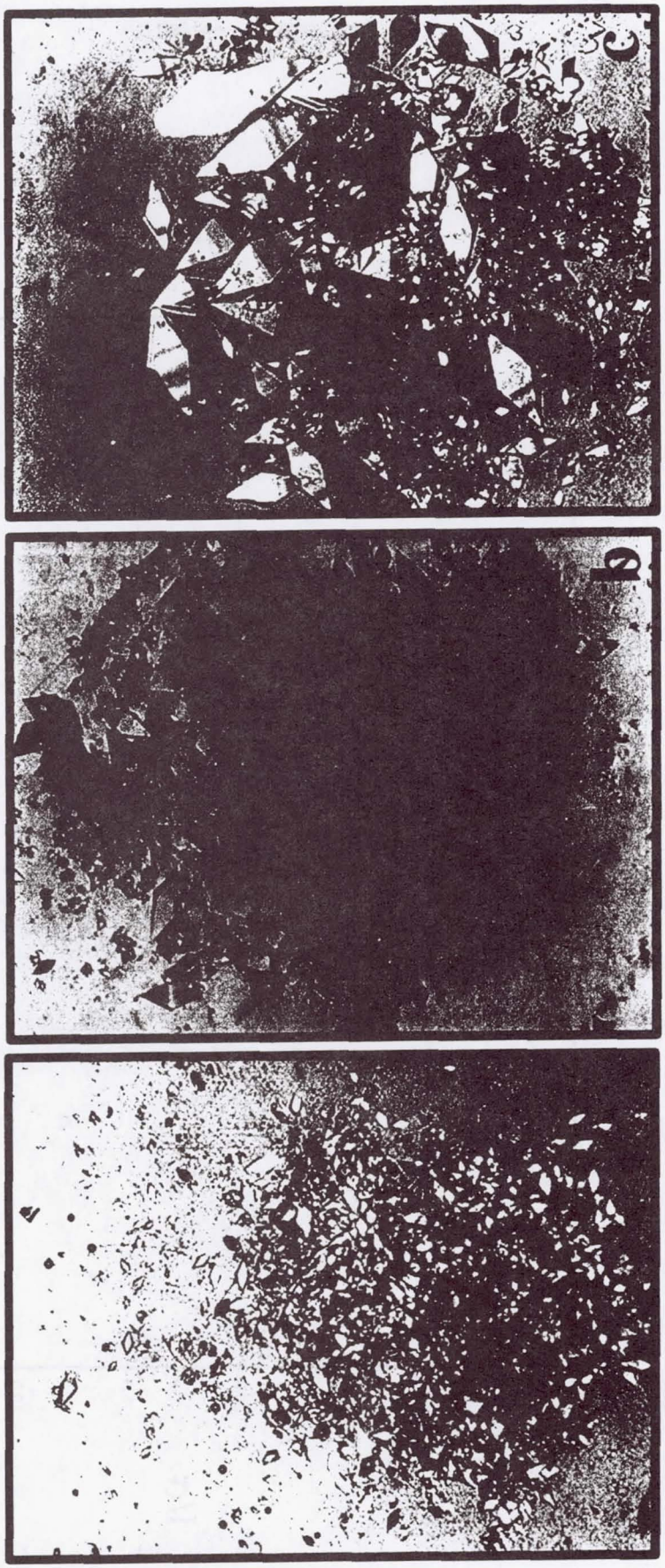

Figure 2

Figure 3

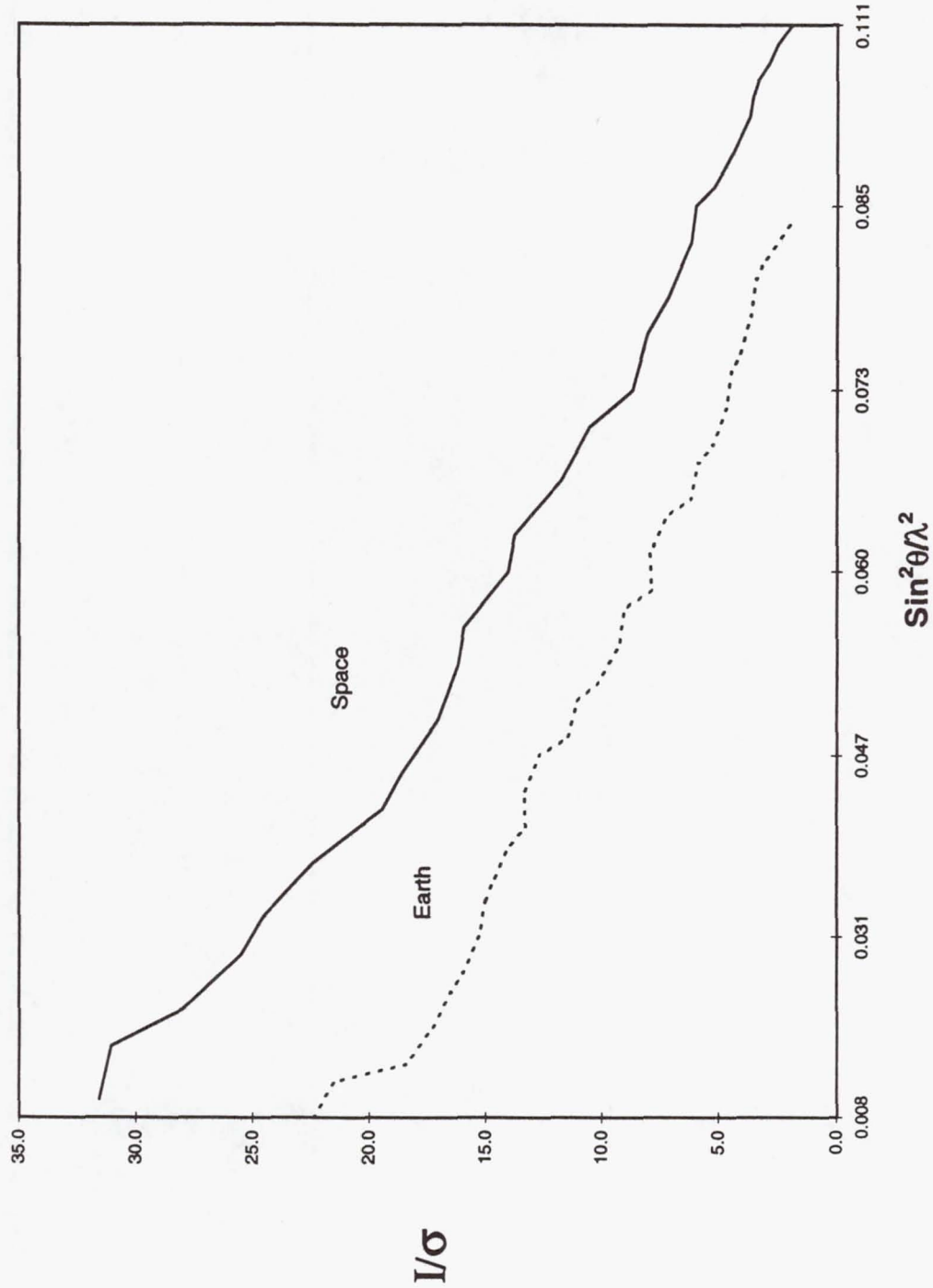
I/σ
35.0
30.0
25.0
20.0
15.0
10.0
5.0
0.0
0.008
0.031
0.047
0.060
0.073
0.085
0.111
Sin²θ/λ²
Space
Earth

Advanced Protein Crystallization Facility (APCF)

Crystallization of the Nucleosome Core Particle

Principal Investigator:

Dr. Timothy Richmond
ETH Zürich
Zürich, Switzerland

Report on Crystallization of the Nucleosome Core Particle during Space Shuttle mission STS-78 using APCF

Armin Mäder and Timothy J. Richmond
Institut für Molekularbiologie und Biophysik
ETH Zürich

7 August, 1997

Reference: APCF/LMS-95-11

Objectives

We asked for participation in the microgravity crystallization program with the aim of improving the X-ray data quality in the resolution range of 1.8-2.8 Å for our crystals of the nucleosome core particle. Specifically, we attempted to obtain crystals with reduced mosaic spread.

Background

The DNA in chromatin of all eukaryotic organisms is organized in arrays of nucleosomes. Two copies of each histone protein, H2A, H2B, H3, and H4 assemble in an octamer that wraps 147 base pairs of DNA around it to form a 206 kD nucleosome core. With the addition of linker DNA and histone H1, the nucleosome is formed. This highly conserved nucleoprotein complex occurs essentially every 200±40 bp throughout all eukaryotic genomes. The repeating nucleosomes further assemble into higher order helices. The nucleosome shapes the DNA molecule both at the atomic level by bending and twisting it, and on the much larger scale of genes by forming a higher order structure.

We have recently determined the atomic structure of the nucleosome core particle containing a defined sequence DNA by X-ray crystallography at 2.8 Å resolution (*Nature* in press). The structure was solved by multiple isomorphous replacement (MIR) using three heavy atom derivatives based on recombinant histone proteins and data collected at the European Synchrotron Radiation Facility (ESRF). This protein/DNA complex, the largest solved to date, shows how four pairs of histone fold domains are responsible for organizing 121 bp of DNA while extensions of the histone fold bind the termini of the DNA superhelix and help stabilize the overall structure. The remainder of the histone molecules, the histone tails, are arranged to contribute the formation of the higher order helix.

The limit of X-ray diffraction data from the nucleosome core particle crystals extends anisotropically to 1.8-2.2 Å and would a permit a molecular structure to be built with greater accuracy than that based on the data to 2.8 Å. This represents an increase of 2.7-fold in the quantity of data available at the higher resolution. At 2.0 Å resolution, even the ordered solvent molecules could be included in the structure. However, the crystal mounting method that is most convenient and that was used for the 2.8 Å data collection puts the long axis of the rod-shaped crystals roughly parallel to rotation axis used to sample diffraction space. This orientation is not ideal because the orthorhombic crystals have cell dimensions of approximately 110 x 200 x 110 Å where the c-axis is along the long axis of the rod. Therefore, the separation of diffraction intensities center to center with respect to the crystal rotation in the vicinity of the h0l projection is only 0.6° for the diffraction intensities at 2 Å resolution. Since the crystals have high mosaic spread, approximately 0.9-1.5° depending on the particular crystal, complete measurement of the high resolution data would not be possible because of overlapping diffraction intensities. The growth of crystals under microgravity conditions was attempted to eliminate this problem stemming from imperfect crystals.

Methods of Data Acquisition and Analysis

X-ray diffraction patterns from crystals grown in space and on the ground were obtained using the Swiss/Norwegian beam line (SNBL) facility at the European Synchrotron Radiation Facility, Grenoble (ESRF). The SNBL optics included a focusing monochromator and mirror. The goniometer and detector consisted of a 30 cm MAR image plate device. The exposures were made using a film to crystal distance to optimize the signal to noise ratio. Exposures were made for 30 to 60 min, allowing us to observe crystal sampled intensities to the diffraction limit of approximately 2.0 Å observed previously on undulator beam lines (ID9 and ID13 lines at ESRF) in 0.5 to 3 minutes. The wavelength used was 0.873 Å with the synchrotron operating at 200 mA in 2/3 fill mode. The beam size at the crystal was nominally 0.3x0.3 mm.

Flight versus Ground Results

We used four 88 ml hanging drop reactors at 20° C during the spacelab flight on Space Shuttle mission STS-78 in June/July 1996. The hanging drop reactors were originally designed to accommodate a protein volume decreasing in the course of the experiment. However, our crystallization conditions are higher in salt concentration at the beginning of the experiment compared to the final equilibrated solution. The HD reactors were modified to allow for the increase in volume. None of the crystallization drops were lost and all were qualitatively recovered at the end of the experiment.

The morphology and size of the space grown crystals did not differ from the ground control crystallization experiments significantly (Table 1).

Reactor	Reservoir buffer mM $MnCl_2$/ KCl	Crystal characteristics
1S	43/48	Many small rods: 100-200 x 100-200 x 500-1000 m Often hexagonal; few holes.
1G	43/48	Many small crystals.
2S	35/40	As for 1S
2G	35/40	Large and small crystals
3S	30/35	Several big crystals: 300-400 x 300-400 x 1000-1500 m Hollow funnels: typical of big crystals.
3G	30/35	Large and small crystals.
4S	24/29	Several large crystals, hollow funnels.
4G	24/29	Large and small crystals.

Table 1. APCF crystal growth experiments.

S - space experiments, G - ground experiments. All initial volumes were 50 ml and increased 1.5-1.8-fold on equilibration. A reservoir volume of 700 ml was dispensed in two 350 ml absorbers. The starting protein concentration was at 8 mg/ml in 84 mM $MnCl_2$, 60 mM KCl and 20 mM Potassium/Cacodylate pH 6.

There were generally many nucleations in both systems with the consequence of limited crystal size. Most crystals were attached to the Teflon piston of the syringe. All crystals grown in HD reactors whether on ground or in space were inferior in morphology and size to our typical crystals grown under very slow vapor diffusion conditions in our laboratory.

Analysis of crystals grown either on the ground or in space showed no discernible differences in the limits of diffraction or in mosaicity under the three sample conditions used to record the diffraction patterns (Table 2).

Sample conditions	Diffraction limits - a* / b* / c* axes in Å	
in X-ray beam	Ground grown	Space grown
HL-0, RT	3.8 / 3.8 / 3.0	3.8 / 3.7 / 2.9
HL-24, RT	3.2 / 3.2 / 2.7	3.2 / 3.2 / 2.8
HL-24/2, -180° C	2.2 / 2.2 / 2.0	2.2 / 2.2 / 2.0

Table 2. Diffraction limits of ground and space grown crystals.
The values for the three principle directions of the diffraction pattern are given. HL-0: harvest liquid (37 mM Potassium Chloride, 40 mM Manganese Chloride, 10 mM Potassium Cacodylate, pH 6.0); HL-24: harvest liquid containing 24% 2,4-methyl-pentandiol (MPD); HL-24/2: harvest liquid containing 24% MPD and 2% Trehalose; RT: room temperature, ~24* C.

The diffraction limit values listed in Table 2 are estimated from direct observation of the diffraction patterns. Mosaicity was also evaluated qualitatively by direct observation estimating the number of diffraction spots that obviously occur on successive exposures in a series of five 0.4° rotations of the crystal.

Conclusions

There were no significant differences in the quality of diffraction from crystals grown on the ground or in space using the modified HD reactor. In both cases, the crystals were not as useful for X-ray data measurement as crystals grown under the optimal laboratory conditions. Factors that contributed to this result are possibly: 1) the HD crystallization reactors could not be adapted to match the optimal laboratory setups, and 2) the time available for space crystallization required that the gradient between protein and buffer volumes reach equilibrium 4 to 5-fold faster than in our standard setups. Additionally, other experimental factors such as vibrations or container surface effects may be more important than the presence or absence of gravity.

Another important point should be considered. Nucleosome core particles require that 24% MPD be added not only to prevent ice formation during cryocooling, but to improve the diffraction limit that is initially observed at room temperature. The crystals undergo a repacking with a concomitant reduction by approximately 7% of the b-axis unit cell length. Since the rearrangement of the particle in the crystals may dominate crystal quality and occurs after crystal growth, it was important to compare crystals at room temperature with and without the addition of MPD. We were interested to see if the resolution limits would be improved by space growth. They were not.

In order to observe the highest resolution diffraction intensities, it is necessary to cool the crystals to -180° C before exposure to X-ray radiation because of their high sensitivity to radiation damage. A crystal survives for only one of the 200 exposures required for a 2 Å data set if exposed to X-rays at higher temperatures (i.e. 4° C), and for 16 exposures at -180° C (15-20% general weakening of the overall intensity in the crystal sampled diffraction pattern). As for room temperature exposures, there were no improvements in space versus ground grown crystals when examined at cryotemperature.

Currently, we are refining our 2.8 Å structure of the nucleosome core particle to 2.0 Å resolution using data collected at the ESRF and crystals grown in the laboratory. We were unable to reduce the mosaic spread of the crystals, but we were able to find a method of mounting the crystals so that the short reciprocal b*-axis is along the direction of the rotation axis during data collection. This procedure eliminated the superposition of diffraction intensities sufficiently well to permitted a complete data set to be collected over 24 crystals at -180° C. Accordingly, we have no further requirement to attempt crystal growth in space for this particular project.

Articles / Presentations

I do not foresee publication of our STS-78 results.

Summary

Crystals of the nucleosome core particle of chromatin were grown in space and on the ground using a device especially designed for crystal growth experiments on the space shuttle. The resulting crystals in either case were generally not as large or perfect morphologically as those grown under more optimal experimental conditions in our laboratory. Crystals grown in space and on the ground using the shuttle device showed no significant differences.

Advanced Protein Crystallization Facility (APCF)

Crystallization of Photosystem I

Principal Investigator:

Dr. Wolf Schubert
Free University of Berlin
Berlin, Germany

Crystallisation of Photosystem I - Results of the LMS Mission

Petra Fromme*, Wolfram Saenger# and Norbert Krauß#

* *Max Volmer Institut für Biophysikalische Chemie und Biochemie, TU Berlin, Str. des 17. Juni 135, 10623 Berlin, Germany*
# *Institut für Kristallographie, FU-Berlin, Takustr. 6, 14195 Berlin, Germany*

Background

Plants and cyanobacteria are able to use light for performing oxygenic photosynthesis This is the main biological process on earth where emissive electromagnetic energy from the sun is converted into chemical energy. The first step of the process, the light induced charge separation across the photosynthetic thylakoid membrane, is catalysed by two large membrane intrinsic protein complexes, the photosystems I and II. Photosystem I (PS I) from the thermophilic cyanobacterium *Synechococcus elongatus* is the largest of the 8 membrane proteins, which have been crystallised so far. It occurs in the cyanobacterial thylakoid membrane as a trimer with a molecular weight of 3 x 340 000 Da; The monomer consists of 11 different polypeptides, coordinating ~100 chlorophyll *a* molecules, 25 carotinoids, 3 [4Fe4S] clusters and 2 molecules of vitamin K1. A structural model of this trimeric Photosystem I has been derived from X-ray structure analysis at 4 Å resolution [Krauß N., Schubert W.-D., Klukas O., Fromme P., Witt H.T. and Saenger W. (1996) *Photosystem I at 4 Å resolution: A joint photosynthetic reaction center and core antenna system* Nature Struct. Biol. 3, 365-370]

Objectives

Photosystem I was crystallised under microgravity on USML-2 with very encouraging results. The volume of the obtained crystals was increased by a factor of 10-20 compared to the terrestrial Photosystem I crystals, the largest crystal having a length of 4mm and a diameter of 1.5 mm. The crystals diffract X-rays to a maximal resolution of 3.4 Å and show a mosaic spread of 0.6 °. A complete native data set was measured from the largest microgravity grown crystal using synchrotron radiation at DESY in Hamburg and evaluated to a resolution of 3.4 Å. This is the best X-ray data set thus far obtained from Photosystem I crystals.

Photosystem I could not be crystallised under optimal conditions during the USML-2 mission. We had to use 20°C for technical reasons; however, the temperature for the best crystallisation of Photosystem I on earth was found to be 4°C. Earth grown crystals of Photosystem I aged at 20 °C for 21 days (which was the flight and transport time during USML-2) do not diffract X-rays to a resolution higher than 5 Å. Crystallisation on LMS was technically feasible at 8°C and performed under this condition in order to further improve the quality of the crystals.

Methods

Two sets of experiments were performed: A) Crystallisation of Photosystem I by dialysis against low salt B) Crystallisation of Photosystem I in the presence of 0.75 M sucrose. The aim of using sucrose in the second set of experiments was to increase the viscosity of the solution, thereby reducing the diffusion rates of salt and protein and to slow down equilibration of the solutions in the reactors. This should lead to a slower growth rate and possibly to a significant reduction of the mosaic spread of the obtained crystals.

For A), small pre-grown crystals of Photosystem I were completely dissolved in buffer A (50 mM $MgSO_4$, 5 mM MES pH = 6.4 and 0.02 % ß-dodecylmaltoside) in order to prepare the protein solution. For B), the crystals were dissolved in buffer B (same as A, but + 1,5 M sucrose). The protein concentration was 80 mg/ml in both cases.

In the APCF microdialysis reactors this solution was dialysed against the same buffers but with reduced salt concentration (equilibration concentration 11 mM $MgSO_4$ for A) and 8 mM for B).

A total of eight APCF reactors were filled according to protocol A, and seven reactors were filled according to protocol B using the same solutions. Of these 15 reactors, 9 were used as ground controls (5 without sucrose, 4 with sucrose,), and 6 were flown in space (3 without sucrose, 3 with sucrose). All ground controls were activated/deactivated at the same time as the flight reactors in space.

Comparison of flight results to ground results

The results are summarised in table 1. In all 9 ground control reactors crystals suitable for X-ray structure analysis were obtained. In contrast, all 6 space reactors contained clear, green solution of Photosystem I, although the control and space chambers were filled under identical conditions.

There are several explanations for this result; the following questions had been addressed:

Have the reactors been activated? -=> yes

- The first possibility for non-crystallisation could be that the space reactors had not been activated. In order to exclude this possibility, the conductivity in the reservoir chamber was measured in all flight and ground control reactors. Without activation of the reactors the conductivity should be as low as conductivity at the beginning of the experiment. This was not the case. All chambers showed conductivities expected for the fully equilibrated chambers with a salt concentration of 11 mM $MgSO_4$.

Is the protein degraded ? => no

- We tested if the protein had degraded in the space reactors (perhaps due to increased temperature during start and landing). This was not the case. The flight protocol shows constant temperature during the whole flight and no degradation bands were visible using SDS gelelectrophoresis.

Is there a nucleation problem? => yes

• Decreased nucleation rate in space was assumed to be the reason for the lack of crystals in the space reactors. In order to test this hypothesis, we added a small crystal to the clear solution (seeding) in one of the space-flown reactors. A shower of small crystals was formed immediately. The same result was observed when a a drop of the clear solution from the space reactors (1 ul) was mixed under a microscope with 1 ul buffer without salt . A large number of small crystal was formed immediately.

These results indicate that the nucleation rate was decreased under microgravity conditions. Figure 1 shows a schematic phase diagram of Photosystem I. The protein solution is undersaturated before activation of the reactors (80mg/ml protein and 50 mM salt). After activation, the salt concentration is first reduced to 30 mM, which on earth is close to the border between metastable zone and the nucleation zone. Finally, the salt concentration is further reduced and the protein concentration in solution decreases due to crystal growth. This crystallisation procedure works perfectly for the ground experiments and was also very successfully used on USML -2 mission (at 20 ^{o}C), were we obtained very large crystals in three out of six chambers. We now address the question whether sedimentation of the preformed nuclei accelerates nucleation on earth.

Does the orientation of the (ground control) reactors have an influence on the nucleation

=> yes

• In order to test this possibility we looked for the orientation of the ground control reactors during crystallisation with respect to the number and location of crystals formed in the reactors.

In 5 of the ground controls the reactors were in **vertical orientation** (**v** in Fig. 2) with the protein reservoirs on top, the salt reservoirs on bottom. In this case the sedimentation of the nuclei would be in direction of the decreasing salt concentration (i.e. nuclei will drift to the dialysis membrane).

4 of the ground controls were in **horizontal orientation** (**h** in Fig. 2). The reactors were lying on the side during crystallisation (this corresponds to a rotation of 90° relative to the vertical orientation . In this case the sedimentation occurs perpendicular to the decreasing salt gradient.

The observed results were in good agreement with these suggestions: In the 5 ground controls with vertically oriented reactors 15-50 crystals were formed per reactor; in the 4 horizontally oriented reactors only 1-4 crystals were grown. All crystals were grown on the earth directed side, i.e. in the vertical orientation (v) all crystals grew on the membrane and in the horizontal orientation all crystals grew on the bottom side of the reactors.

Does microgravity have an influence on the nucleation rate => yes

- The question arises, why we obtained very large, well ordered crystals at 20°C on the USML-2 mission and no crystals at 8°C on the LMS mission. The results of both missions suggest that microgravity has an influence on the nucleation rate. It appears that due to the lack of sedimentation the nucleation rate is dramatically reduced under microgravity conditions. This led to 0-3 nuclei at 20°C, but at 8°C, where the diffusion rate (and therefore also the nucleation rate) is about a factor of two lower, no nuclei with larger than the critical radius were formed.

Conclusion

The results obtained during LMS mission led to new insights in the first events during Photosystem I crystallisation, which are not only useful for further microgravity experiments, but may improve the crystallisation conditions on earth.

It was found that sedimentation of nuclei is significant under terrestrial conditions and increases the nucleation rate during Photosystem I crystallisation. The optimal conditions for crystallisation under microgravity must therefore be tested directly in space. Systematic investigations should be done to further elucidate the primary events during crystallisation of Photosystem I and to show the direct influence of microgravity on nucleation rate and crystal quality for a membrane protein. A larger number of space experiments has therefore to be performed in the future, including the possibility of seeding. If optimal conditions can be found at 8°C, we expect a significant increase of crystal quality.

Summary

The crystallisation of the large membrane protein Photosystem I was investigated under microgravity on the LMS mission. Comparison of the microgravity to the ground control experiments shows a significant influence of the microgravity on the nucleation rate.

Table 1

Reactor number	Location	presence of sucrose	orientation of the reactor *	number of crystals/reactor
319	ground control	no	v	~ 50
119	ground control	no	v	~ 15
130	ground control	no	v	~ 30
320	ground control	no	h	4
105	ground control	no	h	1
133	ground control	yes	v	~ 20
103	ground control	yes	v	~ 40
321	ground control	yes	h	1
318	ground control	yes	h	3
101	microgravity	no		0
322	microgravity	no		0
317	microgravity	no		0
106	microgravity	yes		0
117	microgravity	yes		0
132	microgravity	yes		0

* v = vertical orientation of the reactor
h = horizontal orientation of the reactor

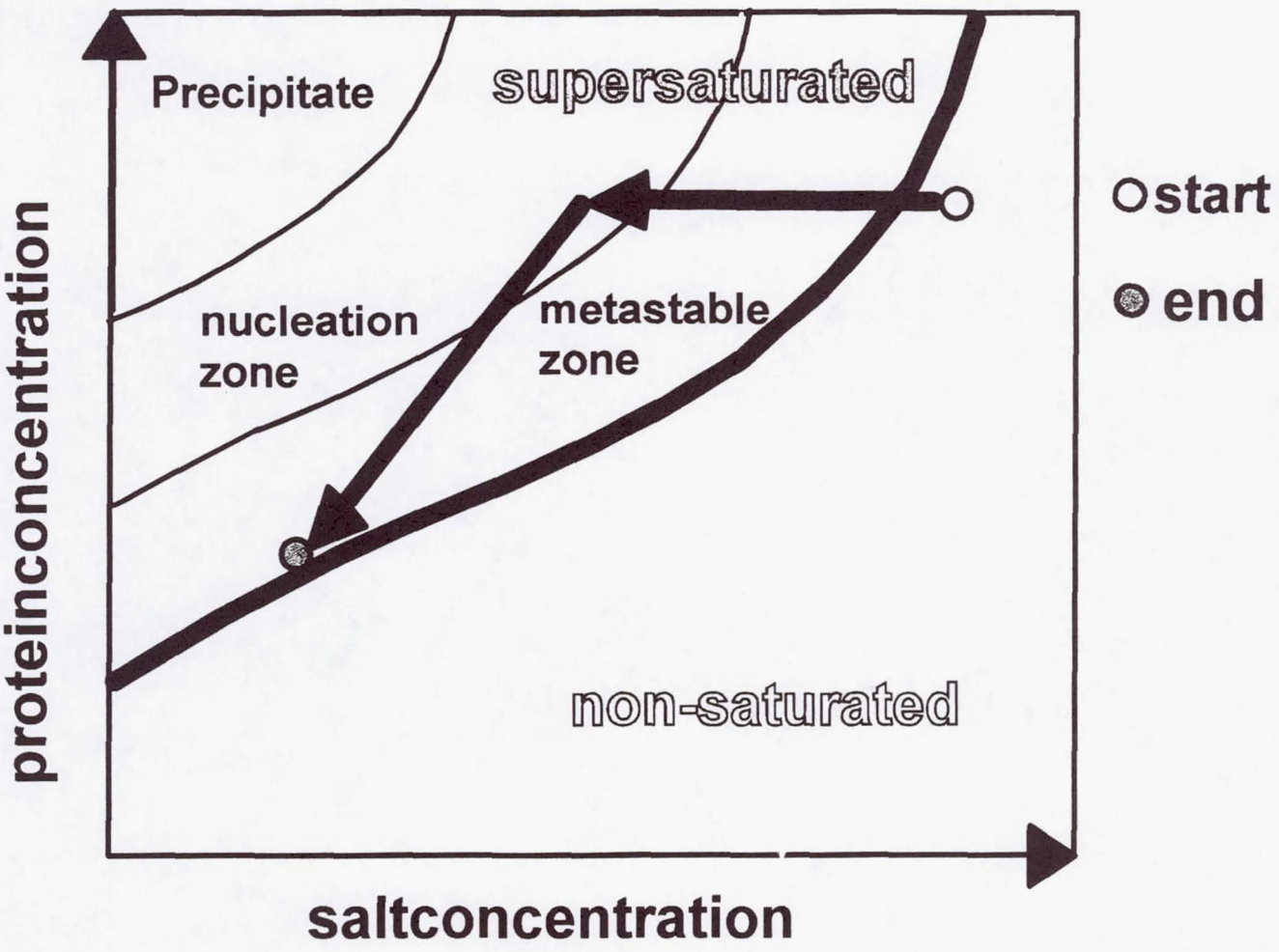
Precipitate
supersaturated
nucleation
zone
metastable
zone
non-saturated
start
end
proteinconcentration
saltconcentration

Advanced Protein Crystallization Facility (APCF)

Mechanism of Membrane Protein Crystal Growth: Bacteriorhodopsin-mixed Micelle Packing at the Consolution Boundary, Stabilized in Microgravity

Principal Investigator:

Dr. Gottfried Wagner
Justus-Liebig-Universität
Giessen, Germany

MECHANISM OF MEMBRANE PROTEIN CRYSTAL GROWTH: BACTERIORHODOPSIN-MIXED MICELLE PACKING AT THE CONSOLUTION BOUNDARY, STABILIZED IN MICROGRAVITY

PI:
Torsten Rothärmel
Gottfried Wagner
Justus-Liebig-University
Department of Biology
Senckenbergstrasse 17
35390 Giessen, Germany

Phone: +49-641-99-35140 / 35142
FAX: +49-641-99-35119
e-mail:
Torsten.Rothaermel@bio.uni-giessen.de
Gottfried.Wagner@bio.uni-giessen.de

Co-I:
Christian Betzel
Markus Perbandt
Institut für Physiologische Chemie
c/o DESY; Geb. 22a
Notkestrasse 85
22603 Hamburg, Germany

Phone: +49-40-8998-4744 / 4745
FAX: +49-40-8998-4747
e-mail:
Betzel@EMBL-Hamburg.de
Markus@unisgi1.desy.de

Abstract

The bacteriorhodopsin crystal growth experiment with the Advanced Protein Crystallization Facility (APCF) on the shuttle mission LMS in June 1996 was done to allow crystal growth of bacteriorhodopsin (BR) at the consolution boundary of bacteriorhodopsin-mixed micelle packing, stabilized in microgravity.
The bacteriorhodopsin crystal growth experiments have resulted in crystals of a) needle-shaped, b) cubic-shaped, c) balk-shaped, and d) small cubic-shaped crystals nucleated on the outer end of needles of multicrystalline clusters.
The average edge length of cubic-shaped crystals under microgravity (163.0 µm) and on ground (59.7 µm), and their density (1.125 g/cm^3) were determined.

Introduction:

Membrane proteins catalyze vital reactions such as solute transport, charge separation and conversion of energy, as well as signal transduction. The proton-pumping bacteriorhodopsin (BR) is a small amphiphilic photochromic retinal protein, found in the purple patches of the cell membrane of *Halobacterium halobium*. As a small membrane spanning protein, it does not exceed the lipid bilayer much on either side (1). Detergent-solubilized bacteriorhodopsin is embedded in micelles of different sizes, as a function of the detergent cocktails used (2, 3). The bacteriorhodopsin molecules form filaments which pack together due to weak and easily disturbed hydrophilic interactions between the loop regions of protruding molecules in aligned filaments (4, 5). Three different habits of bacteriorhodopsin crystals, namely a) needle-shaped, b) cubic-shaped, and c) balk-shaped are compatible with three different micelle sizes, received in detergent solutions after bacteriorhodopsin solubilization (2).
Our experience shows that best bacteriorhodopsin crystals grow close to the consolution boundary, where interaction between detergent micelles is enhanced. Reduced gravitational conditions are favourable due to minimal gravity-driven phase separation.

Results:

Consistent with different micelle sizes observed through dynamic light scattering, three different habits of bacteriorhodopsin crystals, namely a) needle-, b) cubic-, and c) balk-shaped crystals could be obtained. The packing of the molecular rods of bacteriorhodopsin was tight and the crystal morphology exhibited smooth surfaces and sharp edges of up to 1 mm in length, and diffractional power with a resolution limit of up to 3.8 Å, as reported before (2, 4).

The LMS-2 (STS-78) microgravity experiment lead to the growth of cubic-shaped bacteriorhodopsin crystals (Fig. 2) with a 20-fold enlarged volume compared to the ground control (Fig. 1).

Vapour diffusion: Laboratory hardware	Liquid-liquid diffusion: APCF 188 µl in Microgravity	Liquid-liquid diffusion: APCF 188 µl on Ground
84.6 ± 6.5 µm (n = 41)	163.0 ± 7.3 µm (n = 13)	59.7 ± 2.3 µm (n = 39)

Fig. 1: Average edge length of cubic-shaped crystals of bacteriorhodopsin, grown under different conditions.

The cubic habit was stabilized under microgravity conditions, while the ground control showed additional multicrystalline needle clusters.
An altered crystal growth protocol produced multicrystalline needle clusters and single needles both on earth and in microgravity.

The density of cubic-shaped crystals was determined by the method of Matthews (6) and Mikol and Giegé (7). Preliminary results of the determination of crystal density with different Ficoll solutions show a density of 1.125 g/cm^3 after 35 min (Fig. 3).
This preliminary density estimation of cubic-shaped bacteriorhodopsin crystals is slightly lower than the density of purple patches in the membrane from *Halobacteria* with 1.18 g/cm^3 (8). The three-dimensional cubic-shaped bacteriorhodopsin crystals would show an slightly increased content of water compared to the two-dimensional crystalline structure in the purple membrane patches.

A new observation was the nucleation of small cubic-shaped bacteriorhodopsin crystals on the end of single needles from multicrystalline bacteriorhodopsin needle clusters (Fig. 4). The multicrystalline needle clusters grown under microgravity showed a slight increase in diameter compared to the multicrystalline needle clusters grown as ground control.
Nucleation of pseudohexagonal needles and orthorhombic bacteriorhodopsin crystals has been described before on benzamidine crystals (9). The observation that pseudohexagonal bacteriorhodopsin crystals could be nucleated on benzamidin-crystals led to the assumption that the activation energy that determines the nucleation probability was lower on the particular benzamidin surface than in solution.

Interestingly, endparts of the surface of the needles of bacteriorhodopsin multicrystalline needle clusters were able to induce a new crystal morphology, since small cubic-shaped bacteriorhodopsin crystals formed at the end of the needles of multicrystalline needle clusters (Fig. 4).

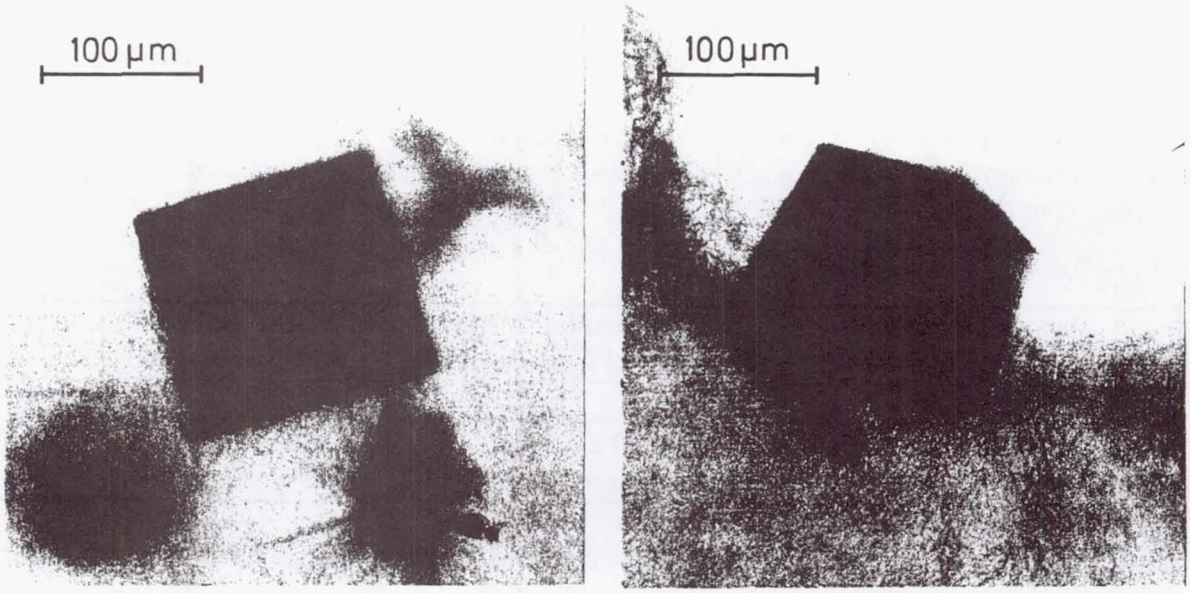

Fig. 2: Cubic-shaped bacteriorhodopsin crystals grown in microgravity with axes of 150 µm in length. The crystal morphology is compact with sharp edges and smooth surfaces.

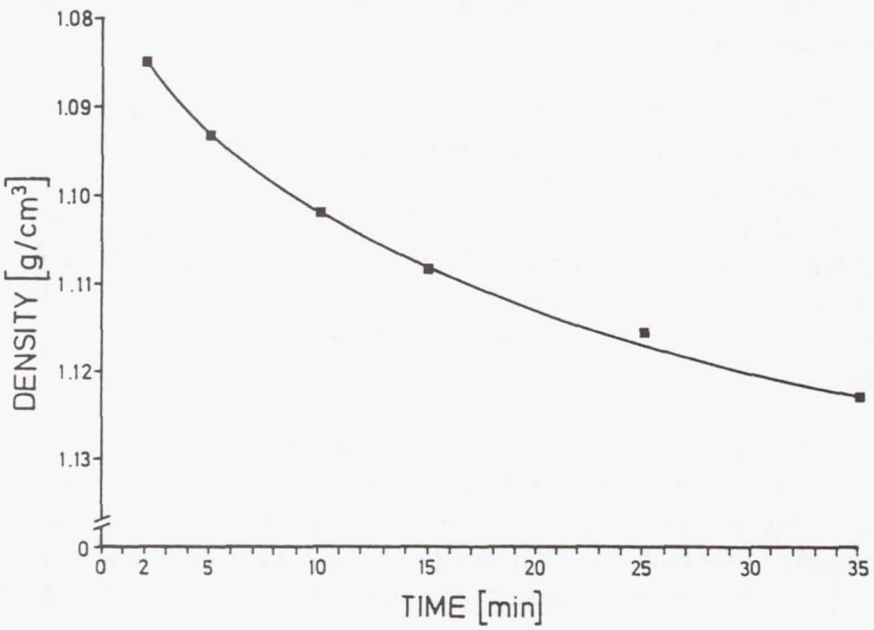

Fig 3: Experimental determination of the density of cubic-shaped bacteriorhodopsin crystals. The density was determined in a step up gradient of Ficoll solutions (from 25-60% w/w) calibrated by estimation with NaH_2PO_4 droplets.

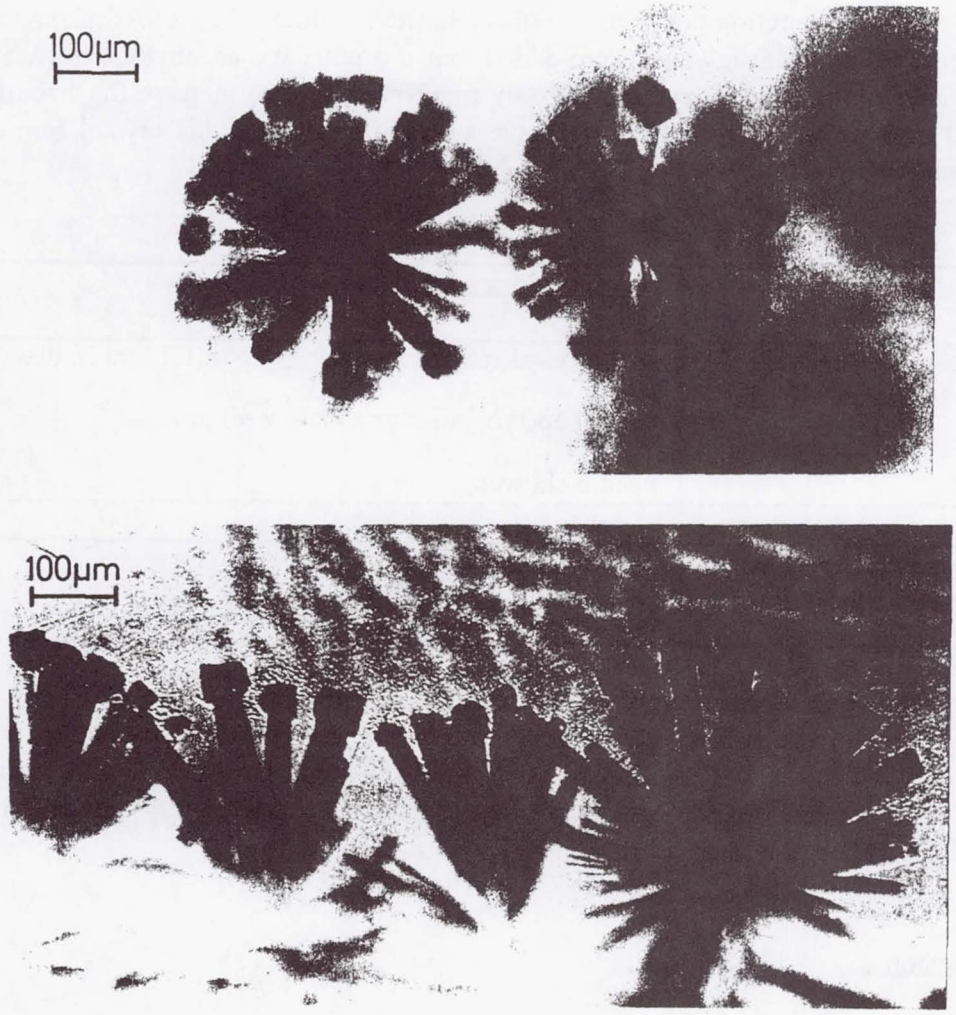

Fig. 4: Multicrystalline bacteriorhodopsin needle clusters with small cubic-shaped crystals on the end of single needles. The multicrystalline needle clusters shown here, are up to 390 µm in diameter; the small cubic-shaped crystals have an edge length up to 45 µm. The clusters fall apart easily.

Another attempt of crystal formation was based on the procedure of seeding. Cubic-shaped and balk-shaped bacteriorhodopsin crystals were transferred in new crystalization set ups of seeding-analogue protocols:

a) The cubic-shaped seeding-crystals dissolved over night after being transferred. The new crystallization set ups led to formation of multicrystalline needle clusters, a few balk-shaped bacteriorhodopsin crystals, and needle-shower (Fig. 5).
b) The balk-shaped seeding-crystallization set ups led to formation of multicrystalline needle clusters and balk-shaped bacteriorhodopsin crystals of increased length and width (Fig. 5).

Electrostatic crosslinkers as additives may have value for optimization of crystallization conditions, since ionic and electrostatic interactions between macromolecules play a role in the crystallization process (10). The linker could act as a multivalent tether, where one end of the linker would interact with a charged surface group of one macromolecule while a second charged group on the same tether could interact with another, and so might influence both pre- and post-nucleation events (10).

Cubic-shaped bacteriorhodopsin crystals formed while the crosslinkers Triglycine, Tetraglycine, and Hexaglycine were added, but did not have an obvious impact on size or appearance of the formed crystals. Gly-Gly free base tended to increase the size of the cubic-shaped crystals on earth, but did not have a clear impact on cubic crystal formation under microgravity.

Seeding-crystals:	New grown crystals:
cubic-shaped crystals edge length: 60-90 µm	multicrystalline needle clusters up to 1.3 mm in diameter balk-shaped crystals up to 840 x 90 µm needle-shower
balk-shaped crystals 300-450 x 30-60 µm	balk-shaped crystals up to 900 x 90 µm multicrystalline needle clusters up to 1.6 mm in diameter

Fig. 5: Bacteriorhodopsin crystal formation in seeding set ups.
Some of the balk-shaped crystals considered new grown in the set up with seeding balk-shaped crystals could be seeding-crystals with increased length, because it was not possible to distinguish between balk-shaped seeding-crystals and new grown crystals of the same habit.

Conclusions:

The chosen crystallization conditions combined with the suppression of gravity-driven convection and sedimentation of bacteriorhodopsin enabled the growth of tightly packed crystals of different habits. Single crystals exhibited a diffractional power with a resolution limit of up to 3.8 Å.
The volume of cubic-shaped bacteriorhodopsin crystalsgrown under microgravity conditions showed a 20-fold enlarged volume compared to the ground control.
A new observation was the nucleation of small cubic-shaped bacteriorhodopsin crystals on the endpart of the surface of needles of multicrystalline needle clusters.
Both effects putatively result from stabilization of the consolution boundary.
Further experiments in microgravity, as a favourable environment of improved crystallo-genesis, provide additional progress in the investigation of difficult membrane proteins such as bacteriorhodopsin.

References

1. D. Oesterhelt, C. Bräuchle, and N. Hampp, Quart. Revs. Biophysics **24**:425-478 (1991)
2. T. Rothärmel, G. Wagner, Ch. Betzel, and M. Perbandt, USML-2 report (1997)
3. E. H. L. Tan and R. R. Birge, Biophys. J. **70**:2385-2395 (1996)
4. G. Wagner, ESA-Proc. Space Station Utilization, SP-**385**:235-238 (Dec. 1996)
5. G. Wagner, ESA J. **18**:25-32 (1994)

6. B. W. Matthews, J. Mol. Biol. **33**:491-497 (1968)
7. V. Mikol and R. Giegé. In: A. Ducruix and R. Giegé (eds.): Crystallization of Nucleic Acids and Proteins. IRL Press, pp 219-239 (1992)
8. D. Oesterhelt, R. Hartmann, H. Michel, and G. Wagner. In: G. Schäfer and M. Klingenberg (eds.): Energy conservation in biological membranes. Springer-Berlin, pp. 140-151 (1978)
9. G. F. X. Schertler, H. D. Bartunik, H. Michel, and D. Oesterhelt, J. Mol. Biol. **234**:156-164 (1993)
10. B. Cudney, S. Patel, K. Weisgraber, Y. Newhouse, and A. McPherson, Acta Cryst. D**50**:414-423 (1994)

Acknowledgement
Flight opportunities provided through DLR/DARA and ESA/ESTEC, and financial support of the experiments in the laboratory through DARA (FKZ 50 WB 91635; 50 WB 9414), are thankfully acknowledged. Andrea Weisert is given special thanks for her support in the determination of the density of crystals.

MECHANISM OF MEMBRANE PROTEIN CRYSTAL GROWTH: BACTERIORHODOPSIN-MIXED MICELLE PACKING AT THE CONSOLUTION BOUNDARY, STABILIZED IN MICROGRAVITY

Torsten Rothärmel*, Gottfried Wagner*, Christian Betzel°, and Markus Perbandt°

* Justus-Liebig-University, Department of Biology, Senckenbergstrasse 17, 35390 Giessen, Germany, e-mail: Torsten.Rothaermel@bio.uni-giessen.de, Gottfried.Wagner@bio.uni-giessen.de

° Institut für Physiologische Chemie, c/o DESY, Geb. 22a, Notkestrasse 85, 22603 Hamburg, Germany, e-mail: Betzel@EMBL-Hamburg.de, Markus@unisgi1.desy.de

The proton-pumping bacteriorhodopsin (BR) is a small amphiphilic photochromic retinal protein, found in the purple patches of the cell membrane of *Halobacterium halobium*.
The experiment was done under microgravity to allow crystal growth of bacteriorhodopsin at the consolution boundary of bacteriorhodopsin-mixed micelle packing and resulted in crystals of a) needle-shaped, b) cubic-shaped (Fig. 1), c) balk-shaped, and d) small cubic-shaped crystals nucleated on the end of needles of multicrystalline clusters (Fig. 2).
The packing of the molecular rods of bacteriorhodopsin was tight and the crystal morphology exhibited smooth surfaces and sharp edges of up to 1 mm in length, and diffractional power with a resolution limit of up to 3.8 Å.
The average edge length of cubic-shaped crystals under microgravity (163.0 µm) and on ground (59.7 µm), and their density (1.125 g/cm^3) were determined. The cubic-shaped bacteriorhodopsin crystals grown in microgravity showed a 20-fold enlarged volume compared to the ground control.
Interestingly, endparts of the surface of the needles of bacteriorhodopsin multicrystalline needle clusters were able to induce a different crystal morphology, since small cubic-shaped bacteriorhodopsin crystals formed at the end of the needles of multicrystalline needle clusters.

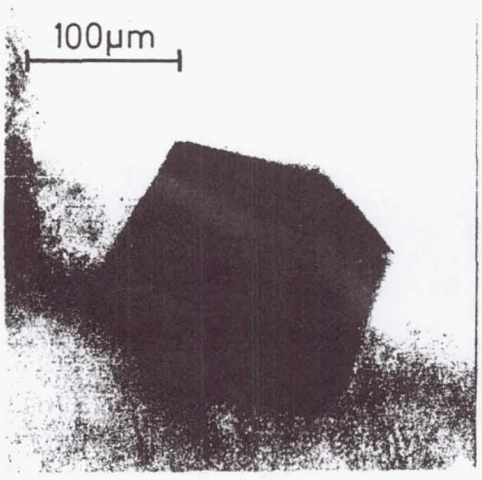

Fig. 1: Cubic-shaped BR crystal grown under microgravity with axes of 150 µm length. The crystal morphology is compact with sharp edges and smooth surfaces.

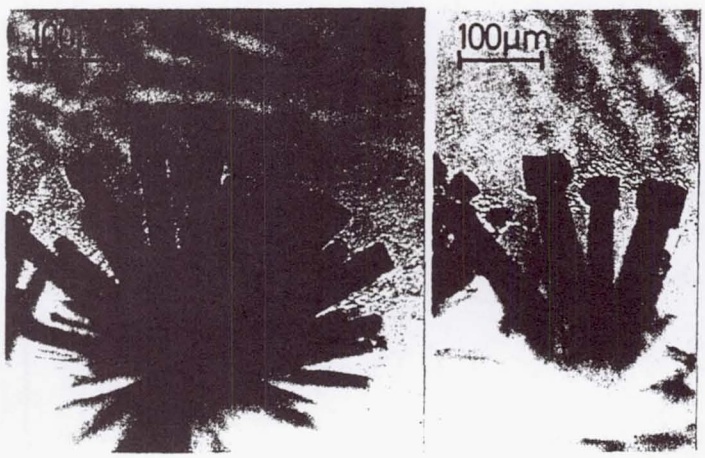

Fig. 2: Multicrystalline BR needle cluster with small cubic-shaped BR crystals on the end of single needles. The multicrystalline needle clusters shown here, are up to 390 µm in diameter; the small cubic-shaped crystals have an edge length of 45 µm.

Advanced Protein Crystallization Facility (APCF)

Crystallization in a Microgravity Environment of CcdB, a Protein Involved in the Control of Cell Death

Principal Investigator:

Dr. Lode Wyns
Free University of Brussels
Brussels, Belgium

CRYSTALLIZATION IN A MICROGRAVITY ENVIRONMENT OF CcdB, A PROTEIN INVOLVED IN THE CONTROL OF CELL DEATH

Prof. Dr. Lode WYNS, Dr. Minh Hoa DAO THI, Dr. Dominique MAES
Department of Ultrastrucutre
Institute of Molecular Biology
Free University of Brussels (VUB)
Belgium

Phone: 32 2 359 02 82
Fax: 32 2 359 02 89
email: ljwyns@vub.ac.be

Introduction

The *E. coli* F-plasmid is very stable inherited in the bacterial population. Plasmid-carrying cells are able to propagate while daughter cells that have not inherited a plasmid copy are selectively killed (Jaffé et al., 1985). The plasmid F-encoded proteins CcdA and CcdB are the key molecules responsible for this postsegregetional killing of bacterial cells. The underlying mechanism is based on a differential decay of the activities of the CcdA and CcdB proteins, the half-life of the cytotoxic CcdB being longer than the half-life of CcdA, that antagonises the CcdB action (Van Melderen, 1994, 1996). When CcdA is absent, CcdB is responsible for cell death, induction of the SOS pathway and inhibition of DNA synthesis (Bex et al., 1983, Karoui et al., 1983; Bailone et al., 1985). CcdA and CcdB are encoded by the *ccd* operon (Miki et al., 1984a,b). They are known to auto-regulate their own expression and it was shown that both proteins acts as a DNA binding repressor, probably after having formed a CcdA/CcdB complex (Tam & Kline, 1989a,b; De

Feyter et al., 1989). Recently it was demonstrated that the CcdB mediated cell-killing involves poisoning of DNA-topoisomerase II complexes (Bernard & Couturier 1992). The Arg462Cys mutation in the DNA gyrase A domain suppresses the lethal character of CcdB. Further experiments showed that, like quinolone antibiotics and a variety of antitumor drugs, CcdB is responsible for gyrase-mediated double-stranded DNA breakage (Bernard *et al.*, 1993). It thus converts the wide-type gyrase in a DNA-damaging agent. This action, which is most likely due to direct binding of CcdB to the DNA gyrase A domain, can be completely reversed by addition of stochiometric amounts of CcdA.

Poisons of eucaryotic topoisomerases are regarded as potent candidates of anti-cancer drugs. Elucidation of the structure and mode of action of the CcdB protein may lead to the design of new antibiotics and anti-tumoral drugs. Effort to crystallise CcdB over the last few years led to the identification of experimental conditions for the growth of several crystal forms. Here we present information concerning the crystallisation behaviour of CcdB and report on a novel crystal form that diffracts to high resolution and is suitable for structure determination. We also report the crystallisation of a mutant that acts as a super killer, probably due to its enhanced affinity for the A subunits of gyrase.

Objectives

- Improvement of crystal quality especially with respect to the systematic twinning problem.
- Crystallization of CcdB mutants using for MIR work.

Materials and Methods

Protein expression and purification of CcdB from Escherichia coli

CcdB was overexpressed in *E. coli* strain MS501 (containing the CcdB permissive mutation R462C in the GyrA gene harbouring plasmid pULB2250). *E. coli* cells were grown at 37°C in LB medium supplemented with 100 mg/l ampicilin and streptomycin. The purification contains the following steps : the ammonium sulphate precipitation using 30-80% cut-off , QEAE column at pH = 8.50 Tris-Hcl buffer ,

gel filtration column.,and finally Mono-S column. using a 0.0 - 1.0 M NaCl gradient. This resulted in a protein showing only a single band on SDS-PAGE and a yield of about 20 mg CcdB per litre of culture. The purified protein was dialysed against water and concentrated to 15.0 mg/ml (assuming a specific absorption coefficient of 16,100 M^{-1} at 280 nm) and subsequently used in crystallisation trials.

Purification of the CcdB Cysteine mutants

The CcdB mutants S70C, S74C, S84C and the double mutant S74C/G77Q were purified by affinity chromatography on activated Thio-Sepharose and washed with buffer containing 50 mM Tris-HCl (pH 7.80) , 1mM EDTA, 0.5M NaCl and 0.1% Triton X-100. and a Mono-Q column using a 0.0 to 1.0 M NaCl gradient. The pure protein was dialysed against water and concentrated before use in crystallisation trials.

Crystallisation

Crystallisation conditions were screened using the hanging drop method and resulted in three crystal forms, the details of which are summarised in Table I. Phase diagrams were also determined by crystallisation using the hanging drop method. For the tetragonal and orthorhombic forms, crystallisations were performed at different pH values, ranging between 6.5 and 9.0, using ammonium sulphate, sodium chloride and sodium acetate as precipitants. For the monoclinic form, the pH was chosen between 4.1 and 4.6 using PEG-6000 or PEG-Me5000 as precipitants. For the double S74C/G77Q, a phase diagram was determined using MPD.

Crystallisation was also attempted in both agarose and silica gels (Robert et al., 1992; Thiessen et al., 1994) for tetragonal and monoclinic forms of CcdB. In agarose gels, the crystallisation have been performed with different concentrations of CcdB ranging from 2.6 - 5.0 mg/ml, using 6%-12% PEG 6000 and 10%-20% PEGMe 5000 as precipitant at pH4.50 for the monoclinic form. For the tetragonal form, the protein concentration was varied between 6.0 and 12.0 mg/ml and the concentration of ammonium sulphate between 0.8 M and 2.0 M. These trials were done both at pH 7.5 and pH 8.5. The agarose concentration was varied from 0 to 2% agarose for all conditions tried. Similarly, the silica gel contents was varied from 2.7 - 5.0 %.

Crystallisation experiments in a microgravity environment of CcdB and its mutants were accepted by ESA for the two missions : USML-2 (1995) and LMS (1996).

Hanging drop (HD) reactors and free interface diffusion (FID) reactors of the *Advanced Protein Crystallisation Facility* (APCF) were used in these experiments. All experiments were duplicated in identical setups on earth, and in the cases where no crystals appeared during the space shuttle mission, the reactors were reactivated on earth after the flight. During the USML-2 mission, one Hanging Drop reactor and one FID reactor were allocated for both the wild type CcdB and for the double mutant S74C/G77Q. During the LMS mission, also a single hanging drop reactor and two FID reactors were available, this time for the wild type protein only.

Data collection and heavy atom screening

Data were collected on an Enraff-Nonius FAST area detector with a rotating anode source operated at 40 kV and 90 mA. Crystals were mounted in capillaries in the usual way and data were collected at 288 K. In the case of monoclinic CcdB, data were also collected at 100 K. These crystals were first transferred to a solution containing of 30% (w/w) PEG 400 and 70% (w/w) of a buffer solution consisting of 100mM sodium acetate buffer pH 4.5, and then shock-frozen in a 100 K nitrogen stream.

Heavy atom derivatives were screened by adding 1 µl of the corresponding compound (dissolved in the mother liquor of the corresponding crystal form) directly to 10 µl hanging drops containing one or more single crystals of monoclinic CcdB. Soaking times and concentrations were varied from 0.1 mM and 1 hour to 25 mM and 5 days, after which they were mounted in glass capillaries and the data collected immediately.

Results and discussion

Tetragonal and orthorhombic crystals

Four years ago, we reported the crystallisation of CcdB in two crystal forms (Steyaert et al., 1993). These were tetragonal and orthorhombic crystals, the details of which are summarised in Table I. Their morphologies are shown in Figure 1. The tetragonal and orthorhombic crystals can be grown using ammonium sulphate, sodium chloride and sodium acetate in the pH range from 6.5 to 9.0. The tetragonal crystals grow most easily, while the orthorhombic form occurs more sporadically,

often together with tetragonal crystals. The asymmetric unit of each of these two crystal forms is rather large, and both crystal forms turned out to be unusable for heavy atom screening.

In the case of the tetragonal form, a 2.7 Å set of data could initially be collected from a crystal grown in ammonium sulphate, but it soon turned out that the crystals often showed no significant diffraction at all. This was especially problematic for crystals grown in sodium acetate, although some of them reached dimensions up to $0.4 \times 0.5 \times 1.5$ mm^3. Also, no suitable heavy atom derivatives could be found.

The orthorhombic crystals allowed for a 2.5 Å native set of data to be collected and consequently, derivative screening was started using these crystals. All prepared potential derivatives were highly non-isomorphous. As apparently all heavy atom compounds tested showed these same results, regardless of concentration and soaking time, a number of native data sets were collected for comparison. Native data from different crystals turned out to be non-isomorphous to each other, the R_{merge}'s being in the range of 30% to 50%.

Monoclinic Crystals

Extensive screening of the crystallisation conditions led to a new, monoclinic, low pH crystal form (Figure 2). These crystals belong to space group C2, with unit cell parameters a = 74.94 Å, b = 36.24 Å, c = 35.77 Å, β = 115.27°. These crystals grow around pH 4.5 using PEG 6000 or PEG-Me 5000 as precipitants. Typically, a drop consisting of 5 µl protein (3 mg/ml in 100 mM MOPS buffer pH =7.0) and 5 µl of 10 -15 % of PEG 6000 or PEG-ME 5000 in 100 mM acetate buffer pH 4.1-4.5. The monoclinic crystal form contains only a single molecule in the asymmetric unit. Therefore, at low pH, CcdB is at most a dimer, the molecular two-fold axis of which coincides with the crystallographic two-fold axis of space group C2..

The zone in which crystallisation occurs is very narrow and the crystals appear only after precipitation has already formed in the drop. Such a narrow crystallisation zone is unusual and makes screening with a wide grid or sparse matrix method difficult. Nevertheless, it is this crystal form that forms the key for obtaining the three-dimensional structure of CcdB, as it is the only one with which we could prepare useful heavy atom derivatives. The crystals that grow spontaneously are highly twinned and are not suitable for data collection. To produce single crystals of

the C2 form, crystallisation was performed by using repeated microseeding in hanging drop and sitting drop setups. The monoclinic CcdB crystals grown in this way turn out to be highly mosaic, and show a large variation in mosaicity from crystal to crystal (0.5° up to 3.0° in unfavourable cases). We were, however, unable to fine tune the crystallisation conditions in order to grow crystals with a lower mosaicity reproducibly, despite extensive effort, including attempts with gel growth and crystal growth in microgravity conditions (see below). This is in contrast to the results obtained with other proteins using similar techniques (Sica et al., 1994, Snell et al., 1995). In fact, high and low mosaicity crystals grow together in the same drop, but there is some tendency of the smaller crystals to be less mosaic. Gel growth resulted in crystals essentially similar in size and diffraction quality as those grown in normal hanging and sitting drop experiments.

For crystals with high mosaicity, usable diffraction can be observed up to about 3.0 Å, while the better crystals show diffraction up to 1.6 Å at room temperature. This diffraction limit was observed both for crystals grown by microseeding and crystals grown in gel. Data collection on a flash frozen crystal (refined mosaicity 0.9°) provided usable data up to at least 1.5 Å (R-merge in the resolution shell from 1.54 to 1.50 Å was 0.146, with a mean I/sigma(I) in this shell of 7.2. Screening for heavy atom derivatives has, until now, resulted in the identification of one single site derivative. This $Hg(Ac)_2$ derivative was prepared by a 20 hours soak in 10 mM mercury acetate. The structure of CcdB will therefore be determined using MIR methods after additional derivatives have been found, or alternatively using MAD on the single site $Hg(Ac)_2$ derivative.

Crystallisation in a microgravity environment

Crystal growth in microgravity conditions was used as a possible solution to overcome the problem of twinning and high mosaicities. The experimental conditions used as well as the outcome of these experiments are summarised in Table II. The number of experiments that could be performed during the two space shuttle missions was limited and the interpretation is complicated by the failure to grow crystals in most of the control experiments on earth. Nevertheless, the fact that crystals could be grown in several reactors during the space shuttle missions, while no crystals appeared in the control experiments on earth do suggest that the

lack of convection and sedimentation has a beneficial effect on protein crystal growth. In the one experiment where both in space and on earth crystals were produced, we did observe a significant decrease of the number of twinned crystals, but no pronounced improvement of the mosaicity was evident.

Crystallisation of cysteine mutants

To look for suitable heavy metal derivatives we decided to make the four following specific serine to cysteine mutants : Ser70Cys, Ser74Cys, Ser84Cys and the double mutant Ser74Cys/Gly77Gln. These mutants were designed for the production of Hg-derivatives in the MIR work and some of them were shown to act as super-killers (Bahassi et al., 1997). No crystals were obtained for the two mutants Ser74Cys and Ser84Cys. The mutant Ser70Cys crystallised in ammonium sulphate as very thin plates, that do not diffract. The double mutant Ser70Cys/Gly77Gln was initially crystallised using MPD as precipitant. The crystals thus formed were thin needles that at most diffract to about 7 Å and do not withstand soaking with mercury salts. Later, well diffracting crystals were formed in the same conditions as where the wild type protein produces the tetragonal form. These crystals are however not isomorphous with the those of the wild type protein. They belong to space group I222 (or $I2_12_12_1$) with unit cell a = 105.58 Å, b = 105.80 Å, c = 91.90 Å and diffract to 2.5 Å resolution (Table I). Although a and b are almost identical and the unit cell constants are very similar to the tetragonal form of the wild type protein, the crystals are not tetragonal. Nevertheless, both crystal forms are probably related, as the tetragonal form of the wild type protein contains a 17 sigma non-origin peak in its Patterson, suggesting a pseudocentering (data not shown).

Conclusions

CcdB is a small dimeric protein that poisons DNA-topoisomerase II complexes. We analysed its crystallisation properties in function of precipitant type, precipitant concentration, pH and protein concentration. This led to a novel crystal form which, in contrast to previously reported crystals, is suitable for structure determination using the MIR method. The space group of this new form is C2, with unit cell parameters a = 74.94 Å, b = 36.24 Å, c = 35.77 Å, β = 115.27°. The asymmetric

unit contains a single monomer. Flash-frozen crystals diffract to at least 1.5 Å resolution, while room temperature diffraction can be observed up to 1.6 Å. The double mutant S74C/G77Q, which acts as a super-killer, crystallises in space group I222 (or $I2_12_12_1$) with unit cell a = 105.58 Å, b = 105.80 Å, c = 91.90 Å. These crystals diffract to 2.5 Å resolution. With the new crystal form we were able to solve the structure of CcdB .as it shown in Figure 3.

Acknowledgements

This work was supported by the Vlaams Interuniversitair Instituut voor Biotechnologie. We thank ESA for the IML-2/APCF grant.

References

Bahassi, E.M., Jaloveckas, D.R. & Couturier, M. (1997) *In preparation.*

Bailone, A., Sommer, S. & Devoret, R. (1985) *Proc. Natl. Acad. Sci. USA* **82**, 5973-5977.

Bernard P. & Couturier M. (1992) *J. Mol. Biol.* **226**, 735-745.

Bernard, P., Kézdy, K., Van Melderen, L., Steyaert, J., Wyns, L., Pato, M., Higgins P., & Couturier, M. (1993) *J. Mol. Biol.* **234**, 534-541.

Bex F., Karoui H., Rokeach L., Drèze P., Garcia L. & Couturier M. (1983) *EMBO J.* **2**, 1853-1861.

De Feyter, R., Wallace, C. & Lane, D. (1989) *Mol. Gen. Genet.* **218**, 481-486.

Jaffé A., Ogura T.& Hiraga S. (1985) *J. Bacteriol.* **163**, 841-849.

Karoui, H., Bex, F., Drèze, P. & Couturier, M. (1983) *EMBO J.* **2**, 1863-1968.

Miki T., Yashioka K. & Horiuchi T. (1984a) *J. Mol. Biol.* **174**, 605-626.

Miki T., Chang Z.-T. & Horiuchi T. (1984b) *J. Mol. Biol.* **174**, 627-646.

Robert, M. C., Provost, K. and Lefaucheux, F. (1992) In *Crystallisation of Nucleic Acids and Proteins. A Practical Approach*, A.Ducruix and R.Giegé eds. Oxford University Press.

Sica, F., Demasi, D., Mazzarella, A., Zagari, A. and Capasso, S. (1994) Acta Cryst. **D50**, 508-511.

Snell, E.H., Weisgerber, S., Helliwell, J.R., Weckert, E., Hölzer, K. & Schroer, K. (1995) *Acta Cryst.* **D51**, 1099-1102.

Steyaert, J., Van Melderen, L., Bernard, P., Dao-Thi, M.-H., Loris, R., Wyns, L., & Couturier, M. (1993) *J. Mol. Biol.* **231**, 513-515.

Tam., J.E. & Kline, B.C. (1989a) *Mol. Gen. Genet.* **219**, 26-32.

Tam J.E. & Kline B.C. (1989b) *J. Bacteriol.* **171**, 2353-2360.

Thiessen, K. J. (1994) *Acta Cryst.* **D50**, 491-495.

Van Melderen, L., Bernard, P., & Couturier, M. (1994) *Mol. Microbiol.* **11**, 1151-1157.

Van Melderen, L., Dao-Thi, M.-H., Lecchi, P., Gottesman, S., Couturier, M. & Maurizi, M.R. (1996) *J. Biol. Chem.* **271**, 27730-27738.

Figure 1. Photomicrograph of tetragonal and orthohombic CcdB. (a) tetragonal crystals grown from ammonium sulphate, (b) tetragonal crystals grown from ammonium acetate, (c) tetragonal crystals grown from NaCl, (d) orthorhombic crystal grown from ammonium sulphate. All photographs are shown on the same scale. The largest crystal in (d) is about 0.8 mm long.

Figure 2 . Monoclinic CcdB crystals. (a) spontaneously grown, heavily twinned monoclinic crystals, (b) monoclinic crystals grown using microseeding, (c) monoclinic crystals grown in agarose gel, (d) space grown monoclinic crystals. All photographs are shown on the same scale. The largest crystal is about 0.3 mm long.

Figure 3 Ribbon representation of the CcdB dimer.The secondary structure element of one monomer are labelled and colour-coded. While the other monomer is shown in grey. The main five-stranded antiparallel ß-sheet is shown in red, the smaller three-stranded "wing" sheet in purple. The C-terminal α-helix is coloured yellow, and the tree isolated turn of 3-helix ochre. Residues identified by mutagenesis to be involved in the killer function of CcdB are shown as ball-and-stick models. The three C-terminal residues (Trp99 Gly100 and Ile101), mutations of which suppress the killer phenotype , are coloured yellow. The three serines, who's mutation to cysteines enhance the killer phenotype (Ser70, Ser74 and Ser84) ,as well as Leu 83(who's mutation to Ile has a similar effect) are coloured light blue. The LysC cleavage site protected by CcdA is indicated by an arrow on each monomer.

Table I. : Crystals of CcdB.

	wild type			S74C/G77Q
	Form I	Form II	Form III	Form IV
Space group	C2	$P4_22_12$	$P2_12_12_1$	I222 or $I2_12_12_1$
Unit cell	a = 74.94 Å b = 36.24 Å c = 35.77 Å β = 115.27°	a = b = 104.4 Å c = 88.9 Å	a = 77.62 Å b = 93.28 Å c = 141.44 Å	a = 105.58 Å b = 105.80 Å c = 91.90Å
Resolution	1.6 Å/1.5 Å*	2.7 Å	2.5 Å	2.5 Å
R_{sym}	0.061/0.056*	0.092	0.070	0.118
Completeness (%)	90.2/84.9*	95.1	93.1	90.2
Multiplicity	6.87/2.33*	2.93	2.97	3.50
Contents of asymm. unit	1 monomer	2 dimers	4 dimers	2 dimers
Solvent contents (%)	35 %	55 %	55 %	55 %

* after cryocooling

Table II : Overview of of the microgravity experiments.

Reactor	Protein drop	Bottom solution/salt chamber	microgravity	earth
USLM-2 HD172	50 µl containing 4.5 mg/ml protein (double mutant S74C/G77Q) in 100 mM MOPS pH7.0	30 µl containing 30% MPD in 100 mM NaAc pH 4.6	small amount of precipitation and a few needle-shaped crystals	larger needle shaped crystals
USLM-2 HD127	30 µl containing 3.7 mg/ml protein in 100 mM MOPS pH7.0	50 µl containing 10% PEG5000 in 100 mM NaAc pH 4.6	heavy precipitation, a large amount of twinned crystals with an average size of 0.3 × 0.2 × 0.2 mm and a few single crystals with average dimensions 0.1 × 0.05 × 0.02 mm	no crystals
LMS HD 154	40 µl containing 4.5 mg/ml CcdB in 100 mM MOPS pH7.0	40 µl containing of 10% PEG-Me5000 in 100 mM NaAc pH 4.1	slight precipitation and a large amount of crystals, mostly single	small, heavily twinned crystals

USLM-2 FID207	115 µl containing 4.5 mg/ml protein (double mutant S74C/G77Q) in 100 mM MOPS pH7.0 mixed with 85 ml salt chamber solution	85 µl containing 2.0 M NaCl and 0.2 M NaAc in 100 mM NaAc pH 4.6	heavy precipitation post-flight re-activation resulted in several needle-shaped crystals	heavy precipitation a large amount of tiny needle-shaped crystals
USLM-2 FID203B	40 µl containing 7.4 mg/ml protein in 100 mM MOPS pH7.0 mixed with 160 ml salt chamber solution	160 µl containing 10% PEG5000 in 100 mM NaAc pH 4.6	slight precipitation One single crystal (0.05 × 0.02 × 0.02 mm) and several larger twinned crystals	heavy precipitation no crystals
LMS FID312B	135 µl containing 4.5 mg/ml CcdB in 100 mM MOPS pH7.0 mixed with 65 ml salt chamber solution	65 µl containing 40% ammonium sulphate in 100 mM HEPES pH 7.5	small amount of precipitation no crystals	heavy precipitation no crystals
LMS FID305B	80 µl containing 4.5 mg/ml CcdB in 100 mM MOPS pH7.0 mixed	120 µl containing 10% PEG5000 in 100 mM NaAc pH 4.1	small amount of precipitation no crystals	heavy precipitation no crystals

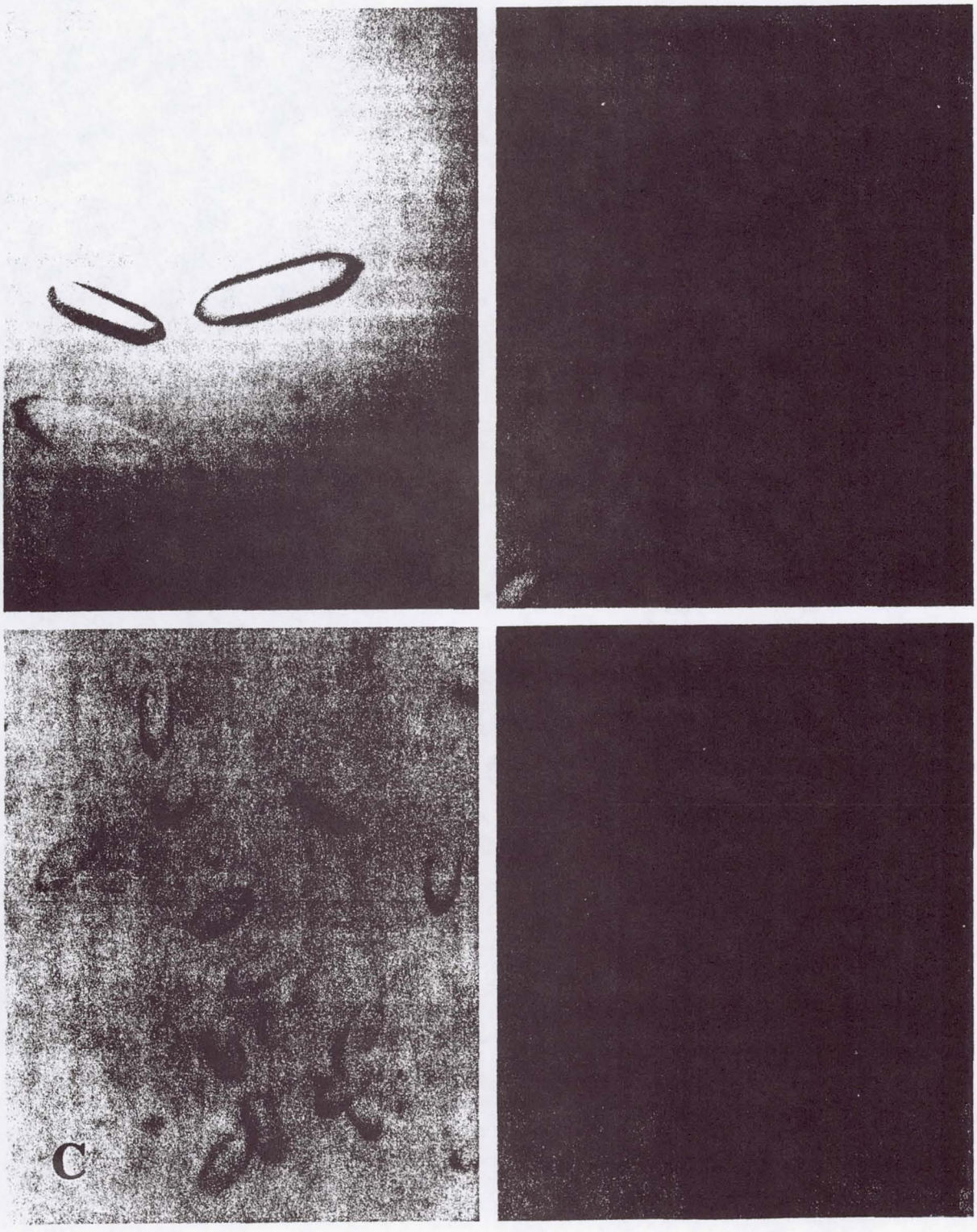

Figure 1

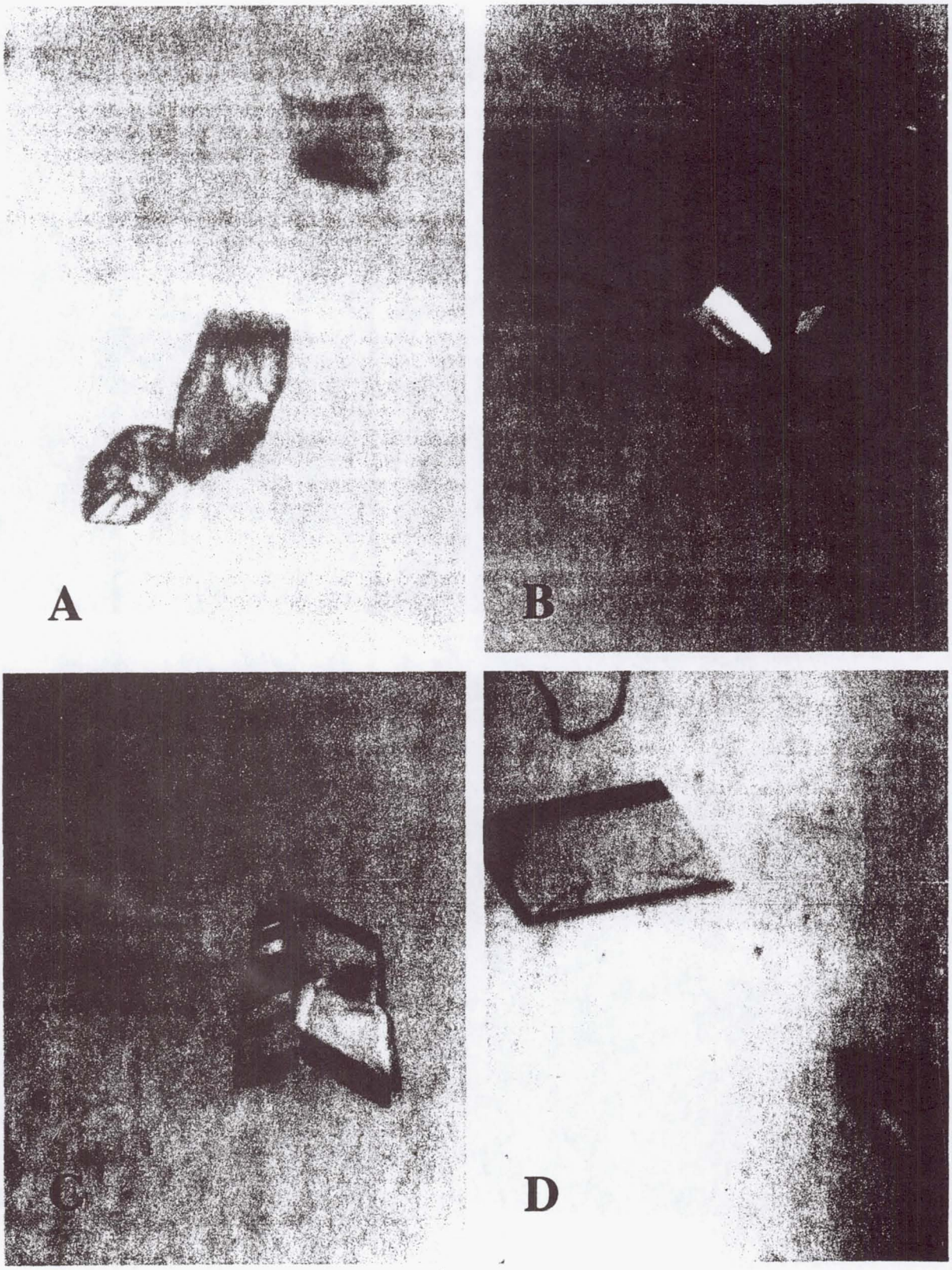

Figure 2

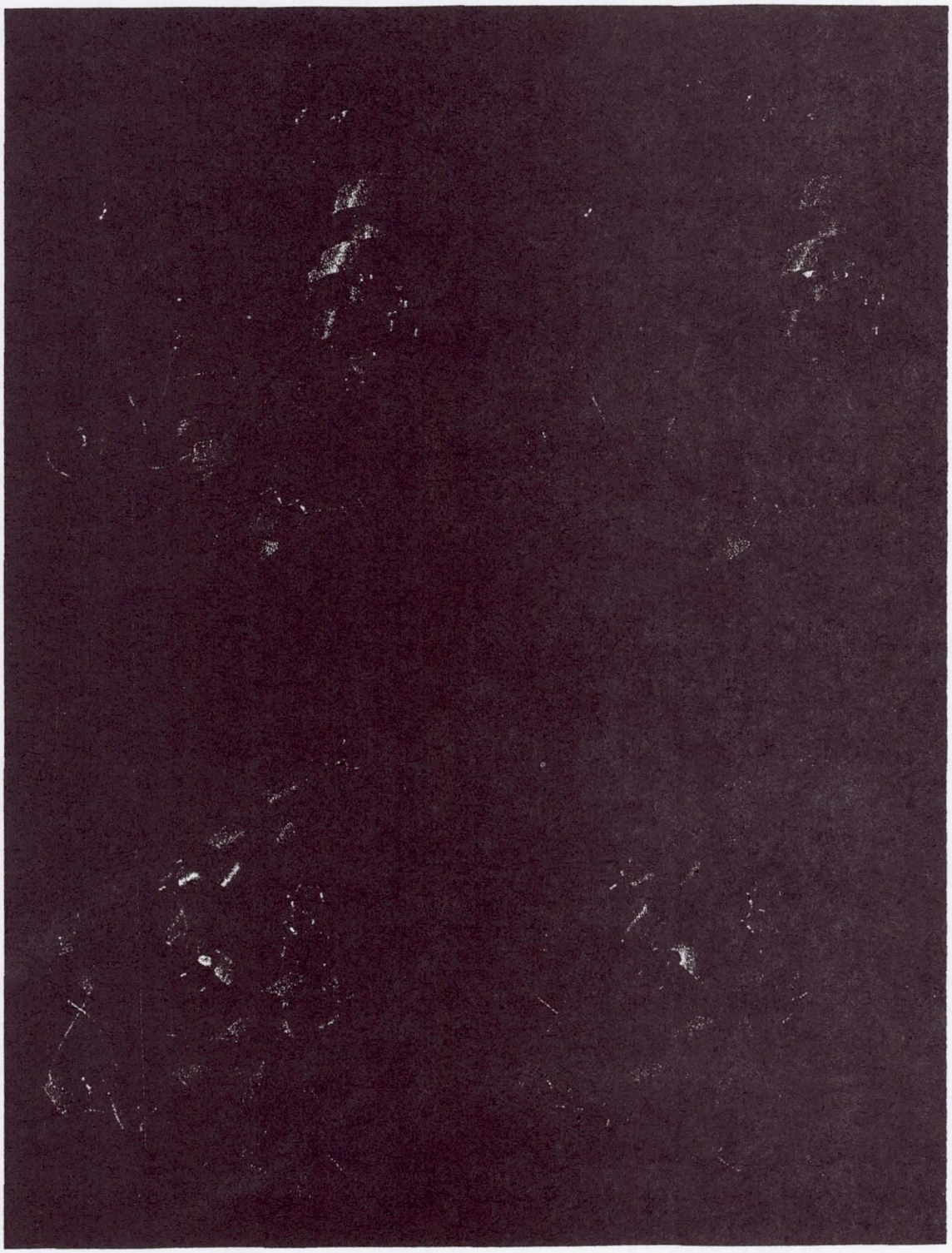

Figure 3

Advanced Protein Crystallization Facility (APCF)

Crystallization of Sulfolobus Solfataricus

Principal Investigator:

Dr. Adriana Zagari
University of Naples
Naples, Italy

A Comparison of Crystals Grown on Earth and in Microgravity in the Advanced Protein Crystallization Facility on the LMS Mission

P.I. Adriana Zagari[a]
e-mail *Zagari@chemna.dichi.unina.it*

Co-Investigators : L. Esposito,[a] F. Sica,[a] G. Sorrentino,[a] R. Berisio [a], L. Carotenuto,[b] A. Giordano[c], C.A. Raia[c], M. Rossi,[c] V.S. Lamzin,[d] K.S. Wilson,[d]

[a]*Centro di Studio di Biocristallografia, CNR and Dipartimento di Chimica, Università di Napoli "Federico II", Via Mezzocannone 4, 80134 Naples, Italy,* [b]*Microgravity Advanced Research & Support Center (MARS), Via Comunale Tavernola, 80144 Naples, Italy,* [c]*Istituto di Biochimica delle Proteine ed Enzimologia, CNR, Via Marconi 10 Naples, Italy, and* [d]*European Molecular Biology Laboratory (EMBL) c/o DESY Notkestrasse 85, D-22603 Hamburg, Germany.*

1. Background

Sulfolobus solfataricus is a hyperthermophilic archaeon, which thrives at a temperature of 87 °C and at a pH of 3.5 in the Solfatara volcanic area near Naples, Italy (Raia *et al.*, 1996). The bacterium expresses an NAD^+-dependent alcohol dehydrogenase (SsADH) which has a potential biotechnological application due to its ability to function in these extreme life conditions.

We obtained crystals of SsADH in the apo and holo form complexed with β-Nicotinamide Adenine Dinucleotide Reduced Form (NADH), on Earth. Both forms diffracted to better than 3 Å resolution. Depending on the crystallization conditions, the crystals can assume various morphologies, but commonly exhibit tail coat-shaped ends. Unfortunately, analysis of their diffraction pattern revealed that the crystals were twinned and hence not suitable to X-ray analysis (Pearl *et al.*, 1993; Sica *et al..*, 1994).

An increasing number of reports in the literature describe a remarkable effect of gravity on protein crystal growth. The density gradient on Earth induces convective flows at the crystal interface and,

according to some authors, this can increase the occurrence of defects, dislocations, and other imperfections (DeLucas & Bugg, 1991; Day & McPherson, 1992). In a microgravitational environment, these density-driven flows are removed, retaining an undisturbed depletion zone around the growing crystals and thus favoring more ordered growth (McPherson, 1993; Rosenberg, Muschol, Thomas & Vekilov, 1996). In addition, protein crystals usually sediment and make contacts with foreign surfaces. These surface effects can be avoided in microgravity, favoring high quality crystal growth. For these reasons we carried out SsADH crystallization experiments on the LMS Mission.

2. Objectives

Our goal was to obtain NADH-complexed SsADH crystals of better quality than those grown on Earth. We wanted to compare the characteristics of ground and microgravity-grown crystals, including the occurrence of twinning. Twinning interferes with crystallographic structure determination, and thus we were particularly interested in testing whether microgravity affects twinning. This was the first time such an experiment was carried out.

3. Methods of data acquisition and analysis

Crystallization data

We carried out pre-flight and flight crystallization experiments in 80 µl vapor diffusion (HD) and in 20 µl free-interface diffusion or dialysis (FID/DIA) reactors of the Advanced Protein Crystallization Facility (APCF) (Bosch, Lautenschlager, Potthast & Stapelmann, 1992). Prior to launch, we received one FID/DIA and three HD reactors from Dornier and we optimized the crystallizing conditions in these reactors. The crystal size during these preparatory trials never reached a dimension larger than 0.3 mm, whereas identical reference trials conducted in Limbro plates produced larger crystals (0.5-0.8 mm) with better morphologies.

Initial trials were carried out using either FID or DIA configuration in the FID/DIA reactor. As a

control, equivalent trials were performed in glass capillaries and in dialysis buttons. The best results were obtained using the FID/DIA reactor with the DIA configuration and this method was then adopted for subsequent experiments.

We conducted space and ground reference experiments in eight crystallization reactors (six HD (80 μl) and two FID/DIA (20 μl) reactors according to the specifications listed in Table 1.

The reactors were filled with protein and other reagent solutions in the laboratory of Prof. W. Weber in Hamburg, Germany. The space reactors were mounted in the APCF and taken to the launch site at the Kennedy Space Center (KSC), USA. The ground control reactors were kept at the EMBL c/o DESY, in Hamburg. About eight hours after the launch, both space and ground reactors were activated and were then deactivated one day prior to shuttle re-entry.

X-ray data

Four microgravity-grown crystals and six ground-grown crystals were analyzed using EMBL X11 beam line synchrotron radiation at the DORIS storage ring at DESY in Hamburg. Data were recorded on a Mar Research image plate detector. Additional experiments were conducted at the Biocrystallographic Center in Naples, Italy from one microgravity grown and a few ground-control crystals and were analyzed using a DIP 2030 image plate detector (Nonius) mounted on a rotating anode operating at 40 kV and 90 mA. All data were processed and refined using the HKL package (Otwinowski, 1993). The crystals belong to space group C2 with one dimer in the asymmetric unit, and the cell parameters are, **a** = 133.0, **b** = 85.7, **c** = 70.5 Å, β = 97°.

3. Flight Results

Crystallization experiments were performed simultaneously on SsADH on Earth and in microgravity. To ensure identical conditions, we used the same reagent solutions, crystallization hardware, and temperatures for both sets of experiments.

Photographs were taken of all APCF reactors one day after landing at KSC. The crystals grown in microgravity inside the DIA reactor are shown in Figure 1a. The space-grown crystals exhibit the

same tail-coat ends as observed in Earth-grown crystals (Fig. 1b). The ground-control DIA reactor contained similar crystals. All the crystals were removed from the DIA reactors, mounted in capillaries and exposed to X-ray radiation. Disappointingly, the large number of the crystals harvested from the HD reactors both in microgravity and on Earth were very small. These crystals diffracted very poorly and could not be used in our analysis. A summary of the space and ground crystallization experiments is reported in Table 1.

Though we started out with identical reagent solutions, we obtained very different results from the HD and DIA reactors. Similar variations have been reported in the literature. For example, during the International Microgravity Laboratory 1 mission, McPherson *et al.* obtained very different results for the protein canavalin and also for satellite tobacco mosaic virus, (Day & McPherson, 1992). The best canavalin crystals were grown by vapor diffusion, whereas the best tobacco mosaic crystals came from liquid-liquid diffusion. In another instance, Chayen *et al.* (1997) described a video-camera observation of microgravity protein crystallization in APCF/HD vapor-diffusion reactors; indeed motion was observed in the growing crystals which was attributed to Marangoni effects, due to the presence of free liquid surfaces open to vapor. Considering our results and those cited in the literature, the importance of the method and the experimental apparatus used in protein crystallization seems quite clear.

To assess crystal quality, we used X-ray diffraction analysis. First, we carried out a comparative analysis for microgravity-grown and Earth-control crystals at the EMBL-DESY facility in Hamburg. Initially, crystals grown in microgravity and on Earth diffracted well, up to 1.8 and 2.5 Å resolution, respectively, indicating an improved microgravity-grown crystal quality. Unfortunately, once exposed to the synchrotron beam, the crystals began to decay and this resulted in an incomplete set of maximum resolution data. We collected a complete data set only from one microgravity-grown crystal, though only to 2.3 Å resolution. The ground-control crystals showed a more rapid decay after a few frames, and so only partial data were collected using the best ground-control crystal. Unfortunately,

analysis of the diffraction pattern revealed that microgravity and ground-control crystals were twinned in a similar manner as previously observed on Earth.

We then conducted the same comparative analysis at our own laboratory using one microgravity-grown crystal and a few ground-control crystals. A complete set of data was obtained from the microgravity crystal, though at a lower resolution than in Hamburg, due to the X-ray source lower intensity. Earth-grown crystals again showed greater damage under exposure to conventional source X-rays and thus only partial data sets could be recorded. As a result, we had to merge data from two crystals.

We were able to index spots on the same crystal lattice in all of the samples. A summary of all X-ray data is shown in Table 2.

5. Conclusions

A number of conclusions can be drawn concerning microgravity protein crystallization:

In terms of size, the SsADH microgravity-crystals are larger than ground-control crystals, though still comparable to the best Earth-grown counterpart. This concurs with several but not all cases cited in the literature). As for resolution, SsADH microgravity-grown crystals achieved significantly higher resolution diffraction data, indicating a reduced statistical disorder. Lastly, though severe decay was observed in all SsADH crystals, the microgravity-grown crystals displayed increased stability when exposed to X-rays. The growth method appeared particularly influential for SsADH; a subject currently being examined by a number of laboratories.

Unfortunately, we found that microgravity-crystals of SsADH complexed to NADH were twinned. This was the first time this phenomenon was tested in microgravity. To see whether different results can be obtained under reduced gravity further studies should be planned to examine other factors known to affect twinning, as e.g. stress and secondary nucleation. In conclusion, there are still a number of questions concerning microgravity protein crystallization which warrant further investigation.

Acknowledgements

We acknowledge ESA and NASA for providing the flight opportunity, Dr. N. Chayen (Imperial College, London, UK) and Dr. L. Mazzarella (University of Napoli, 'Federico II', Italy) for useful suggestions, Dr. R. Bosch and Dr. P. Lautenschlager (Dornier, GmbH, Friedrichshafen, Germany) for assistance with the reactor filling, Dr. W. Weber (DESY, Hamburg, Germany) for hospitality in his laboratory, Dr. G. Wagner (University of Gieβen, Germany) as Project Scientist and Paola Occorsio (Naples) for technical assistance. Access to the EMBL beam lines was funded through the EC HCMP Access to Large Scale facilities Contract, CHGE-CT93-0040. This work was financially supported by the Italian Space Agency (ASI).

6. References

Bosch, R., Lautenschlager, P., Potthast, L. & Stapelmann, J. (1992) *J Cryst. Growth* **122**, 310-316.

Chayen, N. E., Snell, E.H., Helliwell, J.R. & Zagalsky, P. F. (1997) *J. Cryst. Growth* **171**, 219-225.

Day, J. & McPherson, A. (1992) *Protein Sci.***1**, 1254-1268.

DeLucas L.J. & Bugg, C.E. (1991) *Advances in Space Biology and Medicine* **1**, 249-278.

McPherson, A. (1993) *J. Phys.D:Appl.Phys.* **26** B104-B112.

Otwinowski, Z. (1993) DENZO, *An Oscillation Data Processing Program for Macromolecular Crystallography*. Yale University, New Haven, CT, USA.

Pearl, L.H., Demasi, D., Hemmings, A. M., Sica F., Mazzarella, L., Raia, C. A., D'Auria, S., & Rossi, M.(1993).*J. Mol. Biol.*. **229**, 782-784.

Raia C.A., Caruso, C., Marino, M., Vespa, N. & Rossi, M. (1996) *Biochemistry* **35**, 638-647.

Rosenberg, F., Muschol, M., Thomas, B.R. & Vekilov, P.G. (1996) *J. Cryst. Growth* **168**, 1-27.

Sica, F., Demasi, D., Mazzarella, L., Zagari, A., Capasso, S., Pearl, L. H., D'Auria, S., Raia, C; A. & Rossi, M. (1994) *Acta Crystallogr.* D**50**, 508-511.

Legend to Figure 1

Fig.1. a) Photograph of microgravity-grown crystals taken at KSC one day after landing. b)Photograph of a typical NADH-complexed SsADH crystal grown on Earth.

Ground- and microgravity-grown crystals both show typical tail coat-shaped ends.

Table 1. Results of crystallization experiments

Reactor type	No.	Final composition*		Results			
				On Earth		In space	
		SsADH mg/mL)	MPD (%v/v)	N	E (mm)	N	E (mm)
HD	3	11-13	48-50	many	0.10	many	0.10
DIA	1	10	48	10	0.4	5	1.0

* with Tris-HCl buffer, 50mM, pH 8.4, NADH 1mM

N=number of crystals appeared

E=maximum edge

Table 2. Diffraction data of crystals on the ground and in space

Crystal Growth	Diffraction Data							
	Synchrotron Data				Laboratory Data*			
	d1(Å)	d2(Å)	C(%)	R_{sym}	d1(Å)	d2(Å)	C(%)	R_{sym}
Space	1.8	2.3	89	0.08	2.6	3.0	79	0.12
Ground	2.5	3.2	57	0.17	2.9	3.5	72	0.12

d1 = Resolution limit to which significant data are initially observed

d2 = Resolution to which data have been collected

C = Completeness within d2

$R_{sym} = \Sigma[(I_i - \langle I \rangle)^2/\Sigma I_i^2$ where I_i is the measured intensity of an individual reflection, and $\langle I \rangle$ the mean intensity of symmetry-related measurements of this reflection.

*Laboratory data for the ground-grown crystal have been merged from two crystals.

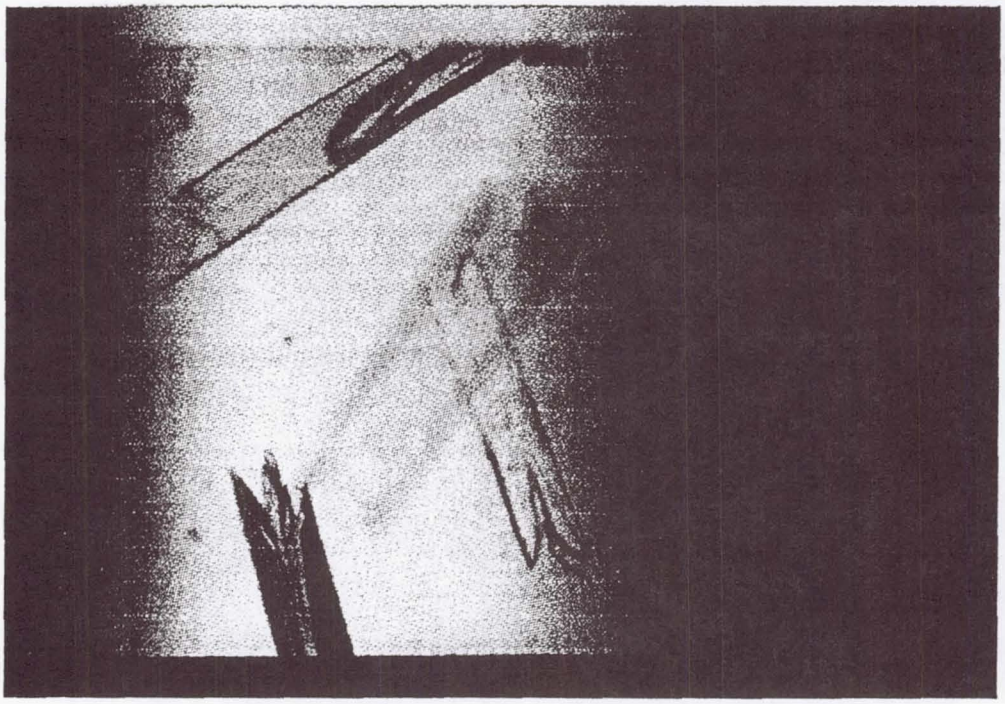

Figure 1A

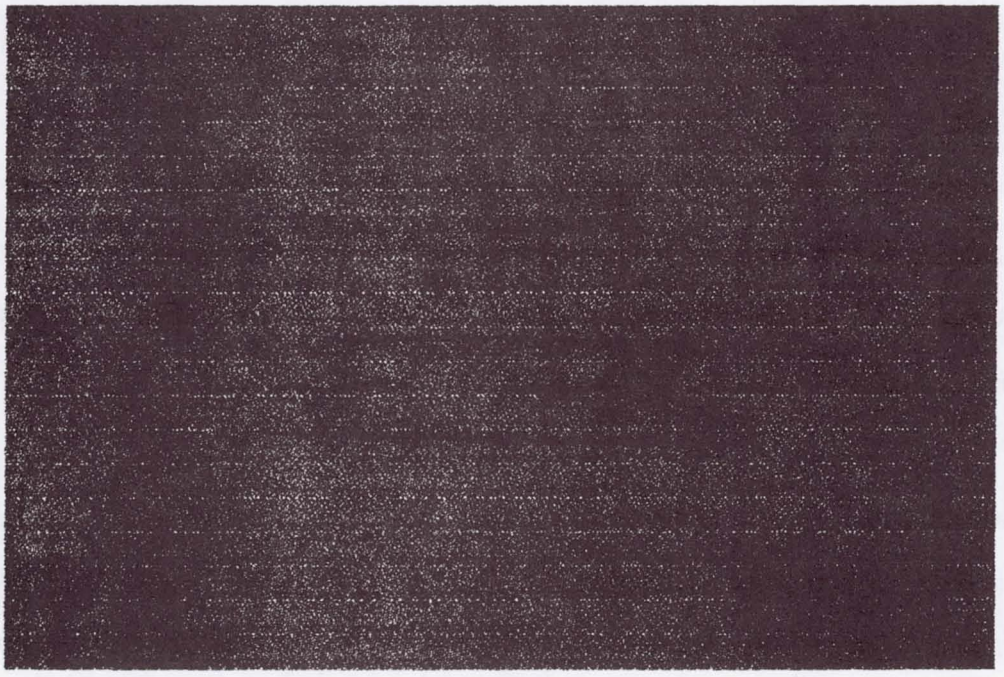

Figure 1B

Bibliographic citations of articles/presentations resulting from the flight

Research Article:

Esposito, L., Sica, F., Sorrentino, G., Berisio, R., Carotenuto, L., Giordano, A., Raia, C.A., Rossi, M., Lamzin, V.S., Wilson, K.S. & Zagari, A. Protein Crystal Growth in the Advanced Protein Crystallisation Facility on the LMS Mission: a Comparison of *Sulfolobus solfataricus* Alcohol Dehydrogenase Crystals Grown on the Ground and in Space. *Acta Crystallographica D* , accepted.

Invited Lecture:

Sica, F., Esposito, L., Sorrentino, G., Berisio, R., Raia, C.A., Rossi, M., Lamzin, V.S., Wilson, K.S. & Zagari, A. Recent results of protein crystal growth in microgravity Joint Annual Meeting Deutsche Gesellschaft fur Kristalwachstum und Kristallzuchtung and Italian Crystallographic Association - Crystal Growth Section 5-7 March 1997, Fribourg (Germany)

Poster presentation:

Esposito L., Sica F., Sorrentino G., Berisio R., Carotenuto L., Raia C., Rossi M., Lamzin V., Wilson K., and A. Zagari Crystallization of *Sulfolobus solfataricus* Alcohol Dehydrogenase in Microgravity . 17th European Crystallographic Meeting, 24-28 Aug. 1997, Lisbon, Portugal.

Oral Presentation:

Zagari A., Sica F., Mazzarella L. Protein Crystal Growth: a Case Study in Microgravity. 27th National Meeting of the Italian Crystallographic Association, 12-14 September Perugia, Italy.

Summary

Alcohol dehydrogenase crystals from *Sulfolobus solfataricus* were grown in the Advanced Protein Crystallization Facility during the U.S. space shuttle's Life and Microgravity Sciences Spacelab mission. Large diffracting crystals were obtained by dialysis and poor quality crystals were obtained by vapor diffusion. The quality of both the space and ground-based crystal was analysed by X-ray diffraction. The space crystals showed improved size and diffraction resolution limit. The phenomenon of twinning, however, which was observed in the Earth-grown crystals, was also present in those grown in space.

Bubble, Drop and Particle Unit (BDPU)

Oscillatory Thermocapillary Instability

Principal Investigator:

Dr. Jean-Claude Legros
Université Libre de Bruxelles
Brussels, Belgium

MICROGRAVITY RESEARCH CENTER

The Life and Microgravity SpaceLab Mission

Oscillatory Thermocapillary Instability

Overview of the Preliminary Results, August 1997

J.C. Legros and Ph. Georis

Service de Chimie Physique E.P., CP165
Université Libre de Bruxelles; 50 Av. F.D Roosevelt,
1050 Bruxelles, Belgium.

Objectives

Investigation of the behaviour of liquids bounded by free interfaces is of prime importance for containerless material processing in microgravity. Crystal growing and purification of high added value multi-component electronic crystal such as GaAs could be one day, an economically profitable space activity. Containerless boundaries around the melt reduce the problems of wall corrosion and contamination. Also eliminated are the structural stresses associated with the separation of the container from solidified material. However, the convection induced by surface tension gradients along the free surface of the melt remains a potential cause for structural and concentrational inhomogeneities as it can induce time dependent flow. The float zone refining method is a containerless technique used on ground for many years to produce high quality slicon crystals for electronic industry. For a high density material such as GaAs, ground based processing is restricted to small crystal since the stabilising effect of the surface tension forces is small with respect to the gravity effect. In microgravity, the maximum diameter of the crystal is much larger and effectively limited by the electrical power needed to melt the sample.

The liquid crystal encapsulation of the GaAs by B_2O_3 has been suggested as an improved method for single crystal processing. The encapsulation of the melt reduces the evaporation of As and helps thus to control the stoichiometry of the GaAs single crystal processed. Moreover, the encapsulant is expected to reduce the intensity of Marangoni convection and also to suppress time dependent flow. This promising idea has recently motivated theoretical and experimental investigations on thermocapillary convection in superposed layers of immiscible liquids. The model case where the temperature gradient is applied perpendicularly to the free interfaces as in the central zone of the melted region of a sample, has been examined on the LMS mission.

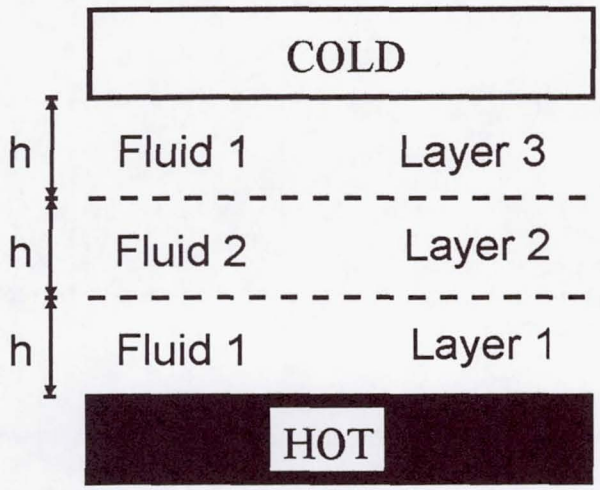

The configuration depicted here is a natural extension of the Marangoni Bénard instability studied on ground for about 100 years. However the mechanism leading to the Marangoni-Bénard instability is very different when both phases adjacent to the interface are taken into account. In the single layer case, the instability results from the competition between dissipation (viscous and thermal) and surface tension forces generated along the free surface by the fluctuations.

When both layers are taken into account, convective motions in the cold layer ($d\sigma/dT < 0$) are stabilising because they are damping thermal gradients at the interface. In this case, the development of the instability will mainly depend on the relative efficiency of heat transfer towards the interface in both layers determined by the heat diffusivity of the liquid. The main consequence of this mechanism is the possibility of oscillatory convection at the threshold. For the symmetrical three layer system, the existence of the oscillatory mode is governed by one parameter: the heat diffusivity of the two liquids have to be close to each other. This criterion for the existence of time dependent flow is so simple that it could be relevant for many practical applications in space or on ground. This experiment aimed at proving the existence of this type of oscillatory mechanism in the configuration of the three layer system that was theoretically predicted so far.

This experiment on the LMS mission on oscillatory convection is a follow up of the IML2 mission where steady convection in a three layer system has been successfully investigated.

Experiment description

The fluids selected for this experiment are n-octane for the external layers (1&3) and methanol for the central one (2). These fluids are transparent, liquid at the ambient temperature, meet the safety requirements and form an interface insensitive to contamination where Marangoni convection can be easily observed. Methanol and n-octane are partially miscible and their miscibility is increasing with temperature. To reduce the mass transfer between the layers, the experiment is operated below the ambient temperature as far as possible. The properties of liquids are listed in table 1.

Table 1 : Fluid properties

	n-octane (1&3)	methanol (2)	(1)/(2)
ν ($m^2 s^{-1}$)	$7.0\ 10^{-7}$	$8.0\ 10^{-7}$	0.875
μ ($kg\ m^{-1}\ s^{-1}$)	$5.51\ 10^{-4}$	$5.62\ 10^{-4}$	0.98
λ ($W\ m^{-1}\ K^{-1}$)	$2.15\ 10^{-1}$	$1.50\ 10^{-1}$	1.43
κ ($m^2 s^{-1}$)	$1.09\ 10^{-7}$	$1.02\ 10^{-7}$	1.07
ρ ($kg\ m^{-3}$)	703	787	0.897
Pr	6.42	7.84	0.82
$\sigma_{n\text{-oct.} - meth}$ ($N\ m^{-1}$)	$4.0\ 10^{-3}$		
$d\sigma_{n\text{-oct.} - meth}/dT$ ($N\ m^{-1}\ K^{-1}$)	$-1.9\ 10^{-5}$		

The heat diffusivities of the liquids are nearly equals, the primary condition for the onset of the oscillatory instability is thus perfectly fulfilled. $d\ \sigma_{meth - n\text{-oct}}/dT$ has been measured in the laboratory using the maximum drop weight method described by Harkins (1952).

Fluid container

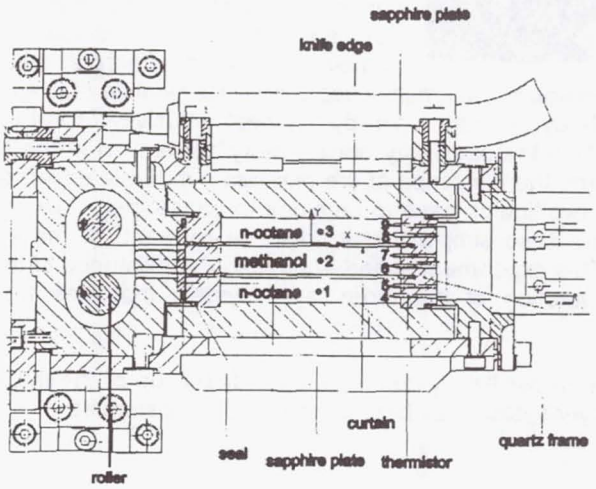

The fluid container is closed on two sides by one centimetre thick sapphire windows. The internal dimensions of the fluid container are 50 mm x 35 mm x 24 mm. Initially, the 8 mm high layers are separated by two stainless steel curtains preventing any mixing before the beginning of the experiment. The boundaries between the layers are maintained leak tight by Chemraz seals moulded on an antiwetting a knife edge. At the beginning of the experiment the curtains are pulled out and slowly wounded (0.25 mm s^{-1}) on rollers creating two free liquid - liquid interfaces subjected to the Marangoni effect. The temperature difference between the

sapphire is then increased step by step until the onset of convection is reached.

Stability of the three layer configuration

In microgravity, the static shapes of connected liquid phases are governed by the interfacial forces only. In the absence of walls, a three layer configuration such as depicted in fig. 1. would be unstable. Indeed, the surface tension forces would act to minimise the surface with respect to the volume of the layers, curving the free interfaces and leading supposedly to connected spherical phases. In a container, the situation is different because the layers may keep a flat shape provided their edges are properly anchored on the solid walls.

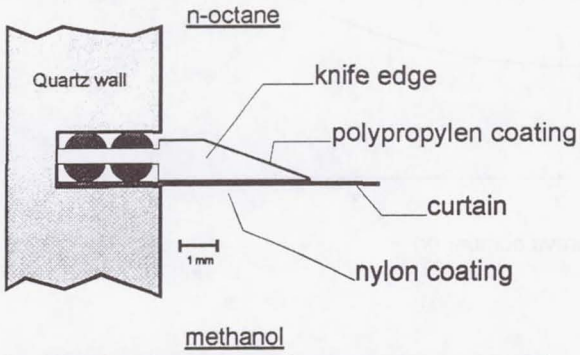

Here, the anchorage is achieved using two stainless steel frames coated on one side with a polypropylen film and with a nylon film on the other side (fig 3). Nylon is wetted preferentially by methanol rather than by n-octane while polypropylen is wetted by n-octane rather than by methanol.

Besides controlling the wetting of the walls, one must ensure that the experimental set up is such that the interfacial tension counterbalances the density difference of the liquids effectively (this is important because of the residual gravity level in the space shuttle). This condition must be fulfilled taking into account that the liquid layers are enclosed in a fixed volume. In the simplified case of the Rayleigh-Taylor instability - the residual gravity is normal to the interfaces - the surface tension stabilises the arrangement for sufficiently short wavelengths.

The critical wavelength λ_m for the onset of the Rayleigh-Taylor instability for two liquids is given by the capillary length (Chandrasekhar 1961). The maximum gravity level acceptable g^* is estimated to 10^{-2} g_0 knowing that when λ_m is larger than the length of the interface, the Rayleigh-Taylor instability cannot start. In the space shuttle, the mean microgravity level being lower than 10^{-4} g_0, the Rayleigh-Taylor instability mechanism will be inactive for the geometry chosen here and indeed has not been observed.

Theoretical and numerical approach

Linear stability analysis

The linear stability analysis is used to compute the critical Marangoni number (or ΔT) for the onset of convection. The linear stability analysis gives also the spatial and the temporal frequencies of the instability.at the onset The linear stability curve is shown on fig. 4; The validity of these results is restricted to system of inifinite extension in the horizontal plane. Also, these results do not apply to the supercritical region where the non linear terms in the energy and in the Navier Stokes equations cannot be neglected. The non dimensional and dimensional values of the critical values are given in table 2. The period of the oscillation is about 5 min and is compatible with the time slice allocated to the experiment (20 hours).

Table 2 : Results of the linear stability analysis

Ma_c	k_c	w_c	ΔT_c	L_c (cm)	Period (s)
1625	1.96	1.53	1.65	2.57	328

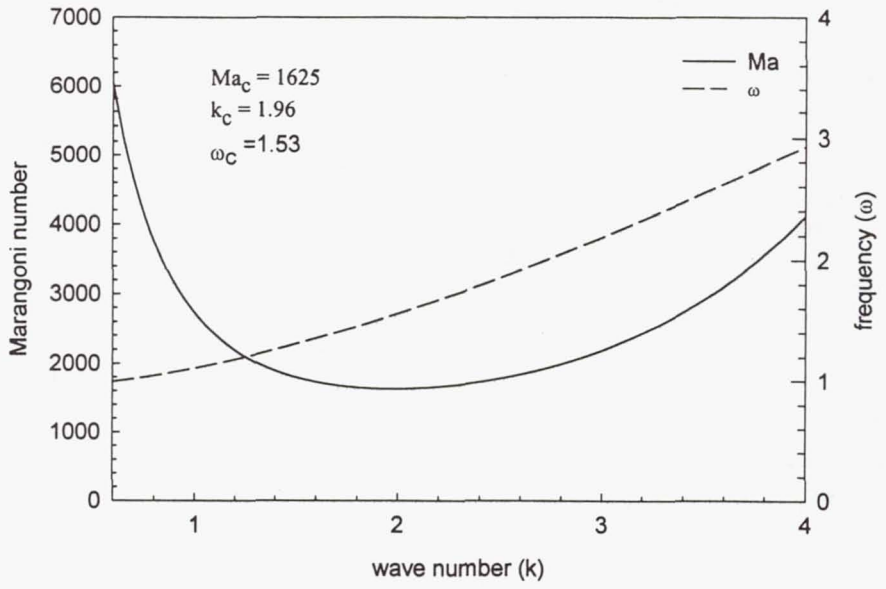

Fig. 4: linear stability analysis

The Marangoni is defined with respect to the parameters of the n-octane layer :

$$Ma = \frac{\frac{d\sigma}{dT}\Delta T\, h_l}{\kappa_l\, \mu_l}$$

2D Finite difference simulations

The non-linear Navier Stokes and the energy equations are solved numerically in 2D for the actual set-up. In each layer l, the dimensionless governing equations expressed in terms of stream function and vorticity are:

$$\partial_t \phi + \partial_z \psi\, \partial_x \phi - \partial_z \phi\, \partial_x \psi = \frac{\nu_l}{\nu_l} \Delta^2 \phi$$

$$\Pr\left(\partial_t T + \partial_z \psi\, \partial_x T - \partial_z T\, \partial_x \psi\right) = \frac{\kappa_l}{\kappa_l} \Delta^2 T$$

where: $\frac{\partial \psi}{\partial z} = v_x$ and $-\frac{\partial \psi}{\partial x} = v_z$, $\quad \Delta^2 \psi = \phi$

with $\Pr = \frac{\nu_l}{\kappa_l}$

The equations are discretised on a uniform rectangular mesh using the centred difference technique and solved using ADI scheme. The Poisson's equation is solved using the Gauss-Seidel relaxation technique. The Navier Stokes, energy and Poisson's equations are solved for the internal nodes in each layer independently then the boundary conditions are applied to compute the value of the vorticity and temperature on the boundary nodes.

Numerical results

Numerically, the onset for the convection is found at $\Delta T=2.2$ °C. The convection is oscillatory at the threshold as predicted by the linear stability analysis. The evolution of the flow pattern (isostream lines and isotherms) for $\Delta T=2.3$ °C is shown here below. The flow pattern is presents a nearly perfect left-right mirror symmetry. The oscillations proceed as follow: two small rolls appear in the centre region of the cell (t=0.8) , they grow while squeezing on the lateral wall the side rolls (t=1.6); this process reapeats one more time during the whole cycle from t=2.

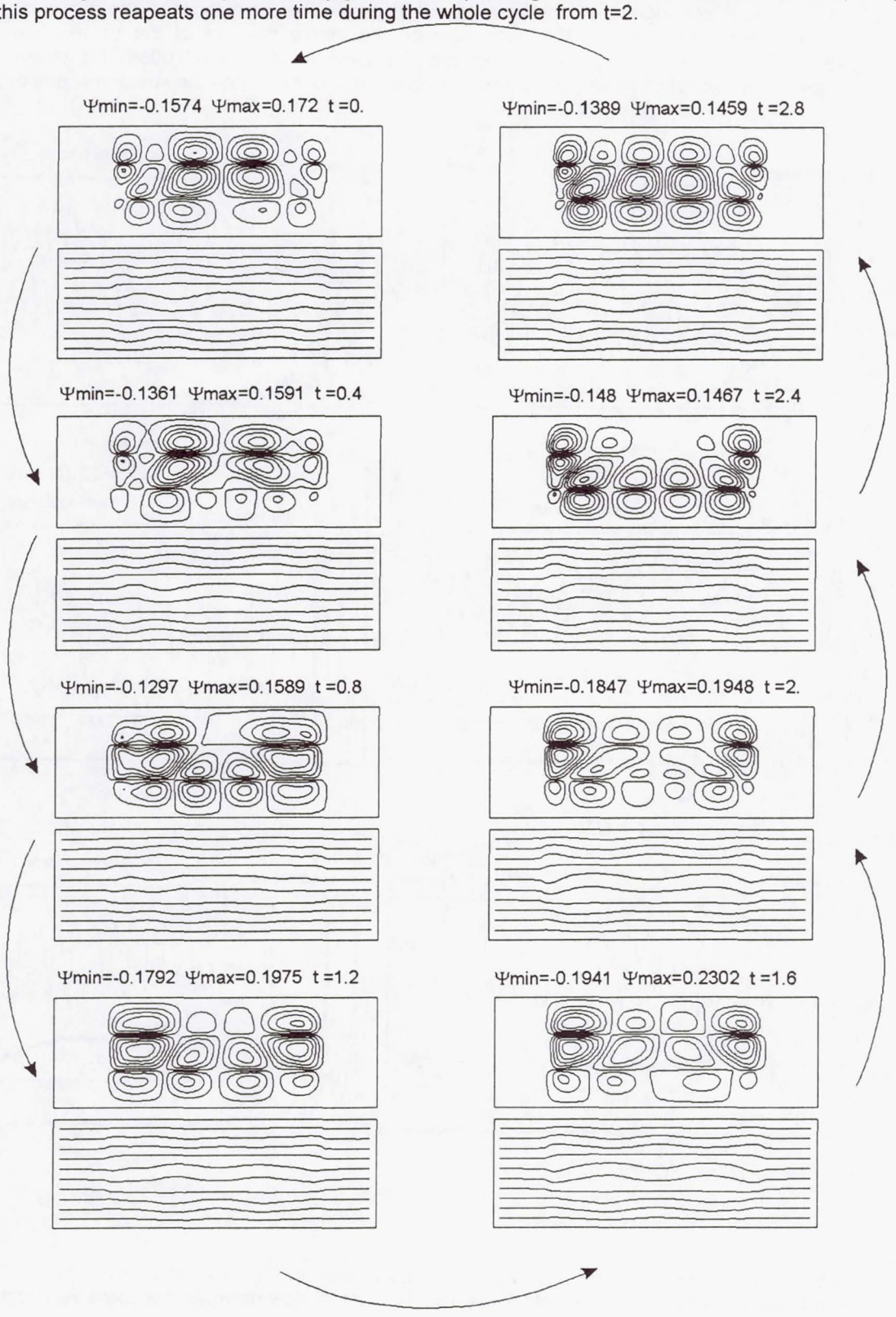

Experimental Results

Temperature

The evolution of temperature recordings inside the methanol layer and the corresponding frequency spectrum are shown here below. At the onset of convection (ΔT=7.5 °C), the oscillation pattern is simple although the amplitude is not regular. The amplitude of the temperature oscillation recorded on the side thermistor and on the centre one are of the same order of magnitude. The frequency spectrum is composed of a dominant peak at f=0.00857 Hz. When ΔT is increased, the oscillation pattern becomes more and more complex and the spectrum composed

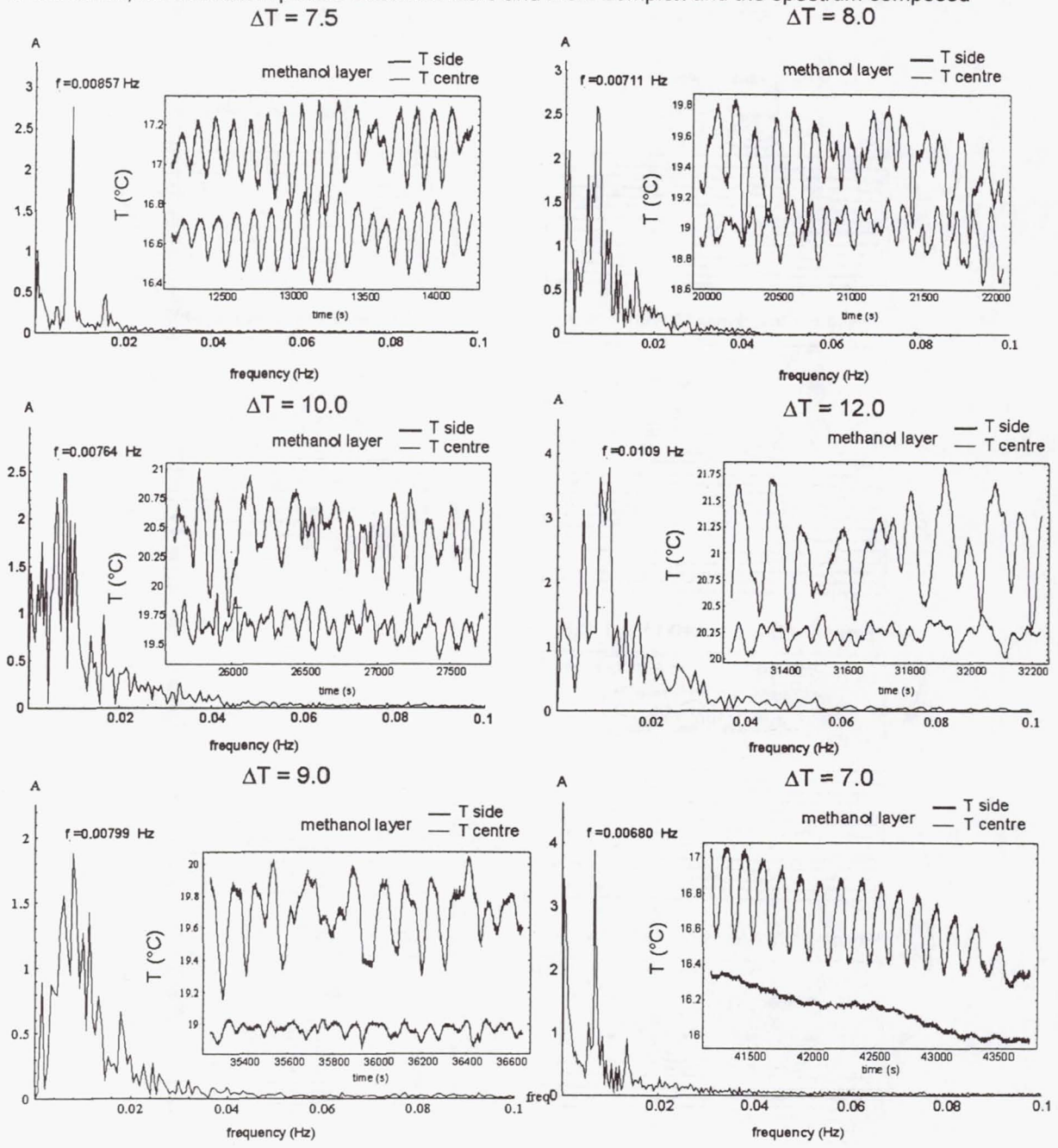

of multiple peaks. After the onset, the main frequency tends to increase as ΔT increased. When DT is decreased back to the threshold value, the oscillations slow down and become very regular

as at the beginning of the experiment. As the experiment goes on, the amplitude of the signal recorded with the side thermistors is decreasing continously. The reason for this unexpected behaviour is still under investigation.

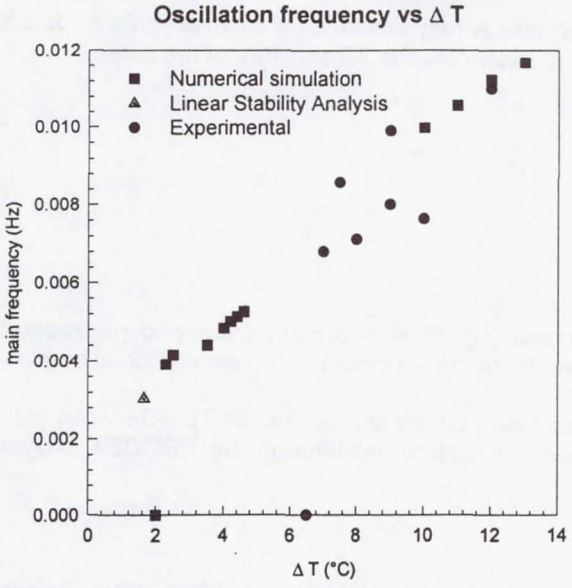

The next figure allows the comparison between the main oscillation frequency for the experimental, numerical and linear stability analysis values. The frequency of oscillations tends to increase as ΔT is increased. Although the critical ΔT for the experiment is much larger than for the numerical one, the oscillation frequencies are of the same order of magnitude. There is also a nice agreement between the linear stability analysis and the numerical computations. It is important to note that no main frequency may be determined in the numerical computation for 5 °C < ΔT < 10 °C because the frequency spectrum is continuous.

The discrepancy between experimental and theoretical ΔT is so large that in cannot be attributed to the imprecision on the physical parameters of the liquids. The interface could be eventually blocked by some impurities but in such a case, the agreement between the experimental and numerical oscillatory frequencies cannot be explained. The large difference observed could be explained by 3 D effects. In the 2D approximation, on of the dimension of the fluid cell is not considered. In the y direction, the fluid cell is only 35 mm long. It is possible that the lateral walls are exerting a strong stabilising effect on the onset of the instability preventing the development of convective mode relying on 3D travelling waves. Once the critical temperature difference becomes large enough, convective mode compatible with restricted geometry will be able to start with a frequency determined by ΔT. This hypothesis has to be checked in the future performing for example 3D computations.

Velocity fields

The quality of the images and the 3D nature of the flow does not allow to visualise the evolution of the velocity field during the whole experiment. More than 1000 velocity maps have been computed using a digital particle image velocimeter developed by ESA. Tracer particles are mainly visible in the central layer and partially visible in the cold methanol layer. An example of the evolution of the velocity field for ΔT=7°C during 3 min. is shown on the last page figure. Two successive fields are separated by 25 s. The convection is unsteady and driven by both interfaces as predicted by the theory and the numerical simulations. The detailed analysis of the velocity field evolution has not been achieved yet.

Conclusions and future plans

This report provides a preliminary overview of the experimental results obtained during the LMS mission. This experiment can be considered as very successful. The curtain concept of the fluid cell has proven to be very efficient. Mechanically stable three layers configurations could be achieved in microgravity playing on the differential wetting properties of the liquids.

For the first time, oscillatory thermocapillary convection has been observed at the onset of the Marangoni-Bénard instability. This experiment demonstrates the existence of an oscillatory mechanism that is a specific feature of multilayer systems. The oscillations are robust, tend to accelerate when the thermal constraint is increased and become complex very close to the threshold. The condition for the existence of these oscillations is very simple and can be fulfilled in many physical systems of practical interest. In the future, this experiment will be proposed for a

new flight if such an opportunity is presented. A refly would allow to investigate in details all the features of this oscillatory mode and also to determine the 3D structure of the flow.

Acknowledgements

The authors are thankful to all the persons, agencies and companies who participated to the success of the LMS mission in general and to the development of the experimental hardware.

The preparation of this experiment has been supported by the SSTC (Services du Premier Ministre, Affaires Scientifiques Techniques et Culturelles) through the PRODEX programme of ESA

Selected bibliography

Bénard, H. 1900 Les tourbillons cellulaires dans une nappe liquide. *Rev. Gén. Sciences Pure Appl.*, **11**, 1261-1271.

Block, M.J. 1956 Surface tension as the cause of the Bénard cells and surface deformation in a liquid film. *Nature* **178**, 650 - 651.
Chandrasekhar, S. 1961 Hydrodynamic and Hydromagnetic Stability, Oxford University Press, 652 p.

Colinet, P., Géoris, Ph., Legros, J.C. & Lebon, G. 1996 Spatially quasiperiodic convection and temporal chaos in two-layer thermocapillary instabilities. *Phys. Rev. E.* **54**, 514-525.

Géoris, Ph., Hennenberg, M., Simanovskii, I.B., Nepomniaschy, A., Wertgeim, I. & Legros, J.C. 1993 Thermocapillary convection in a multilayer. *Phys. Fluids A.* **5**, 1575 - 1582.

Harkins, W.D. 1952 The Physical Chemistry of Films. Reinhold Publishing Corporation, 413 p.

Koschmieder, E.L. 1992 Bénard Cells and Taylor Vortices. Cambridge University Press, 337 p.

Pearson, J.R. 1958 On convection cells induced by surface tension. *J. Fluid Mech.* **4**, 489-500.

Scriven, L.E. & Sternling, C.V. 1963 On cellular convection driven by surface tension gradients : effects of mean surface tension and surface viscosity. *J. Fluid Mech.* **19**, 321-340.

Scriven, L.E. & Sternling, C.V. 1956 Interfacial Turbulence: Hydrodynamic Instability and the Marangoni Effect. *A.I.Ch.E. Journal* **6**, 514-523.

Simanovskii, I.B. and Nepomniashchy A. A. 1993 Convective instabilities in systems with interface. Gordon and Breach Science Publishers, 276 p.

Wahal, S. & Bose, A. 1988 Rayleigh-Bénard and interfacial instabilities in two immiscible liquid layers. *Phys. Fluids* ***31***, 3502 - 3510.

Zeren, W. & Reynolds, W. 1972 Thermal instabilities in two-fluid horizontal layers. *J. Fluid Mech.* **53**, 305-327.

Evolution of the velocity field in the central layer for $\Delta T=7°C$; Two succesive fields are separated by 25 s.

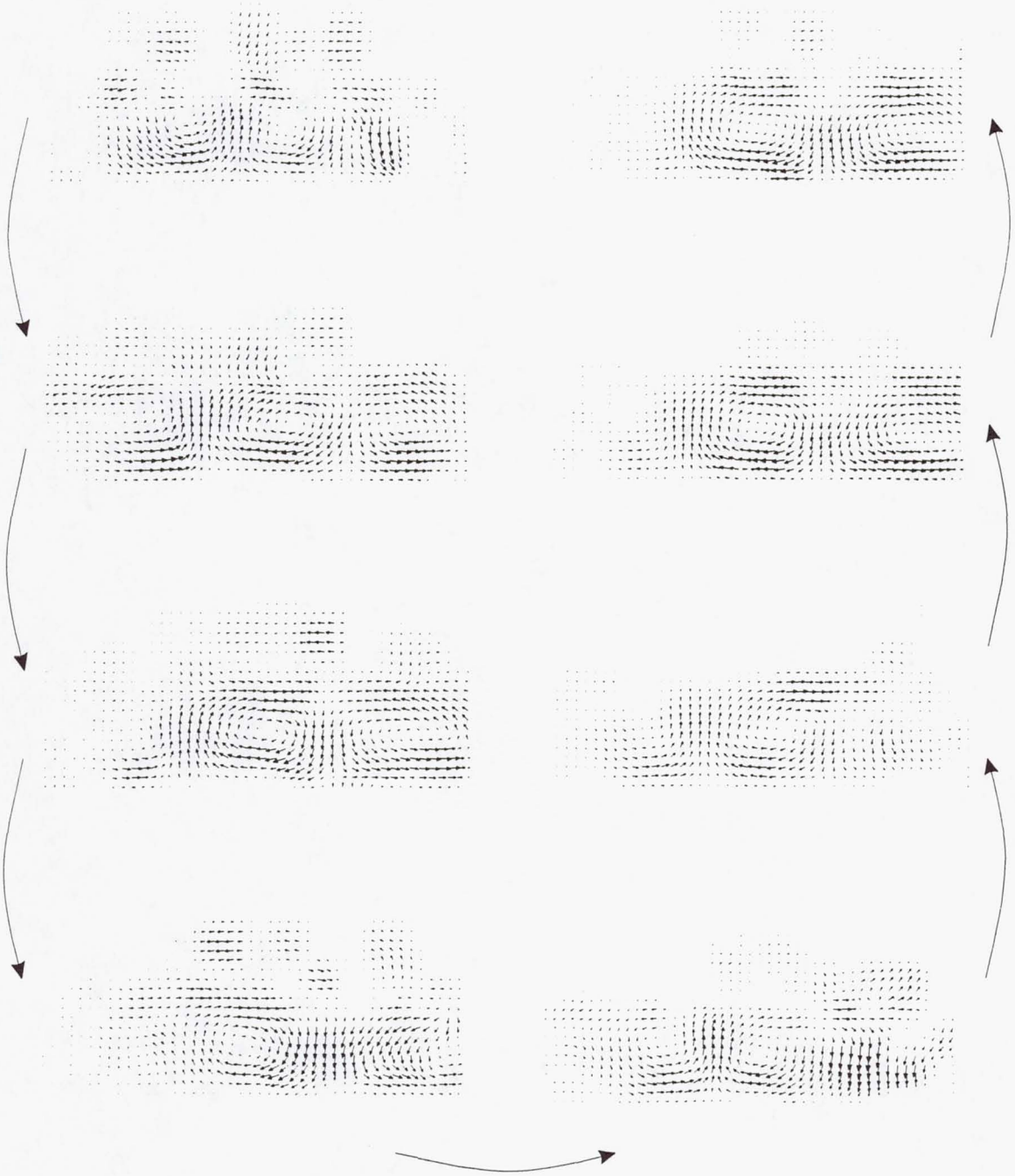

Bubble, Drop and Particle Unit (BDPU)

Thermocapillary Convection in Multilayer Systems

Principal Investigator:

Dr. Jean-Claude Legros
Université Libre de Bruxelles
Brussels, Belgium

Microgravity Research Center
ULB CP 165
50, av. F. Roosevelt
B-1050 Belgium

MICROGRAVITY RESEARCH CENTER

The Life and Microgravity SpaceLab Mission

Thermocapillary Convection in Multilayer Systems

Overview of the Preliminary Results, August 1997.

J.C. Legros and Ph. Georis

Objectives

This experiments aims to observe and measure the features of thermocapillary convection in multilayer systems heated parallel to the interfaces. In the absence of the buoyancy mechanism, heat, mass and momentum transfer inside and between connected liquid phases are due to the interfacial tension gradients along the interfaces. Interfacial tension depends on the temperature and on the composition. For practical reasons in model experiments like this one, interfacial tension gradients are generated imposing different temperature set points on the boundary of the fluids. When one of the fluid phase is a gas, its influence on the flow pattern is neglected because of its low dynamical viscosity. More interesting are the cases wher multiple liquid layers are superposed and submitted to temperature gradients. In such configurations, the specificity of the thermocapillary effect cannot be assessed on the Earth. Indeed, buoyancy and thermocapillary effect will cooperate or compete in the different layers depending on their position. This experiment will provide reliable data set for the validation of the theoretical and numerical models already developed.

The experimental system we are dealing with is shown on fig. 1. The experimental hardware is designed in such a way that both two and three layer configurations may be investigated in the same test container one after each other.

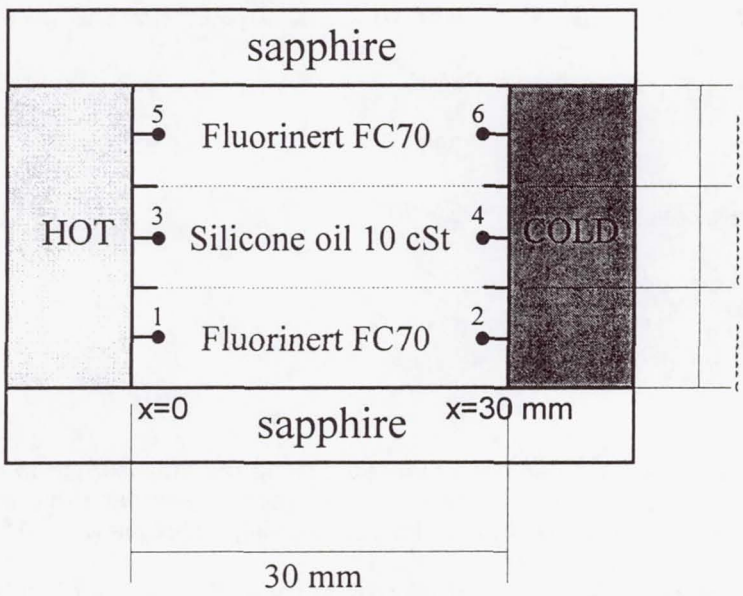

Fig 1. experimental set up

Background

The fluids chosen for this experiment are perfectly immiscible, transparent and inert. Moreover, they form an interface insensitive to contamination. Their properties are summarised in table 1.

Table 1 : Fluids properties

	Fluorinert FC70 (1&3)	Silicone oil 10 cSt (2)	(1)/(2)
ν ($m^2 s^{-1}$)	$13.4\ 10^{-6}$	$9.08\ 10^{-6}$ (35 °C)	1.48
μ ($kg\ m^{-1} s^{-1}$)	$2.55\ 10^{-2}$	$8.40\ 10^{-3}$ (35 °C)	3.04
λ ($W\ m^{-1} K^{-1}$)	$7.00\ 10^{-2}$	$1.34\ 10^{-1}$	0.522
κ ($m^2 s^{-1}$)	$3.44\ 10^{-8}$	$9.51\ 10^{-8}$	0.362
ρ ($kg\ m^{-3}$)	1940	934	2.08
Pr	390	95	4.11
$\sigma_{FC70-Si10cSt}$ ($N\ m^{-1}$)	$6.9\ 10^{-3}$		
$d\sigma_{FC70-Si\ 10cSt}/dT$ ($N\ m^{-1} K^{-1}$)	$-2.7\ 10^{-5}$		

$d\sigma_{FC70-Si\ 10cSt}/dT$ has been measured using the maximum drop weight method described by Harkins (1952). The value obtained is in good agreement with the measurement performed by Burkersroda et al (1994) with the du Noüy ring technique ($2.9\ 10^{-5}$ N m^{-1} K^{-1}).

The temperature dependence for the silicone oil - Fluorinert interfacial tension is only half that of the silicone oil - air.

Fluid container

The fluid container is closed on two sides by one centimetre thick sapphire windows. The internal dimensions of the fluid container are 60 mm x 30 mm x 24 mm. Initially, the layers are separated by two stainless steel curtains preventing any mixing before the beginning of the experiment. The boundaries between the layers are maintained leak tight by Viton seals moulded on an antiwetting frame forming a knife edge. At the beginning of the experiment the curtains are pulled out and slowly wounded (0.25 mm s^{-1}) on rollers creating two free liquid - liquid interfaces subjected to the Marangoni effect.

Stability of the three layer configuration

In microgravity, the static shapes of the connected liquid phases are governed by the interfacial forces only. In the absence of walls, a three layer configuration such as depicted in fig. 1. would be unstable. Indeed, the surface tension forces would act to minimize the surface with respect to the volume of the layers, curving the free interfaces and leading supposedly to connected spherical phases. In a container, the situation is different because the layers may keep a flat shape provided their edges are properly anchored on the solid walls. Here, the anchorage is achieved using two stainless steel frames coated on one side with a Teflon film (fig 2) that prevents the creeping of the silicone oil along the quartz wall. Unlike quartz or stainless steel, Teflon is wetted preferentially by Fluorinert rather than by silicone oil. Thus the Teflon coated sides of the frames are oriented towards the Fluorinert layers.

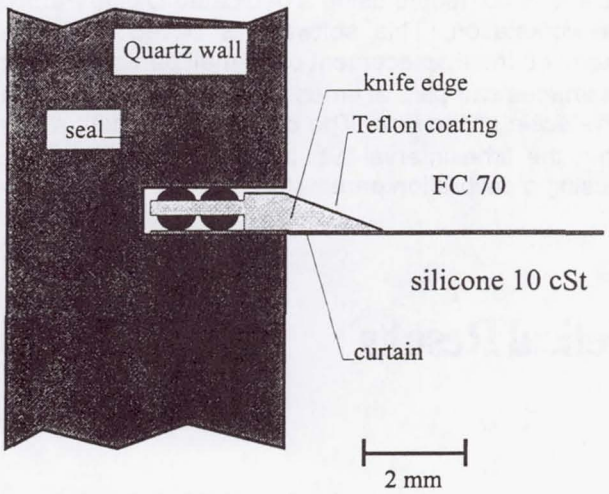

Fig. 2: antiwetting knife edge

Besides controlling the wetting of the walls, one must ensure that the experimental set up is such that the interfacial tension counterbalances the density difference of the liquids effectively (this is important because of the residual gravity level in the space shuttle). This condition must be fulfilled taking into account that the liquid layers are enclosed in a fixed volume.

In the simplified case of the Rayleigh-Taylor instability - the residual gravity is normal to the interfaces - the surface tension stabilises the arrangement for sufficiently short wavelengths. The critical wavelength λ_m for the onset of the Rayleigh-Taylor instability for two liquids of infinite lateral extension is given by the capillary length (Chandrasekhar 1961).

The maximum gravity level acceptable g^* is estimated to 10^{-2} g_0 knowing that when λ_m is larger than the length of the interface, the Rayleigh-Taylor instability cannot start. In the space shuttle, the mean microgravity level being lower than 10^{-4} g_0, the Rayleigh-Taylor instability mechanism will be inactive for the geometry chosen here and indeed has not been observed.

Methods of data acquisition and analysis

Thermal data

The temperature of the layers is measured with six thermistors. The signals are recorded continuously. In high Prandtl number fluid, the velocity field is slaved to the thermal field. The temperature measured locally in the layers is thus correlated to the convective field.

Images

The layers are seeded with tracer particles whose diameter range between 30 and 60 μm. Their density is matching the density of the liquids in order to prevent sedimentation due to the residual gravity level. The test container is shaken just before it is inserted inside the facility so the tracer particles are uniformly suspended in the layers.

The particles are visualised in a 1mm laser light sheet parallel to the longest side of the cell. The particles are sufficiently small to follow perfectly the streamlines of the flow. Their position as function of time is directly correlated to the local velocity of the liquid.

The velocity field in the light sheet plane is computed using a dedicated Digital Particle Image Velocimeter (DPIV) running on a workstation. This software is based on a grey level correlation algorithm allowing to determine the displacement of a small particle patterns with a sub pixel accuracy. Two successive images sampled at times t and $t+\Delta t$ are divided in square cells whose scale is smaller than the scale of the flow. The correlation algorithm determines the displacement of each cell within the time interval Δt. the displacements computed in pixels are then converted in μm s^{-1} using a calibration parameter.

Numerical and Theoretical Results

Analytical Approach

A simple analytical expression describing the convective flow may be found for $L/h \rightarrow \infty$. This technique has been used by several authors and will not be described here. The non-

$$\begin{cases} v_{x1} = k\, z\,(2 - 3\, z) \\ v_{x2} = k\,(-6z^2 + 18z - 13) \\ v_{x3} = k\,(-3\, z^2 + 16\, z - 24) \end{cases}$$

$$\text{with} \quad k = \frac{1}{(4+6M)} \frac{Ma}{A\, Pr}$$

dimensional temperature gradient is assumed constant and equal to the invert of the aspect ratio A^{-1}. The flow being parallel vertical velocity is assumed to vanish everywhere. The horizontal velocity profile along the vertical axis can be computed analytically for the two and the three layer cases.

$$\begin{cases} v_{x1} = l\, z\,(2 - 3\, z) \\ v_{x2} = l\,(-3z^2 + 10\, z - 8) \end{cases}$$

$$\text{with} \quad l = \frac{1}{(4+4M)} \frac{Ma}{A\, Pr}$$

$$\text{where} \quad M = \frac{\mu_2}{\mu_1}, \quad A = \frac{L}{h} \quad \text{and} \quad Ma = \frac{\frac{d\sigma}{dT} \Delta T\, h_1}{\kappa_1\, \mu_1}$$

The analytical forms of the velocity profiles are plotted versus the vertical coordinate on fig. 3.

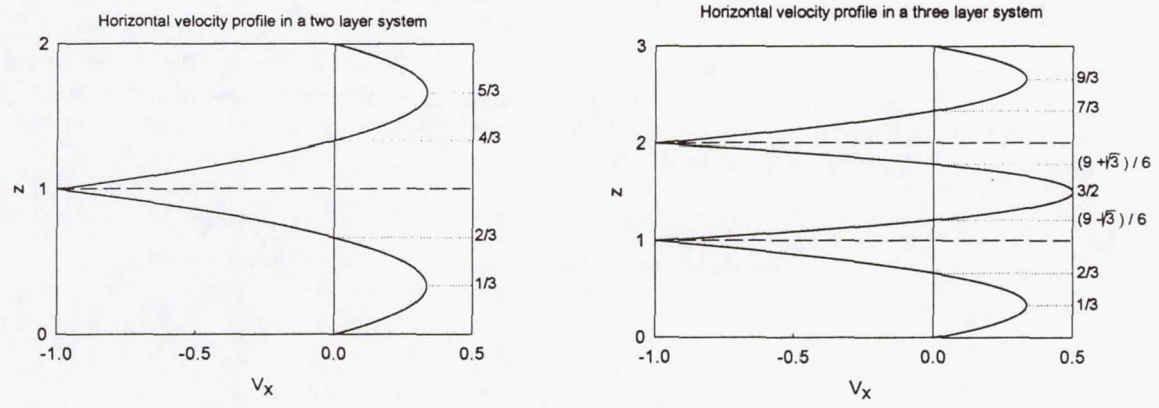

Fig 3: asymptotic velocity profiles for the two and three layer systems

In the two layer system, the velocity profiles in the layers are identical although the configuration is not. In layer 1, the return flow velocity is maximum at z=1/3 where it is one third of the interfacial velocity. In the symmetrical three layer system, the velocity profile has the same symmetry as the physical configuration. The velocity profiles in layers 1 and 3 are identical to those observed in the two layer configuration. The intensity of the return flow in layer 2 is half of the interfacial velocity. The shape of the velocity profile identical to the shape determined for the three layer configuration. The velocity vanishes at h_0=2/3 h. The maximum velocity which is located at h_m=1/3 in the bulk is one third of the velocity at the interface.
l > k indicating that the flow is more intense in the 2 layer case than in the 3 layer case. This is explained by the large shear stress imposed in layer 3 by two moving interfaces.

For the fluids used in the experiment, the dimensional value of the velocity may be found from the physical parameters given in table 1:

V_x max (2layer) = 53.1 μm s^{-1} $°C^{-1}$ ΔT

Vx max (3 layer) = 47.3 μm s^{-1} $°C^{-1}$ ΔT

2D Finite difference simulations

The non-linear Navier Stokes and the energy equations are solved numerically in 2D for the actual set-up. In each layer l, the dimensionless governing equations expressed in terms of stream function and vorticity are:

$$\partial_t \phi + \partial_z \psi \, \partial_x \phi - \partial_z \phi \, \partial_x \psi = \frac{\nu_l}{\nu_l} \Delta^2 \phi$$

$$\mathrm{Pr}\,(\partial_t T + \partial_z \psi \, \partial_x T - \partial_z T \, \partial_x \psi) = \frac{\kappa_l}{\kappa_l} \Delta^2 T$$

where: $\frac{\partial \psi}{\partial z} = v_x$ and $-\frac{\partial \psi}{\partial x} = v_z$, $\quad \Delta^2 \psi = \phi$

The equations are discretised on a uniform rectangular mesh using the centred difference technique and solved using ADI scheme. The Poisson's equation is solved using the Gauss-Seidel relaxation technique. The Navier Stokes, energy and Poisson's equations are solved for the internal nodes in each layer independently then the boundary conditions are applied to compute the value of the vorticity and temperature on the boundary nodes.

Numerical results

The convective pattern for increasing temperature differences have been computed for the two (fig. 4) and the three layer (fig 5.) systems.

The flow patterns as shown on fig. 4 for the Fluorinert FC70 – silicone oil 10 cSt systems are very similar in both layers although the fluids have quite different physical properties. The temperature isotherms are highly distorted large velocity of the interface even for a temperature difference as small as 2.5 °C.

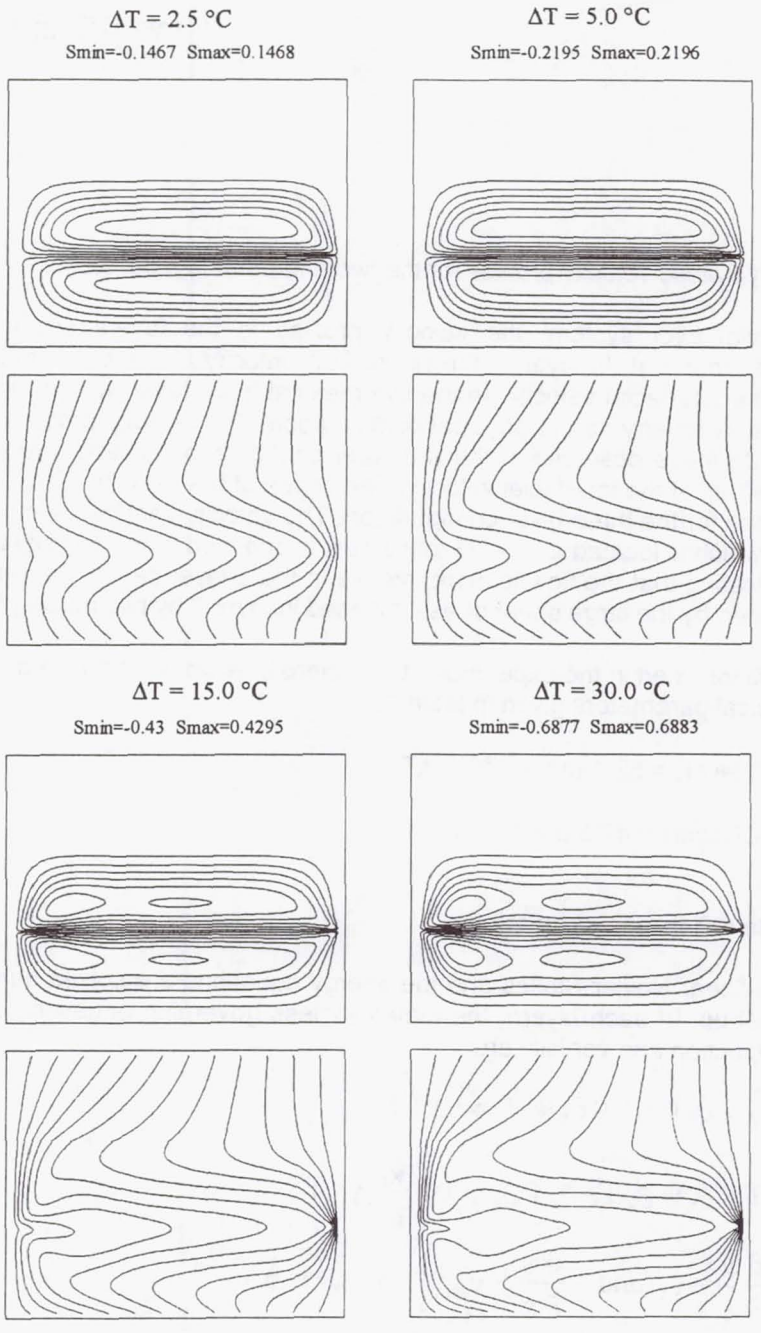

Fig. 4: Steady flow patterns and isotherms in the two layer system FC70 – silicone 10 cSt

For large values of ΔT, recirculation vortices appear in the primary cellular structure. The fluid is strongly accelerated when it reaches the interface near the hot wall. The intense surface tension driven flow is bringing hot liquids near the cold wall where a very steep temperature gradient is created.

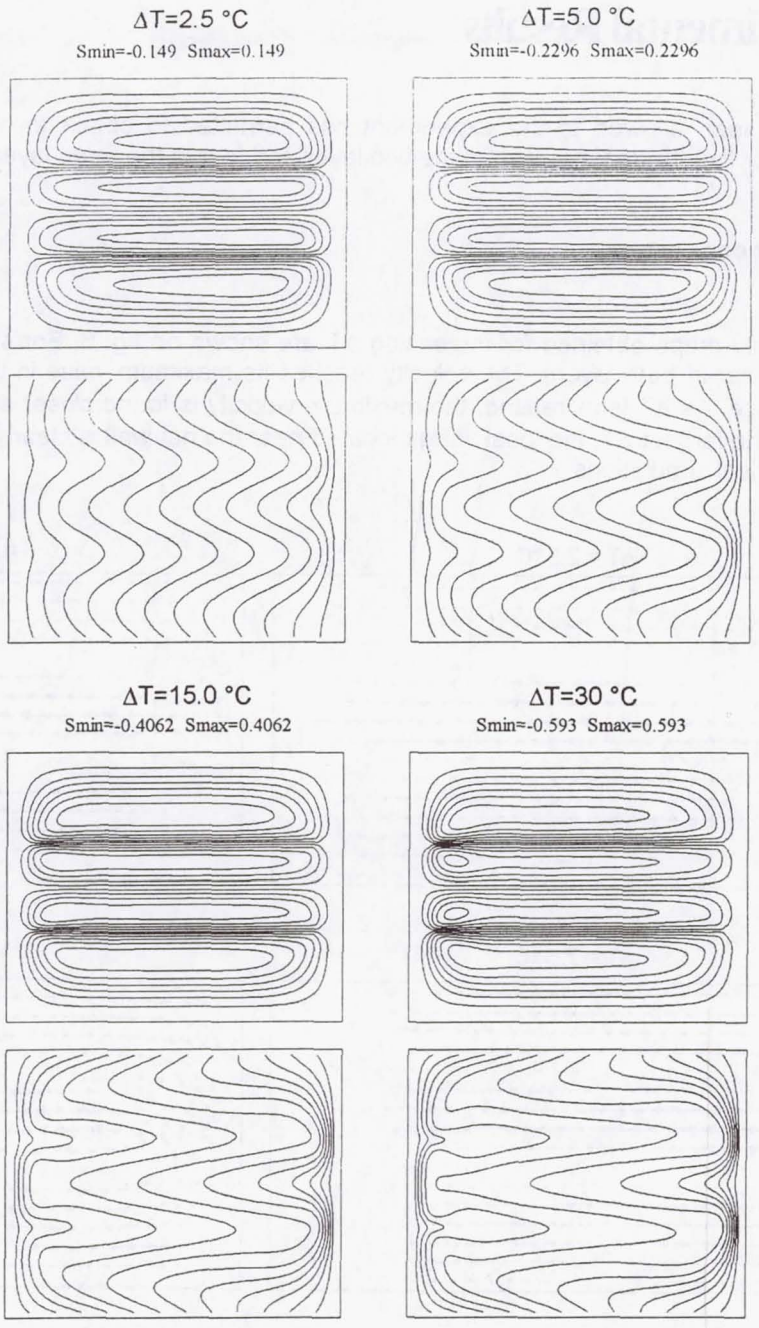

Fig 5: steady flow patterns and isotherms in the three layer system FC70 – si. 10 cSt - FC70.

Steady flow pattern computed for the three layer system are shown on fig. 5. The situation is very different from the two layer case. The flow patterns are reflecting the geometry of the setup. Interfacial motion creates two symmetrical contrarotative vortices in the middle layer. In the lateral layers, the flow pattern is mono cellular with no recirculation even for the largest temperature differences. The deformation of the isotherms is, as compared with the corresponding states of fig. 4, less pronounced.

Experimental Results

The time span allowed to the experiment has permitted to obtain to observe steady flow patterns for five thermal gradient in the two layer and four in the three layer configuration.

Two layer convection

The velocity maps obtained for increasing ΔT are shown on fig. 6. For small ΔT, the flow is mono cellular in both layers. The velocity reaches its maximum value in the central region of the interface. As ΔT is increased, the maximum velocity is found closer and closer to the hot wall. For the largest ΔT, the local vortex located near the hot wall is clearly apparent just as in the numerical simulations

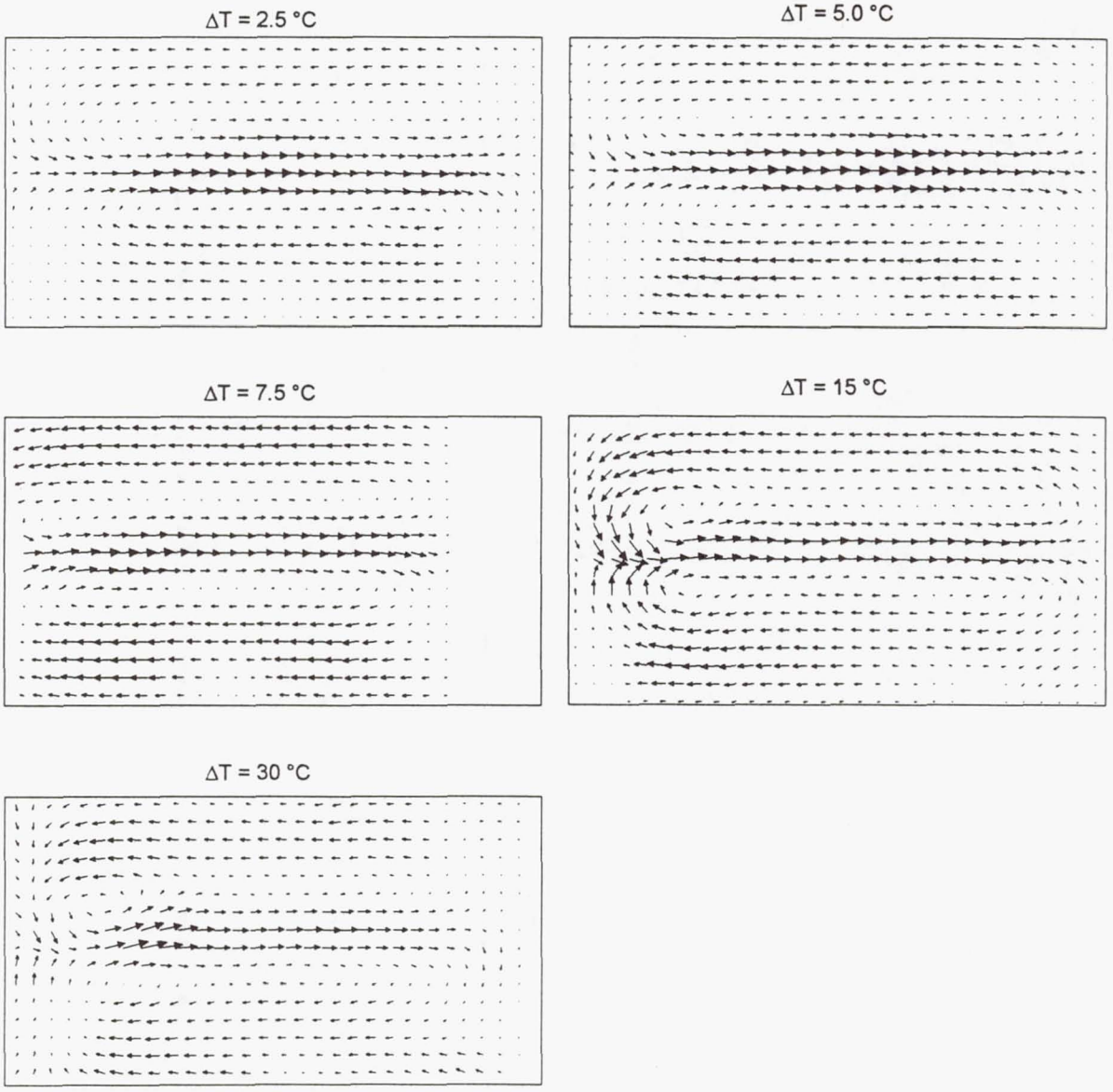

Fig. 6: velocity maps in the two layer system FC70 – silicone 10 cSt

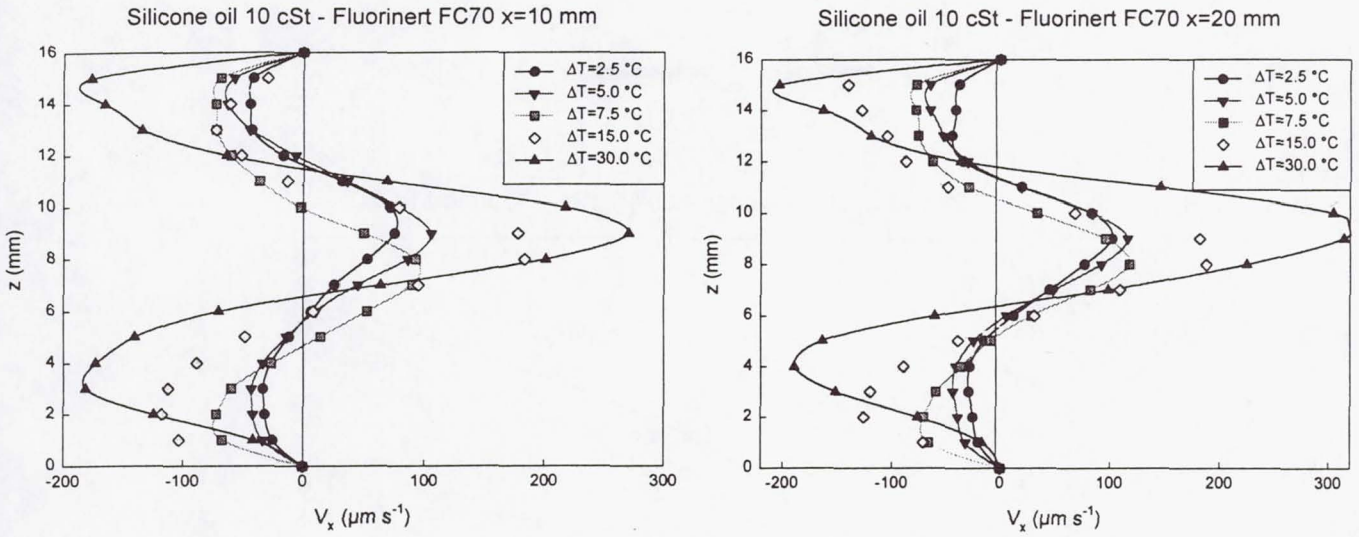

Fig. 7: horizontal velocity profiles at x= 10 mm and x=20 mm

The horizontal velocity profiles along two vertical axis at x= 10 mm and x=20 mm are shown on fig. 7. Because of the thickness of the seal (fig. 2), the velocity of the fluids at the interfaces cannot be determined accurately and is probably underestimated. The intensity of the flow is, as expected proportional to ΔT. Also, it appears that the shape and the intensity of the flow is comparable at x= 10 mm and x = 20 mm.

For the comparison between the asymptotic computation, the numerical simulations and the experimental results, the maximum velocity of the return flow (V_{mrf}) is plotted versus the temperature difference imposed (or the Marangoni number) between the flanges (fig. 8). The experimental data are fitting the following empirical two parameters function:

$$V_{mrf} = V_{\infty}(1 - e^{-a\Delta T})$$

There is a clear discrepancy between the numerical (crossed squares) and the experimental results. For large values of the Marangoni number, V_{mrf} experimental is twice larger than the numerical one. For the sake of verification, the results of the numerical simulations (squares) for large aspect ratio (A=10) and small Marangoni number are in good agreement with the results of the asymptotic approach. The reason for the discrepancy between numerical and experimental values has not been identified yet. Two potential reasons have to be investigated:

In the numerical simulations, the viscosity of the layers is assumed constant which is not the case in reality.

The steep thermal gradient created at the interface near the cold wall is not perfectly modelled in the case of large ΔT.

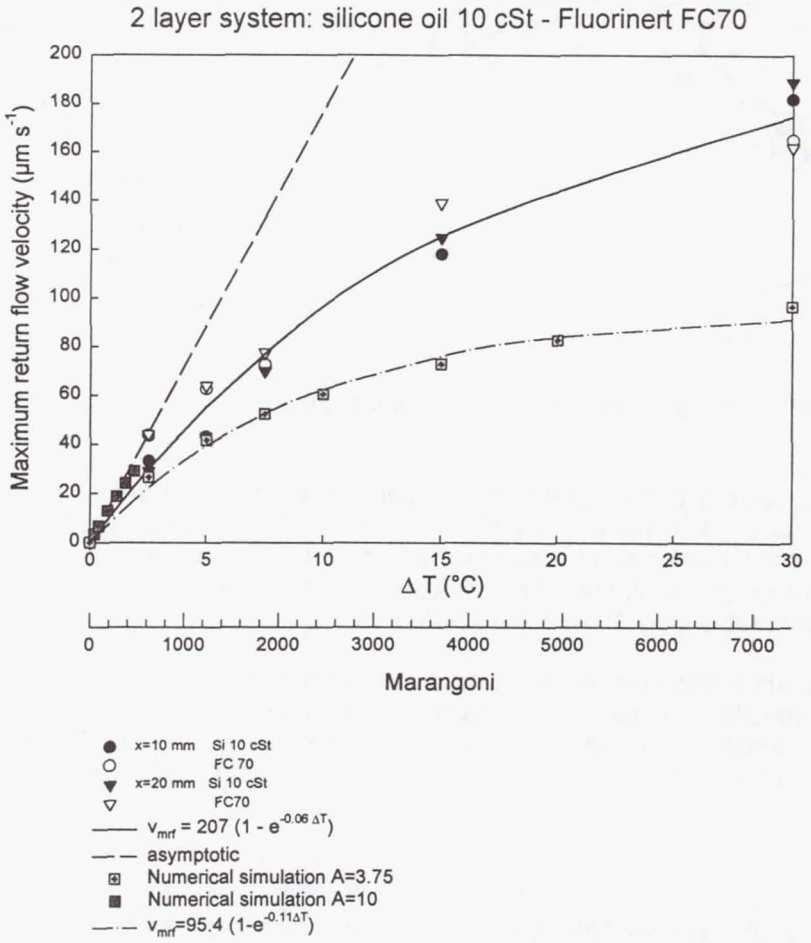

Fig 8 Maximum return flow velocitiy vs ΔT in the two layer system

Three layer convection

The velocity fields measured for increasing ΔT are shown on fig. 9. As simulated numerically, the flow pattern is symmetrical. There are two convective rolls in the central layer.Visually, the convective patterns compare well with the numerical ones excepted for ΔT= 15°C where the tracer particles are not visible everywhere. In general, the quality of the velocity maps obtained for the three layer experiment is lower than for the two layer one. This is mainly due to the accumulation of tracer particles on the interfaces and on the quartz walls.

The shapes of the velocity profiles at x=10 mm and x= 20 mm shown on fig. 10 compare well with the shape found using the aymptotic theory. The symmetry of the flow pattern is clearly apparent on these profiles.

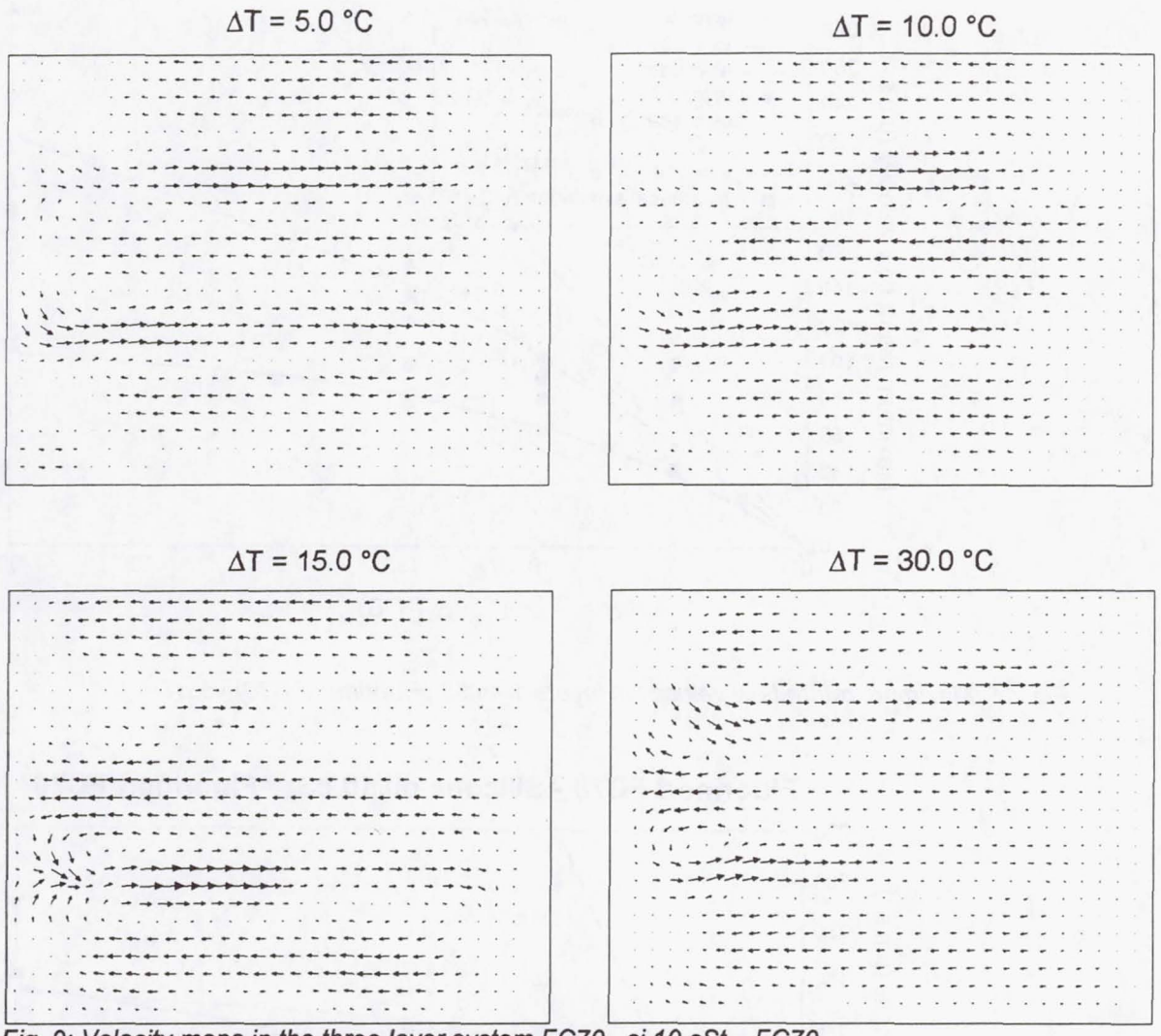

Fig. 9: Velocity maps in the three layer system FC70 –si 10 cSt – FC70

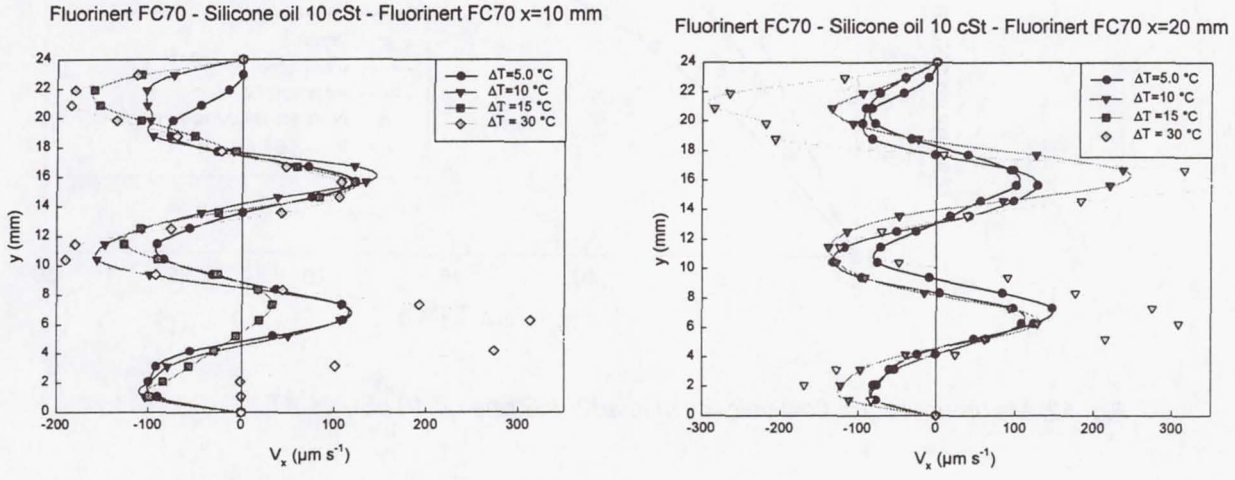

Fig 10: horizontal velocity profiles at x=10 mm and x = 20 mm

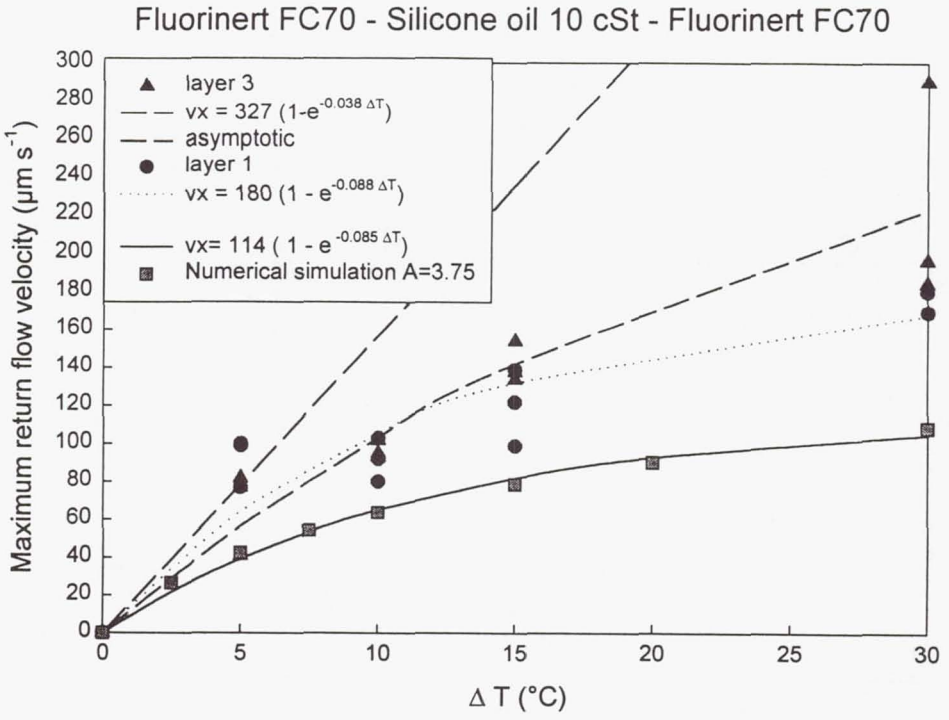

Fig. 11: Maximum return flow velocity in layers 1 and 3 (Fluorinert FC70) vs ΔT

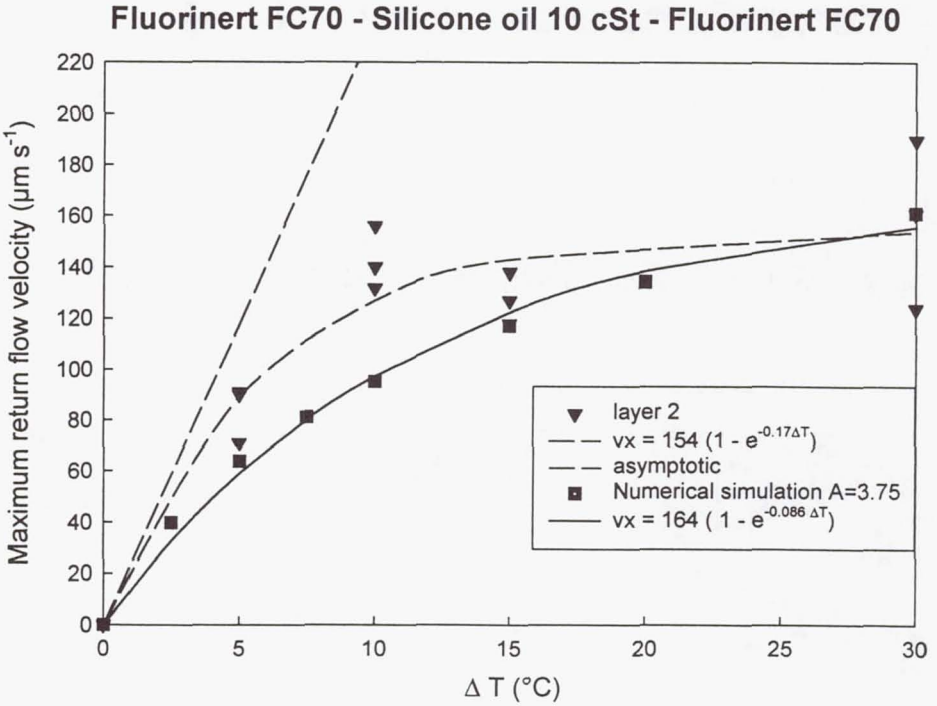

Fig. 12: Maximum return flow velocity in layer2 (silicone oil 10 cSt) vs ΔT

The plots of the maximum return flow velocity shown on fig. 11 and 12 reveal the same discrepancy between numerical and experimental results. The experimental velocities are significantly larger than the theoretical ones. This is mainly the case in the external layers.

Conclusions and future plans

This report provides a preliminary overview of the experimental results obtained during the LMS mission.

This experiment can be considered as very successful. The curtain concept of the fluid cell has proven to be very efficient. Mechanically stable two and three layers configurations could be achieved in microgravity playing on the differential wetting properties of the liquids.

Quantitative velocity fields on the thermocapillary convection in multilayer systems have been obtained. The flow patterns observed are similar to those obtained by numerical simulations. However, the experimental velocitities are significantly larger than the computed ones. The reason for this discrepancy is currently under investigations.

Acknowledgements

The authors are very grateful to Professor J. Koster (Colorado University, Boulder USA) for the use of fluid cell he conceived for the IML2 mission and for the fruitful discussions on thermocapillary convection.

The authors would like also to thank Dr L. Qiu Sheng and Dr B. Roux for their precious advices on the numerical simulation of thermocapillary convection.

The authors are thankful to all the persons, agencies and companies who participated to the success of the LMS mission in general and to the development of the experimental hardware.

The preparation of this experiment has been supported by the SSTC (Services du Premier Ministre, Affaires Scientifiques Techniques et Culturelles) through the PRODEX programme of ESA

Selected bibliography

Burkersroda, C., Prakash, A. & Koster, J. 1994 Interfacial Tension between Fluorinert and Silicone Oils. 1994, *Microgravity Quart.* **4** (2), 93-99.

Chandrasekhar, S. 1961 Hydrodynamic and Hydromagnetic Stability, Oxford University Press, 652 p.

Harkins, W.D. 1952 The Physical Chemistry of Films. Reinhold Publishing Corporation, 413 p.

Peyret, R. & Taylor, D. 1990 Computational Methods for Fluid Flow. Springer Verlag, New-York, 358 p.

Prakash A. and J.N. Koster, "Convection in Multiple Layers of Immiscible Liquids in a Shallow Cavity - I", Int. J. Multiphase Flow Vol. 20, n°2, pp 383-396, 1994.

Prakash A. and J.N. Koster, "Convection in Multiple Layers of Immiscible Liquids in a Shallow Cavity —II", Int. J. Multiphase Flow Vol. 20, n°2, pp 397-414, 1994.

Qiu Sheng L, " Couplage entre forces interfaciales dans un système multicouche de fluides immiscibles avec ou sans effet des forces thermogravitationnelles", Ph D Thesis, 1994 Université de Marseille.

Villers D., »Couplage entre les convections capillaire et thermogravitationnelle », PhD Thesis,1989, Université de Mons Hainaut, Belgium.

Bubble, Drop and Particle Unit (BDPU)

Bubble and Drop Interaction with Solidification Front

Principal Investigator:

Dr. Rodolfo Monti
Università degli Studi di Napoli
Naples, Italy

Bubble and drop interaction with solidification front: scientific results obtained during the LMS mission

Raimondo Fortezza, Dario Castagnolo, Enrico Ceglia
MARS Center
via Comunale Tavernola, 80144, Napoli, Italy

Rodolfo Monti
DISIS, University of Naples
P. Tecchio 80, 80126, Napoli, Italy

Objectives

This report deals with the scientific results obtained during the "MONTI" experiment performed in the BDPU facility flown on board of the Spacelab LMS mission. The objective of the experiment was to study the interaction of drops and bubbles with a moving solidification front. This interaction between the bubbles and the solidification/melting front was studied by analysing the bubble sizes and the front velocity. This will provide us with information on the manner in which bubbles are captured by (or pushed away from) a moving solidification/melting front[7].

This is aimed at better understanding the behaviour of the bubbles when released from or approaching the solid front, and from this we could eventually learn how to prevent the presence of bubbles included in solidified products and how to minimize the impact these bubbles have on the final product.

Finally, in the last part of the experiment water droplets were injected within the melted matrix (a paraffine called Tetracosane). Again, the objective was to study the interaction of these droplets with the solidification front, in order to establish whether they were pushed or engulfed by the front. These results are of great importance in the improvement of production of metal alloys, glasses and ceramics on Earth.

Background

The first part of the experiment was devoted to the study of the interaction between pre-formed gas bubbles (see figures 1 (a) and (b)) and a moving melting/solidification front, obtained by heating a solid tetracosane sample. This sample was contained within the Test Container number 8 (TC#8), placed within the Bubble, Drop and Particle Unit (BDPU), which is a facility developed by the European Space Agency (ESA).

The motivation for performing this experiment in a microgravity environment is that buoyancy and sedimentation effects are negligible, which the study of the interaction possible whithout additional forces acting on the inclusions. One of the negative aspects of the buoyancy effect is that it leads to undesired distortion of the front and an increased velocity of the melting process.

During the initial phase of the experiment the needle side flange was heated up to a temperature of 80°C (greater than the melting temperature Tmelt = 51°C), while the net side flange was maintained at a temperature of 45°C. This allowed us to study the movement of the melting front, and its interaction with the gas bubbles that were released.

As the bubbles detach themselves from the melting front, they are gradually absorbed by the liquid tetracosane, this allowed us to determine the diffusion coefficient of the gas bubbles in the liquid.

After some time both flanges were brought to a temperature of 90°C, and the tetracosane sample was completely melted. At this point, the tetracosane was re-solidified from the needle side, which gave us the possibility to study the behaviour of bubbles (ie. whether they are pushed or engulfed) as a solidification front approaches.

The aim of the experiment was also to investigate if any thermocapillary migration effects could have been detected in the large temperature gradient.

In the second part of the experiment water droplets were injected into the liquid tetracosane. Some difficulties were encountered during the injection procedure, since the droplets exibited a strong wetting capability and did not easily detach themselves from the needle. This problem was overcome by increasing the previously selected dimensions of the droplets and the injection velocity. We then observed the interaction of these larger droplets with the solidification front, in order to establish if the front can modify the shape and the position of the droplets.

Analysis of the flight results

- Observation of bubble release

A post flight analysis of the video images recorded during the experiment onboard the LMS Shuttle mission was carried out. During the first melting phase the position and dimensions of the various bubbles were compared to those set during the filling of the test container on the ground prior to the flight. The following unexpected changes were noted: (i) During the first melting experimental phase, in which the tetracosane specimen is initially melted from one side of the test cell only, bubbles are immediately released as the melting/solidificationfront begins to move away from the heated side. At this point no bubbles had been foreseen, as the first bubbles set within the tetracosane were expected further along the specimen. (ii) As the front approached the various positions along the specimen where bubble release was expected, some bubbles did not appear at all, and others had dimensions that were not the same as those expected (mostly bigger than they should have been). (iii) In the second part of the first melting phase, the cell is also heated from the other side of the solid tetracosane specimen, close to the net of the test container. As the tetracosane near the net begins to melt and the front moves away from the net, a large bubble is visible between the solid tetracosane and the net. This bubble begins to apply pressure to the visible lower end of the solid, causing it to tilt.

The reasons for these changes may be explained by the method that was utilised to fill the test container with the solid tetracosane prior to the flight . The first part of the filling procedure consisted in placing a hollow, truncated-conical mould of solid tetracosane in the test container, such that the flat part of the mould was pressed against the net within the cell. Various slices of solid tetracosane were then successively placed within the hollow part of the mould, until the cell was completely filled with solid tetracosane. These slices contain semi-spherical hollows, that, when placed one against the other, form the desired air bubbles within the tetracosane solid at pre-specified locations. The discrepancies (i) and (iii) described above may be attributed to the fact that at the contact areas between the hollow tetracosane mould and the slices placed within it, small amounts of air were trapped during the filling of the test container, and this air was immediately released in the form of bubbles as the solid regions near the heated flange (i) and the net (iii) in the vicinity of the contact points began to melt. Three reasons can be put forward to try and attempt an explanation for the discrepancies outlined in (ii) above : (a) Air was trapped between the contact areas of the slices placed in the mould during the filling of the test cell. During the experiment, as the tetracosane began to melt near these areas, this air formed micro-bubbles that coalesced in larger ones so that this air was released in the form of unexpected bubbles, or it began to merge with the pre-formed air bubbles to produce bubbles with dimensions larger than that expected. This trapped air may also have caused the pre-formed bubbles to shift from their set positions as the tetracosane began to melt. (b) As the melting front approached the contact areas between the various slices, liquid tetracosane may have flown into these cavities, causing the pre-formed bubbles to shift, and maybe even to merge to form larger bubbles than expected. (c) A combination of (a) and (b). The second reason (b) seems unlikely as no deformation in the melting front where liquid could have flown into the cavities, was noted. As for the explanation of the changes (i) and (iii), (a) above seems to be the more likely reason to explain variation (ii). A video image analysis was also useful in determining the correct orientation of the test cell with respect to the pre-formed bubbles within the tetracosane solid matrix. Figure 2(a) is a video image during the melting phase, upon which a schematic representation of the bubble positions and dimensions (to scale) have been superimposed. It can be clearly seen that the two bubbles being released from the tetracosane solid correspond to the bubbles 10 and 11 in both position and dimension. Eventhough these two bubbles were relatively close to each other they did not coalesce. The larger bubble within the liquid ahead of these two bubbles was not expected, and it probably resulted from the coalescence of bubbles 4 and 7. A further indication of the correct orientation of the test cell is given in figure 2(b). The tetracosane is in the process of releasing two more bubbles, and the superimposed schematic indicates that these bubbles correspond to bubbles 11 and 12. The schematic has been rotated in correspondence to the rotation which the remaining tetracosane solid has undergone as a result of the large bubble pushing against it from the lower part of the cell on the net side. The two larger bubbles in the liquid towards the needle side correspond to bubbles 10 and 11 seen in figure 2(a), while the coalesced bubble of figure 2(b) has moved towards the bottom corner of the needle side.

- **Experimental absorption rate of gas bubbles in tetracosane**

The next step in the analysis of the video images was to determine the rate of absorption of the gas bubbles within the liquid tetracosane during the melting sequence of the experiment. This was done by utilising a video analysis tool developed at MARS Center, which plays the stored images of the experimental sequence at different speeds. This allows one to easily move backwards and forwards to a desired instant of the experiment at a selected speed. The frame which must be analysed is then identified and "captured", allowing one to carry out measurements of the bubble radius and location.Eighteen different bubbles with initial radii varying between 0.4725 and 4.1125 mm were analysed at various instances using the video images recorded from the CCD cameras, providing a "top" and "lateral" view of the test cell. The initial radii were measured just after the bubbles were released from the solid tetracosane into the liquid, and after an interval of time the final radii were measured, from which the experimental decrease in radius with time (absorption rate) was calculated.

- **Theoretical calculation of absorption rate**

From reference [1], the volumetric flow rate of a gas bubble for the diffusion of a gas in a liquid, is given by the following :

$$W = \frac{dV}{dt} = kA\left[\frac{X_{A_\infty} - X_{A_o}}{1 - X_{Ao}}\right] \qquad (1)$$

where V is the volume, t is time, k is the mass transfer coefficient, A is the surface area of the bubble, d is the bubble diameter, X_{Ao} is the concentration of gas at the gas/liquid interface, and $X_{A\infty}$ is the concentration of gas in liquid at a distance far from the bubble. We assume $X_{A\infty}$ equal to zero, since the concentration of air in the tetracosane upon melting is zero, and it is practically negligible compared to the concentration of gas at the gas/liquid interface for the instances in which the eighteen bubbles were analysed. Equation (1) can be re-written as follows :

$$\frac{dr}{dt} = k\left[\frac{X_{Ao}}{X_{Ao} - 1}\right] \qquad (2)$$

where dr/dt is the absorption rate, and X_{Ao} is defined as the ratio between the partial pressure of the bubble and Henry's constant (H). By calculating X_{Ao} and substituting into equation (2), we get :

$$\frac{dr}{dt} = -1.15\text{x}10^{-5}k \qquad (3)$$

In reference [2] the mass transfer coefficient (k) is defined as follows :

$$k = \frac{D_{AB}}{d}\left[2 + 0.31\left(\frac{d3g\Delta\rho}{D_{AB}\rho_l}\right)^{\frac{1}{3}}\right] \qquad (4)$$

where D_{AB} is the diffusion coefficient of the gas in the liquid, and g is the gravitational acceleration. Since g in our case is negligible (of the order of $10^{-6}g_o$), equation (4) can be reduced to the following : $k = \frac{D_{AB}}{r}$ and substituting for k in equation (3), we finally obtain :

$$\frac{dr}{dt} = -1.15\text{x}10^{-5}\frac{D_{AB}}{r} \qquad (5)$$

Since the value of D for air in tetracosane is unknown, equation (5) has been applied using various values of D, and these results were then fitted to the experimental data. From this analysis it has been concluded that a suitable value of D for air in tetracosane is $4\text{x}10^{-5}$ m^2/s. This value is comparable to that for air in water which is between 2 and $3\text{x}10^{-5}$ m^2/s. The theoretical curve is shown plotted versus the experimental data in figure 3.

- **Analysis of the interface shape at the bubble/interface contact point**

Theoretically it has been shown [3] that the solid/liquid interface can take on one of 3 different shapes at the particle/interfacecontact point, depending on the thermal conductivity ratio (α). This is the ratio of the thermal conductivity of the particle (Kg) to the thermal conductivity of the

solid (Ks). For $\alpha<1$, the interface at the contact point is a bump (Figure 4 (a)), for $\alpha=1$, the interface is planar (Figure 4 (b)), and for $\alpha>1$, the interface at the contact point is a trough (Figure 4 (c)). Since the thermal conductivity of air (bubble) is Kg=0.0257 W/m°K, and for tetracosane (solid) it is Ks=0.1580 W/m°K, we have an experimental thermal conductivity ratio, $\alpha=0.163$. In figures 5, it can be seen that, (as is expected theoretically), for $\alpha=0.163$ (ie. <1), the interface shape at the bubble/interface contact point is a bump.

- **Comparison between analytical and experimental bubble velocities.**

The experimental bubble velocities measured for various bubble radii were compared to the analytical bubble velocities calculated from [4] for the case of Stokes buoyancy convection, due to the residual gravity obtained from the OARE accelerometer data ($\approx$0.7 μg). From figure 6 it can be seen that the experimental values are in good agreement with those obtained analytically. We can conclude that the observed bubble migrations are exclusively due to the residual gravity and therefore no Marangoni convection is present. The reason for this is that the non-homogenous liquid contaminates the surfaces of the bubbles preventing a surface tension gradient from forming. This is in accordance with [6], where no Marangoni convection was observed for the case of bubbles in CBr_4.

The presence of a thermal gradient around the bubble is confirmed by figure 7, where we have superimposed an experimental image with one obtained from numerical simulations. The disturbance of the bubble, (which is the coalesced bubble in figure 2(a)), on the thermal field is evident from the figure.

- **Pushing and engulfing of bubbles by advancing solidification front**

From [5] we get the analytical solution of the velocity of the melting/solidification front:

$$|V_f| = 68\sqrt{\frac{1}{t}} \text{ microns/sec} \qquad (6)$$

Figure 8 compares the analytical solution of the front velocity with that measured experimentally, as well as with that obtained from the numerical simulations, and it can be seen that they are all in reasonably good agreement with one another. The experimental images were studied to see whether any pushing of bubbles by the advancing solidification front, whose velocity was measured to be of the order of 1 μm/s, could be observed during the re-solidification process. Most of the bubbles that could be clearly observed were engulfed by the advancing solidification front. An exception, in which one bubble was seen to be pushed by the front, is shown in figure 9: bubble 1, which has a radius of 0.9 mm, is pushed by the front as the bubble comes into contact with the it, while bubble 2, which is aligned with bubble 1, and has a radius of 1.8 mm, is engulfed as it interacts with the moving front.

- **Drop interaction with solidification front**

In the last part of the experiment, some water droplets (diameters between 5 and 10 mm) were injected into the melted tetracosane. Their interaction with an advancing solidification front was analyzed, and no pushing was observed. During the final stages of the experiment, the liquid tetracosane, which still contained the previously injected droplets, was completely solidified from both sides of the test cell. In the post-flight analysis, the solid tetracosane sample was removed from the experimental test cell, and was sliced in order to observe the positions and the shape of the droplets with respect to the final flight configuration. As expected from this study we can conclude that the advancing solidification front does not push or in any way modify the shape of droplets which have dimensions similar to those used in the experiment.

Conclusions and future plans

This experiment allowed us to study the interaction between a solid/liquid front and gaseous/liquid inclusions. We have been able to make a number of important conclusions from our analysis.

The inclusions with diameters in the range 5 -10 mm are engulfed by both the melting and the solidification front.

In spite of the large temperature gradient, no thermocapillary effect was witnessed, because of surface contamination. The observed bubble migration was caused by the residual gravity level.

The absorption of the gaseous particles by the liquid phase and the interface shape at the bubble/interface contact point confirm some of the theoretical expectations.
Future research will be focused on the microscopic interaction between a low melting material solidification front and gaseous inclusions with a much smaller diameter. The intention of this future research is to determine the conditions for which pushing by the front takes place. This is an important point in the fabrication of most composites by melt processing techniques, where the presence of dissolved gas occurs. The management of the insoluble particles is vital to the attainment of the desired physico-mechanical properties.
Also, the solidification regime will be such as to promote either a planar or a non-planar solidification front.

References

1. Bird R,Stewart W,Lightfoot E,"Transport Phenomena",Casa Editrice Ambrosiana,Italy, (1979).
2. Perry R,"Perry's chemical engineers' handbook",Mc Graw-Hill International Editions, (1984).
3. Shangguan D,Ahuja S,Stefanescu D,"An analytical model for the interaction between an insoluble particle and an advancing solid/liquid interface",*Met.Trans.A*,Vol. 23A, Pgs.669-680, (Feb. 1992).
4. Young N,Goldstein J,Block M,"Motion of bubbles in a vertical temperature gradient",*J. Fluid Mech.*, 6, Pgs. 350- 356, (1959)
5. Carslaw H,Jaeger J,"Conduction of heat in solidification", Oxford and Clarendon Press, (1959).
6. Papazian J,Wilcox W,"Interaction of bubbles with solidification interfaces", *AIAA Journal*, Vol.16 No.5, Pgs.447-451, (May 1978).
7. Fortezza R, Castagnolo D, Ceglia E, Tontodonato V, Verzino G, Monti R, "Bubble interaction with solidification front: scientific results obtained during the LMS mission.", Joint Xth European and Vith Russian Symposium on Physical Sciences in Microgravity, St. Petersburg, Russia, 15-21 June 1997.

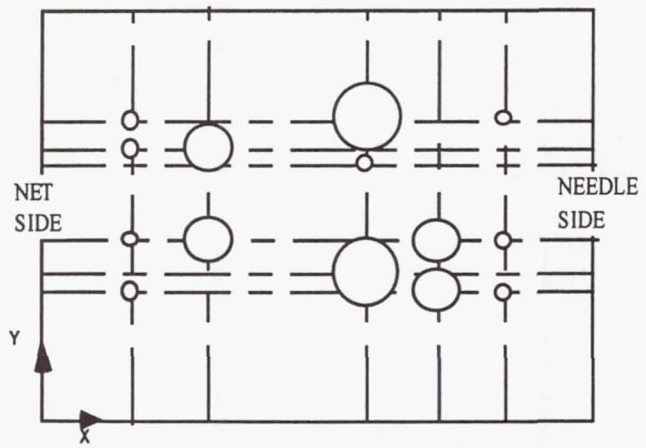

Fig. 1(a) - Initial bubble displacement, view from CCD1 camera.

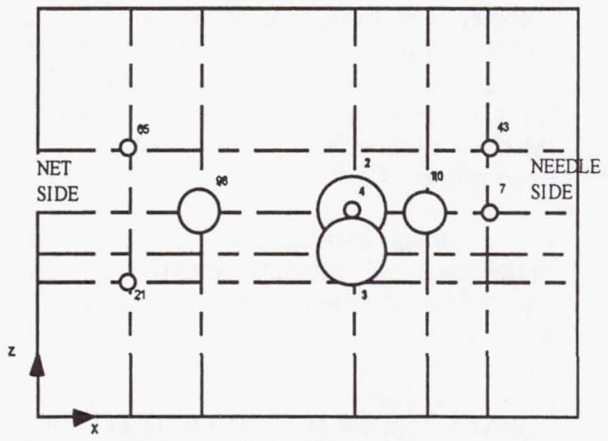

Fig.1(b) - Initial bubble displacement, view from CCD3 camera.

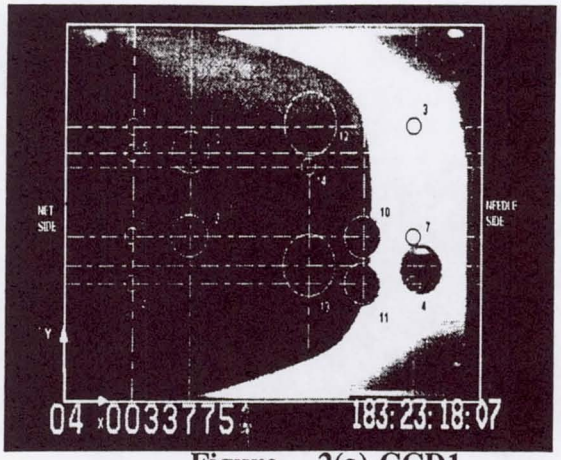

Figure 2(a)-CCD1.

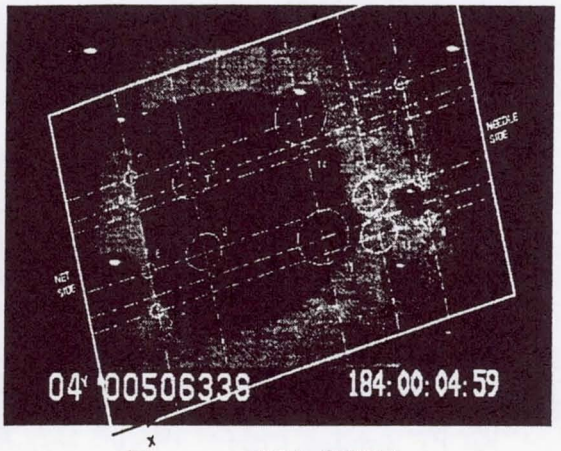

Figure 2(b)-CCD1.

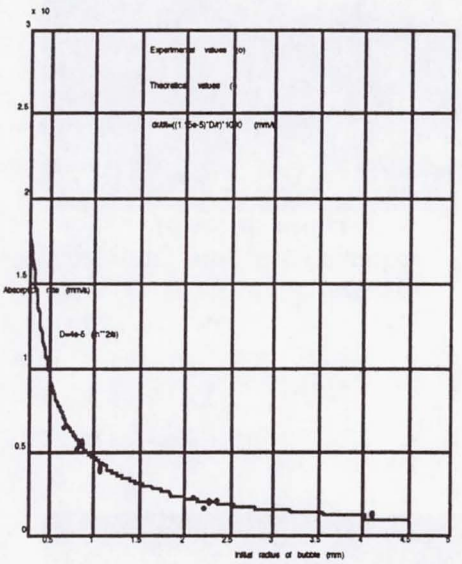

Figure 3. Theoretical vs. Experimental absorption of bubbles in liquid tetracosane.

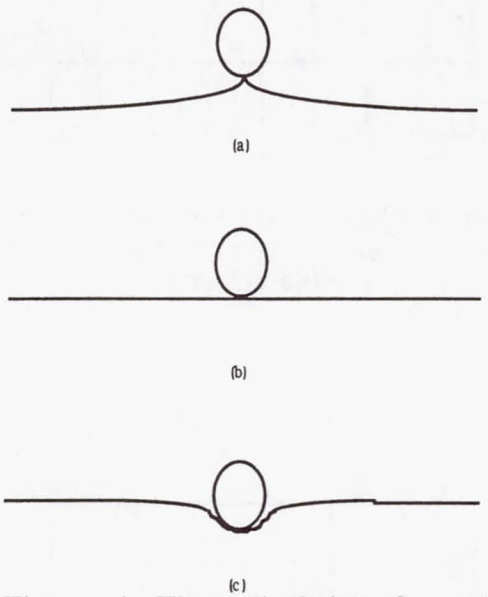

Figure 4. Theoretical interface shape for :(a)α<1,(b)α=1,(c)α>1.

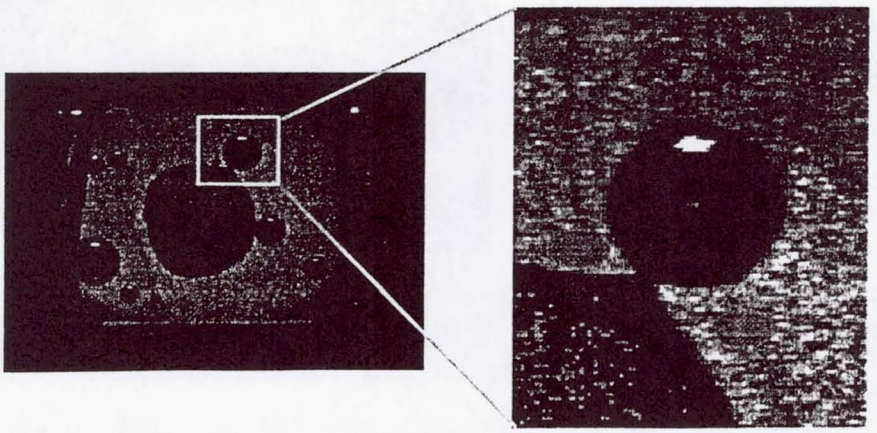

Figure 5. Interface shape at bubble/interface contact point. (α=0.163).

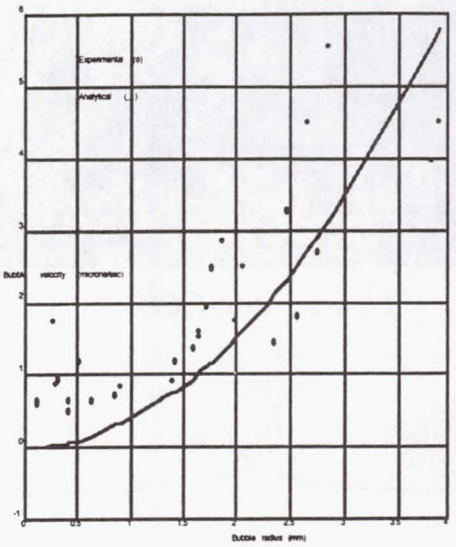

Figure 6. Comparison between analytical and experimental bubble velocities.

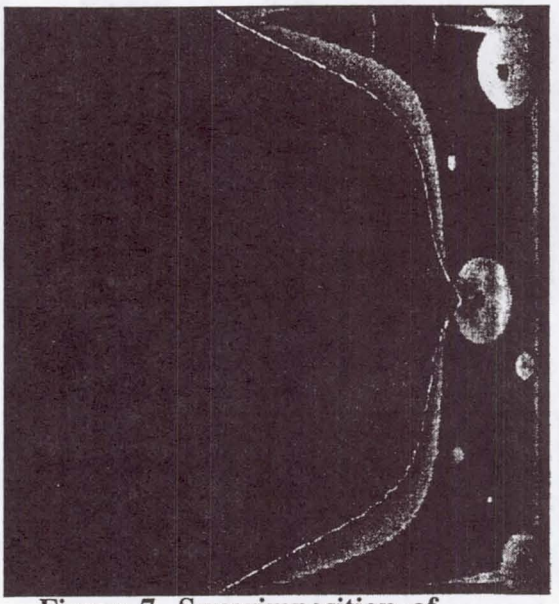

Figure 7. Superimposition of experimental and numerical images.

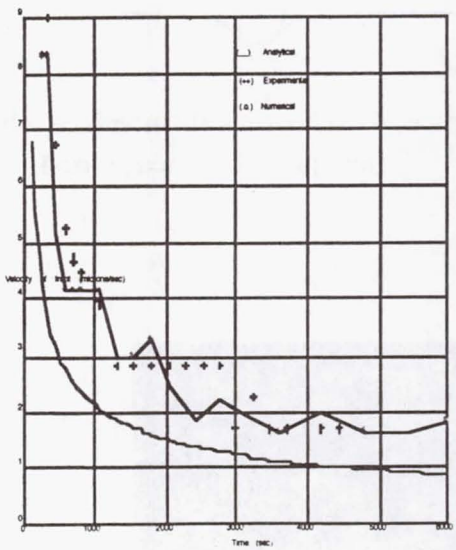

Figure 8. Analytical, experimental and numerical comparisons of front velocity.

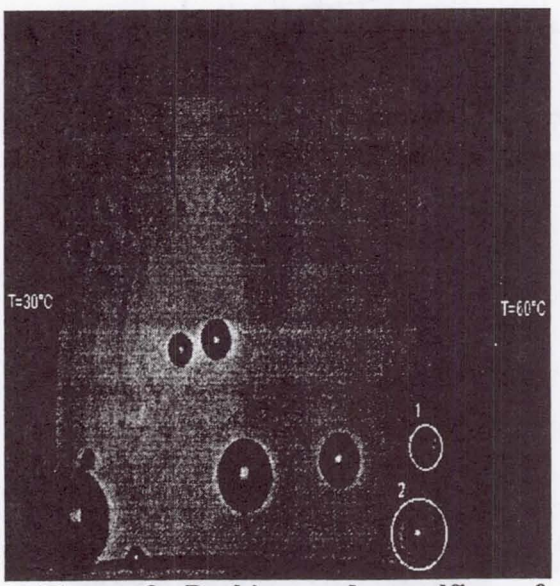

Figure 9. Pushing and engulfing of bubbles by advancing solidification front.

Non-technical summary

Several solidification processes on ground used to produce alloys, glasses and composites are affected by the presence of undesired bubbles and droplets, that cannot be easily removed from the melt. The result is that the quality of these products is poor and should be improved. The buoyancy and sedimentation effects on-ground can be beneficial for the phase separation, but, in particular cases they are not sufficient to obtain the required purity. Alternative methods to remove these inclusions from the melt require futher analysis. The afore-mentioned was the objective of the "MONTI" experiment performed in the BDPU facility flown on board of the Spacelab LMS mission. In particular the aim was to study water droplets and air bubbles inserted in a paraffine wax (Tetracosane) and to evaluate their interactions with a moving solidification front.

From these results it was possible to determine:

- How to manage the inclusions in a liquid matrix and how to remove them by using the pushing action of a moving solidification front.
- How to generate a thermocapillary force capable of displacing the solid and liquid inclusions in a established direction (called Marangoni migration)
- How to prevent the bubble inclusions in solidifying products and how to minimize the impact these bubbles have on the final product.
- How to improve the production of metal alloys, glasses, ceramics and metal matrices on Earth.

The major motivation for carrying out this experiment in a microgravity environment is that buoyancy and sedimentation effects are negligible, so that interactions between solid fronts and inclusions can be carried out without additional external forces. This environment greatly simplifies this study. An example of the negative aspects of the buoyancy effect is that it leads to an undesired distortion of the melting/solidificationfront and to the displacement of the inclusions.

The main conclusions drawn by this experiment are the following:

- The bubbles and droplets with diameters between 5 and 10 mm are engulfed by the front during both the melting and solidification phases of the experiment, in agreement with theory.
- Eventhough a large temperature gradient was established in the liquid phase (40°C/cm), no Marangoni thermocapillary bubble migration was observed, probably due to the surface contamination. The bubble migration which did take place was caused by the residual gravity level (0.7 μg) experienced during the experiment, and measured by the onboard OAREaccelerometer.
- The absorption of the gas bubbles by the liquid tetracosane, and the interface shape at the bubble/interface contact point confirm some of the theoretical expectations.

Futher studies are required to investigate the interaction between a solid interface (both planar and dendritic) and inclusions (gaseous, liquid and solid) characterized by a very small diameter (order of few microns).

Bubble, Drop and Particle Unit (BDPU)

A Liquid Electrohydrodynamics Experiment

Principal Investigator:

Dr. Dudley Saville
Princeton University
Princeton, New Jersey

ALEX

A Liquid Electrohydrodynamics EXperiment

Report On An Experiment Carried Out On The LMS Mission
June & July 1996

Science Team

C. L. Burcham

S. Sankaran

&

D. A. Saville

(Principal Investigator)

Department of Chemical Engineering
Princeton University
Princeton NJ 08544

Final Technical Report - ALEX **A** **L**iquid **E**lectrohydrodynamics E**X**periment

I. *RESEARCH OBJECTIVES*

The experimental foundation of electrohydrodynamics[1] - fluid motions driven by strong electric fields - is weak and the theory proposed by G. I. Taylor[2] (the leaky dielectric model) is relatively untested. To test the theory, experiments were carried out on the electrohydrodynamic stability of liquid bridges.

II. *BACKGROUND*

Electrical forces can be used to manipulate fluids by controlling the shape of an interface or exerting a body force on bulk liquid. For example, liquids can be pumped or sprayed by an appropriately shaped electric field. For apolar liquids (such as organic compounds) where the conductivity is low, relatively high field strengths (1000 V/cm) are needed. Controlling the flow of liquids in micron-scale devices is a rapidly emerging technology*. Here, the design of small scale fluid circuits depends, in part, on understanding the electrical forces and their relation to fluid motion; there are many other applications of electrohydrodynamics. Hence the need for a reliable, well-tested theory for designing apparatus. The current theory, the leaky dielectric model, was invented by G. I. Taylor[2] in the 1960's, but very few quantitative tests have been carried out[1]. We used a liquid bridge as a venue for our experiments. One reason for choosing the bridge configuration is it's simple geometry. In addition, studying the electrohydrodynamic stability enabled us to probe aspects of the theory which had not been previously accessible.

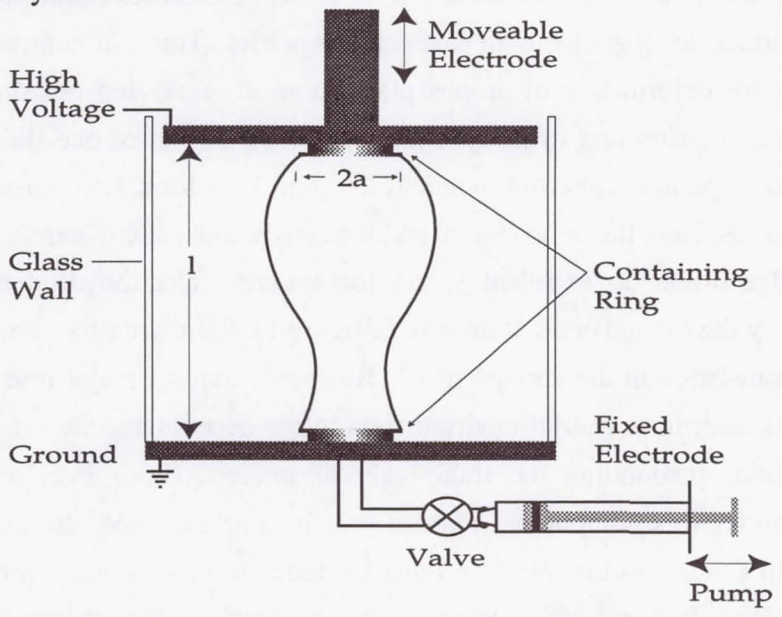

Figure 1. Schematic diagram of a liquid bridge, including features for altering the volume and imposing an electric field.

* A recent newspaper article [*U. S. 1*, January 29,1997] reports work at Orchid Biocomputer, a company founded by the Stanford Research Institute and SmithKline Beecham. They are developing a technology for carrying out a multitude of chemical reactions on a microchip; fluid management is by electrohydrodynamic pumping.

A liquid bridge is a column of liquid pinned to a flat plate at each end (figure 1). Over a century ago, Plateau found that a neutrally buoyant bridge is stable to small perturbations as long as its length, L, is less than it's circumference, πD ($2a = D$, the diameter). Thus, for stability $L/D < \pi$. Interfacial tension plays a dual role. With short bridges, small perturbations are smoothed by the action of interfacial tension. Longer bridges become unstable, also due to interfacial tension. All this derives from the amount of new surface created by a perturbation relative to that in the base configuration. Electrical forces have profound effects. Charging the bridge to bring it to a high potential makes it more unstable since the radially directed electric field opposes surface tension. Conversely, a field aligned with axis of the bridge may stabilize it. The mechanism depends on the presence or absence of free electrical charge.

Fluid bodies composed of perfect dielectric liquids can be maintained in deformed states without motion. A perfect dielectric drop deforms into a prolate spheroid in an applied field; electrical stresses balance interfacial tension on the (static) deformed interface. Non-cylindrical equilibrium bridge configurations are possible, e.g., bridges stressed by an axial field. Bridges with $L/D > \pi$ can be stabilized, up to a point; stability derives from the arrangement of polarization charge induced on the interface.

A leaky dielectric material[1,2] behaves like a dielectric with a small conductivity. In such materials, free charge is transported by ion migration and these liquids behave as Ohmic conductors. The behavior of leaky dielectrics is quite different from perfect dielectrics because free charge congregates at interfaces due to the steep gradients in electrical properties. Thus, in contrast to the situation with a perfect dielectric, the deformation of droplet placed a steady field depends on the delicate balance of electrical, interfacial tension *and* hydrodynamic forces. A droplet of one fluid suspended in another may deform into a prolate spheroid whereas an oblate deformation ensues upon reversing the arrangement of fluids. Here the deformation and the steady shape are dynamic.

A liquid bridge offers an excellent venue for studying electrohydrodynamic stability since its location is fixed by the pinned contact lines (c.f., figure 1). Following the motion of a droplet is more difficult due to translation in the applied field[3]. Buoyancy plays a major role in studying phenomena with free surfaces and, in terrestrial environments, often necessitates the use of an isopycnic system with a matrix fluid surrounding the fluid body of interest. Since interfaces play major roles in electrohydrodynamics this complicates matters greatly. For example, the influence of the electrical properties of both fluids and the interface must be understood, especially processes whereby charge crosses the interface. In our LMS experiment we avoided such problems by using a gas, sulfur hexafluoride - SF_6, as the matrix fluid. At the conditions of the experiment SF_6 behaves as a (very low viscosity) perfect dielectric gas. Neutrally buoyant liquid bridges may take on any one of three configurations: cylindrical, amphora or vase-like, and separated in to two drops. In this experiment, the transitions between these three configurations were studied.

In our experiments the behavior of a given bridge is governed by two dimensionless groups: These are: the aspect ratio, $\beta \equiv L/D$ and $\Delta \equiv a\varepsilon\varepsilon_o E^2/\gamma$, which is the ratio of stabilizing electrical forces to destabilizing interfacial tension forces. The new symbols are: ε, the dielectric constant of the bridge fluid; ε_o, the permittivity of free space; E, the field strength; and γ, the interfacial tension. The other parameters are ratios of mechanical and electrical properties which are fixed for a given fluid pair.

III. *DATA ACQUISITION AND ANALYSIS*

Apparatus Design and Fabrication

The LMS experiment ALEX, the acronym for A Liquid Electrohydrodynamics eXperiment was sponsored by the European Space Agency (ESA) with Daimler-Benz Aerospace as the prime contractor. Two Italian companies: Ferrari Engineering and Laben were responsible, respectively, for the mechanical design and fabrication and electrical design, fabrication and integration. Trek Engineering (USA) built the high voltage power supply. Two test containers - TC4A & TC4B were manufactured and used in the Bubble, Drop & Particle Unit (BDPU), under the overall supervision of ESTEC, the scientific and technological arm of ESA. An especially noteworthy aspect of the experiment is that only 18 months elapsed between the science concept review and the flight aboard the space shuttle Columbia. During the LMS Mission, ALEX was operated by remote control from the Marshall Space Flight Center, Huntsville, Alabama. The success of the experiment demonstrates it is possible to carry out meaningful experiments within a short time span.

Test Container Configurations

Each test container was equipped with a carousel apparatus housing three test cells. One test cell in each container contained a 2-phase mixture, similar to that used in terrestrial experiments to serve as a

Table 1: Test Container Configurations

Cell	Number of Phases	TC 4A	TC 4B
1	1	castor oil	1,000 St. silicone oil
2	2	castor oil eugenol in 12,500 St. silicone oil	castor oil in 1,000 St. silicone oil
3	1	10 X castor oil**	100 X castor oil***

* St. stands for the kinematic viscosity of the fluid measured in 'Stokes.'
** Doped with an electrolyte to raise the conductivity to 10 times that of the neat oil.
*** Doped with an electrolyte to raise the conductivity to 100 times that of the neat oil.

tie-in to ground-based work. The other two cells contained a single liquid to be suspended as a bridge in SF_6, a high field strength dielectric gas. Five of the six cells were operated successfully. In the other cell, a 2-phase cell, the bridge spilled from the retainer rings intended to hold the column in place.

Nevertheless, useful video data were obtained. Overall, nearly 20,000 video images were acquired to depict various stages of the behavior of bridges in both dc and ac fields. Analysis of the images was carried out using image analysis software developed by MARS, an ESA subcontractor. Following the mission, the hardware was recalibrated to verify the data. None of the important calibrations changed, indicating that data collected during the mission are reliable.

Experiment Sequence

The liquid bridge electrohydrodynamic experiments were conducted in a dynamic mode. For the two-phase experiments, experience with previous ground studies provided an accurate estimate of the electric fields necessary for stability. However, since there was no theory or experimental data for single-phase configurations, the electric fields necessary for stability were determined via trial and error in flight. Thus, changes in the configuration were not pre-programmed, but determined based upon the progress of the experiment.

Before a stability experiment was performed, it was necessary to form a liquid bridge. In the two-phase experiments, a short bridge (~1 mm) was created when the TC was filled prior to the launch. For the single-phase experiments, the bridge was built in orbit to avoid spilling fluid from the containing rings during the launch. The first step was to inject a drop of fluid into the containing ring on the fixed electrode. Then the movable electrode was positioned 1.5 cm above the fixed electrode and 12 kV applied. At this field strength (8 kV/cm), the drop is pulled into a shape known as a Taylor cone. Electrical forces cause fluid to be ejected from the tip of the cone towards the movable electrode where it collects inside the containing ring on the electrode. As fluid was transferred from the fixed electrode containing ring, additional fluid was added until the movable electrode containing ring was filled and a drop of fluid visible. Then the voltage was removed and the electrodes brought together until the drops on the containing ring touched and coalesced.

From this point, the single- and two-phase experiments proceeded in essentially the same fashion. The aspect ratio of the bridge was changed by moving the electrode and injecting or withdrawing fluid into the bridge at the appropriate volumetric rate so that a perfect cylinder was formed. At the outset, the aspect ratio was increased until it was close to the Plateau limit, π, and the bridge volume checked to ensure that the configuration was cylindrical. Fluid was added or withdrawn as necessary. Then the stability of the bridge at an aspect ratio just below π was investigated.

Next, the aspect ratio was increased using an electric field to maintain a stable configuration. Commands were sent in real time to increase the field since the field needed for stability was not known *a priori*. Once the desired aspect ratio was achieved, the electric field could be lowered in small steps to examine the transition from cylinder to amphora as well as the pinch-off point. Between voltage steps, the bridge was allowed to assume a steady state configuration. After the pinch-off point was identified, the voltage could be increased to re-establish the bridge. Then, further increases in the

field allowed the sequence of configurations leading to a perfect cylinder to be re-studied. Configurations were analyzed in real time using the image analysis program developed by MARS.

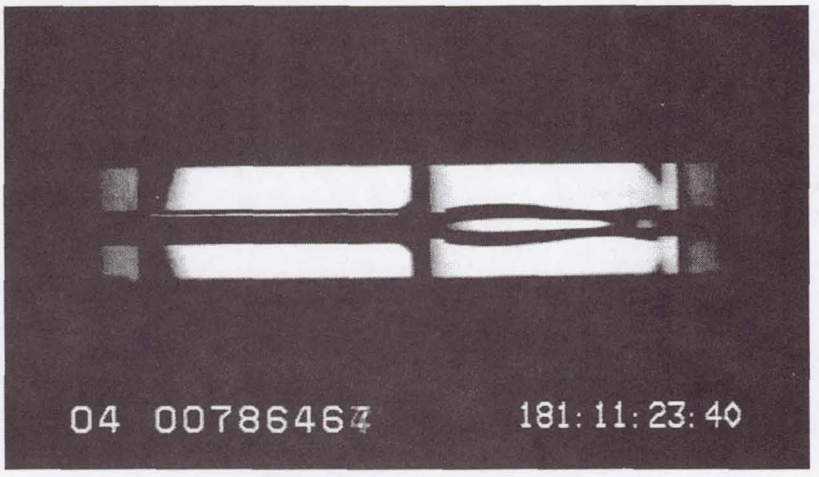

Figure 2: Digitized video image.

The image analysis algorithm produced digitized images (figure 2) and, from the edge coordinates, a trace of the bridge could be reconstructed (figure 3). The edge coordinates were also used to calculate the Fast Fourier Transform (FFT) of the shape and minimum and maximum diameters. The processes of digitization and edge detection proceeded at a rate of 2 to 10 images per second.

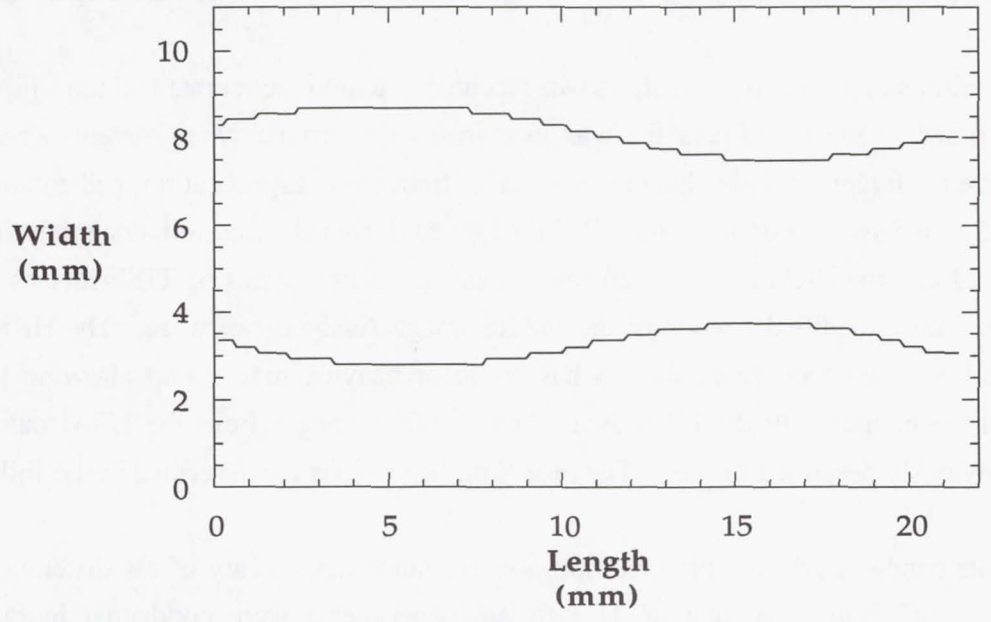

Figure 3: Reconstructed bridge shape.

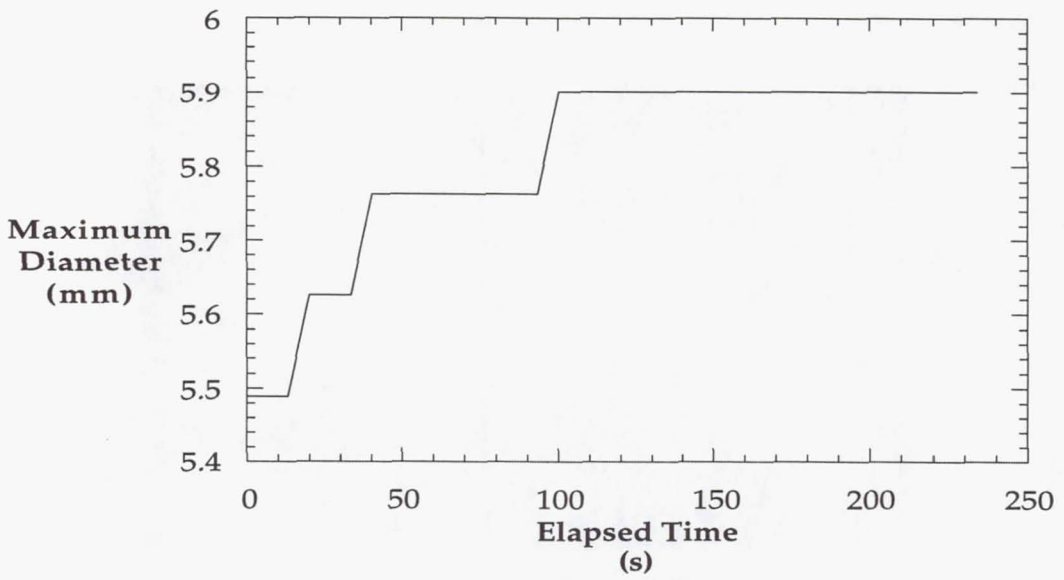

Figure 4: Maximum diameter - time relation during an experiment where the voltage was being lowered.

It was important to observe a sequence of "equilibrium" bridge shapes to identify the various configurations. Once a steady state configuration was established, the voltage was changed and shape changes monitored by following the evolution of the FFT coefficients and maximum or minimum diameter as illustrated in figure 4. A steady state configuration was defined as one which did not change in a certain period. Once steady state is achieved, the voltage was changed again and the process repeated.

Following the mission, all the image analysis was repeated in a more deliberate fashion. First, the telemetry data recorded in the ECIO data file was examined to determine when "events" occurred during the experiment. Events include changes in voltage, frequency, aspect ration, cell rotation, or pumping. The ECIO file was use instead of the MMI files saved during the mission since they include all of the LOS data. Next, the HRM data was reformatted and saved as a series of TIFF images which were then analyzed with a modified version of the MARS Image Analysis Software. The HRM data was used over the live video recordings since it has an accompanying time stamp allowing for the synchronization of the images with the MMI data. Over 17,000 images from the HRM data were analyzed in the previously described fashion. The results of the analysis are described in the following section.

The experiments conducted during the LMS mission examined the stability of six different liquid bridges for AC and DC fields. A total of 41 different experiments were conducted in two test containers, TC 4A and TC 4B, during two separate on-line periods. The experiments involved the effects of DC and AC field levels and frequencies on the stability of bridge with different aspect ratios. Sixteen experiments were conducted the first night, and 25 the next. Each test container had two

single-phase and one two-phase liquid bridge experiment (Table 1). Four of the liquid bridges were single-phase liquid bridges; one with 1000 St. silicone oil, the other three with different electrical conductivity castor oil. The conductivity was adjusted by adding small concentrations of an organic electrolyte, tetrabutylammonium tetraphenylborate, to the castor oil. The two remaining cells were used for two-phase experiments. One of the two-phase experiments reproduced experiments previously conducted on the ground with a liquid bridge of a mixture of castor oil and eugenol in a bath of 12,500 St. silicone oil. The density of the castor oil and eugenol mixture matched that of the silicone oil to within 0.02%. The other two-phase experiment involved a castor oil bridge in a bath of 1,000 St. silicone oil.

Other than an accidental camera dislocation and a minor problem with a limit switch, the test containers and BDPU hardware performed flawlessly. Also the support teams performed magnificently. Support in the POCC by Dornier, MARS, Alenia, Teledyne Brown, NASA, and ESA was invaluable to the success of our experiment. An additional support team made up of engineers from Laben and Ferrari were on hand in Italy but were not utilized extensively during the mission -- a testament to the job done prior to the launch in fabricating and filling the test containers.

Experiments With TC4A

The first night of experiments (TC4A) occupied a 16 1/2 hour period. Cell 2 was rotated into place and examined first. The stability of the bridge without an electric field was examined at aspect ratios of 2.93 and 3.36 for comparison with ground-based work. These experiments were quite successful and will be discussed in § IV.

Next, the carousel was rotated to put cell 3 in place. The Taylor cone procedure was performed successfully creating the initial liquid bridge. Upon increasing the aspect ratio, a large gas bubble was observed in the bridge. Since the bubble was not formed during the Taylor cone procedure, it must have been trapped in the bridge fluid reservoir during filling. Attempts made to destroy the bubble by rupturing and re-forming the bridge were unsuccessful. Even though the motion of the fluid was very violent, it was not sufficient to rupture the bubble. However, this exercise did demonstrate the effectiveness of the grooved containing rings. A final attempt to break the bubble involved withdrawing fluid from the fixed electrode while the air bubble remained fixed to the movable electrode. Although the initial bubble ruptured, another formed. At this point efforts to work with cell 3 were discontinued to conserve time.

Using cell 1, a number of aspect ratios were examined for both AC and DC fields. Again the Plateau limit was probed at aspect ratios of 2.79 and 2.91. Both were stable without a field. However, at an aspect ratio of 2.96, the bridge was found to be unstable without a field - this was attributed to the fact that the volume of fluid inside the bridge was not enough to form a perfect cylinder. This result shows the importance of the real time image analysis software, which allowed us to determine the volume within a bridge both in the deformed and undeformed shape.

The aspect ratio was further increased to 3.23 where various transitions were observed with a DC field. Starting with the bridge broken at the aspect ratio of 3.23, the electric field was increased incrementally until coalescence occurred at $\Delta = 0.14$. Further increases identified the transition from amphora to cylinder at $\Delta = 0.45$. The sequence is depicted in figure 5.

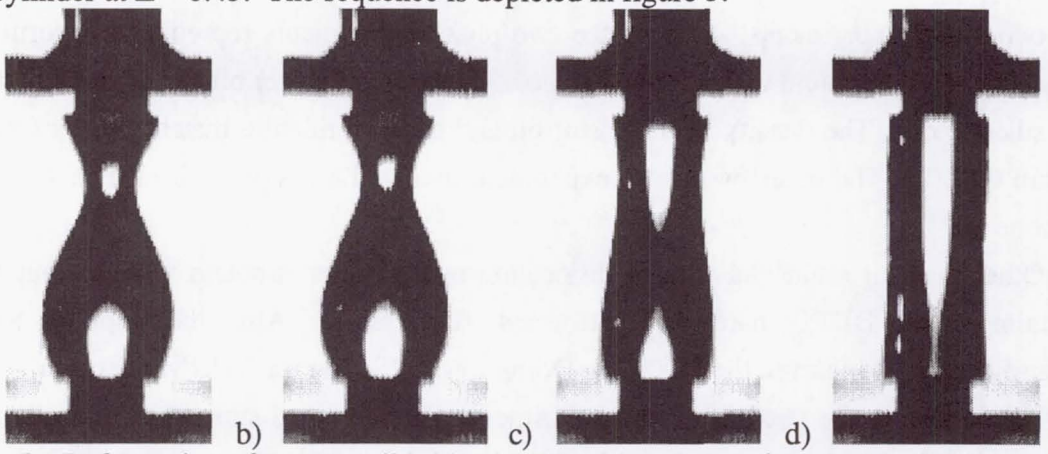

Figure 5a: Deformation of a castor oil bridge in SF_6 with an increasing electric field. Electric field parameter: a) $\Delta = 0.1423$, b) $\Delta = 0.2604$, c) $\Delta = 0.4138$, d) $\Delta = 0.4428$.

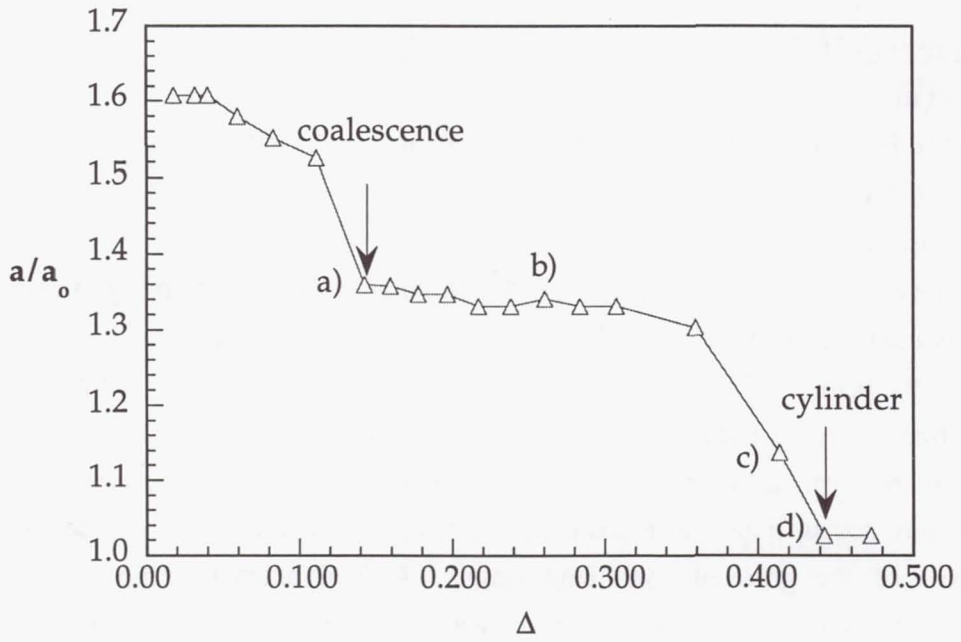

Figure 5b: Maximum bridge radius - electric field parameter relation for an increasing field. The bridge is broken until point 'a' (corresponding to figure 5a) where coalescence occurs. At point 'd', the shape of the bridge becomes a perfect cylinder.

Then, starting from a perfect cylinder, the field was lowered searching for the cylinder-amphora transition. The transition occurred at $\Delta = 0.26$ -- much lower than the transition to a cylinder. The influence of the bridge history on its final geometry was never observed in the ground experiments and was quite unexpected. The pinch-off point occurred at a $\Delta = 0.1$, very close to the coalesce point. This is shown in figure 6.

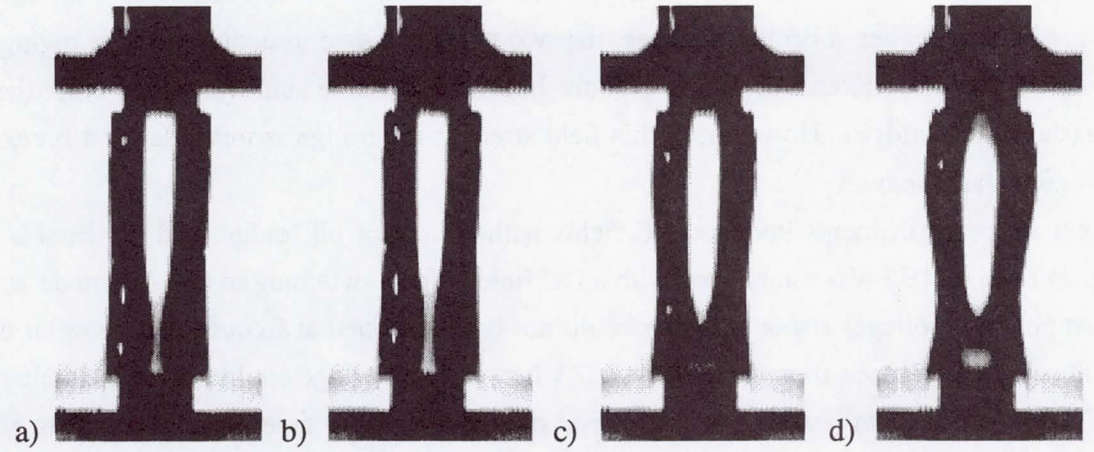

Figure 6a: Deformation of a castor oil bridge in SF_6 with a decreasing electric field. Electric field parameter: a) $\Delta = 0.4138$, b) $\Delta = 0.3325$, c) $\Delta = 0.2374$, d) $\Delta = 0.0961$.

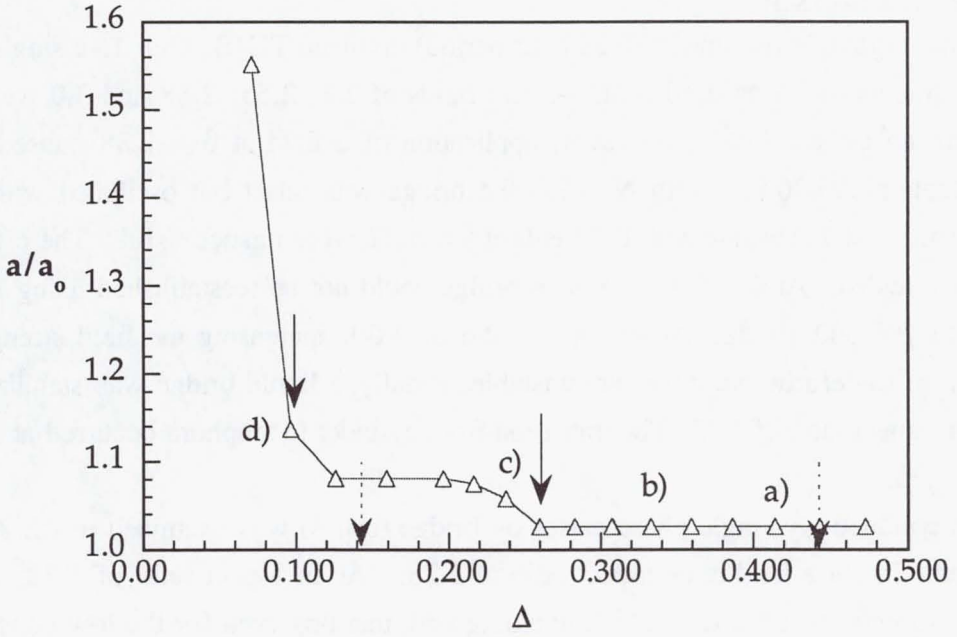

Figure 6b: Maximum bridge radius - electric field parameter relation for a decreasing field. Points correspond to configurations noted in figure 6a.

The aspect ratio was then increased to 4.32, and another DC scan performed. Starting from a broken bridge, coalescence occurred at $\Delta = 0.35$ and the transition to a cylinder at $\Delta = 0.95$. Decreasing the field exhibited the same trend as before, with the amphora transition at $\Delta = 0.6$, and pinch-off at 0.35.

An interesting behavior was observed following pinch-off. After breakup, fluid globules on each retainer ring grew into conical shapes, drew together, and reformed the bridge. Then, the bridge

collapsed and the process repeated itself many times. Such behavior is consistent with the leaky dielectric model since, when a bridge ruptures, the two parts continue to acquire charge owing to the conductivity of the oil. Eventually each globule becomes unstable and coalesces with the other forming a (deformed bridge). However, at this field strength the bridge is unstable so it breaks apart and the process starts anew.

The next set of experiments involved AC fields with the castor oil bridge, cell 3. First a bridge with a aspect ratio of 4.32 was established with a DC field. Upon switching to the AC mode at 20 kV (the highest possible voltage) stable columns could not be maintained at frequencies between 6.6 and 500 Hz. The aspect ratio was then lowered to 3.77 where a stable bridge could not be maintained at 20 kV and 30 Hz. At this point it was necessary to end operations due to time constraints. This behavior in AC fields is quite unexpected since, according to the leaky dielectric model, the bridge should behave as a perfect dielectric at frequencies in excess of the free charge relaxation time.

Experiments With TC4B

The second night of experiments (a 26 hour period) involved TC4B. Cell 1, a single-phase bridge of 1,000 St. silicone oil, was used first. Aspect ratios of 2.3, 2.55, 2.88 and 3.0 were found to be stable without an electric field. However, application of a field at $\beta = 2.88$ caused the bridge to become unstable at $\Delta = 0.8$. With $\Delta > 2.0$ the bridge was intact but oscillated without breaking. Attempts to form a stable bridge with DC fields at $\beta = 3.22$ were unsuccessful. The effects of an AC field were then tested. At $\beta = 2.88$ a broken bridge could not be reestablished using AC fields with frequencies of 200 and 10 Hz. At an aspect ratio of 3.00, increasing the field strength at 200 Hz caused to bridge to deform, but it was not unstable. Finally, a liquid bridge was stabilized with a 500 Hz field at an aspect ratio of 3.22. The transition from cylinder to amphora occurred at $\Delta = 1.55$, and pinch-off at 1.25.

The high conductivity single-phase castor oil bridge (cell 3) was examined next. A stable bridge was observed without a field at an aspect ratio of 2.25. At an aspect ratio of 3.32, the amphora - cylinder transition occurred at $\Delta = 0.45$, coinciding with that observed for the low conductivity castor oil bridge. Unfortunately, the bridge spilled from the contained rings and neither the pinch-off nor the transition from cylinder to amphora was observed. A bridge with $\beta = 3.71$ was briefly examined and found to be a stable amphora at $\Delta = 1.0$. AC experiments at 200 Hz were also conducted at an aspect ratio of 3.71. The column was unstable at 12 kV and broke spilling onto the electrodes in an unrecoverable manner.

The final cell examined was the two-phase cell (cell 2) consisting of a castor oil bridge in 1,000 St. silicone oil. Stable columns were observed at aspect ratios of 2.12, 2.82 and 3.08 without a field. A DC experiment was conducted at an aspect ratio of 3.36. Coalescence occurred at $\Delta = 0.41$. However, just as the transition to a perfect cylinder was occurring at a $\Delta = 0.98$, the column spilled. The spill was recovered, and the aspect ratio increased to 3.54. A scan from $\Delta = 1.0$ to 2.1 found that

the bridge was approaching a cylindrical shape at $\Delta = 2.1$. However, at this point the bridge began to spill again. The aspect ratio was further increased to 3.92. A stable amphora was observed at $\Delta = 11.2$.

A number of AC experiments were also conducted with the two-phase cell. Below the Plateau limit at an aspect ratio of 3.08, a perfect cylinder was observed at 200 Hz for Δ up to 0.5. At an aspect ratio of 3.36 and 10 Hz, a range of Δ's from 0.5 to 3.1 were not sufficient to stabilize the bridge. Although, at an aspect ratio of 3.54 and 200 Hz the bridge was stabilized at $\Delta = 0.83$. Increasing Δ caused the deformation to grow. The final aspect ratio examined was at 3.92 and 200 Hz. The bridge could not be stabilized at the maximum of 20 kV. The bridge became unstable spilling in an unrecoverable manner.

IV. *COMPARISON OF FLIGHT AND GROUND-BASED RESULTS*

With the two-phase system, TC4A-cell 2, transitions from cylinder to amphora and the pinch-off point were found to agree closely with the results of Sankaran and Saville[4] after taking account of the difference between the properties of the two system (Figure 7). The transition from cylinder to amphora occurred at $\Delta = 0.195$, and pinch-off at $\Delta = 0.057$. This compares to the values of $\Delta = 0.18$ and 0.03 reported by Sankaran and Saville[3] for the transition and pinch-off points respectively. This agreement between μ–g and 1-g experiments validates the performance of the flight system for steady fields.

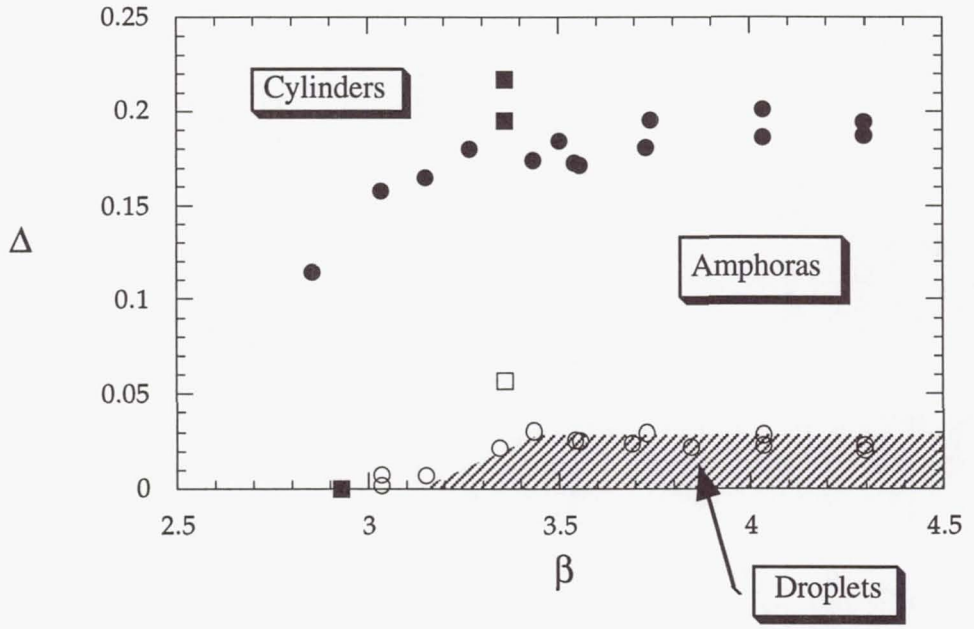

Figure 7. A comparison of flight and ground-based results in a two-phase system.
● & ○ - terrestrial experiments; ■ & ❑ - μg experiments.

V. *COMPARISON OF EXPERIMENT AND THEORY*

At the time of the experiment the leaky dielectric model had not been used to predict the behavior of a pinned bridge. Since that time, Mr. Chris Burcham has completed calculations[5] to predict the stability of a liquid, leaky dielectric bridge in a dielectric gas. A comparison between experimental results for a castor oil bridge and theoretical calculations are shown in figure 8. Although the agreement between theory and experiment for pinch-off is encouraging, it is unexpected since the theory presupposes small perturbations. On the other hand, the lack of agreement for the cylinder-amphora transition is vexing. Two causes, other than the approximations involved in linearization, come to mind. First, it is possible that the bifurcation from cylinder to amphora is continuous, rather than abrupt as suggested by the theory. Another possibility is that the leaky-dielectric model itself is flawed. A large number of approximations are inherent in the model[1] and one or more of these may be at fault. These matters remain under investigation.

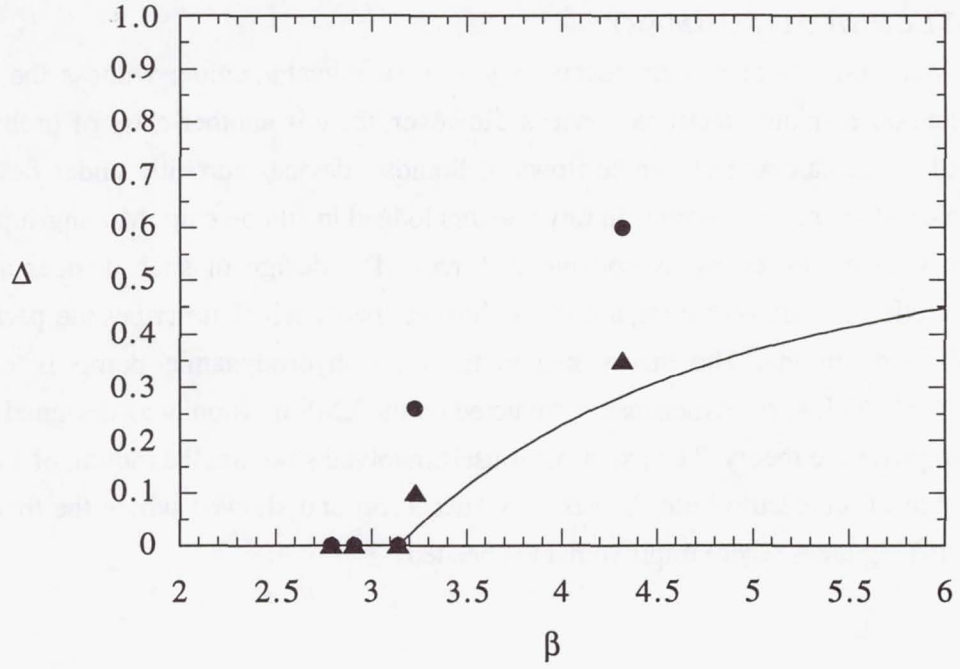

Figure 8. Comparison between theory[6] and experiment for a castor oil bridge in an SF_6 environment. The solid line is a theoretical result for the stability of a liquid bridge subject to small perturbations. States above the line are stable; those below the line are unstable. The experimental points were obtained in experiments during the LMS mission - TC4A, cell 1: ● - cylinder-amphora transition; ▲ - amphora - drop transition ('pinch-off').

VI. *SUMMARY & CONCLUSIONS*

The ALEX apparatus performed as designed and produced a considerable amount of useful data. The primary goal, to test the leaky dielectric model in the liquid bridge configuration, was achieved. As with any successful scientific experiment, as many new questions and ideas were raised as were answered. Thus, the ability of the model to address issues of stability with a gas-liquid interface in DC fields was demonstrated. Theory and experiment appear in agreement, although some questions remain.

The situation with AC fields is less clear. According to the theory, leaky dielectric materials should behave as perfect dielectrics if the frequency is high enough. Thus, a bridge which can be stabilized by a DC field should be stable in a AC field, albeit at a higher field strength. This was not generally the case in our experiments. Accordingly, additional work with this aspect of the model is needed to elucidate the behavior of leaky dielectrics in AC fields.

VII. *NON-TECHNICAL SUMMARY*

Many aspects of modern technology involve miniaturization; witness the proliferation of computers and other micro-electronic devices. However, there is another class of problems which can be addressed if one can control minute flows of liquids - devices currently under development carry out a multitude of chemical reactions in tiny reactors lodged in silicon chip. Moving liquid to and from the reactors is done with electrohydrodynamic forces. The design of such devices as well as other applications relies, in part, on having a well-established theory which describes the performance of the pumps and fluid circuits. The theory behind the electrohydrodynamic pump is called the leaky dielectric model. ALEX, the experiment conducted on the LMS mission, was designed to provide data to test and improve the theory. The experiment itself involved studying the motion of a column of fluid in the presence of an electric field. It was very successful and showed where the theory is strong as well as identifying areas where improvement is needed.

VIII. *BIBLIOGRAPHIC CITATIONS*

1. C. L. Burcham & D. A. Saville 'Electrohydrodynamic Stability of Liquid Bridges'
AICHE Annual Meeting, Chicago, November 96.

IX. *BIBLIOGRAPHY*

[1] D. A. Saville 1997 Electrohydrodynamics: The Taylor-Melcher leaky dielectric model *Annual Review of Fluid Mechanics* **29** 27-64.

[2] G. I. Taylor. 1966 Studies in electrohydrodynamics I. The circulation produced in a drop by an electric field. *Proc. Roy. Soc.* A291:159-66.

[3] O. Vizika & D. A. Saville 1992 The Electrohydrodynamic Deformation of Drops Suspended in Liquids in Steady and Oscillatory Electric Fields. *Journal of Fluid Mechanics* **239** 1-21.

[4] S. Sankaran & D. A. Saville 1993 Experiments on the stability of a liquid bridge in axial electric field. *The Physics of Fluids A* **5** 1081-1083.

[5] C. L. Burcham 1997 Ph.D. Thesis, Department of Chemical Engineering, Princeton University.

Bubble, Drop and Particle Unit (BDPU)

Boiling on Small Plate Heaters under Microgravity and a Comparison with Earth Gravity

Principal Investigator:

Dr. Johannes Straub
Technical University Munich
Munich, Germany

Report prepared for LMS final science review, Montreal, Canada, August 1997

BOILING ON SMALL PLATE HEATERS UNDER MICROGRAVITY AND A COMPARISON WITH EARTH GRAVITY

J. Straub, M. Steinbichler, G. Picker

Lehrstuhl A für Thermodynamik, TU München

Boltzmannstr. 15, 85748, Garching, Germany

M. Zell

DASA GmbH, Dornier

88039 Friedrichshafen

ABSTRACT

The boiling heat transfer on five miniature heaters of different size and shape has been measured under microgravity conditions during the LMS mission and under earth gravity after the mission in 1996. These experiments were conducted as basic studies of boiling heat transfer in microgravity and as simulations for the direct emersing cooling of small electronic devices by boiling heat transfer, which becomes more and more important due to high thermal loads of modern electronic components.

The boiling process was studied in the liquid FREON 123, which was considered as an alternative refrigerant which is not endangering the ozone layer. The boiling heat transfer was determined by a simultaneous measurement of the heat-flux and the temperature of the heater. The boiling process was observed in two perpendicular observation directions with different types of optical diagnostics, provided by the BDPU facility.

Several boiling modes, like cavitation and sparkling boiling, as well as the cavitational thermocapillary supported flow-mode, thermocapillary jet boiling and saturated boiling have been observed during the experiments, depending on the subcooled liquid state and the overall heat flux. Under microgravity surface tension driven convection plays an important role in the boiling heat transfer on the miniature heaters. The observations under earth gravity show significant differences especially in terms of bubble size, departure diameter and induced flow-pattern. Astonishingly a remarkable influence of the gravity level on the heat transfer could not be measured. That confirmed earlier observation that the evaporation in the liquid wedge between the solid heater and the bubble interface, the capillary force, the surface tension and the wetting condition play the most important role in the boiling process.

INTRODUCTION AND OBJECTIVES

During the LMS Spacelab mission of NASA in July 1996 pool boiling experiments under microgravity conditions were performed. These experiments are utilized five different small sized and shaped thermistors. These thermistors were used simultaneously as heating elements and as resistance thermometers. Three of these five heating elements were plate shaped with the diameters of 3, 1.5 and 1 mm, respectively. The other two heating elements were thermistor beads, with nearly spherical diameters respectively 1.4 and 0.4 mm. The experiment called BOIL „ A simulation for the cooling of small electronic devices" /1/ was accomplished in the BDPU (Bubble, Drop and Particle Unit), which was a Spacelab multi-user facility for fluid physics experiments, operated by the European Space Agency, ESA. This facility was already used during the IML-2 mission in 1994.

This boiling experiment was conducted together with a second experiment called NUBUC „Study of vapor bubble growth in a supersaturated liquid" /2/, utilizing the same hardware, which was designed and build according to this purpose. The original planning foresaw an equal sharing of the available microgravity time for both of the experiments. However a major share of the available microgravity time was used for the boiling experiment, whose primary results will be discussed on the following pages. Thanks to the replanning efforts of the NASA team from the MSFC Operation Support Center in Huntsville, AL, additional time for both experiments was available. After disintegration from the Spacelab the experiment was repeated on ground with the flight hardware, the identical fluid, and the same

experimental sequences, in order to guarantee comparable boiling data both under microgravity as under earth gravity.

The scientific objectives of the boiling experiments were the following:

a) A study of the primary mechanisms of pool boiling on five different sized and shaped microheaters under excellent microgravity conditions and a comparison of the microgravity data with reference data gained under comparable conditions under normal gravity.
b) A observation typical dynamic processes as bubble formation, growth, departure, departure diameter, and coalescence, in order to determine the influence of the gravity level on these dynamic processes.
c) The separation of gravity dependent and gravity independent mechanisms on the boiling process.
d) The investigation of the heat transfer coefficients for very small plate shaped and hemispherical microheater under microgravity and normal earth gravity.
e) The study of the influence of the size and shape of the heating element on the overall heat transfer coefficient under microgravity and normal earth gravity.
f) The acquisition of a large data base of boiling data for the development of new correlations for the boiling heat transfer under microgravity.
g) A comparison with the boiling data gained during IML-2.
h) A study of the feasibility of boiling heat transfer, using this technique for the cooling of high powered microelectronic components directly immersed into a liquid and its application in space and on earth.

APPLICATION

The performance of integrated circuits and high powered electronical components was enhanced considerably during the last years. This increase was mostly combined with an decrease in size This causes serious problems, because most of the electric power disperses into expense heat, which must safely be transferred from the electronic component, in order to protect from overheating and possible destruction. As protection from any critical overheating, an efficient and stable method of cooling must be found and applied. One of the most promising methods is boiling heat transfer in dielectric liquids. Several authors /3-6/ investigated boiling heat transfer on integrated circuit chips or simulated microheaters that were directly immersed into a pool of liquid. These liquid pools were normally environmentally safe refrigerants, with appropriate vapor pressure curves. These experiments were performed under earth conditions, where the buoyancy and the buoyancy induced convection supported the vapor and heat transport away from the heater.

Naturally our main interest lied still, in spite of possible future technical applications, mainly in the basic fundamentals of the boiling process and its mechanisms. Former experiments /1,8,11/ demonstrated that the applied correlations loosed their validity quickly, if they were extrapolated to higher or lower gravity level. Therefore it was justified to ask whether gravity really should be considered the dominant mechanism of the boiling heat transfer process.

BACKGROUND

In contrast to existing theories and correlations e.g. /10/ former boiling experiments with various geometries under microgravity /8/ demonstrated clearly that the influence of gravity is much less as predicted. However, for these experiments large heating elements were used, therefore no information existed about very small heaters. For large heating elements it was obvious that the temperature and heat flux measured was only an integral value, which neglected local and spatial variations in temperature and heat flux due to bubble dynamics. Therefore the usage of small heating elements promised a considerably better information about the boiling phenomena encountered, because the measuring resolution is higher.

Other authors e.g. /12/ predicted that under the absence of gravity a small heating element should immediately be covered with vapor, leading to film boiling and corresponding with it to high heater temperatures, since buoyancy is the driving force of vapor removal from the heating surface. Hence the question arised, if the boiling process can still be a suitable mechanism for an efficient cooling of small electronic elements under microgravity? Future application of the boiling process for cooling of electronical components in space applications and on earth depended from a solution to this question.

EXPERIMENTAL EQUIPMENT

BDPU Facility

During the LMS Spacelab mission on STS 78 the experiment was conducted in the ESA multi-user facility BDPU (Bubble, Drop and Particle Unit), designed by ALENIA, Italy. Multi-user facility meant that it could be used for a wide variety of specific scientific needs. The BDPU provided the power supply, data acquisition and two perpendicular observation directions, with a wide variety of optical devices like background illumination, two different types of interferometers, a point diffraction and a wollaston interferometer and a light sheet for the study of flow fields with particle image velocimetry. Each observation path was recorded by a video camera or an extra 16 mm film camera. Furthermore the BDPU provided the interface to the Spacelab and the Shuttle system for the video and data link direct to the Operation Support Center at the NASA-MSFC in Huntsville. There, the principal investigators and their teams could observe the experimental runs during the mission in real time video and all important experimental data were directly available. The experiments in the BDPU were controlled by telecommanding from ground and the essential experimental parameters were adjusted depending on the observed data. This system ensured that a maximum of scientific results could be obtained.

Test Container

The test container was refurbished from the test container used during IML-2 according to the new requirements of the experiment by the companies Daimler Benz Aerospace,Dornier, Germany, in cooperation with Ferrari Engineering, Italy. The container was set in the facility and electrically connected by one of the astronauts. It had the size of 45x15x30 cm^3. Because of safety reasons the container had a triple containment. It had to be ensured that in case of a leakage of the fluid system no gas of the evaporating liquid was released into the Spacelab environment. The liquid cell had an internal dimension of about 50 x 50 x 50 mm^3 with a nearly spherical shape on the inside. It had four windows of sapphire with 40 mm optical diameter for the two perpendicular observation directions. To change the pressure of the liquid in the test cell and to compensate the vapor volume in order to keep the pressure constant during boiling a bellows was used with the counter pressure imposed by nitrogen. A small gas compressor supplied a small pressure vessel with the necessary compressed nitrogen, to guarantee the counter pressure on the liquid side of the bellows. By the means of two valves on the nitrogen side of the pressure system the pressure inside the fluid cell could be adapted to its appropriate value.

Two Peltier elements on the lateral walls of the fluid cell were used simultaneously for heating or cooling. The temperature could be controlled within $\pm$ 0.05 K. The Peltier elements dissipated the heat to the avionics air duct through two heat pipes. The test liquid in the fluid cell was FREON R123, which had replaced the environmental endangering FREON R11. Nine identical small sized thermistors were directly placed in the liquid to measure the liquid temperature distribution in the vicinity of the heating elements. Originally three plate heaters and three spot heaters were additionally placed inside the test cell. Unfortunately the smallest spot heater was already damaged beyond recovery during the first experiment run at the beginning of the mission. The plate heaters were circular with the diameters of 3, 1.5 and 1mm . The remaining spot heaters of nearly spherical size had a bead diameter of 1.4 and 0.4 mm. As an example for one of the spot heaters see **Fig. 1**

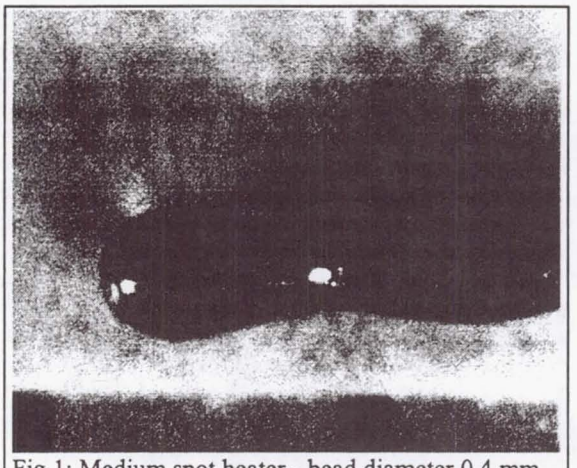

Fig.1: Medium spot heater - bead diameter 0.4 mm

These thermistor used as heaters had a special temperature-resistance characteristic, which was determined well before the mission. The thermistors themselves were covered by a glass coating in order to protect the semi-conductor material, which provided the necessary resistance characteristic. The plate heaters were designed as circular copper plates with a thermistor glued into, with a special glue of high thermal conductivity. These copper plates were integrated in a basis material characterized by a high melting point and low thermal conductivity, in order to minimize loss of heating power due to conduction in the material.. However, because of the glass coating the temperature measured was not equal to the wall temperature, which determined the nucleation temperature and the evaporation of the liquid. Therefore the real wall temperature had to be calculated from the power input and the measured inner temperature during the evaluation stage of the data.

The spot heaters and plate heaters could be controlled with constant temperature as well as constant power. Constant temperature meant that the heat flux adapted according the physical circumstances of the boiling state with a constant superheat, whereas constant power meant that the wall temperature adapted to the physical circumstances with the power dissipation held constant. This adaptation was influenced by the pressure level, respectively the fluid state and the heat transfer coefficient of the boiling process. Each experiment run with different heat fluxes or temperatures was conducted at a constant fluid temperature and pressure level. Afterwards the boiling run was repeated at the same liquid state with another heater. Whenever five boiling curves for the available five heaters were acquired the fluid state was changed and the whole procedure started again.

During the evaluation stage the appropriate wall temperature T_w had to be calculated from a steady-state conduction equation. Since all thermistors were nearly spherical the heat conduction equation simplified to one-dimensional steady-state conduction. With the power input to the thermistor $\dot{Q}$, determined by the voltage and current at the heater and the inner temperature T_i of the heater according to its resistance characteristic the real wall temperature could be calculated according to following equation

$$\dot{Q} = \frac{T_i - T_l}{R_l + R_\alpha} \qquad (1)$$

where T_i is the inner temperature of the thermistor, T_l is the bulk liquid temperature recorded in the cell, R_λ is the thermal conductivity resistance of the thermistor coated with glass and could be determined, if the geometry was assumed spherical and the inner diameter r_1 of the semi-comductor, and the outer diametere r_2 of the glass coating were known

$$R_\lambda = \frac{(r_2 - r_1)}{\lambda_g 4\pi r_1 r_2} \quad . \qquad (2)$$

This assumption is justified because in the case of pure heat conduction to the liquid at lower heater temperature a nearly spherical temperature field was observed in the interferometer.

The heat transfer resistance R_α to the liquid was given by

$$R_\alpha = \frac{1}{\alpha 4 \pi r_2^2} \quad . \tag{3}$$

With eq. (1) the total thermal resistance $R_\lambda + R_\alpha$ of the thermistor was determined, and respectively with eq. (3) the heat transfer coefficient α. The wall temperature on the outside of the glass coating of the thermistor T_w could be determined as:

$$T_w = T_i - \dot{Q} R_\lambda \quad . \tag{4}$$

The heat loss to the cylindrical not heated part of the thermistor was calculated as a fin and is proportional to T_i - T_l. The heat losses were considered in the calculation of the heat flux. These calculations were valid for all of the heaters as long as spherical or nearly spherical geometries were considered and the appropriate geometrical dimensions and thermal properties were used. Concerning the plate heaters, which were thermistors glued into copper plates further thermal resistance has to be considered. However since the thickness of the copper plate was very small and the thermal conductivity of copper was about 400 times higher than the thermal conductivity of the glass coating of the thermistor, the influence of the copper could be neglected within reasonable accuracy. Nevertheless heat losses due to dissipation into the basis material, the copper plates were integrated in, were considered in the calculations. These simplification were backed by the readings of a very tiny measuring thermistor (bead size 0.05 mm) which was assembled in the copper mantle of the large plate heater (3mm diameter), which showed good agreement between the calculated and measured wall temperatures.

EXPERIMENTAL PROCEDURE

The temperature of the fluid cell was set to the desired value, and while stirring the liquid in the test cell was heated up to the set temperature. After the set temperature was reached the pressure level was adapted according to the desired subcooling or saturation. Then the stirrer was switched off and the movement of the liquid calmed down within 2 minutes.

Then the chosen heater was either controlled in constant temperature or constant power. The heater inner temperature or power dissipation was slowly increased in 10 steps up to the maximum value. After the maximum level was reached the power/temperature was then slowly decreased in fifteen steps until the beginning state was reached again. The maximum power and inner temperature levels of each heater varied according to their sizes and resistance characteristics. Since for every experiment run the number of changed parameters was about 40 parameters a special software was developed, to simplify and to quicken the changing process.

The power dissipation $\dot{Q}$ and the inner temperature T_i were measured during the whole experimental run. At each temperature / power level the boiling process was maintained for about 20 seconds. The measured data clearly showed that this time interval was easily enough for steady state conditions at the heater surface, since the steady state conditions were reached after approximately two seconds.

All measurement data was recorded with a frequency of 8 Hz and linked down directly to the control center of MSFC in Huntsville.

The experiment controlling software consisted of three boiling runs, which were conducted with three different heaters. After completion of the three boiling runs, a new run with the other two heaters was completed. The pressure was raised up to 14 bar in order to condense any excess vapor. A new pressure/subcooling level was adjusted and again the five boiling runs were completed. After completion of all the desired pressure levels at one fluid state, a new fluid temperature value was set and everything started over again. The measured boiling curves normally started with pure conduction until the necessary nucleation wall temperature was reached, then the boiling process set in. Unfortunately almost at no fluid state the critical heat flux condition could be achieved. This fact is mainly due to the high thermal resistance of the glass coating of the heating elements. Therefore mostly only nucleate boiling curves could be measured.

PRELIMINARY RESULTS

Boiling Sequence

The experiments were carried out at constant bulk liquid temperatures T_l = 30, 40, 50, 70, 80, 90, 100, 110 °C and at various thermistor inner temperatures T_i and power levels $\dot{Q}$. The maximum achievable inner temperature T_i. was averagely

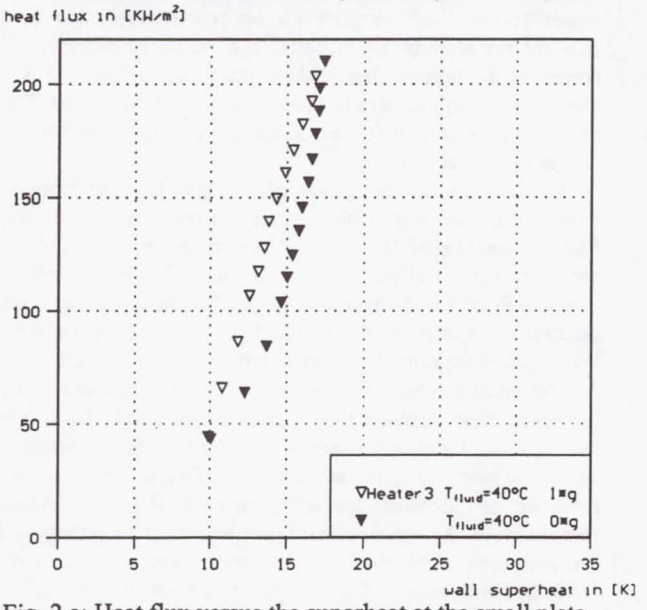

Fig. 2 a: Heat flux versus the superheat at the small plate heater

250 °C, depending on the resistance-temperature characteristic of the heater. The maximum power dissipation $\dot{Q}$ of the heaters ranged from 0.8 W for the larger heaters and 0.3 W for the

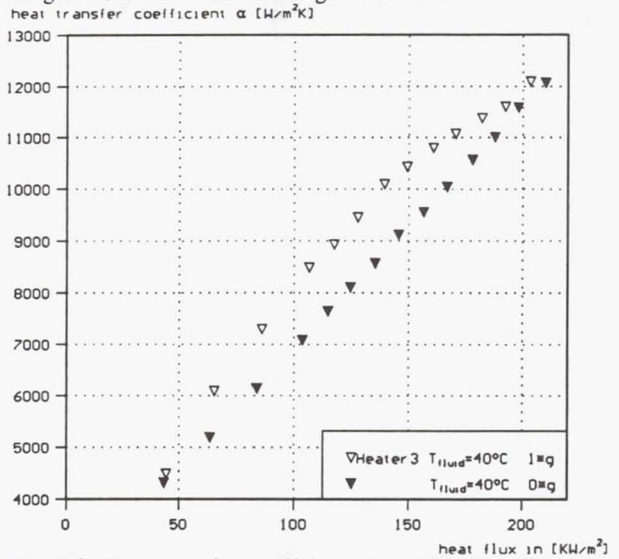

Fig. 2. b: Heat transfer coeffcients versus the heat flux at the small plate heater

smaller ones.

During the course of one experimental sequence three boiling curves where done at one predefined fluid state and pressure level. One boiling curve consisted of 20 different temperature or power levels. Each temperature or power level was held constant for at least 20 seconds. The measured voltage and current at the heaters clearly show that this waiting time was more than enough for steady state conditions at the heaters. The steady state conditions were reached in a time interval of maximal two seconds.

In **Fig. 2a and b** the results of a conducted experimental sequence for one of the plate heaters at saturation pressure and fluid temperature of 40 °C are shown as an example. **Fig. 2a** shows the time averaged heat flux $\dot{q}$ versus the wall superheat, respectively the difference of the wall temperature and the saturation temperature of the liquid ΔT_{sat}. Since the pressure level equaled the saturation pressure at a fluid temperature of 40 °C, the saturation temperature was 40 °C. **Fig. 2b** shows the averaged heat transfer coefficient α, defined with the temperature difference between wall and saturation temperature, versus the heat flux $\dot{q}$. Also included in **Fig. 2a and b** are the reference measurements conducted on earth. For the reference measurements the identical hardware and the same refrigerant had been used. Additionally the reference experiment runs were conducted with exactly the same heater temperature and power levels, in order to guarantee the reproducibility of the measured reference data.

It can be clearly seen , that a remarkable influence of the gravity level cannot be identified. The averaged microgravity data points are shown with closed symbols, whereas the averaged reference data points are shown with open symbols. Considering the shape of the boiling curves it is easy to see that both the microgravity data and the reference data show the same qualitative tendency. This strongly indicates that even without the presence of gravity induced buoyancy still the same hydraulic and thermodynamic forces are responsible for the boiling process. Therefore considering the buoyancy a primary mechanism of the boiling process cannot be contained.

Heat Transfer

Saturated liquid state:

The heat transfer for saturated liquid conditions under microgravity (full symbols) at the fluid temperatures of 40°C, 60 °C and 80 °C is shown in **Fig. 3**. together with the

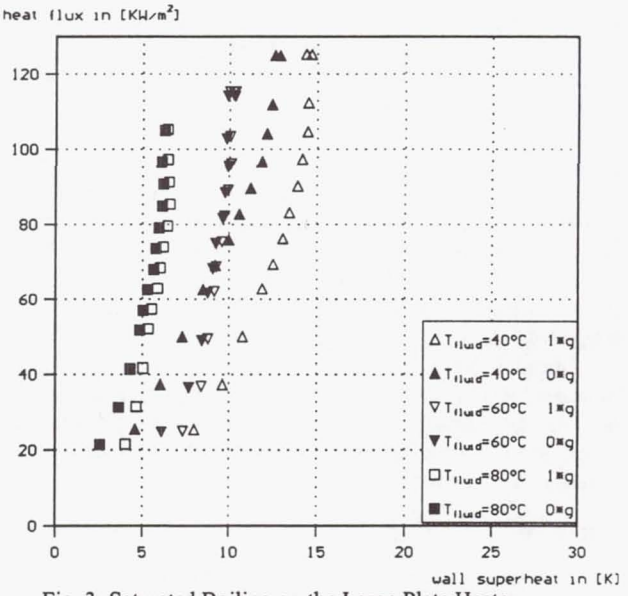

Fig. 3: Saturated Boiling on the Large Plate Heater

corresponding normal earth gravity data (open symbols) for the large plate heater .

The appropriate boiling curves shifted with increasing pressure level from 40°C to 80°C to lower superheating, averagely from 15 K to 8 K. This fact was in good agreement with the existing theories, which predicted lower necessary superheats with increasing system pressure. The comparison of the microgravity nucleate boiling curves and the normal gravity nucleate boiling curves yielded interesting results. At each fluid temperature of 60 °C and 80 °C the heat transfer under microgravity showed almost no difference to the heat transfer under normal gravity. At the saturation fluid state of 40 °C the heat transfer coefficients under microgravity were even up to 20-30 % higher compared to the reference heat transfer coefficients measured on earth. This indicated that the heat transfer under microgravity was more efficient. These observation confirmed our previous findings /8,11,13/ that the influence of the gravity level in the nucleate boiling regime is neglectable.

In any case it is obvious that the influence of the gravity level on the heat transfer is not correlated very well by equations developed for boiling heat transfer under earth gravity. The usage of the well known correlation from Rohsenow /9/ at the same fluid states, heater geometries and at same heater conditions yields the following influence of system acceleration, respectively the gravity level.

$$\frac{\dot{q}_{\mu g}}{\dot{q}_{1g}} = \left(\frac{a}{g}\right)^{\frac{1}{2}} \qquad (5)$$

Measurements during the shuttle flight showed that the average residual gravity a/g is about 10^{-4} and lower. Equation (5) predicts that the heat flux therefore should decrease to 1 % of its normal gravity value. The boiling curves clearly show that this was not the case at all, even for the small geometries. Therefore it seemed that probably the interfacial tension and the wetting characteristics are the more dominant mechanisms than the gravity induced buoyancy and can replace the buoyancy induced convection easily. A more detailed discussion of these effects can be found in /8,11/. In case of the boiling curve at 40°C it also seems that the gravity hems the heat transfer process somehow. This could be explained with the following fact. Due to the absence of buoyancy induced convection the thermal boundary layer under microgravity at the heaters surface is thicker compared to earth gravity and the superheat higher. Therefore the boiling process under microgravity sets in at lower heat fluxes, since the excess heat has to be transported by pure conduction. Therefore while under earth gravity conditions the heat transfer is still managed by convection and conduction, under microgravity boiling is already established. This could explain why the heat transfer coefficient is higher under microgravity in the region of low heat fluxes. Concerning higher heat fluxes, where both under microgravity and earth gravity the boiling process is established, the better heat transfer can be explained by the heater area, the boiling process takes place on. Since under normal gravity the excess heating power is transferred to the surrounding liquid by evaporation and conduction, certain local surface areas are still not in the nucleate boiling regime. In contrast to this almost the complete surface area under microgravity is affected by the vigorous boiling process. Taking all this into account a slightly higher heat transfer coefficient at higher heat fluxes under microgravity could be explained.

Subcooled liquid state:

For the saturated liquid state at 70 °C the subcooled boiling heat transfer data has been evaluated for the large plate heater along the isobaric line of p = 3.79 bar (corresponding to 70 °C saturation state), **Fig 4.**

With increasing liquid subcooling the wall superheat ΔT_{sat} was reduced, as predicted by theory. Again the heat transfer coefficient under microgravity and normal earth gravity showed no remarkable deviation. In contrast to the saturated liquid states the light sheet and the interferometric images showed that under microgravity with increasing subcooling of the liquid a strong thermocapillary flow developed, which supported the heat removal away from the surface of the heater, see **Fig 5.**

Therefore it seemed that under subcooled conditions other mechanisms on the boiling process besides the interfacial tension and the wetting characteristic became important. The

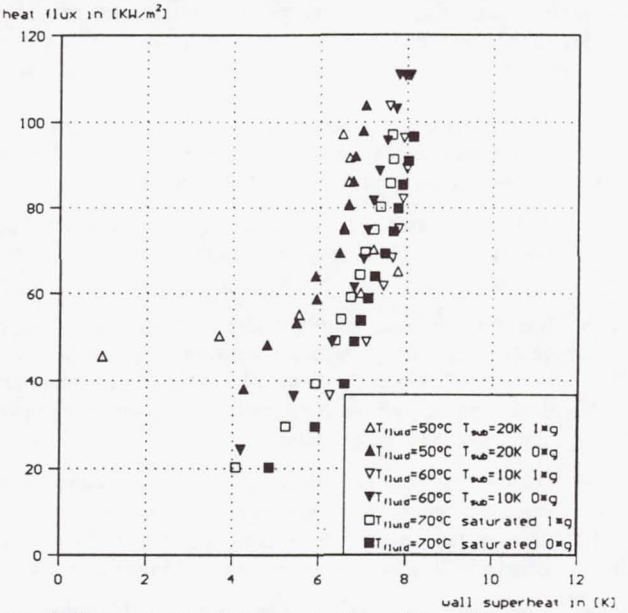

Fig..4: Subcooled boiling on the Large Plate Heater

development of this thermocapillary flow originated in surface tension gradients from the bubbles base to the bubble top, and was totally independent of gravity.

Resulting from the experiments it can be stated that the gravity induced buoyancy still is not the primary mechanism responsible for the boiling process. In subcooled liquid states this strong thermocapillary flow could be one of the reasons for the not predicted efficient heat transfer. Further evaluation of the particle image velocimetry, which are under evaluation right now should improve the understanding of the importance of this

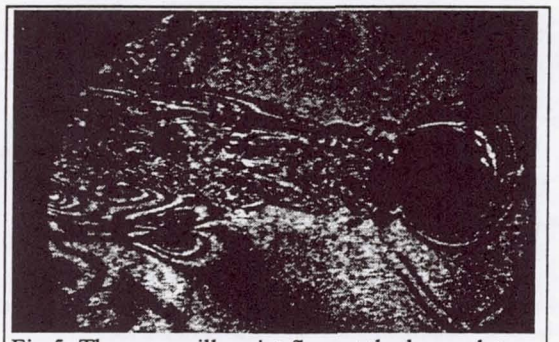

Fig.5: Thermocapillary jet flow at the large plate heater

thermocapillary flow.

CONCLUSIONS

From these boiling experiments at saturated and subcooled liquid conditions performed at small heaters under microgravity and earth gravity the following conclusions can be obtained.

- The boiling process seemed to be almost independent of the system acceleration, respectively the gravity level. This fact is consistent with earlier microgravity experiment.
- The gravity based buoyancy is deemed as a parameter of the boiling system with only small influence in the nucleate boiling region.
- Interfacial tension, capillary forces momentum of vapor generation, wetting behavior between solid surfaces and liquid and vapor, and in subcooled fluid states the thermocapillary jet are considered as the main mechanisms in the nucleate boiling regime.
- For the first time in boiling study the thermocapillary jet mode was observed for moderate subcooling states and the flow pattern could be studied by the utilization of differential interferometry and particle image velocimetry.
- Even under microgravity boiling is a very efficient process of heat transfer. Moreover the boiling process is self-stabilizing, since a strong increase in the heat flux only leads to a moderate increase of the wall temperature, as long as the boiling process is maintained in the nucleate boiling regime. Therefore the boiling process would allow a very fail-safe application for direct immersing cooling of high powered electronic microelements in all space systems. For these kind of applications the liquid conditions like fluid temperature and pressure level can easily be adapted.
- The final evaluation should allow more detailed statements of the boiling process, since during the mission a wide variety of fluid states with five different geometries could be studied.

This report describes only a few preliminary results from the LMS mission. The evaluation of the data is still going on. Detailed qualitative and quantitative correlations, which combine measured heat-flux, wall temperature and fluid state with the observed bubbles sizes and flow-patterns, will be generated.

FUTURE PLANS

The experimental work will be continued under earth gravity. The same hardware and refrigerant, which were used during the mission will be utilized for continued laboratory experiments, where the influence of the heater surface orientation in respect to the vector of the system acceleration on the boiling process will be investigated and finally compared with the results from the LMS mission.

NOMENCLATURE

a	acceleration
g	earth gravity
p	pressure
$\dot{Q}$	heat flux
r	radius
R	thermal resistance
T	temperature

Greek Symbols

α	heat transfer coefficient
λ	thermal conductivity
σ	surface tension
μg	microgravity

Subscripts

g	glass
i	center (inner core)
l	liquid
sat	saturation
sub	subcooled
w	wall
α	heat transfer
λ	heat conduction

LITERATURE

/1/ Johannes Straub, Gerold Picker, Marcus Steinbichler,Josef Winter and Martin Zell; *Heat Transfer and Various Modes Of Bubble Dynamics On A Small Hemispherical Heater UnderMicrogravity and 1g Condition;Eurotherm Seminar No. 48,Ed. D.Gorenflo ,D.B.R. Kenning, Ch. Marvillet,1996, pp. 265-275*

/2/ Johannes Straub; Gerold Picker; Martin Zell; *Study of Vapor Bubble Growth in supersaturated liquid;* Proc. 30th Nat. Heat Conf. 1995 Portland USA, Vol. 3,pp. 29-37, Eds.: S.S. Sadhal et al

/3/ Kazuyoshi Fushinobu, Takao Nagasaki, Tadashi Saitoh, Atsushi Ui and Kunio Hijikata; *Boiling Heat Transfer Characteristics from very small heaters on a substrate;* Heat Transfer 1994 Proc of the 10th Int. Heat Conf. Brighton U.K., Vol. 5, pp. 51-56, Ed. by J. Hewitt

/4/ Baker, E.; *Liquid Immersion Cooling of Small Electronic Devices;* Microelectronics and Reliability, 1973, Vol. 12, pp. 163-173

/5/ Bar-Cohen, A.; *Fundamentals of Nucleate Pool Boiling of Highly-Wetting Dielectric Liquids;* ASI Proceedings, Cooling of Electronic Systems, Izmir, Turkey, 1993, pp. 415-455, Ed. by S. Kakac

/6/ Bergles, A. E. & Bar-Cohen, A; *Immersion Cooling of Digital Computers;* ASI Proceedings, Cooling of Electronic Systems, Izmir, Turkey, 1993, pp. 539-621, Ed. by S. Kakac

/7/ Nagasaki, T., Hijikata, K., Fushinobu, K., & Saitoh, T.; *Boiling Heat Transfer from a Small Heating Element;* 3, ASME Winter Annual Meeting, New Orleans

/8/ Straub, J., Zell, M., and Vogel, B.; *Pool Boiling in a Reduced Gravity Field;* Proc. Ninth Int. Heat Transfer Conf., Jerusalem, Israel, 1990, Ed. G. Hetsrony, Vol. 1, pp. 91-112, Hemisphere, New York 1990

/9/ Forster, H. K., Zuber, N.; *Dynamics of Vapor Bubbles and Boiling Heat Transfer;* AICHE J., vol. 1, 1955, pp. 531 - 534

/10/ Rohsenow, W. H.; *A Method of Correlating Heat Transfer Data for Surface Boiling of Liquids;* Trans. ASME Ser. C, J. Heat Transfer 74, pp. 969-976

/11/ Straub, J.; *The Role of Surface Tension for Two-Phase Heat and Mass Transfer in the Absence of Gravity;* Experimental Thermal and Fluid Science 1994, 9, pp. 253-273

/12/ Bakrhu, N., Lienhard, J. H.; *Boiling from small cylinders;* Int. J. Heat Mass Transfer 1972, vol. 5, pp. 2011-2025

/13/ Johannes Straub, Stefan Micko; *Boiling On A Wire Under Microgravity Condtions - First Results From A Space Experiment Performed In May 1996; Eurotherm Seminar No. 48,Ed. D.Gorenflo,D.B.R. Kenning, Ch. Marvillet,1996, pp. 275-282*

ACKNOWLEDGMENT

We like to express our appreciation to all, who made this research possible. Especially we are grateful to the Space Shuttle crew of STS 78, NASA headquarters, the mission manager, the mission scientist and the team of NASA Operation Support Center in Huntsville, AL, to ESA and ESA/ESTEC for providing the BDPU facility and the test container, the individuals of the industrial companies designing and building the facility and the test container of Alenia, Laben, Ferrari and Dornier. Furthermore we thank all individuals and teams supporting us during the mission and we gratefully acknowledge the support of the Germany Space Agency DARA in the contract 50 WM 9566.

Science Report on the LMS mission (BDPU, TC3-Straub).

Boiling on a miniature heater - A simulation for cooling of small electronic devices under microgravity

During the boiling experiment on six small heaters of different geometry about 300 single experiment cycles were conducted at 9 different fluid temperatures, ranging from 30°C to 120°C. At each fluid temperature a variety of fluid pressures (saturated and subcooled) were investigated with each of the available heaters. Besides the study of boiling phenomena we investigated the nucleation on small heating elements with low heat fluxes. Especially the optical images, combined with the electronical data showed surprising effects, which were not observed ever before. The real time particle image velocity processing confirmed these effects. The boiling heat transfer presented in common literature of heat transfer, used for the design of heat exchangers, predicts a strong influence of gravity on the heat transfer process. In contrast to the present state of art our findings showed, that under microgravity the boiling heat transfer is still as efficient as under normal earth gravity. In contrast to the existing theory our findings show that the influence of earth gravity is less than predicted, and the heat transfer in a microgravity environment is still as efficient, sometime seven more efficient than in the environment at normal gravity. A possible reason for this could be the strong stream flow which develops at certain fluid states around the heating elements. It was the first time that this strong stream flow could be observed and studied as functions of liquid parameters and heat fluxes. This stream flow causes a strong pumping effect without any mechanical parts carrying away the heat produced by our heating elements. Generally it can be stated, that these new results could lead to new theories, which describe the boiling process more accurately than existing theories, and will provide a further advance in the calculation and design of heat exchangers for application on earth and in space.

Bubble, Drop and Particle Unit (BDPU)

Thermocapillary Migration and Interactions of Bubbles and Drops

Principal Investigator:

Dr. Shankar Subramanian
Clarkson University
Potsdam, New York

Thermocapillary Migration and Interactions of Bubbles and Drops

Principal Investigator: R. Shankar Subramanian, Clarkson University, U.S.A.
Co-Investigators: R. Balasubramaniam, NASA Lewis Research Center and
Günter Wozniak, Bergakademie Freiberg, Germany
Team Member: Peer H. Hadland, Clarkson University, U.S.A.

Summary

Experiments were performed aboard the LMS mission of the Space Shuttle in summer 1996 in the BDPU on isolated air bubbles and Fluorinert FC-75 drops as well as on interacting bubbles/drops migrating in a temperature gradient in a Dow-Corning DC-200 series silicone oil of nominal viscosity 10 centistokes. The data, recorded in the form of videotape images as well as cine images in selected runs, have been analyzed. Preliminary results are reported here. The behavior of the isolated objects is consistent with earlier observations made aboard the IML-2 mission while the range of Reynolds and Marangoni numbers has been extended substantially over that in the IML-2 experiments. Results on interacting drops and bubbles display interesting and unanticipated features. In some experiments, drops are found to follow a sinuous three-dimensional trajectory. In others, trailing drops and bubbles are found to move off the axis of the cell when migrating behind a leading drop or bubble which moves along the axis. In this type of run, if the trailing drop is sufficiently large, it is found to pass the leading drop. It is conjectured that this behavior of the trailing objects is influenced by the thermal wake behind the leading object. Also, since Fluorinert dissolves in silicone oil to some extent it is possible that the composition wake left by a drop, which takes a long time to dissipate, influences the motion of drops that are injected subsequently. Finally, behavior similar to that observed in IML-2, namely that a small leading drop slows the movement of a larger trailing drop moving along the cell axis, was observed as well.

1. Objectives

The objectives of this flight experiment were to conduct a detailed exploration of interactions between pairs of bubbles and pairs of drops, to determine velocity distributions by the use of tracer particles in the case of bubble motion, and finally to explore the motion of isolated bubbles and drops for parameter values beyond those which could be reached in prior IML-2 experiments.

2. Background

When a drop or bubble is introduced into a second fluid in which there exists a temperature gradient, the drop (or bubble is implied from hereon) will move (1). Such motion is a consequence of the variation of the interfacial tension along the interface

between the drop and the continuous phase. Reviews of the literature on this subject may be found in Wozniak *et al.* (2) and Subramanian (3). This movement is termed thermocapillary migration, and can be important in materials processing in space, and in separation processes used in long duration space excursions for recycling and on the surface of the moon.

The speed at which a drop migrates can be obtained by solving the governing continuity, Navier-Stokes, and energy equations along with the associated boundary conditions. When convective transport effects are important, the problems are nonlinear. The relative importance of convective transport of energy when compared to conduction can be judged from the magnitude of the Péclet number whereas a similar ratio for momentum transport is described by the Reynolds number, Re. When a velocity scale characteristic of thermocapillary migration is used, the Pèclet number is known as the Marangoni number, Ma. The Capillary number also is another parameter that influences the shape of the drop. However, shape deformations were difficult to detect from the video and cine images from the LMS experiments. The definitions of the Reynolds and Marangoni numbers are given below.

$$\mathrm{Re} = \frac{R v_0}{\nu} \tag{1}$$

$$Ma = \frac{R v_0}{\kappa} \tag{2}$$

Here, R is the radius of the drop, ν the kinematic viscosity of the continuous phase, and κ its thermal diffusivity. The reference velocity, v_o, is defined below.

$$v_0 = \frac{|\sigma_T||\nabla T_\infty| R}{\mu} \tag{3}$$

In the above, μ is the dynamic viscosity of the continuous phase, σ_T is the rate of change of interfacial tension with temperature, and ∇T_∞ is the temperature gradient imposed in the continuous phase fluid.

In the linear limit when the Reynolds and Marangoni numbers are negligible, the contribution of thermocapillarity can be extracted from experiments on the ground. Therefore, experiments designed to explore thermocapillary migration on the ground are subject to this important limitation; some of this experimental work is discussed in references (2,3).

To better explore the parameter space in the Reynolds and Marangoni numbers than is possible on the ground, investigators have attempted to carry out experiments in reduced gravity conditions. The previous studies, as discussed by us in Balasubramaniam *et al.* (4), were subject to many limitations which raise questions regarding the utility of the data. Therefore, in summer 1994, we performed thermocapillary migration experiments in reduced gravity under conditions closer to those assumed in theoretical models. We used air bubbles and Fluorinert FC-75 drops migrating in a Dow-Corning DC-200 series silicone oil of nominal viscosity 50

centistokes. The apparatus in which the experiments were performed was the Bubble, Drop, and Particle Unit (BDPU) built under the auspices of the European Space Agency. Our experiments, carried out aboard the IML-2 mission of the Space Shuttle, yielded good data on isolated drops up to a Reynolds number of 0.85 and a Marangoni number of 280, and on isolated bubbles up to a Reynolds number of 2.2 and a Marangoni number of 810. In the case of air bubbles, the data were found to be generally consistent with our predictions from a numerical solution of the governing equations as well as an asymptotic theoretical result obtained by Balasubramaniam and Subramanian (5). Also, we were able to perform preliminary experiments on pairs of drops injected one after the other along the long axis of the test cell. These drops migrated along the axis, and we made the remarkable observation that a relatively small leading drop can significantly slow down a larger trailing drop while itself moving as though it is unaffected by the large drop. We hypothesized that this was a consequence of the thermal wake behind the leading drop which is a region of weakened temperature gradient. The fluid in the wake will wrap around the trailing drop and can cause the driving force for the motion, which is the temperature variation over its surface, to be reduced.

In an attempt to explore further the interactions between pairs of drops and pairs of bubbles and to extend the range of values of Marangoni and Reynolds numbers, we performed follow-on flight experiments aboard the LMS mission of the Space Shuttle in summer 1996. The same fluids, air and Fluorinert FC-75, were used for the bubble and drop phases, respectively, and a silicone oil of nominal viscosity 10 centistokes was employed for the continuous phase. This choice was made so as to be able to extend the maximum Marangoni number by approximately a factor of 5, and the corresponding maximum Reynolds number by a factor of approximately 25. Also, tracer particles dispersed in the silicone oil were used in the air bubble migration experiments in order to track the flow in the continuous phase during the migration process. In addition, the Point Diffraction Interferometry (PDI) system used in IML-2 was refined by the European Space Agency to incorporate a Wollaston Prism with a divergence angle of 10 degrees, so that interferometry was able to provide quantitative information on temperature fields in the LMS experiments involving gentle temperature gradients. Except for these modifications, the procedures and the experiments were similar to those in IML-2, described in the final report for that flight experiment (6). A secondary objective of the LMS experiments was to gather data at small values of the Marangoni number; the IML-2 data on air bubbles showed significant departure from theoretical predictions in the range 5-40. However, this proved difficult to accomplish because of the reduced viscosity of the liquid and poor communication conditions with the Shuttle (resulting in frequent loss of Real Time TV coverage and commanding capabilities) during the low temperature gradient run in which this objective was to have been accomplished.

3. Methods of Data Acquisition and Analysis

The experiments were performed in the BDPU which was provided by the European Space Agency through a cooperative arrangement with the National Aeronautics and Space Administration. The apparatus consists of a "facility" which provided power, optical diagnostics and illumination, imaging facilities including a

video camera and a motion picture camera, and other sundry support services. Within this facility, a test cell that was specific to the experiment was inserted by the payload specialist on the Shuttle when needed.

Conceptually, the experiments were simple. Within a test cell mounted in the facility and filled with a suitable liquid, a temperature gradient was established, followed by the introduction of a bubble or a drop as desired. The subsequent motion of the object, in the direction of the applied temperature gradient, was recorded for later analysis on videotape on the ground as well as on cine film on board the Shuttle in selected experiments. When a bubble or drop reached the hot wall, it was extracted and another was introduced after a small waiting period.

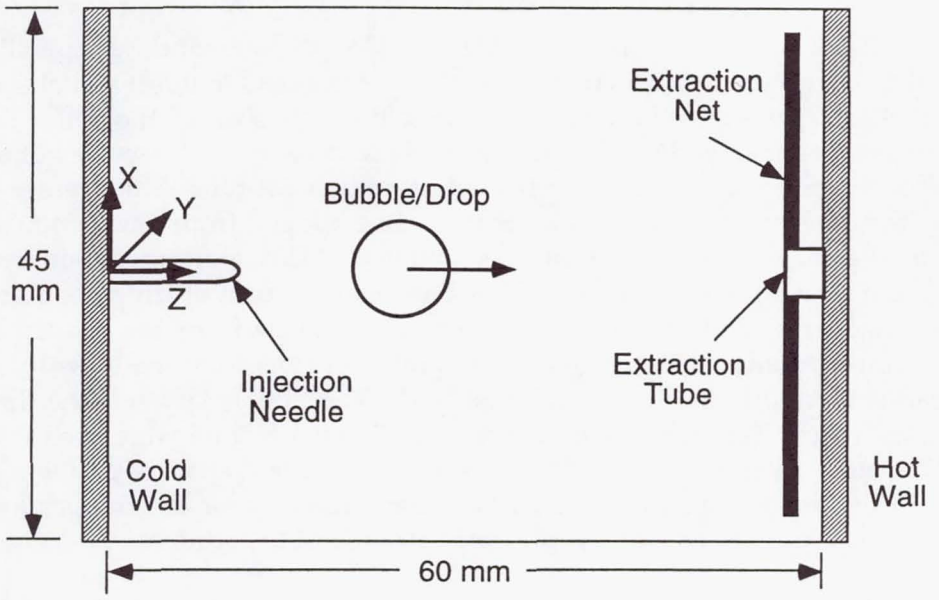

Figure 1. Schematic of Test Cell

The heart of the experimental apparatus is the test cell shown schematically in Figure 1. Two rectangular test cells were available. Both were of identical dimensions, measuring 60 x 45 x 45 mm in the interior. This cavity was filled with a Dow-Corning DC-200 series silicone oil of nominal viscosity 10 centistokes in both cells. As mentioned earlier, the silicone oil in the bubble cell contained a small concentration of tracer particles provided by Dornier GmbH from Germany. It was possible to maintain the two end walls (made of aluminum) in the long dimension of the cell at fixed known temperatures so that a temperature gradient could be established in the z-direction. Within the cavity, an injection needle was available when needed. When not in use, the tip was flush with the cold aluminum surface at its center. It was possible to introduce air bubbles in one test cell, and Fluorinert FC-75 drops in the other cell. The diameters of the bubbles varied from approximately 1.3 to 14.4 mm, and those of drops ranged from 2.1 to 14.3 mm. After a bubble or drop completed its traverse, it was possible to extract it from the hot wall using an extraction tube mounted at the center of a net.

The equipment provided red background illumination and the opportunity to capture images of the interior of the test cell on videotape on the ground. Also, a limited amount of cine film was available, and was used to capture images during selected runs at suitable framing rates.

In any given run, the procedure was first to establish the desired temperature gradient over a period of 2 hours. This period included approximately 30 minutes in which the liquid in the cell was stirred by back and forth movement of the net, followed by a quiescent period lasting approximately 90 minutes. This was followed by the injection, traverse, and subsequent extraction of bubbles or drops. At low temperature gradients, interferometry images received on the ground were used as a diagnostic tool to determine when the temperature field became steady.

At the end of the heating period, when real time TV and commanding capability were available, the experiment was initiated by sending a command to inject a bubble or drop of a specified size at a specified position along the long axis of the cell. The traverse of the object was followed on the ground while recording it. When the bubble reached the opposite wall, it was usually extracted using a small tube at the center of that wall. After the passage of a sufficient amount of time, judged from interferometry images where available, the next injection was initiated. This waiting period was usually of the order of 3 minutes. For a pair of bubbles or a pair of drops, suitable commands were packaged and sent up to the apparatus to perform the sequential double injection automatically. When a sufficient number of runs were made with one temperature gradient, another gradient was employed. The bubble cell and the drop cell were each used twice. Temperature gradients of 0.33 and 1 K/mm were used with bubbles, and 0.25 and 1 K/mm with the drops. A run with a temperature gradient of 0.067 K/mm with the bubble cell yielded no usable data due to poor communications between the orbiter and ground caused by the "safe" attitude of the orbiter.

A total of 64 bubble runs and 74 drop runs were recorded on videotape, and 35 bubble runs and 38 drop runs on cine film. Of these, 53 bubble runs and 67 drop runs were analyzed. The rest either contained objects too small to be measured precisely or presented other problems that precluded analysis. A sufficient number of runs were made on isolated drops and bubbles to extend the range of Reynolds and Marangoni numbers beyond those encountered in the IML-2 experiments. The remaining experiments focused on interacting drops and bubbles. While we introduced pairs of bubbles and pairs of drops deliberately in selected runs, sometimes a collection of two or more objects was introduced by the injection system even when the objective was to inject a single object.

4. Results and Discussion

4.1 Isolated Bubbles and Drops

One of the objectives in performing experiments on isolated drops and bubbles was to look for shape deformation. Deformation would be most likely to occur in the case of large bubbles and drops which moved very rapidly. The video and cine images

were analyzed using an automated computerized system developed by NASA Lewis Research Center. This worked by selecting single frames and tracking the boundary of the object involved. For rapidly moving objects, the image on a single frame was sufficiently blurred in the direction of motion that any deformation could not be measured due to the uncertainty in the measurement of the diameter in that direction. In cases where both diameters could be measured precisely, they were found to be equal to each other to within the uncertainty of the measurement.

Since the position of the objects was followed throughout the traverse it was possible to calculate the velocity at various locations in the cell. The velocity changed during the traverse because of the initial acceleration of the bubble or drop upon release from the injector as well as due to the change of physical properties (principally viscosity) with temperature. Therefore, the velocity was never truly steady for any given bubble or drop. In the case of bubbles, a quasi-steady velocity can be expected to be achieved after the bubble has moved a distance equal to its own diameter. We selected data near the center of the cell as being the best to present. In the case of drops, a quasi-steady state would be achieved only when a quasi-steady temperature gradient field is established within the drop. This restriction resulted in obtaining quasi-steady velocities of drops only up to approximately 6 mm in diameter. In the case of larger drops, the data must be considered transient throughout the run. For a drop of diameter 6 mm, it was necessary to obtain data a bit beyond the center of the cell in order to assure that a quasi-steady had been reached. In the isolated bubble runs, the Reynolds number varied from 0.8 to 87 while the corresponding Marangoni number ranged from 51 to 5800. In the case of the drops, the range of Reynolds number was 0.14 to approximately 10 and the corresponding range of Marangoni number was 14.6 to approximately 600.

In Figure 2, the velocity data on isolated air bubbles are plotted in scaled form and compared with available predictions. The velocity of a bubble is scaled using the velocity it would have in the limit of negligible values of the Reynolds number and the Marangoni number given in reference (1). The various physical properties are evaluated at the estimated temperature in the undisturbed fluid at the x-y plane containing the center of the bubble. Typical uncertainty estimates are shown in the figure. Also shown on the same drawing are data from IML-2 experiments. Note that the data are consistent with those obtained during the IML-2 mission while covering a wider range of values of the Marangoni number. Included in the drawing for comparison is a theoretical prediction obtained from a finite difference solution of the governing continuity, momentum, and energy equations for the quasi-steady velocity and temperature fields and bubble velocity (7). The model also assumes a spherical bubble in an infinite extent of fluid, and Newtonian and incompressible flow with constant physical properties, except for the interfacial tension which is assumed linear with temperature. Also included is our prediction in the asymptotic limit of large Marangoni number for negligible Reynolds number. It is evident from Figure 2 that the data support the qualitative trend predicted from the quasi-steady theory.

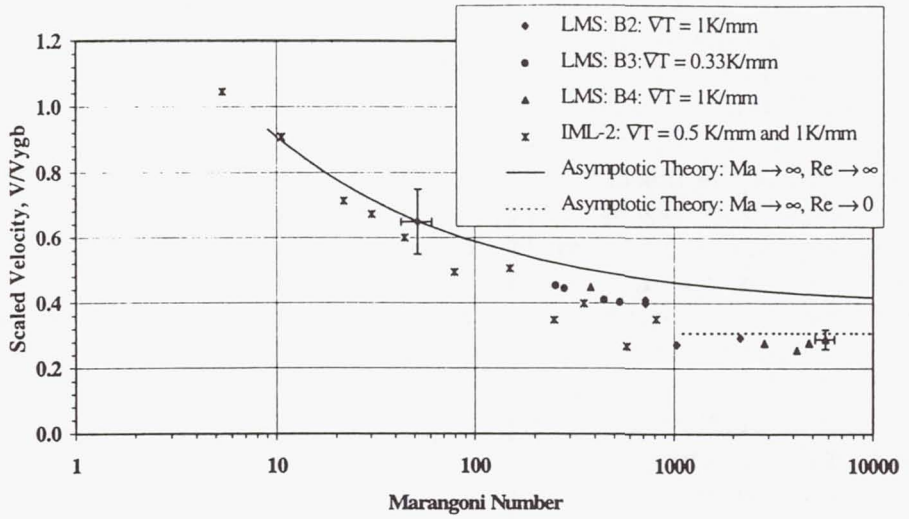

Figure 2. Scaled velocity of isolated bubbles plotted against the Marangoni number and compared with IML-2 data and results from two asymptotic theoretical predictions for large values of the Marangoni number. The reference velocity used for scaling is the value expected when convective transport effects are negligible.

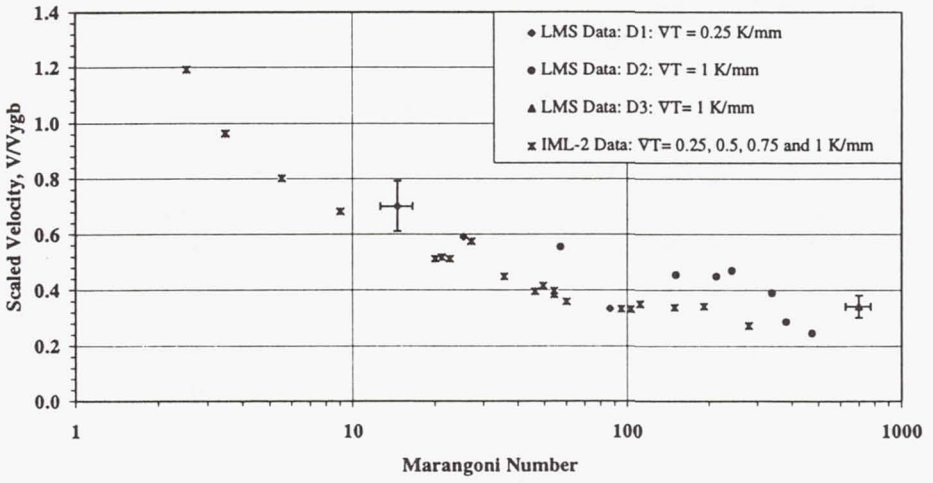

Figure 3. Scaled velocity of isolated drops plotted against the Marangoni number and compared with IML-2 data. The reference velocity used for scaling is the value expected when convective transport effects are negligible.

In Figure 3, we show a drawing similar to Figure 2, but for Fluorinert FC-75 drops. These data display a trend very similar to that shown by bubbles in Figure 2. The reference velocity is once again the predicted velocity at negligible values of Reynolds and Marangoni number from reference (1). Again, the IML-2 data are included for comparison purposes. At present, no theoretical predictions are available for comparison with these data.

4.2 Interacting Drops and Bubbles

One of the principal objectives of the LMS experiments was to explore interactions between pairs of bubbles and pairs of drops. Therefore, several runs were made in which such pairs were deliberately introduced. When a small bubble follows a large bubble, the leading large bubble moves away so rapidly that it is not possible to observe any significant interaction effects between the two objects; the same holds true for drops. Therefore, virtually all the usable interaction runs were of the type where a small leading drop/bubble was followed by a larger object.

While we indeed observed behavior similar to that in IML-2 experiments on pairs of drops as mentioned earlier, we shall focus here on some remarkable new observations. First, in several experiments we observed a leading bubble or drop moving straight along the axis of the cell while a trailing object released a small distance behind the leader moved away from the axis in the positive or negative x-direction in Figure 1. This movement was typically only by a few mm in that direction but was clearly measurable. We observed the same behavior on the part of bubbles as well as drops. In some other experiments on Fluorinert drops we found even more interesting behavior. In the very first drop run, when we attempted to inject a single drop, four drops were introduced instead by the injector. The first of these moved straight along the axis of the cell, deviating from that axis only by about 0.5 mm by the time it reached the hot wall. However, the second drop was found to execute a three dimensional trajectory which may be described as sinuous for lack of a better term. The movement of this object was principally in the direction of the applied temperature gradient. However, it was evident from the video image that the object moved back and forth in the x-direction as it moved along the z-axis. In addition, the interferometry view of this run revealed the object also moved back and forth in the y-direction in the same manner. However, this motion in the y-direction began initially in phase with that in the x-direction, but after about two oscillations, fell out of phase so that the trajectory can be visualized as evolving into a helix. The third object also began its movement in a manner similar to that of the second object, but its oscillations were larger in amplitude. The fourth drop was very small and exhibited somewhat similar behavior.

The above fascinating behavior on the part of interacting drops was not confined to the first run. With the same temperature gradient, we observed four experiments in which the pattern was observed. In two of these runs, even the leading drop exhibited sinuous motion.

Explaining the behavior of interacting drops is not trivial. Clearly the wake of the first object must play an important role in causing it. One can envision a thermal wake behind the leading object in the case of both the bubble and drop experiments.

This is a relatively thin region in which the temperature field is presumably axisymmetric and the temperature gradient is weaker than that in the undisturbed fluid. Whereas in IML-2, the trailing drop moved straight along the axis when influenced by this wake, in some LMS experiments, it appears that slight asymmetries in the positioning of the second object with respect to the wake caused the fluid in the wake to wrap around this object asymmetrically; in turn, this must have led to an asymmetry in the temperature gradient distribution on its surface which must have caused the resulting movement away from the axis of the cell. The more interesting sinuous behavior is also more difficult to explain because it involves a somewhat periodic return of the object to the axis and movement past the axis in the other direction. Since this was only observed in the drop runs, it also is possible that the dissolved Fluorinert FC-75 in the silicone oil is playing some role. If one assumes thermodynamic equilibrium corresponding to the prevailing temperature at each location on the drop surface, then dissolved FC-75 should not make any difference to the interfacial tension gradient on the drop surface and one must look beyond this for explanations. Another important difference is that thermal diffusion is much more rapid than species diffusion in the silicone oil; one can expect a difference of two orders of magnitude between the two diffusivities. This suggests that thermal wakes would dissipate relatively quickly and composition wakes would take much longer to do so. Since the sinuous paths were indeed noted even with a leading object in a run wherein there was a long wait after the previous run, thermal wakes are less likely to be the reason for the occurrence of these trajectories.

4.3 Diagnostics

In runs involving gentle temperature gradients, interferometry images using the PDI system with a Wollaston Prism were successfully received on the ground and recorded on videotape. The PDI system failed to provide any useful information in runs at the higher gradients. Also, in the drop experiments, the very first drop left a trail of dissolved Fluorinert FC-75 in its wake. The numerous fringes due to the refractive index gradients resulting from the composition variations made the interpretation of later interferometry images from the drop cell for temperature field information not possible. The best bubble run for interferometry was analyzed by G. Wozniak and his students at Bergakademie Freiberg and the resulting temperature field was found to be qualitatively consistent with that one would expect. Quantitative comparisons still need to be performed when predictions are made for this run. The best drop run was that involving the very first drop. Even this run shows problems in the interpretation behind the drop due to the wake of dissolved Fluorinert. However, in the forward portion of the domain in the direction of movement of the drop, the field is qualitatively as expected.

In some selected runs, tracer particles were illuminated using a laser light sheet and their movements recorded on videotape. These images need to be analyzed using an automatic system at NASA Lewis Research Center. We intend to perform this analysis as soon as proper training is received in the use of the analysis system.

5. Conclusions and Future Plans

This is a preliminary report based on observations made on isolated and interacting bubbles and drops moving in a temperature gradient under reduced gravity conditions in the LMS mission. The results for the migration velocity of isolated air bubbles qualitatively extend the range of values of the Marangoni number investigated in earlier IML-2 flight experiments. The data are consistent with those from IML-2 and with theoretical predictions. The data on isolated drops display similar trends even though theoretical predictions are not yet available for comparison. Experiments on multiple drops and bubbles show evidence of wake effects from a leading object. In some cases, the trailing bubble or drop moves off the axis of the cell; large trailing drops pass the leading drop in this way. In other experiments, trailing drops exhibit a sinuous three-dimensional trajectory. It is conjectured that these types of behavior, which imply non-axisymmetric fields, may be caused by a combination of factors arising from the thermal and compositional wakes from the leading drop working in conjunction with slight asymmetries. The data on runs involving tracer particles remain to be analyzed using the automatic analysis system at NASA Lewis Research Center.

6. Acknowledgments

The work described herein was supported by NASA's Microgravity Sciences and Application Division through NASA Grant NAG3-1122 from the Lewis Research Center to Clarkson University. Also, support by the German Space Agency (DARA) through DARA Grant 50WM9582-0 to G. Wozniak is gratefully acknowledged.

7. Bibliographic Citations of Articles/Presentations Resulting from the Flight

Articles in preparation

"Thermocapillary Migration of Isolated Bubbles and Drops at Relatively High Marangoni number in Reduced Gravity, " by P.H. Hadland, R. Balasubramaniam, G. Wozniak, and R.S. Subramanian.

"Interactions among Drops and among Bubbles Undergoing Thermocapillary Migration," by R. Balasubramaniam, P.H. Hadland, G. Wozniak, and R.S. Subramanian.

"Temperature and Flow Fields around Bubbles Executing Thermocapillary Motion," by G. Wozniak, R. Balasubramaniam, P.H. Hadland, and R.S. Subramanian.

Presentation

"Thermocapillary Migration of Drops and Bubbles in Reduced Gravity – Preliminary Results from LMS Flight Experiments," P.H. Hadland, R. Balasubramaniam, G. Wozniak, and R.S. Subramanian, Poster Presentation at the Gordon Conference on Gravitational Effects in Physicochemical Systems, Henniker, NH, June 1997.

8. References Cited

1. N. O . Young, J. S. Goldstein, and M. J. Block: The motion of bubbles in a vertical temperature gradient, J. Fluid Mech., Vol. 6, 1959, pp. 350-356.

2. G. Wozniak, J. Siekmann, and J. Srulijes: Thermocapillary Bubble and Drop Dynamics Under Reduced Gravity --- Survey and Prospects, Z. Flugwiss. Weltraumforsch, Vol. 12, 1988, pp. 137-144.

3. R. S. Subramanian: The Motion of Bubbles and Drops in Reduced Gravity, in Transport Processes in Bubbles, Drops, and Particles, edited by R. Chhabra and D. De Kee, Hemisphere, New York, 1992, pp. 1-41.

4. R. Balasubramaniam, C.E. Lacy, G. Wozniak, and R.S. Subramanian: Thermocapillary Migration of Bubbles and Drops at Moderate Values of the Marangoni Number in Reduced Gravity, Phys. Fluids, Vol 8, No. 4, 1996, pp. 872-880.

5. R. Balasubramaniam and R.S. Subramanian: "Thermocapillary Bubble Migration -- Thermal Boundary Layers for Large Marangoni Numbers," Int. J. Multiphase Flow, Vol. 22, 1996, pp. 593-612.

6. R. S. Subramanian, R. Balasubramaniam, C.E. Lacy, and G. Wozniak: "IML-2 Final Science Report on Thermocapillary Migration and Interactions of Bubbles and Drops."

7. R. Balasubramaniam and J. E. Lavery: Numerical Simulation of Thermocapillary Bubble Migration Under Microgravity for Large Reynolds and Marangoni Numbers, Num. Heat Transfer A, Vol. 16, 1989, pp. 175-187.

Thermocapillary Migration and Interactions of Bubbles and Drops

Principal Investigator: R. Shankar Subramanian, Clarkson University, U.S.A.
Co-Investigators: R. Balasubramaniam, NASA Lewis Research Center and
Günter Wozniak, Bergakademie Freiberg, Germany
Team Member: Peer H. Hadland, Clarkson University, U.S.A.

Brief non-Technical Summary

Drops and bubbles will be encountered in various materials processing applications in reduced gravity as well as in the recycling of life-sustaining substances such as water and oxygen in long-duration space excursions. On the Earth, drops and bubbles move due to the action of gravity. In reduced gravity, other mechanisms will be developed for moving these objects when needed. For instance a temperature gradient can be used to move a drop. The variation of temperature around the periphery of the drop causes gradients of interfacial tension which act to move the fluid around the drop and by reaction the drop migrates typically toward warm fluid. This is known as thermocapillary motion.

Experiments were performed aboard the LMS mission of the Space Shuttle in summer 1996 in the BDPU on air bubbles and Fluorinert FC-75 drops migrating in a temperature gradient in a Dow-Corning DC-200 series silicone oil. The movement was recorded on videotape and cine film and analyzed frame-by-frame later on the ground. Also, interferometry images were recorded on video and analyzed for the temperature distribution around the moving bubbles. The results on the motion of single bubbles or drops are consistent with those from our earlier experiments on the IML-2 mission in summer 1994 and permit us to extend the range of the relevant parameters. These results also are in general agreement with available theoretical predictions. In the case of interacting bubbles or drops, we observed very interesting physical behavior which was not seen in our earlier flight experiments. It was found that a bubble will sometimes move away from the axis of the cell when trailing a small leading bubble. If it is sufficiently large, it will pass the leading bubble. The same behavior was observed in the case of drops. In addition, we found in some experiments that drops followed a three-dimensional trajectory which resembles a helix. These phenomena appear to be due to complex effects arising from the thermal and compositional wakes left by the leading object, and we are working on developing a good physical understanding of the observed behavior.

Bubble, Drop and Particle Unit (BDPU)

Nonlinear Surface Tension Driven Bubble Migration

Principal Investigator:

Dr. Antonio Viviani
Seconda Università di Napoli
Naples, Italy

BDPU on LMS TC#6

Non Linear Surface Tension Driven Bubble Migration

P.I. : Antonio Viviani
Seconda Università di Napoli
Aversa, Italy

The experiment has been the follow-up of the "Bubble Behavior under Low Gravity" experiment performed during the IML2 mission in 1994 which was a milestone in the field of thermocapillary (or Marangoni) bubble migration, i.e. the motion of bubbles in a liquid subjected to a thermal gradient due to the dependence on the temperature of the surface tension at the liquid-bubble interface. In fact, for the very first time, it was shown the existence of liquids where thermocapillary migration of bubbles occurs from hot liquid towards the colder one, opposed to the classical Marangoni migration where bubbles move from colder liquid to the hot one.

In particular, it was demonstrated that in some saturated aqueous solutions of long chain alcohols (such as normal-heptanol used in the experiment), due to the particular dependence on the temperature of the surface tension at the interface with air, the bubbles can migrate from the "hot" side to the "cold" one, the latter being now the pole of minimum surface tension. This is very relevant to applications of space material sciences since that behavior of the interface tension with respect to the temperature is the same of the one shown, at very higher (1000-1500 °C) temperatures, by a wide class of materials of high technological interest.

The diagram of the surface tension versus the temperature of normal heptyl alcohol shows a parabolic behavior with a minimum around 40°C, in the case of thermodynamic equilibrium, that is, each point of the diagram is obtained by measuring the surface tension at the interface between the solution and air with the solution saturated at the given temperature (static surface tension measurement).

In the experimental configuration, with a linear temperature distribution imposed along the Test Cell, that means in dynamic condition, the most relevant result is that the position of minimum of the surface tension is not at 40°C; in fact, the bubbles injected did not stop in the corresponding position in the cell; they moved toward the coldest temperature, even though, their non-linear velocity of approach to the cold wall seems to slow down to rest at a temperature around 10°C. Being the operative temperatures of the cell in the range 10-90°C, the possible stop of the bubble around the temperature of 10°C could have been disturbed by the distortion in the thermal field that occur in the surrounding of the wall and/or of the extraction net of the cell.

The LMS experiment fully confirmed the findings of the IML2; moreover by putting the temperature of the cold wall to 5°C it has been detected the stopping of the bubble around 8-10° C. So it remains open the puzzling problem (as defined by Prof. Manuel G. Velarde) of explaining why the surface tension minimum location in presence of flow does change with respect to the static value.

A detailed analysis of all data collected during the mission is unfortunately still missing and will be reported at International Conferences. It is also planned to submit a paper on the results of both the experiments (IML2 and LMS) to the Physics of Fluids Journal.

Space Acceleration Measurement System (SAMS) / Orbital Acceleration Research Experiment (OARE)

Project Scientist:

Dr. Roshanak Hakimzadeh
NASA Lewis Research Center
Cleveland, Ohio

ONE YEAR REPORT FOR SAMS AND OARE ON STS-78/LMS

Roshanak Hakimzadeh
NASA Lewis Research Center, Cleveland, Ohio 44135
Tel: (216) 433-8738, E-mail: roshanak@lerc.nasa.gov

1. INTRODUCTION

The Life and Microgravity Spacelab (LMS) payload flew on the Orbiter Columbia on mission STS-78 from June 20th to July 7th, 1996. The LMS payload on STS-78 was dedicated to life sciences and microgravity experiments. Two accelerometer systems managed by the NASA Lewis Research Center (LeRC) flew to support these experiments, namely the Orbital Acceleration Research Experiment (OARE) and the Space Acceleration Measurements System (SAMS). In addition, the Microgravity Measurement Assembly (MMA), managed by the European Space Research and Technology Center (ESA/ESTEC), and sponsored by NASA, collected acceleration data in support of the experiments on-board the LMS mission. OARE downlinked real-time quasi-steady acceleration data, which was provided to the investigators. The SAMS recorded higher frequency data on-board for post-mission analysis. The MMA downlinked real-time quasi-steady as well as higher frequency acceleration data, which was provided to the investigators.

The Principal Investigator Microgravity Services (PIMS) project at NASA LeRC supports principal investigators of microgravity experiments as they evaluate the effects of varying acceleration levels on their experiments. A summary report [1] was prepared by PIMS to furnish interested experiment investigators with a guide to evaluate the acceleration environment during STS-78, and as a means of identifying areas which require further study. The summary report provides an overview of the STS-78 mission, describes the accelerometer systems flown on this mission, discusses some specific analyses of the accelerometer data in relation to the various activities which occurred during the mission, and presents plots resulting from these analyses as a snapshot of the environment during the mission.

Numerous activities occurred during the STS-78 mission that are of interest to the low-gravity community. Specific activities of interest during this mission were crew exercise, radiator deployment, Vernier Reaction Control System (VRCS) reboost, venting operations, Flight Control System (FCS) checkout, rack excitation, operation of the Life Sciences Laboratory Equipment Refrigerator/Freezer (LSLE R/F), operation of the JSC Projects Centrifuge, crew sleep, and attitude changes. The low-gravity environment related to these activities is discussed in the summary report.

2. ACCELEROMETER SYSTEMS

Two NASA LeRC accelerometer systems, OARE and SAMS, measured the low-gravity environment of the Space Shuttle Columbia during the STS-78 mission. The OARE was designed to measure quasi-steady accelerations from below 1×10^{-8} g up to 2.5×10^{-3} g. It is mounted near

the center of gravity of the space shuttle vehicle. On STS-78, the SAMS unit was located in the Spacelab module in rack 7 in support of LMS experiments. Three SAMS triaxial sensor heads (TSH) were located remotely at experiment sites (Table 1). The signals from these sensor heads were filtered by low-pass filters with cutoff frequencies listed in Table 1. These signals were then sampled, and the data were recorded on optical disks.

The MMA unit on LMS consisted of four Microgravity Sensor Packages (MSPs) and one Accelerometer Spatiale Triaxiale Electrostatique (ASTRE). The MSPs are triaxial sensor heads capable of measuring disturbances in the 0.1 to 100 HZ range. The ASTRE is a quasi-steady sensor designed to measure disturbances at frequencies below 1HZ. The ASTRE and one MSP reside within the MMA unit which was located in rack 3. The remaining three MSP sensor heads were located remotely at the BDPU (Rack 8), AGHF (Rack 3) and APCF (Rack 7) experiment sites within the Spacelab.

3. COORDINATE SYSTEMS

The OARE data is typically presented in the Orbiter body coordinate system (X_b, Y_b, Z_b). In this coordinate system, the direction from tail to nose of the Orbiter is $+X_b$. The direction from port wing (left wing) to starboard wing (right wing) is $+Y_b$, and the direction from the top of the fuselage to the Orbiter belly is $+Z_b$. This coordinate system is centered at the center of gravity (C.G.) of the Orbiter [1].

The SAMS data is typically presented in the Orbiter structural coordinate system (X_o, Y_o, Z_o). In this coordinate system the direction from nose to tail of the Orbiter is $+X_o$. The direction from port wing to starboard wing is $+Y_o$, and the direction from the Orbiter belly to the top of the Orbiter fuselage is $+Z_o$. This coordinate system is centered at the tip of the Orbiter external fuel tank [1].

4. COLUMBIA MICROGRAVITY ENVIRONMENT - STS-78

The microgravity environment measured by an accelerometer system on the Orbiter has many components. The quasi-steady microgravity environment is related to orbital phenomena such as aerodynamic drag and rotational motion and to gravity gradient effects based on the distance from the Orbiter center of gravity. In addition to these quasi-steady acceleration, all ongoing operations of crew life support systems and activities and operations of the Orbiter, crew, carrier, and experiments tend to have transient and vibratory components that contribute to the background acceleration environment. The following subsections describe some of the most interesting events which contributed to the microgravity environment during the mission.

4.1 Radiator Deploy

The STS-78 Space Shuttle Mission Report [2] lists the time of the port radiator deploy as MET 002/03:23:53. Following the examination of the SAMS data around this time frame, it was concluded that this time corresponds to the end of the radiator deploy operation. Three 25-second windows were chosen, corresponding to the times before, during and after the deploy operations. For each period PSDs were computed from the SAMS TSH a data acquired, and the Root-Sum-of-Squares (RSS) of the three axes were plotted in overlapping fashion (Figure 1). It can be seen from Figure 1 that the PSD for the during-deploy period shows the addition of a 6.30 HZ and a 9.47 HZ peak, which do not appear in either the before deploy or after deploy periods. These two peaks may be related to the motor which drives the radiators away from the payload bay doors. The after deploy period shows the addition of a 3.37 HZ peak which does not appear in the before deploy spectrum.

4.2 VRCS Reboost Demonstration

During LMS, a detailed test objective called the Vernier Reaction Control System Reboost Demonstration was performed. During this test, the Orbiter was in a -XLV/-ZVV attitude while two pairs of VRCS jets (F5L/F5R and L5D/R5D) were alternately fired in a precise pattern to slightly raise the Orbiter's attitude. This pattern can be seen in Figure 2 where the forward (FWD) and AFT vernier jet firings are indicated by the top and bottom rows of "+" markers, respectively. As a result, the Orbiter was ratcheted to a higher altitude as is suggested by the pitch angle data plotted in Figure 2. The acceleration vector magnitude during this test did not exceed 2.5×10^{-3}g, and was nominally below about 1×10^{-3}g which is of the order of the background acceleration environment. Reference 1 gives more detailed analysis of this activity.

4.3 Flight Control System Checkout

Approximately one day before the scheduled re-entry, a two-part checkout procedure is performed to verify operations of the FCS. The first part of this check-out is to use one of the three Auxiliary Power Units (APUs) to circulate hydraulic fluid in order to move the rudder, elevons, and ailerons of the Orbiter. For LMS, APU number 2 was used for the checkout procedure. As the APU is activated, it vents an exhaust gas in the $-Z_b$ direction. The result of this exhaust is similar in nature to a VRCS jet firing. The exhaust gas can range from nearly 0 to 30 pounds of force. The exhaust does not vent as a steady stream, but cycles at approximately 1 to 1.5 HZ.

From the SAMS data it was seen that the FCS phase 1 checkout lasted for approximately 5 minutes (MET 015/18:01 - MET 015/18:06). As seen from Figure 3, the effect of the FCS checkout on the microgravity environment was to cause impulse accelerations of roughly 5×10^{-3}g on the X_o-axis, with the Y_o- and Z_o-axes acceleration spikes reaching above the 1×10^{-2}g level. From this data there is indication of a damping behavior following a spike, with impulse relaxation time of approximately 4 seconds. No excitation in the 1 to 1.5 HZ region was detected, perhaps

due to this region of the spectrum having been masked due to an increase in broad-band noise. The impulsive transients which occur roughly every 20 seconds during the checkout procedure are the cause of the increase PSD noise floor.

No disturbance to the microgravity environment were detected during the phase 2 of the FCS checkout procedure, as expected, as this is a test of the electronics and command channels.

4.4 Venting Operations

Supply and waste water dumps are performed using nozzles on the port side of the Orbiter. Figures 4 and 5 show a simultaneous supply/waste water dump and a supply water dump, respectively. These water dumps show contributions to the Y_b-axis and, unexpectedly, to the Z_b-axis. The reason for the Z_b-contribution is unknown at this time.

Another venting system, the Flash Evaporator System (FES), is a component of the Orbiter Active Thermal Control System. The flash evaporators are located in the aft fuselage of the Orbiter. No discernible effects of FES operations were seen in the OARE data for this mission.

4.5 Orbiter Attitude

The LMS mission was flown predominantly in two attitudes: -XLV/+ZVV and -ZLV/-XVV. Figure 6 is a plot of the OARE data for the entire LMS mission. The effect of the attitude on the data is most apparent in the X_b-axis, and during the sleep periods (Figure 6). The nominal accelerations observed for the X_b-axis during these quiet periods consist of two levels. The two levels observed result from the different rotational and gravity gradient effects imparted on the X_b-axis data for the two attitudes flown. Similar, less obvious level changes are observable in the Z_b-axis data.

Figures 7 and 8 are eight-hour plots of the OARE data with the Orbiter in the -ZLV/-XVV and -XLV/+ZVV attitudes, respectively. These Figures show crew sleep periods, from which the contributions from the atmospheric drag to the total quasi-steady acceleration can be seen. Figure 7 shows that atmospheric drag is the dominating component on the X_b-axis, and Figure 8 shows it to dominate on the Z_b-axis.

4.6 Crew Sleep

Analysis of the SAMS and MMA data has shown that during crew sleep periods, the primary quieting is in the lower frequency (below 5 Hz) regime [1]. Also, an unidentified sinusoidal signal of frequency around 12.3 Hz was apparent during these periods.

4.7 Ergometer Exercise

During this mission, ergometer exercise was performed in both the Spacelab module and on the flight deck. Analysis of the SAMS data has shown that this type of exercise resulted in a disturbance with frequency about 2 to 3 Hz on all three axes, most notably the Y_o- and Z_o-axes. More detailed analysis of exercise can be found in Reference 1.

4.8 Rack Excitation

During the BDPU experiment operations, it became necessary for Payload Specialist Jean-Jaques Favier to close the front-panel of the BDPU experiment module in Rack 8 of the Spacelab. Acceleration data from SAMS TSH A, which was mounted on the BDPU Rack, is shown in Figure 9 for this time frame. As seen, the transitory disturbance induced by this action is prevalent on the Y_o- and Z_o-axes. The acceleration vector magnitude during this operation peaked at about $3x10^{-3}g$ [1].

4.9 Life Sciences Laboratory Equipment Refrigerator/Freezer

Two LSLE R/F units were flown side-by-side in Rack 9.From the SAMS data it is appears that two acceleration signals with frequencies around 22.00 and 23.07 Hz are the primary disturbances seen from the two LSLE R/F units. Harmonics of the fundamental frequencies of 22.00 and 23.07 Hz are seen at approximately 44 and 46 Hz. In addition to these signals, signal aliasing is believed to be present [1].

A third signal, with frequency of 23.61 Hz, and with a harmonic at 47.00 Hz, and aliases at 48.64 and 51.34 Hz is believed to be related to the LSLE R/F units.

4.10 JSC Projects Centrifuge

A centrifuge was mounted in Rack 12 of the Spacelab module. Analysis of the SAMS TSH C data and the MMA MSP APCF and MSP BDPU data show the disturbance generated by the centrifuge which had a rotational frequency of 39.8 Hz. Two other lower frequency disturbances at 15.7 and 24.1 Hz are thought to be related to the operation of the centrifuge [1].

5. CONCLUSIONS

The microgravity environment of the Space Shuttle Columbia was measured during the STS-78 mission using three accelerometer systems, namely the NASA LeRC OARE and SAMS, and the European MMA. The OARE provided investigators with real-time quasi-steady acceleration measurements. SAMS recorded higher frequency data on-board, which was analyzed post-mission. The MMA provided investigators with real-time quasi-steady and higher frequency

acceleration measurements. The microgravity environment related to several different Orbiter, crew, and experiment operations was presented and interpreted.

A radiator deploy, the Flight Control System checkout, and the vernier reaction control system reboost demonstration had minimal effects on the acceleration environment. Frequency components at 6.3 and 9.47 Hz were present in the SAMS data during the port radiator deploy. These frequencies may be related to the motor which drives the radiators away from the payload bay doors. During the FCS checkout period, regular impulse accelerations of about $5x10^{-3}$ to $10x10^{-3}$g were evident in the SAMS data. Flash Evaporator System venting had no noticeable effect on the environment while supply and waste water dumps caused excursions of $2x10^{-6}$ to $4x10^{-6}$g in the Y_b and Z_b directions. Crew sleep and ergometer exercise periods can be clearly seen in the acceleration data, as expected. Accelerations related to the two Life Science Laboratory Equipment Refrigerator/Freezers were apparent in the data with fundamental frequencies of 22 and 23 Hz. These signals showed different characteristics than on previous missions. The cause for the differences is being investigated. Accelerations caused by the JSC Projects Centrifuge were evident at about 40 Hz. Disturbances at 15.7 and 24 Hz appear to be temporally related.

The SAMS and MMA MSP sensor data compare well for the times studied. No detailed comparisons have been made for the OARE and MMA quasi-steady, ASTRE sensor data.

REFERENCES

1. R. Hakimzadeh, et. al. *"Summary Report of Mission Acceleration Measurements for STS-78"*, NASA TM 107401.

2. STS-78 Space Shuttle Mission Report, NSTS-37409, August 1996.

Sensor Head	Cutoff Frequency	Sampling Rate (samples/sec)	Sensor Location
TSH A	10 Hertz	50	Rack 8 (behind front panel)
TSH B	10 Hertz	50	Rack 3 (behind front panel)
TSH C	25 Hertz	125	Rack 7 (behind SAMS)

Table 1. STS-78 SAMS Head Locations

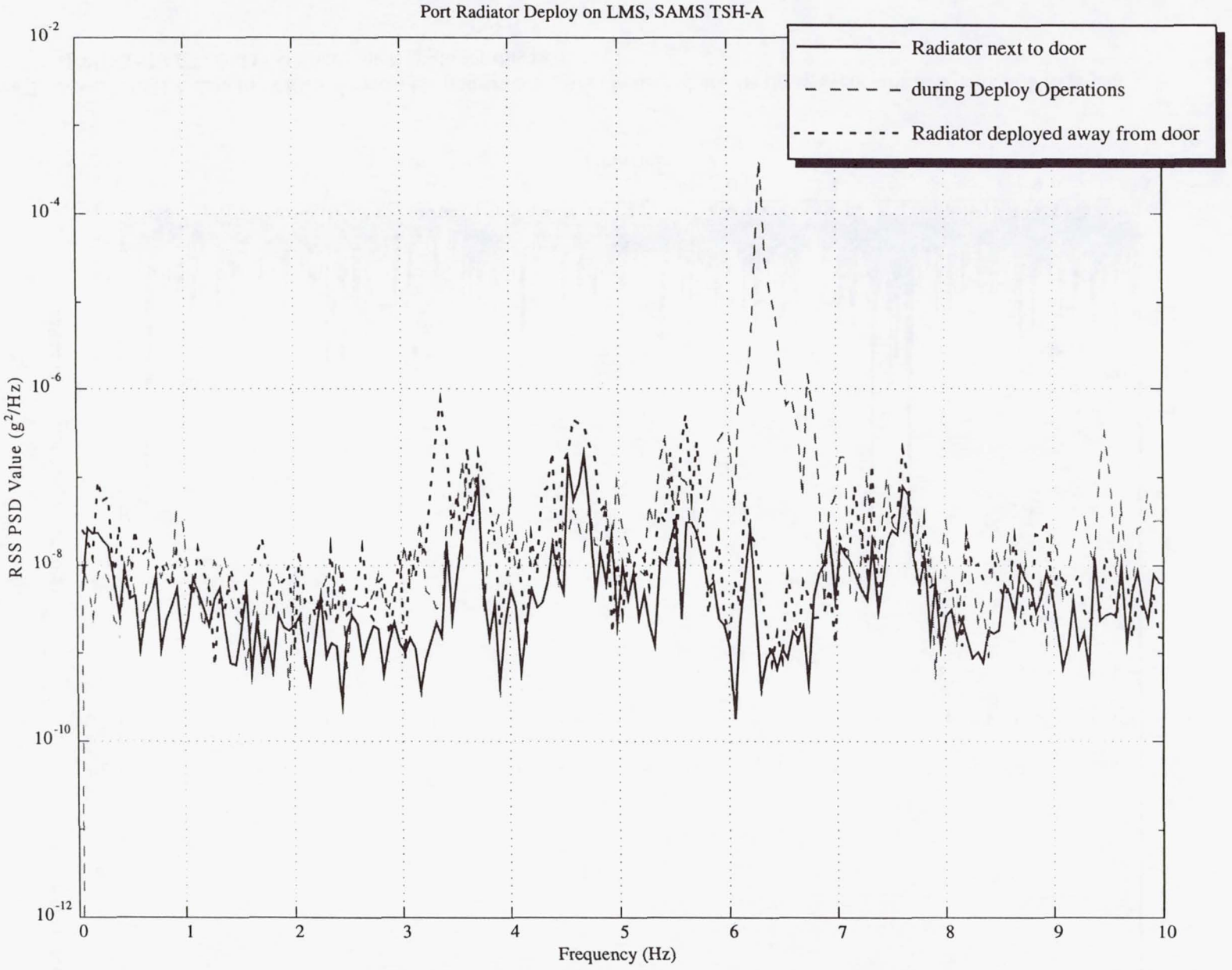

Figure 1. SAMS TSH A data PSDs for periods before, during, and after port radiator deploy. Note differences at 3.37, 6.30, and 9.47 Hz.

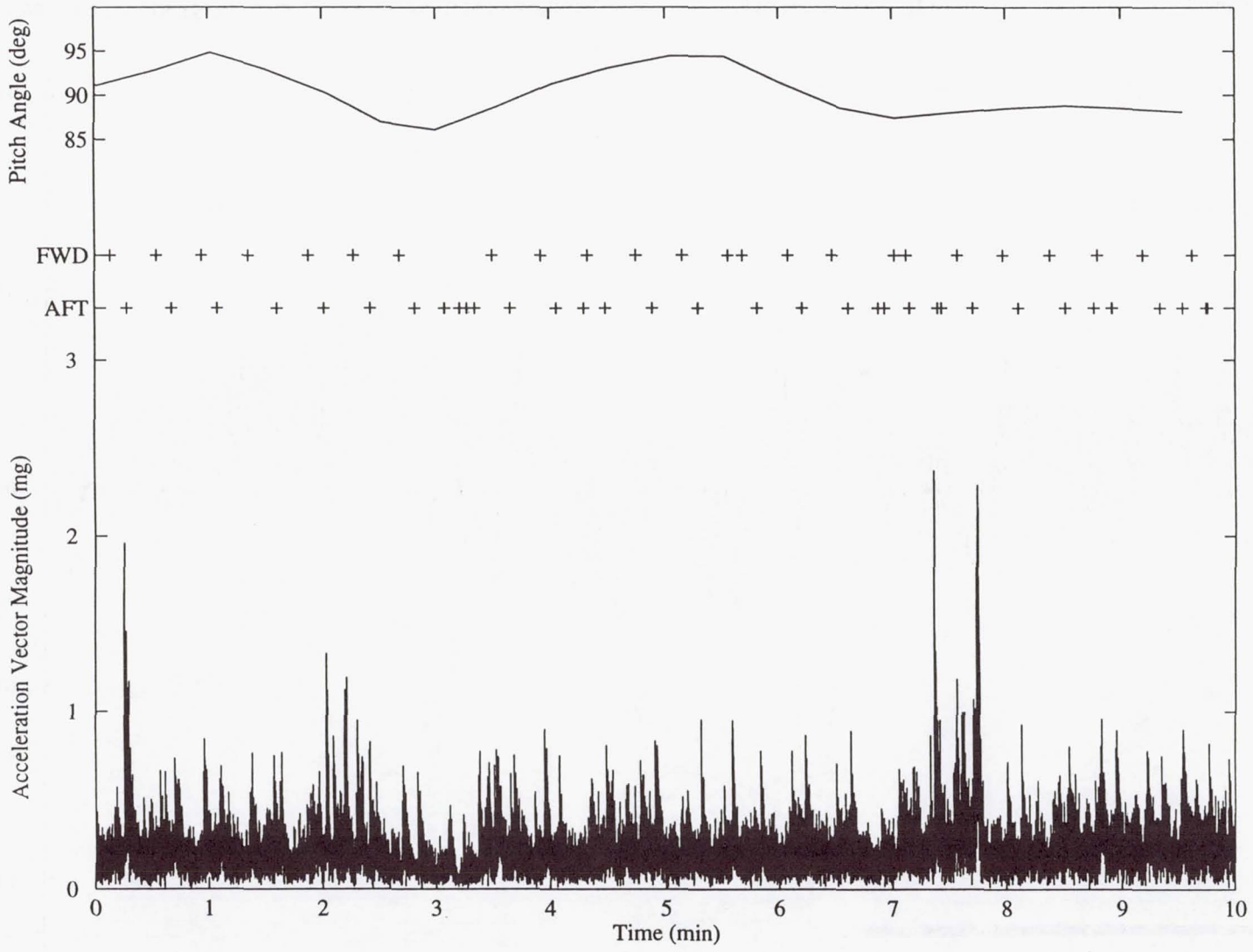

Figure 2. SAMS TSH A data for VRCS Reboost Demonstration. Also indicated are the firing events for two pairs of VRCS jets (FWD and AFT) and the Orbiter pitch angle for this period.

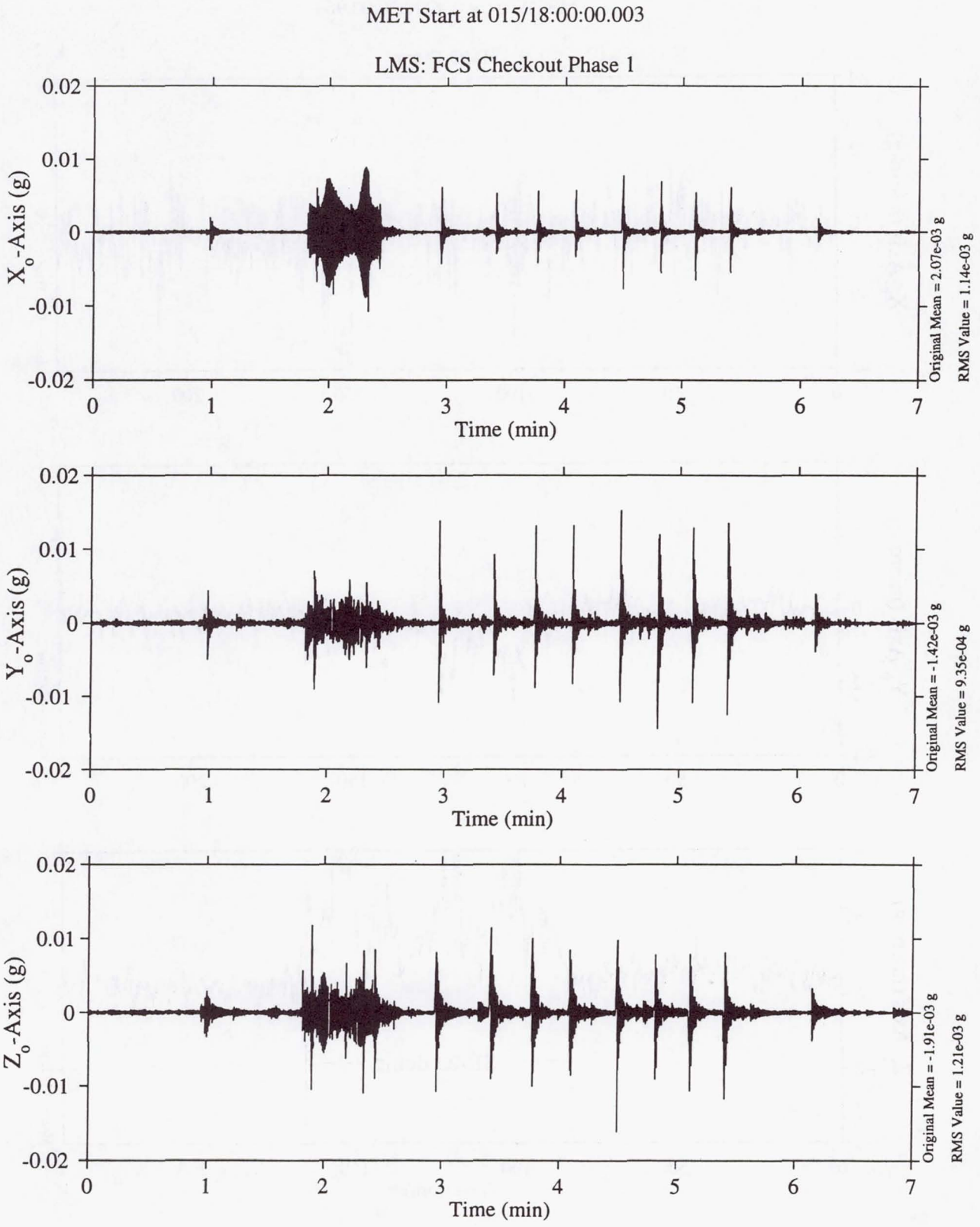

Figure 3. SAMS TSH A data for Flight Control System checkout phase 1

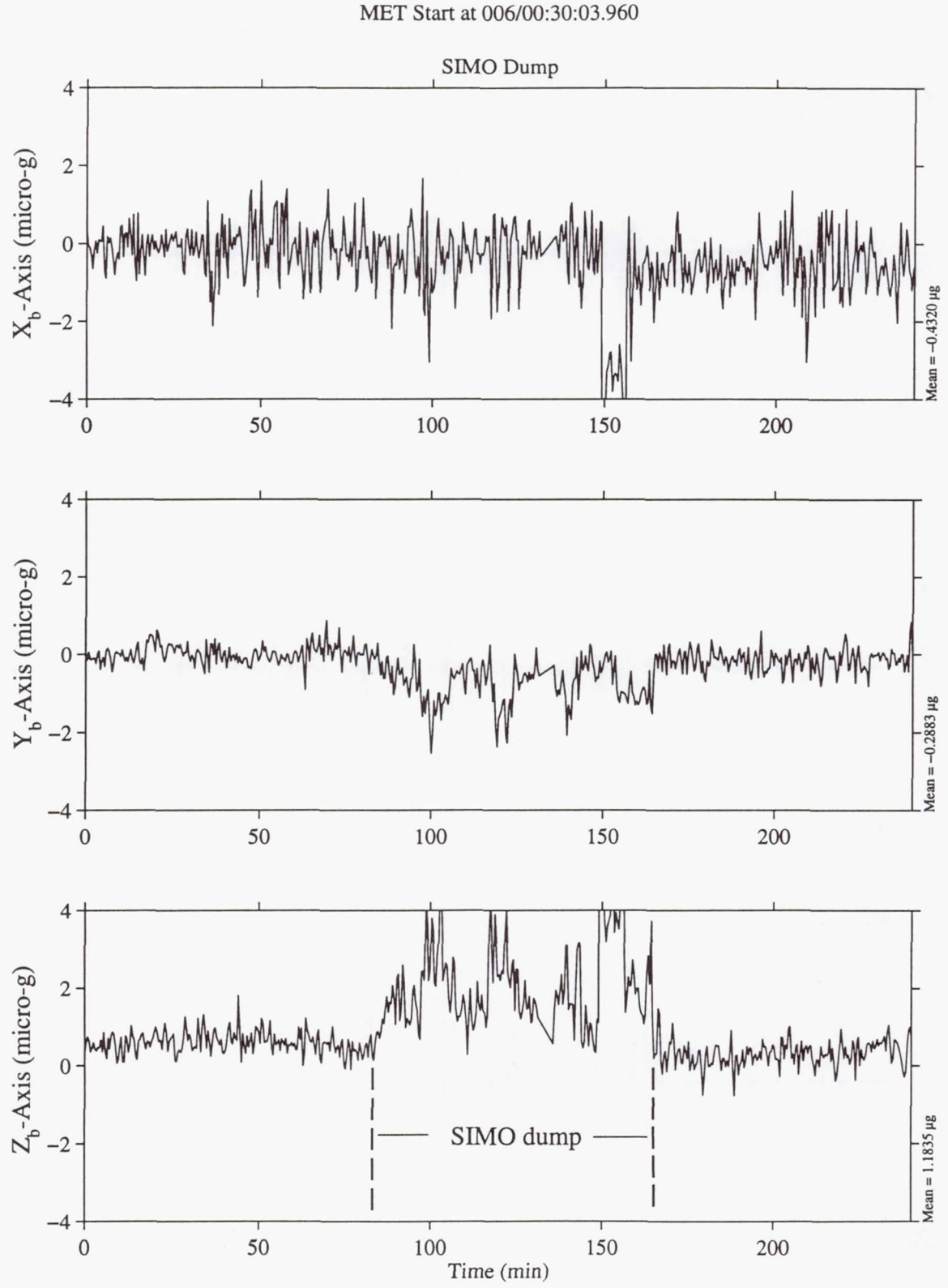

Figure 4. OARE data collected during a simultaneous supply and waste water dump at MET 006/00:30

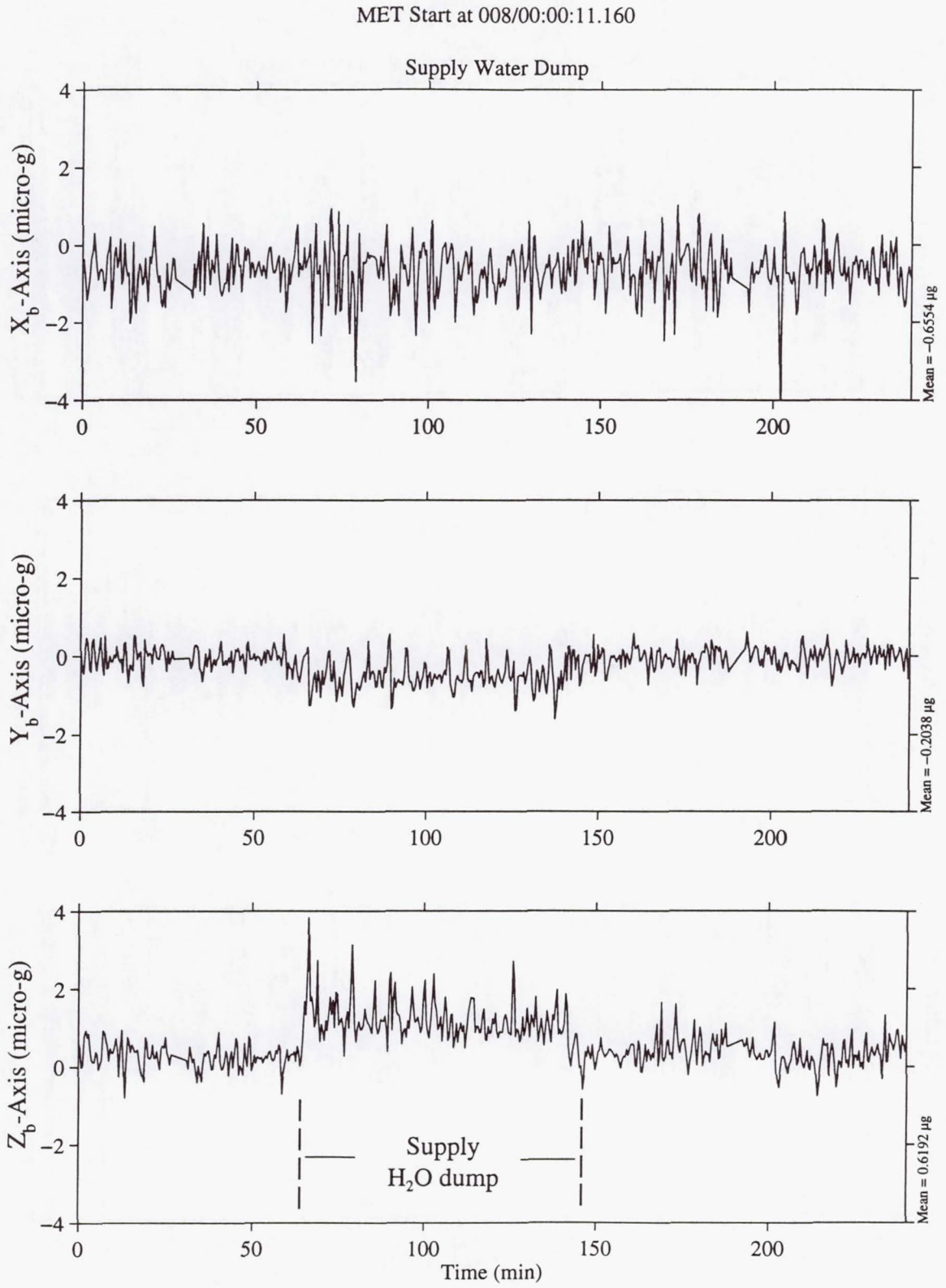

Figure 5. OARE data collected during a supply water dump at MET 008/00:00.

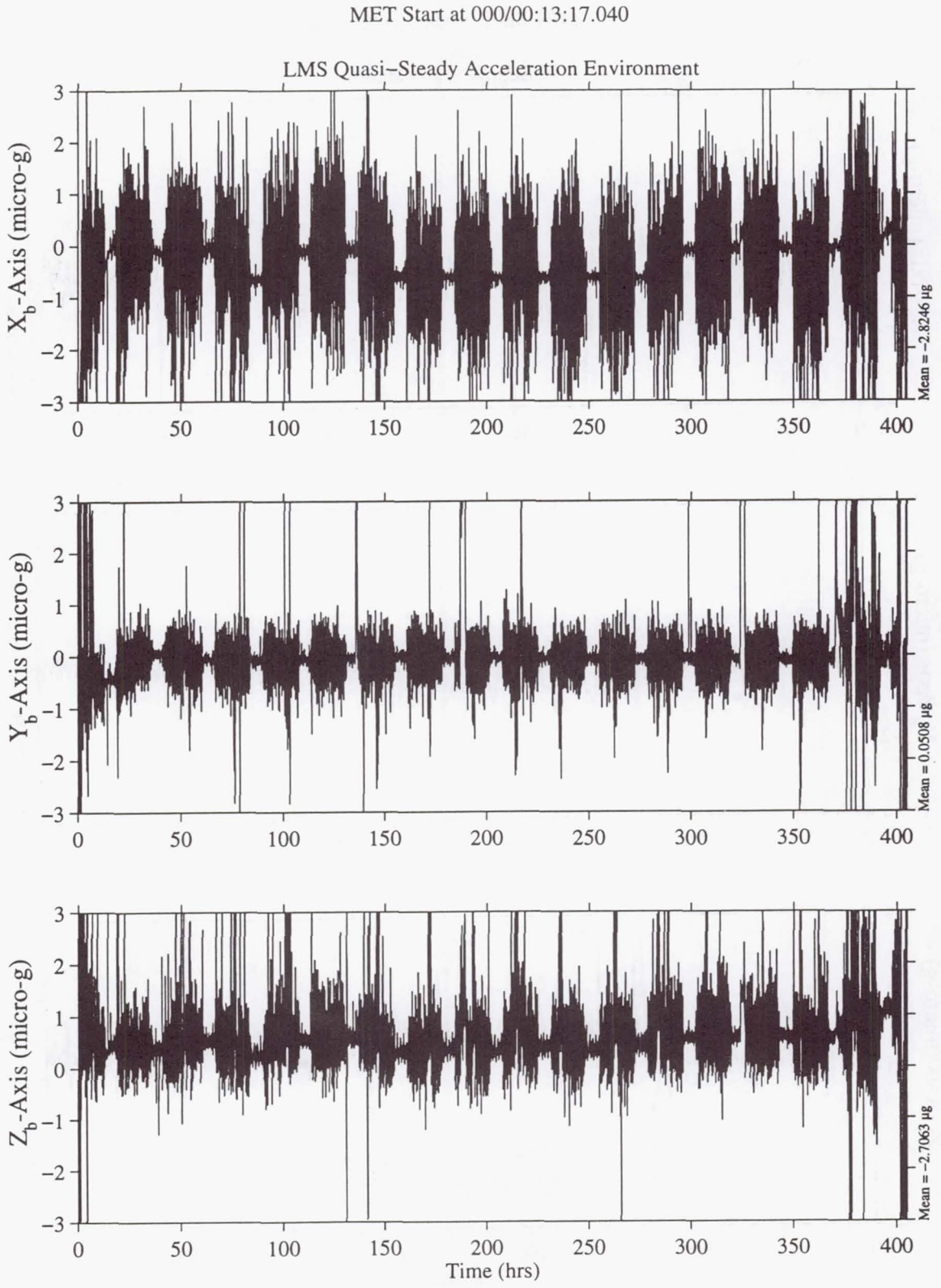

Figure 6. Trimmean filtered OARE data for the STS-78 mission.

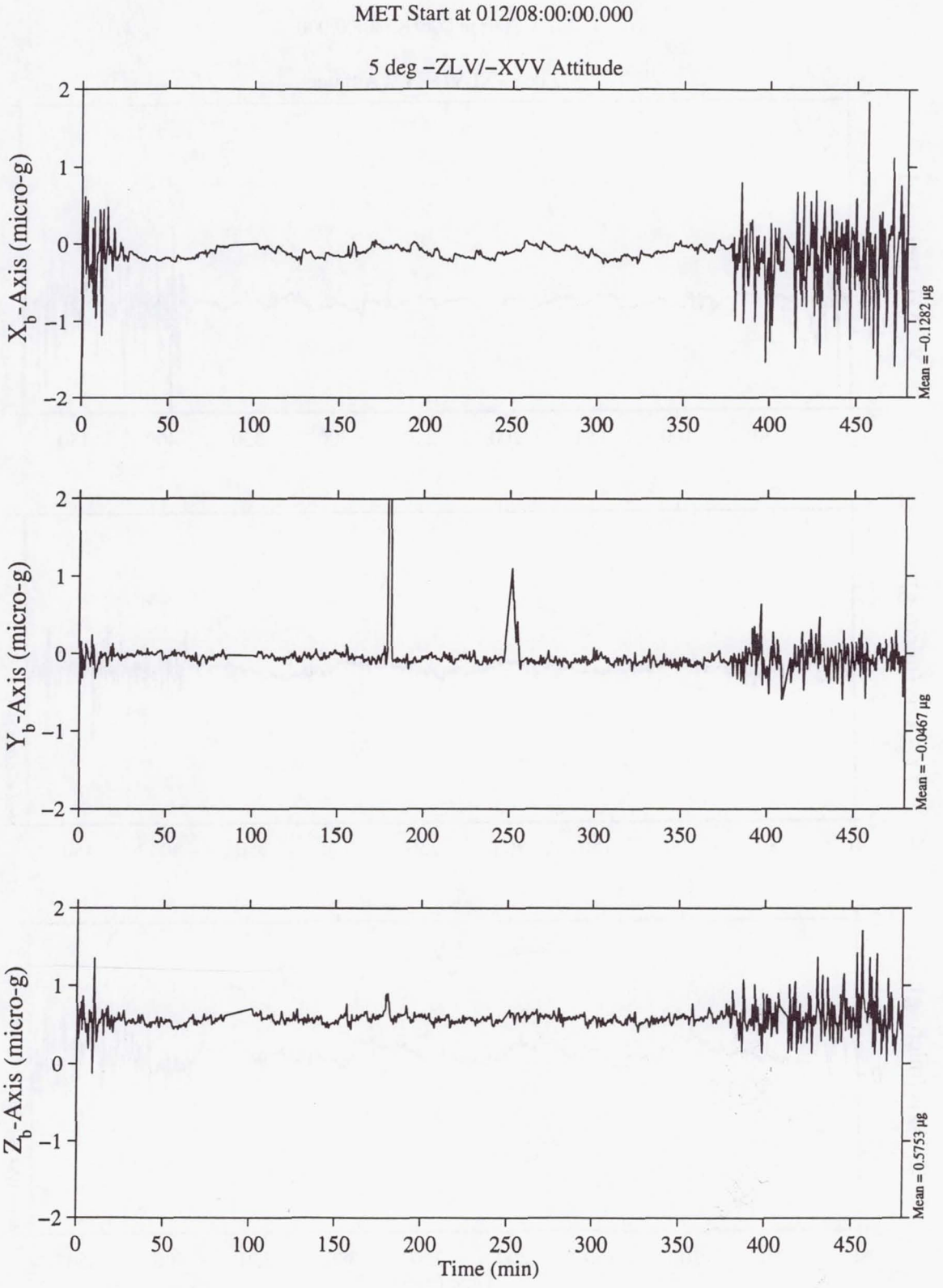

Figure 7. Trimmean filtered OARE data for STS-78 with Columbia in -ZLV/-XVV attitude, MET start 012/08:00.

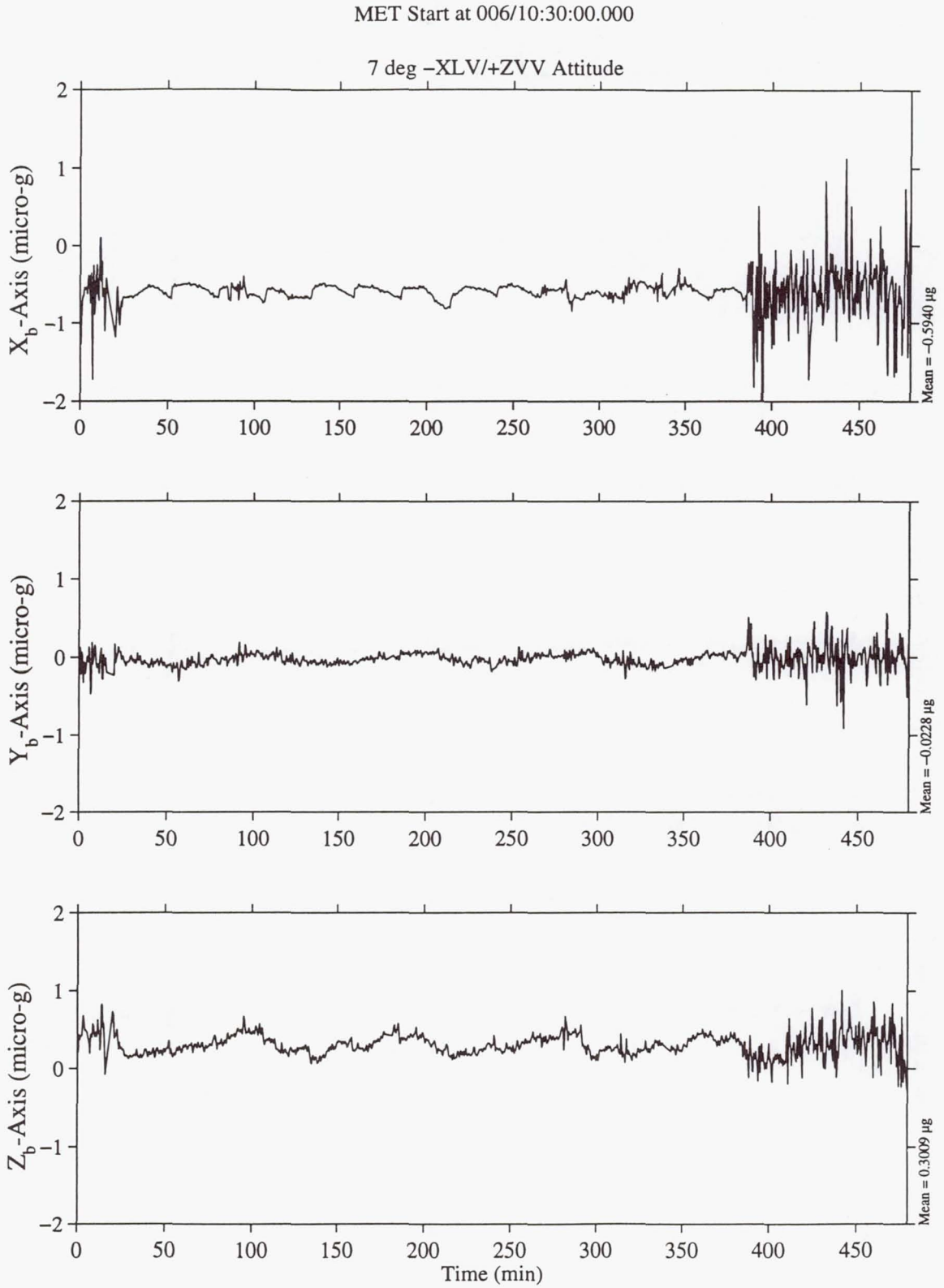

Figure 8. Trimmean filered OARE data for STS-78 with Columbia in -XLV/+ZVV attitude, MET start 006/10:30.

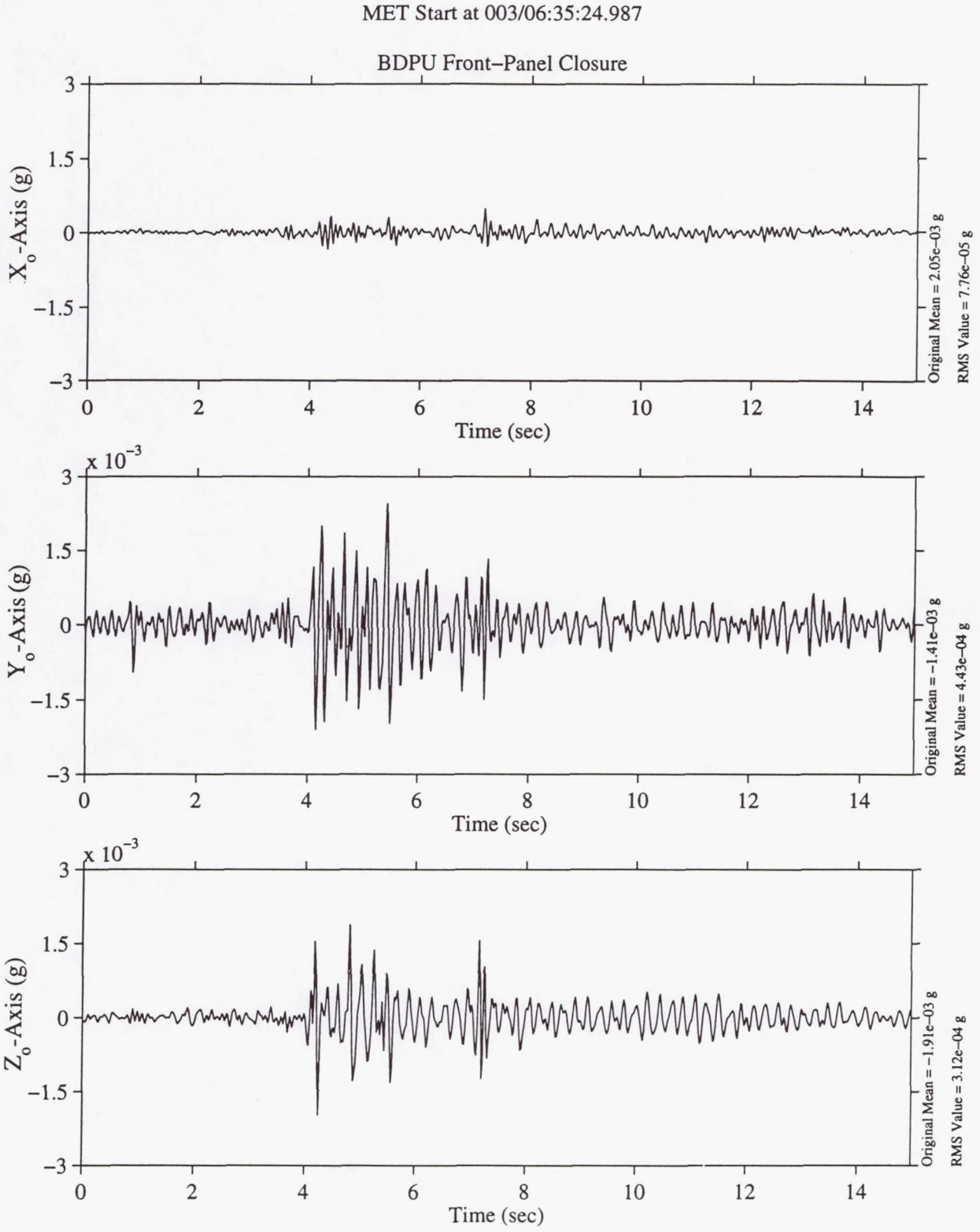

Figure 9. SAMS TSH A data for BDPU panel closing, MET 003/06:35:24.987.

Animal Enclosure Module (AEM)

Role of Corticosteroids in Bone Loss During Space Flight

Principal Investigator:

Dr. Tom Wronski
Univesity of Florida
Gainesville, Florida

FINAL REPORT

ROLE OF CORTICOSTEROIDS IN BONE LOSS DURING SPACE FLIGHT*

PRINCIPAL INVESTIGATOR: THOMAS J. WRONSKI, PH.D.
DEPARTMENT OF PHYSIOLOGICAL SCIENCES
UNIVERSITY OF FLORIDA
GAINESVILLE, FL 32610

CO-INVESTIGATORS: BERNARD P. HALLORAN, PH.D.
DEPARTMENT OF MEDICINE
UNIVERSITY OF CALIFORNIA
SAN FRANCISCO, CA 94121

SCOTT C. MILLER, PH.D.
RADIOBIOLOGY DIVISION
UNIVERSITY OF UTAH
SALT LAKE CITY, UT 84112

*Designated as the AEM experiment aboard the space shuttle Columbia (STS 78) during the LMS mission.

OBJECTIVES

The primary objective of this research project is to test the hypothesis that corticosteroids contribute to the adverse skeletal effects of space flight. To achieve this objective, serum corticosteroids, which are known to increase during space flight, must be maintained at normal physiologic levels in flight rats by a combination of adrenalectomy and corticosteroid supplementation via implanted hormone pellets. Bone analyses in these animals will then be compared to those of intact flight rats that, based on past experience, will undergo corticosteroid excess and bone loss during space flight. The results will reveal whether maintaining serum corticosteroids at physiologic levels in flight rats affects the skeletal abnormalities that normally develop during space flight. A positive response to this question would indicate that the bone loss and decreased bone formation associated with space flight are mediated, at least in part, by corticosteroid excess.

BACKGROUND

Space flight is known to induce alterations in calcium homeostasis. Gemini, Apollo, and Skylab astronauts exhibited hypercalciuria and negative calcium balances (1-3). Since the skeleton is the major reservoir of calcium in the body, increases in the urinary excretion of calcium presumably reflect bone loss. Photon absorptiometry revealed that the bone mineral density of the calcaneus declined by approximately 4% in Skylab crewmembers after 84 days of orbital flight (4). More recently, bone ultrasound and quantitative computed tomography detected losses of from 4 to 13% of primarily cancellous bone in the calcaneus and tibia of a cosmonaut stationed on MIR for 6 months (5). Although it is commonly assumed that the observed bone loss is due primarily to increased bone resorption, recent biochemical data indicate that decreased bone formation may also be involved (5).

Bone histomorphometric analyses are necessary to define more completely the skeletal effects of space flight. Unfortunately, such analyses are not feasible in astronauts due to the traumatic nature of the bone biopsy procedure. For this reason, bone histologic studies in experimental animals subjected to space flight are of considerable interest. Rats placed in orbit aboard Soviet Cosmos biosatellites and the space shuttle exhibited an inhibition of periosteal bone formation (6-8) and loss of cancellous bone in the long bone metaphysis (9-12). Calcium kinetic analyses (13) and measurements of the number of osteoclasts (9-

12), the bone resorbing cells, indicate that bone resorption was not increased in rats during space flight. On the other hand, the number of osteoblasts, the bone forming cells, was found to be decreased in rats subjected to space flight (9-12). Therefore, the observed loss of cancellous bone in flight rats appears to be due primarily to an inhibition of bone formation rather than a stimulation of bone resorption.

It is commonly assumed that the adverse skeletal effects of space flight are due to loss of mechanical loading in a weightless environment. Nevertheless, some lines of evidence suggest that other factors may be involved. If the bone changes induced by space flight are due solely to mechanical unloading, these changes should be confined to weightbearing bones. However, skeletal abnormalities have been detected in bones of flight rats that lack a weightbearing function such as the maxilla, mandible, and calvarium (14-16). These findings may be interpreted as evidence that the skeletal effects of space flight are systemic rather than confined to weightbearing bones. The failure of on-board centrifugation to prevent the inhibition of periosteal bone formation in flight rats (17) also indicates that microgravity is not solely responsible for bone loss during space flight.

Endocrine factors in general and corticosteroids in particular may be involved in the etiology of the apparently systemic skeletal effects of space flight. In support of this concept, plasma cortisol was found to be significantly increased in Skylab astronauts for the duration of their long-term missions (1). Several investigators have reported that adrenal hypertrophy occurred in rats placed in orbit aboard Cosmos biosatellites (2,3). Exogenous administration of corticosteroids induces marked hypercalciuria (18) and skeletal alterations that are similar to those observed during space flight, including cancellous bone loss (19-21), decreased numbers of osteoblasts (22-24), and an inhibition of periosteal bone formation (24,25).

In summary, the above findings suggest that the changes in calcium homeostasis and bone associated with space flight may be mediated, at least in part, through the action of corticosteroids. This hypothesis has not been adequately tested to date. The current research project is designed to manipulate serum corticosteroids by a combination of adrenalectomy and exogenous supplementation with implanted hormone pellets. Maintenance of equivalent physiologic levels of serum corticosteroids in flight and ground-based rats with subsequent bone analyses will determine whether corticosteroid excess is essential for the development of skeletal abnormalities during space flight.

METHODS

The experimental animals were male Sprague Dawley rats that were 6 weeks of age and weighed an average of 165g at launch. All rats were anesthetized with an IM injection of ketamine hydrochloride (50 mg/kg body weight) and xylazine (10 mg/kg body weight) and subjected to bilateral adrenalectomy or sham surgery at 4 days prior to launch. At the time of surgery, pellets composed of cholesterol with dissolved corticosterone and aldosterone were implanted in each adrenalectomized (ADX) rat. The proper doses of the hormones to achieve normal circulating levels of corticosterone and aldosterone were established in prior supporting ground-based studies. Each sham-operated rat was implanted with a placebo cholesterol pellet. On the day before launch, all rats were injected SC with calcein at a dose of 15 mg/kg body weight to label bone forming surfaces. Shortly afterwards, six ADX flight rats and six sham flight rats were loaded in each of two animal enclosure modules (AEM) and transported to the space shuttle Columbia for launch on 6/20/96 (STS-78). On the day of launch, baseline ADX and sham rats were sacrificed for collection of serum and bone samples. Other ADX and sham rats were placed in ground-based AEMs or standard vivarium (VIV) cages. The experiment therefore consisted of the following 8 groups of rats (N=6/group):

1. Baseline ADX
2. Baseline Sham
3. Flight ADX
4. Flight Sham
5. AEM ADX
6. AEM Sham
7. VIV ADX
8. VIV Sham

After a 17 day space flight, the ADX and sham flight rats were necropsied between 4 and 6 hours after landing. Serum samples were collected and stored at -80°C until their corticosterone and aldosterone concentrations were measured by radioimmunoassay techniques. The adrenal glands in sham rats were carefully dissected free of adjacent tissues and weighed with a Mettler balance. Various bones including both tibiae, femora, lumbar vertebrae, and caudal vertebrae were stripped of musculature. The left tibia was frozen for subsequent measurements of bone dry and ash weights. Other bones were placed in 10% phosphate-buffered formalin for 24 hours for tissue fixation. The bone samples were then dehydrated in increasing concentrations of ethanol and embedded undecalcified in methyl methacrylate. For cancellous bone analyses, longitudinal sections were cut at a thickness of 4 µm with an AO Autocut/Jung 1150 microtome. These sections were stained according to the Von Kossa method with a tetrachrome

counterstain for measurements of cancellous bone volume (%), osteoclast surface (%), an index of cancellous bone resorption, and osteoblast surface (%), an index of cancellous bone formation. All data were collected in cancellous bone tissue at distances greater than 1 mm from the growth plate-metaphyseal junction to exclude the primary spongiosa.

The distal half of the right tibia was dehydrated in ethanol and acetone, then embedded undecalcified in a styrene monomer that polymerizes into a polyester resin (Tap Plastics, San Jose, CA). The tibial diaphysis 1-2 mm proximal to the tibiofibular junction was then sawed into 50-75 μm thick cross sections with a Buhler Isomet low speed saw. Cortical bone area, cortical width, and marrow area were measured in these cross sections. Other measurements include the area of newly formed bone between the calcein label and the periosteal surface as well as the distance between the calcein label and the periosteal surface at 100 μm intervals around the periphery of cortical bone. This distance was divided by the time interval between administration of the calcein label and landing (18 days) to calculate periosteal mineral apposition rate. Similarly, the area of newly formed cortical bone along the periosteal surface was divided by the same time interval to calculate the periosteal bone formation rate.

All histomorphometric measurements were performed with the Bioquant Bone Morphometry System (R&M Biometrics Corp., Nashville, TN). Data are expressed as the mean for each group $\pm$ SD. Statistical differences among groups were evaluated by ANOVA followed by Fisher's Protected Least Significant Difference (PLSD) test for multiple comparisons. P values less than 0.05 were considered to be significant.

RESULTS

All rats gained substantial body weight during the course of the experiment (Figure 1). The ADX and sham flight rats exhibited at least as much weight gain as the ground-based AEM and VIV rats. In fact, the mean body weight of the ADX flight group was slightly but significantly increased compared to the mean body weight of all other groups. These findings indicate that space flight was well tolerated by the flight rats.

Mean values for adrenal gland weights for the 4 sham groups are shown in Figure 2. The sham flight group had significantly increased adrenal gland weights compared to baseline and ground-based AEM and

VIV sham groups. This finding is consistent with adrenal hypertrophy and corticosteroid excess in sham flight rats.

Figures 3 and 4 depict mean values for serum corticosterone and aldosterone, respectively. Sham flight rats exhibited a significantly higher mean value for serum corticosterone by at least a factor of 2 compared to all other groups. This finding undoubtedly reflects a stress response to re-entry and postflight handling in these animals. The ground-based AEM and VIV sham groups also exhibited at least a strong trend for increased serum corticosterone compared to all 3 ADX groups. In contrast, the mean value for serum corticosterone remained at 50-60 ng/ml in all ADX groups, which is equivalent to normal physiologic levels of the hormone in rats. Similarly, mean serum aldosterone (Figure 4) was maintained at the normal physiologic level of approximately 100 pg/ml in the 3 ADX groups. Therefore, the implanted hormone pellets were found to successfully deliver normal levels of corticosterone and aldosterone to the systemic circulation of ADX rats.

The dry and ash weights of the left tibia (data not shown) were significantly greater in the flight, AEM, and VIV groups than the baseline groups due to growth of the former groups during the experimental period. However, no significant differences in tibial dry and ash weights were detected among the flight groups (ADX and sham) and the ground-based AEM and VIV groups (ADX and sham).

Data for cancellous bone volume in the proximal tibial metaphysis are shown in Figure 5. The mean values were nearly the same for all 8 groups of rats with no significant differences among them. ADX and sham flight rats also did not exhibit even a trend for decreased cancellous bone volume in the lumbar vertebra, caudal vertebra, and femoral neck (data not shown). Similarly, osteoclast surface (Figure 6), an index of bone resorption, and osteoblast surface (Figure 7), an index of bone formation, varied little in the proximal tibial metaphysis of all groups. These cellular variables also did not differ in the lumbar and caudal vertebrae of flight rats (ADX and sham) compared to the ground-based AEM and VIV rats (data not shown).

Structural data for cortical bone in the tibial diaphysis are shown in Figures 8-10. A growth-related increase in cortical bone area and width was detected in the older flight, AEM, and VIV groups compared to the younger baseline groups. However, when comparing rats of the same age, these variables did not differ in the flight groups (ADX and sham)

compared to the AEM and VIV groups. Marrow area was nearly the same in all 8 groups of rats.

Age-related decreases in periosteal bone formation rate (Figure 11) and periosteal mineral apposition rate (Figure 12) occurred in the flight, AEM, and VIV groups compared to the baseline groups. However, the mean values for these variables were very similar in the flight groups (ADX and sham) compared to the ground-based AEM and VIV groups.

CONCLUSIONS

All preflight procedures were accomplished as planned. The rats were successfully adrenalectomized (ADX) and the implanted hormone pellets delivered physiologic levels of corticosterone and aldosterone to the systemic circulation. The substantial increase in body weight that occurred in all rats indicated that the ADX/supplemented rats were healthy and that the flight rats tolerated space flight well. The observed adrenal hypertrophy in the intact sham flight rats was also a positive finding in that it was suggestive of corticosteroid excess in these animals.

Unfortunately, the experimental objective, which was to test the hypothesis that corticosteroids contribute to bone loss during space flight, could not be achieved due to lack of bone changes in intact flight rats. These animals exhibited normal cancellous bone mass at several different skeletal sites. Furthermore, both cancellous and cortical bone formation were found to be normal in flight rats compared to ground-based control rats. The results clearly indicate that space flight has minimal effects on bone mass and bone formation in rapidly growing rats. This finding is surprising in view of previous reports of cancellous bone loss (9-12) and an inhibition of bone formation (6-12) in rats subjected to space flight. However, it is important to note that the rats from most of these previous studies were older than the rats from the current study. In addition, the former rats were often housed singly while in space compared to the group housing for the animals of our experiment. Finally, the strain of the rats also varied among the different flight experiments. Therefore, the negative findings of the current study emphasize the importance of rat age, strain, and housing conditions for the development of bone changes during space flight. These factors are crucially important for the planning of future experiments involving use of rats as an animal model for the adverse skeletal effects of space flight.

REFERENCES

1. Leach, C.S., S.I. Altschuler, and N.M. Cintron-Trevino. Med. Sci. Sports Exer. 15:432-440, 1983.

2. Portugalov, V.V., E.A. Savina, A.S. Kaplansky, et al. Aviat. Space Environ. Med. 47:813-816, 1976.

3. Grindeland, R.E. FASEB J. 4:10-15, 1990.

4. Lutwak, L., G.D. Whedon, P.A. LaChance, J.M. Reid, and H.S. Lipscomb. J. Clin. Endocrinol. 29:1140-1156, 1969.

5. Collet, P., D. Uebelhart, L. Vico, L. Moro, D. Hartmann, M. Roth, and C. Alexandre. Bone 20:547-551, 1997.

6. Morey, E.R., and D.J. Baylink. Science 201:1138-1141, 1978.

7. Wronski, T.J., and E.R. Morey. Am. J. Physiol. 244:R305-R309, 1983.

8. Wronski, T.J., E.R. Morey-Holton, S.B. Doty, A.C. Maese, and C.C. Walsh. Am. J. Physiol. 252:R252-R255, 1987.

9. Jee, W.S.S., T.J. Wronski, E.R. Morey, and D.B. Kimmel. Am. J. Physiol. 244:R310-R314, 1983.

10. Vico, L., D. Chappard, A.V. Bakulin, V.E. Novikov, and C. Alexandre. Physiologist 30:545-546, 1987.

11. Vico, L., S. Bourrin, C. Genty, S. Palle, and C. Alexandre. J. Appl. Physiol. 75:2203-2208, 1993.

12. Zerath, E., D. Godet, X. Holy, C. Andre, S. Renault, M. Hott, and P.J. Marie. J. Appl. Physiol. 81:164-171, 1996.

13. Cann, C.E., and R.R. Adachi. Am. J. Physiol. 244:R327-R331, 1983.

14. Roberts, W.E., P.G. Mozsary, and E.R. Morey. Physiologist 24:575-576, 1981.

15. Simmons, D.J., J.E. Russell, F. Winter, P. Tran Van, A. Vignery, R. Baron, G.D. Rosenbert, and W.V. Walker. Am. J. Physiol. 244:R319-R326, 1983.

16. Simmons, D.J., M.D. Grynpas, and G.D. Rosenberg. FASEB J. 4:29-33, 1990.

17. Morey, E.R., R.T. Turner, and D.J. Baylink. In: Final Reports of U.S. Experiments Flown on the Soviet Satellite Cosmos 936, S.N. Rosenzweig and K.A. Souza (eds.), NASA TM 78526, 1978, pp. 135-183.

18. Hansen, J.W., G.S. Gordan, andd S.G. Prussin. J. Clin. Invest. 52:304-315, 1973.

19. Sissons, H.A., and G.J. Hadfield. J. Anat. 89:69-78, 1955.

20. Storey, E. Clin. Orthop. 30:197-216, 1963.

21. Bressot, C., P.J. Meunier, M.C. Chapuy, E. Lejeune, C. Edouard, and A.J. Darby. Metab. Bone Dis. 1:303-309, 1979.

22. Simmons, D.J., and A.S. Kunin. Clin. Orthop. 55:201-215, 1967.

23. Jee, W.S.S., H.Z. Park, W.E. Roberts, and G.H. Kenner. Am. J. Anat. 129:477-480, 1970.

24. Li, M., Y. Shen, B.P. Halloran, B.D. Baumann, K. Miller, and T.J. Wronski. Bone 19:81-88, 1996.

25. Stanisavljevic, S., H. Roth, A.R. Villanueva, and H.M. Frost. Henry Ford Hosp. Med. Bull. 10:179-184, 1962.

BIBLIOGRAPHY

Wronski, T.J., M. Li, S.C. Miller, Y. Shen, B.M. Bowman, and B.P. Halloran. Lack of an effect of space flight on bone mass and formation in rapidly growing rats. Abstract submitted for presentation at the 1997 ASGSB meeting.

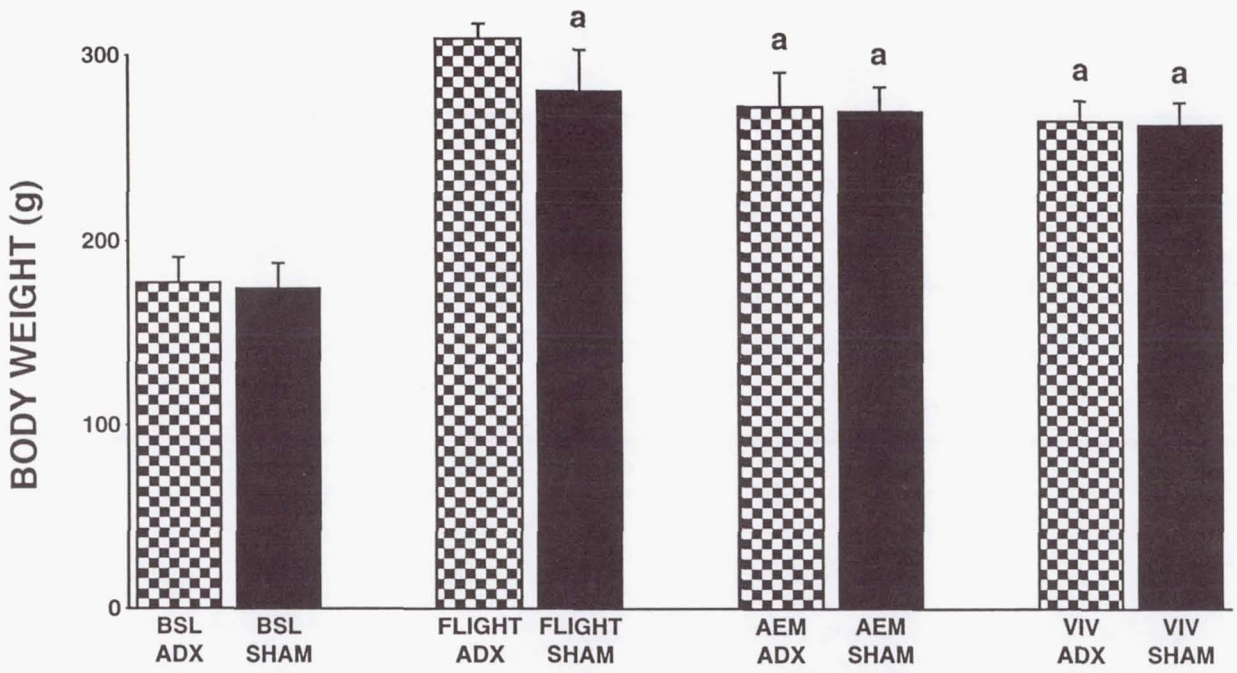

a: vs Flight ADX ($p < 0.05$)

b: vs Flight Sham ($p < 0.05$)

c: vs AEM ADX ($p < 0.05$)

d: vs AEM Sham ($p < 0.05$)

e: vs VIV ADX ($p < 0.05$)

FIGURE 1

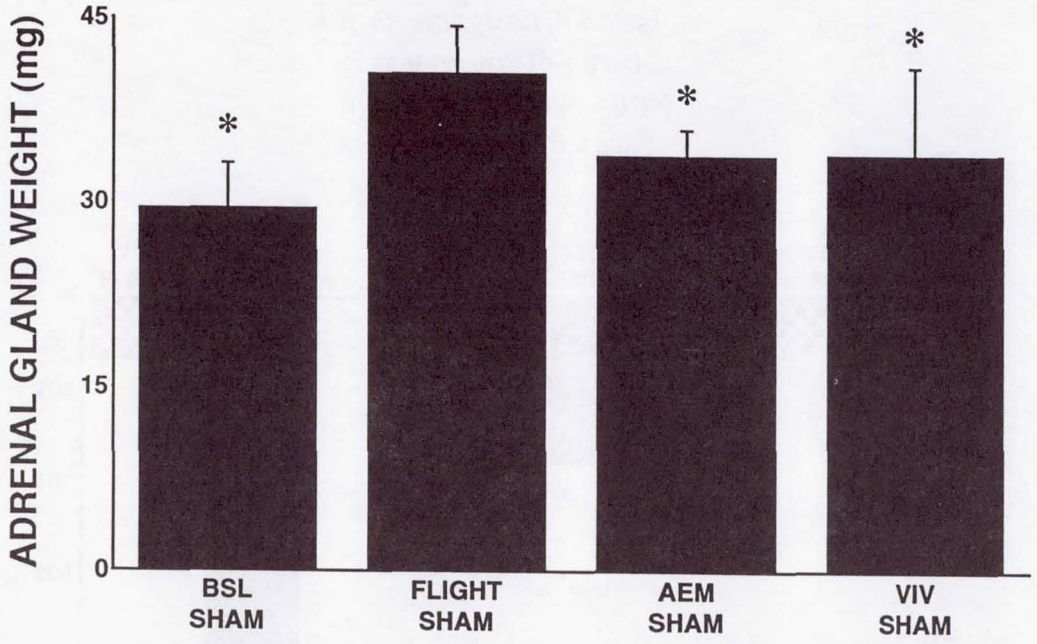

* Significantly different from FLIGHT SHAM group ($p < 0.05$)

FIGURE 2

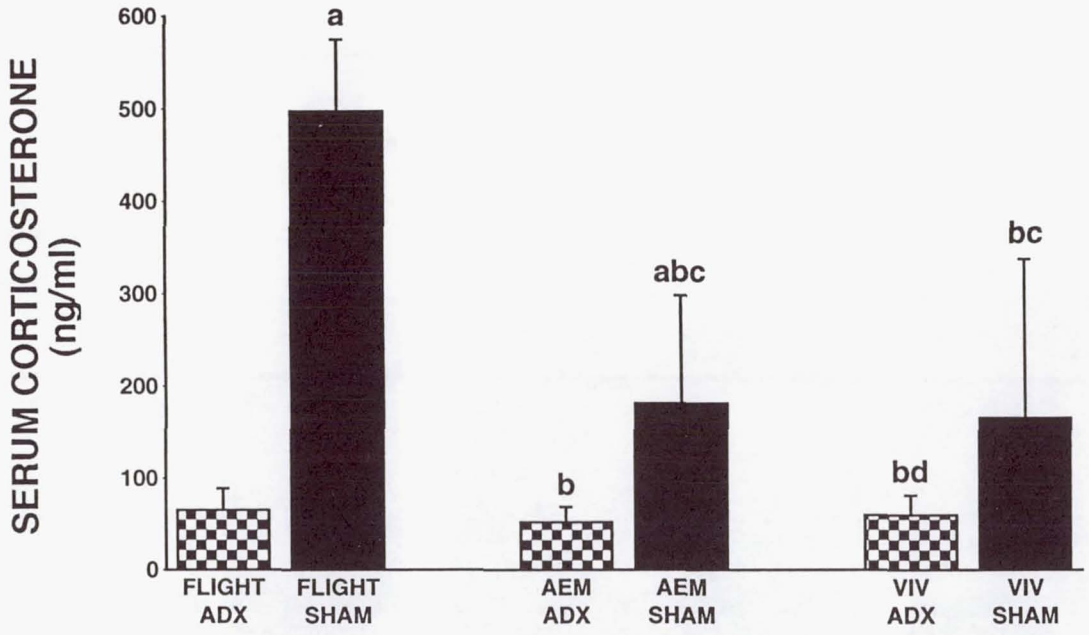

a: vs Flight ADX ($p < 0.05$)
b: vs Flight Sham ($p < 0.05$)
c: vs AEM ADX ($p < 0.05$)
d: vs AEM Sham ($p < 0.05$)
e: vs VIV ADX ($p < 0.05$)

FIGURE 3

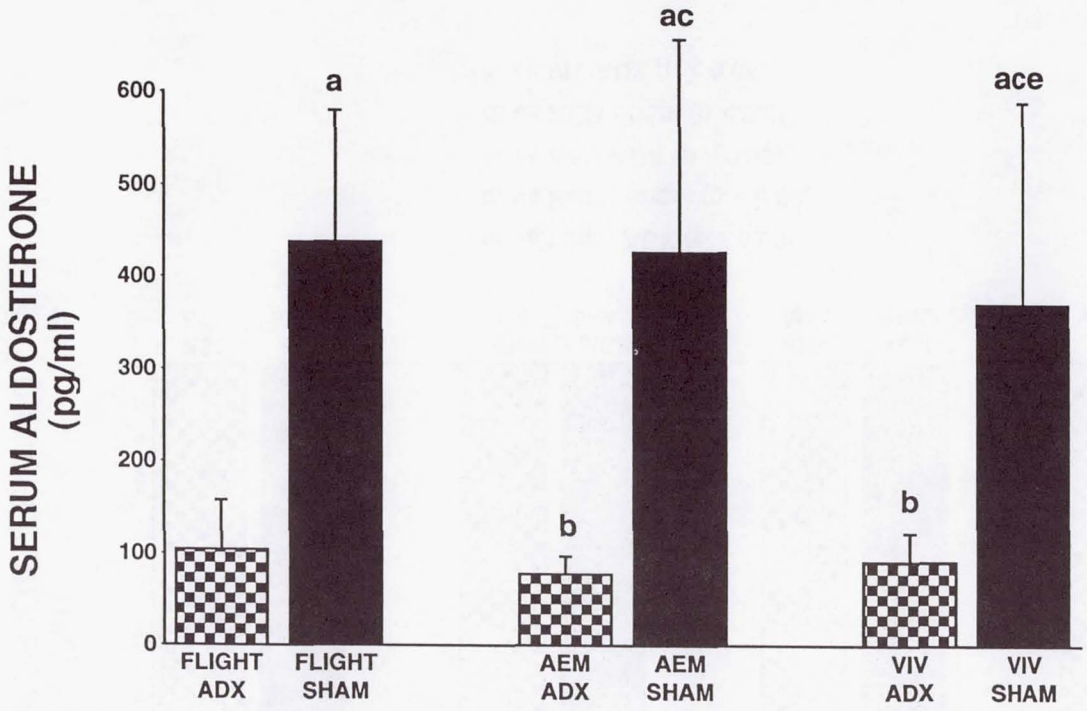

a: vs Flight ADX ($p < 0.05$)
b: vs Flight Sham ($p < 0.05$)
c: vs AEM ADX ($p < 0.05$)
d: vs AEM Sham ($p < 0.05$)
e: vs VIV ADX ($p < 0.05$)

FIGURE 4

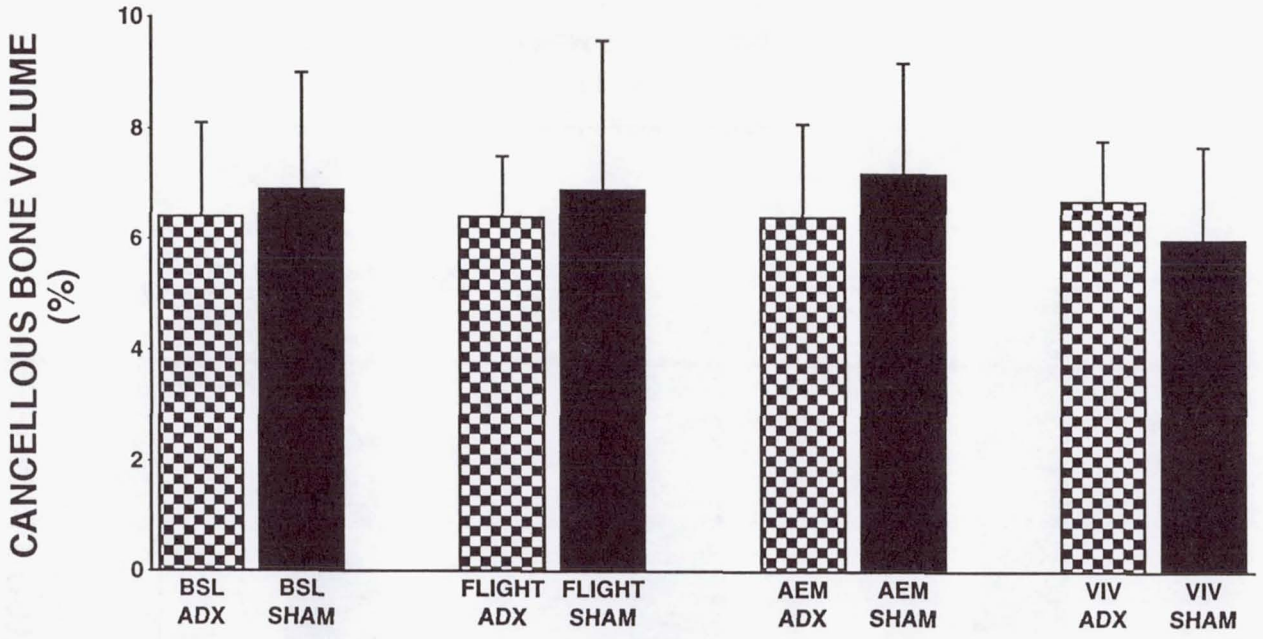

a: vs Flight ADX ($p < 0.05$)

b: vs Flight Sham ($p < 0.05$)

c: vs AEM ADX ($p < 0.05$)

d: vs AEM Sham ($p < 0.05$)

e: vs VIV ADX ($p < 0.05$)

FIGURE 5

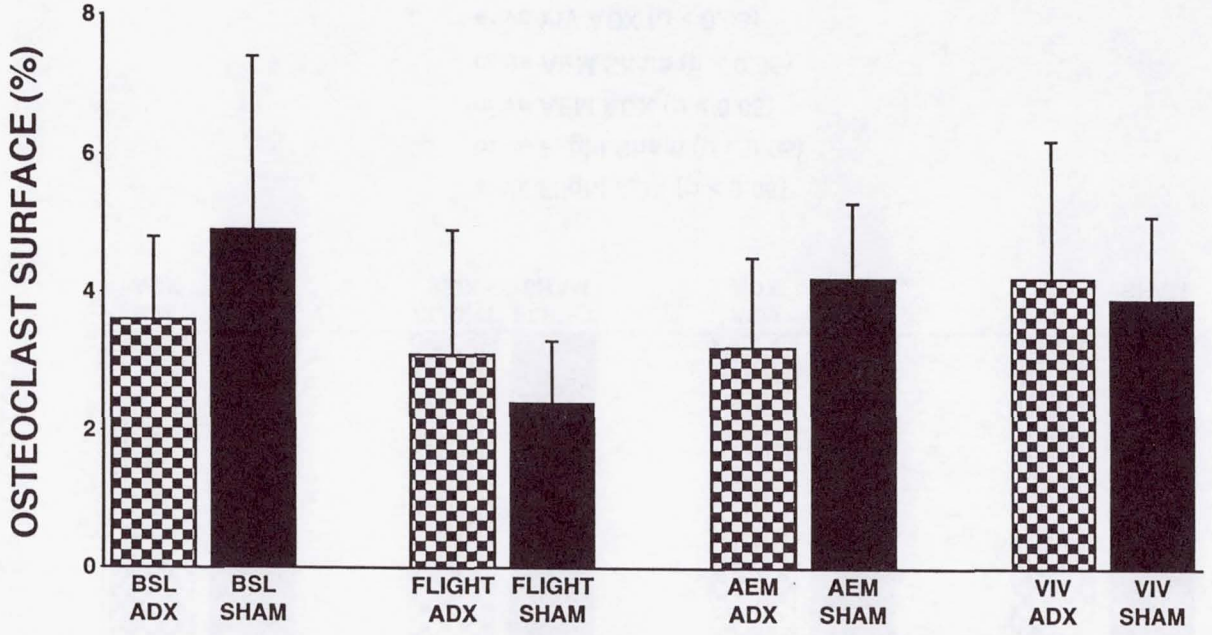

a: vs Flight ADX ($p < 0.05$)

b: vs Flight Sham ($p < 0.05$)

c: vs AEM ADX ($p < 0.05$)

d: vs AEM Sham ($p < 0.05$)

e: vs VIV ADX ($p < 0.05$)

FIGURE 6

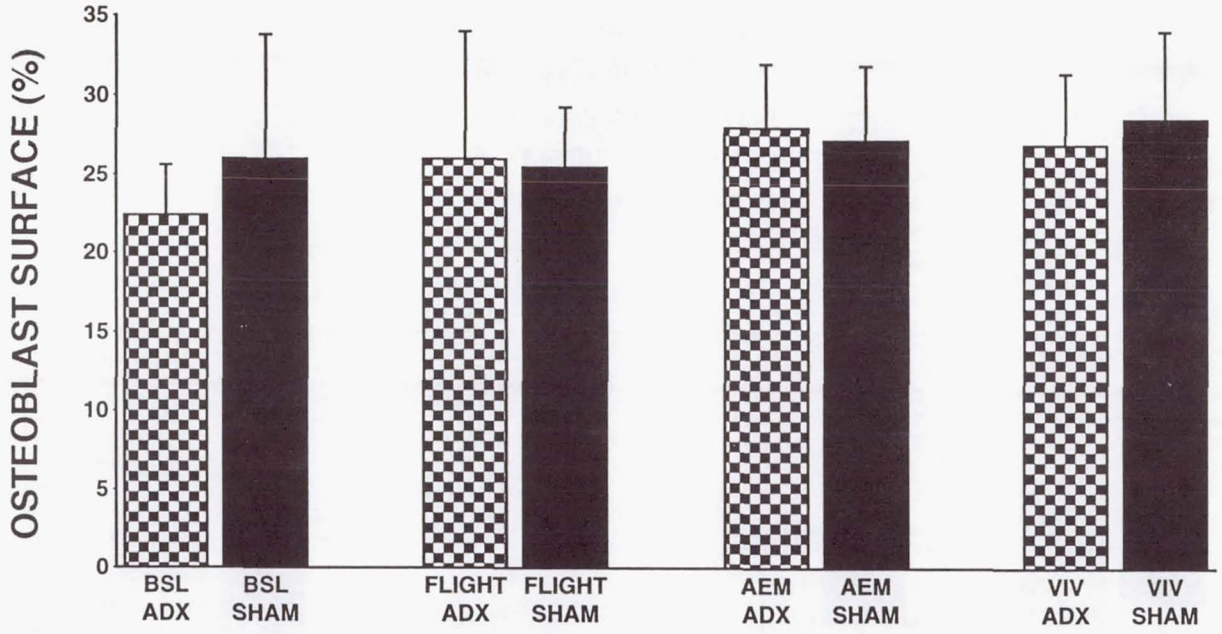

a: vs Flight ADX ($p < 0.05$)

b: vs Flight Sham ($p < 0.05$)

c: vs AEM ADX ($p < 0.05$)

d: vs AEM Sham ($p < 0.05$)

e: vs VIV ADX ($p < 0.05$)

FIGURE 7

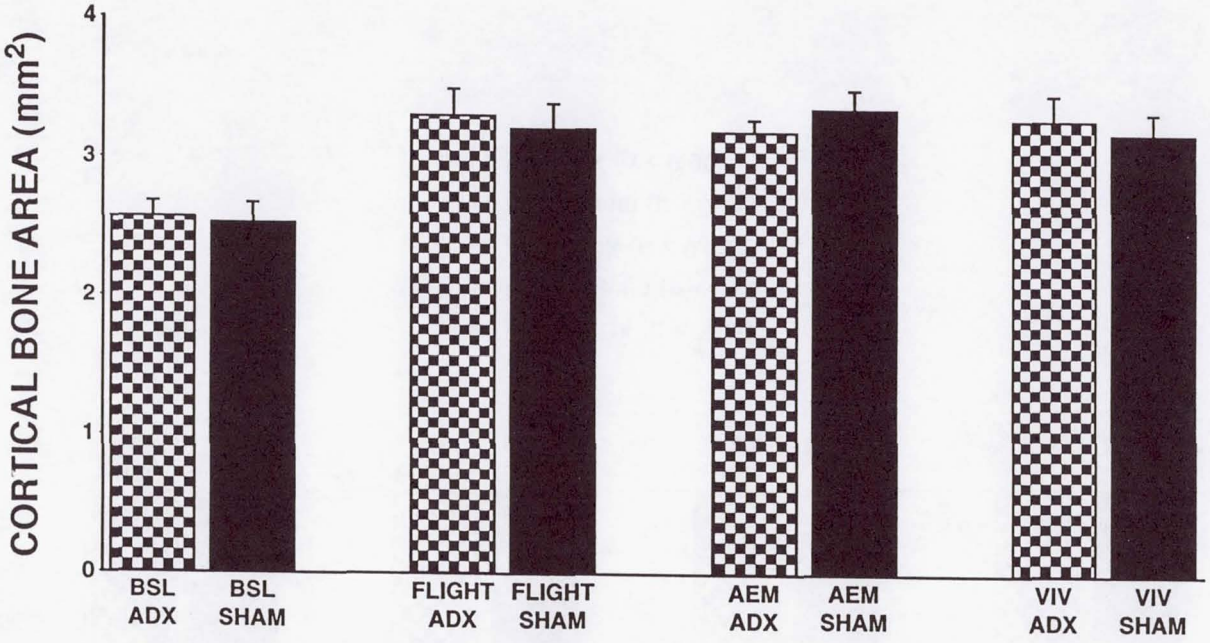

a: vs Flight ADX ($p < 0.05$)
b: vs Flight Sham ($p < 0.05$)
c: vs AEM ADX ($p < 0.05$)
d: vs AEM Sham ($p < 0.05$)
e: vs VIV ADX ($p < 0.05$)

FIGURE 8

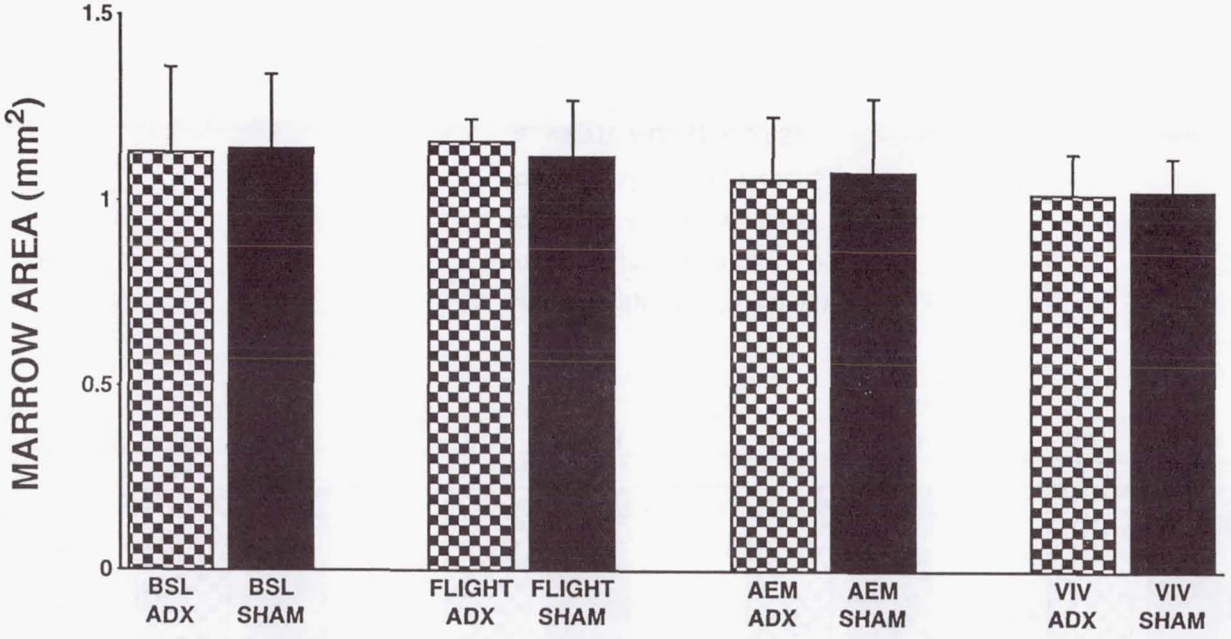

a: vs Flight ADX ($p < 0.05$)
b: vs Flight Sham ($p < 0.05$)
c: vs AEM ADX ($p < 0.05$)
d: vs AEM Sham ($p < 0.05$)
e: vs VIV ADX ($p < 0.05$)

FIGURE 9

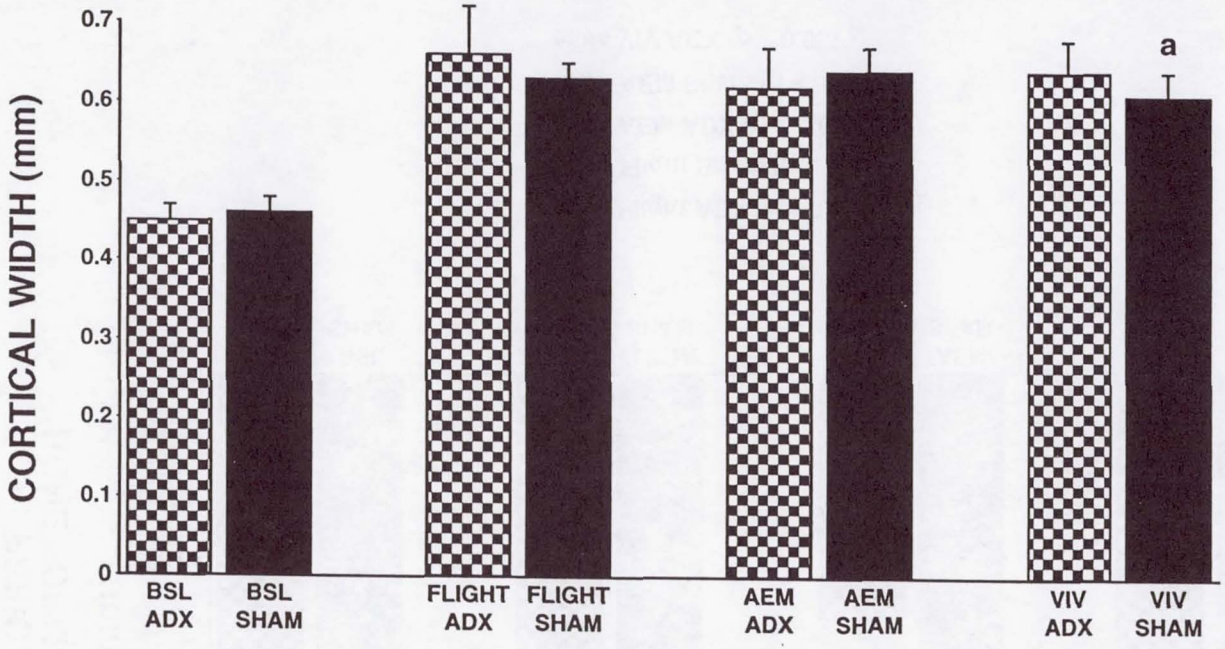

a: vs Flight ADX ($p < 0.05$)
b: vs Flight Sham ($p < 0.05$)
c: vs AEM ADX ($p < 0.05$)
d: vs AEM Sham ($p < 0.05$)
e: vs VIV ADX ($p < 0.05$)

FIGURE 10

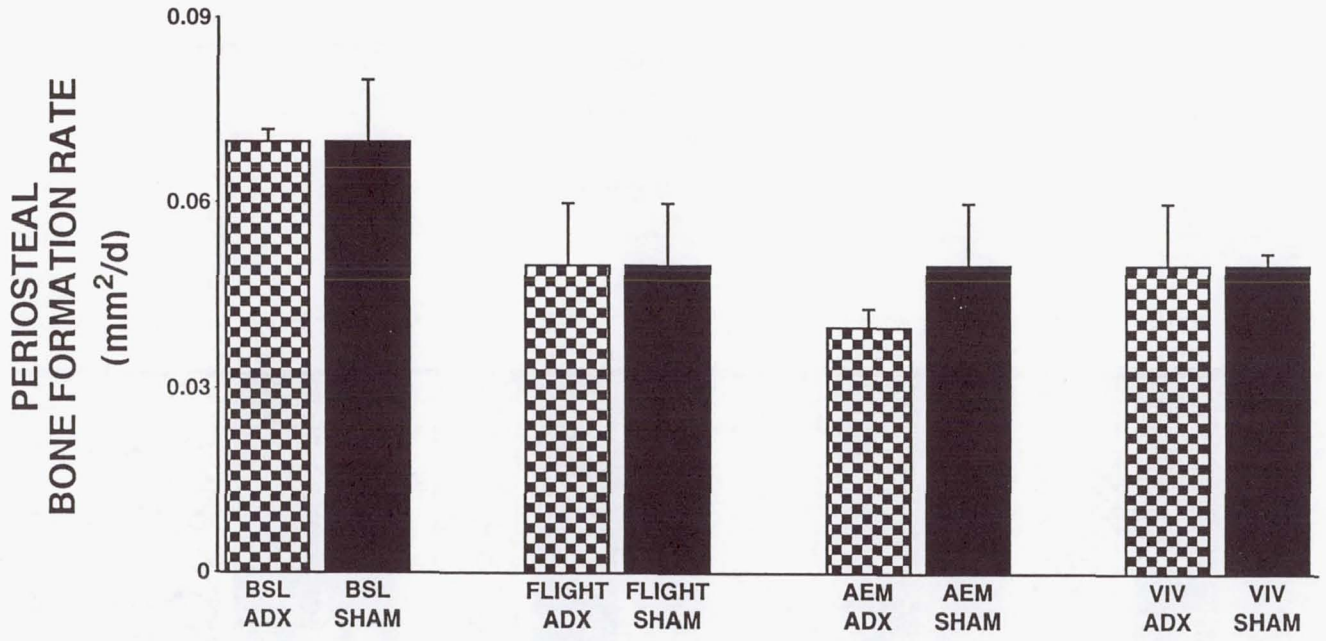

a: vs Flight ADX ($p < 0.05$)

b: vs Flight Sham ($p < 0.05$)

c: vs AEM ADX ($p < 0.05$)

d: vs AEM Sham ($p < 0.05$)

e: vs VIV ADX ($p < 0.05$)

FIGURE 11

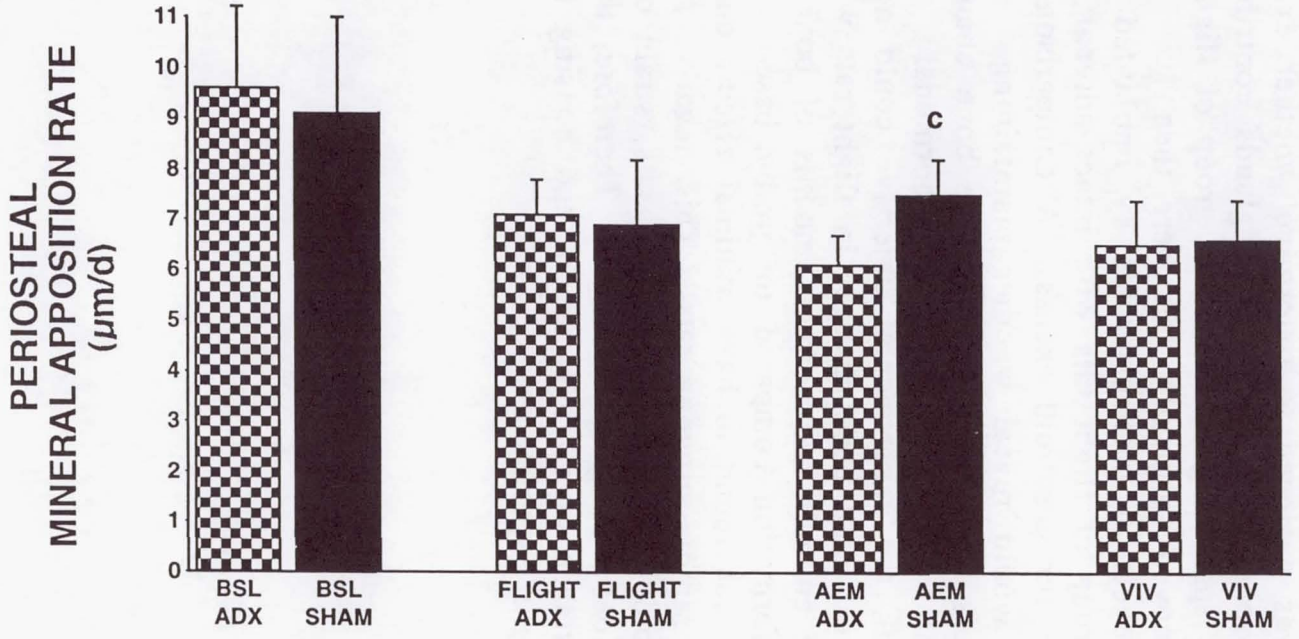

a: vs Flight ADX ($p < 0.05$)
b: vs Flight Sham ($p < 0.05$)
c: vs AEM ADX ($p < 0.05$)
d: vs AEM Sham ($p < 0.05$)
e: vs VIV ADX ($p < 0.05$)

FIGURE 12

NON-TECHNICAL SUMMARY

Corticosteroid hormones that are secreted by the adrenal glands in response to stressful situations are known to be increased during space flight. These hormones are also known to have adverse effects on bone. Therefore, the experiment was designed to determine whether excess secretion of corticosteroid hormones by the adrenal glands contributes to the bone loss associated with space flight. A certain group of flight rats had their adrenal glands removed surgically, but were then supplemented with normal levels of corticosteroids by implanted hormone pellets. Another group of flight rats with intact adrenal glands would presumably experience corticosteroid excess. A comparison of bone between these groups would reveal whether maintaining corticosteroids at normal levels in flight rats affects the bone changes that occur during space flight. Although the planned hormonal manipulations were successful, the experimental objective could not be achieved due to lack of the expected bone changes in flight rats with intact adrenal glands. These animals had normal amounts of bone mass and normal levels of bone formation compared to ground-based control rats. Therefore, space flight was found to have minimal effects on bone mass and bone formation in rapidly growing rats. This negative result may be a consequence of rapid bone growth in young rats, strain of rat, and/or group housing conditions during space flight. Therefore, the findings emphasize the importance of rat age, strain, and housing for the planning of future space flight experiments.

JSC Human Life Sciences Project

E029 - Magnetic Resonance Imaging after Exposure to Microgravity

Principal Investigator:

Dr. Adrian LeBlanc
The Methodist Hospital
Houston, Texas

Final Report for Experiment E029: Life and Microgravity Spacelab

July 21, 1997

1. TITLE

Magnetic Resonance Imaging After Exposure To Microgravity

2. ORGANIZATION

Baylor College of Medicine and The Methodist Hospital
Houston, Texas 77030

3. INVESTIGATORS

Principal Investigator: Adrian LeBlanc, Ph.D.
Professor
Baylor College of Medicine
Houston, TX

Co-Investigators: Linda Shackelford, M.D.
Johnson Space Center, NASA
Houston, TX

Harlan Evans, Ph.D.
Assistant Professor of Medicine,
Baylor College of Medicine
and Krug Life Sciences, Houston, TX

Chen Lin, Ph.D.
Assistant Professor
Department of Medicine,
Baylor College of Medicine, Houston, TX

Thomas Hedrick, M.D.
Assistant Professor
Department of Radiology,
Baylor College of Medicine, Houston, TX

INTRODUCTION

A number of physiological changes have been demonstrated in bone, muscle and blood from exposure of humans and animals to microgravity. Determining mechanisms and the development of effective countermeasures for long duration space missions is an important NASA goal. Historically, NASA has had to rely on tape measures, x-ray and metabolic balance studies with collection of excreta and blood specimens to obtain this information. The development of magnetic resonance imaging (MRI) offers the possibility of greatly extending these early studies in ways not previously possible; MRI is also non-invasive and safe, i.e., no radiation exposure. MRI provides both superb anatomical images for volume measurements of individual structures and quantification of chemical/physical changes induced in the examined tissues. DEXA is a noninvasive technique that employs low dose x-rays to measure bone, fat and lean tissue composition. This proposal will apply MRI and DEXA technology to examine changes resulting from exposure to microgravity in 5 different areas: muscle, intervertebral disc, bone marrow, body composition, and fluid distribution.

OBJECTIVES

1. Measure the muscle volumes of the calf, thigh, and back using MRI before and after flight. These data will be compared with pre and post flight muscle performance measurements. Determine the total body lean tissue mass using DEXA.

2. Determine the changes in the MRI muscle volumes and DEXA soft tissue distribution between R+0 and R+2 days. Determine the calf muscle transverse relaxation time (T2) before and after flight.

3. Determine the change in intervertebral disc size and spine length in the lumbar spine after flight and determine the rate of recovery after return to one G.

4. Determine the bone marrow T2 and cellularity of L3 before and after flight using MRI spectroscopy.

BACKGROUND AND PURPOSE

Space flight without effective countermeasures causes significant loss in muscle mass and strength, similar to horizontal bed rest (1-5). It is believed that these losses are at least partially responsible for degraded muscle performance observed following space flight (3). Our measurements on the crew of Spacelab mission SLJ/STS47 demonstrated significant muscle-specific atrophy after only 8 days in weightlessness (6). We repeated these MRI muscle measurements on the 17 day LMS mission and included more extensive recovery measurements after flight.

Research studies indicate that normal ambulation is necessary for intervertebral disc health

(7-11). Unloading of the spinal column for long periods of time, as in space flight, may result in adaptive changes which may require significant time for readaptation on return to one G and possibly in some degree of permanent change after prolonged weightlessness. The results of our 5 and 17 week horizontal bed rest studies demonstrated that overnight or longer bed rest causes expansion of the disc area, reaching an equilibrium value of about 22% (range 10-40%) above baseline within the first 4 days of bed rest (12). We have shown that following 8 days of space flight, disc area returns to baseline within a few days of ambulation (12). This proposal repeated these measurements on the longer LMS mission to determine if (1) longer exposure to weightlessness would result in post-flight changes and (2) whether measurements taken early after flight would demonstrate the expected disc expansion during flight. For this purpose, this proposal measured the cross-sectional area of intervertebral lumbar discs and vertebral length (L1-L5) before and at several time points after flight including recovery day.

Our bed rest studies demonstrated fluid accumulation in the lower limbs following reambulation which can result in significant error in the estimation of muscle atrophy depending on when measurements are performed-this misinterpretation of the degree of atrophy may impact muscle performance estimates (13). The physiological explanation for these fluid changes is not understood. Two possibilities are: (1) fluid redistribution from the upper body to the lower because of the change in the gravity vector and (2) fluid accumulation resulting from muscle repair caused by post-flight damage and/or rebuilding muscle lost during weightlessness (14-16). We examined this using DEXA and MRI on R+0 and R+2 days, an elapsed time during which significant muscle volume (MRI) or mass (DEXA) change would not be expected. In addition to volume and mass changes, we measured T2 of the calf muscles before and after flight. Exercise is known to cause a transient fluid shift which resolves in less than 45 minutes (17-18) while muscle damage causes changes that evolve more slowly and may last several days to weeks (19-20). We have previously reported that T2 values are elevated shortly after reambulation but not during bed rest, suggesting that fluid has been retained in the limbs compared to bed rest or pre-bed rest (21).

Several space experiments have documented altered hematopoietic activity which may be related to cellularity changes in the bone marrow (22-23). It is known from bone biopsies, for example, that marrow fat increases 100% during the first 20 weeks of paralysis (24). Rats flown aboard Cosmos (19-21 days) have shown increases in marrow fat of 150 - 200% in the tibia and humerus while rats undergoing rear limb suspension have shown even larger increases, +685 and +500% in marrow fat of the tibia and humerus respectively as well as decreases in bone formation (25). These studies may also have relevance to bone atrophy that occurs during space flight and bed rest. It is speculated that adipose cells serve as a store of energy required for hematopoiesis, it may serve a similar purpose for control of osteolytic or osteoblastic activity. One objective of our Life and Microgravity Spacelab (LMS) experiment was to document this expected change in the marrow composition using a noninvasive MRS technique developed in our laboratory(26). The percent fat and cellular

portion of the marrow was measured in L3 before and after flight.

Body composition (bone, fat, lean) are affected either directly or indirectly by space flight (27-30). DEXA derived body composition was determined to complement the fluid shift and muscle loss measurements described above.

METHODS

MRI (magnetic resonance imaging) and DEXA (dual energy x-ray absorptiometry) imaging of the crewmembers of the Spacelab mission, LMS, was performed prior to flight on days L-(50-51), L-(29-31) days and post flight on R+0, R+2, R+10, and R+30 days. Two hours and 15 minutes per session were required except on R+0 when an abbreviated MRI was used because of time restrictions. The total time on R+0 was about 45 minutes for MRI and 15 minutes for DEXA for a total time of about 1 hour. The MRI unit used was a 1.5 Tesla Siemens machine located at The Methodist Hospital in Houston except on R+0 when a portable 1.0 Tesla G.E. instrument was brought to the landing site. In addition to the nominal imaging protocol, additional abbreviated MRI sessions were requested (Astronaut office, IRB, LMS crew) for bone marrow spectroscopy measurements only. These sessions required about 20 minutes and were obtained at various times depending on crew availability and the differences in the observed MRI values from baseline. All crewmembers received a DEXA scan using a Hologic 2000 device located at The Methodist Hospital in Houston or at the Kennedy Space Center. For the bed rest control study conducted at Ames Research Center, 8 male subjects received whole body DEXA scans using a Lunar Corp, DPX scanner and MRI scans using a 1.5 Tesla Siemens magnet located at O'Conner Hospital. The O'Conner unit was located about 5 miles from Ames. The DEXA and MRI imaging were obtained during the week prior to bed rest, on the last day of bed rest and again 24 to 48 hours after reambulation. For the bed rest study, the subjects were transported by stretcher and ambulance to the imaging sites during the bed rest portion of the study or by automobile during the ambulatory phase.

A. MRI

In order to minimize the effects of fluid shifts caused by lying after standing upright, crewmembers are recumbent for a minimum of 10-15 minutes before the start of data acquisition and the order in which the measurements are made was kept the same from one imaging session to the next. The imaging sequence was spine and back followed by the limb measurements. For the limb imaging, the feet were positioned in a holder to minimize movement during image acquisition and to insure repositioning. The portion of the limb being imaged was suspended while the non-imaged portion was supported with foam supports. An RF shield was positioned caudally to the imaged portion of the leg. For the thigh and calf muscles 32, 1 cm slices are obtained using a Te=10 (flight) or 20 (bed rest) msec, Tr=800 (flight) or 1500 (bed rest) msec and a 256x512 matrix. For the back muscles, a similar protocol is used except 20, 0.5 cm slices centered on L3 were obtained

using a spine coil. A phantom was imaged during each imaging session to correct for any changes in pixel size.

Calf muscle T2 was measured by repeating the calf region scan using the same receiver gain at Te=50 msec. T2 values for each muscle pixel were calculated by comparing the image intensity at Te=10msec and Te=50msec. T2 values of each individual muscle were obtained by averaging the T2 for all the pixels within that muscle. Because of time constraints, T2 measurements were not made on the bed rest subjects.

For the spine imaging, the subjects were positioned so that the imaging area was centered within the L3 vertebra, determined from a sagittal scout view. A coronal scout image was used to position a 1 cm slice of interest through the center of the spinal column. A 3 slice gradient echo sequence, Te=7 msec, Tr=800 msec with 1 acquisition and a 256 x 256 matrix was used. A phantom was imaged during each imaging session to correct for any changes in pixel size. Disc area was obtained for discs T12-L1, L1-2, L2-3, L3-4, L4-5 from the number of pixels in each image.

To measure the fat and water percentages in vertebral bone marrow, volume selective proton spectra were obtained using a surface receive coil. A cubic volume of interest of 15mm x 15mm x 15mm located in the center the L3 vertebral body was selected based on the initial scan of the spine region. A Gradient Inversion Spectroscopy technique was used to acquire spectra at Te = 12, 18, 24, and 30 ms with Tr = 2s. The images were corrected for T2 weighting by exponential extrapolation of the spectra obtained at various TE. The intensities of fat and water were calculated by integrating the areas under the fat and water peaks after baseline correction. Bone marrow cellularity was determined from the fat to water peak areas. Since the spectroscopy software was not available on the O'Conner Hospital magnet at the time of the start of the study, pre-bed rest spectroscopy measurements were not obtained. Measurements however were made at end of bed rest and on R+2 and R+15 days.

B. DEXA

A whole body DEXA scan was performed at the time of the MRI scans. The DEXA scan required approximately 15 minutes and gives a radiation exposure of less than 1 mrem. The whole body scan was analyzed for bone mineral density (BMD), soft tissue, lean, and fat. In order to examine fluid redistribution between the upper body and the lower limbs, the soft tissue values of the legs was divided by the whole body soft tissue minus the legs. This ratio was used to compare pre-flight with post-flight.

RESULTS

A. STATISTICAL ANALYSIS

Unless otherwise noted the data were analyzed using repeated measures ANOVA with a Tukey-Kramer or Dunnett multiple comparison test when the ANOVA was significant. Significance was chosen as a $p<0.05$.

B. MUSCLE VOLUME

There were 8 bed rest subjects, however, one subject was not able to enter the MRI magnet head forward because of claustrophobic reasons and therefore only leg imaging was done on this individual. Therefore, only 7 subjects were imaged for the back and spine measurements. The muscle volume for the 7-8 subjects were analyzed using repeated measures ANOVA for the 3 time points (pre-bed rest, last day of bed rest, and 1-2 days after reambulation). Table 1 gives the results as a percent change from baseline at the end of bed rest and during reambulation. These results show that all regions demonstrated significant loss during bed rest except the psoas. The gastrocnemius and anterior calf were no longer significant after 1-2 days of reambulation, presumably because of fluid shifting into the lower limbs-see later section on fluid shift for discussion.

The 4 flight crew received two baseline measurements. For this report the values for both time points were averaged and all individual data points were expressed as a percent change from the average baseline. The data were analyzed statistically as above for the 5 time points, pre, R+0, R+2, R+10, and R+30 days- table 2 gives these results. The R+0 data for the crew is not comparable to the bed rest subject's end of bed rest data since the flight crew were not recumbent after flight, but were in wheelchairs for one to several hours prior to imaging. The R+2 day data is however, comparable between the two studies. Overall, the changes at R+2 seen in the flight crew and bed rest subjects are quite similar, i.e., there are no changes in the psoas, anterior calf and gastrocnemius; the percent change in the soleus, quadriceps, hamstrings and intrinsic back muscles are significant and similar. By R+10 days there were no significant differences from baseline in any of the muscle groups. This is different than SLJ/STS47 (8 day mission) which showed some muscle deficit remaining at R+14 days. The R+0 volume changes after LMS are somewhat greater than SLJ/STS47 obtained on R+1 while the R+2 LMS data are somewhat less than the SLJ data obtained on R+1. These data demonstrate the importance of imaging time for post-flight measurements of muscle volume. We will correlate these muscle changes with muscle performance data from other investigators when this data becomes available. Table 3 shows the muscle volume data from the 8 day SLJ/STS47 Spacelab mission for comparison.

C. FLUID REDISTRIBUTION

The above muscle volume data at R+0 and R+2 days, clearly indicates that fluid moves into

the lower limbs and possibly other muscles after flight or bed rest. For the bed rest subjects above, there was little difference between the end of bed rest data and 1-2 days after reambulation for most muscles except the calf-these changes ranged from 3-6%. We have seen much larger changes, 10-15%, after longer duration bed rest, probably reflecting a response to a relatively overloaded condition after bed rest. The flight data, although showing a slightly different pattern, was in general similar to bed rest. The physiological explanation for these fluid changes is not understood. Two possibilities are: (1) Muscle is dehydrated during weightlessness or bed rest because of fluid redistribution. After return from spaceflight or bed rest, fluid redistributes from the upper body to the lower because of the change in the gravity vector. (2) A second possibility is that there is fluid accumulation resulting from muscle repair caused by post-flight damage and/or rebuilding muscle lost during weightlessness. In the first case, if muscle becomes dehydrated during space flight or bed rest and subsequently rehydrates following reambulation or return to one G, a key question is what is the most appropriate time to measure muscle atrophy, R+0, R+2, R+10 days or some other post-flight time. In second situation, R+0 is the most appropriate time for measurement.

We attempted to investigate possibility number 1 by examining the soft tissue ratio of the legs to upper body from the DEXA scan before during and after bed rest or flight. Table 4 and 5 give these ratios for the bed rest and flight data respectively. While there was a shift during bed rest, this returned to baseline within 1-2 days after bed rest since there is no apparent difference between R+2 and baseline. There was no significant change in the pre-flight and post-flight ratios indicating that the inflight shift to the upper body from the legs has already reverted back to baseline by the time measurements were taken on R+0. There is no evidence for an increased ratio after flight. This might indicate that gravity dependent fluid shift is not responsible for the muscle swelling seen post-flight.

In order to investigate possibility number 2, we measured T2 of the calf muscles. T2 is sensitive to changes in tissue water/protein content. The graphs 1-4 show the calf T2 for the 4 flight crew. Statistical testing showed that the R+2 and R+10, but not R+30 data for the anterior calf and soleus were significantly above baseline. The T2 fro the gastrocnemius ANOVA did not reach significance, $p=0.07$. These results appear to show an elevated T2 at R+2 and sometimes at both R+2 and R+10 which returns toward baseline by R+30. This would indicate that fluid accumulation does occur during this time period after flight, but returns toward the baseline condition by R+30 days. We cannot rule out that T2 is elevated during flight or immediately thereafter, e.g., on R+0. We did not attempt to measure muscle T2 on R+0 because the magnet strength of the portable machine was different than the instrument used for the pre and post-flight measurements. However, it seems unlikely that T2 would be elevated during flight since fluid shifts out of the lower limbs during flight and not into the legs. Also, we have shown that measurements in bed rest do not change muscle T2, but that T2 is elevated following reambulation. The data from the present experiment are consistent with the bed rest data. Interestingly, in 2 individuals, the T2 was still elevated at R+10 when muscle volume differences are not apparent, but performance decrements are

still apparent (Narici). No T2 data was obtained during the bed rest study as previously mentioned. The muscle volume, soft tissue and the T2 data suggest that the most accurate time to obtain muscle atrophy measurements may be before or shortly after reambulation for bed rest and shortly after return to one G in the case of space flight. Reambulation causes a movement of fluid and swelling of muscle that lasts several weeks and is probably associated with muscle damage and/or repair.

D. INTERVERTEBRAL DISC

Table 6 gives the percent change from baseline in the intervertebral area for the bed rest subjects. During bed rest, prior to reambulation, the discs are expanded about 12% above baseline. This is considerably less than the 22% average that we observed previously during 5 and 17 weeks of bed rest (12). This difference may result from the difference in the two bed rest studies, i.e., 6 degree head-down at Ames versus horizontal bed rest in Houston. The head-down condition is likely to provide greater weightbearing on the discs compared to the horizontal condition. There were no residual effects after 1-2 days of reambulation similar to our 5 week bed rest studies. This is also reflected in the spine length measurements, Table 8, which showed about 3.5 mm increase in length during bed rest which normalizes to baseline values by 1-2 days post bed rest. Table 7 gives the cross-sectional disc areas for the flight crew. There is no evidence of disc expansion on R+0. There seems to be slight, but nonsignificant decrease in disc area post-flight. The spine length data of the flight crew is given in Table 9. Because of a missing data point, one way ANOVA was performed on this data instead of repeated measures ANOVA. This data shows a lengthening of the spine relative to baseline on R+0, which appears to be at variance with the disc area measurements. An explanation may be that the disc cross-sectional area reverts back to baseline more quickly than the spine curvature which contributes to spine length as well as disc size. The crew were seated rather than recumbent prior to imaging. Sitting loads the disc about the same as when standing, but might provide support for the back slowing the readaptation process for spinal curvature. There is a tendency for spine length to be decreased post-flight similar to the cross-sectional disc area measurements. These small post-flight changes which were not observed in the Ames or in our previous bed rest studies may have some relevance for longer space missions.

E. BONE MARROW

The proton spectroscopy data (T2 Water, T2 Fat, and Percent Water) were analyzed for three subgroups of subjects (four astronauts, seven normal controls, and seven bed rest subjects). The data available for the astronauts included two pre-flight measurements and 6-7 post-recovery measurements. For the bed rest subjects there were three measurements, end of bed rest, R+2 and R+15 days post reambulation. The normal controls had 4 to 11 observations over an 85 week period.

Immediately post-flight no significant change in the fraction of the water (cellular) component

was found although subsequent post-flight measurements may indicate some change, figure 5. There appeared to be a small decrease in the T2 of the cellular component post-flight, but what was surprising was the increase in T2 in all crewmembers that was clearly evident by the final data collection point at 30 days post-flight. We obtained IRB and astronaut permission to obtain additional measurements when the crewmember's time and schedule permitted. These data are shown in figure 6. For 3 of the 4 crewmembers, the T2 remains elevated above baseline for more than 4 months after landing. These data appeared to show a consistent pattern post-recovery: an increase followed by a reduction. The data were analyzed using non-linear regression models, e.g. a Farazdaghi and Harris growth curve model. Although the data pattern was consistent with this model, the limited number of data points for each astronaut precluded a good fit of the model to each individual. However, an exponential growth curve model fit to the data indicated a statistically significant change over elapsed time for the astronauts. In addition to these models, a linear-linear piecewise regression was fit to the data. This is a four parameter model since it requires two linear regressions to be fit. From a visual perspective, this model gave the best fit. Even though the estimated R^2 was greater than 0.80, the number of parameters for the model left only three degrees of freedom for error which produced 95% confidence intervals (CI) that included '0'. Because of the number of data points 90% CI's, would be a better choice. The same model was fit to all four astronauts simultaneously. This produced a good visual fit, but because of the different data patterns for each individual gave an R^2 of only 0.36. The astronaut data did not show a change in the T2 of the fat component, figure 7. Standard linear regression with the other variables for the controls and bed rest subjects indicated, in general, no statistically significant deviations from a non-time-related flat response figures 8-10.

Since the fraction of the cellular portion of the marrow is changing only slightly if at all, we believe that the observed T2 change in the cellular component represents a change in the cellular composition of the marrow. One explanation for this change might increased hematopoiesis to replace lost red cells following flight since the loss of red cell mass during short duration weightlessness is documented. However, the time frame of the T2 response is much longer than needed to replace lost red cells which should be completed within one month after flight. Another explanation for the post-flight T2 response might be increased osteoblastic activity which might be expected to have a longer time frame. In support of this, our 17 week bed rest studies demonstrated an increase in bone formation markers compared to pre-bed rest after reambulation; alkaline phosphatase by 50% and osteocalcin by 33% (31). These findings have significant implications for medical research on earth as well as microgravity. The results of this portion of the project are the most intriguing of our findings.

F. BODY COMPOSITION

Tables 10-11 give the whole body BMD for the bed rest subjects and flight crew. The BMD did not change with bed rest or flight although one point at R+10 appeared to show an increase. It was reported (12th Man in Space Symposium, Euro/Mir 97) that BMD was not

altered immediately after flight (n=1), but did show a decrease several weeks after flight. Our data (n=4) does not show a decrease after bed rest or flight. The R+10 day increase in BMD is presumably not significant since the R+0 and R+30 day values are the same as baseline. Also the increase at R+10 days, 2%, is within expected instrument precision. In any case, it is an increase not a decrease. Subregional analysis showed no significant change in the lumbar spine or pelvis BMD. These results indicate that the reported post-flight BMD decrease after the 20 day Euro/Mir 97 mission is probably not correct. The whole body lean tissue values are given in Tables 12-13. There was no significant change in whole body lean for the flight crew, but a small change was statistically evident for the bed rest study during bed rest and at R+2 days. It is important to point out that lean tissue measurements using DEXA cannot distinguish between fluid changes from actual changes in muscle mass. The bed rest subjects demonstrated no change in total body fat, Table 14, while the flight crew showed a loss in total body fat, Table 15, that appeared to persist up to at least 10 days after the flight. The differences between the flight and bed rest lean and fat results may reflect variation in the diet and or physical activity of the two groups and possibly sample size. Table 16 gives the reported flight crew body weights before and after flight which shows a loss during flight which is not significant by R+10 days although the mean weight is still about 2 Kg less than baseline. The DEXA data would suggest that most of this loss was due to fat.

CONCLUSIONS

Clearly, the most interesting findings of our experiment was the unexpected finding of the dramatic changes in bone marrow following flight. The significance of these findings needs further work, but we could speculate that if these changes represent a response of the trabecular skeleton to loading, measurements such as these may provide an early indicator of bone formation. This information might be useful in assessing early the response to countermeasures against space flight or osteoporosis associated with aging. Assuming that alterations that result in bone loss with aging or other causes are at least partially rooted in the bone marrow, these findings could lead to a better understanding of the basic physiology of the remodeling process with disease. It may be possible to investigate bone specific changes in remodeling in response to loading or from other types of interventions. We would like to verify the findings on LMS on another short-term (8-17 days) shuttle mission with a design to intentionally follow these changes after flight. It would also be interesting to investigate women entering the menopause and correlate ultimate changes in BMD over 1-2 years versus the changes occurring in the marrow.

We did not observe any residual expansion of the intervertebral discs as seen after long duration bed rest, rather we did observe some slight contraction in the discs following flight which might be important after long duration weightlessness.

As expected, our MRI measurements demonstrated small decreases in muscle volume in the calf, thigh and back similar to the changes after 17 days of bed rest. There was fluid

movement into the lower limb as evidenced by MRI volume changes between R+0 and R+2 and increases in T2 on R+2 and in some cases on both R+0 and R+10 days. Our data suggest that reambulation after flight or bed rest causes swelling of muscle that lasts several weeks and is probably associated with muscle damage and/or repair.

There were no significant changes in total body BMD or lean tissue after flight, but there appeared to be loss in total body fat which paralleled changes in total body weight.

ACKNOWLEDGEMENT

The cooperation and interest of the crew in obtaining the measurements for this experiment is appreciated. In particular our research group would like to express our appreciation to the crew for their willingness to undergo the additional MRI scans to elucidate the evolution of the bone marrow T2 phenomena-we are aware of their busy post-flight schedule and the inconvenience in fighting Houston traffic to reach the Medical Center. We also thank the bed rest subjects for participating in the study conducted at Ames Research Center.

We would also like to thank Mel Buderer, James Downey, Victor Schneider, Sarah Arnaud and their staff for support for the bed rest and flight studies.

REFERENCES

1. Thornton W.E.; and Rummel J.A. Muscular Deconditioning and its Prevention in Space Flight. In: Dietlein L. (ed) *Biomedical Results from Skylab*. U.S. Govt. Printing Office, Washington, DC, pp. 191-197, 1977.
2. Whedon G.D.; Lutwak L.; Rambaut P.C.; Whittle M.W.; Smith M.C.; Reid J.; Leach C.S.; Stadler C.R.; and Sanford D.D. Mineral and Nitrogen Metabolic Studies, Experiment M071. In: Dietlein L. (ed) *Biomedical Results from Skylab*. U.S. Govt. Printing Office, Washington, D.C., pp 164-174, 1977.
3. Hayes JC; McBrine JJ; Roper ML; Stricklin MD; Siconolfi SF; Greenisen MC. Effects of Space Shuttle Flights on Skeletal Muscle Performance. FASEB J 6:A1770, 1992.
4. LeBlanc A.; Gogia P.; Schneider V.; Krebs J.; Schonfeld E.; Jhingran S.; and Johnson P. Calf Muscle Area and Strength Changes After Five Weeks of Horizontal Bed Rest. *Am. J. of Sports Medicine* 16:624-629, 1988.
5. LeBlanc A.D.; Schneider V.S.; Evans H.J.; Pientok C.; Rowe R.; and Spector E. Regional Changes in Muscle Mass Following 17 Weeks of Bed Rest. *J. Appl. Physiol.* 73(5):2172-2178, 1992.
6. LeBlanc A; Rowe R; Schneider V; Evans H, Hedrick T; Regional Muscle Loss After Short Duration Space Flight *Aviation, Space, & Env Med.* 66(12):1151-1154, 1995.
7. Hansson T.; and Roos B. The Relation Between Bone Mineral Content, Experimental Compression Fractures, and Disc Degeneration in Lumbar Vertebrae. *Spine* 6:147-

153, 1981.
8. Holm S.; and Nachemson A. Nutritional Changes in the Canine Intervertebral Disc After Spinal Fusion. *Clin. Ortho. Rel. Res.* 169:243-258, 1982.
9. Keller T.S.; Hansson T.H.; Abram A.C.; Spengler D.; and Panjabi M.M. Regional Variations in the Compressive Properties of Lumbar Vertebral Trabeculae, Effects of Disc Degeneration. *Spine* 14:1012-1019, 1989.
10. Kurowski P.; and Kubo A. The Relationship of Degeneration of the Intervertebral Disc to Mechanical Loading Conditions on Lumbar Vertebrae. *Spine* 11:726-731, 1986.
11. Pedrini-Mille A.; Maynard J.A.; Durnova G.N.; et. al. Effects of Microgravity on the Composition of the Intervertebral Disk. *J. Appl. Physiol.* 73:26s-32s, 1992.
12. LeBlanc AD; Evans HJ; Schneider VS; Wendt RE III; and Hedrick TD. Changes in Intervertebral Disc Cross-sectional Area with Bed Rest and Space Flight. *Spine* 19(7):812-817, 1994.
13. A. LeBlanc, R. Rowe, H. Evans. Muscle Volume Changes After Overnight and Long Duration Bed Rest. Society For Magnetic Resonance Imaging in Medicine and Biology. U. of Liverpool, United Kingdom. June 26 - July 2, 1994.
14. Kasper CE, White TP, Maxwell LC. Running during recovery from hindlimb suspension induces transient muscle injury. APS 533-539, 1990.
15. Riley DA; Bain JLW; Thompson JLT; Trappe P; Costill D; Fitts RH. Histochemical, Immunohistochemical, and Ultrastructural Studies of Unloaded and Reloaded Human Gastrocnemius and Soleus Muscles. ASGSB Bulletin (9)1: Abstract 123, October 1995.
16. Riley DA; Ellis S; Slocum GR; Sedlak FR; Bain JLW; Krippendorf BB; Lehman CT; Macias MY ; Thompson JL; Vijayan K; De Bruin JA. In-flight and postflight changes in skeletal muscles of SLS-1 and SLS-2 spaceflown rats. APS 133-144, 1996.
17. Conley MS; Meyer RA; Bloomberg JJ; Feeback DL; Dudley GA Noninvasive Analysis of Human Neck Muscle Function. Spine Vol 20(23):2505-2512, 1995.
18. Disler DG; Cohen MS; Krebs DE; Roy SH; Rosenthal DI. Dynamic Evaluation of exercising leg Muscle in Healthy Subjects with Echo Planar MR Imaging: Work Rate and Total Work Determine Rate of T2 Change. JMRI Vol 5(5):588-594, September/October, 1995.
19 Fleckenstein JL; Weatherall PT; Parkey RW; Payne JA; Peshock RM. Sports-related muscle injuries: evaluation with MR imaging. Radiology 1989; 172:793-8.
20. LeBlanc AD; Jaweed M; Evans H. Evaluation of Muscle Injury Using Magentic Resonance Imaging. Clin J Sport Med 3:26-30, 1993.
21. LeBlanc AD; Evans H; Schonfeld E; Ford J; Schneider V; Jhingran S; Johnson P. Changes in Nuclear Magnetic Resonance (T_2) Relaxation of Limb Tissue With Bed Rest. MR in Med. 4:487-492, 1987.
22. Johnson PC. The Erythropoietic Effects of Weightlessness. In: *Current Concepts in Erythropoiesis*, ed. C.R. Dunn, Chapter 12. John Wiley & Sons Ltd., 1983.
23. Udden MM, Driscoll TB; Pickett MH; Leach-Huntoon CS; Alfrey CP. Decreased

Production Of Red Blood Cells In Human Subjects Exposed to Microgravity. J Lab Clin Med: April, 1995.

24. Minaire P; Meunier P; Edouald C; Bernard J; Courpron P; and Bourrat J. Quantitative Histological Data on Disuse Osteoporosis; Comparison with Biological Data. *Calcif Tissue Res* 17:57-73, 1974.
25. Morey-Holton E; and Wronski TJ. Animal Models for Simulation of Weightlessness. *Physiologist* 24(6):545-548, 1981.
26. Lin C; Wendt R; Evans H; Rowe R; Hedrick T; and LeBlanc A. Eddy Current Correction in Volume Localized Magnetic Resonance Spectroscopy. J. of MRI 4:823-827, 1994.
27. VS.Oganov, AI.Grigoriev, LI.Voronin, AS.Rakmanov, AV.Bakulin, V.Schneider, A.LeBlanc. Bone Mineral Density in Cosmonauts After 4.5-6 Month Long Flights Aboard Orbital Station MIR. Aerospace And Environmental Medicine 26(No.5-6):20-24, 1992.
28. Schneider VS, LeBlanc AD, Huntoon CL. Prevention of Space Flight induced Soft Tissue Calcification and Disuse Osteoporosis. Acta Astronautica 29:139-140, 1993.
29. Schneider V, V Oganov, A LeBlanc, A Rakmonov, L Taggart, A Bakulin, C Huntoon, A grigoriev L Veronin. Bone and Body Mass Changes During Space Flight. Acta Astronautica 36:463-466, 1995.
30. A. LeBlanc, V. Schneider, LL Shackelford, S. West, V. Ogavov, A. Bakulin, L. Veronin. "Bone Mineral and Lean Tissue Loss After Long Duration Spaceflight".American Society for Bone and Mineral Research, Seattle, Washington, September 7-11, 1996.
31. A.LeBlanc, V.Schneider, E.Spector, H.Evans, R.Rowe, H. Lane. Calcium Absorption, Endogenous Secretion and Endocrine Changes During and After Long-Term Bed Rest. Bone 16(4):301S-304S, 1995.

PRESENTATIONS

"Vertebral Bone Marrow Changes Following Space Flight" A LeBlanc, C Lin, H Evans, L Shackelford, S West, T Hedricks. 12th Man In Space Symposium, Washington, DC, June 8-13, 1997.

"T2 Vertebral Bone Marrow Changes After Space Flight" American Society for Bone Mineral Research, Cincinnati, Ohio, September 10-14, 1997.

"Magnetic Resonance Imaging After Exposure to Microgravity"
A LeBlanc, C Lin, H Evans, R Rowe, L Shackelford, T Hedricks. LMS One Year Science Review, Montreal, Quebec, August 20-21, 1997.

NON-TECHNICAL SUMMARY

Researchers have found a number of physiological changes in bone, muscle and blood from exposure of humans and animals to microgravity. Determining mechanisms and the development of effective countermeasures for long duration space missions is an important NASA goal. Magnetic resonance imaging (MRI) offers the possibility of greatly extending these early studies; MRI provides both superb anatomical images of individual structures and quantification of chemical/physical changes induced in the examined tissues. In addition, MRI is non-invasive and safe. Dual photon x-ray absorptiometry (DEXA), commonly used clinically to evaluate osteoporosis, is a noninvasive technique that employs low dose x-rays to measure bone, fat and lean tissue composition. This experiment used MRI and DEXA technology to examine changes resulting from exposure to microgravity in 5 different areas: muscle, intervertebral disc, bone marrow, body composition, and fluid distribution.

Our MRI measurements demonstrated decreases, 3-12%, in muscle volume in the calf, thigh and back similar to changes after 17 days of bed rest-within 10 days after flight these differences from baseline were no longer apparent. Our data suggest that reambulation after flight or bed rest causes swelling of muscle that lasts several weeks and is probably associated with muscle damage and/or repair.

It is generally believed that there is significant expansion of the intervertebral disc during weightlessness as observed during bed rest simulation. Research studies suggest that normal ambulation is necessary for intervertebral disc health and that extended time in microgravity may have deleterious effects on disc health. We did not observe any significant residual changes in the intervertebral discs after flight.

The most interesting finding of our experiment was the dramatic MRI change in bone marrow found following flight. The significance of these findings needs further work, but we speculate that if these changes represent a response of the trabecular skeleton to mechanical loading, measurements such as these may provide an early indicator of bone formation. This would be useful in assessing the early response of techniques designed to prevent bone loss from space flight, aging, or other causes. Assuming that bone marrow is an essential element in the process that leads to changes in bone mass, these findings could provide a better understanding of the basic physiology of the remodeling process in particular alterations caused by aging or disease. It may be possible to investigate region specific changes in bone remodeling in response to mechanical loading or other interventions.

TABLE 1

BED REST MUSCLE VOLUME - PERCENT CHANGE FROM BASELINE ± SD

MUSCLE	BED REST*	p	R+1/2 DAYS	p
Anterior Calf (n=8)	-5.7 ± 3.2	<0.001	-2.5 ± 1.9	NS
Soleus (n=8)	-10.0 ± 3.0	<0.001	-5.5 ± 2.3	<0.001
Gastroc (n=8)	-8.4 ± 3.1	<0.001	-2.2 ± 3.1	NS
Soleus & Gastoc (n=8)	-9.4 ± 2.9	<0.001	-4.3 ± 2.1	<0.001
Quads (n=8)	-5.6 ± 1.7	<0.001	-4.8 ± 2.2	<0.001
Hams (n=8)	-3.7 ± 3.1	<0.01	-3.7 ± 1.5	<0.01
Intrinsic Back (n=7)	-6.3 ± 2.9	<0.001	-6.2 ± 1.8	<0.001
Psoas (n=7)	-1.0 ± 1.3	NS	0.1 ± 1.4	NS

* Measured on day 16 of bed rest, ANOVA with Tukey-Kramer multiple comparison test.
p = compared to baseline
n = number of subjects

TABLE 2

FLIGHT CREW MUSCLE VOLUME - PERCENT CHANGE FROM BASELINE ±SD, n=4

MUSCLE	L-50/51	L-29/31	R+0	P	R+2	P	R+10	P	R+30	P
ANTERIOR CALF	-0.2 ±0.6	0.2 ±0.6	-3.3 ±2.9	<0.05	-2.4 ±2.2	NS	1.0 ±3.2	NS	0.6 ±1.7	NS
SOLEUS	-0.1 ±1.3	0.1 ±1.3	-9.8 ±3.7	<0.01	-7.1 ±2.5	<0.01	-3.2 ±4.6	NS	-1.6 ±2.0	NS
GASTROC	-0.9 ±1.2	0.9 ±1.2	-12.4 ±3.6	<0.01	-2.5 ±4.6	NS	4.0 ±9.5	NS	0.3 ±4.7	NS
SOLEUS & GASTROC	-0.4 ±1.2	0.4 ±1.2	-10.8 ±3.0	<0.01	-5.4 ±3.1	<0.05	-0.5 ±6.3	NS	-0.9 ±2.8	NS
QUADS	-0.4 ±1.0	0.4 ±1.0	-7.4 ±5.0	<0.01	-4.1 ±4.3	<0.05	-2.6 ±3.7	NS	-0.9 ±2.5	NS
HAMS	-0.3 ±0.4	0.3 ±0.4	-2.8 ±5.5	NS	-4.2 ±3.7	<0.05	0.4 ±4.3	NS	1.1 ±1.9	NS
INTRINSIC BACK	-0.6 ±1.0	0.6 ±1.0	-10.0 ±5.6	<0.01	-7.9 ±1.2	<0.01	-7.9 ±1.2	NS	-0.3 ±1.5	NS
PSOAS	-0.5 ±1.1	0.5 ±1.1	-5.0 ±2.1	<0.01	0.6 ±3.5	NS	0.6 ±3.5	NS	1.2 ±1.0	NS

Table 3

Change in Muscle Volume of Four Crewmembers of Shuttle Flight STS-47. Values are expressed as the Percent Change from the Average of Three Preflight Measurements.

	CALF		THIGH		LUMBAR	
Crewmember†	Anterior	Soleus+ Gastroc	Quadriceps	Hamstrings	Intrinsic	Psoas
			Recovery +1 Day			
1	-4.3	-5.4	---	-7.2	-4.8	-0.9
2	-4.3	-5.2	-4.1	-6.2	-14.5	-7.2
3	-2.3	-6.9	-4.5	-10.1	-7.9	-0.8
4	-4.6	-7.5	-9.4	-8.7	-14.2	-3.6
Mean	-3.9	-6.3	-6.0	-8.0	-10.3	-3.1
±SE	0.5	0.6	1.7	0.9	2.4	1.5
*p	0.005	0.005	0.071	0.002	0.023	0.129
			Recovery +15/16 Days			
1	-1.5	-0.1	---	-3.2	-2.0	2.1
2	-1.3	-1.2	-0.3	-2.1	-7.4	-2.5
3	-5.3	-8.2	-6.2	-6.6	-5.4	-4.6
4	-5.0	-8.3	-7.9	-7.2	-9.0	-4.4
Mean	-3.3	-4.4	-3.1	-4.8	-5.9	-2.4
±SE	1.1	2.2	2.3	1.3	1.5	1.6
*p	0.058	0.058	0.175	0.032	0.029	0.224

* Repeated measures ANOVA using means contrasts and a Greenhouse-Geisser adjustment factor.

† All crewmembers took the salt/water orthostatic countermeasure prior to landing; crewmembers 3 and 4 underwent LBNP 1-2 days before landing; crewmember number 1 performed regular exercise during flight.

TABLE 4

Bed Rest - Ratio of Legs to Upper Body Soft Tissue

SUBJECT	PRE-BED REST	BED REST	R+1/2
249	0.55	0.52	.053
374	0.52	0.50	0.54
405	0.50	0.49	0.49
420	0.47	0.45	0.46
428	0.57	0.52	0.54
435	0.53	0.50	0.50
439	0.52	0.46	0.50
457	0.51	0.48	0.52
MEAN	0.52	0.49	0.51
SD	0.03	0.02	0.02
P VALUE		<0.01	NS

TABLE 5

Flight Crew - Ratio of Legs to Upper Body Soft Tissue

CREW MEMBER	PRE-FLT	R+0	R+2	R+10	R+30
LMS1	0.50	0.49	0.51	0.52	0.50
LMS2	0.54	0.54	0.55	0.56	0.55
LMS3	0.52	0.54	0.54	0.55	0.55
LMS4	0.59	0.56	0.57	0.57	0.58
MEAN	0.54	0.53	0.54	0.55	0.55
SD	0.04	0.04	0.03	0.02	0.03
P VALUE		NS	NS	NS	NS

TABLE 6

BED REST-INTERVERTEBRAL DISC CROSS-SECTIONAL AREA, PERCENT CHANGE FROM BASELINE

	Disk Number					
	T12-L1	L1-L2	L2-L3	L3-L4	L4-L5	Average
Subject-249						
Bedrest	-3	7	-1	11	12	5
R+1	-12	5	-1	4	12	2
Subject-405						
Bedrest	1	11	32	35	19	19
R+2	-17	1	5	2	10	0
Subject-420						
Bedrest	10	32	8	11	21	16
R+2	-4	3	0	2	6	1
Subject-428						
Bedrest	4	-1	16	3	0	5
R+2	-1	1	8	-3	-6	-0
Subject-435						
Bedrest	17	11	10	8	15	12
R+1	-7	2	-4	-1	2	-2
Subject-439	28	26	8	-1	13	15
Bedrest	5	7	1	1	1	3
R+1						
Subject-457						
Bedrest	6	6	14	8	8	8
R+1	-3	-9	0	-4	-4	-4
All Subjects						
Bedrest	9	13	12	11	13	12
p	<0.05	<0.01	<0.01	<0.05	<0.01	<0.01
R+(1-2)	-6	2	1	0	3	0
p	NS	NS	NS	NS	NS	NS

TABLE 7

FLIGHT CREW-INTERVERTEBRAL DISC CROSS-SECTIONAL AREA, PERCENT CHANGE FROM BASELINE

	T12-L1	L1-L2	L2-L3	L3-L4	L4-L5	AVERAGE	p
			LMS-1				
L-50	1	-1	-0	-1	3	0	
L-29	-1	1	0	1	-3	-0	
R+O	-5	5	-4	1	-9	-2	
R+2	3	2	3	2	-4	1	
R+10	-6	-3	-7	-1	-17	-7	
R+30	2	6	-1	1	-4	1	
			LMS-2				
L-51	6	1	-0	-1	-4	0	
L-29	-6	-1	0	1	4	-0	
R+O	-6	-4	-3	-1	0	-3	
R+2	-5	1	-5	-3	4	-1	
R+10	-15	-9	-11	-10	-2	-9	
R+30	-10	-8	-8	-2	-2	-6	
			LMS-3				
L-50	-0	1	-0	*	1	0	
L-31	0	-1	0	*	-1	1	
R+O	-3	-6	-3	*	-1	-6	
R+2	-3	-3	-6	*	3	-1	
R+10	+	-4	-5	*	-1	-8	
R+30	0	-4	-3	*	-2	-5	
			LMS-4				
L-50	-1	3	-1	2	-3	-0	
L-30	1	-3	1	-2	3	0	
R+O	-3	-3	-0	-2	4	-1	
R+2	-11	-7	-2	-3	-1	-5	
R+10	-13	-2	-5	-3	-5	-6	
R+30	2	3	-1	4	-0	2	
			ALL SUBJECTS				
L-(50/51)	1	1	-1	-1	-1	0	
L-(29/31)	-1	-1	1	1	1	0	
R+0	-4	-2	-3	-5	-1	-2	NS
R+2	-4	-2	-2	-0	1	-2	NS
R+10	-9	-5	-7	-9	-6	-6	<0.01
R+30	-1	-1	-3	-4	-2	-1	NS

* Problem measuring disk.
\+ Not available due to scan positioning

TABLE 8

BED REST - CHANGE IN SPINE LENGTH (mm), DISC T12-L1 TO DISC L4-L5

	SUBJECTS								
	249	405	420	428	435	439	457	AVERAGE ALL SUBJECTS	p
BEDREST	1.7	3.2	4.5	3.7	4.8	4.6	2.1	3.5	<0.001
R+1/2	-0.4	0.7	0.8	-0.6	0.6	-0.0	-0.1	0.2	NS

TABLE 9

FLIGHT CREW - CHANGE IN SPINE LENGTH (mm), DISC T12-L1 TO DISC L4-L5

	CREWMEMBERS					
	LMS-1	LMS-2	LMS-3	LMS-4	AVERAGE ALL CREWMEMBERS	p*
L-50/51	0.1	-0.3	0.1	0.4	0.1	
L-29/31	-0.1	0.3	-0.1	-0.4	-0.1	
R+0	2.7	2.0	1.5	1.4	1.9	<0.01
R+2	0.3	-0.7	-1.2	-1.7	-0.8	NS
R+10	-1.5	-2.0	-	-1.7	-1.7	<0.05
R+30	0.3	-1.2	-2.0	-0.7	-0.9	NS

* One way ANOVA was done because of missing data point.

TABLE 10

Bed Rest - Whole Body BMD (gm/cm²)

SUBJECT	PRE BED REST	BED REST	R+1/2
249	1.269	1.258	1.270
374	1.260	1.275	1.267
405	1.407	1.426	1.406
420	1.174	1.169	1.174
428	1.290	1.288	1.309
435	1.135	1.122	1.111
439	1.365	1.400	1.388
457	1.144	1.146	1.141
MEAN	1.255	1.260	1.258
SD	0.099	0.112	0.109
P VALUE		NS	NS

TABLE 11

Flight Crew - Whole Body BMD (gm/cm²)

FLIGHT CREW	PRE-FLT	R+2	R+10	R+30
LMS1	1.095	1.087	1.119	1.083
LMS2	1.256	1.259	1.277	1.262
LMS3	1.147	1.167	1.187	1.167
LMS4	1.171	1.164	1.197	1.164
MEAN	1.167	1.169	1.195	1.169
SD	0.067	0.070	0.064	0.073
P VALUE		NS	<0.01	NS

TABLE 12

Bed Rest - Whole Body Lean Tissue (kg)

SUBJECT	PRE-BED REST	BED REST	R+1/2
249	57.06	57.19	57.11
374	53.51	51.41	52.23
405	62.98	59.92	61.69
420	58.68	55.47	56.70
428	64.33	63.43	62.66
435	55.53	52.68	53.60
439	60.38	57.17	57.75
457	56.26	55.27	55.91
MEAN	58.59	56.56	57.20
SD	3.74	3.84	3.58
P VALUE		<0.01	<0.01

TABLE 13

Flight Crew - Whole Body Lean Tissue (kg)

FLIGHT CREW	PRE-FLT	R+0	R+2	R+10	R+30
LMS1	57.08	53.42	57.13	55.6	57.2
LMS2	58.28	57.21	56.86	60.42	58.31
LMS3	63.06	64.42	65.24	66.14	64.22
LMS4	58.18	58.71	59.19	58.84	59.8
MEAN	59.15	58.44	59.60	60.25	59.88
SD	2.66	4.56	3.89	4.41	3.08
P VALUE		NS	NS	NS	NS

TABLE 14

Bed Rest - Whole Body Fat Tissue (kg)

SUBJECT	PRE BED REST	BED REST	Δ	R+1/2	Δ
249	16.74	16.37	-0.37	15.86	-0.88
374	13.43	14.84	1.41	14.18	0.74
405	23.79	23.63	-0.16	22.87	-0.92
420	28.83	30.15	1.32	29.95	1.12
428	26.69	27.93	1.24	26.02	-0.67
435	20.69	23.05	2.35	22.59	1.89
439	33.48	34.15	0.67	34.08	0.60
457	8.30	7.88	-0.42	7.49	-0.81
MEAN	21.49	22.25	0.75	21.63	0.13
SD	8.38	8.74	1.00	8.74	1.09
P VALUE		NS		NS	

TABLE 15

Flight Crew - Whole Body Fat Tissue (kg)

CREW MEMBER	PRE-FLT	R+2	Δ	R+10	Δ	R+30	Δ
LMS1	25.99	22.52	-3.47	23.77	-2.22	24.45	-1.54
LMS2	19.80	18.48	-1.32	18.02	-1.78	20.11	0.30
LMS3	22.92	19.80	-3.12	19.48	-3.44	18.43	-4.49
LMS4	15.87	12.60	-3.27	13.77	-2.10	14.29	-1.58
MEAN	21.14	18.35	-2.79	18.76	-2.38	19.31	-1.83
SD	4.33	4.19	0.99	4.13	0.73	4.20	1.98
P VALUE		<0.01		<0.05		NS	

Δ = Difference from baseline

TABLE 16

Crew Body Weight (kg)*

	PRE-FLT°	R+0	Δ	R+2	Δ	R+9	Δ	R+30	Δ
LMS1	87.67	80.80	-6.87	83.18	-4.49	83.86	-3.81	86.82	-0.90
LMS2	84.88	80.34	-4.54	0.45	-4.43	83.41	-1.47	84.77	-0.11
LMS3	92.31	90.34	-1.97	90.00	-2.31	90.91	-1.40	88.64	-3.67
LMS4	79.16	74.55	-4.61	77.05	-2.11	7.95	-1.21	79.09	-0.07
Mean	86.00	81.51	-4.49	82.67	-3.33	84.03	-1.97	84.83	-1.19
SD	5.50	6.54	2.00	5.49	1.30	5.31	1.23	4.14	1.70
p		<0.01		<0.05		NS		NS	

* Weights taken with crewmen clothed without shoes. Scales were at various locations at JSC and KSC. Weights showing 2 decimal places were converted from pounds.

° Average of L-60 and L-30 except for L-60 of LMS1 which appeared aberrant-used L-90 in place of L-60 for this data point.

Δ Difference from baseline.

Figure 1. LMS–1 Calf Muscle T2

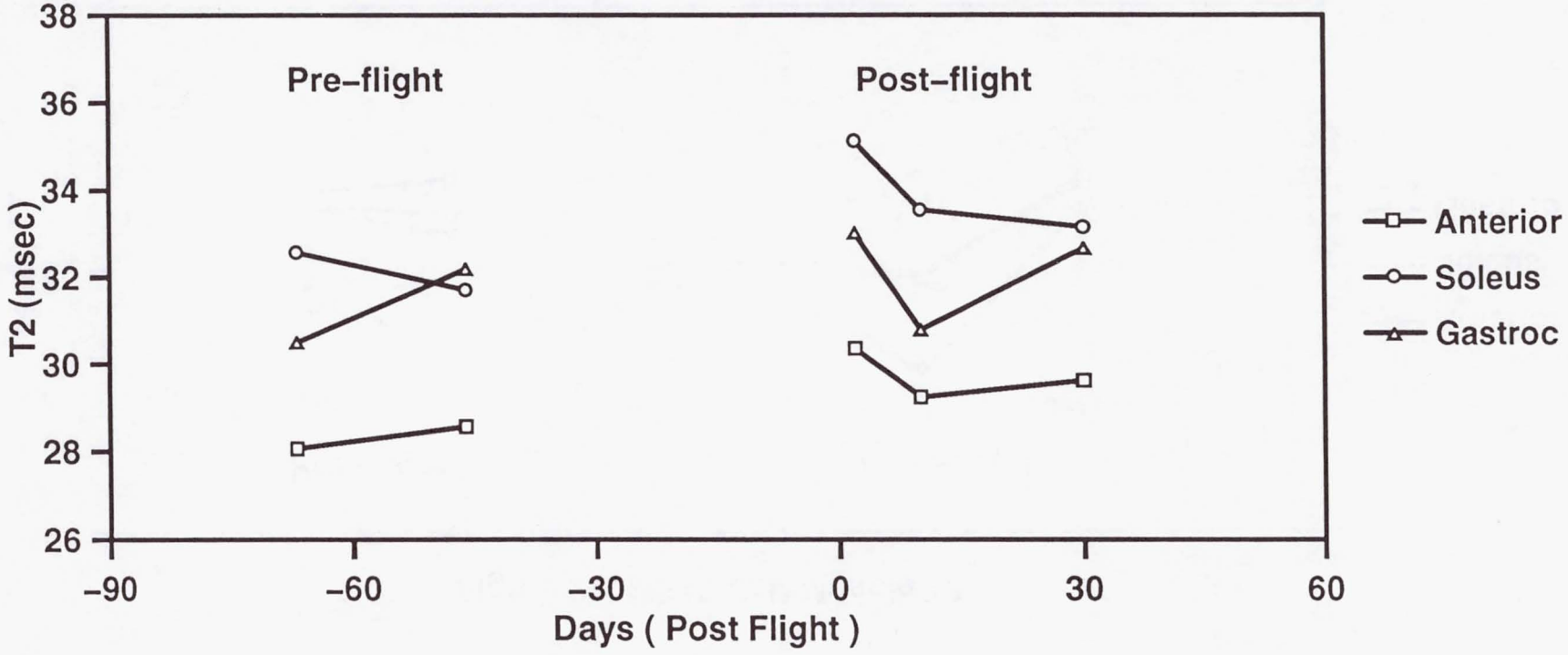

Figure 2. LMS–2 Calf Muscle T2

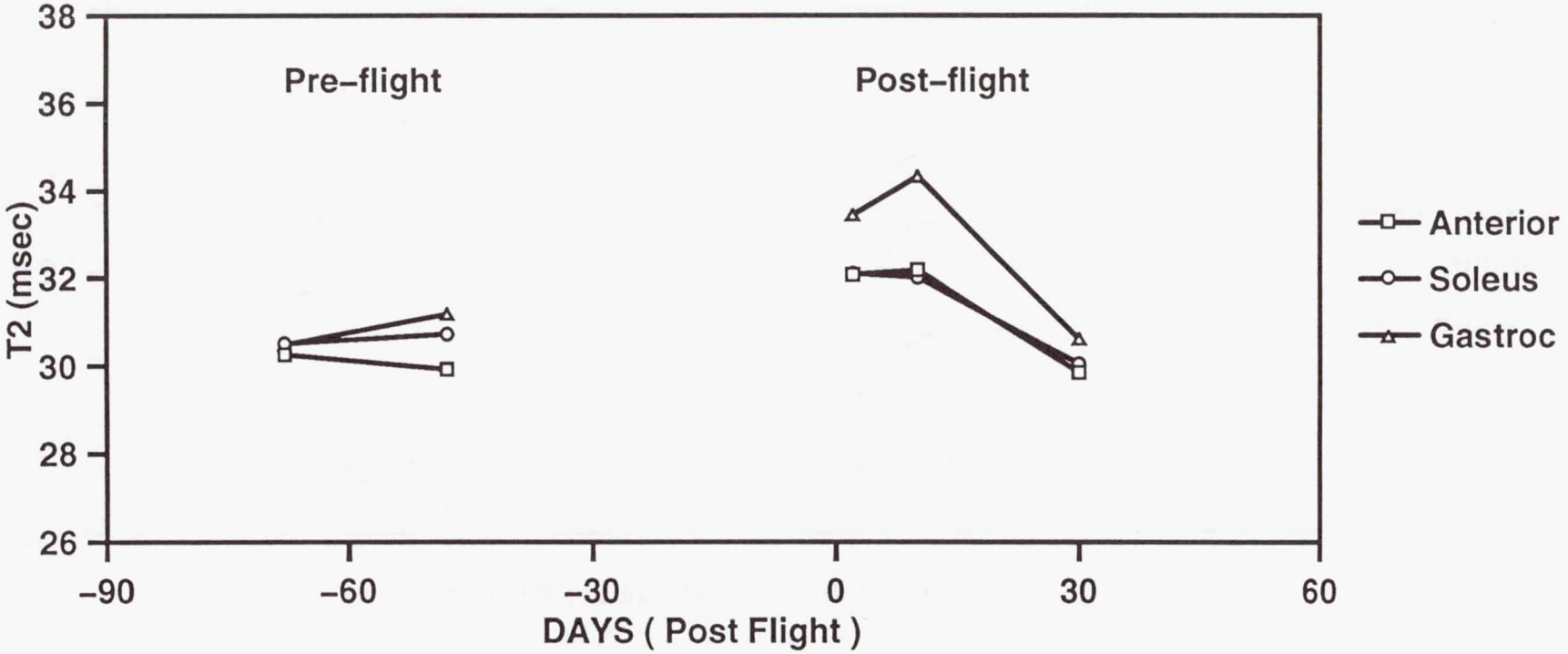

Figure 3. LMS–3 Calf Muscle T2

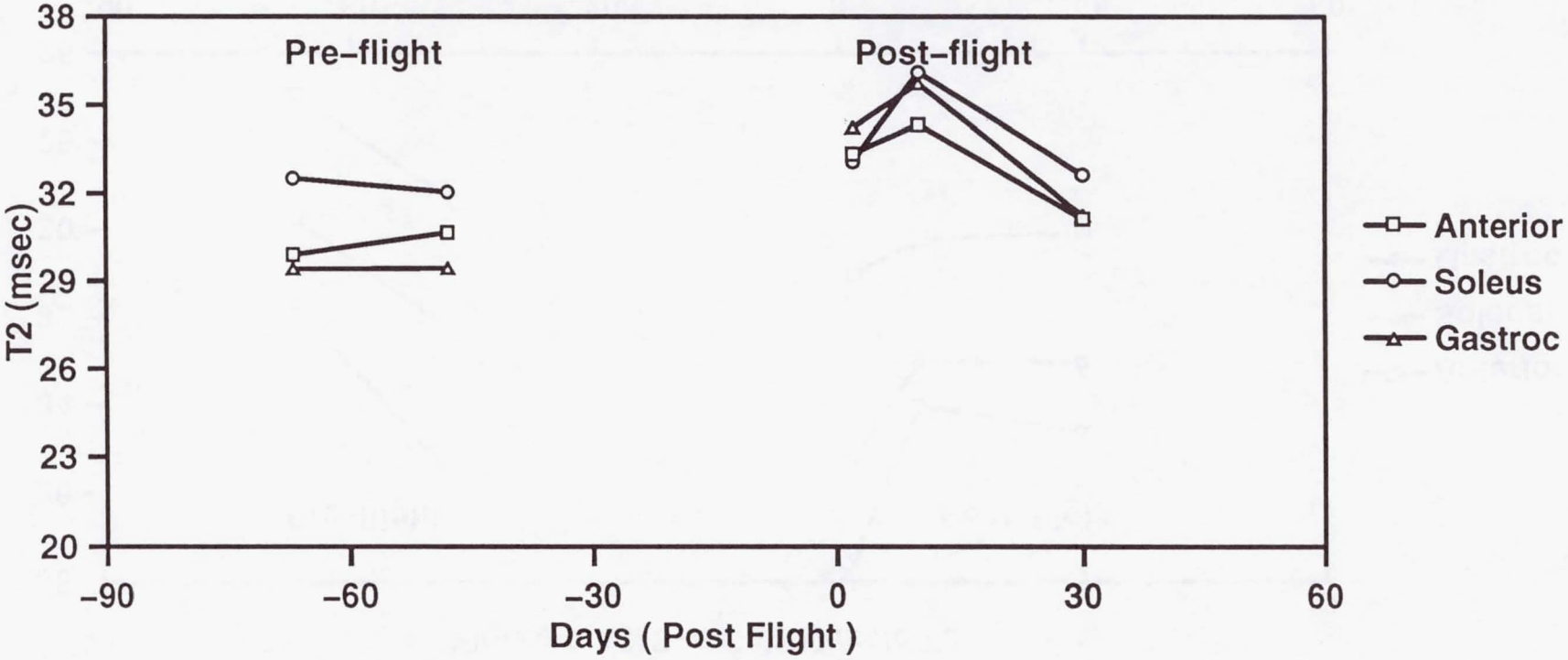

Figure 4. LMS–4 Calf Muscle T2

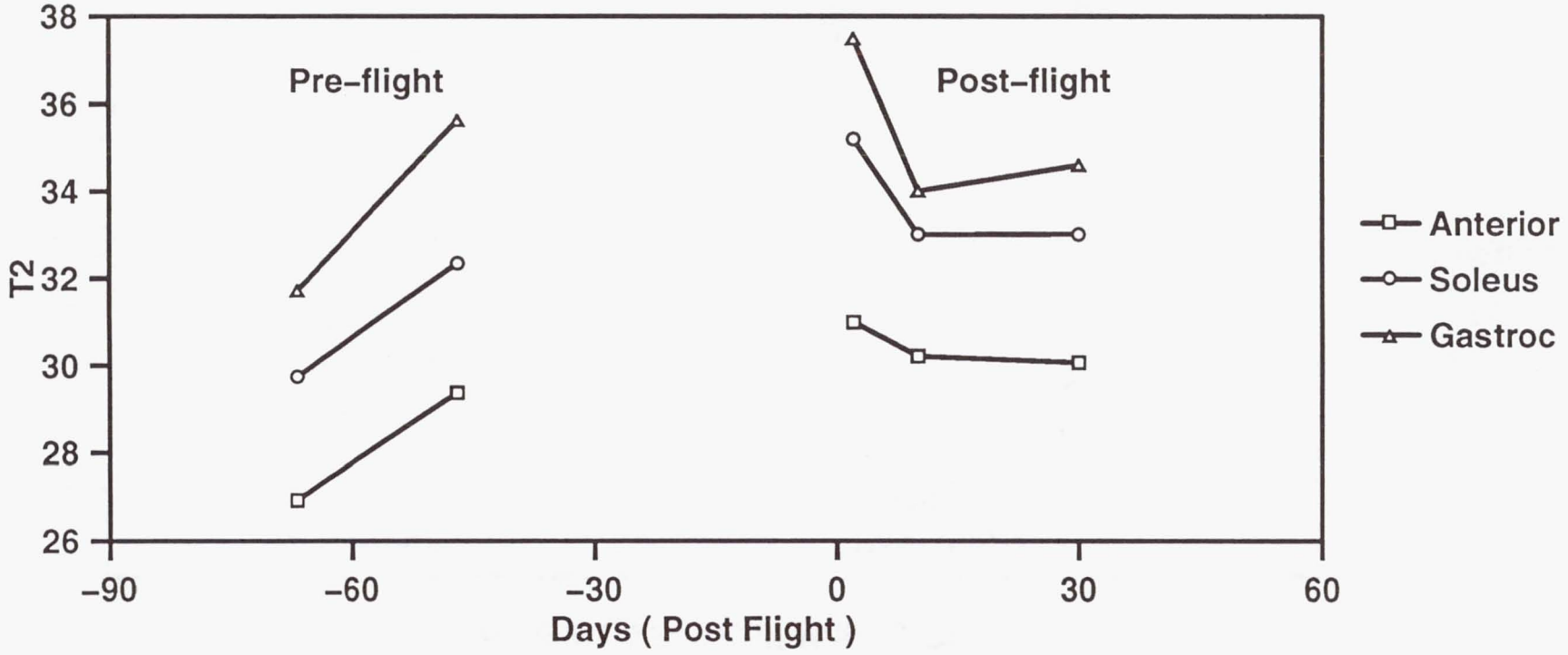

Figure 5. L3 Bone Marrow Water Percentage – Astronauts

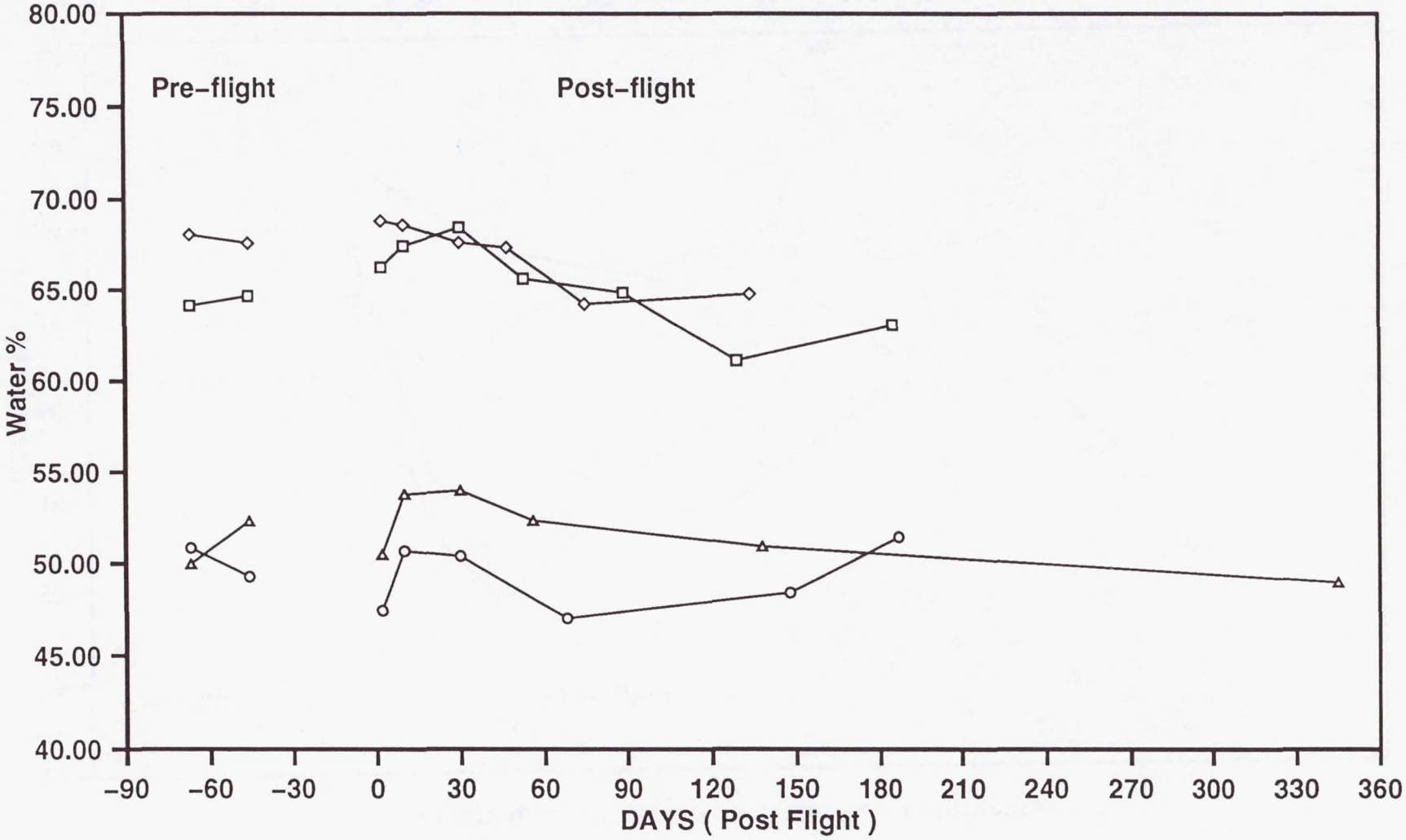

Figure 6. L3 Bone Marrow Water T2 – Astronauts

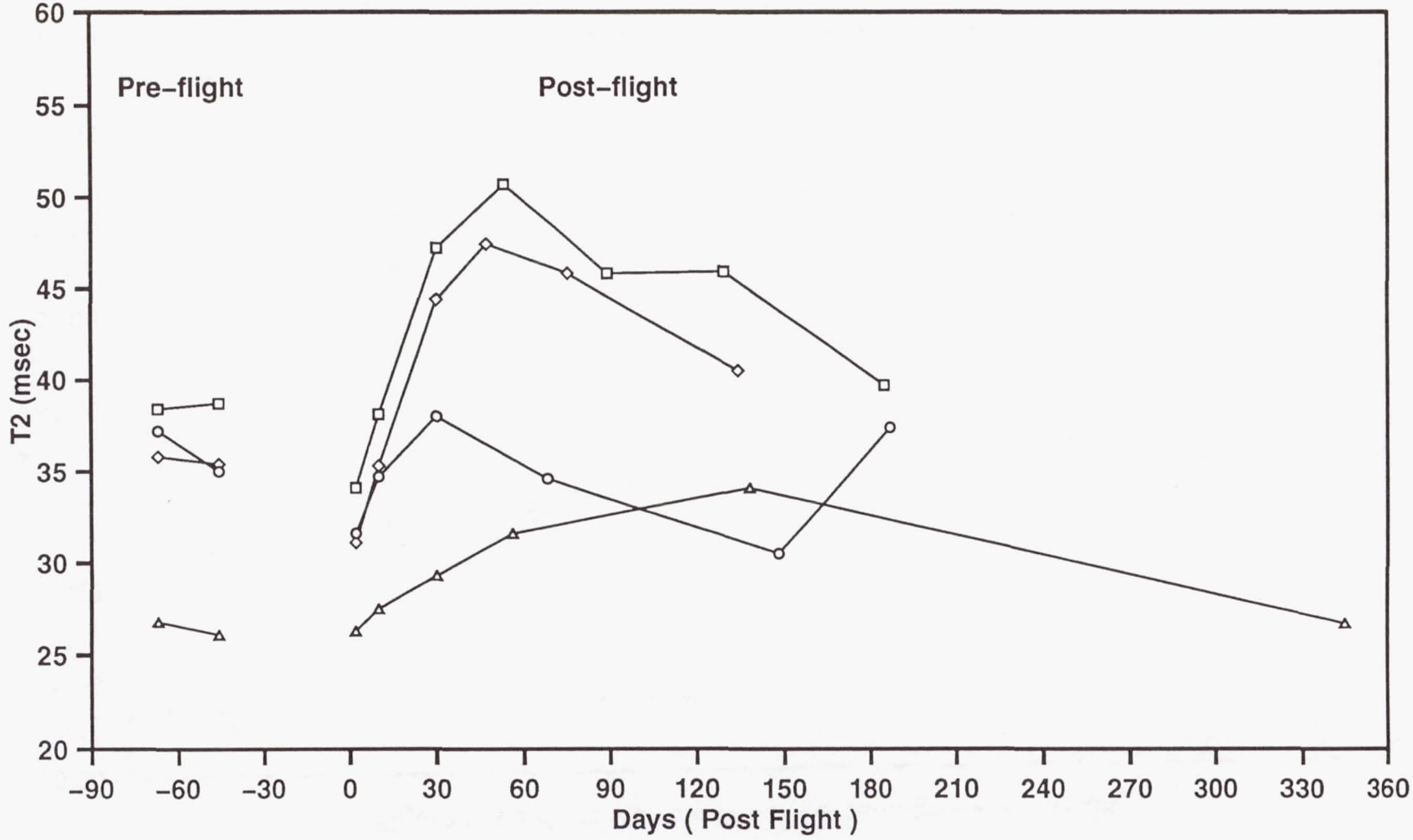

Figure 7. L3 Bone Marrow Fat T2 – Astronauts

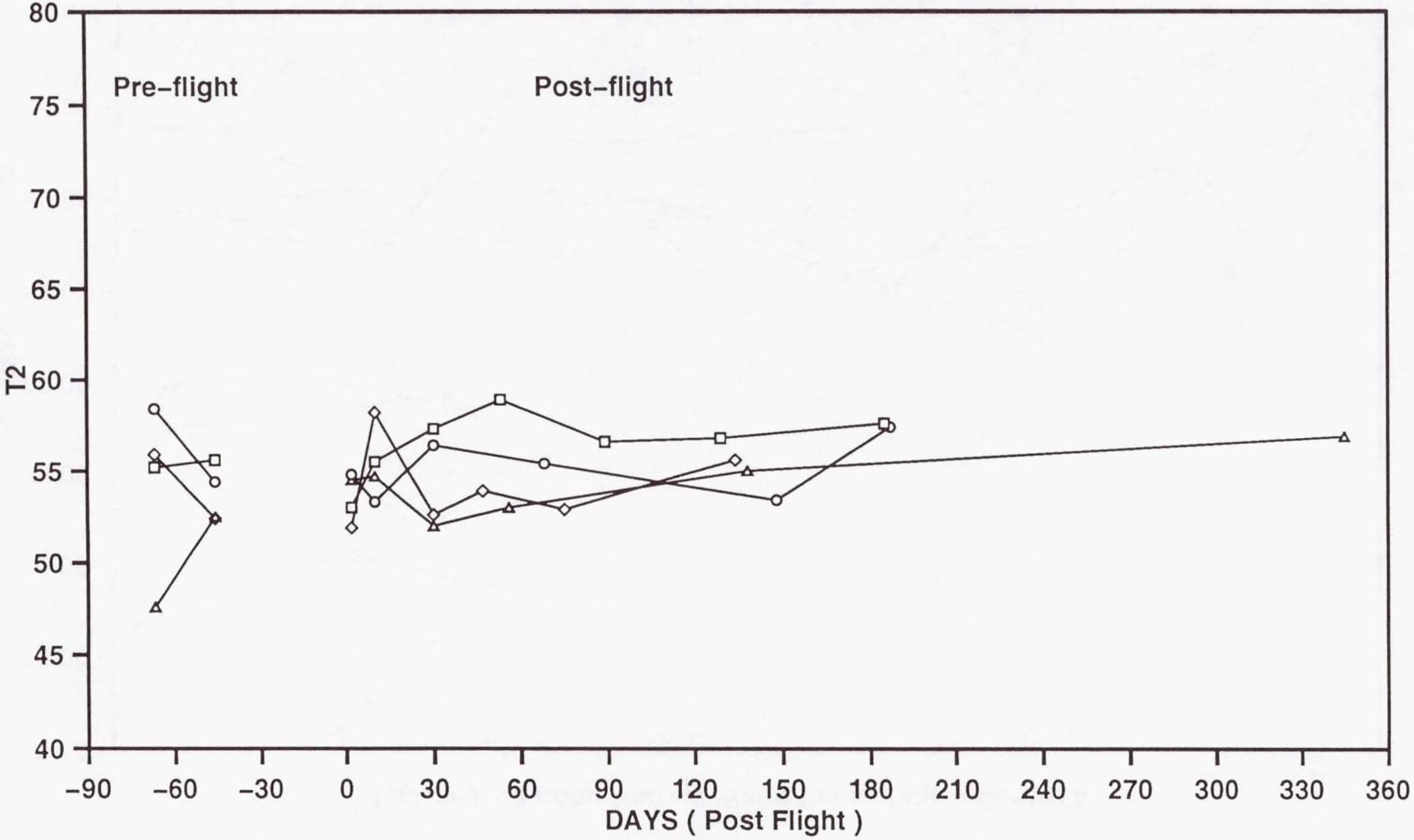

Figure 8. L3 Bone Marrow Water Percentage – Controls

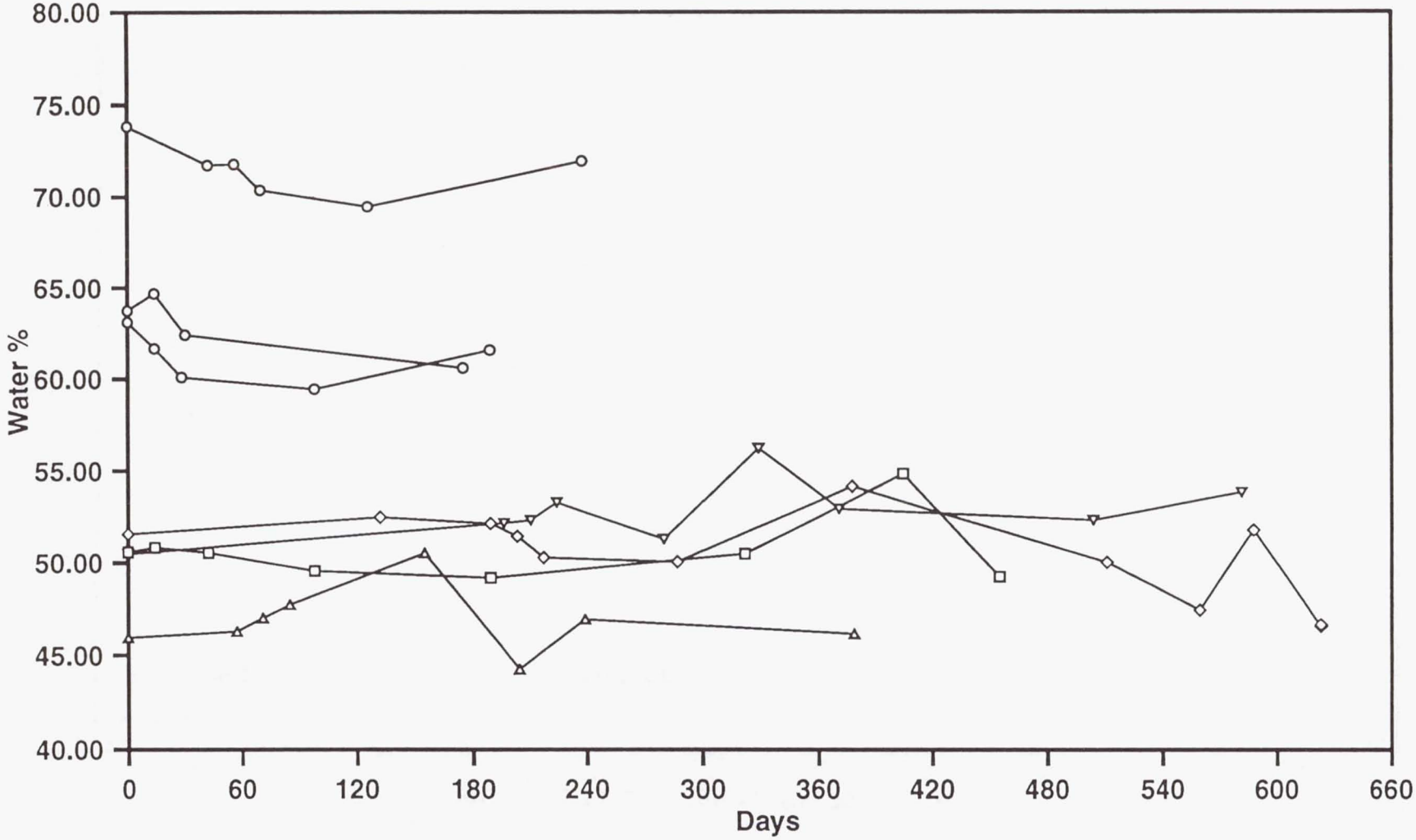

Figure 9. L3 Bone Marrow Water T2 – Controls

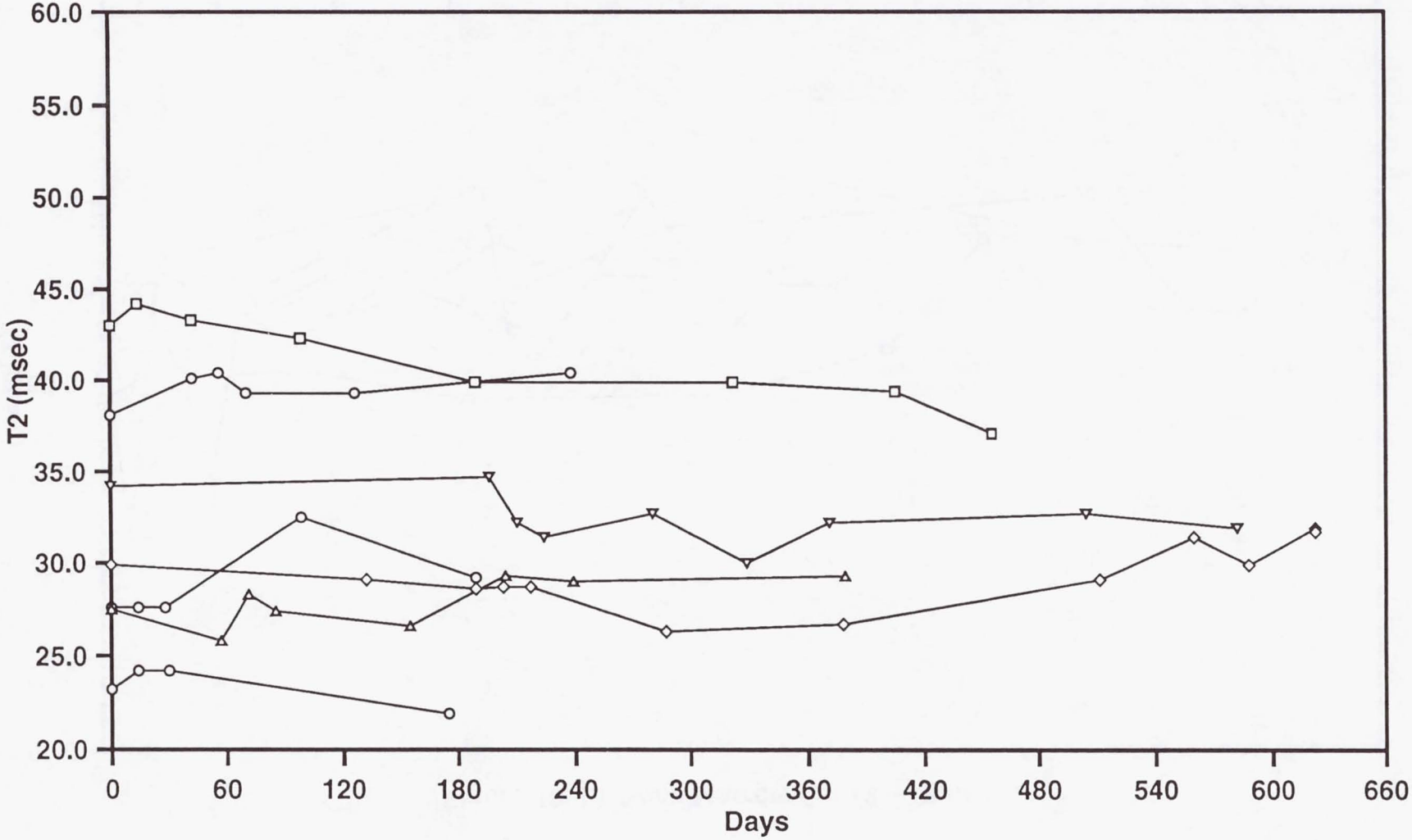

Figure 10. L3 Bone Marrow Fat T2 – Controls

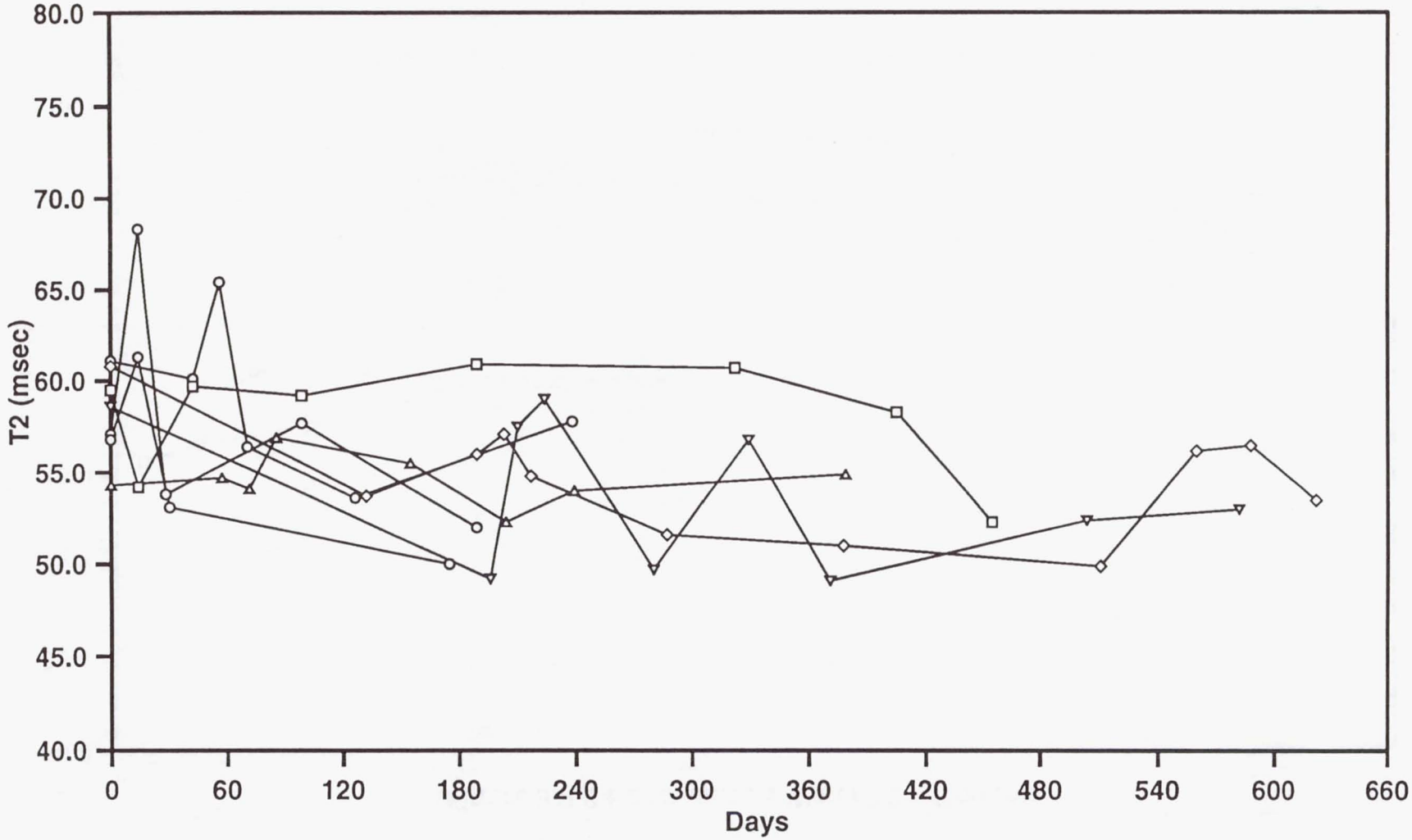

JSC Human Life Sciences Project

E030 - Extended Studies of Pulmonary Function in Weightlessness

Principal Investigator:

Dr. John B. West
University of California, San Diego
La Jolla, California

One Year Post-Flight Science Report
LMS One Year Science Review
Saint-Hubert, Quebec, Canada

Extended Studies of Pulmonary Function in Weightlessness
Astronaut Lung Function Experiment -- ALFE
E-030

Principal Investigator:
John B. West, MD., Ph.D.
University of California, San Diego
Department of Medicine
9500 Gilman Drive
La Jolla, CA 92093-0931

Co-Investigators:

G. Kim Prisk, Ph.D.
University of California, San Diego

Ann R. Elliott, Ph.D.
University of California, San Diego

Manuel Paiva, Ph.D.
Universite Libre de Bruxelles, Belgium

1. Objectives

On Life and Microgravity Spacelab (LMS), we extended our very productive studies in Spacelabs SLS-1, SLS-2, and D-2 of the changes in pulmonary function in microgravity (μG). This was done by studying the effects of exercise on pulmonary function in μG, and additionally by studying changes in chemoreceptive control of ventilation in μG. These measurements will clarify the ventilatory responses to both exercise and changes in inspired O_2 and CO_2, and therefore give information on the function of the chest wall and respiratory muscles. We performed a comprehensive battery of pulmonary function tests both on the ground, and inflight, before and after 85% of maximal exercise testing performed by another experiment (E-920). These studies will shed light on the effects of the known alterations in the distribution of ventilation, perfusion, ventilation-perfusion ratio, and body fluids on the exercise stressed lung, on the mechanical and muscular behavior of the lung and chest wall, and on the chemoreceptors that may contribute to dyspnea in μG.

The objectives of the experiment were:

I. Determine the effect of exercise on the lung in μG. Subjects performed a battery of pulmonary function tests immediately after exercise including measures of cardiac output and lung water, pulmonary diffusing capacity and its subdivisions, and measures of the inhomogeneity of pulmonary ventilation, perfusion, and ventilation-perfusion ratio, and measure metabolic rate via resting oxygen consumption and carbon dioxide production.

II. Further investigate the alterations in intra-acinar gas mixing in μG. Following up on unexpected results from SLS-2 in the area of gas mixing alterations within the acinus of the lung in μG, the inhomogeneity of ventilation tests were modified by altering the inspiratory flow rates to increase the information return from them.

III. Determine separately the pattern of chest wall and abdominal movement during normal ventilation, exercise ventilation and induced hyperventilation. While performing the studies, subjects were instrumented with a respiratory inductance plethysmograph (RIP), a non-invasive device that allows continuous monitoring of the motion and contribution of the rib cage and abdomen. While the subject is not on the mouthpiece, unperturbed measurements of inspiratory and expiratory times were made.

IV. Determine the ventilatory response to carbon dioxide during μG, and pre- and post-flight. Subjects performed a hypercapnic response test in which they rebreathed from a bag containing some CO_2 in a hyperoxic gas mixture.

V. Determine the ventilatory response to acute hypoxia pre- and post-flight. Subjects rebreathed a low O_2 gas mixture from a bag in which the CO_2 was actively removed to maintain isocapnia in the face of increased ventilation and decreasing O_2.

2. Background

The LMS project originated from a proposal submitted in response to AO-84, and which was initially manifested on the SLS-3 flight. This proposal in turn stemmed from our (then

planned) SLS-1 and SLS-2 investigations. Those investigations are now complete, and many of the results have been reported. The publications to date from SLS-1, D-2, and SLS-2 are listed below. The mission team has been involved with the SLS-1, SLS-2, D-2, and EuroMir-95 flights.

3. Methods

Hardware

The hardware flew on both SLS-1 (STS-40) and SLS-2 (STS-58), and is documented in the publications arising from those missions. A complete description of the system is available in Guy et al. (1991a). Briefly, the system centers around a bag in box system. Gases are dispensed into the bags within the box, and the subject controls the breathing path based on prompts presented on an alphanumeric display. Flow was measured with a Fleisch #2 pneumotachograph in the wall of the bag in box which was coupled to a Validyne MP-45 differential pressure transducer. Gas concentrations were measured at the lips of the subject with a quadrupole mass spectrometer (GASMAP).

For LMS, a new microcomputer was used. This provided the ability to directly store data on board on magneto-optical disk cartridges, as well as providing better display capabilities for the crew member. Completely new software was developed and flown. The Respiratory Inductance Plethysmograph (RIP) was borrowed from its previous use on D-2 (STS-55) and packaged to operate as a stand-alone unit. New RIP suits were developed.

The flow measuring system was calibrated before and after measurements by integration of flow from a 3 liter calibration syringe. Alinearities of the flowmeter were determined preflight using the method of Yeh et al. (1982) and corrected for in the analysis. The mass spectrometer was calibrated according to manufacturer instructions preflight and the calibration checked daily by sampling all the gas mixtures carried on board. Mass spectrometer sample transport time was determined daily by sampling a sharp puff of CO_2 containing gas and correcting for the delay in the subsequent analysis.

Test Sequence and Data Collection Schedule

Subjects performed a predefined sequence of pulmonary function tests on themselves. The sequence was:

REB – Rebreathing Cardiac Output and Diffusing Capacity
SSB – Slow single breath test and high oxygen REB
QDT – Distribution of pulmonary perfusion
SBH – Slow single breath test with breathhold
RGE – Resting Gas Exchange
FSB – Fast Single Breath test
RGE -- Resting Gas Exchange
FBH – Fast Single Breath test with Breathhold
COV – Control of Ventilation (CO_2 rebreathing response)

This sequence was performed prior to exercise, and 10 minutes after the completion of the 85% $\dot{V}O_2$(max) ramp exercise protocol of the E-920 experiment. In addition to the four payload crew, who each performed the protocol pre- and post-exercise, additional data were collected on two of the orbiter crew who performed the protocol pre-exercise only. Additional pre-exercise data was also collected on the payload crew on some flight days in which E-920 exercise was not scheduled. The actual sequence of data collection is described below. For

convenience, data collection sessions scheduled over two day periods (e.g., FD-8 and FD-9) in which the crew were split across the two days are referred to as a single session (FD-8). Data collected in 1G were with the subject seated on a tall chair, with the legs extended somewhat below the chair (a draftsman's chair)

In addition to the above PFT sequence, an isocapnic hypoxic rebreathing response test was performed pre-exercise only, in the pre- and post-flight periods only.

Day	Pre-Exercise PFT	Pre-Exercise Hypoxic Response	Post-Exercise PFT
L-90	X	X	
L-60	X	X	X
L-30	X	X	X
L-15	X	X	X
FD-2	X		
FD-4	X		X
FD-8	X		X
FD-12	X		
FD-15	X		X
FD-17	X		
R+0	X		
R+1	X	X	X
R+5	X	X	X
R+9	X	X	
R+15	X	X	

Test Details and Data Analysis

REB – Rebreathing Cardiac Output and Diffusing Capacity. Beginning at residual volume (RV), subjects inspired a test mixture containing 0.3% $C^{18}O$, 0.6% C_2H_2 and 10% Argon. The test mixture also contained either 21% O_2 or 85% O_2, allowing determination of the pulmonary capillary blood volume and membrane diffusing capacity from the diffusing capacity measurements. High oxygen measurements were made immediately following the slow single breath test, and a 30 second period of oxygen pre-breathing. In flight, a loss of the oxygen mixture resulted in a contingency procedure of 30 seconds of pure oxygen pre-breathing using an emergency breathing mask to be implemented. In all cases however, an alveolar oxygen percentage of at least 80% was achieved for the high oxygen test.

Analysis of the rebreathing was performed using a modification of the method of Sackner et al. (1975). A linear least squares fit to the logarithmically corrected soluble gas concentration was performed to the alveolar plateau data from breath number 3 of the rebreathing period to the end.

SSB – Slow single breath test; SBH – Slow single breath test with breathhold; FSB – Fast Single Breath test; FBH – Fast Single Breath test with Breathhold. These four tests form a suite of single breath tests designed to shed light on previously unexpected findings from SLS-2. During that mission, helium and sulfur hexafluoride phase III slopes unexpectedly

reversed, with SF_6 slope actually becoming flatter than that of He in μG after a breathhold. These results suggest that there is either some change in acinar conformation or in the propagation of the cardiac pressure wave through the lung (Prisk et. al, 1996). Interestingly the effect is not seen in the short periods of μG in parabolic flight (Lauzon et. al, 1997).

All prior single breath tests were performed with inspiratory flow rates of 0.5 l/sec. In this suite of tests, we varied inspiratory flow rate between 0.25 l/sec (the slow tests) and 1.0 l/sec (the fast tests) altering the position of the stationary front between convective and diffusive gas transport in the lung periphery. The addition of a breathhold in some tests allows time for some diffusive equilibration to occur.

Because of the loss of the O_2 mixture which contained the He and SF_6, only pre-exercise single breath measurements on the four payload crew could be made on FD-2 and FD-4, after which the gas supply was exhausted.

QDT – Distribution of pulmonary perfusion. This test was a repeat of the hyperventilation breathhold study performed in SLS-1 and SLS-2. Subjects hyperventilate for 20 seconds to lower overall lung CO_2, and then breathhold at TLC for 15 seconds. During the breathhold, CO_2 evolves at a rate proportional to regional pulmonary blood flow, marking regions of different perfusion. Markers of inhomogeneity are cardiogenic oscillations and a terminal change in CO_2 concentration after airways closure (Prisk et. al, 1994). This test was included in the LMS mission to examine the effects of exercise on pulmonary blood flow in μG.

RGE – Resting Gas Exchange. A measure of resting metabolic rate and gas exchange status. Subjects breathe quietly on the mouthpiece for 120 seconds during which time only inspired flow is measured (bag volume limitations preclude the collection of the exhalate during this period). This is followed by 60 seconds of breathing during which both inspiration and expiration are recorded. The test terminates with a slow controlled exhalation from TLC to RV during which time the range of intra-breath respiratory exchange ratio can be determined, providing an indication of the range of $\dot{V}_A/\dot{Q}$ present in the lung (Prisk et al., 1995).

COV – Control of Ventilation (CO_2 rebreathing response). The method of Read (1967) was utilized. Subjects rebreathed from FRC from a bag filled with 60% O_2, 5% CO_2, the balance N_2. As O_2 was consumed, and CO_2 produced the bag concentrations changed, although even at the completion of the test, O_2 level in the bag was still hyperoxic (>21%) ensuring no stimulation of the hypoxic chemoreceptive system. Subjects rebreathed from the bag for 4 minutes, or until the CO_2 level reached 10%, or until the subject voluntarily terminated the test. Ventilation was recorded on a breath by breath basis and the plot of VE vs. CO_2 used to determine the CO_2 responsiveness.

RIP -- Respiratory Inductance Plethysmography. Throughout the sequence of tests, subjects wore a close fitting lycra suit with wires embedded at the level of the nipples and the umbilicus. The RIP system developed for the D-2 mission was used, and provided with an independent power supply for the LMS mission. The RIP was calibrated during the sequence by a series of iso-volume manueuvers where the subject made small inspiratory efforts against a closed glottis or airway. This provides a measure of the relative gains of the rib cage and abdominal bands of the system. Total gain determination was derived from the periods of quiet breathing on the mouthpiece during which time, total respired volume is measured by the flowmmeter in the bag-in-box system.

Hypoxic Response. We used a modified form of the system of Rebuck and Campbell (1974). Using a separate system (Mackey, 1996) subjects rebreathed from FRC from a bag initially containing air. As subjects rebreathed from the bag, CO_2 rose and O_2 fell. A scrubber circuit containing a fan, whose speed was controlled by a computer, and a canister filled with soda lime drew air from one end of the bag, and returned it to the other. A computer measured the end tidal CO_2 as the subject exhaled and adjusted the fan speed to allow CO_2 to rise in the bag, or to remove CO_2 so as to maintain a constant end-tidal CO_2 from the subject. End-tidal CO_2 was held at a level approximately 0.3% above the resting end-tidal CO_2 level of the subject as determined in a 30 second period of quiet breathing prior to the start of rebreathing. Subjects continued to rebreathe until inspiratory oxygen in the bag fell below 7.5%. Blood oxygen levels were monitored with a Nellcor N-200 pulse oximeter on the finger of the subjects. The total system delay between SaO_2 and inspired gas concentrations was determined by measuring the delay between the first inspiration of air at the end of the rebreathing period, and the nadir of the SaO_2 recording, and was typically ~20 seconds. SaO_2 was then time shifted by this delay to correspond with the other signals and the response determined from the breath by breath $\dot{V}_E$ vs. SaO_2 plot.

Statistical Treatment

We followed the same statistical approach used on prior spaceflights. Subjects acted as their own controls. For pre-exercise data only, we included all sessions detailed in table 1, and included data from 6 subjects (four payload crew plus the two orbiter crew on whom we obtained significant amounts of inflight data). Preflight data were tested for stability, and then pooled to form a single baseline. Measurements were then tested on a day by day basis, and as grouped periods of inflight and postflight.

When considering the effects of exercise, data were resampled to include only the four payload crew (who were the only subjects in which we have post-exercise data), and the number of days under consideration reduced to only those shown in table 1 when post-exercise data were collected. Preflight data were tested for stability, and then pooled to form a single baseline. Measurements were then tested on a day by day basis, and as grouped periods of inflight and postflight, as well as for pre-exercise or post-exercise. Differences between pre- and post-exercise were tested for in all cases. Note that because of the resampling necessary in this process, numbers for pre-exercise measurements from the "exercise" data set do not necessarily match numbers derived from the data set involving all 6 crew, as fewer subjects and days are involved.

In all cases, results are expressed as a percentage of preflight, pre-exercise baseline data and data are normalized on an individual basis to this value. Thus the preflight pre-exercise value is by definition 100%, and the SE is a measure of the intra-subject variability only. This normalization process allows pooling of data from subjects with a wide range of sizes.

4. Results and Discussion

REB – Rebreathing Cardiac Output and Diffusing Capacity. Lung volumes determined from argon dilution during the rebreathing tests show a consistently different pattern form that seen in SLS-1 and SLS-2. In this mission, both RV and FRC were elevated compared to preflight controls, RV by ~20%, and FRC by ~12% (figures 1 and 2), while in prior missions we observed a decrease (Prisk et al., 1993; Elliott et al.,1994). There are however significant differences in the data collected in the control period. In the ground data collected

during LMS, subjects were seated in a high chair, which likely prevented descent of the diaphragm; and as a consequence, lowered FRC measured in 1G. In the data collected in μG however, subjects were in more of an upright posture, without the attendant constraints placed on the diaphragm. Similarly, we hypothesized that the reduction in RV seen in μG in SLS-1 was as a result of the removal of the dependent weight of the lower lung present in 1G. It seems that when subjects are seated however, the support of the raised diaphragm raises FRC somewhat accounting for the increase we saw in μG. Of note in the RV data are the results from R+0 which show a significantly elevated RV, which is abolished in all subsequent postflight data which are constant from R+1 on. This likely stems from the cardiovascular instability of the subjects immediately upon return to 1G, with an unwillingness to fully exhale to RV with the attendant negative cardiovascular consequences of something approaching a valsalva maneuver. Examination of the lung volume data pre- and post-exercise shows no differences as a result of exercise, a result we expected in these data.

Figures 3, 4 and 5 respectively show the cardiac output, heart rate and cardiac stroke volume measured from acetylene uptake during the flight. Once again, the changes in cardiac output and stroke volume observed during LMS were smaller than those seen during SLS-1 (Prisk et al., 1993), and SLS-2 (unpublished observations). This difference is likely due to the different control conditions used in LMS and these other missions (sitting vs. standing), and emphasizes the importance of gravity on venous return from the lower extremities. Even a relatively modest change from standing to an erect sitting posture markedly increases the control cardiac output and thus lowers the apparent effect of microgravity. The modest increases that we see in cardiac output (which are not significant) and in stroke volume are intermediate between the changes we previously observed between standing and μG, and between supine and μG.

Of note is the observation that both cardiac output and stroke volume initially increase upon entry into μG, and thereafter begin to decrease. However, after day 12, there is a substantial increase in both these variables, which is not accompanied by a concomitant increase in heart rate (figure 4). We had previously noted a modest increase in cardiac output and stoke volume on day 9 of SLS-1, and attributed that to either an anticipatory effect as the end of the mission approached, or resulting from increased workload associated with the de-orbit preparations. A similar observation remains unexplained from the SLS-2 results. For comparison, the graphs of cardiac output from SLS-1 and SLS-2 are shown in figure 6. Since we again see an increase in both cardiac output and stroke volume late in flight during LMS, we are lead to the conclusion that some competing adaptation mechanism is at work that becomes dominant to the reduction in cardiac output that occurs, presumably secondary to a continuing reduction in circulating blood volume during the early phase of adaptation to μG. Whether the late mission increase in cardiac output and stroke volume has a neurological origin is at present unknown, but the observation may be of considerable interest in the adaptation to long duration exposure to μG.

The determination of the changes in pulmonary tissue volume (V_t) following was confounded by the slow dynamic response of the GASMAP to acetylene. This precluded our ability to accurately resolve the initial inspired acetylene which is critical in the determination of V_t. Calculating V_t using an assumed inspired concentration produces a large increase in V_t that is unphysiological, leading us to believe this to be a measurement artifact (because we believe these data to be erroneous, they are not shown). Further, prior observations of V_t in μG made in the absence of exercise indicate a small decrease (Verbanck, 1997). Despite the questions surrounding the reliability of the V_t measurements in absolute terms, pre- and post-exercise measurements are subject to the same error, and can therefore be compared. There

were no differences in V_t measured pre- and post-exercise suggesting that the 85% exercise level used in the inflight protocol was not detrimental to the fluid balance of the lung.

Diffusing capacity measurements made under normoxic conditions show a pattern similar to that seen on previous missions (Prisk et al., 1993, Verbanck et al., 1997). D_L is raised in μG and remains constant for the duration of the flight (figure 7). The magnitude of the increase is greater in this mission than in SLS-1, but differences in both the choice of maneuver (in this case, a rebreathing maneuver, in SLS-1, a single breath technique), and in the choice of position for the ground control measurements (see above) contribute to this. The rapid change and return again suggest that a strictly mechanical process is involved in the changes in D_L, as was suggested from SLS-1. Pre- and post-exercise D_L measurements both preflight and inflight show no difference except on FD-15, when a small, but likely physiologically insignificant difference was seen. This again suggests that the 85% of $\dot{V}O_2$max exercise protocol used in flight produces not deleterious consequences to the pulmonary system in terms of fluid balance in the lung. High oxygen measurements of diffusing capacity were very variable inflight, perhaps due to the off nominal procedures we were forced to employ following the loss of the high oxygen gas tank. As a consequence, they, and the subdivisions of D_L calculated from them will not be further discussed.
Of interest is the incomplete return of D_L to baseline on R+0 (figure 7). These measurements were made rapidly following return to 1G, and without the subject's ambulating. The higher value on R+0, (which is statistically different from all other post flight days) suggests that the fluid balance state of the subject's is different on R+0, perhaps as a result of the fluid loading prior to reentry (which was not a feature of all crew on SLS-1). A similar effect is visible in the cardiac output data (figure 3) where $\dot{Q}_c$ is actually elevated on R+0, and stroke volume (figure 5) is slightly above preflight baseline prior to large decreases in both variables on R+1.

Single Breath Tests: Changes in acinar inhomogeneity in μG. A preliminary analysis of the data relating to acinar inhomogeneity are available at this time. Only limited inflight data were available because of the loss of the O_2 Mix tank pressure during pre-launch activities or during launch. Preflight and postflight data were not different and have been combined. Because of limited inflight gas supplies, data collection was limited to pre-exercise studies only on the four payload crew only.

This experiment was designed to throw light on the possible mechanisms operating at the acinar level that cause inhomogeneity of ventilation. Data from both SLS-2 (Prisk et al., 1996), and D-2 (Paiva, unpublished observations) suggest that in μG, acinar gas mixing changes considerably, especially in smaller subjects, although the cause of this is at present completely unknown, and the result was unexpected. Data collected in periods of shor- term μG in the KC-135 suggest that the effect is not present in only 25 seconds (Lauzon et al., 1997). The results point to changes in the manner in which the quasi-stationary diffusion front that forms between inspired and resident gas is spread in the lungs, and consequently how gas is mixed. By using gases of widely different diffusivity (He and SF_6), different breathold times (0 and 10 seconds, allowing different times for mixing) and different inspiratory flow rates (0.25 l/sec and 1.0 l/sec) which alters the position of the diffusion front (faster inspiration, more peripheral) we hoped to be able to examine how these interaction between diffusive and convective gas mixing was altered by μG. This mixing occurs in regions of lung that were traditionally thought to be too small to be affected by gravity.

The results from this study show that the anomalous responses we observed in SLS-2 and in D-2, are not a universal event, and vary markedly between subjects. Unfortunately the limited number of inflight observations severely limits our ability to draw substantial conclusions

from this data set. Accordingly, the comments below are highly speculative and may not stand up to further scrutiny.

Helium data (figure 8) shows a marked effect of μG, with substantially lower phase III slopes in μG compared with 1G. Further, breathholding reduces phase III slopes considerably, except for slow inspirations in μG (figure 8A, right). In these tests, at slow inspirations the diffusion front is much more central than in the other tests, suggesting that even the highly diffusible helium is unable to equilibrate between units of differing concentration because they are too far apart. That this happens only in μG is puzzling, and suggests some alteration in gas transport may indeed occur in this situation.

Sulfur hexafluoride results (figure 9) again show a reduction in phase III slope in all circumstances, except that of slow inspirations in μG in which there is no change in phase III slope compared to 1G after a 10 second breathhold. In contrast, when the inspiration is faster, phase III slope is considerably reduced, suggesting that the determinants of phase III slope in μG are sufficiently close to that with a distally located diffusion front, the cardiogenic action during breathholding and the effects of diffusion are able to lower the existing concentration gradients between lung units.

The differences between He and SF_6 phase III slopes are shown in figures 10 and 11. These differences previously showed marked reductions in μG, that were even larger following a breathhold in μG (Prisk et al., 1996). In these subjects however, there are no reductions in μG. However an interesting difference exists between the results from the slow inspirations (0.25 l/sec, proximal diffusion front), which show no effect of breathhold or μG, and those performed at a fast inspiratory rate (1.0 l/sec, distal diffusion front) which show a marked reduction in the SF_6-He phase III slope difference following a breathhold. Whether this is an artifact introduced by the sparse nature of the data set is at present unknown, but if it holds up to closer scrutiny is suggestive of the theory that the changes we observed in SLS-2 and D-2 relate to conformational changes in the most peripheral parts of the lung.

QDT – Distribution of pulmonary perfusion. Data from this test are still under analysis.

RGE – Resting Gas Exchange. Analysis of resting gas exchange showed no clear and consistent trends in the data, either inflight or postflight. Accordingly, we present only average data from preflight, inflight and postflight.

Resting gas exchange may be changed by changes in the atmosphere the subjects are in. Figures 12 and 13 show inspired oxygen and CO_2 levels encountered during the mission. FIO_2 was slightly elevated inflight (by ~ 1.3%). Despite an apparent large increase in inspired CO_2, the absolute value of the increase was small (~0.2%, or 2 Torr). Such an increase is below the level likely to cause any alteration in resting ventilation based on data obtained in the CO_2 exposure study performed in a chamber in Germany (Elliott et al., 1997). The slight increase in inspired CO_2 post exercise inflight likely reflects the increased CO_2 load in the Spacelab resulting from the exercise itself.

Expired gas tensions show a slight increase in end tidal O_2 that inflight mirrors the changes in inspired levels (figure 14). Similarly CO_2 is slightly elevated inflight (figure 15). The absolute magnitude of these changes are small (O_2 ~ 2.3 mmHg, CO_2 ~1.6 mmHg). Postflight however, there is a reduction in expired O_2 and an increase in expired CO_2, possibly suggesting a slight change in the setting of the resting ventilation levels. A similar increase in end tidal CO_2 was seen in the SLS-1 and SLS-2 results (Prisk et al., 1995). Post exercise

there are modest reductions in both expired O_2 and CO_2 in all states, although the cause is at present unclear.

Neither total minute ventilation (figure 16), nor respiratory frequency (figure 17) show any significant changes either as a result of spaceflight, or as a result of exercise. Similarly, the SLS-1 and SLS-2 data show little or no change in these parameters. The absence of a change post exercise indicates that subjects had fully recovered from the modest bout of exercise to which they were subjected, and suggests that there was no residual effect of this exercise on resting ventilation. Ventilatory drive, as indicated by T_I/T_{TOT} was slightly elevated by microgravity and remained so postflight (figure 18), but the change was small. Ventilatory drive seemed unaffected by exercise.

Gas exchange ($\dot{V}O_2$, fig 19; $\dot{V}CO_2$ fig 20) was slightly elevated inflight, and clearly elevated postflight. This increase likely explains the changes in post flight end tidal O_2 and CO_2 (figures 14, 15), which occurred in the absence of large changes in ventilation. The cause of this increase is unknown. On previous missions, there was a modest increase in gas exchange inflight, but this returned to baseline postflight (Prisk et al., 1995).

Overall the data suggest only small or no changes in the resting gas exchange status of the subjects, and no adverse effects of the bout of exercise the subjects were required to perform.

Data from the slow controlled exhalation, during which time intra-breath respiratory exchange ratio (and subsequently the range of $\dot{V}_A/\dot{Q}$ in the lung) is calculated are still under analysis.

COV – Control of Ventilation (CO_2 rebreathing response). There were no apparent changes in the hypercapnic control of ventilation due to μG per se as evidenced by either the slope of the CO_2 response curve (ventilation as a function of CO_2) (see figure 21), or in the Ventilation measured at a PCO_2 of 60 mmHg (figure 22). However, the maximum CO_2 reached at the end of the 4 minutes of CO_2 rebreathing figure 23) was significantly reduced by μG. The cause of this reduction is at present unknown and still under investigation.

Exercise increased the CO_2 responsiveness of the subjects both in 1G, and in μG, although the variability of the measurements makes these increases non-significant. In all cases exercise reduced the maximum PCO_2 reached at the end of the rebreathing period (figure 23), although the magnitude of this reduction in μG was much greater than in either the preflight or postflight periods. The decrease in CO_2 levels during the rebreathing is curious given the lack of any large change in $\dot{V}CO_2$ (see figure 20). Whether it indicates anything of physiological significance is yet to be determined.

RIP -- Respiratory Inductance Plethysmography. Data from the RIP system are still under analysis.

Hypoxic Response. The hypoxic ventilatory response measurements were performed preflight and postflight only, and were only performed during the pre-exercise PFT sessions, and we attempted to reduce their arterial oxygen saturation to 75%.

Hypoxic ventilatory response was elevated postflight compared to preflight (although the changes failed to reach statistical significance at the $p< 0.05$ level) when considering both the slope of the response (figure 24) and the ventilation at and arterial oxygen saturation of 75% (figure 25). Of particular note are the data collected on R+1 which show a marked increase in response, and a considerably larger variability in the results compared to all other

postflight and preflight measurements. The increase in the ventilatory response is mirrored in both tidal volume and frequency data (not shown) which both show substantial increases in both magnitude and variability on R+1.

These data suggest that there are likely substantial changes in the hypoxic ventilatory response as a result of μG. Because of the logistical constraints imposed by the postflight data collection scenario, we were unable to obtain HVR data on R+0, immediately following spaceflight. However it appears likely that had we been able to perform these measurements, an even higher response would have been seen. Similarly, the data are suggestive of an increased sensitivity to hypoxia in μG. Further, the data were collected under nearly normocapnic conditions, with end tidal CO_2 being controlled to only very slightly above the subject's normal end tidal value. It is known that there is synergism between the hypoxic and hypercapnic ventilatory reponses. Thus, it seems likely that the inflight studies of the HVR which will be performed during Neurolab, during which we will control CO_2 to an elevated isocapnic level will yield interesting and provocative results.

5. Conclusions

Despite the loss of the O_2 Mix tank and limited data collection capability, significant data were obtained during LMS. There are few differences to be found between the pre-exercise and post-exercise data. We attribute much of this to the severe descoping that was forced upon the experiment by the inflight restriction of an exercise level of only 85% of maximum $\dot{V}O_2$. We are therefore unable to provide any substantial conclusions regarding the effect of heavy exercise on the lung in μG. However it appears that modest exercise has no adverse effects on lung function in μG. Further data interpretation will have to wait for more complete analyses and publication of detailed papers.

6. Bibliography

Elliott, A.R., G. K. Prisk, H.J.B. Guy, and J.B. West. Lung volumes during sustained microgravity on Spacelab SLS-1. *J. Appl. Physiol.*, 77:2005-2014, 1994.

Elliott, A.R., G.K. Prisk, H.J.B. Guy, J.M. Kosonen, and J.B. West. Forced expirations and maximum expiratory flow-volume curves during sustained microgravity on SLS-1. *J. Appl. Physiol.* 81:33-43, 1996.

Eliott, A.R., G.K. Prisk, C Schöllmann, and U. Hoffmann. Hypercapnic ventilatory response in humans before, during and after 23 days of low level CO_2 exposure. *Aviat. Space and Environ. Med.* In, Press, 1997

Guy, H.J., G.K. Prisk, and J.B. West. Pulmonary function in microgravity: Spacelab4 and beyond. *Acta Astronaut.* 17:1139-1143, 1988.

Guy, H.J.B., G.K. Prisk, and J.B. West. Testing pulmonary function in Spacelab. *SAE Technical paper Series, #911565.* Twenty-first International Conference on Environmental Systems, San Francisco, CA July 15-18, 1992 1-5, 1991a.

Guy, H.J.B., G.K. Prisk, A.R. Elliott, and J.B. West. Maximum expiratory flow-volume curves during short periods of microgravity. *J. Appl. Physiol.* 70:2587-2596, 1991b.

Guy, H.J.B., G.K. Prisk, A.R. Elliott, R.A. Deutschman III, and J.B. West. Inhomogeneity of pulmonary ventilation during sustained microgravity as determined by single-breath washouts., *J. Appl. Physiol.*, 76: 1719-1729, 1994.

Lauzon, A.-M., G.K. Prisk, A.R. Elliott, S. Verbanck. M. Paiva, and J.B. West. Paradoxical helium and sulfur hexafluoride single-breath washouts in short-term vs. sustained microgravity. *J. Appl. Physiol.* 82:859-865, 1997.

Mackey, M.E. Automatic Control of Alveolar Gases in a Hybrid Rebreathing Circuit. Masters Thesis, University of California, San Diego, 1996.

Prisk, G.K., H.J.B. Guy, A.R. Elliott, R.A. Deutschman III, and J.B. West. Pulmonary diffusing capacity, capillary blood volume and cardiac output during sustained microgravity. *J. Appl. Physiol.*, 75:15-26, 1993.

Prisk, G.K., H.J.B. Guy, A.R. Elliott, and J.B. West. Inhomogeneity of pulmonary perfusion during sustained microgravity on SLS-1., *J. Appl. Physiol.*, 76: 1730-1738, 1994.

Prisk, G.K., H.J.B. Guy, A.R. Elliott, M. Paiva, and J.B. West. Ventilatory inhomogeneity determined from multiple-breath washouts during sustained microgravity on Spacelab SLS-1. *J. Appl. Physiol.*, 78:597-607, 1995.

Prisk, G.K. A.R. Elliott, H.J.B. Guy, J.M. Kosonen, and J.B. West. Pulmonary gas exchange and its determinants during sustained microgravity on Spacelabs SLS-1 and SLS-2. *J. Appl. Physiol.* 79:1290-1298, 1995.

Prisk, G.K., A.-M. Lauzon, S. Verbanck, A.R. Elliott, H.J.B. Guy, M. Paiva, and J.B. West. Anomalous behavior of helium and sulfurhexafluoride during single-breath tests in sustained microgravity. *J. Appl. Physiol.* 80:1126-1132, 1996.

Rebuck, A.S. and E.J.M. Campbell. A clinical method for assessing the ventilatory response to hypoxia. *Am. Rev. Respir. Dis.*. 109:345-350, 1974.

Sackner, M.A., D. Greeneltch, M.S. Heiman, S. Epstein, and N. Atkins. Diffusion capacity, membrane diffusing capacity, capillary blood volume, pulmonary tissue volume and cardiac output measured by a rebreathing technique. *Am. Rev. Respir. Dis.* 111:157-165, 1975.

Verbanck, S., D. Linnarsson, G.K. Prisk, and M. Paiva. Specific ventilation distribution in microgravity. *J. Appl. Physiol.* 80:1458-1465, 1996.

Verbanck, S., H. Larsson. D. Linnarsson, G.K. Prisk, J.B. West, and M. Paiva. Pulmonary tissue volume, cardiac output and diffusing capacity in sustained microgravity. *J. Appl. Physiol.* In Press, 1997.

West, J.B., H.J.B. Guy, A.R. Elliott, and G. K. Prisk. Respiratory system in microgravity. In: *The Handbook of Physiology Section 4: Environmental Physiology.* M.J. Fregly and C.M.

Blatteis (eds). New York, Oxford University Press. pp. 675-689, 1996.

Yeh, M.P, R.M. Gardner, T.D. Adams, and F.G. Yanowitz. Computerized determination of pneumotachometer characteristics using a calibrated syringe. *J. Appl. Physiol.* 53:280-285, 1982.

7. Summary

The Astronaut Lung Function Experiment (ALFE) studied the effects of moderate exercise in μG on the lung and investigated changes in the chemical control of ventilation that are hypothesized to occur upon exposure to μG. The analysis completed to date suggests that moderate exercise in μG has no adverse consequences on the lung, although the effects of extreme exercise remain unknown. There were no changes in the ventilatory response to inhaled carbon dioxide caused by μG. However, based on measurements that were only able to be performed before and after the LMS mission, it seems likely that the ventilatory response to lowered oxygen levels in the blood (in this case caused by breathing a low oxygen mixture during a portion of the experiment) is increased in μG. Such a heightened response has the potential to disrupt sleep, and sleep is known to be of poor quality during μG . This effect will be directly investigated during the upcoming Neurolab Spacelab mission in 1998.

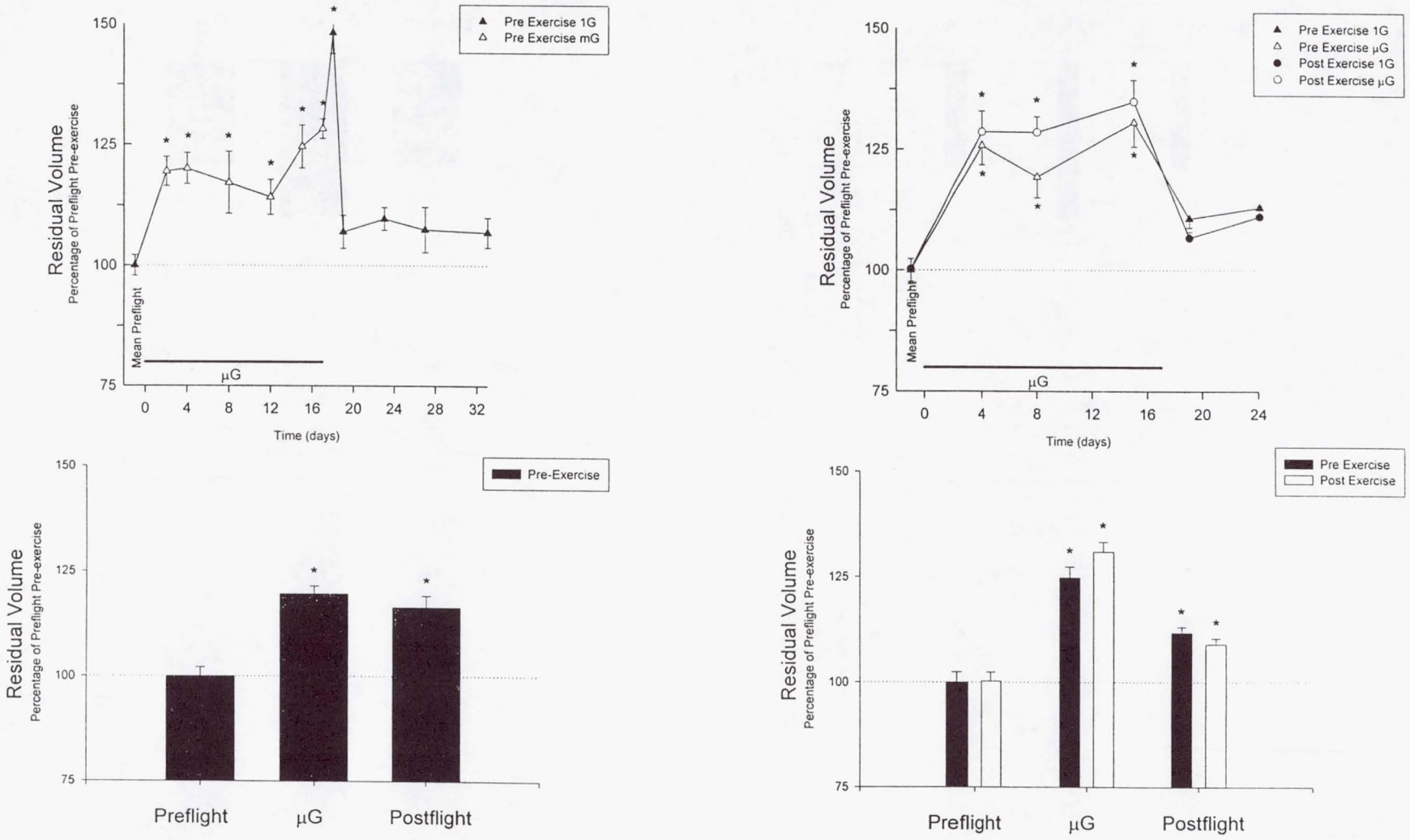
Residual Volume
Percentage of Preflight Pre-exercise
Pre Exercise 1G
Pre Exercise mG
Mean Preflight
μG
Time (days)
Pre Exercise 1G
Pre Exercise μG
Post Exercise 1G
Post Exercise μG
Pre-Exercise
Pre Exercise
Post Exercise
Preflight
μG
Postflight

figure 1

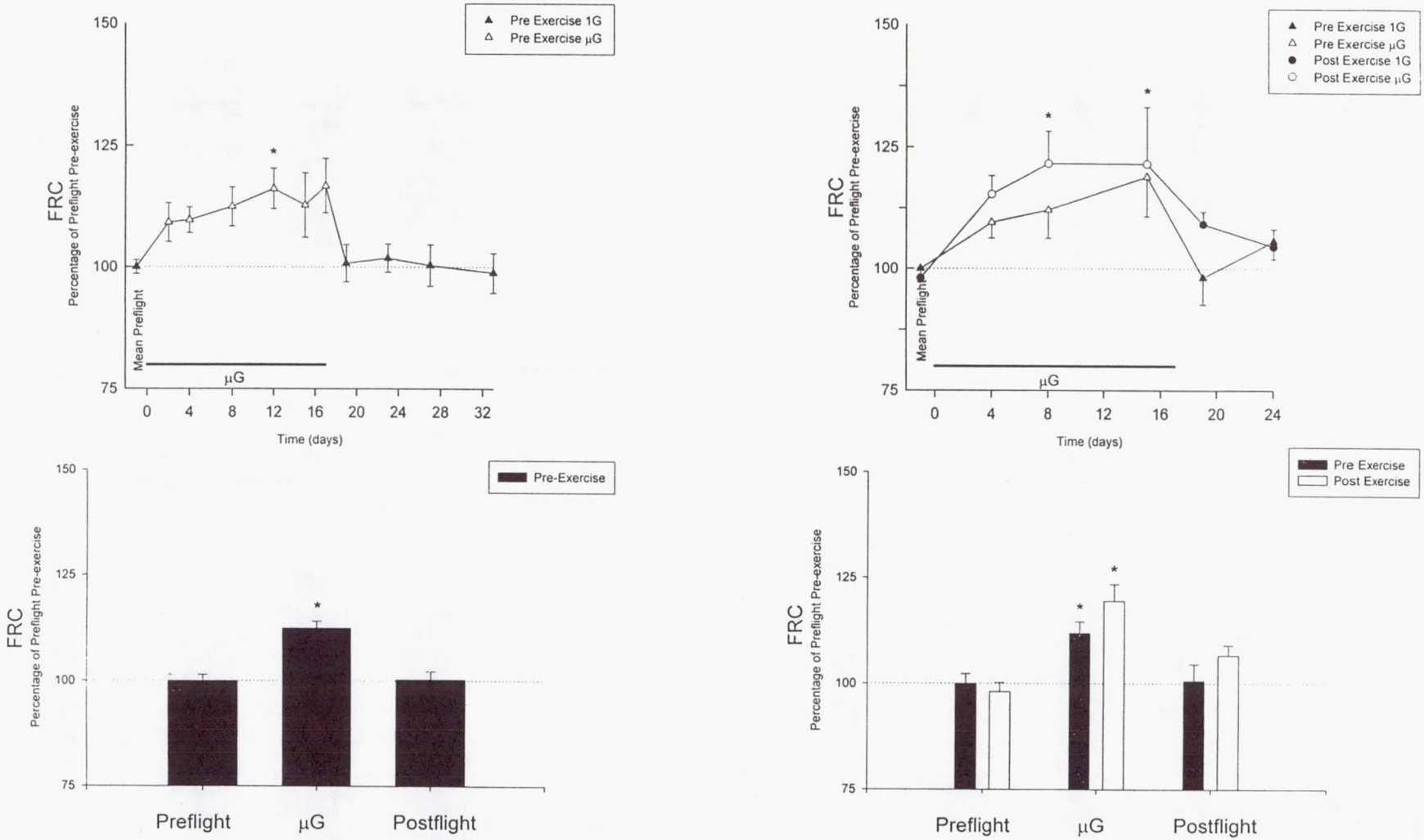
Pre Exercise 1G
Pre Exercise µG
Post Exercise 1G
Post Exercise µG
FRC
Percentage of Preflight Pre-exercise
Mean Preflight
µG
Time (days)
Pre-Exercise
Pre Exercise
Post Exercise
Preflight
µG
Postflight

figure 2

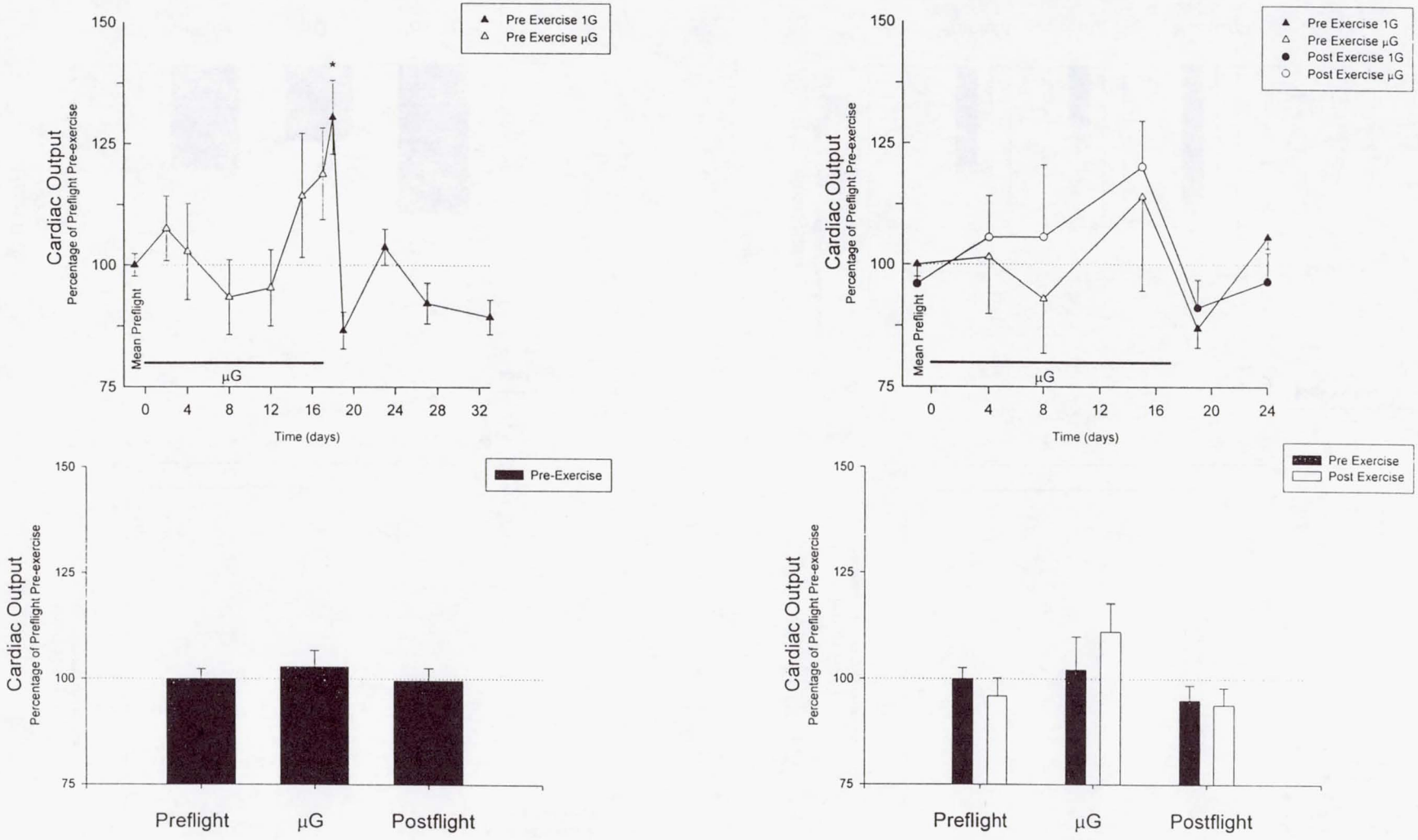
Pre Exercise 1G
Pre Exercise µG
Post Exercise 1G
Post Exercise µG
Cardiac Output
Percentage of Preflight Pre-exercise
Mean Preflight
µG
Time (days)
Pre-Exercise
Pre Exercise
Post Exercise
Preflight
µG
Postflight

figure 3

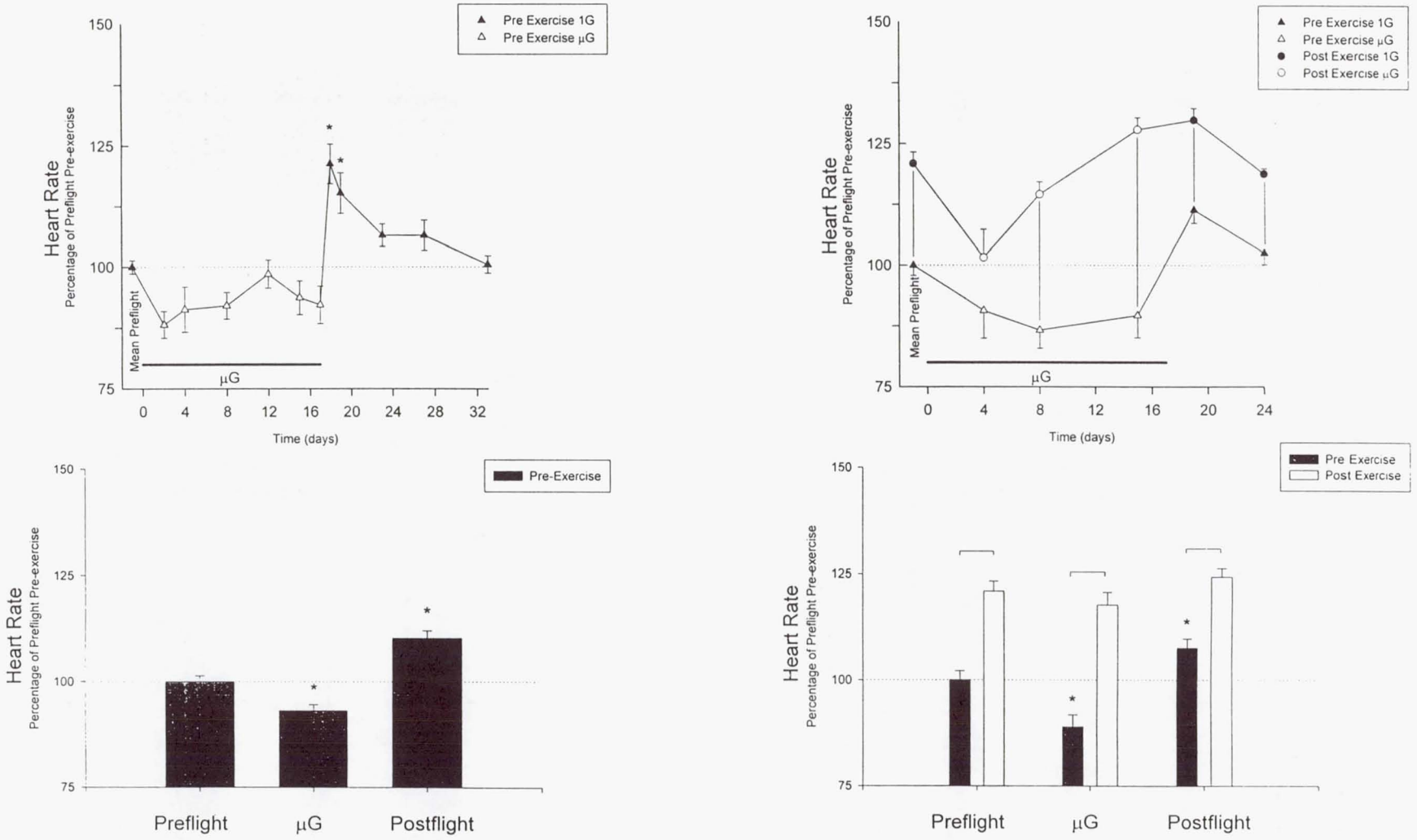
Pre Exercise 1G
Pre Exercise µG
Heart Rate
Percentage of Preflight Pre-exercise
Mean Preflight
µG
Time (days)
Post Exercise 1G
Post Exercise µG
Pre-Exercise
Pre Exercise
Post Exercise
Preflight
µG
Postflight

figure 4

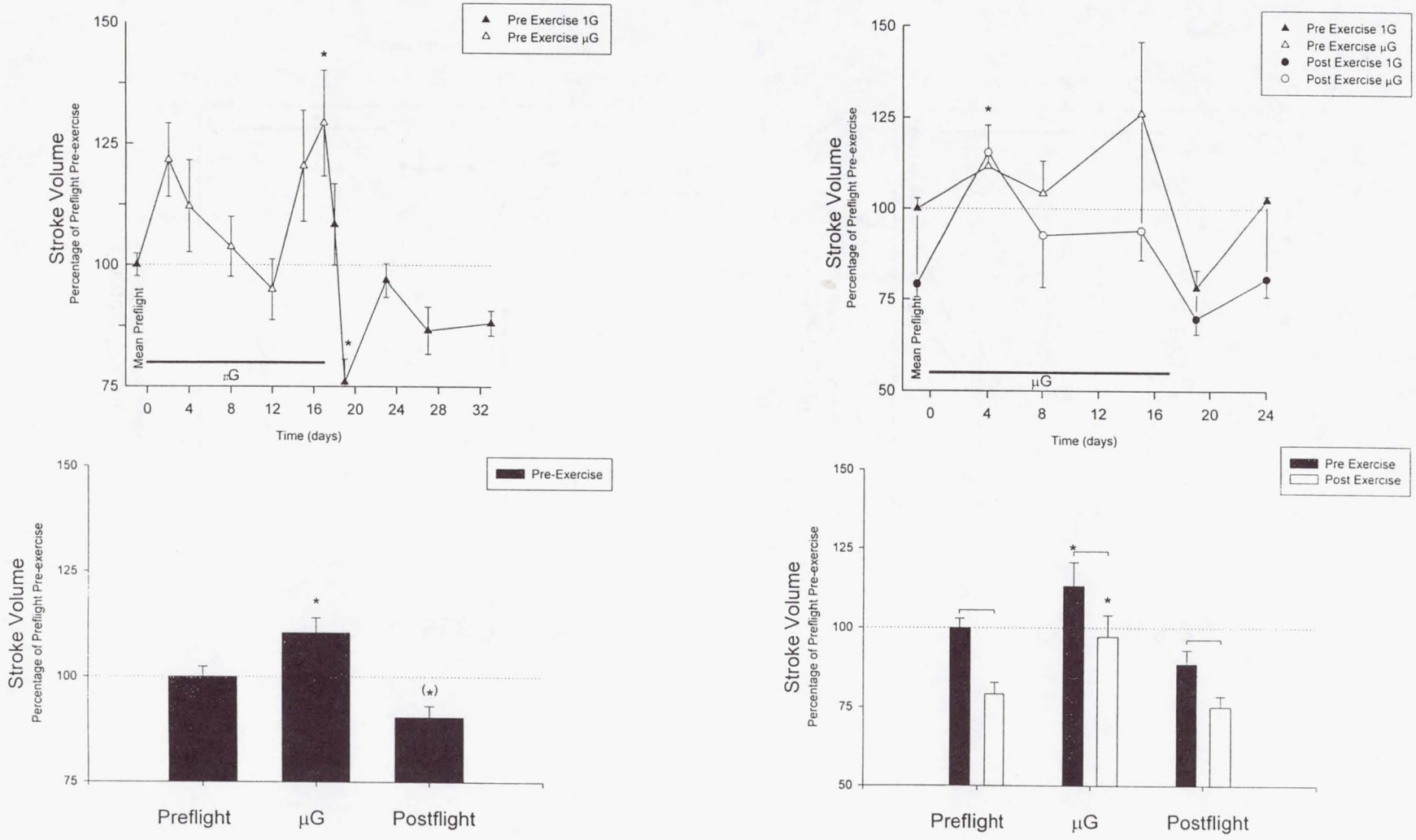
Pre Exercise 1G
Pre Exercise μG
Post Exercise 1G
Post Exercise μG
Stroke Volume
Percentage of Preflight Pre-exercise
Mean Preflight
μG
Time (days)
Pre-Exercise
Pre Exercise
Post Exercise
Preflight
μG
Postflight

figure 5

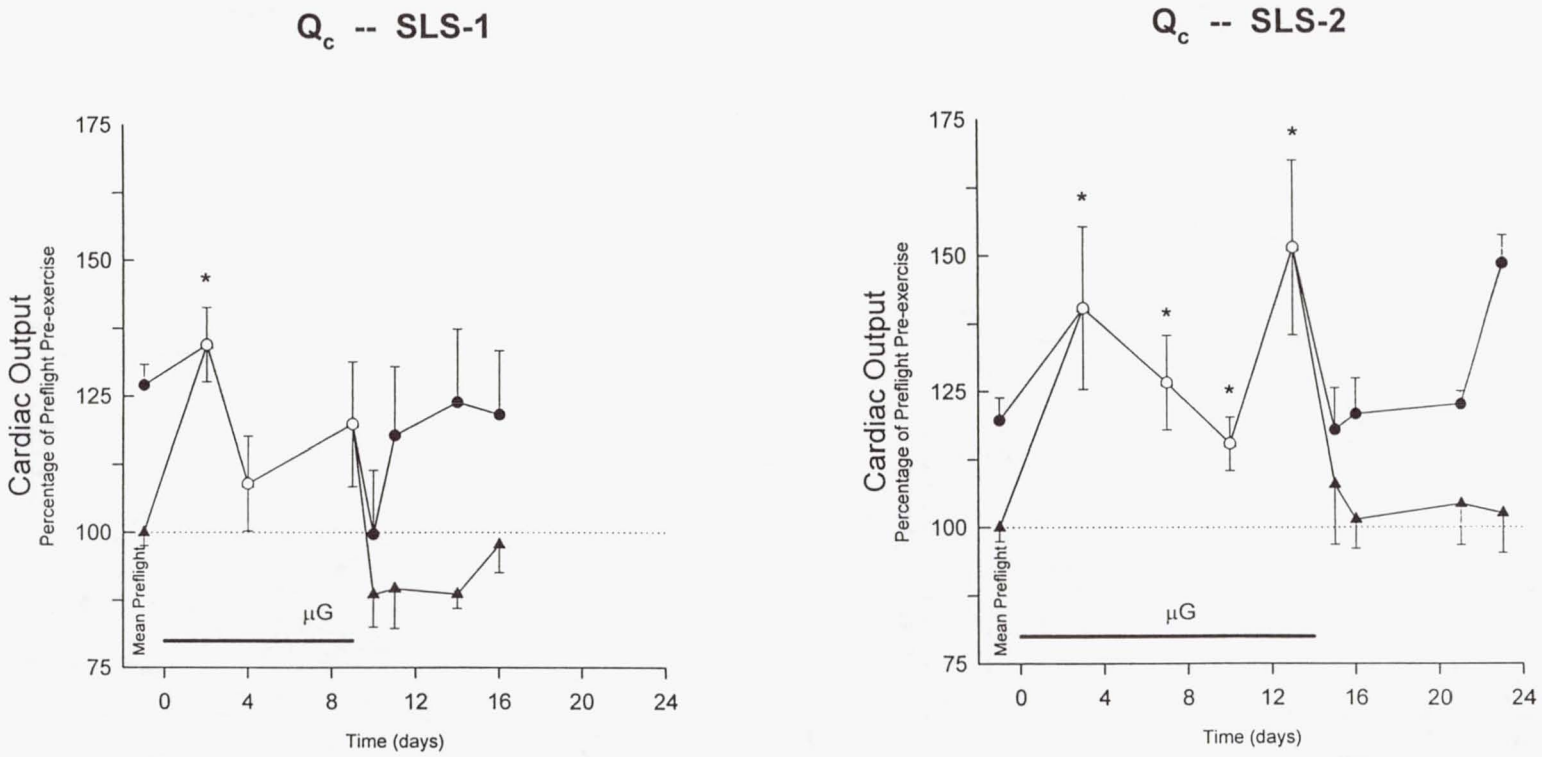
Q_c -- SLS-1
Cardiac Output
Percentage of Preflight Pre-exercise
175
150
125
100
75
Mean Preflight
μG
0
4
8
12
16
20
24
Time (days)
Q_c -- SLS-2
Cardiac Output
Percentage of Preflight Pre-exercise
175
150
125
100
75
Mean Preflight
μG
0
4
8
12
16
20
24
Time (days)

figure 6

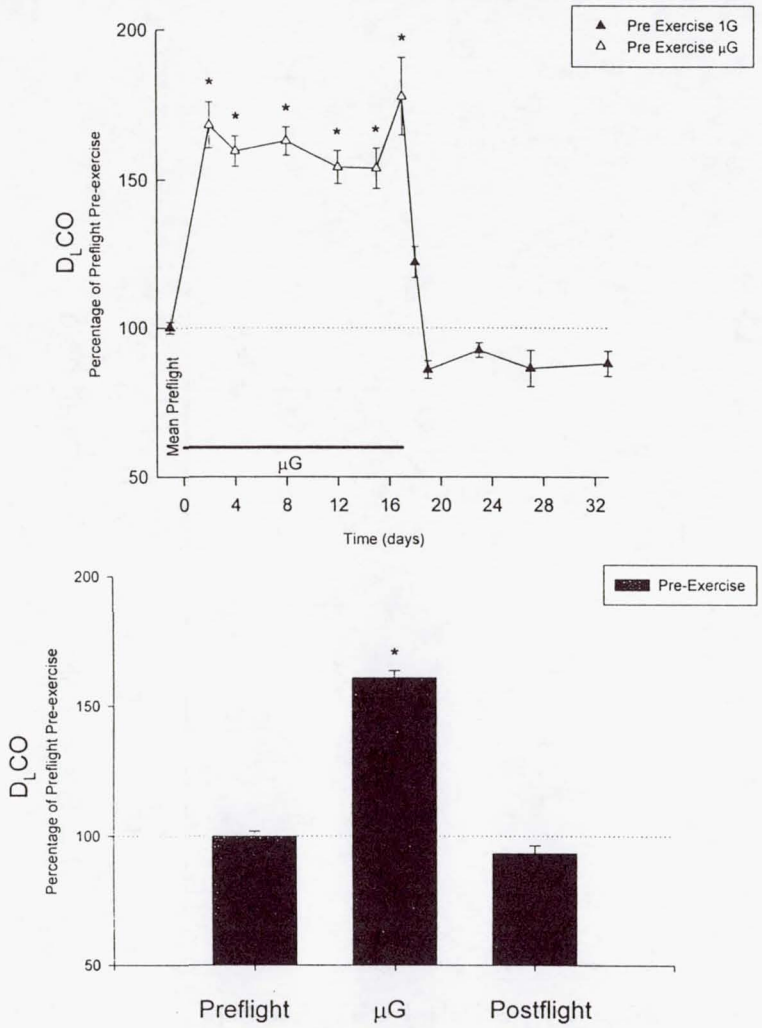
Pre Exercise 1G
Pre Exercise µG
D_LCO
Percentage of Preflight Pre-exercise
Mean Preflight
µG
Time (days)
Pre-Exercise
Preflight
µG
Postflight

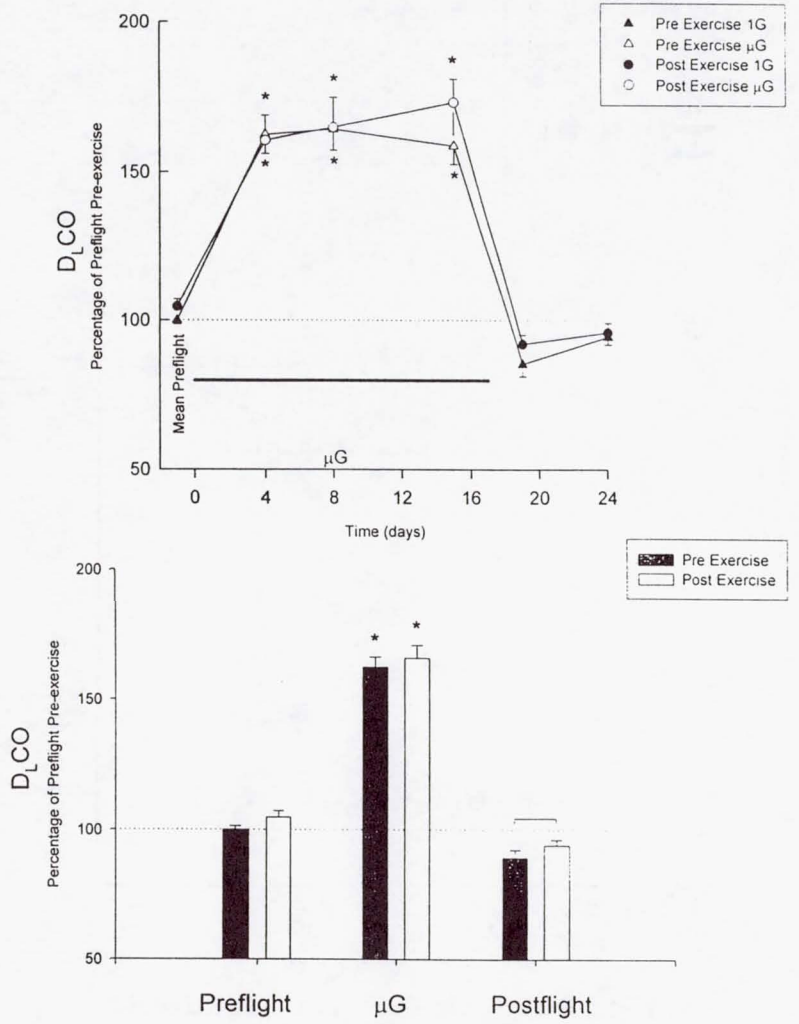
Pre Exercise 1G
Pre Exercise µG
Post Exercise 1G
Post Exercise µG
D_LCO
Percentage of Preflight Pre-exercise
Mean Preflight
µG
Time (days)
Pre Exercise
Post Exercise
Preflight
µG
Postflight

figure 7

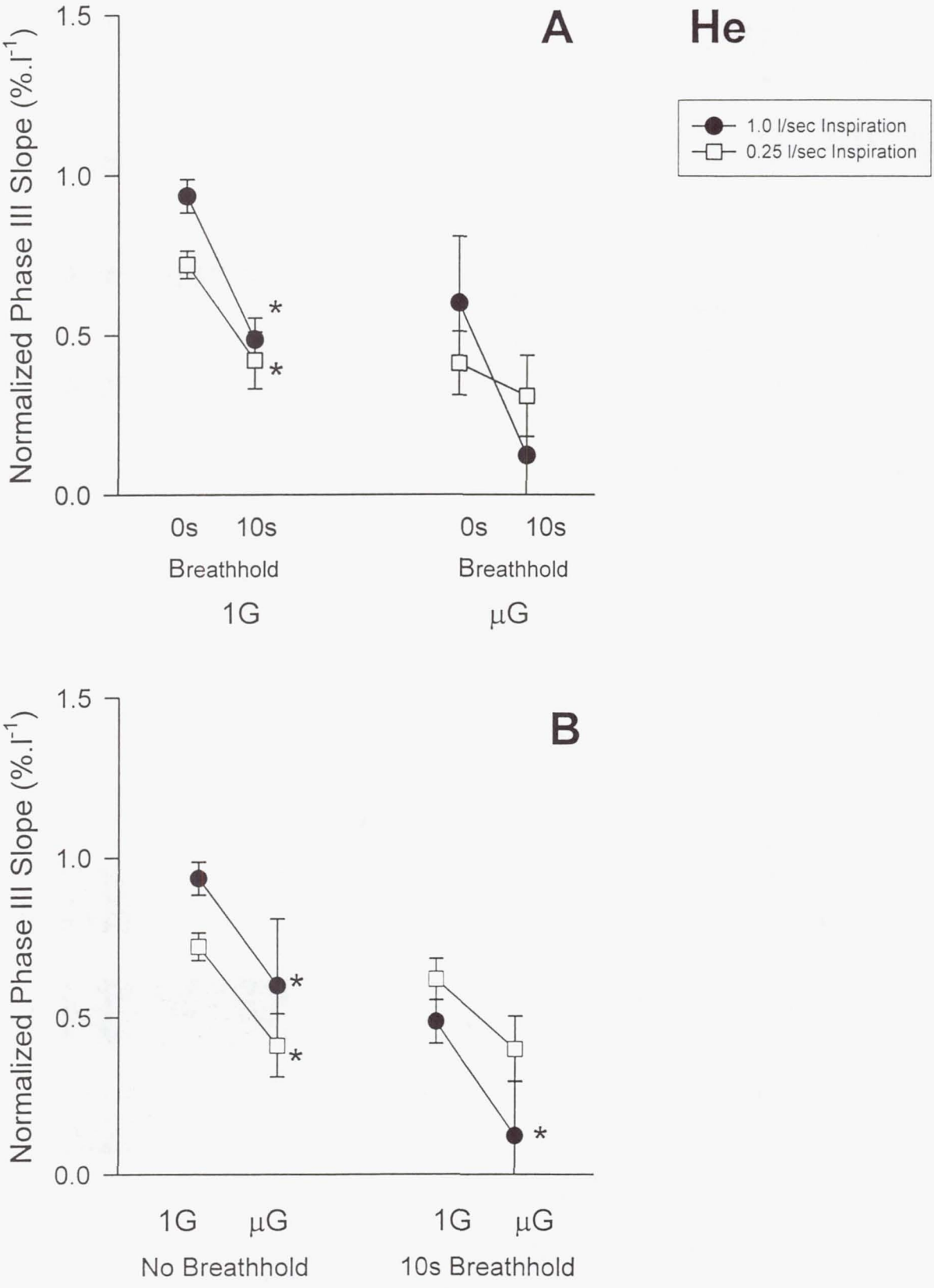
A
He
1.0 l/sec Inspiration
0.25 l/sec Inspiration
Normalized Phase III Slope (%.l-1)
1.5
1.0
0.5
0.0
*
*
0s
10s
Breathhold
1G
0s
10s
Breathhold
μG
B
Normalized Phase III Slope (%.l-1)
1.5
1.0
0.5
0.0
*
*
*
1G
μG
No Breathhold
1G
μG
10s Breathhold

figure 8

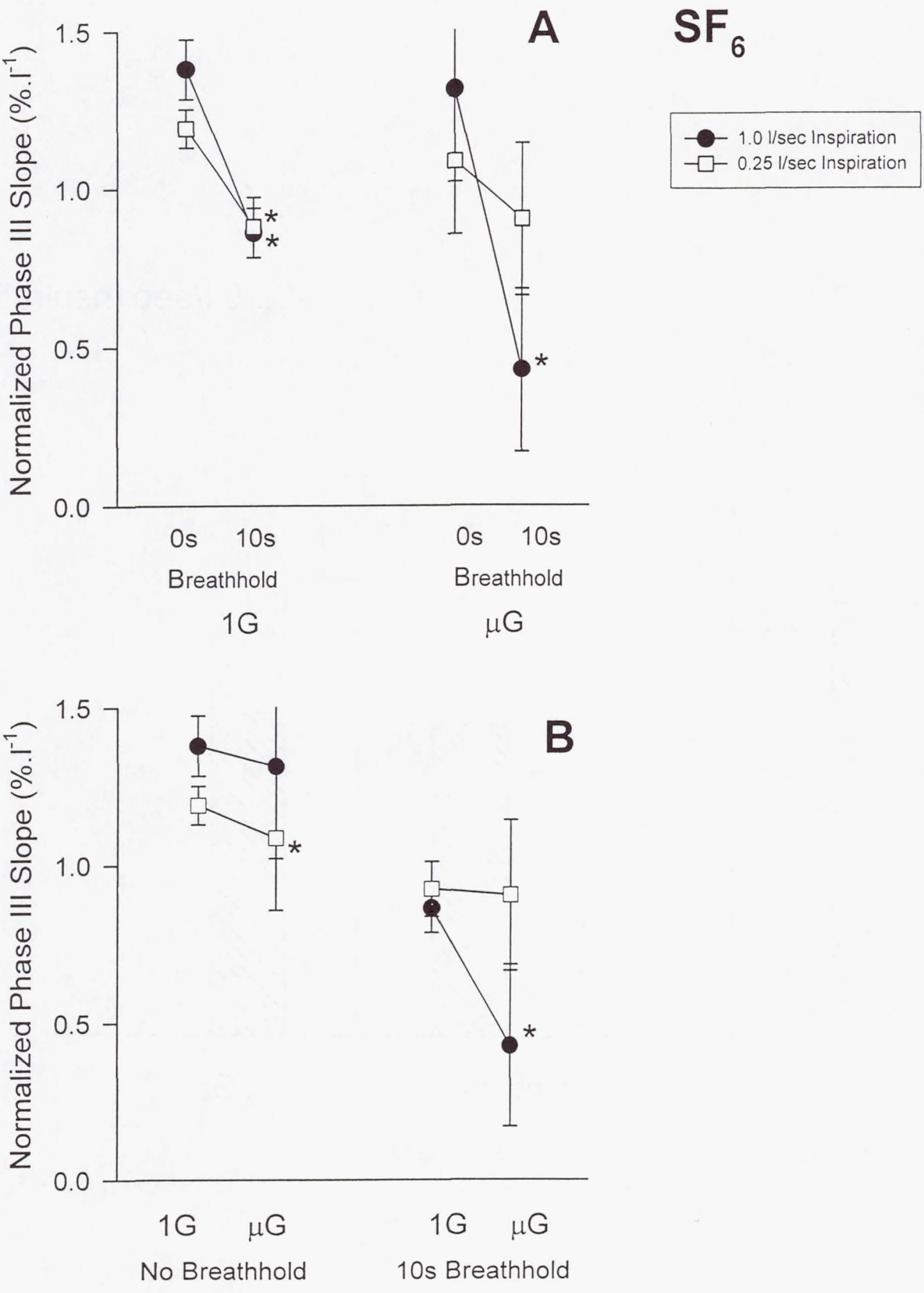
A
SF_6
1.0 l/sec Inspiration
0.25 l/sec Inspiration
Normalized Phase III Slope (%.l^{-1})
1.5
1.0
0.5
0.0
*
*
*
0s
10s
Breathhold
1G
0s
10s
Breathhold
μG
B
Normalized Phase III Slope (%.l^{-1})
1.5
1.0
0.5
0.0
*
*
1G
μG
No Breathhold
1G
μG
10s Breathhold

figure 9

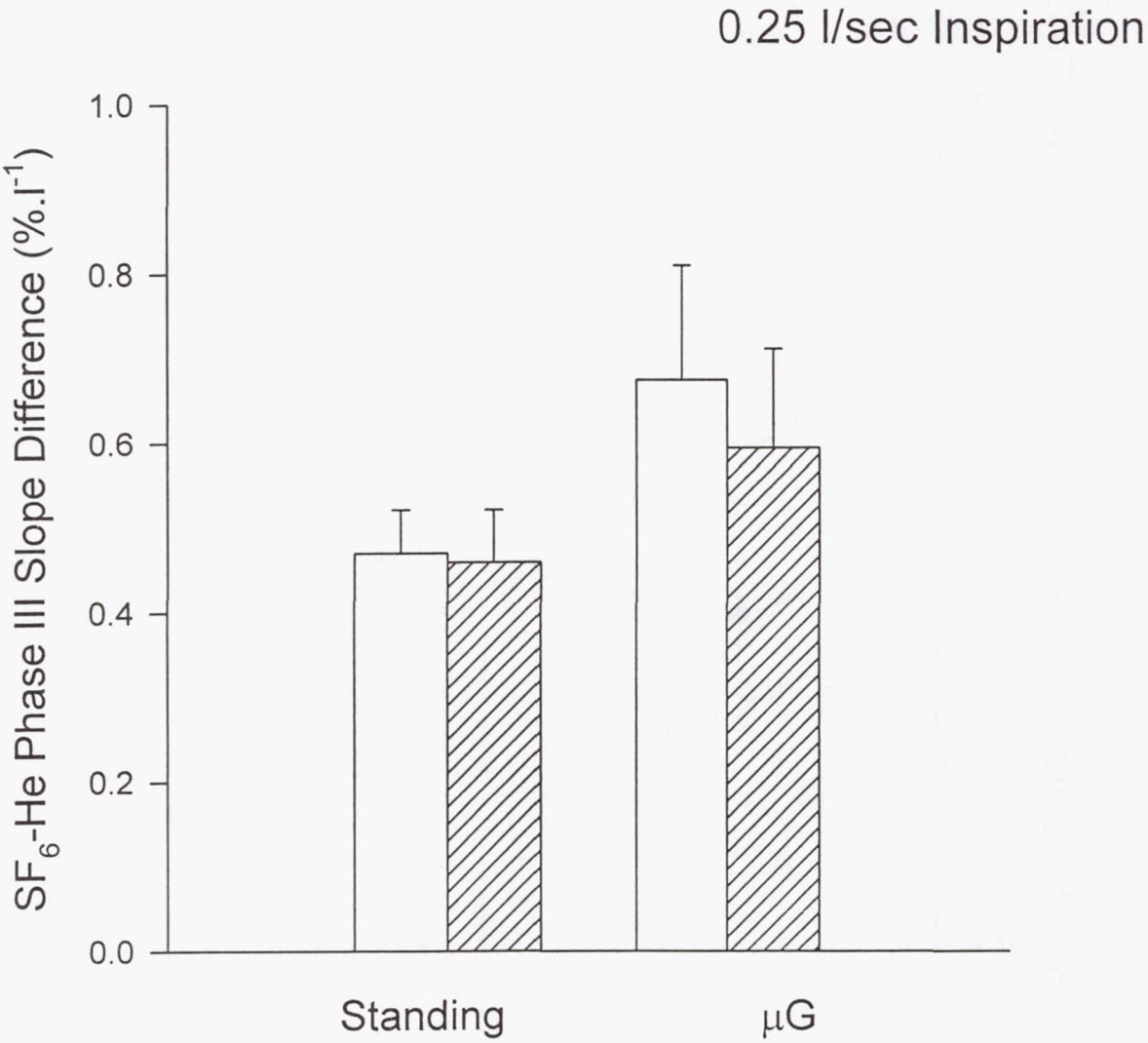
0.25 l/sec Inspiration
SF6-He Phase III Slope Difference (%.l-1)
1.0
0.8
0.6
0.4
0.2
0.0
Standing
μG

figure 10

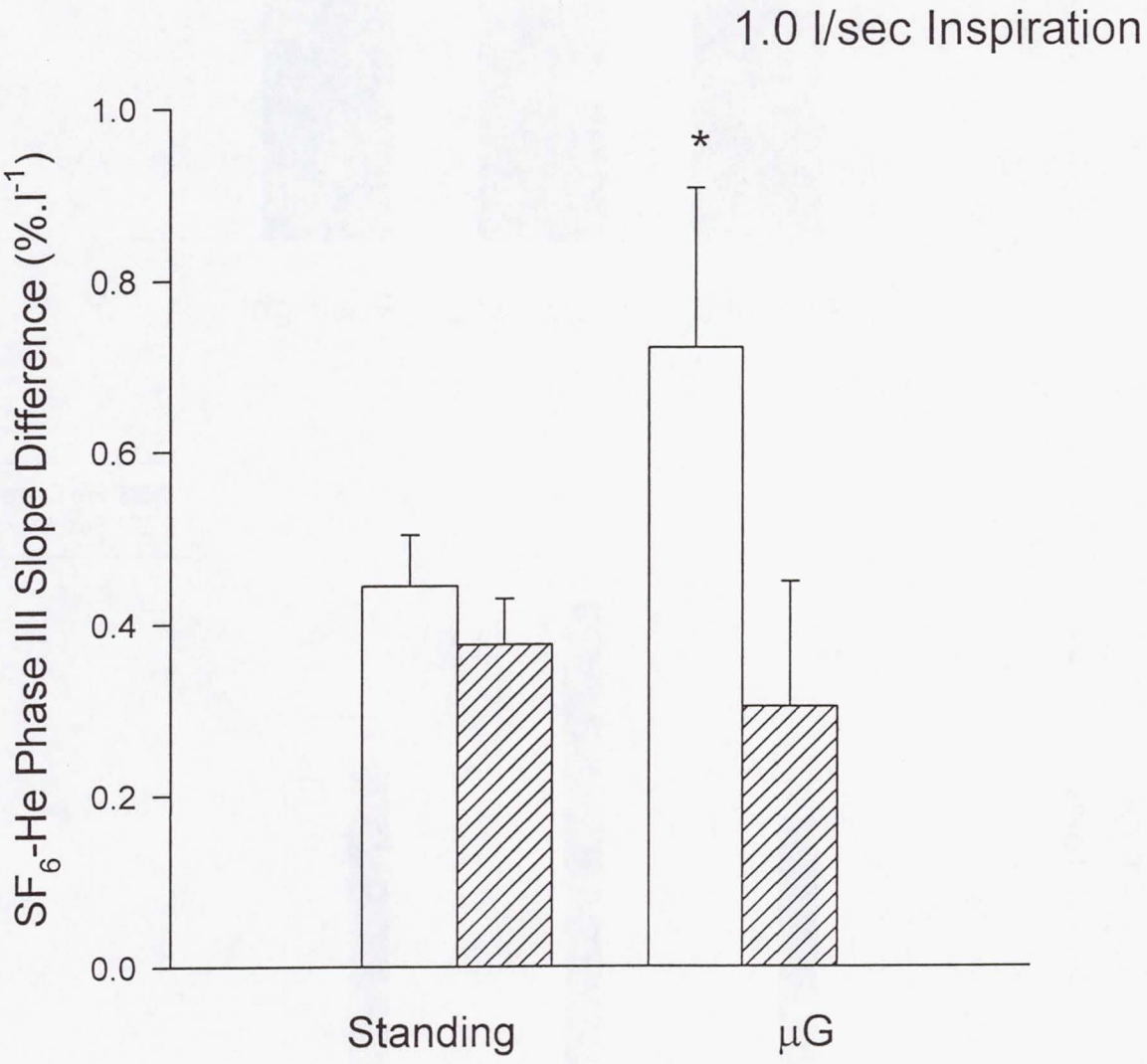
1.0 l/sec Inspiration
SF6-He Phase III Slope Difference (%.l-1)
1.0
0.8
0.6
0.4
0.2
0.0
*
Standing
μG

figure 11

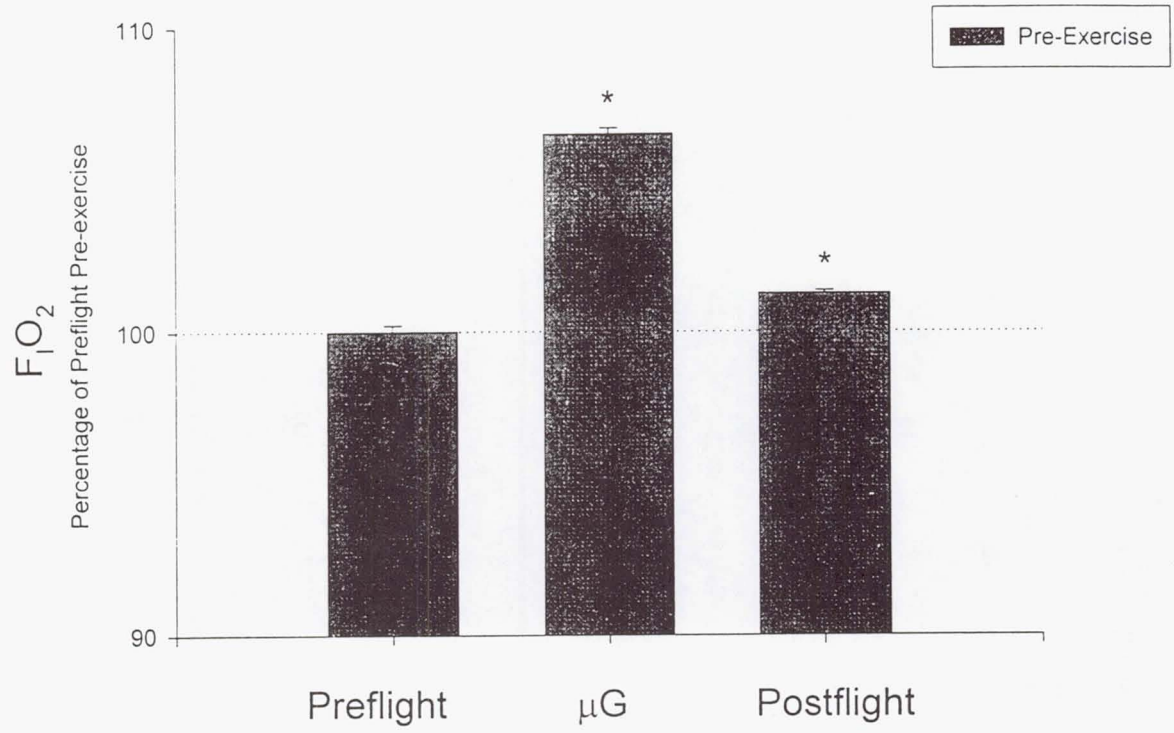
Pre-Exercise
110
100
90
F_IO_2
Percentage of Preflight Pre-exercise
*
*
Preflight
μG
Postflight

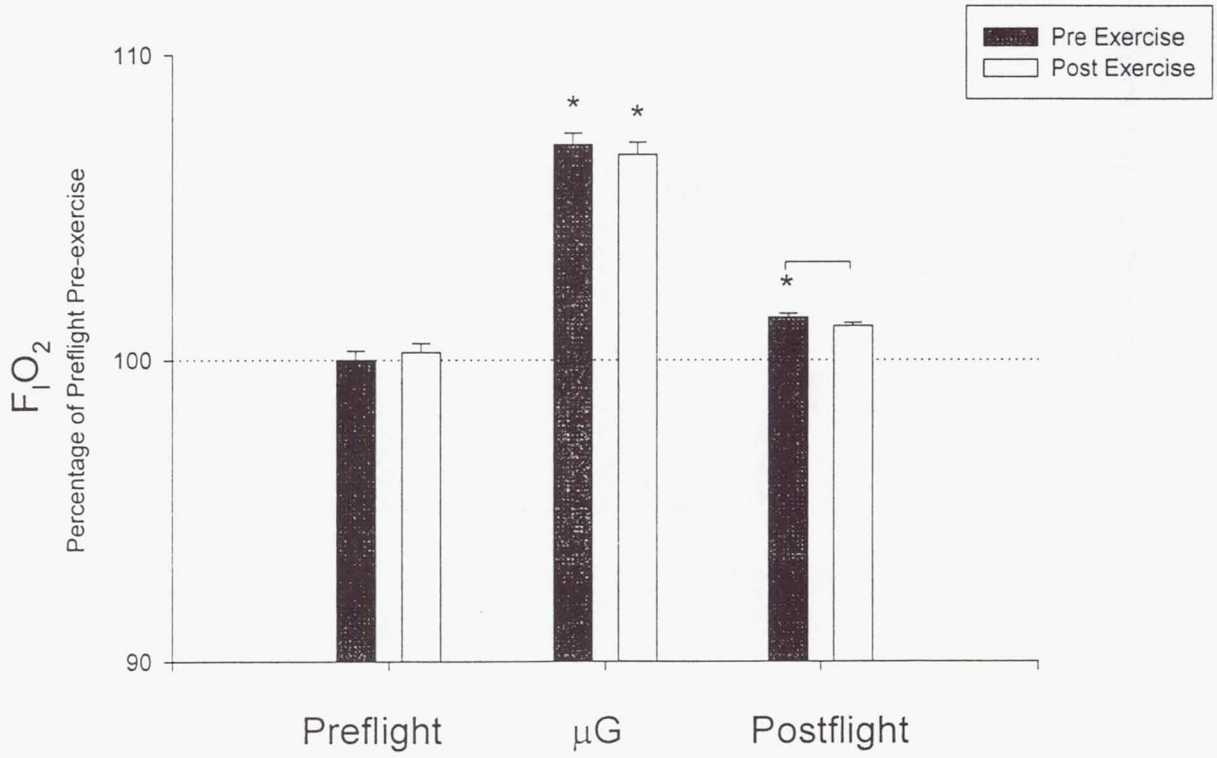
Pre Exercise
Post Exercise
110
100
90
F_IO_2
Percentage of Preflight Pre-exercise
*
*
*
Preflight
μG
Postflight

figure 12

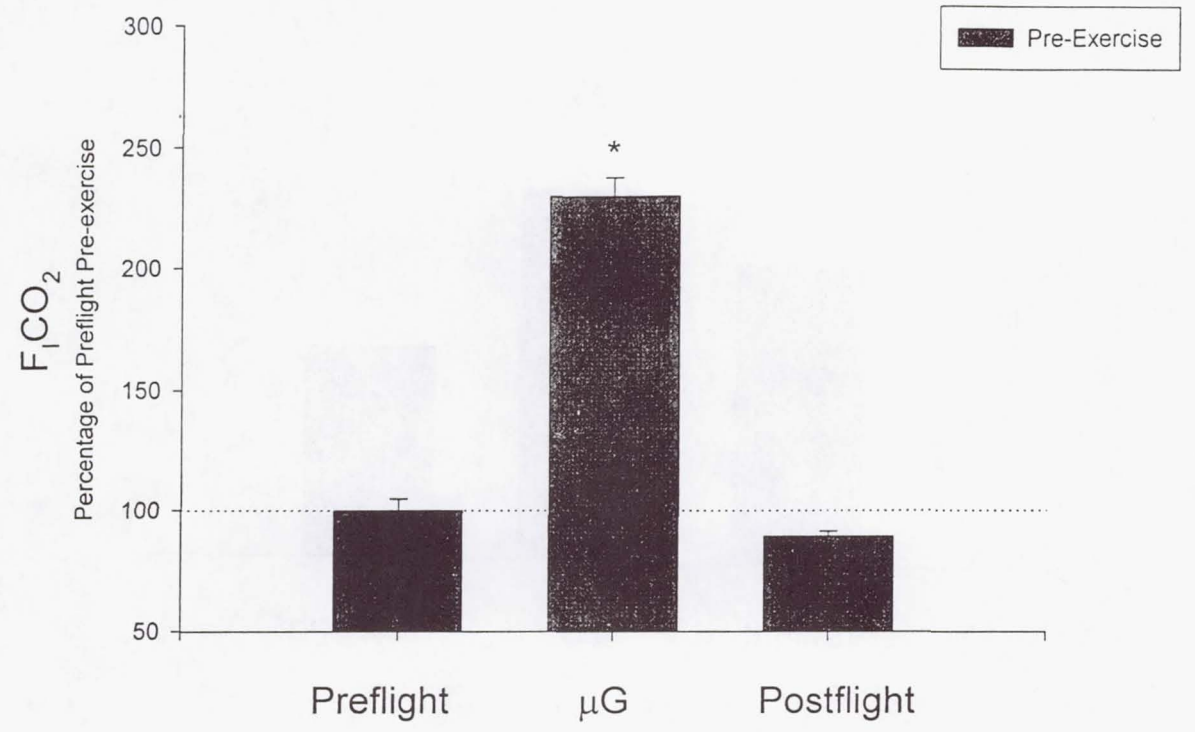
Pre-Exercise
300
250
200
150
100
50
F_ICO_2
Percentage of Preflight Pre-exercise
*
Preflight
μG
Postflight

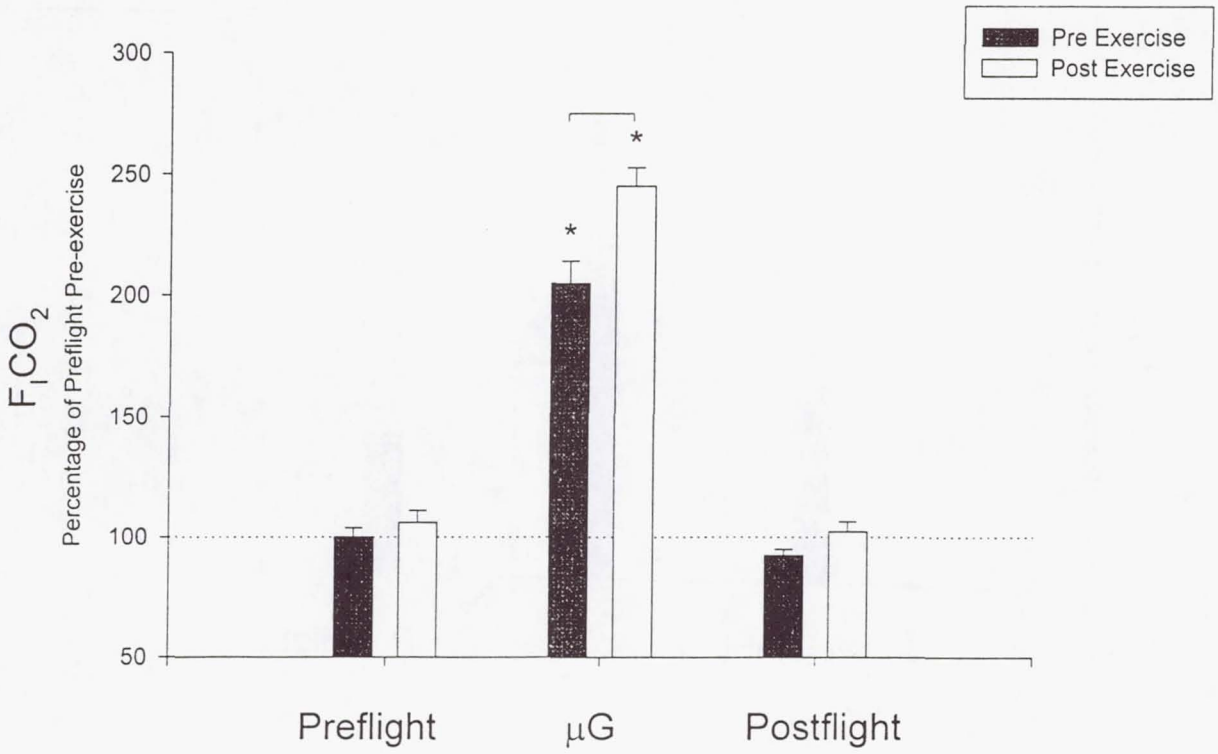
Pre Exercise
Post Exercise
300
250
200
150
100
50
F_ICO_2
Percentage of Preflight Pre-exercise
*
*
Preflight
μG
Postflight

figure 13

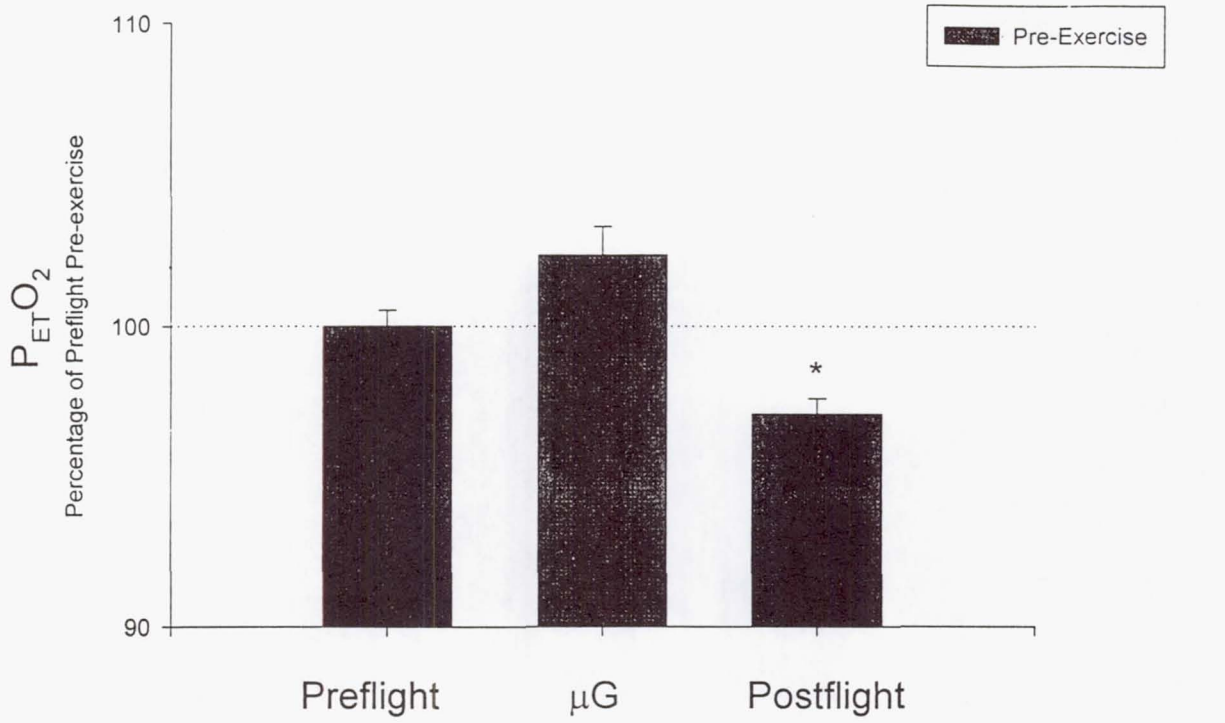
Pre-Exercise
110
100
90
$P_{ET}O_2$
Percentage of Preflight Pre-exercise
*
Preflight
μG
Postflight

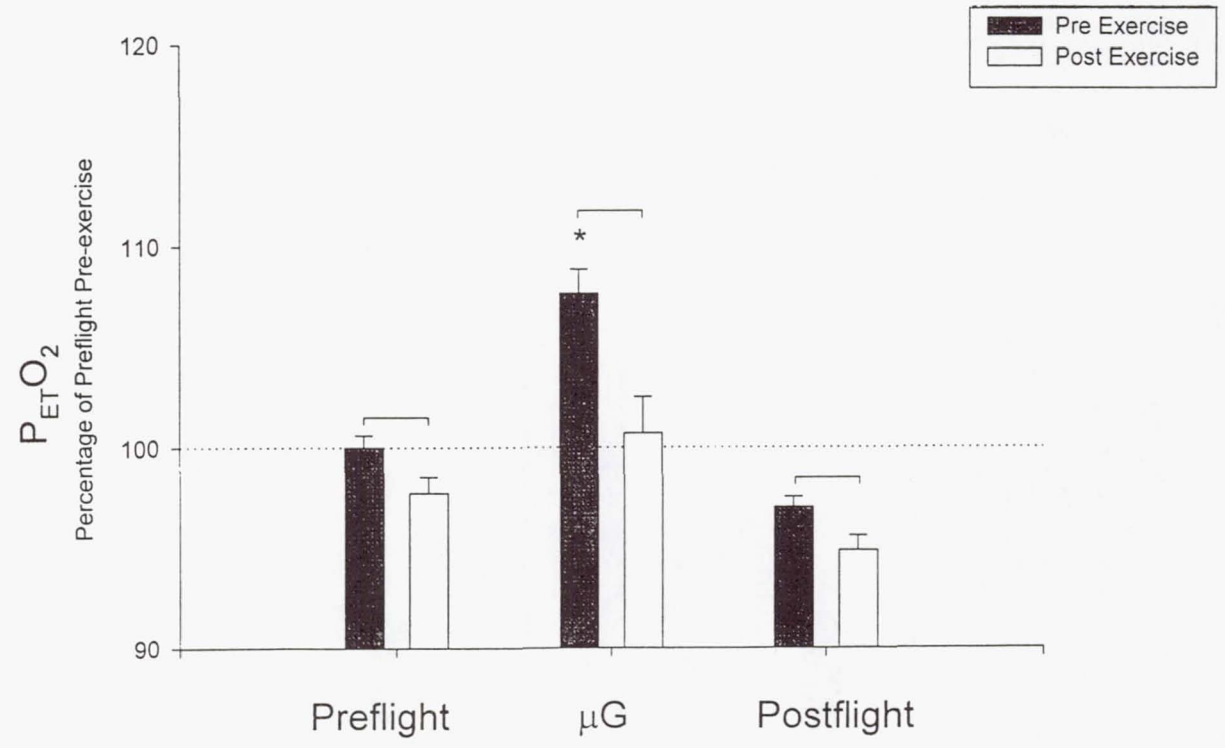
Pre Exercise
Post Exercise
120
110
100
90
$P_{ET}O_2$
Percentage of Preflight Pre-exercise
*
Preflight
μG
Postflight

figure 14

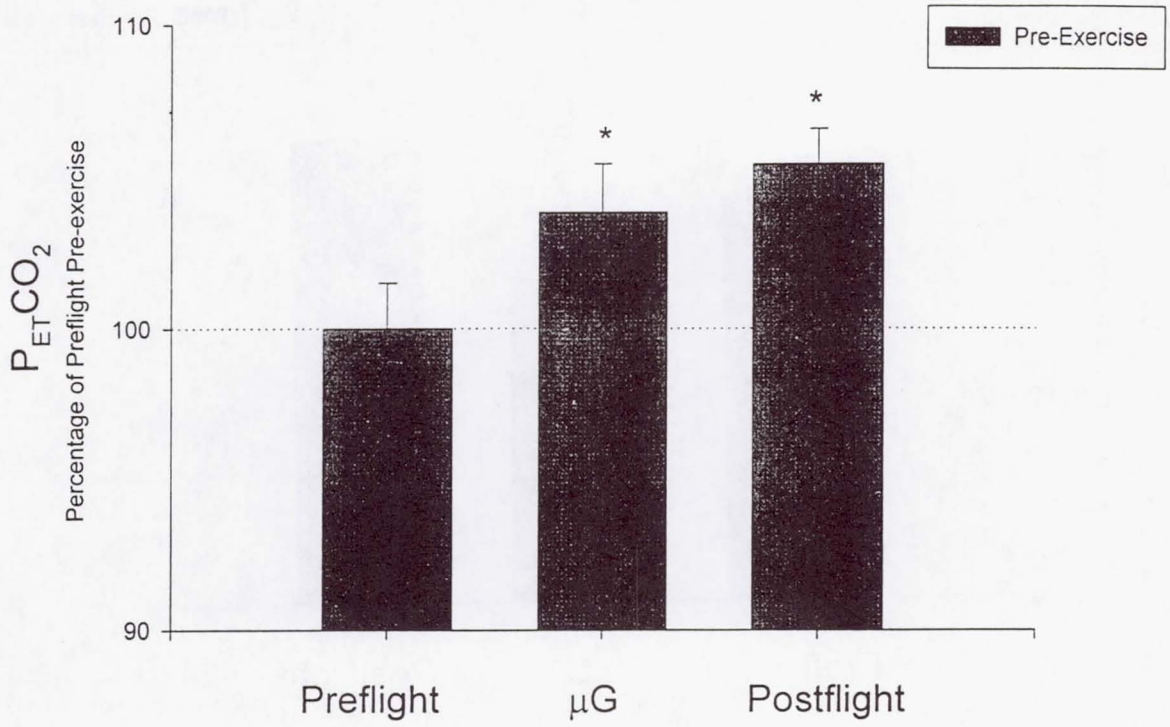
Pre-Exercise
110
100
90
$P_{ET}CO_2$
Percentage of Preflight Pre-exercise
*
*
Preflight
μG
Postflight

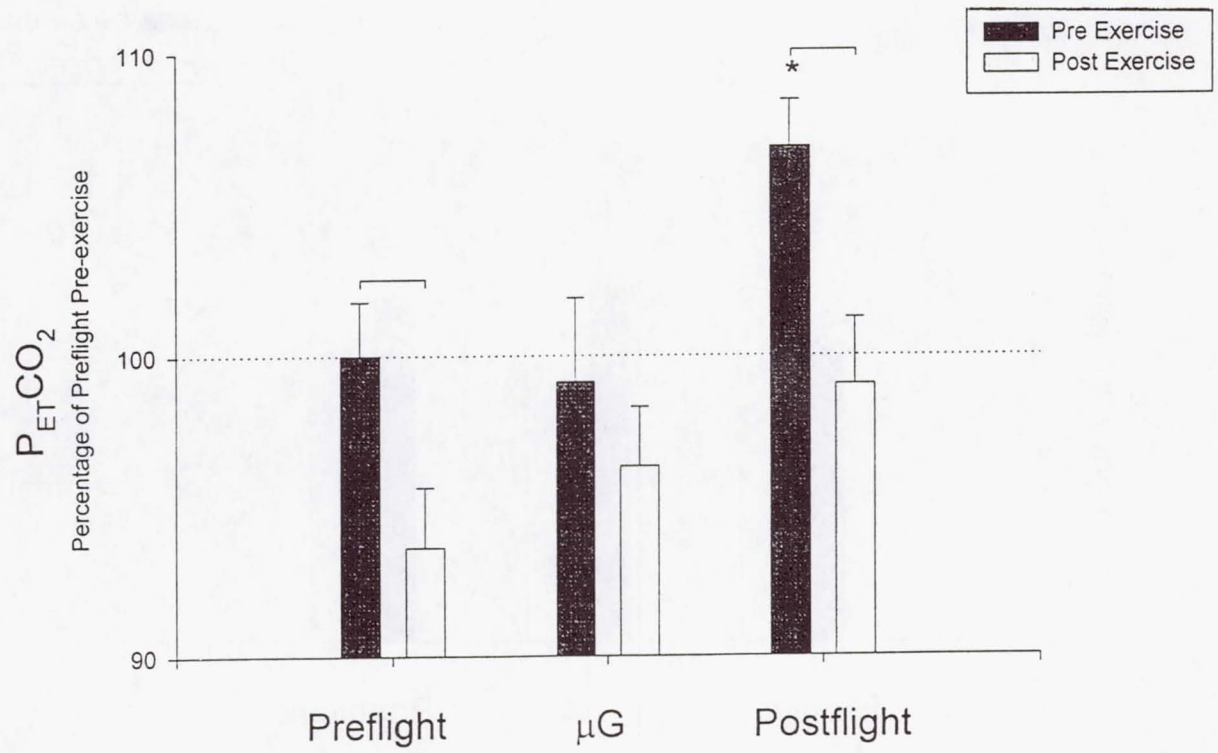
Pre Exercise
Post Exercise
110
100
90
$P_{ET}CO_2$
Percentage of Preflight Pre-exercise
*
Preflight
μG
Postflight

figure 15

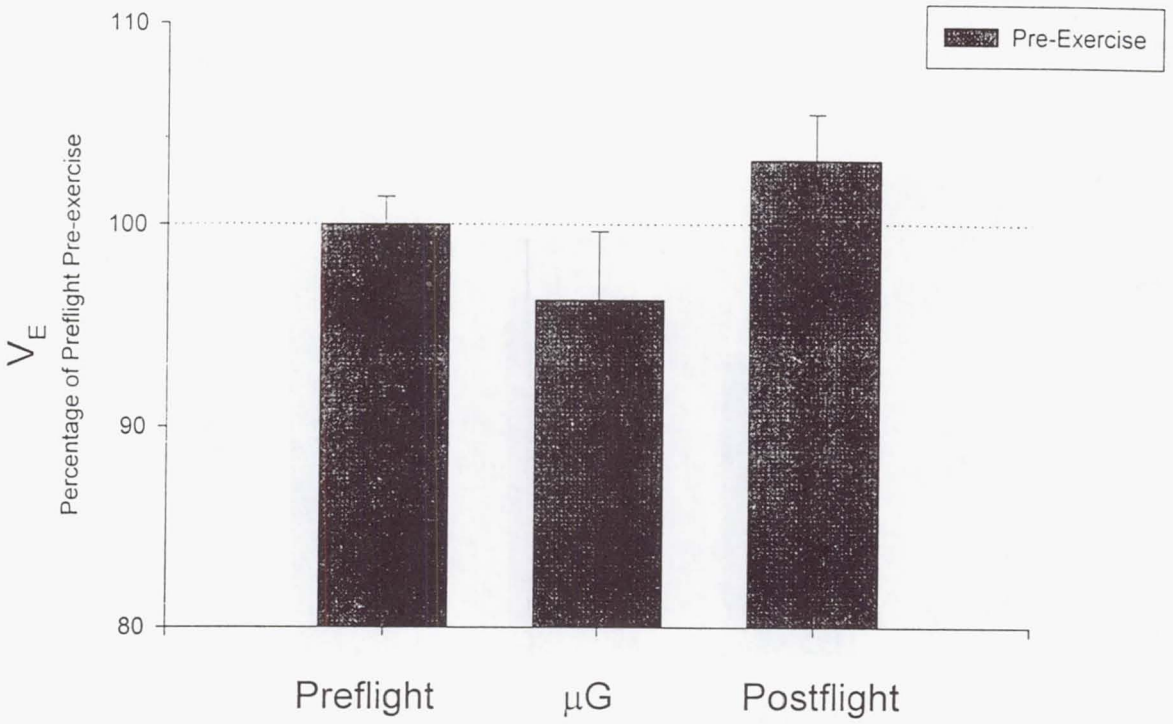
Pre-Exercise
110
100
90
80
V_E
Percentage of Preflight Pre-exercise
Preflight
μG
Postflight

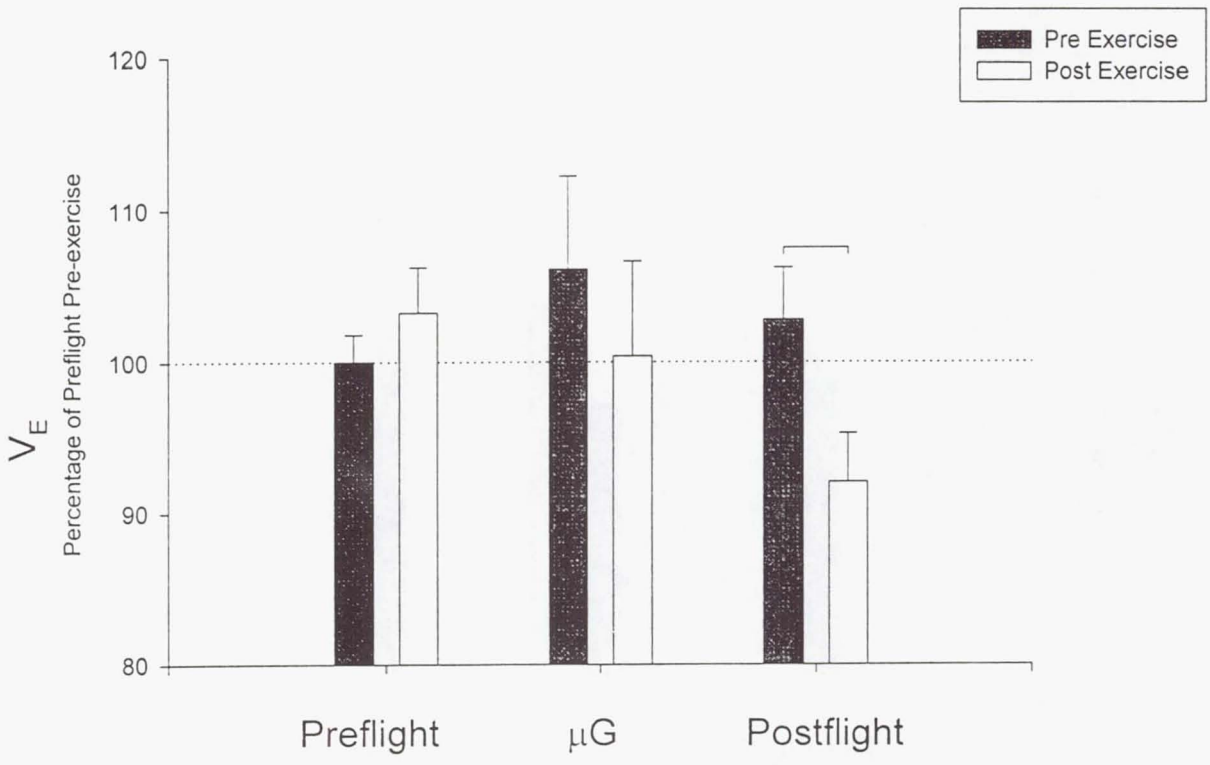
Pre Exercise
Post Exercise
120
110
100
90
80
V_E
Percentage of Preflight Pre-exercise
Preflight
μG
Postflight

figure 16

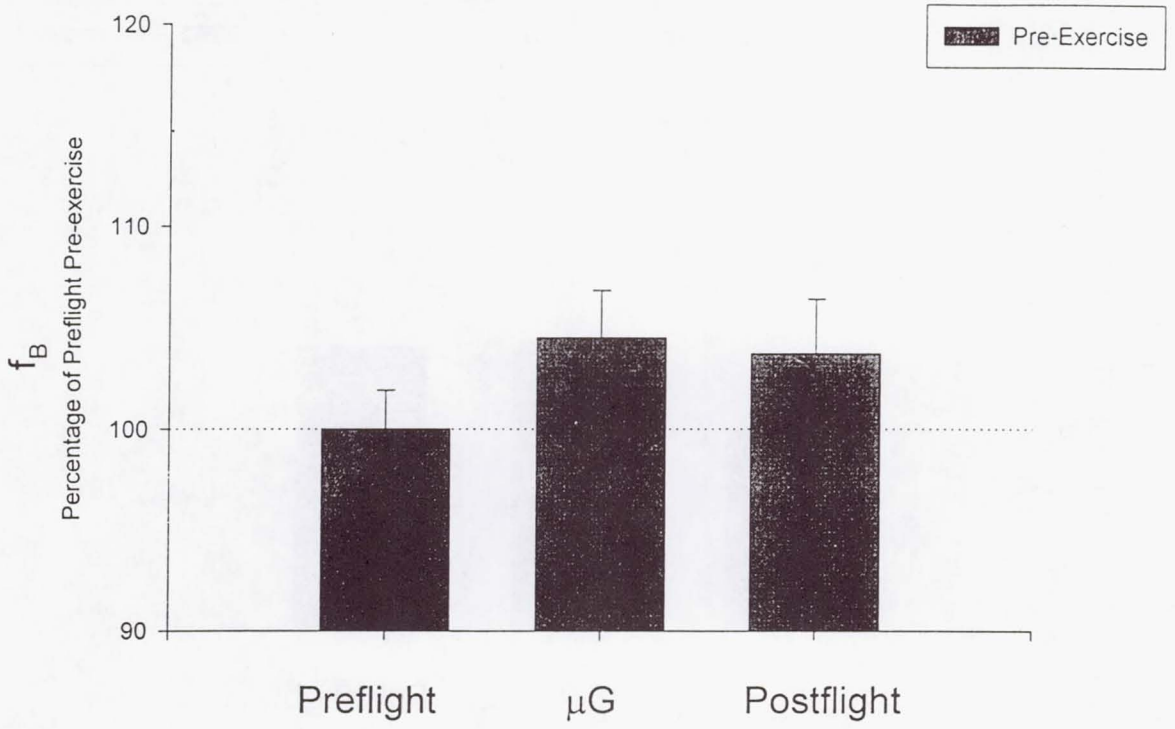
Pre-Exercise
120
110
100
90
f_B
Percentage of Preflight Pre-exercise
Preflight
μG
Postflight

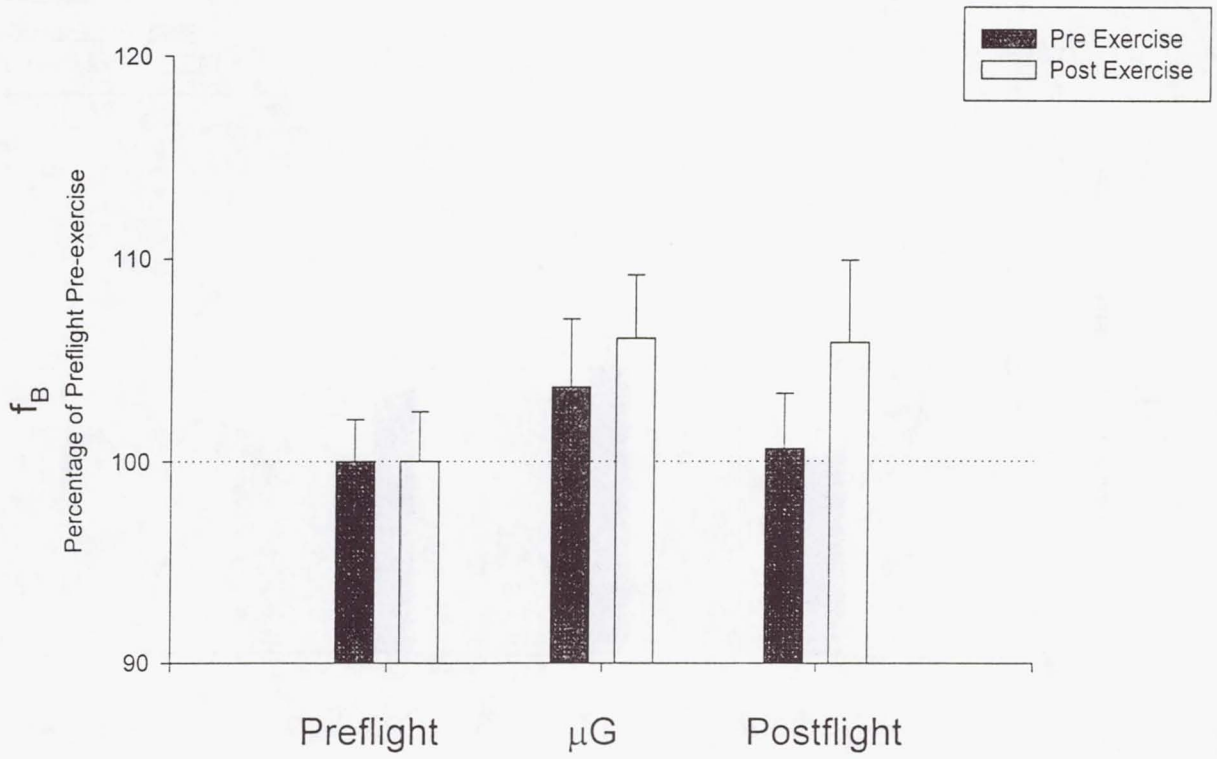
Pre Exercise
Post Exercise
120
110
100
90
f_B
Percentage of Preflight Pre-exercise
Preflight
μG
Postflight

figure 17

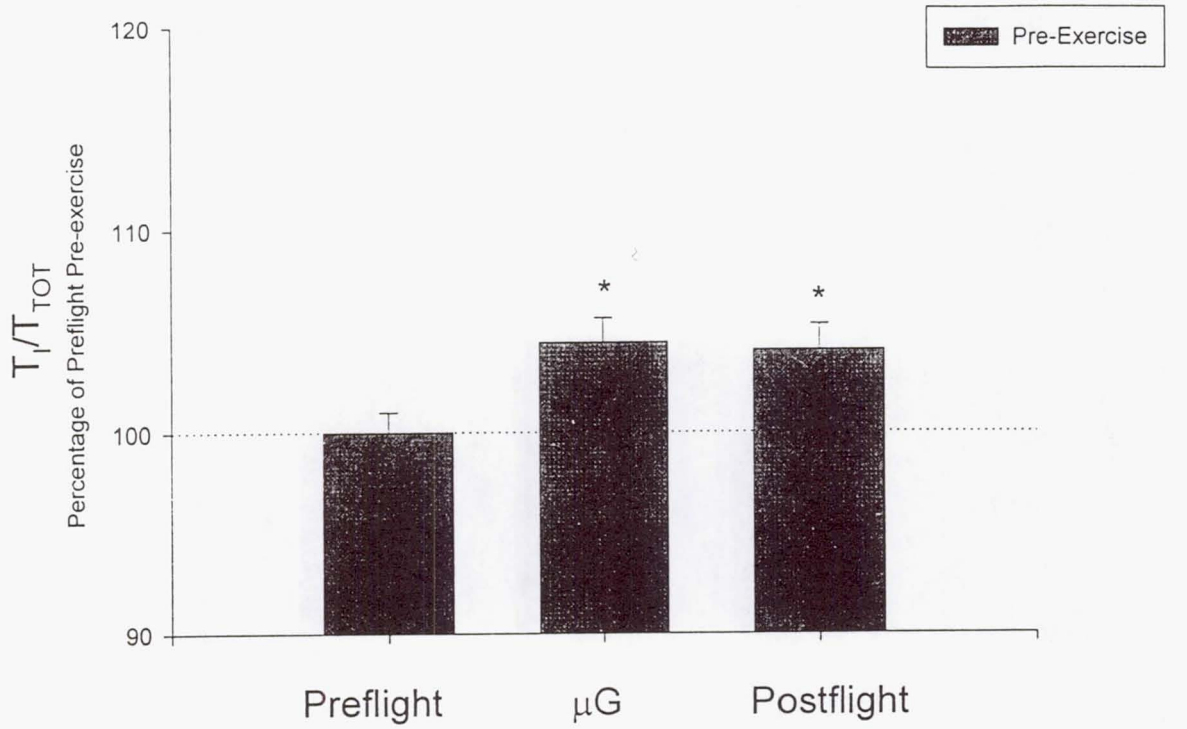
Pre-Exercise
120
110
100
90
T_I/T_{TOT}
Percentage of Preflight Pre-exercise
*
*
Preflight
μG
Postflight

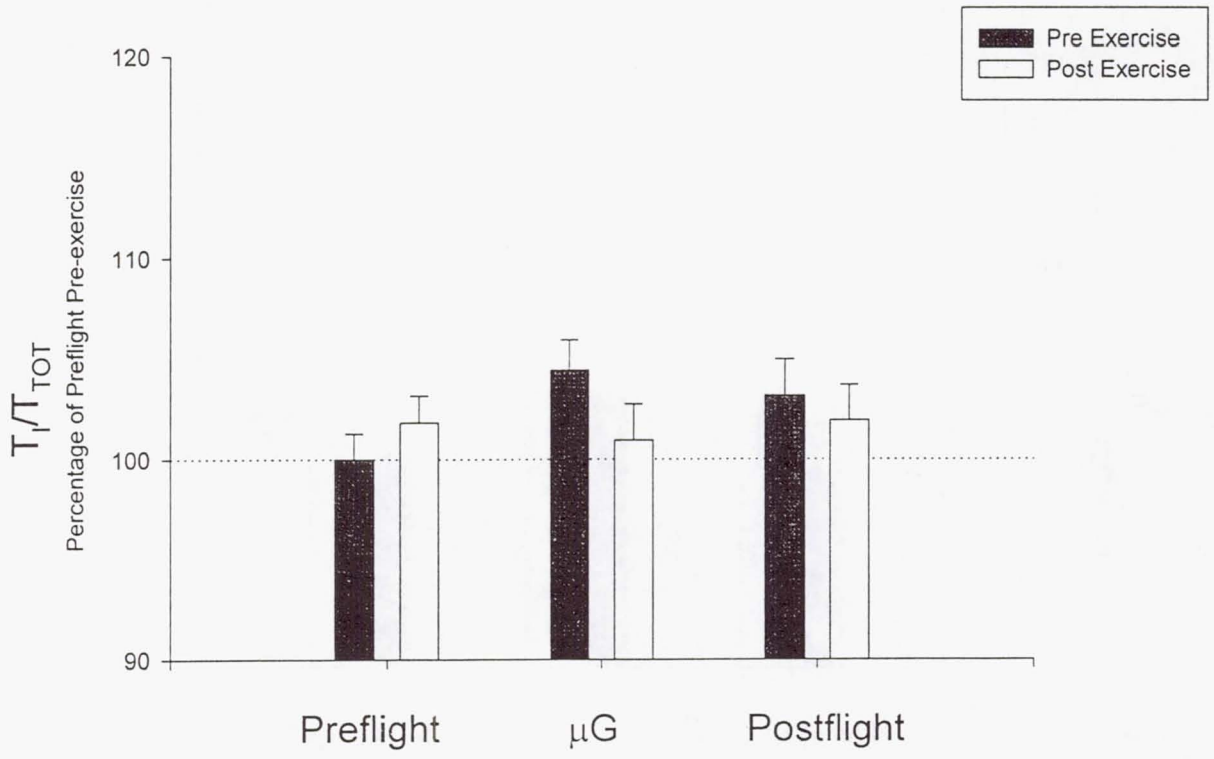
Pre Exercise
Post Exercise
120
110
100
90
T_I/T_{TOT}
Percentage of Preflight Pre-exercise
Preflight
μG
Postflight

figure 18

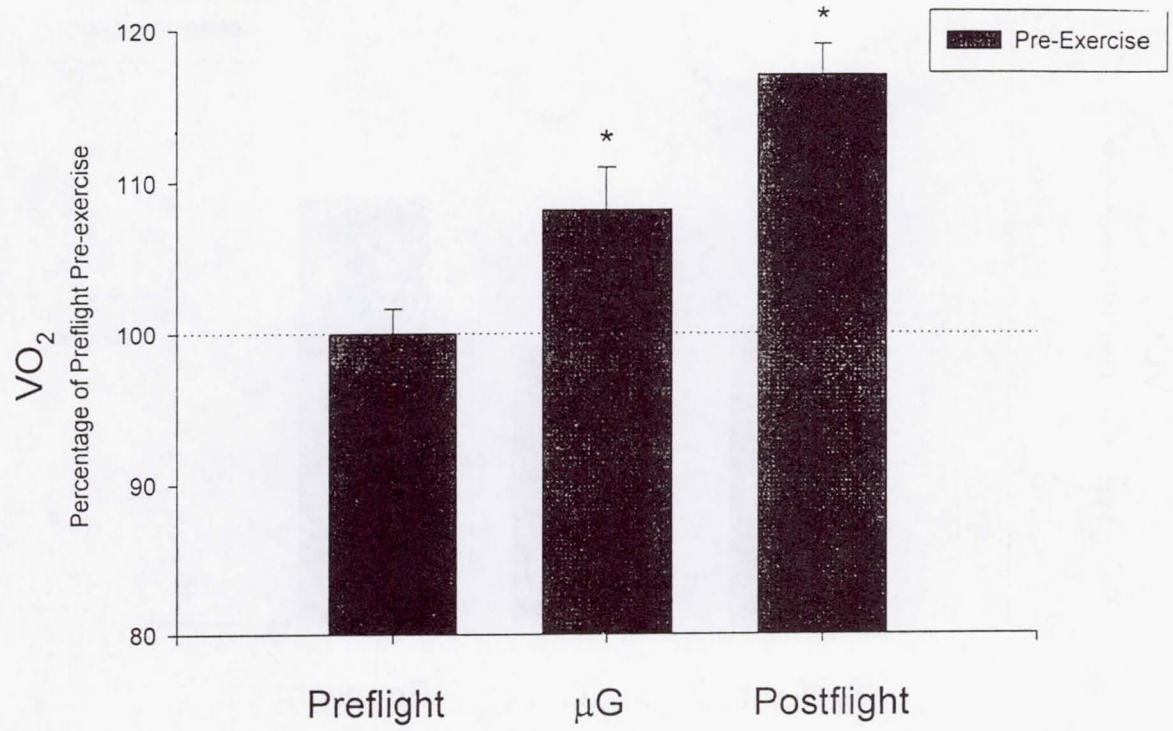
Pre-Exercise
120
110
100
90
80
VO_2
Percentage of Preflight Pre-exercise
*
*
Preflight
μG
Postflight

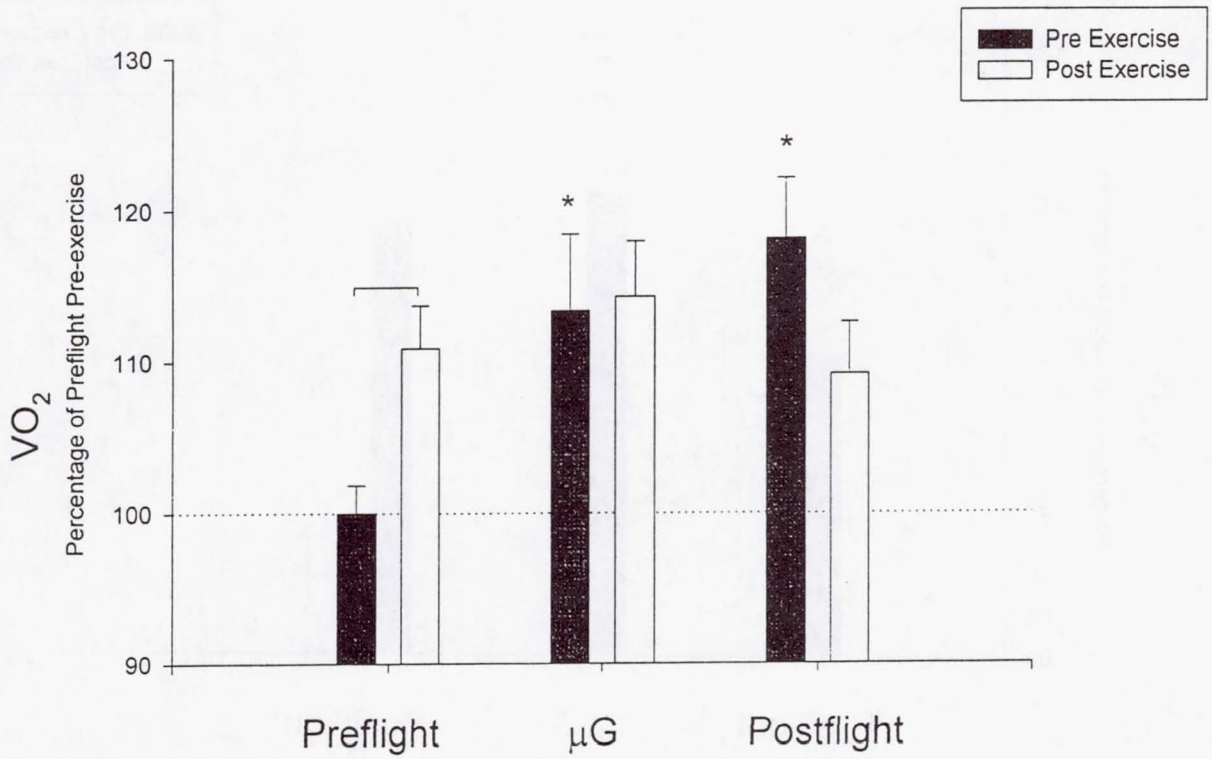
Pre Exercise
Post Exercise
130
120
110
100
90
VO_2
Percentage of Preflight Pre-exercise
*
*
Preflight
μG
Postflight

figure 19

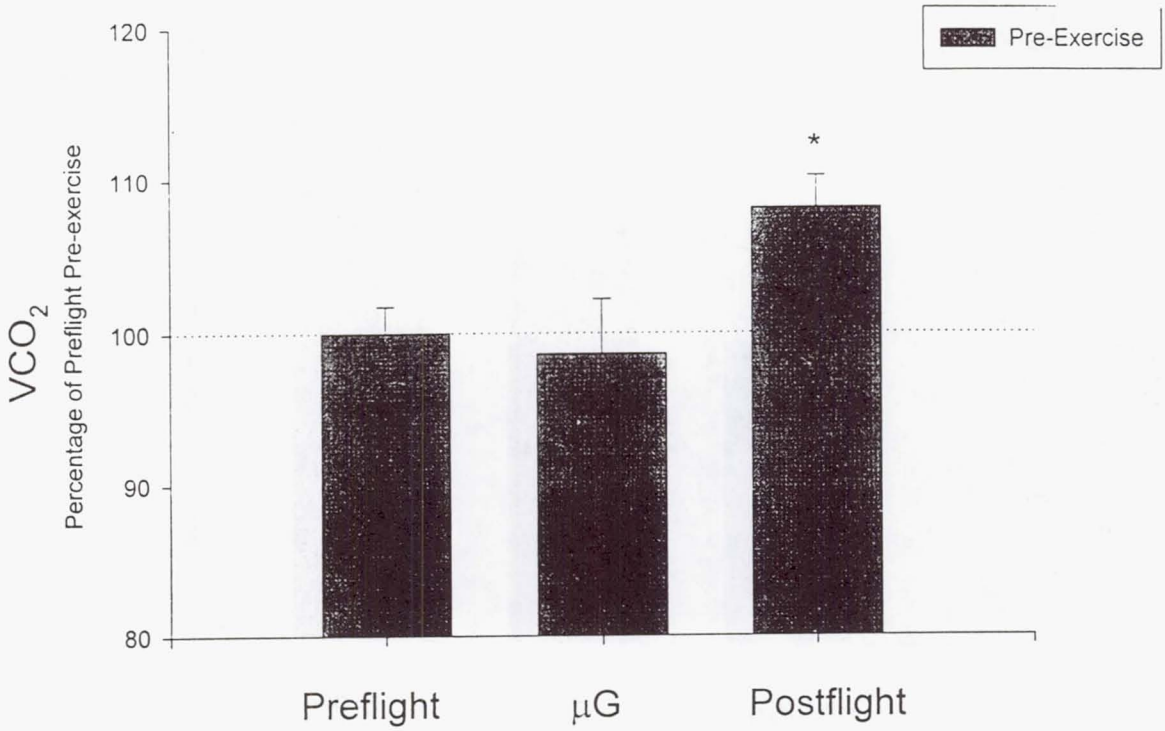
Pre-Exercise
120
110
100
90
80
*
VCO_2
Percentage of Preflight Pre-exercise
Preflight
μG
Postflight

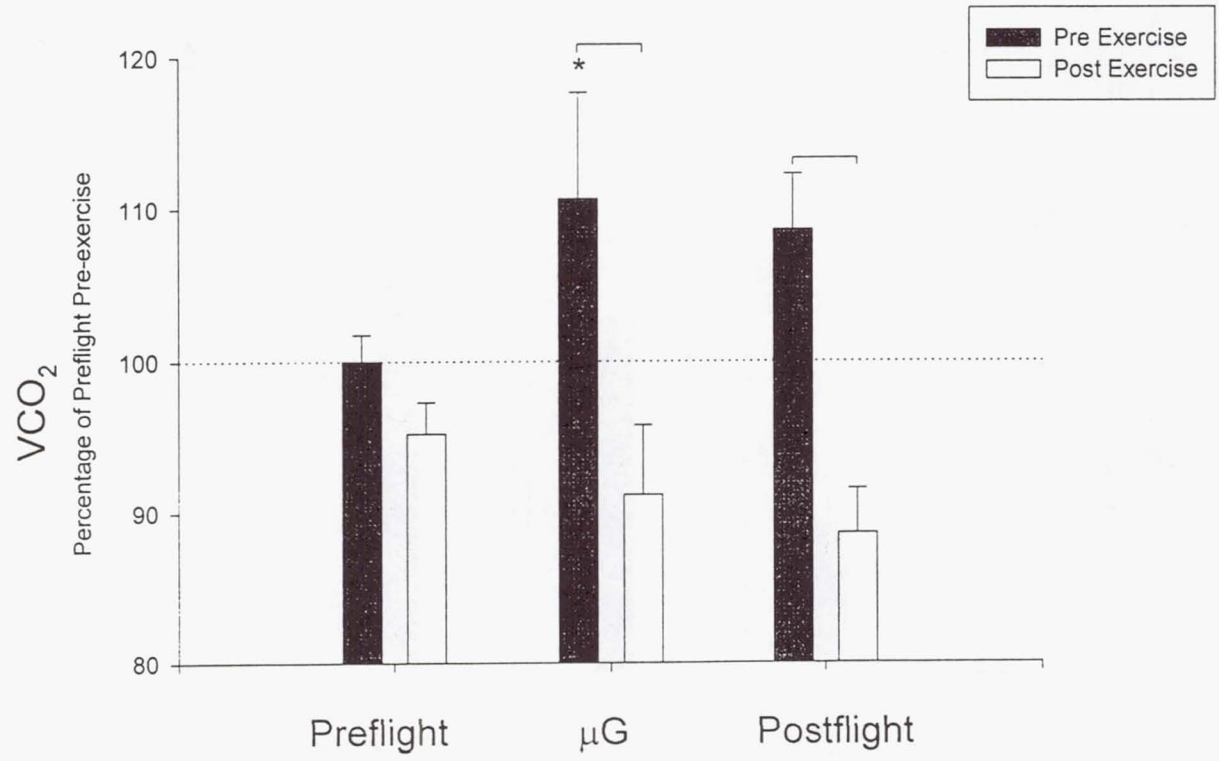
Pre Exercise
Post Exercise
120
110
100
90
80
*
VCO_2
Percentage of Preflight Pre-exercise
Preflight
μG
Postflight

figure 20

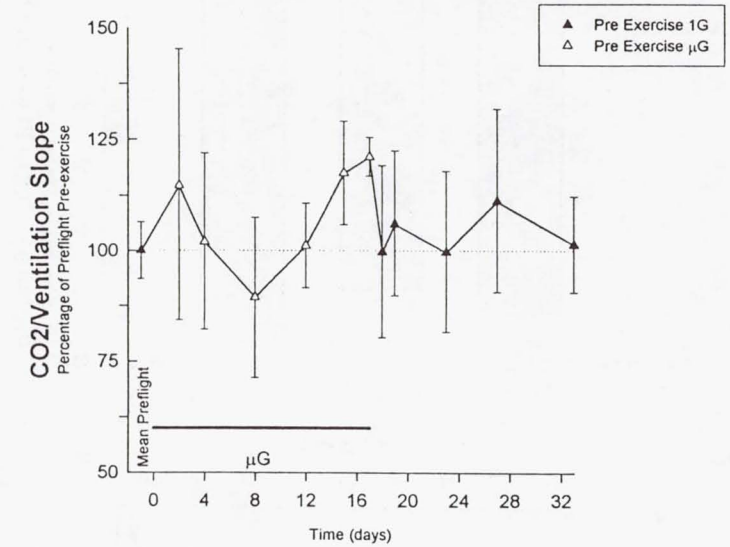
Pre Exercise 1G
Pre Exercise µG
CO2/Ventilation Slope
Percentage of Preflight Pre-exercise
150
125
100
75
50
Mean Preflight
µG
0
4
8
12
16
20
24
28
32
Time (days)

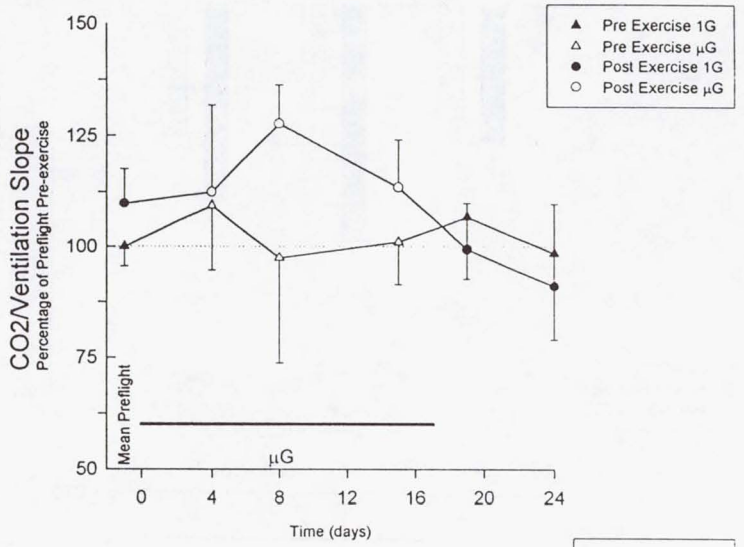
Pre Exercise 1G
Pre Exercise µG
Post Exercise 1G
Post Exercise µG
CO2/Ventilation Slope
Percentage of Preflight Pre-exercise
150
125
100
75
50
Mean Preflight
µG
0
4
8
12
16
20
24
Time (days)

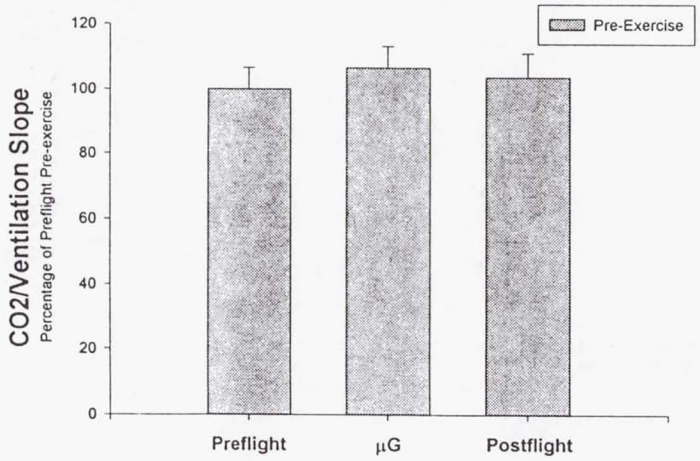
Pre-Exercise
CO2/Ventilation Slope
Percentage of Preflight Pre-exercise
120
100
80
60
40
20
0
Preflight
µG
Postflight

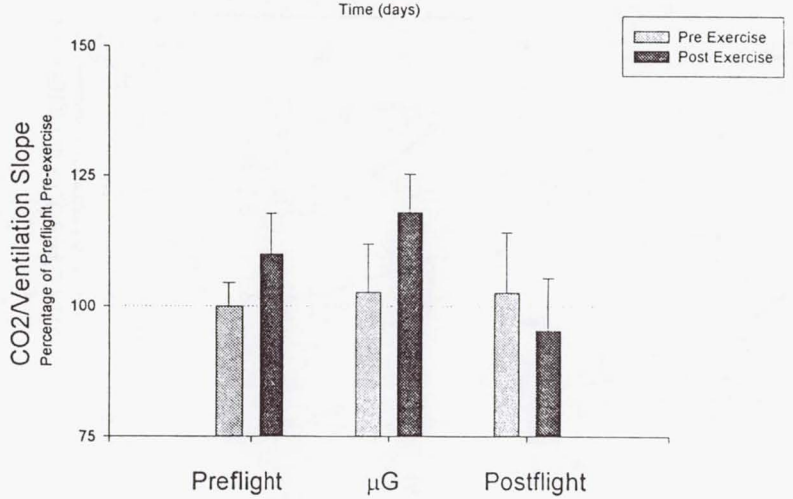
Pre Exercise
Post Exercise
CO2/Ventilation Slope
Percentage of Preflight Pre-exercise
150
125
100
75
Preflight
µG
Postflight

figure 21

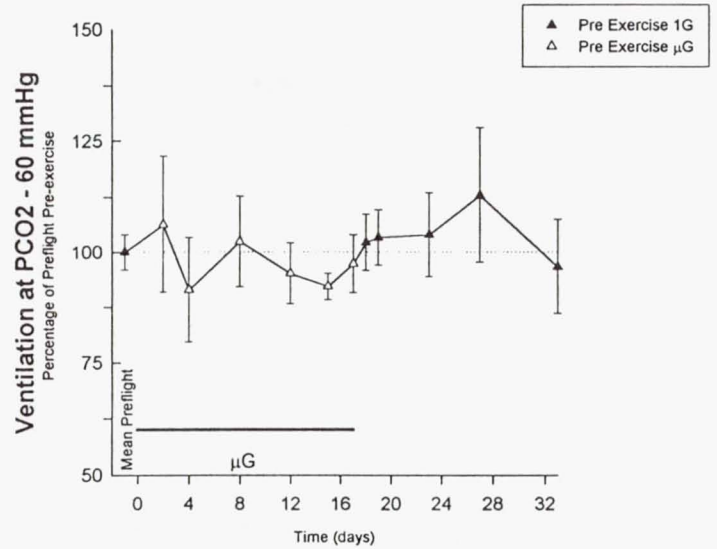
Pre Exercise 1G
Pre Exercise µG
Ventilation at PCO2 - 60 mmHg
Percentage of Preflight Pre-exercise
150
125
100
75
50
Mean Preflight
µG
0
4
8
12
16
20
24
28
32
Time (days)

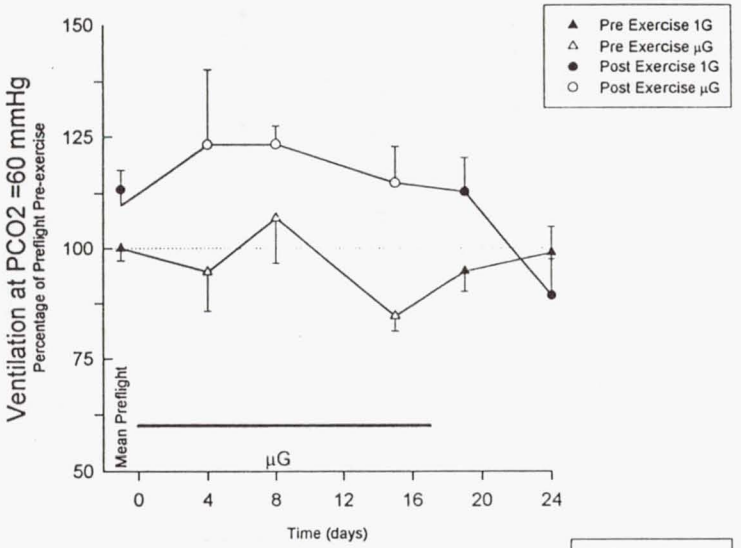
Pre Exercise 1G
Pre Exercise µG
Post Exercise 1G
Post Exercise µG
Ventilation at PCO2 =60 mmHg
Percentage of Preflight Pre-exercise
150
125
100
75
50
Mean Preflight
µG
0
4
8
12
16
20
24
Time (days)

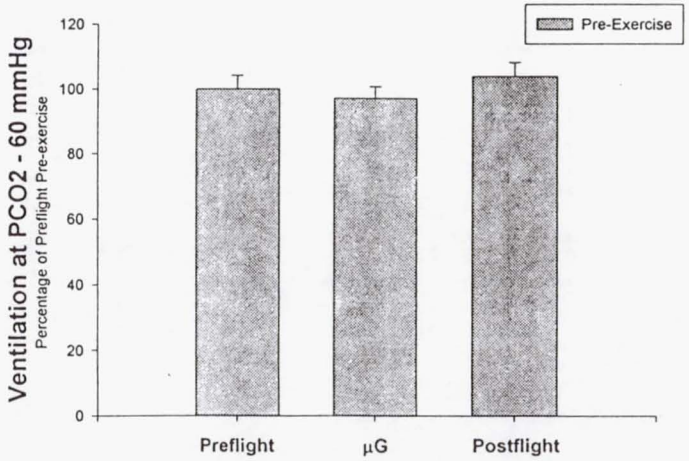
Pre-Exercise
Ventilation at PCO2 - 60 mmHg
Percentage of Preflight Pre-exercise
120
100
80
60
40
20
0
Preflight
µG
Postflight

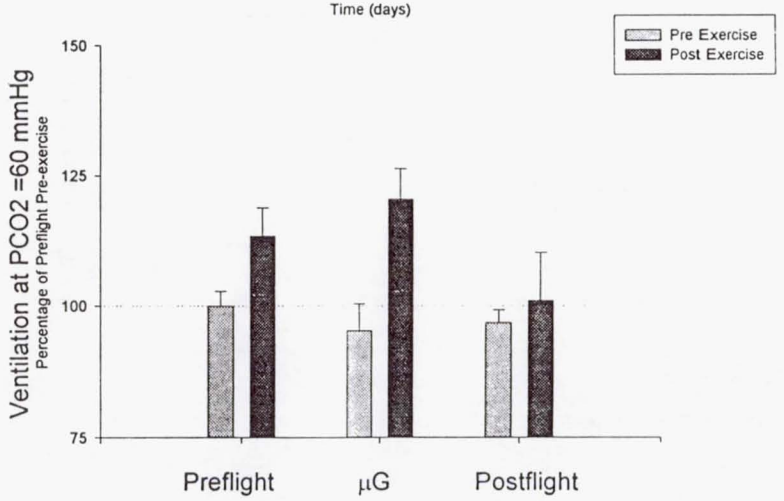
Pre Exercise
Post Exercise
Ventilation at PCO2 =60 mmHg
Percentage of Preflight Pre-exercise
150
125
100
75
Preflight
µG
Postflight

figure 22

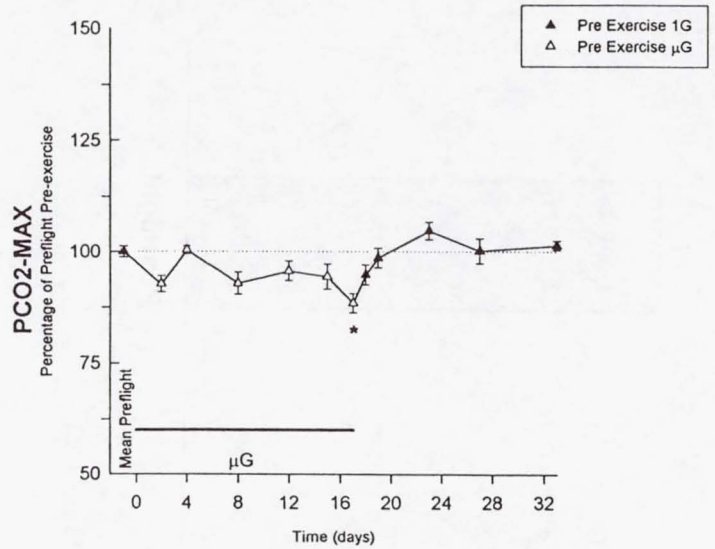
Pre Exercise 1G
Pre Exercise µG
PCO2-MAX
Percentage of Preflight Pre-exercise
150
125
100
75
50
Mean Preflight
µG
0
4
8
12
16
20
24
28
32
Time (days)

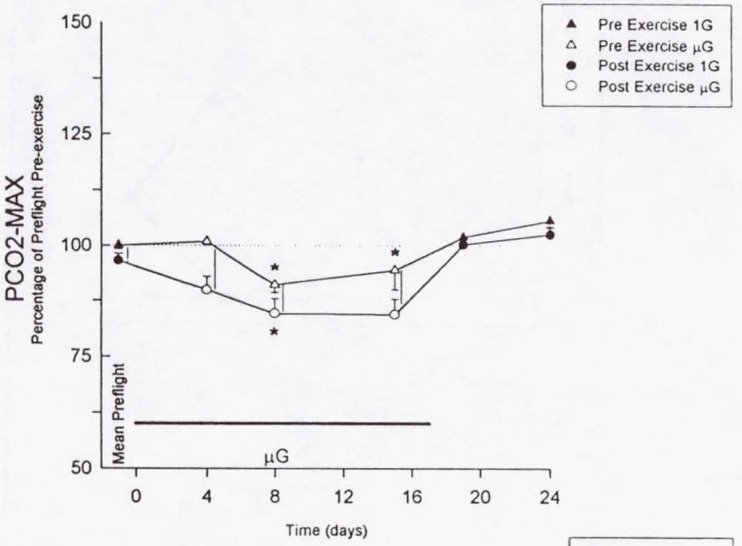
Pre Exercise 1G
Pre Exercise µG
Post Exercise 1G
Post Exercise µG
PCO2-MAX
Percentage of Preflight Pre-exercise
150
125
100
75
50
Mean Preflight
µG
0
4
8
12
16
20
24
Time (days)

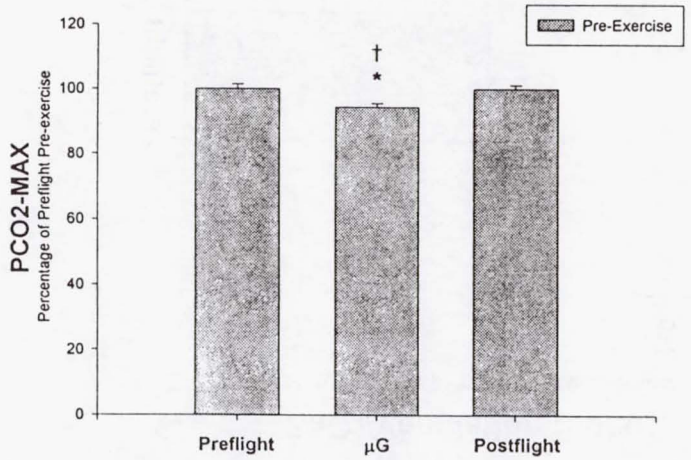
Pre-Exercise
PCO2-MAX
Percentage of Preflight Pre-exercise
120
100
80
60
40
20
0
†
Preflight
µG
Postflight

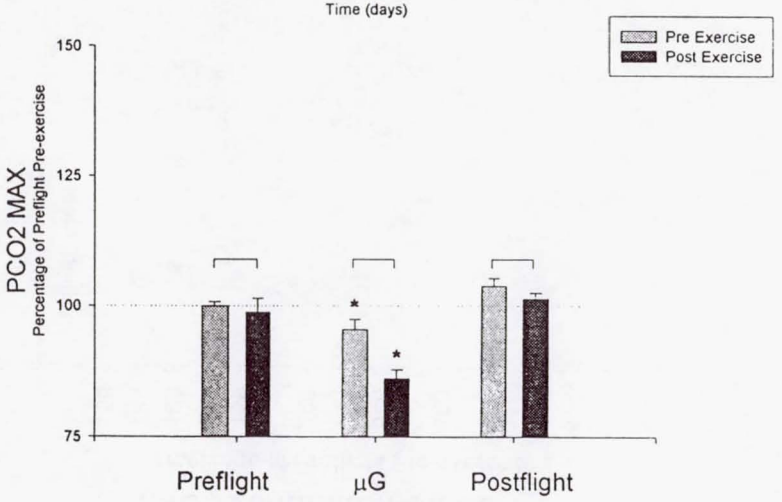
Pre Exercise
Post Exercise
PCO2 MAX
Percentage of Preflight Pre-exercise
150
125
100
75
Preflight
µG
Postflight

figure 23

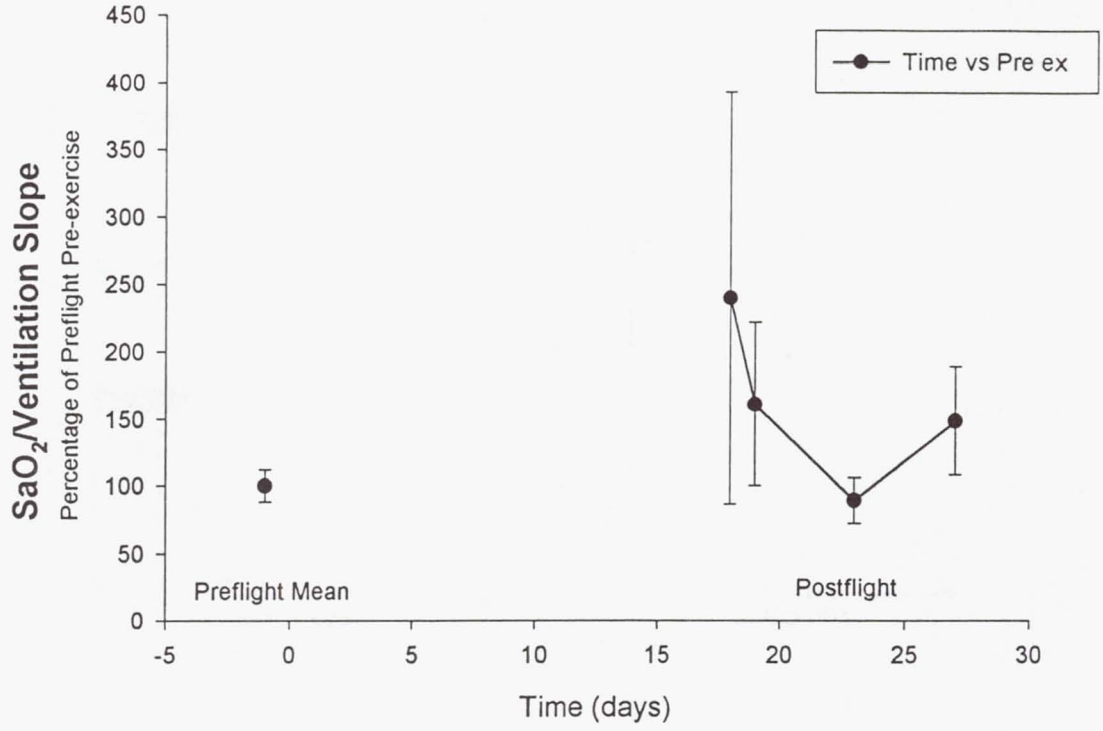
Time vs Pre ex
SaO_2/Ventilation Slope
Percentage of Preflight Pre-exercise
450
400
350
300
250
200
150
100
50
0
Preflight Mean
Postflight
-5
0
5
10
15
20
25
30
Time (days)

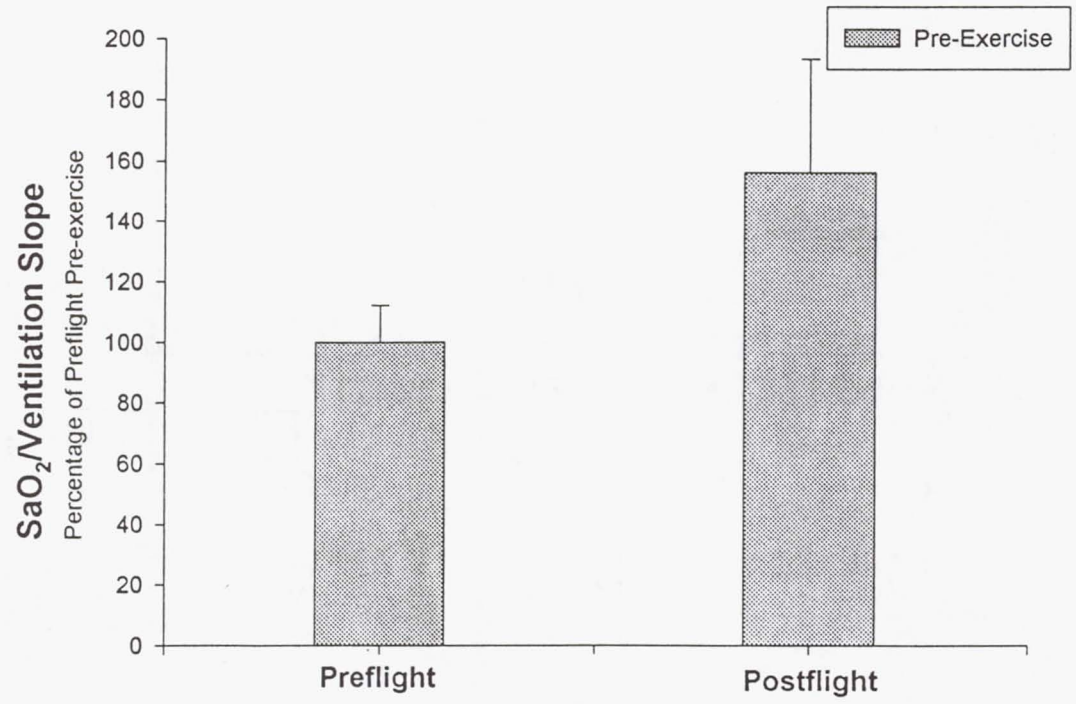
Pre-Exercise
SaO_2/Ventilation Slope
Percentage of Preflight Pre-exercise
200
180
160
140
120
100
80
60
40
20
0
Preflight
Postflight

figure 24

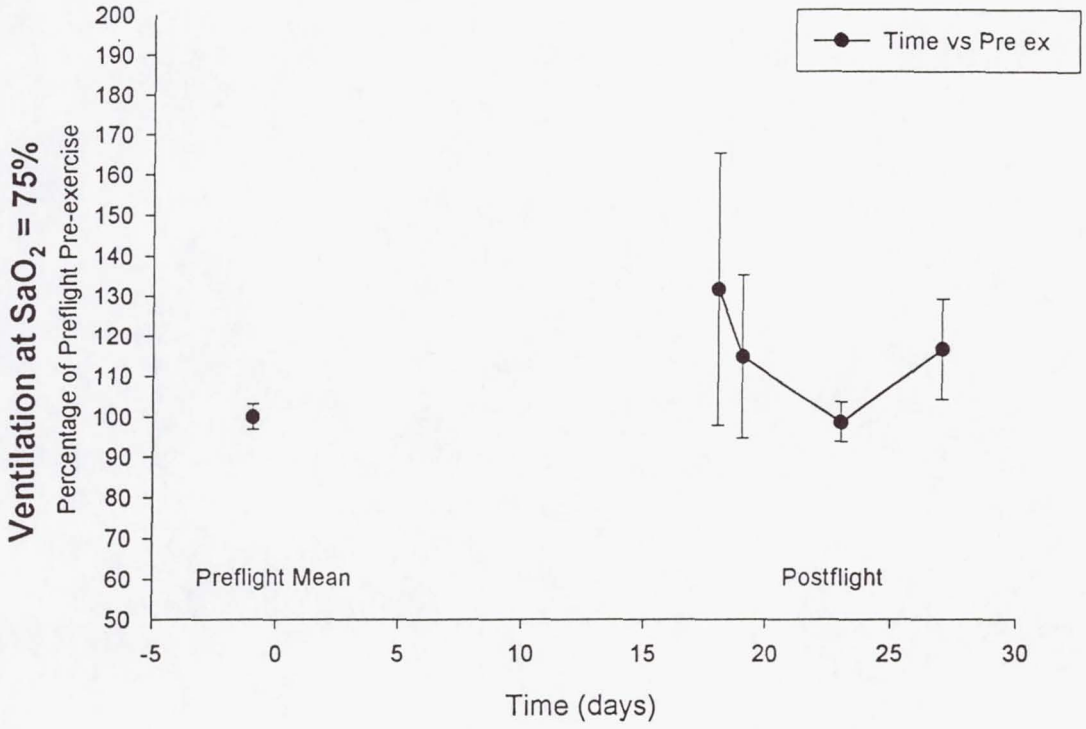
Time vs Pre ex
Ventilation at SaO_2 = 75%
Percentage of Preflight Pre-exercise
200
190
180
170
160
150
140
130
120
110
100
90
80
70
60
50
Preflight Mean
Postflight
-5
0
5
10
15
20
25
30
Time (days)

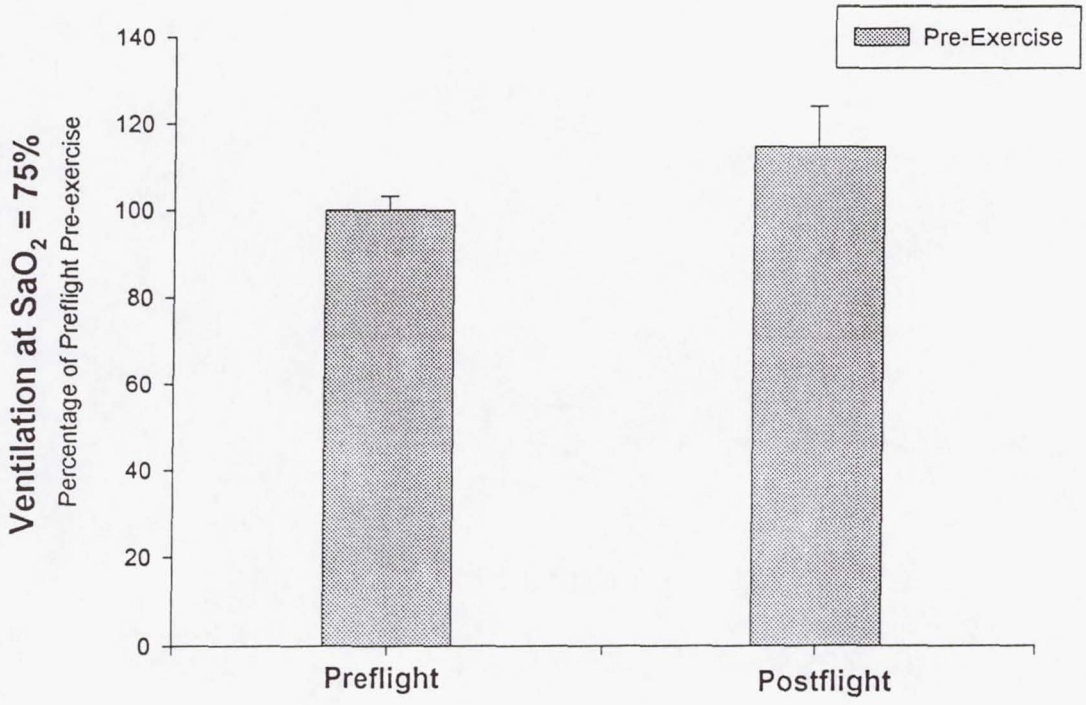
Pre-Exercise
Ventilation at SaO_2 = 75%
Percentage of Preflight Pre-exercise
140
120
100
80
60
40
20
0
Preflight
Postflight

figure 25

JSC Human Life Sciences Project

E074 - Direct Measurement of the Initial Bone Response to Spaceflight in Humans

Principal Investigator:

Dr. Christopher Cann
University of California, San Francisco
San Francisco, California

One Year Symposium Report: LMS E074

Christopher E. Cann, Ph.D.
University of California, San Francisco

Introduction and Objectives

Changes in calcium metabolism during spaceflight are well documented, but the exact mechanism which initiates this process still is not understood. E074, Direct Measurement of the Initial Bone Response to Spaceflight in Humans, was designed to determine which of several physiologic processes could be responsible for the calcium and bone changes seen in flight. While the changes seen in short term flight are of little clinical significance, understanding these processes is key to developing rational countermeasures for skeletal alterations in long term spaceflight, and may also be useful in the evaluation of individual astronaut skeletal responses to microgravity.

The design of E074 was optimized to evaluate the transient adaptive responses of the human calcium and skeletal homeostatic systems to microgravity exposure. Previous investigations on SLS-1 and SLS-2 (E305, Pathophysiology of Mineral Loss in Spaceflight) addressed the specific questions 1) does serum calcium increase in flight, 2) if so is it primary or secondary to an increase in parathyroid hormone, and 3) are there adaptive effects of the system to any hormonal changes which might occur? The results from SLS-1 and SLS-2 suggested that there was a primary increase in serum calcium and compensatory decreases in PTH and later the active vitamin D hormones and intestinal calcium absorption, but technical problems prevented a good answer about the magnitude of this increase and the adaptations to it. The lessons learned from SLS-1 and SLS-2 were, however, incorporated in the planning for the LMS mission and led to a very good final experimental protocol.

The adaptation of calcium metabolism and skeletal homeostasis to a stimulus can occur over several time frames. We addressed all 3 time frames during which we expected to see alterations: immediately on insertion to microgravity (response at the cellular level), 1-5 days into flight (response at the bone tissue level), and weeks to months after flight (response at the bone organ level).

Hypotheses

Hypothesis 1. Exposure to microgravity causes a rapid and sustained release of calcium from the bone, leading to hypercalcemia. The early release of calcium from bone may not be due to an increase in osteoclastic activity or number, but could come from a leak in the membrane separating the "bone fluid compartment" from the blood. Osteoclastic resorption probably also increases, but at a later time.

Hypothesis 2. Exposure to microgravity will cause an increase in the activation frequency for osteoclasts, increasing bone resorption on a time scale of days with sustained hypercalcemia. The calcium homeostatic system will attempt to adapt to this hypercalcemia with a series of hormonal responses, but because the hypercalcemia is primary, these normal adaptive responses will lead to a net decrease in bone balance.

Hypothesis 3. The increase in osteoclast activation and subsequent bone resorption will lead to a transient in bone balance, with resorption remaining elevated weeks or possibly months after flight.

Methods

Hypothesis 1. Serum ionized and total calcium, pH, and parathyroid hormone were measured in blood samples obtained preflight and during the first 4 days inflight. All processing of blood, whether on the ground or inflight, was done with identical procedures to minimize the possibility of artifacts. If the serum ionized calcium is increased and it is a primary increase, the serum PTH should decrease. This is tested by comparing the time course of Ca++ vs PTH early in flight, and by testing to see that the relationship follows that expected for normal individuals. The origin of any increase in serum ionized calcium is identified by using a stable calcium isotope (Ca-48) as a tracer.

Hypothesis 2. Serum calcium, PTH, and vitamin D metabolites, urine deoxypyridinoline (a bone collagen breakdown product) and calcium and tracer calcium were measured as a function of time. An increase in osteoclastic resorption several days into flight due to an increased number of osteoclasts should be evident by an increase in the excretion of deoxypyridinoline and calcium in the urine and a decrease in the ratio of Ca-48 to total calcium in the urine. Serum PTH should be depressed and remain low as long as the calcium-releasing stimulus persists. Later in flight (>8-10 days), 1,25-dihydroxyvitamin D production in the kidney should be depressed as a result of reduced 1-alphahydroxylase activity secondary to PTH suppression.

Hypothesis 3. 24-hour urine calcium and deoxypyridinoline excretion were measured along with serum markers of bone metabolism for 3 months prior to flight until approximately 2 months postflight. If the spaceflight induced an increase in bone resorption which followed a normal bone remodeling cycle, markers of bone resorption and formation would still be elevated 2 months postflight, indicating that the skeleton had not yet readapted to a 1-G steady state.

Results

Hypothesis 1

Figure 1 shows the results of the early response of serum ionized calcium to spaceflight. The first data point on launch day (day 0) is taken before breakfast and represents the last preflight sample. Because sample processing (freezing) could result in some alterations to blood gases, both raw results for Ca++ and those normalized to pH 7.4 are shown. By 3 hours into flight, Ca++ was elevated over baseline values, then decreased back near baseline by day 3. The later rise (days 5-8) can be explained by an increase in bone resorption due to increased numbers of osteoclasts whose proliferation was stimulated by spaceflight.

Figure 2 shows the time course of parathyroid hormone concentration relative to the serum ionized calcium. PTH is reduced in response to elevated serum Ca++ even at the 3 hour time point inflight and shows the expected negative relationship over the first 8 days of flight. This indicates that the calcium homeostatic system is responding normally as expected, as is seen in Figure 3 where there is a close negative correlation between Ca++ and PTH over the preflight, inflight and postflight periods.

Serum Ionized Calcium Preflight
and Early Inflight (n=4, mean +/- sd)

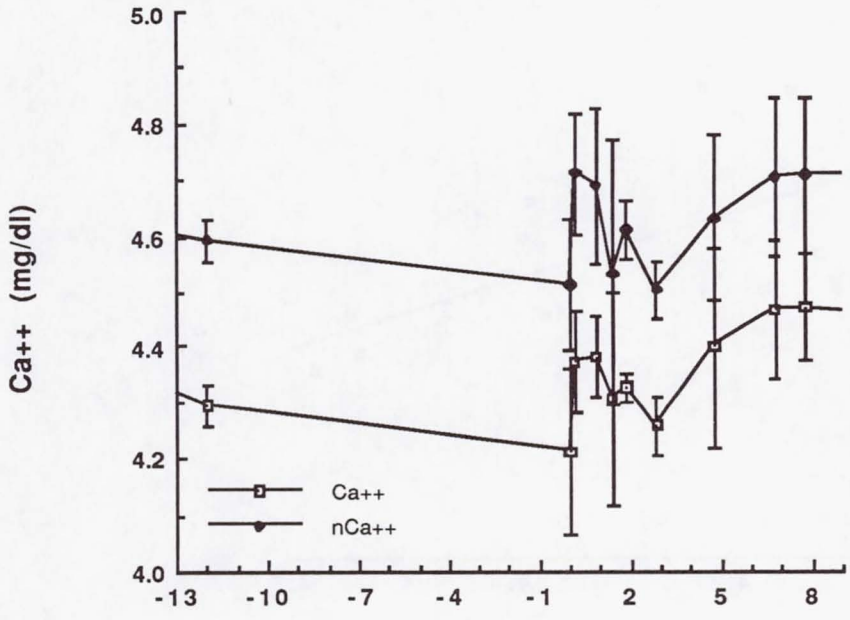

Serum Ionized Calcium and PTH Preflight
and Early Inflight (n=4, mean +/- sd)

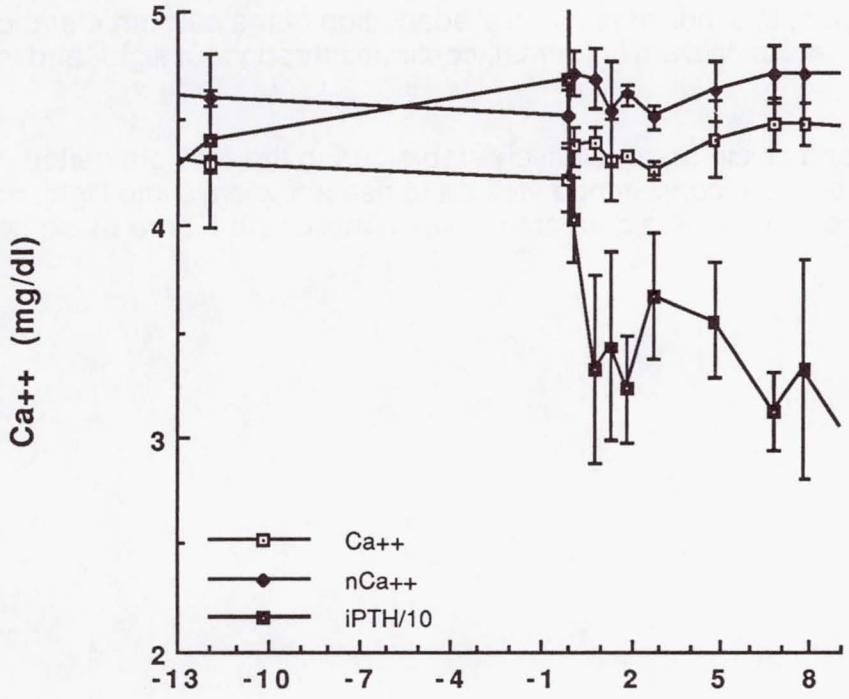

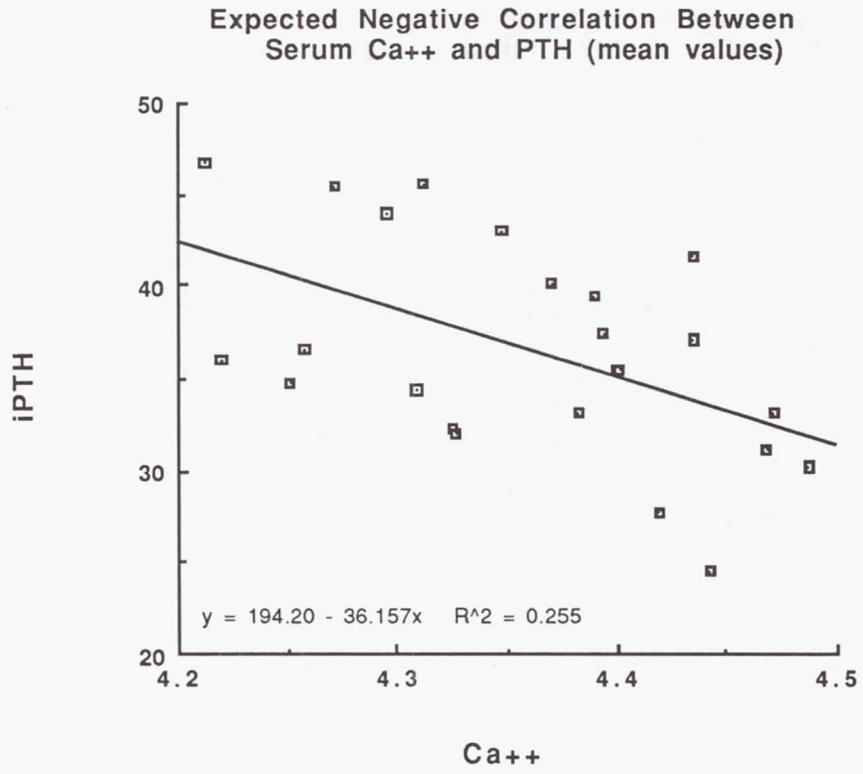

Hypothesis 2

Figure 4 shows the relationship between serum ionized calcium for the flight and early recovery periods, demonstrating the same strong negative relationship as was seen in the early flight period. Again, this indicates that the adaptation of the calcium metabolic system to an increase in serum calcium is normal, continues throughout flight, and is not impaired at recovery.

Urine deoxypyridinoline and calcium are relatively stable during the preflight period while the astronauts are eating a consistent diet, start to rise a few days into flight, and remain elevated after recovery. Limited data are shown in this graph Figure 5), so no error bars are given.

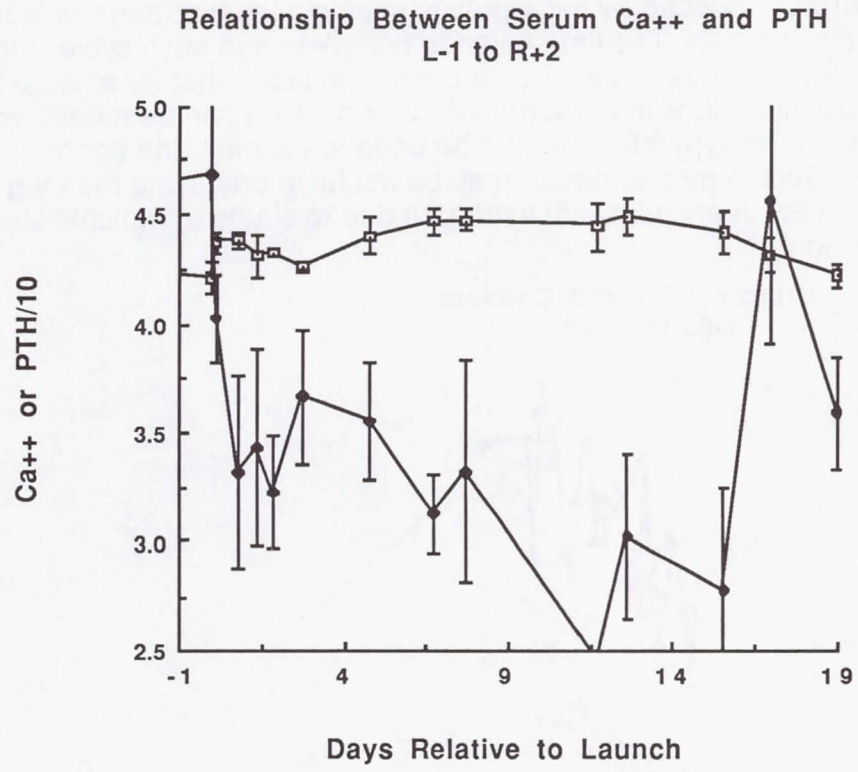

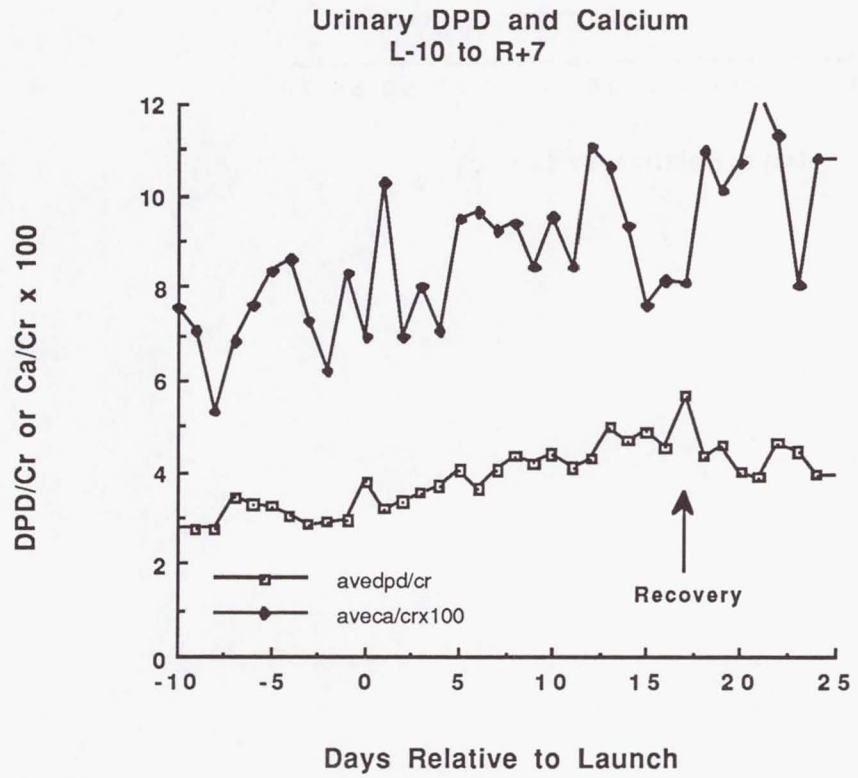

Hypothesis 3

An increase in bone resorption induced by microgravity should persist through at least one bone remodeling cycle in adults. The time taken to complete one such cycle is in the range of 4 months to 2 years in humans. Figure 6 and 7 indicate that for at least 2 months postflight there are alterations in calcium metabolism which can be measured. The quantitative elevation of deoxypyridinoline can be used to estimate the bone resorption rate in mg/day. Such a measurement may be useful in predicting the long term net change in bone mass in an individual astronaut due to single or multiple short term exposures to spaceflight.

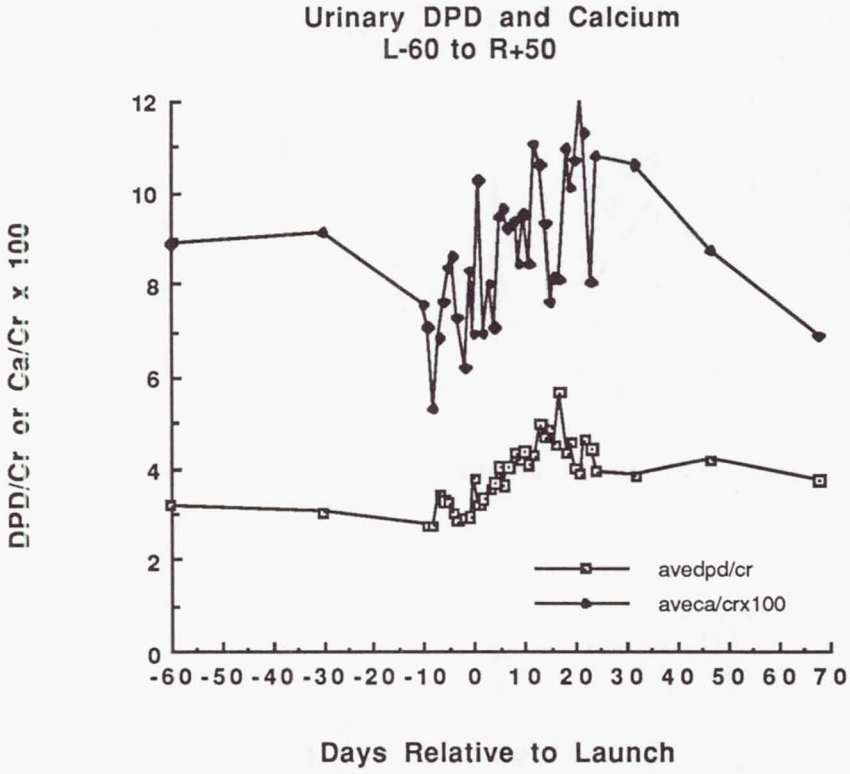

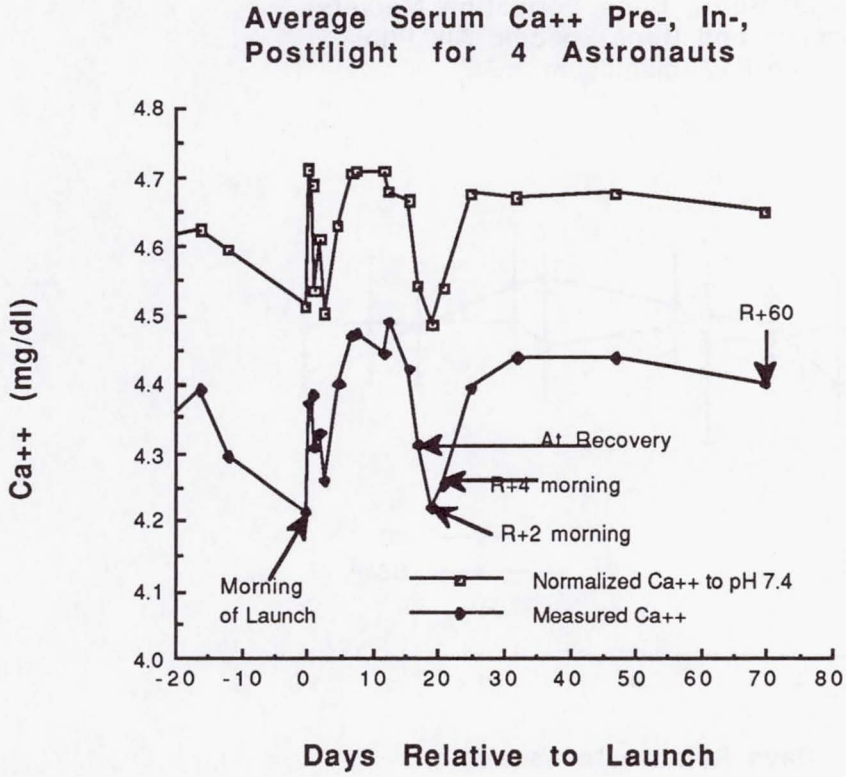

Ancillary Findings

One hypothesis for the decrease in bone following spaceflight has been the possibility that in addition to bone resorption or breakdown being increased, formation of new bone to replace that lost may not occur normally. The basis of this hypothesis comes from animal studies, primarily in rats but with some small amount of data from primates as well, where mineralization of bone is impaired and new osteoblasts are not produced. However, it is also well known that the increased endogenous corticosteroid production from stress will reduce bone formation, so a reduction in formation or indices of formation could be due either to a direct effect on osteoblasts through unloading or mediated by humoral agents.

We measured two markers in the serum which are considered to be specific for bone formation under most circumstances, bone specific alkaline phosphatase and osteocalcin (Figure 8). We found no effect of flight on BSAP. Osteocalcin was reduced for the first few days of flight, then increased back to baseline levels and remained there during flight and the first few days of recovery. This response is more consistent with a cause of stress of flight than of a bone response, although the bone response cannot be ruled out.

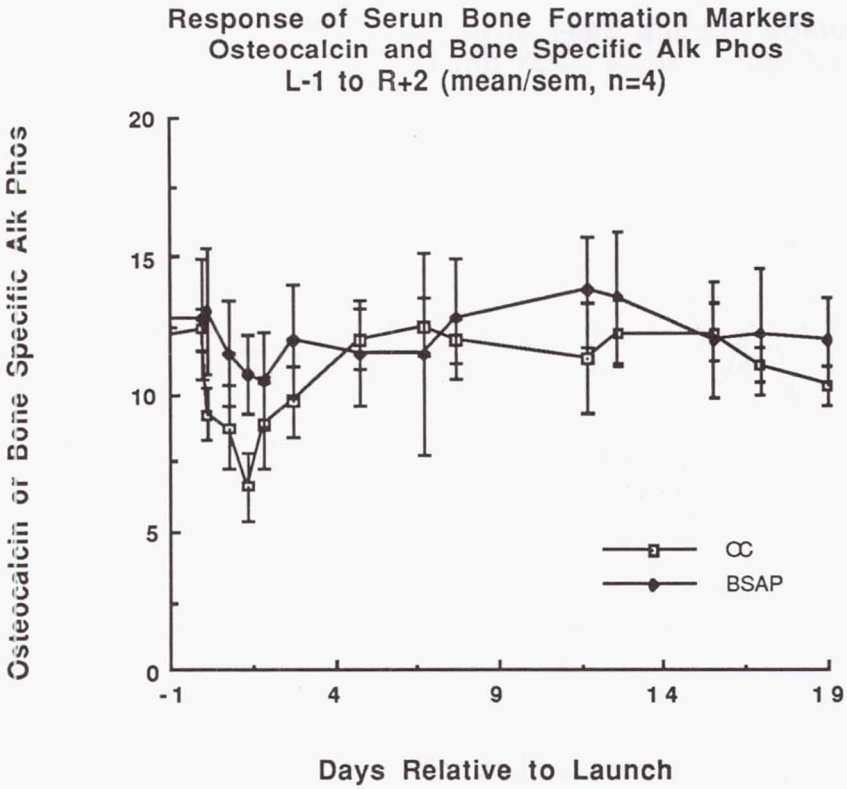

Unexpected Findings

Possible Metabolic Acidosis

Early findings of increased serum ionized calcium and significantly decreased blood pH in samples from SLS-2 led us to investigate the possibility that there were changes in blood acid-base balance which could be contributing to the metabolic changes we saw. Through comprehensive laboratory investigations, we concluded that most if not all ot the increase in blood CO2 that we saw in those samples was an artifact of blood processing (although we have still not identified the source of the increased CO2). Because of this, special care was taken to obtain and process blood samples for LMS with a procedure where any such artifacts would be minimized, using the same hardware, processing time and temperatures expected inflight. Through the diligent efforts of the crew and ground support personnel, we believe that the samples we obtained for LMS are free of artifact.

Figures 9 and 10 show the serum pH and calculated hydrogen ion concentration pre, in and postflight. There is approximately a 10% increase in the blood H+ concentration inflight, which returns toward baseline postflight. This is paralleled by a decrease in urine chloride inflight (Figure 11), which is consistent with the hypothesis that metabolic acidosis exists during spaceflight. This could occur if there is a decrease in peripheral vascular resistance, pooling of capillary blood increasing its residence in the periphery, and increased serum chloride to balance the H+ ions. This is an exciting hypothesis which we hope to explore further.

Response of Serum pH to Flight
L-1 to R+2 (mean/sem, n=4)

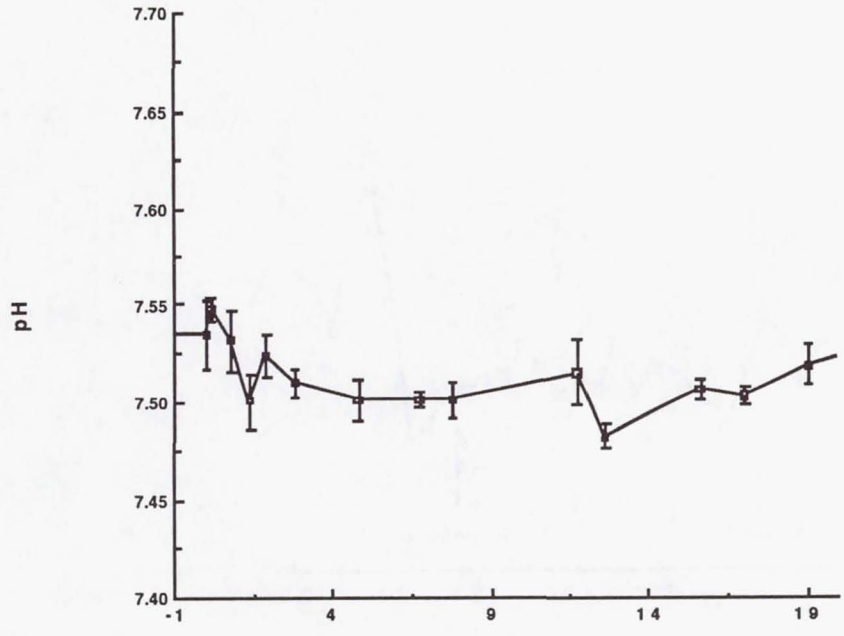

Serum H+ Concentration
Pre, In, and Postflight

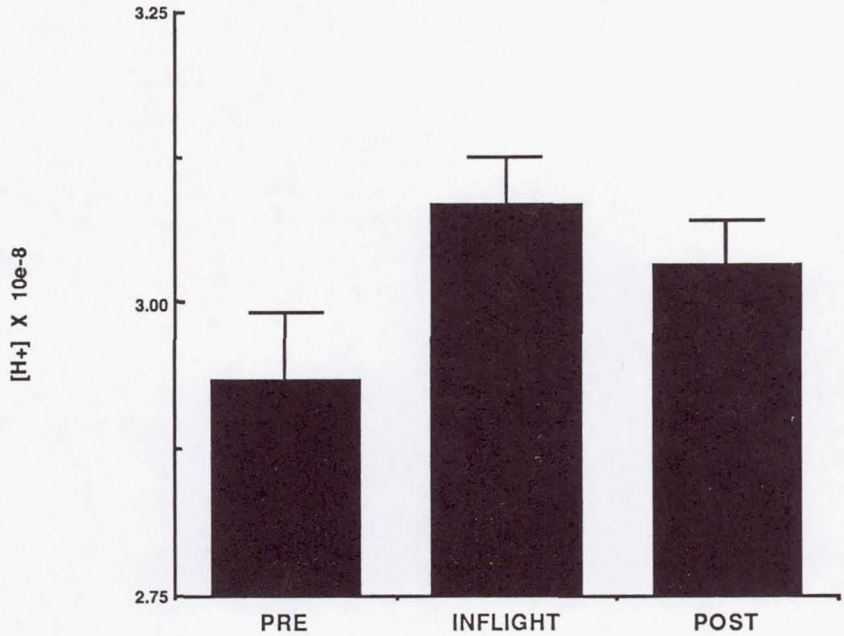

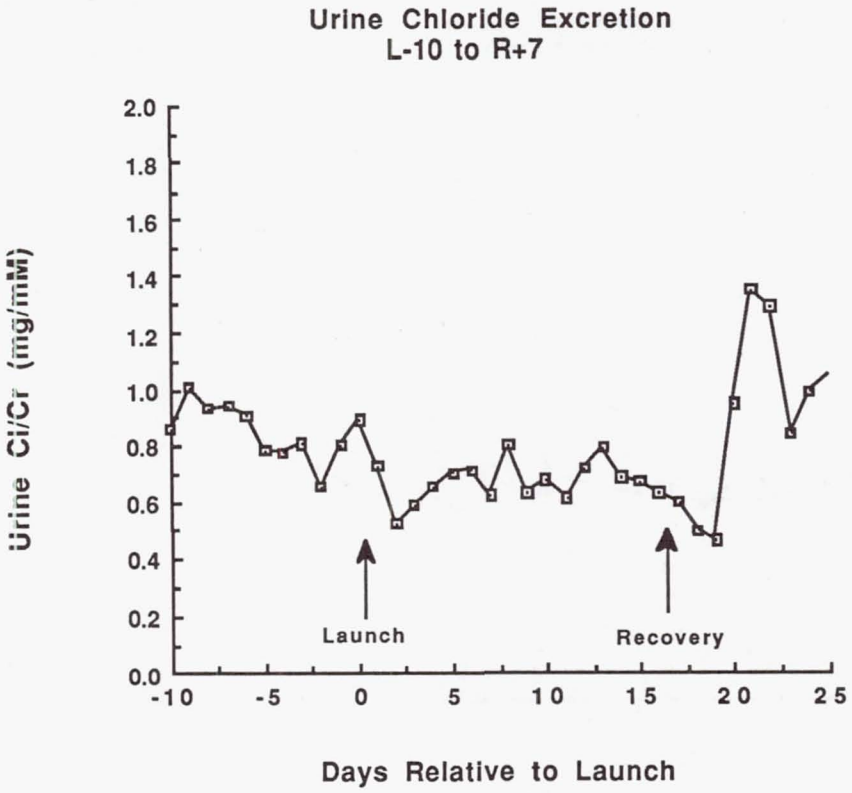
Urine Chloride Excretion
L-10 to R+7
Urine Cl/Cr (mg/mM)
2.0
1.8
1.6
1.4
1.2
1.0
0.8
0.6
0.4
0.2
0.0
-10
-5
0
5
10
15
20
25
Launch
Recovery
Days Relative to Launch

Conclusions and Speculation

Bone resorption increases relatively early in spaceflight (3-5 days). Serum ionized calcium is increased as a result and remains elevated throughout the duration of the flight.

The normal adaptive responses of a decrease in serum PTH as ionized calcium is increased occur.

The effect of a short term exposure to spaceflight is still manifest 2 months postflight with increased bone turnover and possibly elevated serum calcium.

Serum ionized calcium is elevated as early as 2 hours into flight, and PTH is already decreased as an adaptive response. This is too early for an increase in osteoclastic bone resorption due to recruitment of new cells, which occurs as expected by 3-5 days. In addition, urine DPD is not increased early, but occurs on the same expected time scale of 3-5 days. There may be another mechanism for the early increase in serum ionized calcium.

Serum pH is decreased, with a slight (5%) increase in blood H+ concentration as early as 2 hours. Urine pH does not change significantly, but urine chloride excretion is decreased early. These findings are consistent with a slight metabolic acidosis occurring immediately upon exposure to microgravity. However, the serum ionized calcium is increased even when normalized to pH 7.4, so the increase in H+ cannot explain completely the increased Ca++.

Speculation: Decrease in peripheral capillary resistance and pooling of blood in the extremities leads to increased residence time for the blood in the capillary beds. Blood acid content is increased slightly, and may lead to alterations in renal handling of calcium. This should be investigated further to see if the response is sufficient to warrant prophylactic treatment with bicarbonate or other agents.

Bottom Line: Two and a half weeks of spaceflight induces a bone remodeling transient which lasts at least 2 months after return to earth. The increase in bone resorption occurs within 3-5 days as expected, and there is no evidence for a depression of bone formation at this point, except for a transient decrease possibly related to a stress response. Calcium metabolism is altered within 2 hours of launch, possibly due to a slight metabolic acidosis caused by the shift of blood to the peripheral capillary beds, and there may be renal effects in response to this as well.

JSC Human Life Sciences Project

E401 - The Effects of Microgravity on Skeletal Muscle Contractile Properties

Principal Investigator:

Dr. Paolo Cerretelli
Université de Genève
Geneva, Switzerland

The Effects of Microgravity on Skeletal Muscle Contractile Properties

Investigation E401

Final report

Principal Investigator: Paolo Cerretelli, M.D., Ph.D., Dept. de Physiologie, Centre Médical Universitaire, Université de Genève, Switzerland

Co-Investigators: Marco Narici, Ph.D, Consiglio Nazionale delle Ricerche, I.T.B.A., Reparto Fisiologia, Milan, Italy

Bengt Kayser M.D., Ph.D., Dept. de Physiologie, Centre Médical Universitaire, Université de Genève, Switzerland

P Cerretelli

Prof. Paolo Cerretelli
E401-Principal Investigator

Date: July 21st, 1997

CMU Ref: E401-PEMS PF02

The Effects of Microgravity on Skeletal Muscle Contractile Properties Experiment E401 STS-78

Final Report

I. Introduction

Exposure of humans and lower mammals to either actual or simulated spaceflight has been shown to lead to muscle wasting and weakness (Berg et al. 1991, Dudley et al. 1989, Hather et al. 1992, LeBlanc et al. 1988, Thomason and Booth, 1990). By and large, the data on lower mammals and humans indicate that postural muscles are less resistant to atrophy than non-postural muscles, (c.f. Thomason and Booth, 1990). The functional implications of atrophy may be evaluated by studying changes in skeletal muscle contractile features. Muscle function of humans exposed to spaceflight had so far been assessed through strength measurements performed under conditions of voluntary activation by the nervous system. Changes in voluntary contraction force may therefore arise from either muscular or neural factors or both. On the contrary, by stimulating the muscle directly it is possible to measure force beyond the volitional control of the subject and assess aspects of muscle contractility, which cannot possibly be determined from voluntary contractions. The use of this technique thus provides an objective measure of the functional status of skeletal muscle since contractions are at a precise level of activation. These contractile parameters, as studied by means of percutaneous muscle stimulation, have been shown to be fibre type-specific, resulting in changes of twitch characteristics, loss of force at specific frequencies of stimulation and changes in fatigabilty (Russel *et al.* 1983; Lopes *et al.* 1982, Russel *et al.* 1984; Church *et al.* 1984, Davies et al. 1987). Percutaneous muscle stimulation has previously been used to investigate the changes in human muscle contractile properties induced by bedrest deconditioning (Davies et al. 1987, Cerretelli et al. 1996), but never by spaceflight. This investigation was therefore set out to evaluate changes in muscle function of the human triceps surae induced by spaceflight, by-passing neural control, through direct muscle electrical stimulation.

A. Hypothesis

The hypothesis of the present study was that muscle atrophy induced by spaceflight would alter the contractile features of the human plantar flexors. Spaceflight was expected to lead to a decrease in electrically elicited contraction force as well as in muscle size. Given the difference in fibre composition of the soleus and gastrocnemius (88% type I for the SOL and 48% for the GAS, 16) it was expected that a greater atrophy of the soleus, apparently being more vulnerable to atrophy than the gastrocnemius (Thomason

and Booth, 1990), would lead to: i) faster contraction and relaxation times, ii) tetanization at higher stimulation frequencies, iii) and an increase in fatiguability. If instead, both the soleus and gastrocnemius atrophied to the same extent, no change in twitch characteristics, a non frequency-dependent loss of torque, and no change in fatiguability would be expected.

In addition, the comparison of the results of the voluntary versus the electrically induced torque would allow assessing changes in voluntary drive induced by spaceflight.

B. Objectives of the experiment

The aim of experiment E401 was to assess the changes in the electrically evoked isometric contractions of the human triceps surae (TS) during 17-day spaceflight.

Specifically, this study was set out to determine if spaceflight modified:

1. The relation between stimulus intensity and maximum twitch-torque
2. The relation between the TS twitch-torque and ankle joint angle
3. The maximum voluntary strength of the TS as well as the ability to voluntarily activate all TS motor units
4. The relationship between the frequency of stimulation and torque
5. The resistance to fatigue during repeated electrically evoked contractions
6. The force per cross-sectional area of the TS muscle group (evaluated in collaboration with experiment E029).

II. Methods of data acquisition and analysis

The contractile characteristics of the triceps surae were investigated during both voluntary and electrically-evoked isometric contractions using the percutaneous electrical muscle stimulator (PEMS, ESA instrument, developed by C.I.R., Switzerland) and recording the torque generated with the torque-velocity dynamometer (TVD, ESA instrument, developed by E.T.H., Zurich, Switzerland). In each testing session five PEMS protocols were performed according to the following order:

1. Supramaximal Current Intensity (SMCI) determination. The TS was stimulated with 50 μs pulses at an ankle angle of 15 degrees dorsiflexion, increasing the stimulation intensity from an initial 100 mA up to a maximum of 800 mA (in 50 mA steps), and monitoring the twitch torque developed with the TVD, until no further increase in torque was observed.

2. Angle-torque relationship (ATR). Twitches were measured at 7 different angles of the ankle joint (30, 25, 15, 5 degrees plantar flexion (PF), and 5, 15, and 20 degrees

dorsi flexion (DF) (degrees relative to the TVD foot plate), two twitches per angle, 5 seconds apart.

3. Maximum voluntary contraction (MVC) with super-imposed twitches. Three isometric MVCs (at 20 degrees DF), each lasting 4 seconds and interspaced by 20 seconds were performed. During each contraction, the degree of muscle activation was assessed using the twitch super-imposition technique (Merton 1954). This consists of single stimuli (two) at SMCI, in response to which, if the contraction is submaximal, an increase in force on top of the voluntarily contraction is obtained. It thus allows to identify submaximal central neural drive during MVC.

4. Frequency-torque relationship (FTR). This was obtained by stimulating the muscle at varying frequencies. Three twitches (5 seconds between each twitch) were given followed by consecutive trains of pulses, each 1 second in duration at 10, 20, 30, and 50 Hz. This was performed with a current intensity of 60% SMCI. This lower SMCI had to be used to minimize the subject discomfort at the higher frequencies. The stimulation intensity of 60% of SMCI, referred to the muscle twitch. At 50 Hz, because of temporal summation, the torque generated was about 85% of that produced at the same frequency using 100% SMCI. Furthermore, previous tests conducted in the author's laboratory, showed that the shape of the FTR curve obtained at 60% SMCI matches that obtained at 100% SMCI. This showed that the portion of the muscle reached by the stimulation is maximally activated and behaves as the whole muscle. So, 60% SMCI were regarded as a good compromise between subject's tolerance to the test and scientific outcome.

5. Fatigue test. During this protocol the fatigability of the TS was tested during 120 s stimulation at 60% SMCI using trains of stimuli at 20 Hz lasting 350 ms repeated once per second. From this test a fatigue index (F.I.) was calculated as the ratio between the torque of the last (120th) over that of the 1st contraction.

6. Calf muscle plus bone CSA (CSAm+b). CSAm+b was determined anthropometrically from circumference (measured at the site of maximum circumference obtained before the flight) after subtraction of subcutaneous fat by conversion of lateral and medial calf skinfolds into adipose tissue thickness using the equations of Jones *et al.* (1986).

Experimental schedule

Before the flight, PEMS protocols 1 to 5 were on L-90 (actual L-87,-86, -85, -84, -83), L-60 (actual L-50, and L-45), L-30 (actual L-31 and L-30). On L-15 (actual L-12)

protocols 1 to 5 were also repeated.
Calf CSAm+b was measured on all subjects on L-30 (L-31 and L-30)

During the flight (FD1=20 June '96) PEMS protocols 1 to 5 were performed on FD3/4, FD8/9, FD13/14 and FD16.

During the recovery period PEMS protocols 1 to 5 were carried out on R+2 (actual R+2), R+4 (actual R+4), R+8 (actual R+8), R+15 (actual R+15), R+30 (actual R+30).
Calf CSAm+b was measured on R+2, R+8, R+15 and R+30

III. Results

Twitch angle-torque relationship (ATR)

During the flight, no significant changes in ATR relation were observed. However, during recovery, significant decreases in twitch peak torque (PTw) at joint angles comprised between 20 deg of dorsiflexion (DF) and 5 deg of plantar flexion (PF) were found on days R+4, R+8, R+15 and R+30 (Fig. 1a). The largest decreases occurred on R+8 at which PTw was reduced by about 20% ($p<0.01$-0.05), irrespective of joint angle, across angles from 20 deg DF to 5 deg PF (Fig. 1b). No significant changes in PTw were present beyond 5 deg PF.

Twitch characteristics

Time to peak tension showed no significant changes during spaceflight and recovery. Half-relaxation time (1/2RT) significantly decreased during the flight (-18% on FD8 and -8% on FD16), and on recovery day R+2 (-7%); thereafter, 1/2RT values were not different from pre-flight.

Frequency torque relation

No changes in FTR were found during the flight, while a progressive downward-shift in the ATR curves occurred during recovery. For all stimulation frequencies (1, 10, 20, 30 and 50 Hz) the nadir of the decrease in peak torque (PT) was reached on R+8 and was on average 24.0% (<0.01, Fig. 2a). On R+15, PT values from 1 to 50 Hz were still below (-13%, $P<0.05$) those obtained before the flight. The loss of PT was not frequency dependent since no significant differences were found between the percent PT loss at each frequency. This effect was clearly shown by normalizing torques at all frequencies for those developed at 50 Hz, as a result of which all FTR curves matched with that obtained before the flight (Fig. 2b).

Maximum voluntary contraction and tetanic torque

No change in MVC was found during the flight, but a progressive increase up to 17% ($P<0.01$) was observed throughout recovery (Fig. 3). The increase in MVC was accompanied by an increased capability, in all crewmembers, in twitch-occlusion, showing an improved ability in motor unit recruitment.
By contrast, the tetanic torque at 50 Hz (PT50) showed a significant decrease throughout recovery, reaching its nadir (-22%, $P<0.01$) on R+8 (Fig. 3).

CSAm+b and Torque/CSAm+b

Calf CSAm+b was significantly reduced (-7%, $P<0.01$) after the flight on days R+2 and R+4. Thereafter, a progressive recovery was observed and on R+30 CSAm+b was back to its pre-flight values.
A significant decrease (-19%, $P<0.01$) in tetanic torque at 50Hz normalized for calf CSAm+b (PT50/CSAm+b) was found during recovery on R+8.

Fatigability

A significant increase in the fatigability (decrease in F.I.) was found during recovery on days R+8, R+15 and R+30. This increase in fatigability, showing a nadir on R+15 (16%, $P<0.01$, Fig. 4), was due to a greater decrease in the torque values at the end than that at the beginning of the fatigue test.

IV. Conclusions

The present results on electrically evoked human gastrocnemius muscle function assessed during the NASA-LMS mission (Shuttle flight STS-78), show a significant impairment in contractile parameters during recovery, but not during spaceflight. The observed decrease in muscle tetanic torque (24%) was greater than the decrease in calf CSAm+b (7%) as shown by a significant decrease in tetanic torque/CSA. The latter finding is in agreement with a reported decrease in soleus fibres specific tension observed by Widrick et al. (1996) in the same study and may indicate the presence of muscle damage during the re-loading phase in 1-G. Fatigability of the triceps surae was found to increase by 16% after the flight. This seems partly explained by the decrease in half-relaxation time, but could also be due to muscle damage. It seems noteworthy that also for in the quadriceps, of the same crewmembers, Tesch and Berg (1996) also found fatigability to be increased. The paradoxical increase in MVC during recovery is likely explained by a submaximal neural activation at the beginning of the study, however, other neural factors such as antagonist muscles activation or a training effect may be involved too.

V. Bibliography

Berg, H.E., G.A. Dudley, T. Häggmark, H. Ohlsén, and P.A. Tesch. Effect of lower limb unloading on skeletal muscle mass and function in humans. *J. Appl. Physiol.* 70: 1882-1885, 1991.

Cerretelli, P., Narici, M., Kayser, B., and Barattini P. (1996) Effects of bedrest deconditioning on human calf muscle contractile properties. In: Life and Microgravity Sciences Spacelab mission: Human Research Pilot Study. NASA Technical Memorandum 110395, pp. 16-20.

Church, J.M., S.Y.Choong and G.L.Hill. Abnormalities of muscle metabolism and histology in malnourished patients awaiting surgery: effects of a course of intravenous nutrition. Brit. J. Surg. 79: 563-569, 1984.

Davies, C.T.M., Rutherford, I.C., and Thomas, D.O. (1987). Electrically evoked contractions of the triceps surae during and following 21 days of voluntary leg immobilization. Eur J Appl Physiol 56:306-312.

Dudley, G.A., M.R. Duvoisin, V.A. Convertino, and P. Buchanan. Alterations of the in vivo torque-velocity relationship of human skeletal muscle following 30 days exposure to simulated microgravity. *Aviat. Space Environ. Med.* 60: 659-663, 1989.

Edgerton V.R., Zhou M.-Y, Ohira Y., Klitgaard, H., Jiang, B., Bell, G., Harris, B., Saltin, B., Gollnick, PD., Roy, R.R., Day, M.K., & Greenisen (1995). Human fibre size and enzymatic properties after 5 and 11 days of spaceflight. J Appl. Physiol. 78:1733-1739.

Hather, B.M., G.R. Adams, P.A. Tesch, G.A. Dudley. Skeletal muscle responses to lower limb suspension in humans *J. Appl. Physiol.* 72: 1493-1498, 1992.

Jones, P.R.M., P.S.W. Davies, and N.G. Norgan. Ultrasonic measurements of subcutaneous adipose tissue thickness in man. *Am. J. Phys. Anthrop.* 71: 359-363, 1986.

LeBlanc, A.D., P. Gogia, V.S. Schneider, H.J. Evans, C. Pientok, R. Rowe, and E. Spector. Calf muscle area and strength changes after five weeks of horizontal bed rest. *Am. J. Sports Med.* 16: 624-629, 1988.

Lopes MD, Russell DR, Whitwell J, Jeejeebhoy KN. Skeletal muscle function in malnutrition. Am. J. Clin. Nutr. 36: 602-610, 1982.

Merton PA. Voluntary strength and fatigue. J. Physiol. (London) 123: 553-564, 1954.

Russell DR, Leiter LA, Whitwell J, Marliss EB, Jeejeebhoy KN. Skeletal muscle function during hypocaloric diets and fasting: a comparison with standard nutritional parameters. Am. J. Clin. Nutr. 37: 133-138, 1983.

Russell DR, Walker PM, Leiter LA, Sima AAF, Tanner WK, Mickle DAG, Whitwell J, Marliss EB, Jeejeebhoy KN. Metabolic and structural changes in skeletal muscle during hypocaloric dieting. Am. J. Clin. Nutr. 39: 503-513, 1984.

Thomason, DB, and Booth. Atrophy of soleus muscle by hindlimb unweighting. J.Appl. Physiol. 68: 1-12,1990.

Fig 1. *a*) Angle torque relation before and after spaceflight (during not shown because n.s.), (*b*) Percent decrease in torque on R+8 (mean±SE, **=P<0.01)

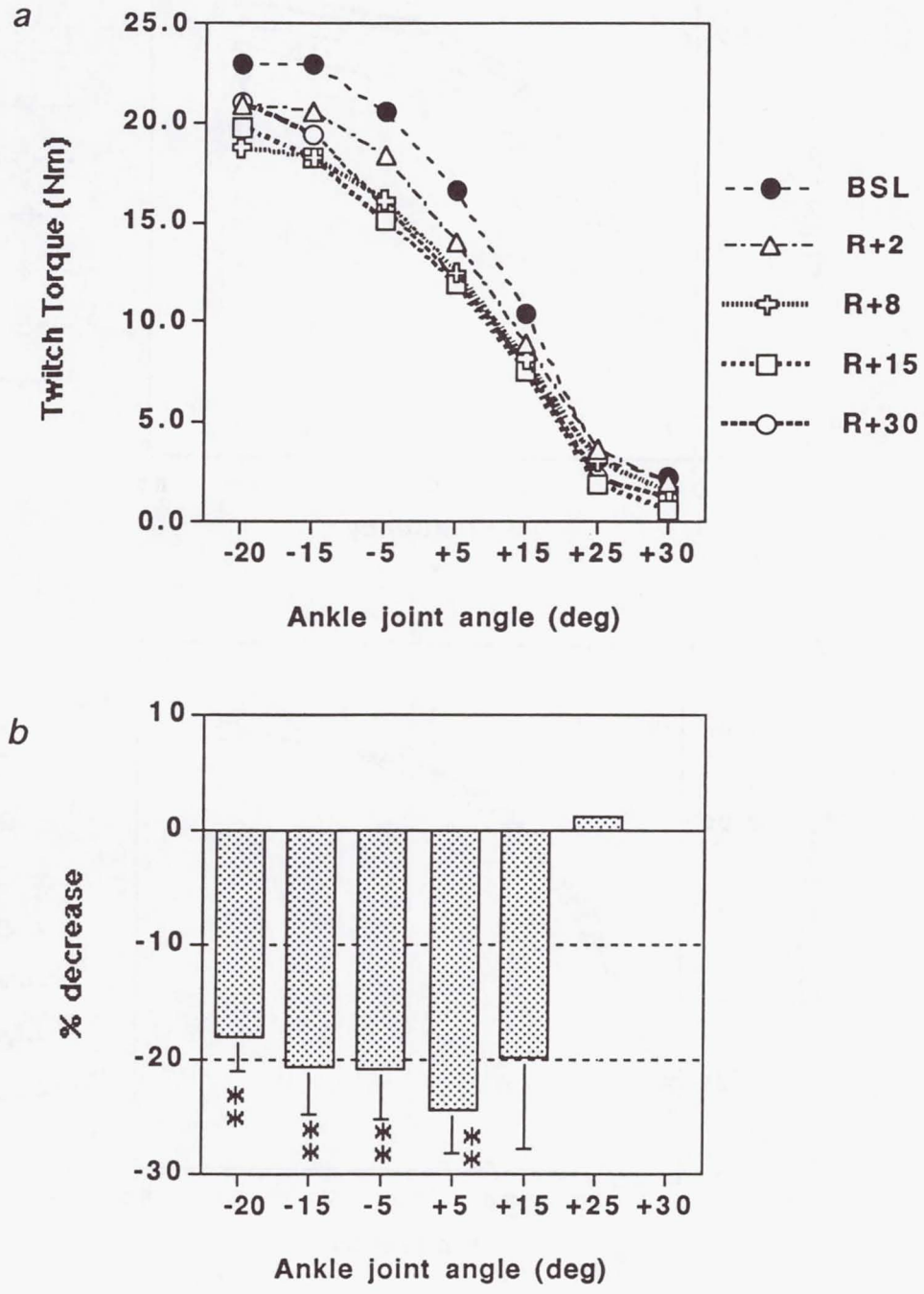

Fig. 2. Frequency-Torque relation in absolute values (*a*), and normalized for the torque at 50 Hz (*b*), before, during and after spaceflight. (*=P<0.01)

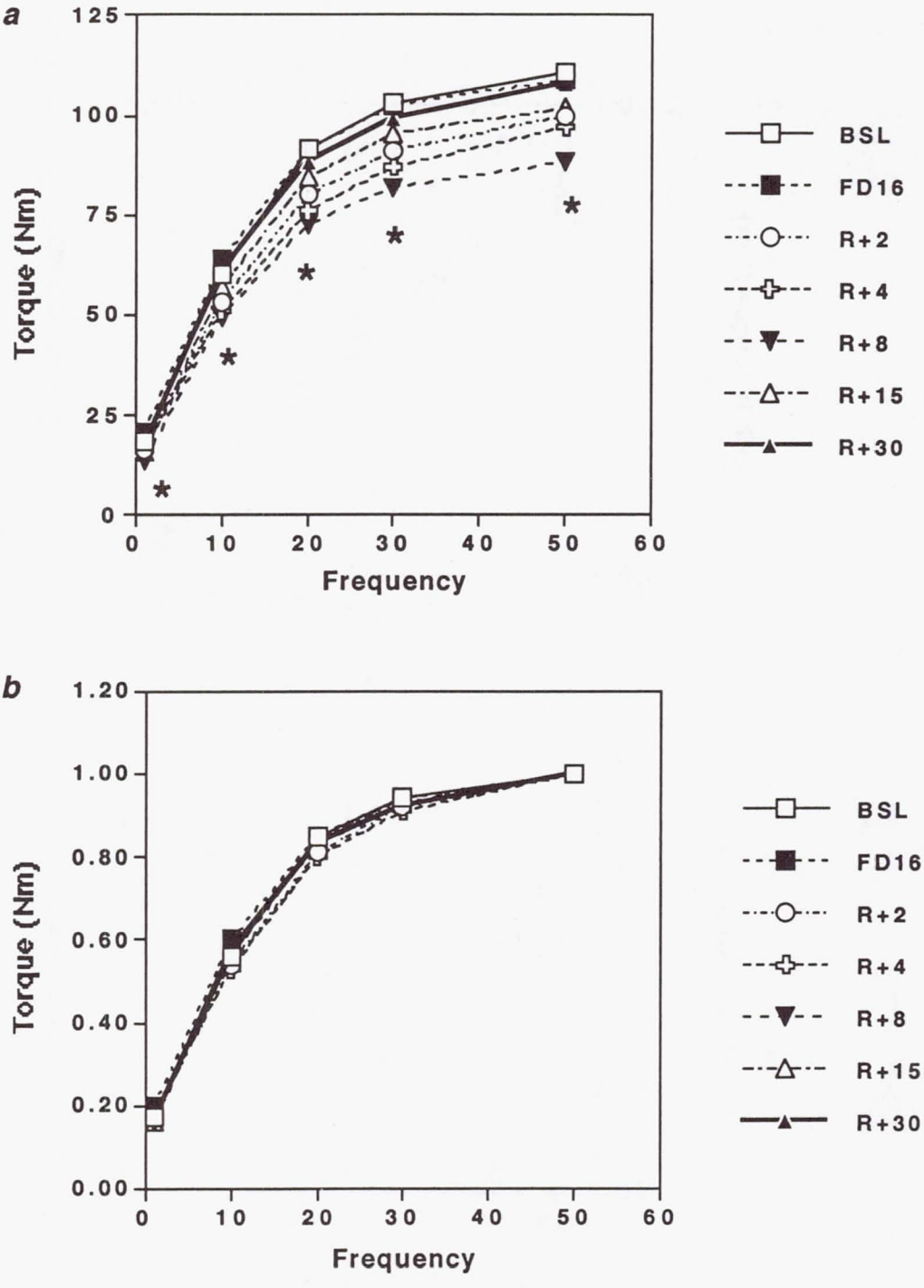

Fig. 3: Maximum voluntary contraction (MVC) and tetanic torque at 50 Hz (T50), before, during and after spaceflight (means±SE)

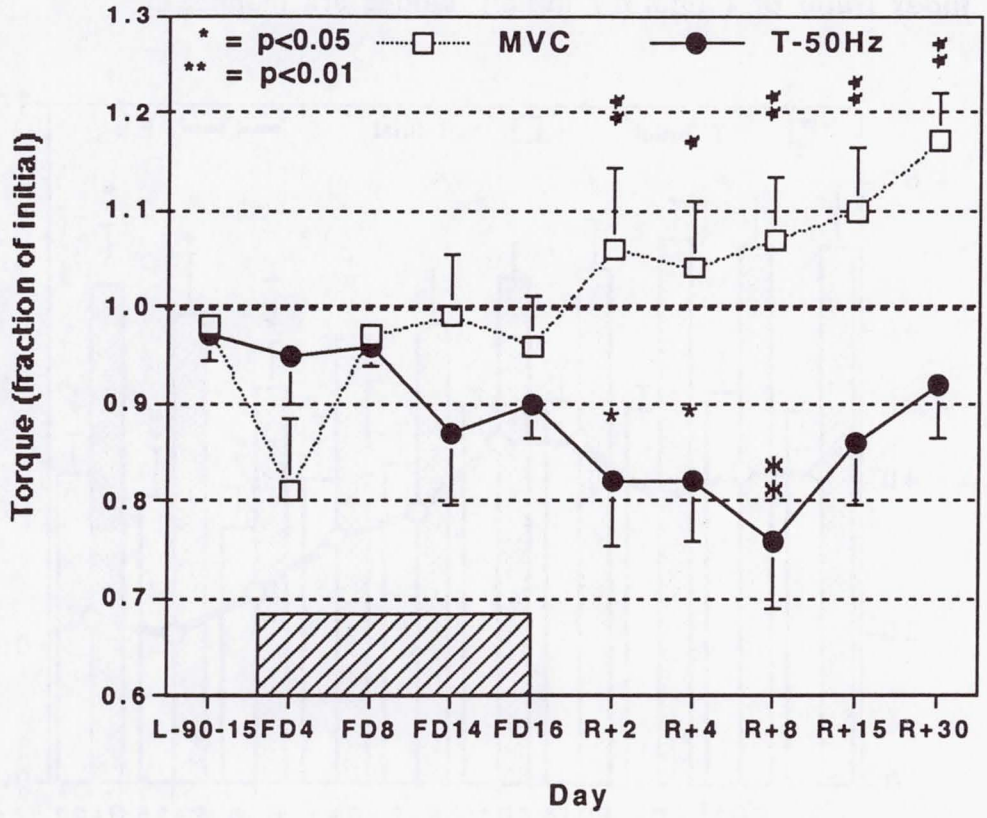

Fig. 4: Triceps surae fatigability before, during and after spaceflight. T initial and T final is the torque produced by the first and last contractions in the fatigue test; F.I. is the fatigue index (ratio of T final / T initial). Values are mean±SE.

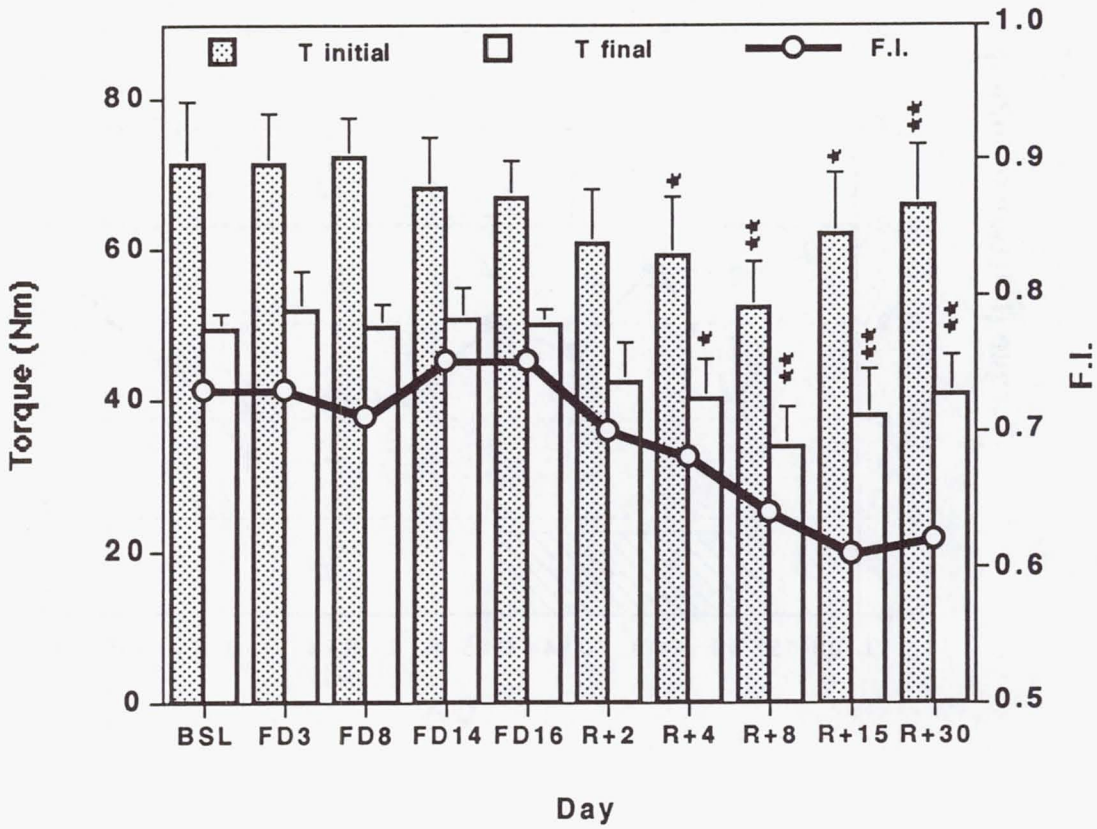

JSC Human Life Sciences Project

E407 - Effects of Microgravity on the Biochemical and Bioenergetic Characteristics of Human Skeletal Muscle

Principal Investigator:

Dr. Pietro di Prampero
Università degli Studi di Udine
Udine, Italy

E 407: Final Report

Effects of Microgravity on the Biomechanical and Bioenergetic Characteristics of Human Skeletal Muscle

Carlo Capelli[1], J. Denoth[2], S. Milesi[1], E. Stüssi[2] and P. E. di Prampero[1].

[1] Dipartimento di Scienze e Tecnologie Biomediche, Università degli Studi di Udine, Via Gervasutta 48, I-33100 UDINE (Italy)

[2] Biomechanics Laboratory, ETH, Wagistraße 4, CH-8952 SCHLIEREN (Switzerland)

Principal Investigator: Dr. Pietro Enrico di Prampero

✉ Dipartimento di Scienze e Tecnologie Biomediche, Università degli Studi di Udine, Via Gervasutta 48, I-33100 UDINE (Italy);
Tel: +39 432 520188;
Fax: +39 432 600828
fisioud@dstb.uniud.it

Theoretical Backgrounds

Long term space flights are known to affect muscle structure and function, essentially because of the absence of the constant pull of gravity. However, the extent and the ultimate reasons thereof are only partially understood. Therefore, investigations concerning the muscular activity as a function of the time spent in microgravity are of great interest from both the theoretical and practical points of view. Indeed, on the one hand they will allow us to gain a deeper understanding of the basic aspects of muscle contraction. On the other, they will provide useful suggestions on how to improve the countermeasures for preventing microgravity deconditioning.

Skeletal muscle transforms chemical energy into mechanical energy. This takes place during muscle contraction which is normally triggered by voluntarily induced nerve stimulation. Muscle contractions can be subdivided into three general categories: i) isometric, wherein the muscle is not permitted to shorten, so that the result of the contraction is the generation of force only, ii) concentric, wherein the force applied to the muscle is lower than the maximal the muscle is able to produce; as a consequence the muscle shortens, thus performing external mechanical work (force times distance shortened), iii) eccentric, wherein the force applied to the muscle is greater than the maximal; the muscle is therefore forcibly lengthened, thus absorbing mechanical work.

The maximal force the muscle can produce under isometric conditions depends on its length; it attains a peak at a length approximately equal to the "physiological" length of the muscle in vivo; it is less at greater or smaller lengths.

The speed at which a muscle shortens is a function of the force imposed on the muscle. For concentric contractions, the force velocity relationship is hyperbolic, the velocity increasing from zero (when the force is equal to the maximal isometric) to a maximum when the force is zero (unloaded contraction). For eccentric contractions, the velocity of shortening is negative (the muscle becomes

longer); it increases (becomes more negative) only slightly for forces not much larger than the isometric; for greater forces the increase in speed becomes much larger.

As a first approximation, skeletal muscles can be viewed as being constituted by the contractile machinery and by an elastic system in series transmitting the force generated by the machine to the appropriate lever arms, thus smoothing and damping the responses of the system.

The mechanical events of the contraction are elicited and preceded by electric signals which can be recorded by appropriately positioned electrodes applied to the skin. These electric signals, defined Electromyogram (EMG) yield information concerning the activity of the different motor units.

Phenomenologically, muscle function is completely characterised when the following basic aspects are known:

i. force length characteristics of the contractile component;
ii. force length characteristics of the series elastic component;
iii. force velocity characteristics of the contractile component;
iv. activation pattern of the motor units

Present knowledge of the biomechanics of isolated muscles is rather satisfactory (e.g. see Carlson and Wilkie, 1974; Woledge, Curtin, and Homsher, 1985). However, our understanding of the functional characteristics of human muscles in vivo is less complete. In addition, long term space flights are known to affect muscle structure and function (Nicogossian, 1989; Grigoriev and Egorov, 1991), to an extent and in a manner, as yet only partially understood. Therefore, investigations concerning the biomechanics of human muscle function on Earth and in microgravity are of great interest from both the theoretical and practical points of view.

Moreover, previous experience accumulated by this group of researchers (Antonutto et al., 1995) demonstrated that the maximal explosive power of the lower limbs, i.e. the maximal power developed during a very sort (0.25 - 0.30 s) all-out effort of the lower limbs, such as a maximal standing high jump off both feet, was substantially reduced after space flight. Indeed, on the occasion of the Euromir 94 and Euromir 95 missions it was observed that the maximal explosive power was reduced to about 70 % of the preflight value after one month in microgravity (one subject) and to about 50 % after six months (three subjects). Indirect but convincing arguments suggest that a large fraction of this decrease is due to a modification of muscle control and co-ordination in space, tending to favour smooth and slow motor patterns, as opposed to forceful, explosive ones.

The results of the present study will allow us to gain a deeper understanding of the effects of microgravity on muscle function per se. It will therefore become possible to better disentangle the extent to which the decline of the explosive power after space fight is due to changes of motor control and co-ordination and to changes of muscle activity per se.

Objectives of Experiment

The fundamental questions are:

i. the force length characteristics of the contractile component;
ii. the force length characteristics of the series elastic component;
iii. the force velocity characteristics of the contractile component;
iv. the motor units activation pattern

of the biceps and triceps brachii and of the triceps surae of four crew members before, during, and after the space flight. In a first step these fundamental characteristics are described by:

i. the isometric torque - angle relationship;

ii. iEMG - isometric torque relationship;

iii. torque - angular velocity;

iv. iEMG - isokinetic torque relationship.

Methods, Experimental Protocol and Data Analysis

Subjects. The experiments were performed on four male astronauts (43 ± 2 yr; 183 ± 4 cm; 86 ± 3 kg) who participated in the LMS -STS 78 mission which took place from June 20th 1996 to July 7th 1996. The subjects were tested four times before the flight to obtain base line data and three times during the flight. After the flight, measurements were taken on four occasions (see Figure 1).

Torque. Muscular torque, as given by the product of the force generated by the muscles times the lever arm, was assessed by means of the Torque Velocity Dynamometer (TVD) constructed in the Laboratory of Biomechanics of the Swiss Federal Institute of Technology (Zurich, Switzerland). The TVD allows one to measure the angular velocity, the angular position and the torque during predefined types of contractions of the flexors and extensors of the elbow and of the ankle. The following contraction types have been studied: i) isometric, wherein the position of the joint was fixed and the torque measured, and ii) isovelocity, wherein the angular velocity was imposed and the torque measured; iii) the same as under ii), but during eccentric contractions, i.e. where the force exceeded the maximal isometric and the muscle was forcibly lengthened. Since the axis of rotation of the TVD was aligned with that of the ankle or of the elbow and since the activity of all accessory agonist and antagonist muscle groups was essentially negligible, the conclusions derived from the experiments apply to the tested muscle groups only, and define the characteristics thereof.

EMG. Surface myoelectric activity (EMG) of the *biceps brachii, triceps brachii, gastrocnemius lateralis, soleus* and *tibialis anterior* were recorded during the experiments placing silver - silver chloride electrodes on predefined positions (Zipp, 1982). The day before launch the locations contours were marked on the skin with a permanent ink pen and, to maintain consistent placements of the electrodes during the experiments performed in flight, the subjects were asked to refresh these contours daily.

EMG signals were fed to a physiological signal conditioner (PSC, NASA). Together with Torque and angular position (α) signals, they were then converted by means of an A/D converter (500/1000 Hz) (National Instruments, USA) interfaced to a portable computer (Think Pad, IBM, USA) and operating at a sampling frequency of 500 Hz (for angular position, velocity and torque) and of 1000 Hz (for EMG signal). During experiments on flight, data were recorded on optical disk and, in parallel, on a tape running on a portable tape recorder (HR 30, TEAC). When possible, they were also down linked to the Space Monitoring Area at the L. Johnson Space Centre in Houston to allow investigators to check the quality of the traces.

Experimental protocol. The experimental protocol pre-, in- and post-flight consisted in a series of predetermined profiles repeated at regular intervals on the TVD to form an experimental block. A single profile had a duration of about 8 s, wherein several TVD modes were combined as indicated in Table 1. The EMG was recorded throughout.

1. After placing the surface electrodes for EMG recording on the agonist and antagonist muscle groups, the subject entered the TVD and the necessary strapping and safety controls were performed. The lever arm of the TVD was automatically positioned to the appropriate angle (see Table 1) and the subject was asked to exert a Maximal Voluntary Contraction (MVC) and to maintain it for the whole duration of the profile.

2. The profile was started in the Isometric (IM) mode and the torque (T) was measured. Duration of this phase: 2 s plus a random interval ranging from 0 to 0.5 s. Independent variable: angle; dependent variable: T.

3. The TVD switched automatically to the Isokinetic (IK) mode. The joint angle was decreased (or increased) by a given amount at a predetermined angular velocity. The duration of this phase was 0.2 s for the Isokinetic concentric (IKc) mode and of 0.4 s for the Isokinetic eccentric (IKe) mode. The angle attained was maintained for 1.8 s plus a random time ranging from 0 to 0.5 s. An angular velocity equal to 50 % of concentric velocity, and in opposite direction, was then applied for the same duration (IKc: 0.2 s; IKe: 0.4 s). Thus, after 2.4 s plus the random time (0 to 0.5 s) from the onset of movement the original joint angle was reached again. Duration of this phase: 2.4 s + random time. Independent variable: angular velocity; dependent variable: T.

4. The TVD switched again to the IM mode. The original position was maintained for 2 s. Independent variable: angle; dependent variable: T.

5. The profile was followed by a pause of 50 s.

6. This single profile was followed by a second one wherein phases 2 to 4 were repeated at a sub maximal, pre-set Torque level, corresponding to 50 % of the individually established pre-flight MVC. In this case a screen appropriately positioned in front of the subject allowed him to check that, in phase 2 and 4, the exerted torque was indeed close to the required 50 % level.

7. A pause of 30 s followed.

The above described two profiles set had a total duration of about 96 s, subdivided into about 8 s of activity at 100 % MVC, 50 s pause, about 8 s at sub maximal level, 30 s pause. Angular velocities (concentric and eccentric) and angles are reported in Table 1. The torque corresponding to the 50 % MVC sub maximal level of muscular activation was set, for each individual and each muscle group, on the basis of the isometric torque attained by the subject during a

preliminary series of maximal voluntary contractions performed shortly before the first experimental session. Afterwards, this level was kept constant throughout the study and applied for all the tested angles.

As indicated in Table 1, we investigated 7 double profile sets and since each double profile was repeated twice, an experimental block on a given muscle lasted about 22.5 min.

The experiments were performed four times before flight (at days L-90, L-60, L-30 and L-15), three times in flight (FD 2, 3, 4; FD 7, 8, 9; FD 13, 14, 15) and four times after flight (R+1, 2; R+4, 5; R+8, 9; R+15, 16) (see Figure 1).

To run the experiments, a computerised procedure, developed by NASA according to the requirements of the investigators, was utilised. This procedure, running on the portable PC, made it possible to load via serial port the profiles into the TVD, to execute the profiles in the proper order while acquiring and storing EMG, torque, velocity and angle signals and to provide on the screen a visual feedback of the Torque and angle outputs to the subject.

Data were analysed off-line by means of automatic, computerised routines developed for this aim at the Laboratory of Biomechanics of ETH in Zurich according to the following methods.

a. Isometric Torque (T_{im}, N m): T_{im} values at 100 % of MVC and at sub maximal level were always obtained as the mean of the Torque signal over an interval of 500 ms. In each profile, the three values of T_{im} corresponding to the two angles α_0 and α_1 were determined: i) at α_0 and at α_1 just before the TVD lever arm moved to the new angle; ii) at α_0 again, 100 ms after the completion of the second movement (Fig. 2A).

b. iEMG during isometric contraction (iEMG, mV): the EMG raw signal corresponding to the time interval (Δt) over which T_{im} was calculated, was band-pass filtered (20 - 200 Hz), rectified, smoothed by means of a moving average with a time window of 75 ms, integrated and finally divided by Δt to obtain the average values in mV of the integrated, rectified myoelectric surface signal

(iEMG) representative of the electrical activity of the muscles (Basmajan and De Luca, 1985).

c. Isokinetic Torque (T_{ik}, N m): T_{ik} in either eccentric or concentric contractions was calculated as follows. The Torque signal corresponding to the first 40 ms after the onset of the movement was omitted. T_{ik} was then calculated as the average over the following 50 ms together with the corresponding mean angular velocity (ω, degrees s^{-1}). (Fig. 2B).

d. iEMG during isokinetic contraction (iEMG, mV): raw EMG signal was time-shifted by 30 ms so as to take into account the electro-mechanical delay (EMD) existing from muscular activation and corresponding mechanical output. Then, iEMG was calculated over the same time interval wherein T_{ik} was obtained applying the same procedure as for the iEMG of T_{im}.

Analysis of the data during isometric contractions has been completed both for Torque and EMG signals, whereas it is still in progress for the isokinetic protocols.

For each experimental session and tested muscular group, the individual T_{im} values at 100 % and 50 % of maximal activation were plotted as a function of α and fitted by means of a second order polynomial: $T_{im} = a_0 + a_1 \alpha + a_2 \alpha^2$. This allowed us to calculate, for elbow flexors and extensors and for ankle plantar flexors, the interpolated values of T_{im} at $\alpha = 0$, i.e. at the angular positions of 100 and 90 degrees of the elbow and ankle joints, respectively. This method, rather than considering the single T_{im} values corresponding to each angle, allowed us to obtain a reliable index of the individual muscular performance resulting from a statistical interpolation calculated on a broad set of data. Furthermore, it must be underlined that T_{im} at $\alpha = 0$ does not correspond to the maximal torque the subject can exert with muscles at that given joint. As such, its value may change as consequence of changes in the force-length relationship. The same kind of analysis was then applied to the iEMG values calculated during isometric

contraction so as to obtain the interpolated iEMG at the same angular position as for T_{im}.

As an example of the applied method, T_{im} values at 100 % of MVC of the elbow flexors and ankle plantar flexors in one subject are plotted as a function of the angular position α in Fig. 3A and 3B along with the regression equation fitting the data. The large full dot corresponds to the T_{im} obtained setting $\alpha = 0$ in the regression equation: it indicates T_{im} at 100 degrees for the elbow or at 90 degrees for the ankle. In the same Figures, the iEMGs of the *biceps brachii* and of *gastrocnemius lateralis* during the same set of measurements are also reported along with the equations fitting the data and the interpolated values at 100 or 90 degrees.

Statistics. Differences among the T_{im} and iEMG average values obtained in each single session were evaluated by means of the Friedman test, i.e. the analogous of the 2 - ways ANOVA in the non parametric domain. Pairwise differences were evaluated by means of the Wilcoxon non parametric test (Daniel, 1991). Average values are reported with their standard deviations, if not otherwise specified.

Results

Individual T_{im} and iEMG values were first normalised dividing them by the average of the corresponding values obtained on all sessions after flight.

In Fig 4A the normalised T_{im} at 100 % MVC of the flexors and extensors of the elbow and that of the plantar flexors is reported as a function of the day from launch. The average value of T_{im} of elbow extensors turned out to be significantly larger ($P < 0.05$) during flight than before flight. On the contrary, the average value of T_{im} of the plantar flexors was significantly smaller in flight than before ($P < 0.05$). Moreover, T_{im} of the plantar flexors post-flight was larger than before flight, although not significantly so ($0.05 < P < 0.1$). T_{im} assessed at sub

maximal level of muscular activity did not show, as expected, any significant variation during the whole period (Fig. 4B).

The normalised values of the *biceps and triceps brachii* iEMG during elbow flexion at 100 % MVC and at sub maximal level of activation are reported in Fig. 5A and 5B as a function of day from launch. No significant differences were detected either for agonist (*biceps brachii)* or for the antagonist (*triceps brachii*). On the contrary, iEMG assessed from *triceps brachii* during elbow extension at 100 % MVC and at sub maximal level increased significantly in the early phases of the flight. The increase of neuromuscular activity gradually subsided during the following days to attain the pre - flight level on the fifteenth/sixteenth day of microgravity exposure (upper panels of Fig. 6A and 6B). Also in the case of elbow extension, no significant variations of the antagonist (*biceps brachii*) iEMG was detected throughout the study (lower panels of Fig 6A and 6B).

The iEMGs during plantar flexion were calculated from surface EMG of *gastrocnemius lateralis* and of *soleus;* they showed significant variations in flight ($P < 0.05$) both at 100 % of MVC and at sub maximal activation (Fig 7A and 7B). iEMG assessed at 100 % MVC kept increasing during flight (Fig 7A), whereas those corresponding to the sub maximal level of activation very early in flight attained a value higher than that prevailing in pre-flight condition and declined slightly thereafter (Fig. 7B).

Discussion

Because of the low number of the subjects and in view of the fact that the results obtained during isokinetic contractions have not yet been completely analysed, the comments that follow must be considered with some caution. Within these limits, a few findings are worth underlining.

During flight, the neuromuscular system seemed able to maintain an unchanged capability of maximal recruitment of motor units. In fact, iEMG at 100 % of MVC of *biceps brachii, gastrocnemius lateralis* and *soleus* remained almost stable throughout the study, whereas that of *triceps brachii* increased in the early phases of flight and remained high thereafter until return on Earth. In this connection, it is worth pointing out that the observed increase of the iEMG of the latter muscle could not have been caused by cephalic fluids shift taking place at the onset of microgravity exposure (Greenleaf, 1977) since this phenomenon should have affected to the same extent all the EMG signals recorded from both the agonists and antagonists of the upper limbs.

The increase of *triceps brachii* iEMG was accompanied by a consensual and significant increase of the T_{im} of the elbow extensors. As a consequence, the ratio between mechanical output (T_{im}) and electrical activity, i.e. iEMG of *triceps brachii*, remained almost constant over the period of the study both at 100 % of MVC and at sub maximal level (Fig. 8A and 8B). Thus, early in flight there seemed to occur a sort of dishinibition of this muscle group which, however, gradually subsided in the course of the mission. When considering that *triceps brachii* is a "non antigravity" muscle, this phenomenon is similar to that reported by Edgerton and Roy (1996, 1997) who showed an increase of the electrical activity of the flexors (non antigravity), as compared to the extensors (antigravity) muscles of the lower limbs early in flight. Furthermore, a significant reduction of the activation of the extensors muscle and an increase of that concerning the flexors were in fact consistently reported in the resting and standing conditions during microgravity exposure. This was thought to reflect a

generalised flexor bias of muscle activation which, however, was progressively restored in the course of the flight (Edgerton and Roy, 1996, 1997). The present data suggest that a similar release of inhibitory inputs, whose causes are still unknown, may also occur at the level of the forearm extensors.

In the early phases of flight, T_{im} of the plantar flexors attained a value significantly lower than pre-flight; however, it progressively recovered in orbit to attain, after fifteen days of mission, a value close to control (Fig. 4B) without any further change upon return on Earth. In this case, however, there was a clear dissociation between muscular performances in terms of T_{im} and iEMG: the neuromuscular activity of *soleus* and of *gastrocnemius lateralis*, in fact, was higher in the early phases of the flight as compared to the control situation. This phenomenon was reflected by the consensual drop of the Torque to iEMG ratio (Fig 9A and Fig 9B) particularly evident in the *soleus* muscle at 100 % of MVC and, for both the *soleus* and *gastrocnemius*, at sub maximal level of contraction. In fact, the drop of electrical activation at the two level of voluntary contraction may be well explained by the dramatic activation of the antigravity, extensor muscles of the lower limb commonly found after the onset of microgravity (Edgerton and Roy, 1996, 1997). Also the gradual recover of the iEMG taking place during flight agrees with the progressive recovery of the activity level of the extensors described by others and taking place in the course of the mission (Edgerton and Roy, 1996). However, the drops of plantar flexors T_{im} to *soleus* and *gastrocnemius lateralis* iEMGs ratios were clearly unexpected and it does deserve some words of comment. The drop of the T_{im} to iEMG ratios indicates the sudden occurrence of a microgravity effect negatively affecting the electromechanical coupling of this muscle. In fact, a drop of the T_{im} to iEMG ratio indicates that the involved muscle is able to develop a lower level of tension in response of the same electrical activation. This finding agrees well with the data recently reported by others and concerning the relationship between maximal isometric torque of lower limb extensors and surface electromechanical activity of

quadriceps muscles (Berg and Tesch, 1996). In that case, a significant decrease of maximal T_{im} of quadriceps was documented after only ten days of lower limb unilateral unloading and it was paralleled by a consensual drop of the corresponding Torque to iEMG ratio. This marked drop of maximal force, as well as its fast recovery after reambulation, was not accompanied neither by a proportional decrease of muscle mass nor by the impairment of maximal recruitment capability. In addition, it has been recently documented by this group that significant and progressive drop of the T_{im} to EMG ratio of the plantar flexors was progressively developing during seventeen days of head - down tilt bed rest (Milesi et al., 1997).

Hence, an unidentified factor (or a series of them) may contribute to the drop of maximal force affecting some specific antigravity muscle of the lower limb and taking place very early in flight and during lower limb unloading. Moreover, the muscle functions seem to recover in a time span shorter than the period of exposure to microgravity.

In conclusion, and within the limits mentioned at the beginning of the discussion, we think that future research in microgravity should aim at: i) a better description of the time course of the effects on muscle tension and motor units recruitment and; ii) a clear understanding of the specific factor (s) underlying this phenomenon.

Bibliography

1) Antonutto, G., C. Capelli, M. Girardis, P. Zamparo, P.E. di Prampero. Effects of microgravity on muscular explosive power of the lower limbs in humans. *Acta Astronautica* 36 (8-12): 473-478, 1995.

2) Basmajan J.V. and C. J. De Luca. In: "*Muscle Alive. Their Functions Revealed by Electromyography*", Williams & Wilkins, Baltimore, 1985, pp. 94 - 100.

3) Berg, H.E. and P.A. Tesch. Changes in muscle function in response to 10 days of lower limb unloading in humans. *Acta Physiol. Scand.* 157: 63-70, 1996.

4) Carlson, F.D., Wilkie, D.R. (1974). Muscle Physiology. Prentice-Hall, Inc. Englewood Cliffs, N.J., USA, PP. 170 + iv.

5) Daniel W. W. *Biostatistics: a Foundation for analysis in health sciences*, J. Wiley & S., NY, 1991, pp. 576 - 630.

6) Edgerton V. R. and R. R. Roy. Neuromusclar adaptations to actual and simulated space flight. In "*Handbook of Physiology, Section 4, Environmental Physiology, Vol 1*", M.J. Fregly and C. M. Blatteis eds., Oxford Un. Press, NY 1996, 1996, pp. 721 - 763.

7) Edgerton V. R. and R. R. Roy. Response of skeletal muscle to space flight, Chapter 7. In "*Fundamentals of Space Life Sciences, Vol 1*", Krieger, Malabar, 1997, pp. 105 - 116.

8) Greenleaf J.E., E.M. Bernauer, H. L. Young, J.T. Morse, R.W. Staley, L.T. Juhos and W. Van Beaumont. Fluid and electrolyte shifts during bed rest with isometric and isotonic exercise. J. Appl. Physiol. 42: 59 - 66, 1977.

9) Grigoriev, A.I, Egorov, A.E. (1991). The effects of prolonged space flights on the human body. In: *Advances in Space Biology and Medicine*, vol. 1. Ed. by S.L. Bonting. JAI Press Inc. London, England. PP. 1-35.

10) Milesi S., C. Capelli, J. Denoth, T. Hutchinson, S. B. Arnaud, E. Stüssi and P. E. di Prampero. Effects of 17 days of bed rest on the maximal voluntary isometric torque and neuromuscular activation of the plantar and dorsal flexors of the ankle. 18th Annual International Gravitational Physiology Meeting, Copenhagen, 20th - 25th April 1997.

11) Nicogossian, A.E. (1989). Overall physiological responses to space flight. In: *Space Physiology and Medicine*. Ed. by A.E. Nicogossian, C. Leach Huntoon, S.L. Pool. Lea & Febiger, Philadelphia London. PP. 139-153.

12) Woledge, R.C., Curtin, N.A., Homsher, E. (1985). *Energetic Aspects of Muscle Contraction*. Academic Press, London. PP. 360 + xiii.

13) Zipp, P. Recommendations for the standardisation of lead position in surface electromyography (EMG). *Eur. J. Appl. Physiol.* 50: 41-54, 1982.

Figure Legend

Figure 1: Schedule of the experiments performed pre-flight, in -flight and post-flight. Numbers in the boxes indicate the subjects evaluated in each experimental session.

Figure 2A: Experimental traces obtained during elbow flexion at 100 % of MVC (profile # 3) are reported in Figure 2A. In the upper panel, the trace of the angular position α is plotted as function of the time. ω_0 (concentric, 57.3 degrees s^{-1}) and ω_1 (eccentric, -28.6 deg s^{-1}) refer to the two angular velocities tested in this profile. In the middle panel, the thick parts of the Torque trace indicate the intervals over which T_{im} was calculated. In the lower panel, raw EMG of *biceps brachii* is plotted after band-pass filtering.

Figure 2B: Typical traces obtained during isokinetic - eccentric action of the ankle plantar flexors. Thick parts of the traces indicate the intervals over which T and ω (angular velocity) were calculated during isokinetic experiments.

Figure 3A: T_{im} (N m) and iEMG (mV) as a function of angular position (degrees) obtained during at 100 % MVC the elbow flexors in one subject. The lower X axis refer to angles measured from an elbow angle of 100 degrees and defined to be the reference position (0 degree); upper X axis refer to the TVD angle. Large full dots correspond to T_{im} and iEMG obtained substituting 0 for α in the regression equations (see text for details).

Figure 3B: Same as in Figure 3A, but for T_{im} and iEMG assessed during sub maximal activation of the ankle plantar flexors. PF = plantar flexors; DF = dorsiflexion.

Figure 4A: Normalised T_{im} of the elbow flexors (upper panel) and extensors (middle panel) and of the plantar flexors (lower panel) at 100 % of MVC is plotted as function of the days from launch.

Figure 4B: The same as in Figure 4A, but referring to sub maximal activation of the three muscle groups.

Figure 5A: Normalised iEMGs of the *biceps brachii* (agonist during elbow flexion) at 100 % MVC, and of the antagonist *triceps brachii* are plotted as function of the days from launch. Points without SD were obtained from less than three values and were not considered in the statistical analysis.

Figure 5B: The same as in Figure 5A, but referring to sub maximal activation of the elbow flexors. Points without SD were obtained from less than three values and were not considered in the statistical analysis.

Figure 6A: Normalised iEMGs of the *triceps brachii* (agonist during elbow extension) at 100 % MVC and of the antagonist *biceps brachii*, are plotted as function of the days from launch. Points without SD were obtained from less than three values and were not considered in the statistical analysis.

Figure 6B: The same as in Figure 6A, but referring to sub maximal involvement of the elbow extensors. Points without SD were obtained from less than three values and were not considered in the statistical analysis.

Figure 7A: Normalised iEMGs of the *gastrocnemius lateralis* and of *soleus* (agonists during ankle plantar flexion) at 100 % of MVC and of the antagonist *tibialis anterior* are presented as a function of days from launch.

Figure 7B: The same as in Figure 7A, but referring to sub maximal activation of the plantar flexors. Values of the *tibialis anterior* are not presented because of the paucity of the available data.

Figure 8A: Normalised T_{im} to iEMG ratios at 100 % of MVC of the elbow are plotted as function of the days from launch. Upper panel reports T_{im} to iEMG ratio obtained dividing T_{im} of the flexors of the elbow to the *biceps brachii* iEMG; lower panel refers to elbow extensors and *triceps brachii* iEMG. Points without SD were obtained from less than three values and were not considered in the statistical analysis.

Figure 8B: The same as in Figure 8A, but referring to sub maximal activation of the two muscle groups. Points without SD were obtained from less than three values and were not considered in the statistical analysis.

Figure 9A: Normalised T_{im} to iEMG ratios at 100 % of MVC of the ankle are plotted as function of the days from launch. Upper panel refers to T_{im} to iEMG ratio obtained dividing Tim of the plantar flexors to iEMG of soleus; lower panel was obtained dividing T_{im} to iEMG of gastrocnemius lateralis. Points without SD were obtained from less than three values and were not considered in the statistical analysis.

Figure 9B: The same as in Figure 9A, but referring to sub maximal activation of the plantar flexors.

Fig. 1

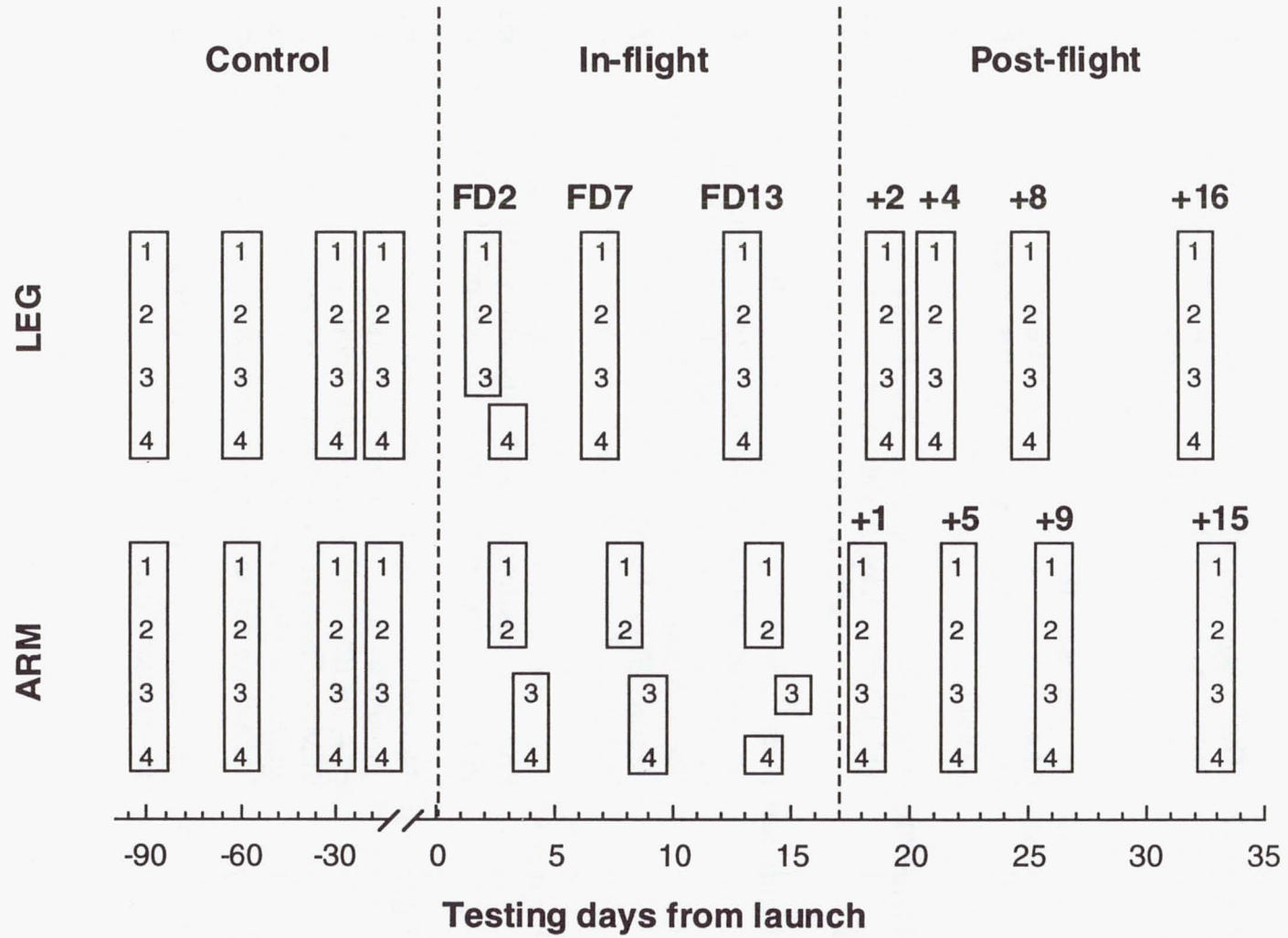
Control
In-flight
Post-flight
FD2
FD7
FD13
+2
+4
+8
+16
+1
+5
+9
+15
LEG
ARM
-90
-60
-30
0
5
10
15
20
25
30
35
Testing days from launch

Fig. 2A

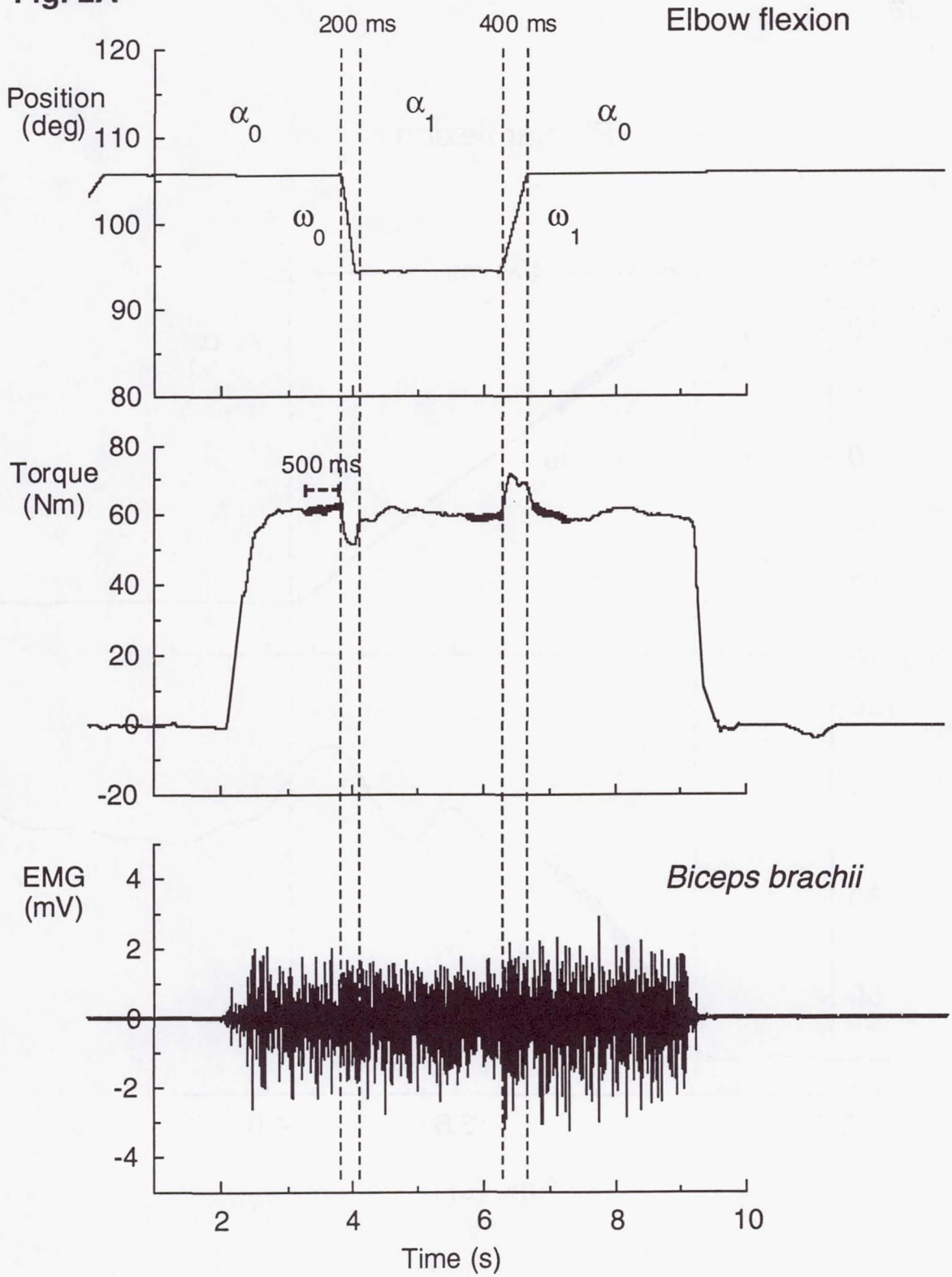
Elbow flexion
200 ms
400 ms
Position (deg)
120
110
100
90
80
α_0
α_1
α_0
ω_0
ω_1
Torque (Nm)
80
60
40
20
0
-20
500 ms
EMG (mV)
4
2
0
-2
-4
Biceps brachii
2
4
6
8
10
Time (s)

Fig. 2B

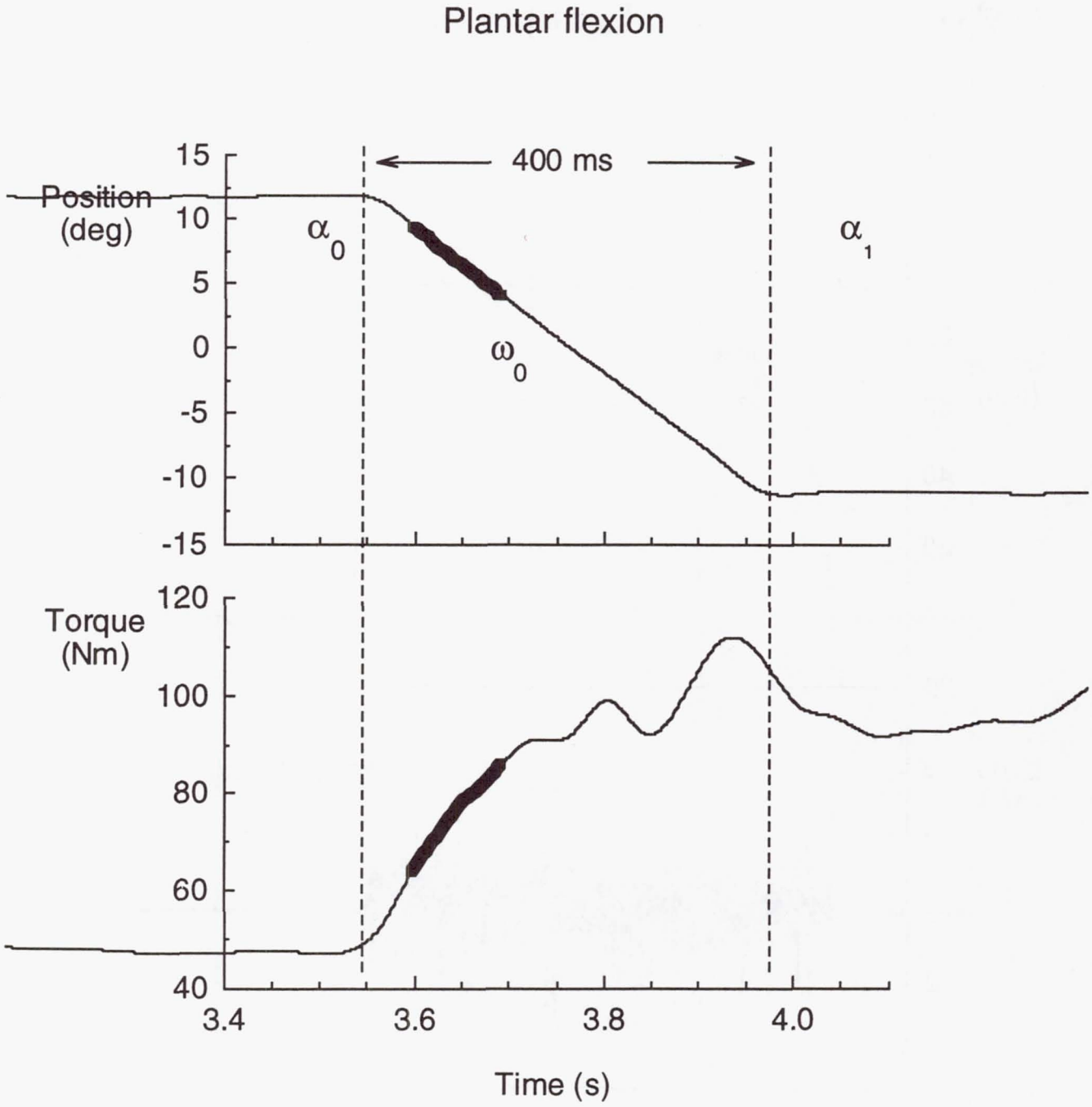
Plantar flexion
400 ms
Position
(deg)
15
10
5
0
-5
-10
-15
α_0
α_1
ω_0
Torque
(Nm)
120
100
80
60
40
3.4
3.6
3.8
4.0
Time (s)

Fig. 3A Elbow flexion at FD14 interpolation= $a_0 + a_1 \alpha^2 + a_2 \alpha^2$

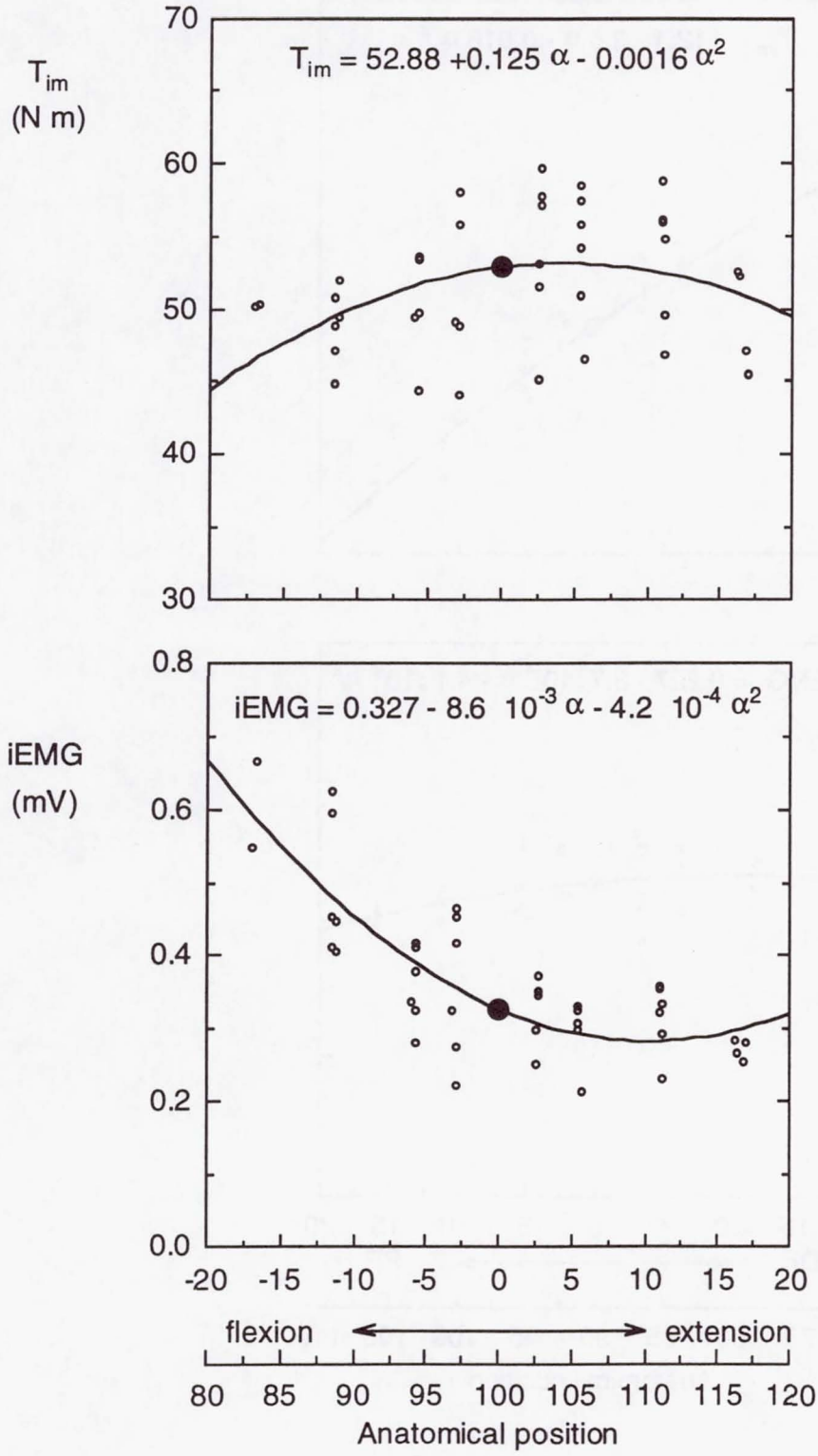

Fig. 3B

Plantar flexion at L-15 interpolation= $a_0 + a_1 \alpha + a_2 \alpha^2$

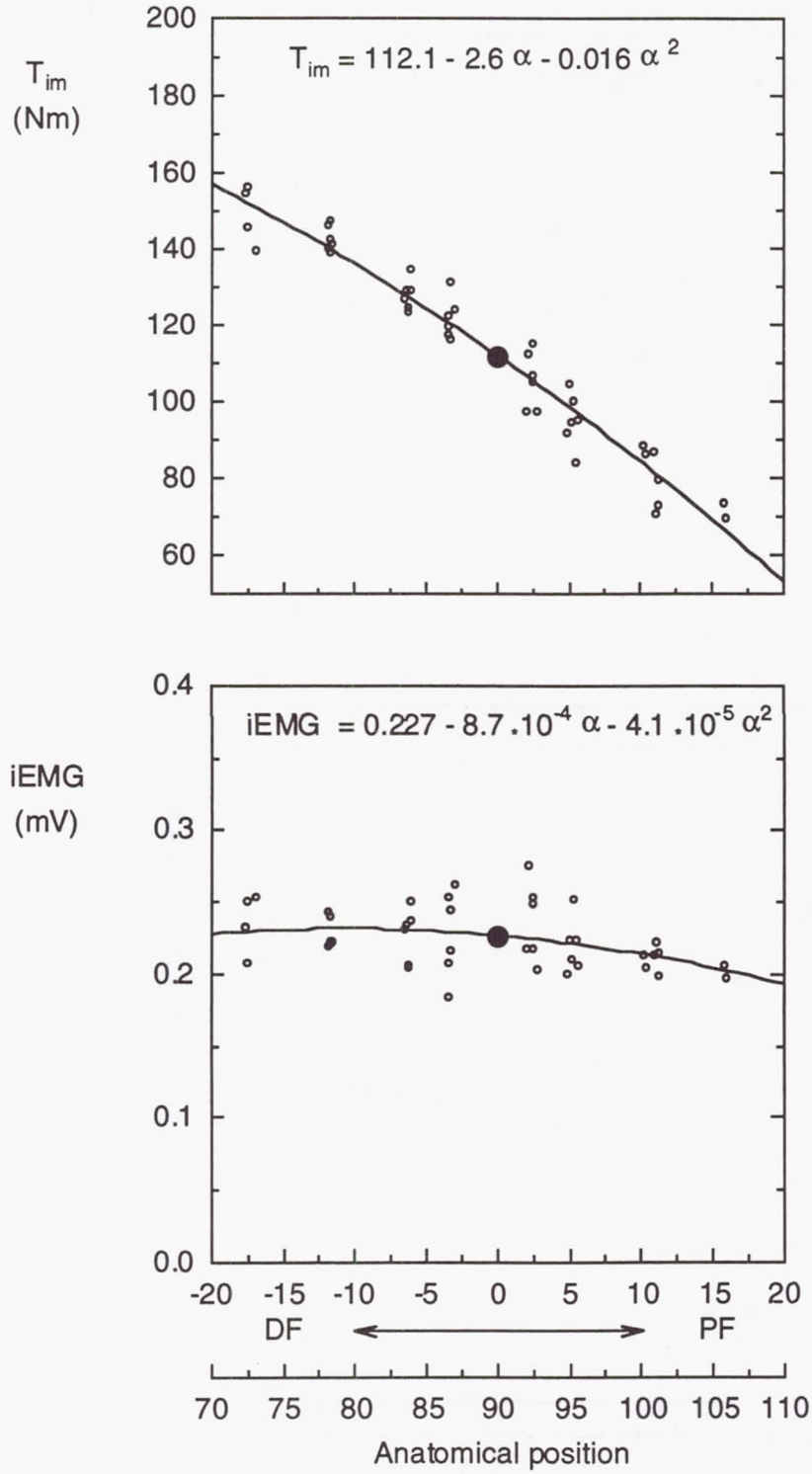

Fig. 4A

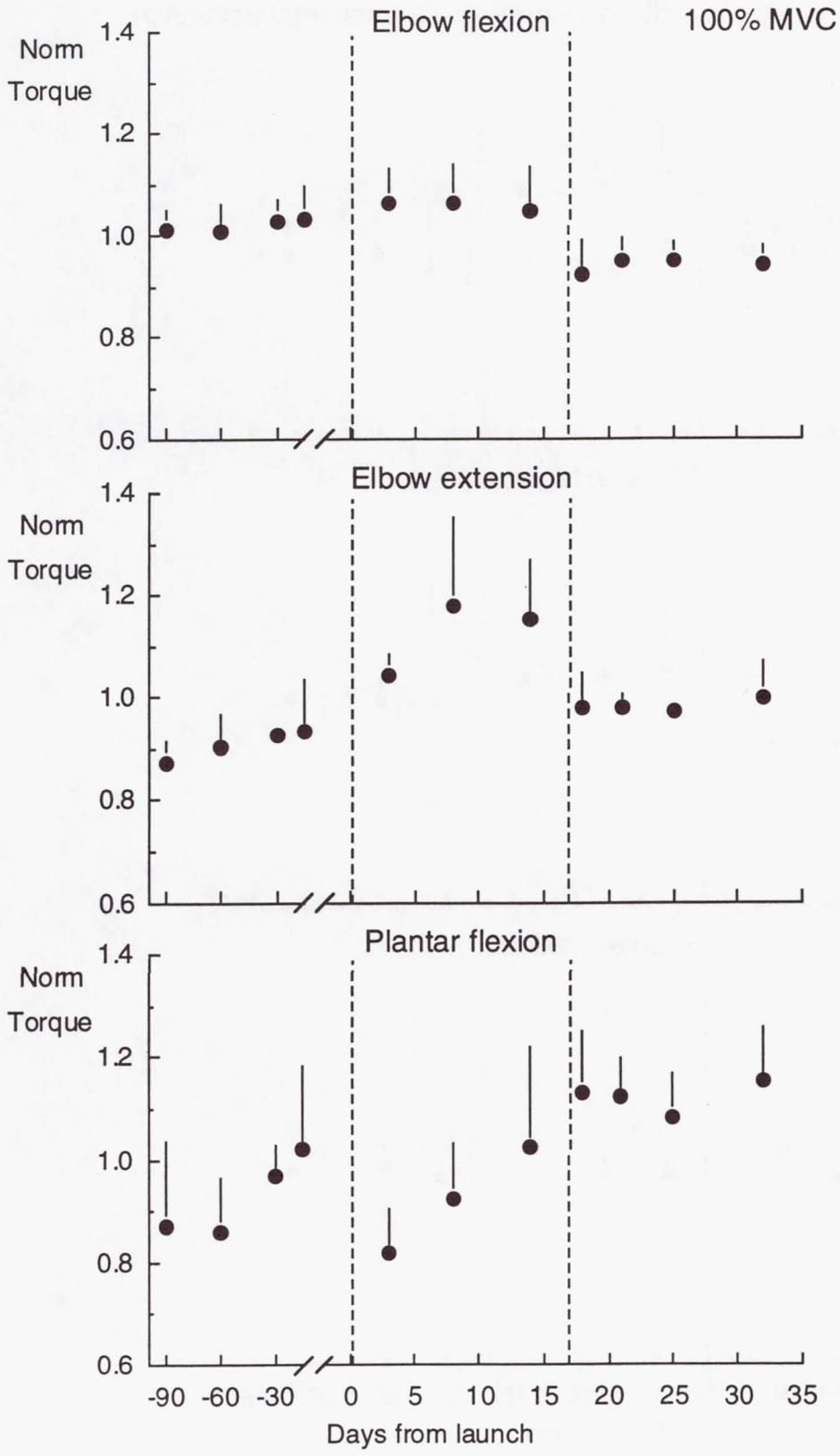
Elbow flexion
100% MVC
Norm Torque
1.4
1.2
1.0
0.8
0.6
Elbow extension
Norm Torque
1.4
1.2
1.0
0.8
0.6
Plantar flexion
Norm Torque
1.4
1.2
1.0
0.8
0.6
-90 -60 -30 0 5 10 15 20 25 30 35
Days from launch

Fig. 4B

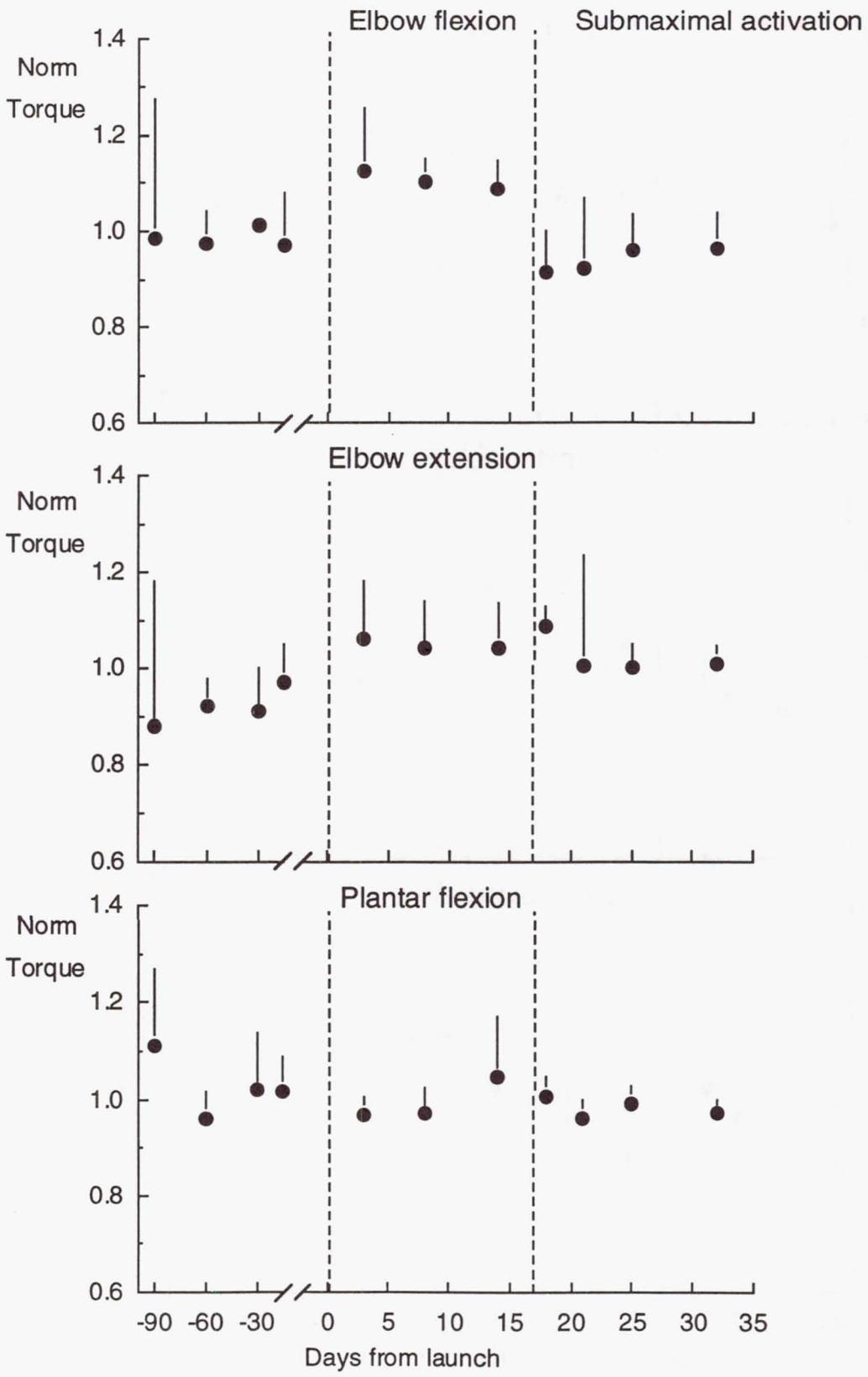
Elbow flexion
Submaximal activation
Norm Torque
1.4
1.2
1.0
0.8
0.6
Elbow extension
Plantar flexion
-90 -60 -30 0 5 10 15 20 25 30 35
Days from launch

Fig. 5A

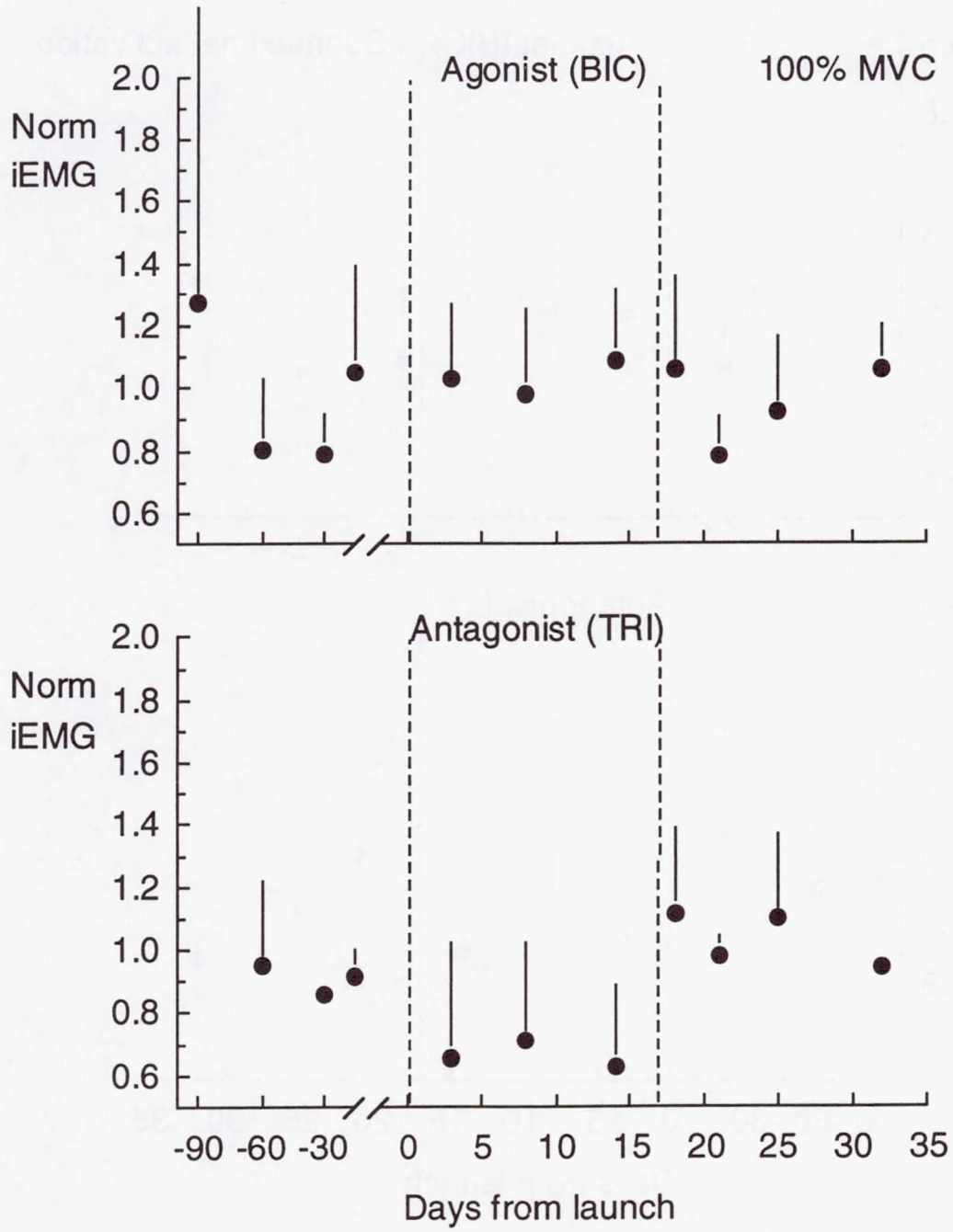
Agonist (BIC)
100% MVC
Norm iEMG
2.0
1.8
1.6
1.4
1.2
1.0
0.8
0.6
Antagonist (TRI)
Norm iEMG
2.0
1.8
1.6
1.4
1.2
1.0
0.8
0.6
-90 -60 -30 0 5 10 15 20 25 30 35
Days from launch

Fig. 5B

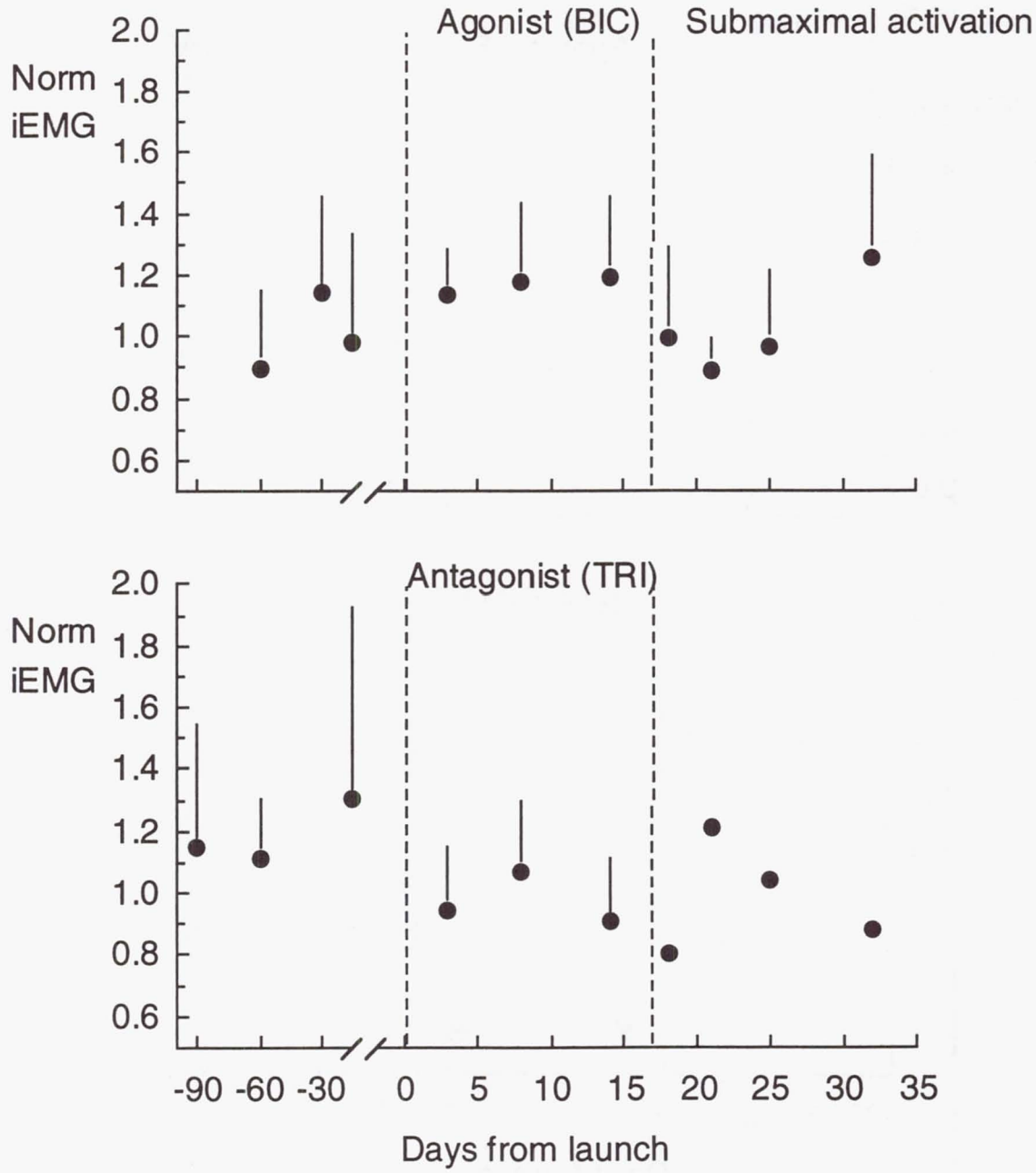
Agonist (BIC)
Submaximal activation
Norm iEMG
2.0
1.8
1.6
1.4
1.2
1.0
0.8
0.6
Antagonist (TRI)
Norm iEMG
2.0
1.8
1.6
1.4
1.2
1.0
0.8
0.6
-90 -60 -30 0 5 10 15 20 25 30 35
Days from launch

Fig. 6A

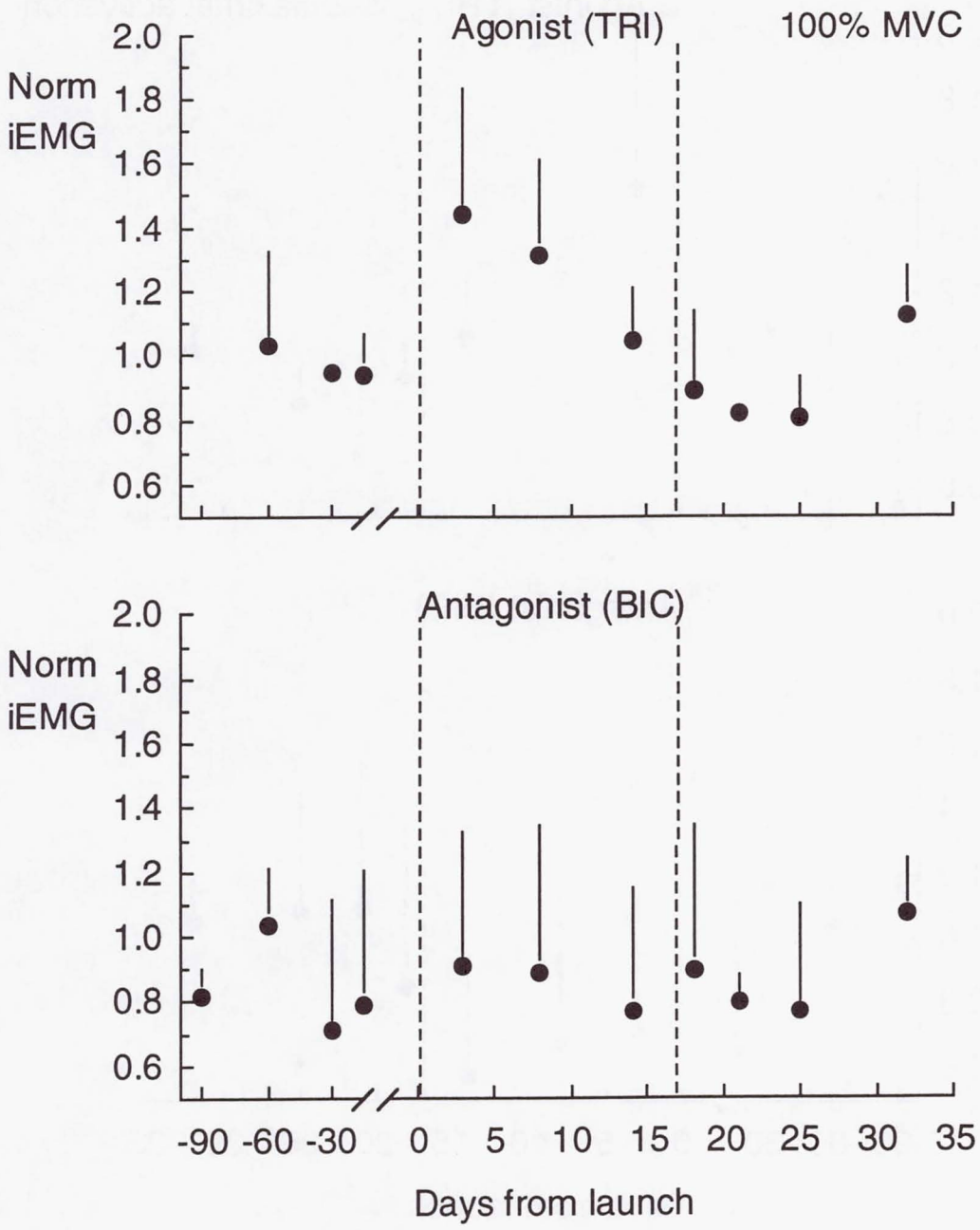
Agonist (TRI)
100% MVC
Norm iEMG
2.0
1.8
1.6
1.4
1.2
1.0
0.8
0.6
Antagonist (BIC)
Norm iEMG
2.0
1.8
1.6
1.4
1.2
1.0
0.8
0.6
-90 -60 -30 0 5 10 15 20 25 30 35
Days from launch

Fig. 6B

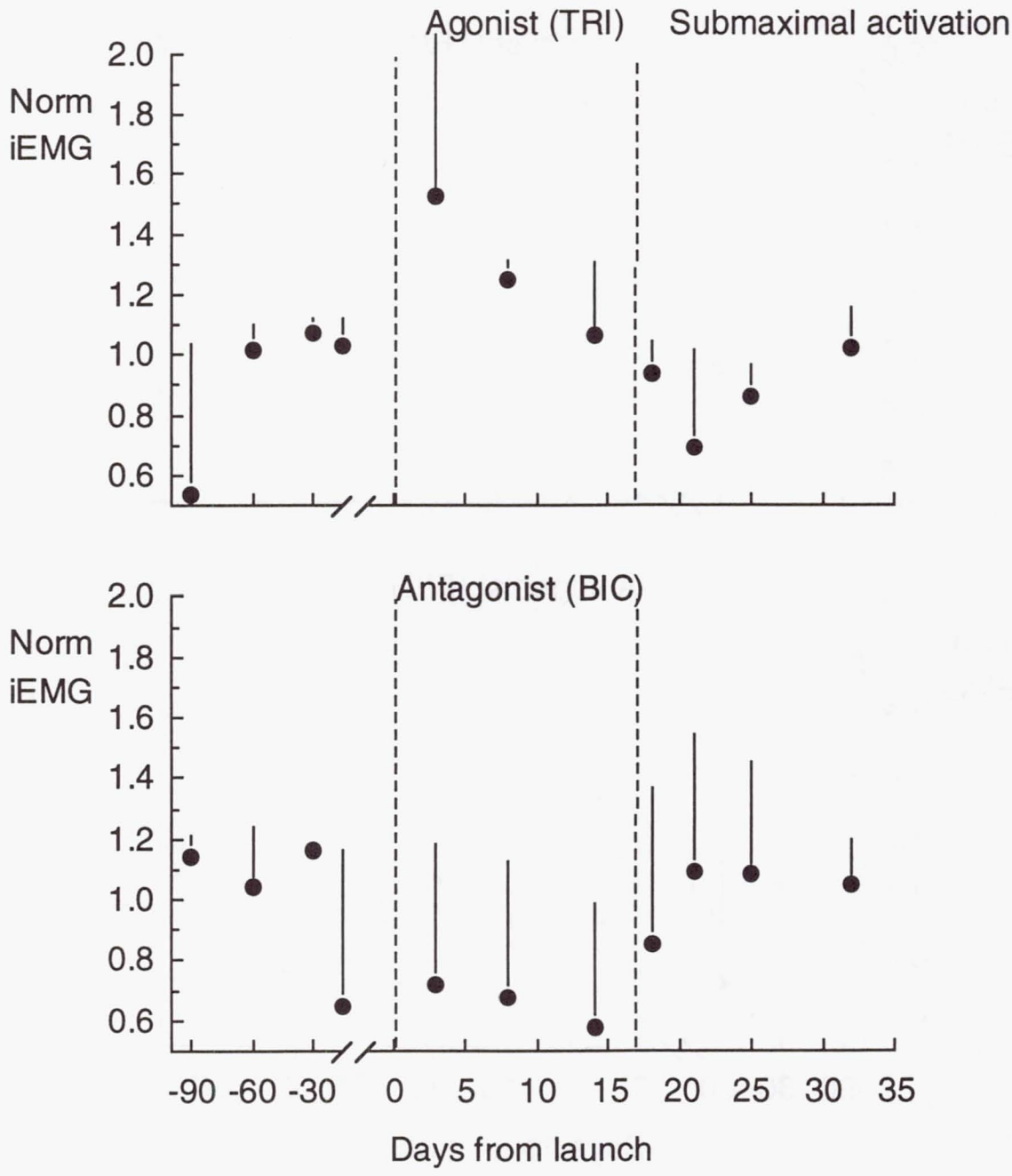
Agonist (TRI)
Submaximal activation
Norm iEMG
2.0
1.8
1.6
1.4
1.2
1.0
0.8
0.6
Antagonist (BIC)
Norm iEMG
2.0
1.8
1.6
1.4
1.2
1.0
0.8
0.6
-90 -60 -30 0 5 10 15 20 25 30 35
Days from launch

Fig. 7A

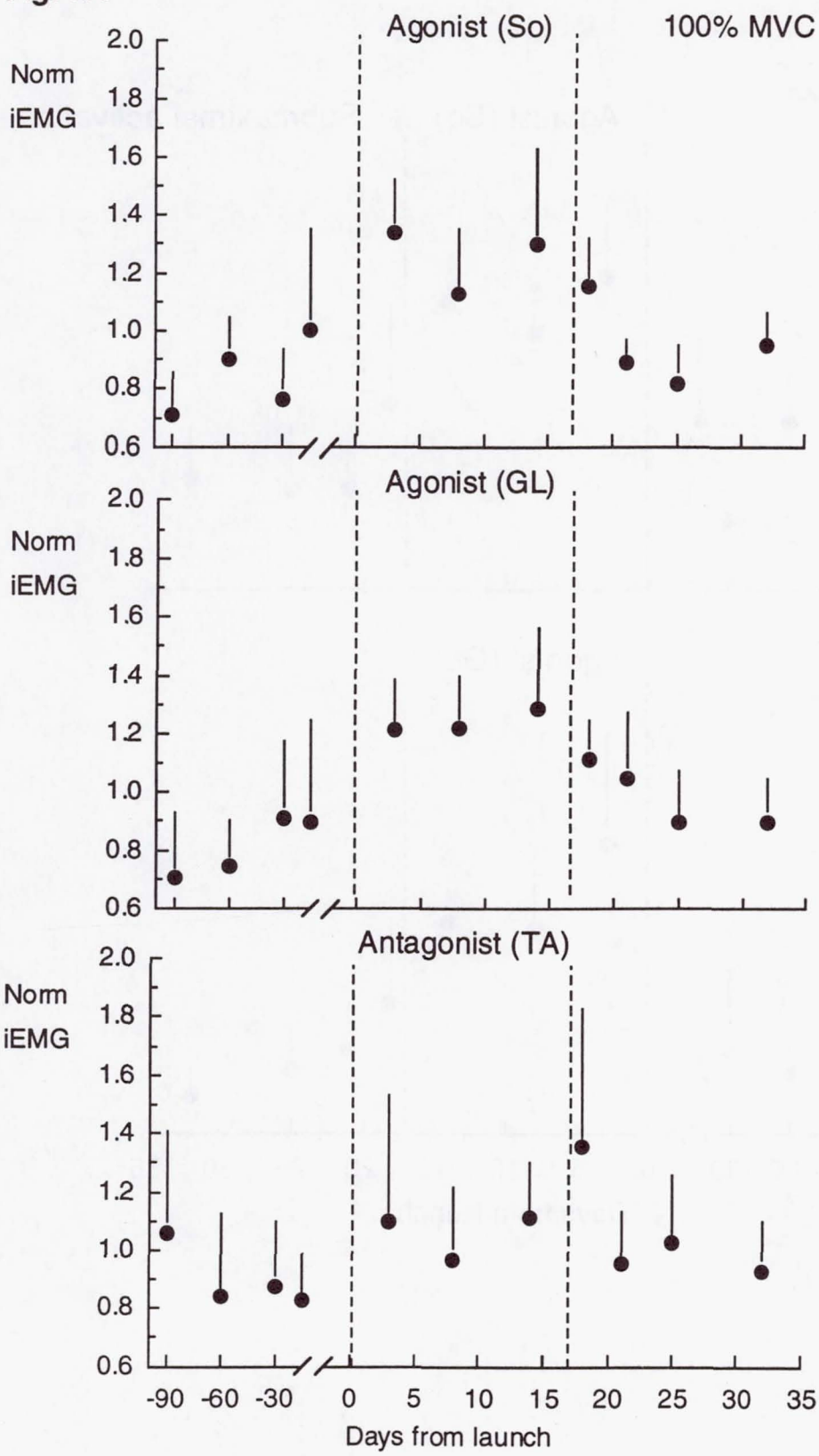
Agonist (So)
100% MVC
Norm iEMG
2.0
1.8
1.6
1.4
1.2
1.0
0.8
0.6
Agonist (GL)
Norm iEMG
Antagonist (TA)
Norm iEMG
-90 -60 -30 0 5 10 15 20 25 30 35
Days from launch

Fig. 7B

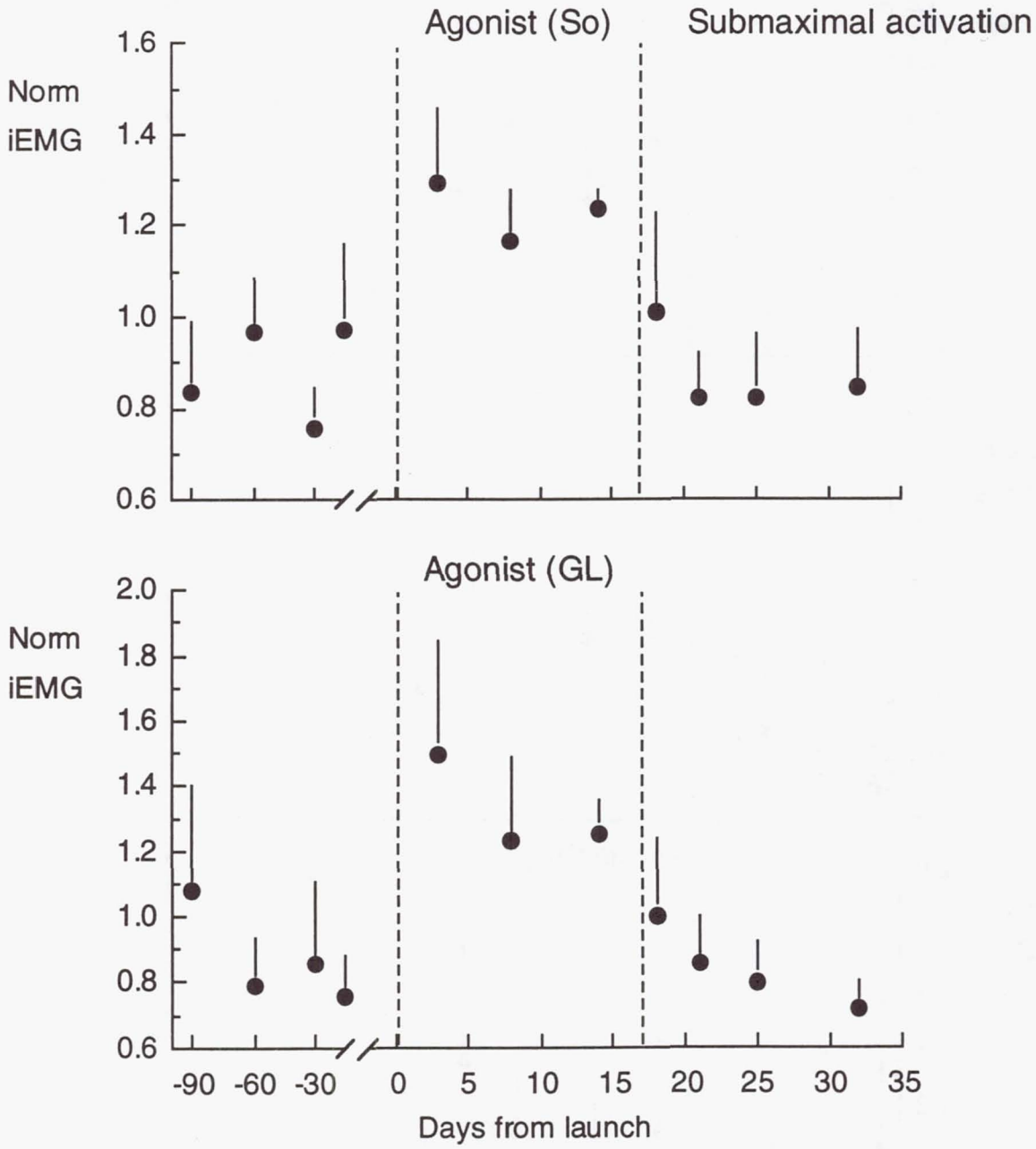
Agonist (So)
Submaximal activation
Norm iEMG
1.6
1.4
1.2
1.0
0.8
0.6
Agonist (GL)
Norm iEMG
2.0
1.8
1.6
1.4
1.2
1.0
0.8
0.6
-90 -60 -30 0 5 10 15 20 25 30 35
Days from launch

Fig. 8A

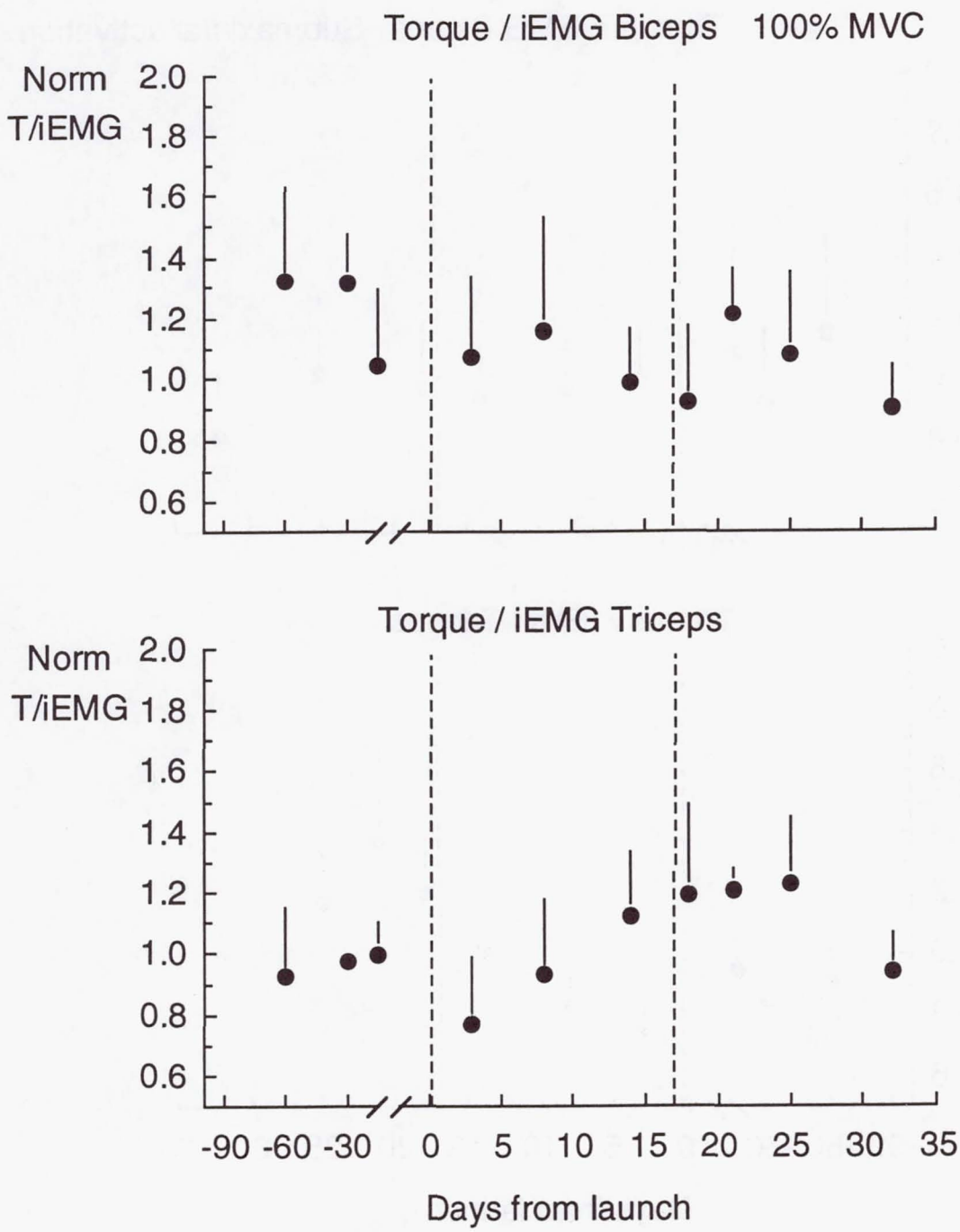
Torque / iEMG Biceps 100% MVC
Norm T/iEMG
2.0
1.8
1.6
1.4
1.2
1.0
0.8
0.6
Torque / iEMG Triceps
Norm T/iEMG
2.0
1.8
1.6
1.4
1.2
1.0
0.8
0.6
-90 -60 -30 0 5 10 15 20 25 30 35
Days from launch

Fig. 8B

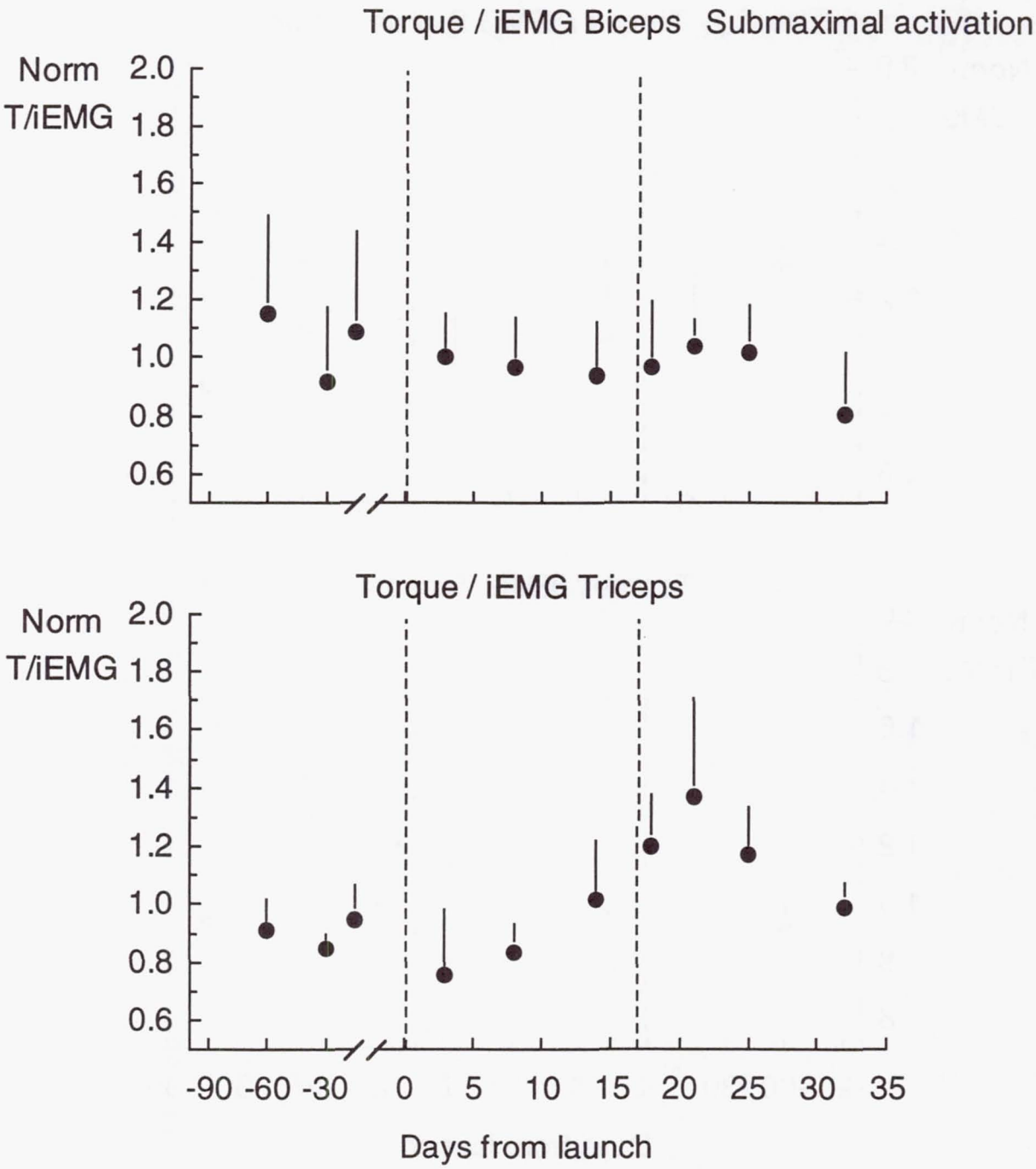
Torque / iEMG Biceps Submaximal activation
Norm T/iEMG
2.0
1.8
1.6
1.4
1.2
1.0
0.8
0.6
Torque / iEMG Triceps
Norm T/iEMG
2.0
1.8
1.6
1.4
1.2
1.0
0.8
0.6
-90 -60 -30 0 5 10 15 20 25 30 35
Days from launch

Fig. 9A

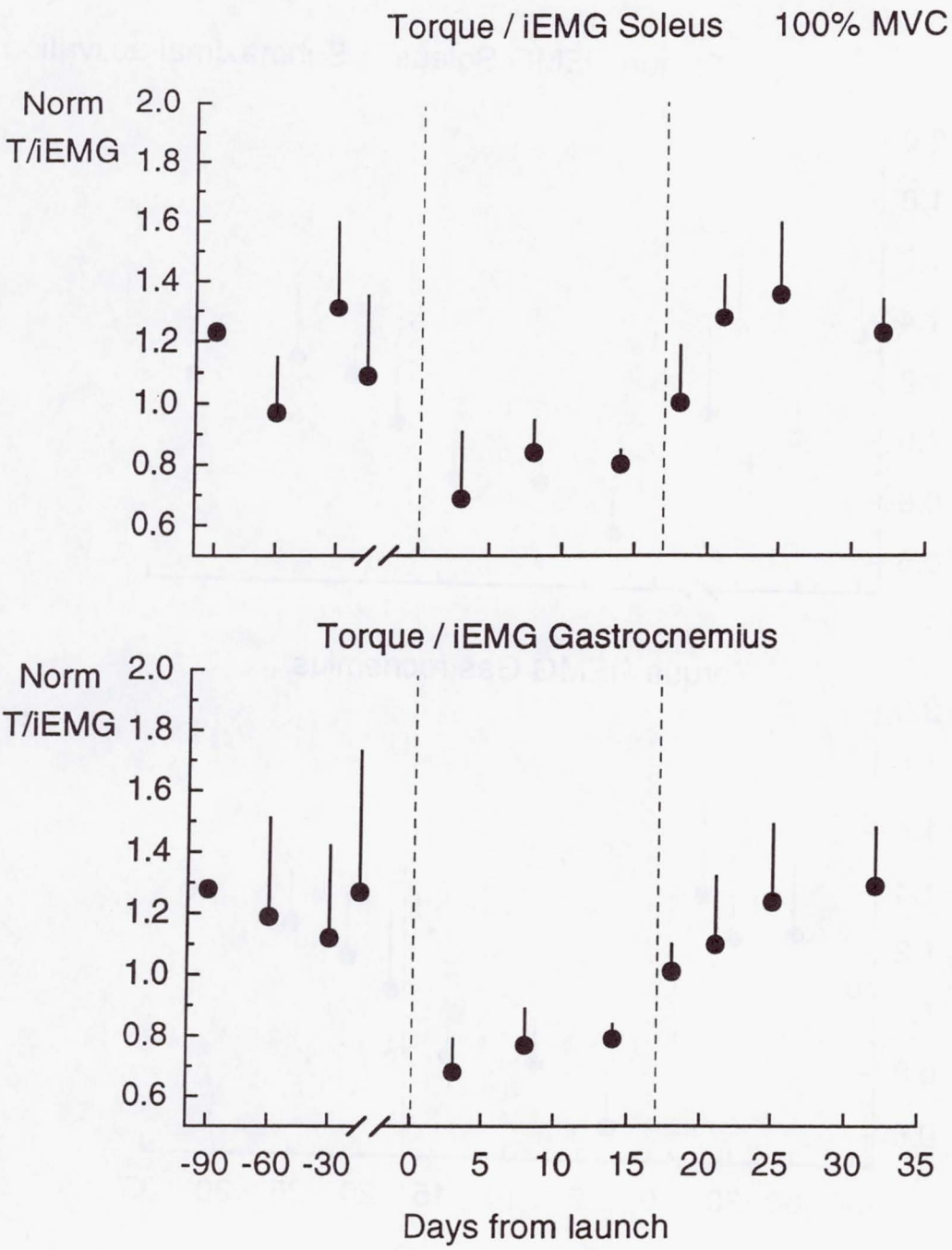
Torque / iEMG Soleus 100% MVC
Norm T/iEMG
2.0
1.8
1.6
1.4
1.2
1.0
0.8
0.6
Torque / iEMG Gastrocnemius
Norm T/iEMG
2.0
1.8
1.6
1.4
1.2
1.0
0.8
0.6
-90 -60 -30 0 5 10 15 20 25 30 35
Days from launch

Fig. 9B

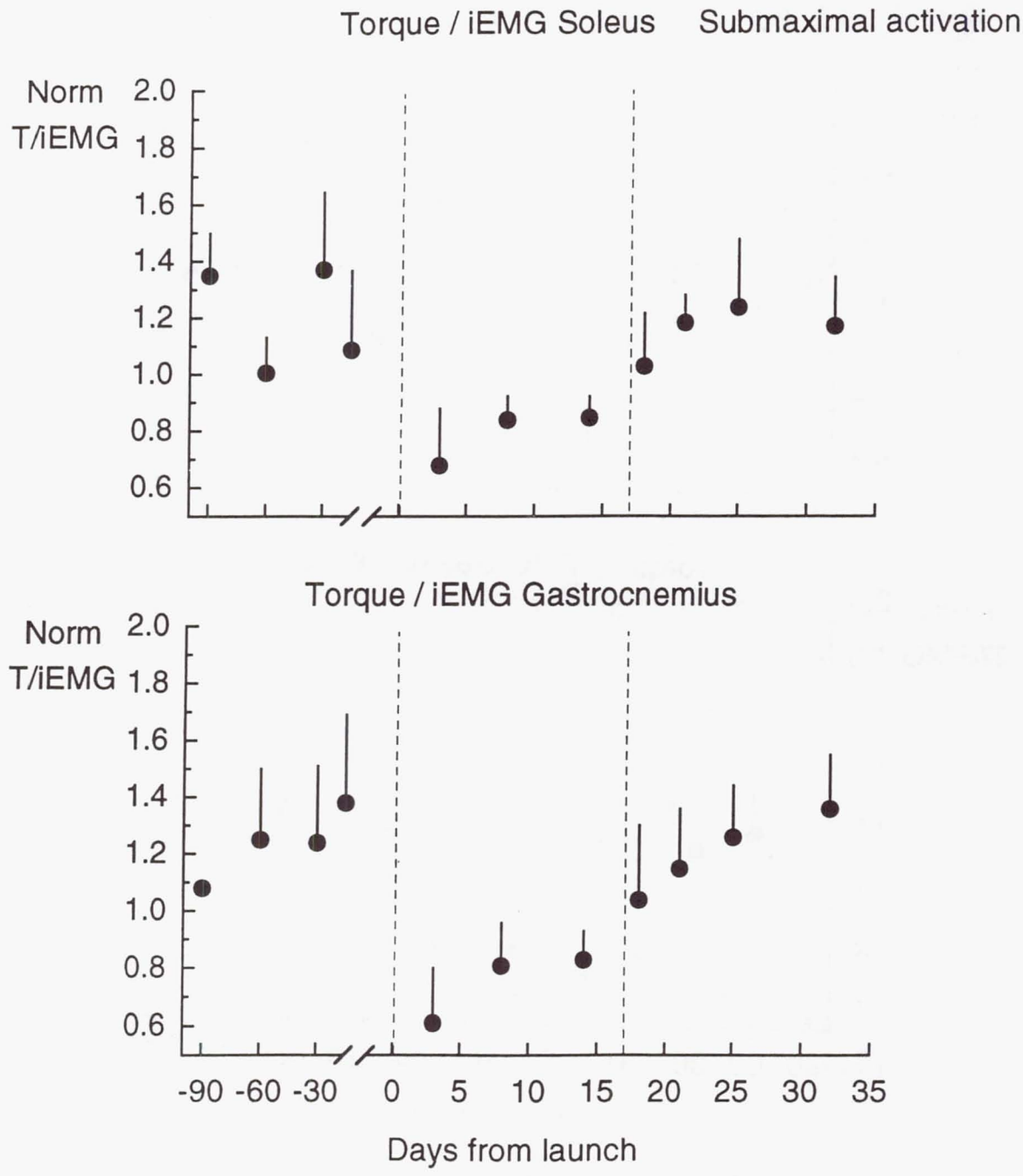
Torque / iEMG Soleus
Submaximal activation
Norm T/iEMG
2.0
1.8
1.6
1.4
1.2
1.0
0.8
0.6
Torque / iEMG Gastrocnemius
Norm T/iEMG
2.0
1.8
1.6
1.4
1.2
1.0
0.8
0.6
-90 -60 -30 0 5 10 15 20 25 30 35
Days from launch

E 407: Non Technical Report

Effects of Microgravity on the Biomechanical and Bioenergetic Characteristics of Human Skeletal Muscle.

Carlo Capelli[1], S. Milesi[1], J. Denoth[2], E. Stüssi[2] and P. E. di Prampero[1].

[1]Dipartimento di Scienze e Tecnologie Biomediche, Università degli Studi di Udine, Via Gervasutta 48, I-33100 UDINE (Italy)

[2]Biomechanics Laboratory, ETH, Wagistraße 4, CH-8952 SCHLIEREN (Switzerland)

P.I.: Pietro Enrico di Prampero

Long term space flights are known to impair muscle function mainly because of the loss of muscle mass. This loss of muscle mass is an early event upon microgravity exposure; it affects especially the antigravity muscles of the lower limbs. In addition, a substantial remodelling of the muscle structure and a reorganisation of the neuromuscular control systems also occur during space flight and may contribute to the impairment of muscle maximal performances. Furthermore, recent findings show that short term lower limb unloading simulating microgravity may bring about a substantial drop of the maximal force of the leg extensors which is not accompanied neither by loss of muscle mass nor by changes of the maximal recruitment capability of muscle motor units. Hence, an unidentified factor (or a series of them) may contribute to the drop of maximal force of some antigravity muscles of the lower limbs and taking place very early upon lower limb unloading. Hence, the aim of the present study was: i) to quantify the extent as to which short term space flight affects mechanical muscle performance and neuromuscular recruitment and; ii) to describe the time course with which these phenomena occur.

To this aim, maximal and sub maximal force during static and dynamic contractions of the extensors and flexors of the elbow and of the plantar flexors of the ankle were studied in four astronauts who participated in the 17 days long LMS mission which took place from June 20th 1996 to July 7th 1996. The electric surface activity (integrated electromyogram, iEMG) of some of these muscles was also simultaneously recorded. Measurements were taken four times before flights, three times in-flights and four times after flight.

The iEMG at maximal voluntary contraction remained stable or even increased on flight, thus showing that the neuromuscular system was able to maintain an unchanged capability of maximal motor units recruitment.

Maximal static force of the elbow extensors was significantly larger during than before flight. This was due to the higher electrical activity with which these muscles were activated and suggests a drop of the inhibitory inputs normally prevailing in normogravity on this muscle groups of the upper limb.

Maximal static force of the plantar flexors, especially in the early phases of flight, was lower than pre-flight. In this case, however, the surface electrical activity of the activated muscles remained high and, as a consequence, the ratios of the maximal force to iEMG were lower. This indicates the sudden occurrence of microgravity effect negatively affecting the electromechanical coupling of this muscle groups and agrees with several, recent findings obtained during short-term lower limb unloading.

Future research in microgravity should aim at: i) a better description of the time course of the effects on muscle tension and motor units recruitment and; ii) a clear understanding of the specific factor (s) underlying this phenomenon.

JSC Human Life Sciences Project

E410 - Torso Rotation Experiment

Principal Investigator:

Dr. Douglas Watt
McGill University
Montreal, Quebec, Canada

Final Science Report

Spacelab LMS Investigation E410

Principal Investigator:

Douglas Watt, M.D., Ph.D.
McGill University
Montreal, Canada

BACKGROUND

Space motion sickness occurs in about 50% of all astronauts and cosmonauts. It is certainly unpleasant, can lower crew efficiency and thus the amount of work that can be done on a given flight, and could conceivably be hazardous, particularly during an extra-vehicular activity or urgent re-entry within a short time of launch. To date, there are no reliable ground-based tests to predict who will be affected, little knowledge of how to prevent the disorder once in space, and no fully acceptable means of treating the symptoms once they appear.

Torso rotation (TR) is a motor strategy in which the head is turned by rotating the torso and the eyes move with the head. Continuous torso rotation on the ground often leads to motion sickness. In the weightlessness of parabolic or orbital flight, many individuals have been seen to move their heads and upper bodies as a unit. Sometimes this is intended to combat motion sickness by reducing head movements, but often it precedes symptoms. Regardless, if deliberate TR on the ground causes motion sickness, inadvertent TR in space should have the same effect. If symptoms are already present, it would actually make them worse, but with a large enough delay that the cause-effect relationship might not be noticed.

Based on a series of inter-related, ground-based experiments (summarized in Bouyer, 1995), the underlying mechanism of torso-rotation-induced motion sickness seems to be excessive vestibular suppression leading to altered central processing of vestibular inputs. While transient cancellation of the vestibulo-ocular and other reflexes is a normal part of every gaze refixation that includes head movement, torso rotation increases the "duty cycle" of this process to an abnormally high level. This leads to changes that are not immediately reversible and that seem to be interpreted as a temporary vestibular malfunction. Vestibular pathology in general usually leads to severe motion sickness.

OBJECTIVES

The broad goal of the Torso Rotation Experiment (TRE) was to determine if astronauts adopt torso-rotation-like motor strategies while in weightlessness and if these changes carry over to the immediate post-flight period. Specifically, we wanted to learn if the eyes were stabilized relative to the outside world during spontaneous, self-generated head rotations (normal behaviour, utilizing vestibular reflexes) or relative to the head (requiring suppression).

METHODS

Data Acquisition

The equipment used to monitor eye, head and torso rotations is shown in Figure 1. It consisted of surface electrodes for yaw-axis electro-oculogram (EOG) recording and two separate electronics units that were mounted securely on the head and upper back, all interconnected with flexible cables. Removable data packs were used to store the results of each experiment session. There were no external controls on the electronics units as they were turned on, self-tested and programmed each time a data pack was inserted. Cues to the operator were provided by a single LED and a beeper and included codes for normal operation, the need for an EOG calibration, the end of the experiment, a low battery condition or an electronic problem.

The head-mounted unit contained a 3-axis angular velocity transducer (maximum 1000°/sec), an EOG pre-amplifier, an isolation amplifier for electroshock protection and a thermistor to monitor transducer temperature. The back-mounted unit contained another 3-axis rate sensor (maximum 300°/sec), a temperature sensor, a calendar clock, an auto-resetting EOG amplifier, other signal

conditioning amplifiers, anti-aliasing filters, a 12 bit analog to digital converter, a Motorola 68000 series microprocessor and a battery pack. Each data module contained 5 megabytes of flash EPROM data storage and 32 kilobytes of conventional EPROM program storage. This was sufficient for 43 minutes of continuous data acquisition.

Figure 1. Free-floating subject performing Torso Rotation Experiment during the Life and Microgravity Spacelab mission.

EOG signals were filtered (low pass below 200 Hz using 8 pole Bessel filter) and sampled at 512 Hz. Head yaw velocity was filtered (low pass below 50 Hz using 2 pole Bessel filter) and sampled at 128 Hz. All other rate sensor channels were filtered in a similar fashion but sampled at 64 Hz. It should be noted that measured head and upper torso angular velocities were almost totally restricted to less than 10Hz.

In addition to the direct measurement of eye, head and body rotations, subjects were videotaped whenever they were wearing the TRE equipment. Full coverage was obtained during pre and post-flight test sessions and most in-flight activity was also recorded. These data assisted interpretation of the EOG and rate sensor signals and were used to determine what the subject had been doing when unusual movement patterns were detected.

Pre and Post-Flight Procedures

Ground-based testing used the same type of data acquisition system as the flight experiment. The subject began by standing in the middle of a 3 metre diameter circle. EOG calibration was carried out by staring at a single, distant target and rotating the head to both sides in a series of short steps. Pure yaw and pure pitch rotations were also performed to provide information necessary for transforming rate sensor information to the anatomical axes during data analysis. Then, following tape-recorded cues, each subject performed a pseudo-random series of gaze refixations to eye-level targets located every 22.5° along the circle. During 6 minutes, 19 refixations of 22.5° to the left were performed, 14 of 22.5° to the right, 19 of 45° to the left, 27 of 45° to the right, 22 of 90° to the left and 20 of 90° to the right. Instructions were to look at each of the indicated targets in turn, using whatever combination of eye, head and body movements felt most comfortable and natural. The session ended with another series of calibration maneuvers.

In-Flight Procedures

Test sessions in weightlessness were less structured, consisting of passive monitoring of eye, head and body rotations during spontaneous, ad lib crew activity. This was possible because a relatively large proportion of naturally occurring gaze refixations occur about the yaw axis (i.e. to the left or right), so an acceptable data yield could be achieved even though precise EOG recordings can only be obtained for lateral eye movements. Each session began with the subject unstowing and putting on the TRE equipment and inserting a data module into the back-mounted unit to begin data acquisition. This was accomplished with the assistance of a second crewmember. For the following 43 minutes, the subject performed other activities, stopping only briefly every 5 minutes to re-calibrate the EOG and rate sensor recordings using methods similar to those employed on the ground. When the TRE equipment signalled that the data module was full, it was pulled out and the equipment was removed.

Motion Sickness Reports

After the completion of each experimental session, subjects were requested to complete a motion sickness report. This consisted of a list of seventeen signs and symptoms of motion sickness which could be rated on a none / mild / moderate / severe basis. It also included a numerical rating of overall discomfort level, ranging from 0 (all is well) through 10 (unhappy but can control) to 20 (out of control and vomiting). Both individual symptoms and overall discomfort were to be described as they had occurred before, during and after the Torso Rotation Experiment.

Data Reduction

For technical reasons, the net gain of the circuits used to amplify EOG signals was 2361 in three TRE units and 1000 in the remaining one. In the case of data obtained with the latter unit, all recorded eye movements were multiplied by 2.361 and appropriate amplifier re-sets were added to make the results conform to the more general standard.

The data from each individual experimental session were then computer-processed to reduce noise and to automatically identify saccades, amplifier resets, higher frequency motion artifacts, eyelid blinks and noise in the form of electromyographic activity and electromagnetic interference. The digital signal processing technique employed was a quadrature mirror filter pair with thresholding. The result was that smaller, high frequency signals were considered to be noise and were removed. Larger, high frequency signals were considered to be events and were flagged for future exclusion. Lower frequency signals were generally accepted by the processing. As a consequence, temporary drifts such as those caused by disturbances of EOG electrode half-cell potentials had to be identified and extracted manually at a later stage of data reduction. Figures 2 and 3 are examples of ground-based and flight results respectively, after processing. Figure 4 illustrates how saccades that occurred with the head fixed, and eye blink artifacts, were removed from the data.

After the first phase of automated analysis was complete, human pattern recognition ability was used to identify all EOG and rate sensor calibrations in the data files. These distinctive movements, partly illustrated in Figure 5, occurred at the beginning and end of each ground-based session and on nine or ten occasions during the in-flight experiments. In all cases, data recorded before the first calibrations were then flagged for future exclusion. For ground-based experiments only, all results after the last calibrations were also marked for trimming. Finally, a few short-duration, low frequency drifts were identified in the EOG signal and excluded from further analysis. These were usually the result of the subject rubbing or adjusting the surface electrodes.

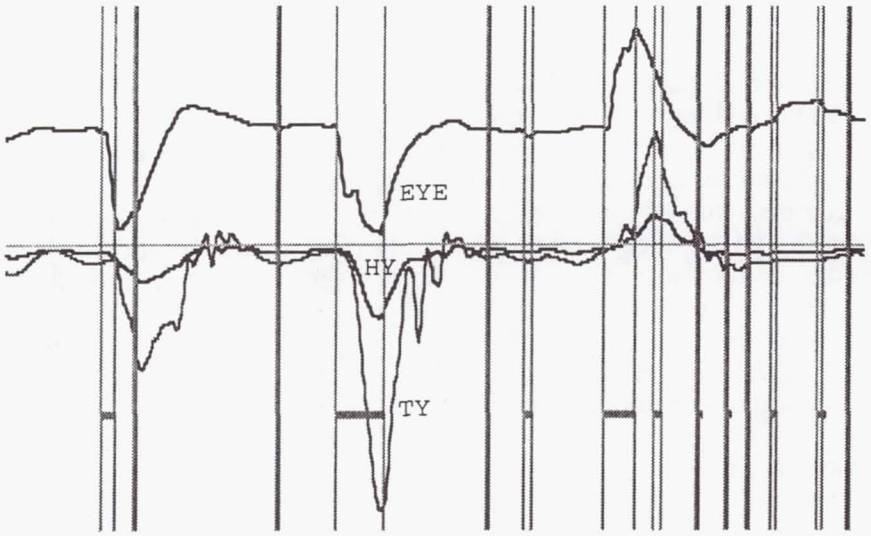

Figure 2. These data were recorded 30 days before launch and consist of three consecutive gaze refixations of about 45°. In this and the following 3 figures, eye position, head yaw-axis velocity and torso yaw-axis velocity have been labelled EYE, HY and TY respectively. TY always appears bigger than HY because a more sensitive rate sensor was used to record upper torso rotations. The vertical lines connected by horizontal bars represent sections trimmed out by the computer. Each record is 10 seconds in duration.

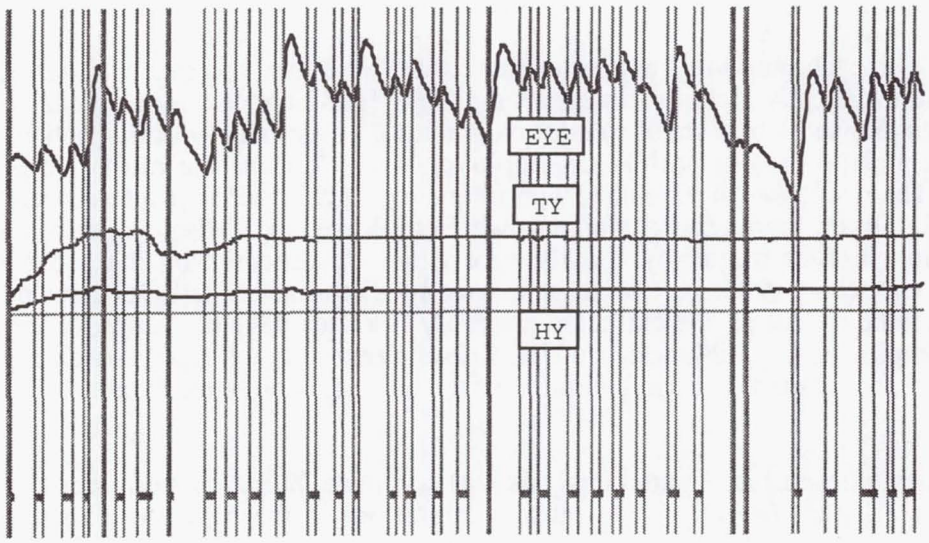

Figure 3. This data segment was recorded on Flight Day 15 and is an example of visual tracking during a prolonged, yaw-axis rotation. Rotation rate is approximately 90°/sec and is particularly steady during the last 7 seconds. This is easily accomplished in weightlessness but would require a servo-controlled rotator on the ground.

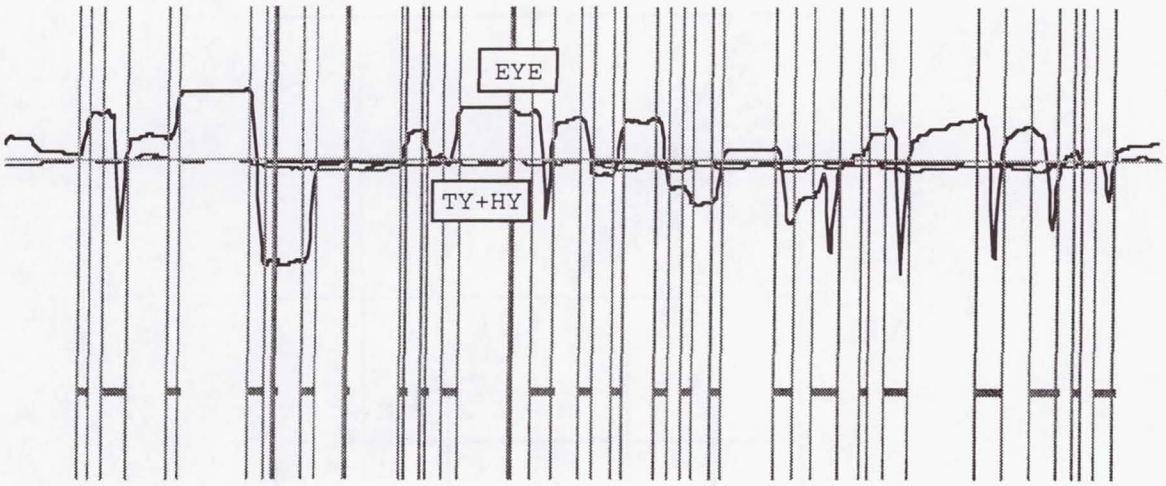

Figure 4. This is an example of saccadic eye movements and eye blink artifacts recorded when the head was not moving. The computer has identified and extracted all of them.

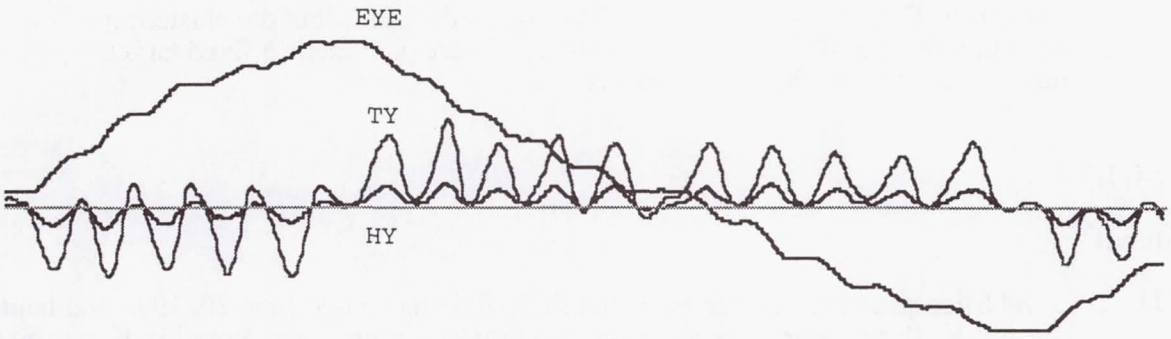

Figure 5. The step-wise pattern of torso, head and eye movements associated with each EOG calibration maneuver was easy to identify. Beyond their obvious use in relating eye to head movements, these segments had to be excluded from further analysis because the subjects were deliberately staring at an external target.

Digital signal processing continued with the definition of the three dimensional unit vector generated as the head was rotated during the EOG calibration maneuvers. On the basis of this vector, a small amount of error tolerance and a velocity threshold of 15°/sec, all periods of "pure" head yaw rotation were identified. Eye position as recorded by electro-oculography was then converted to eye velocity using a 151 term ideal differentiator with windowing and the resulting signal re-filtered using the same noise extraction procedure as before. Finally, EOG gain was calculated for each session by plotting eye velocity as a function of head velocity during EOG calibration maneuvers and by performing a linear regression fit to the resulting graph (Figure 6). The average R^2 value across all pre, in and post-flight sessions was 0.87±0.17.

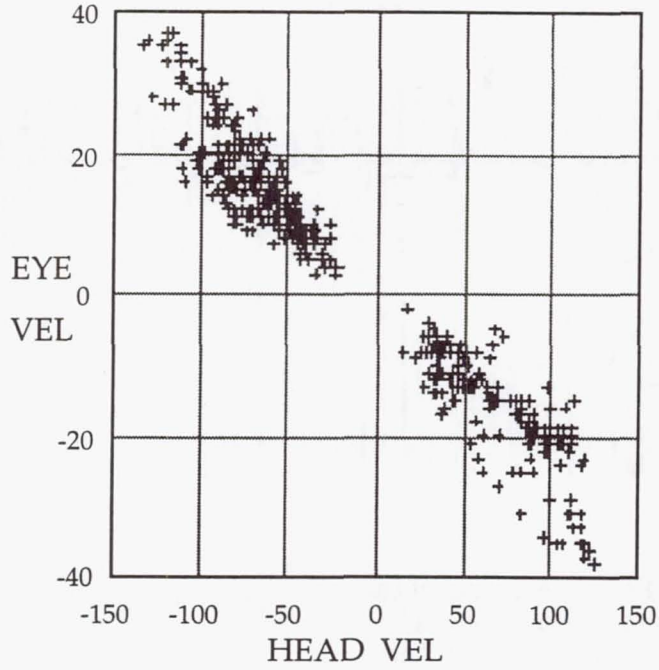

Figure 6. Eye velocity versus head velocity during an EOG calibration maneuver. Both measures are plotted in engineering units, but the clustering of points along a -45° slope indicates the eyes were pointing at a fixed target during the step-wise head movements.

RESULTS

General

The Life and Microgravity Spacelab mission (STS-78) launched on June 20, 1996 and landed on July 7. During the flight, four crewmembers participated in the Torso Rotation Experiment, acting as subjects and providing assistance to each other as required. None had been in space before. Their test schedule has been summarized in Table 1. All four were also tested on the ground at 90, 60 and 30 days before flight, on landing day, and 2 and 5 days after landing.

Flight Day	Subjects Tested
1	1,2,3,4
7	1,2,3,4
12	2,3
13	1
15	2,3,4

Table 1. In-flight testing schedule for TRE subjects.

In-flight testing was carried out as planned with only two minor exceptions. Subject 4 had to install a new battery pack after 16 minutes of his Flight Day 15 test. Subject 2 had to use the alternate set of TRE equipment when he received an "electronic failure" message at the beginning of his Flight Day 15 experiment. Neither problem could be reproduced after landing but the latter one was probably related to a reversible flash memory anomaly. In any case, they had no impact on the experiment. All ground-based sessions were completed without incident.

Data yield following the reduction process was consistent and as anticipated. On average, 0.73±0.19 minutes remained out of the 6 minute ground-based tests and 0.84±0.27 minutes out of the 43 minute in-flight experiments. The much lower in-flight yield (on a percentage basis) was expected because of the less structured nature of the task.

Pre-Flight

Following the data reduction process described above, the remaining results consisted of periods during which the subject was performing pure yaw-axis head movements, with all calibration maneuvers, saccades, artifacts and periods of inactivity excluded. It was then possible to determine if the eyes were being stabilizing relative to the outside world or relative to the body during self-generated head rotations by plotting eye velocity relative to head velocity on a point-by-point basis.

As an aid to interpreting these graphs, Figure 7a summarizes where data points would lie under various conditions. If the subject's eyes were always stabilized relative to the outside world, eye velocity (relative to the head) and head velocity (relative to space) would be equal but in opposite directions. By contrast, if the eyes were always stabilized relative to the body, only head velocity would change. In real life, one might expect a tendency to move back and forth between the two strategies (arrows), with a change in weighting towards the latter in the presence of increased vestibular suppression. To detect these potential changes, the plots have been divided into seven sectors as shown in Figure 7b and the number of data points calculated for each sector.

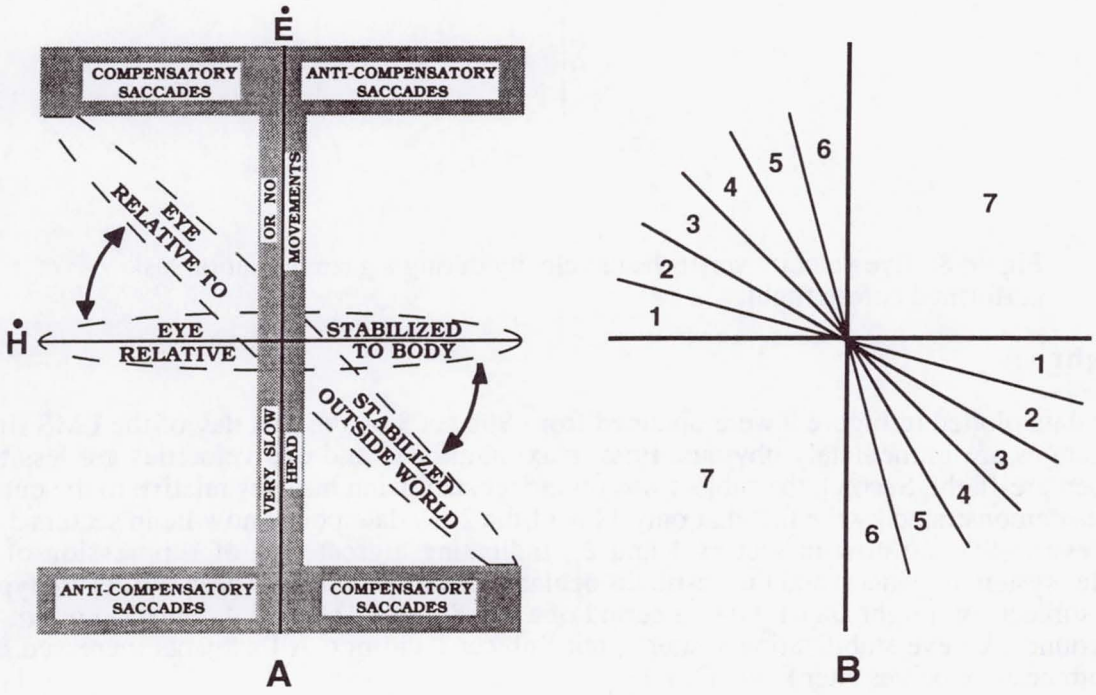

Figure 7. (a) Theoretical scatter diagrams of eye velocity as a function of head velocity. The shaded area indicates where the computer would have identified and trimmed compensatory, anti-compensatory and head-fixed saccades, and periods of very little or no head movement. (b) Division into sectors for further analysis.

Figure 8 is an example of results obtained 30 days before flight from Subject 3. Eye velocity has been plotted as a function of head velocity, up to a maximum of 400°/sec. A quick inspection of the graph suggests that the subject was usually stabilizing his eyes relative to the outside world as he performed the required series of gaze refixations. Indeed, 72% of the 3049 data points plotted here fall into sectors 3 and 4, close to the 45° slope that would indicate perfect stabilization. Note also that less than 16% of the data points lie in sector 7. These results are typical of Subjects 2, 3 and 4. Subject 1 was similar to the others in most respects, but he seemed less inclined to stabilize his eyes relative to the outside world.

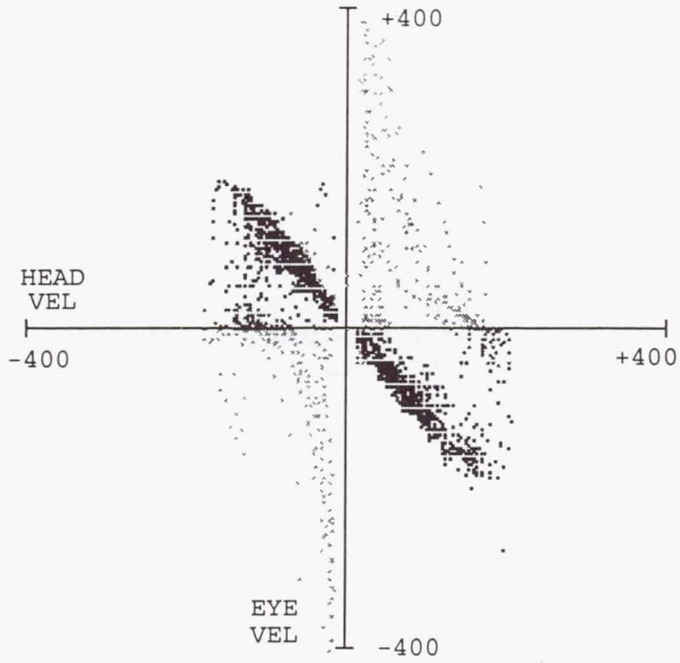

Figure 8. Eye velocity versus head velocity during a gaze refixation task performed before flight.

In-Flight

The data plotted in Figure 9 were obtained from Subject 3 on the first day of the LMS flight. Two changes are immediately obvious. First, maximum head and eye velocities are less than those seen pre-flight. Second, the subject was no longer stabilizing his eyes relative to the outside world, as demonstrated by the fact that only 11% of the 2419 data points now lie in sectors 3 and 4. However, 69% are now in sectors 1 and 2, indicating a great deal of suppression of the vestibular system in general and the vestibulo-ocular reflex in particular. These results are typical of all 4 subjects on Flight Day 1. Over a period of days, Subjects 2, 3 and 4 tended to return to a more ground-like eye stabilization strategy, but Subject 1 did not. All subjects increased their maximum head velocities after Flight Day 1.

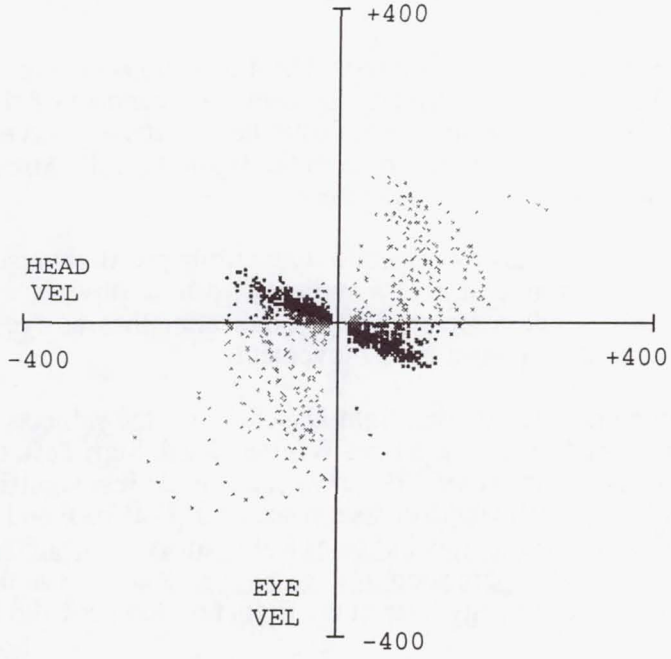

Figure 9. Eye velocity versus head velocity during ad lib, in-flight activity.

Post-Flight

Figure 10 is an example of results obtained from Subject 3 on landing day. The data are similar in every respect to those obtained pre-flight from the same subject (Figure 8), indicating a rapid return to a normal pattern of eye stabilization. This was true of all subjects, although the strategy adopted by Subject 1 was still a bit unusual, as had been noted pre-flight.

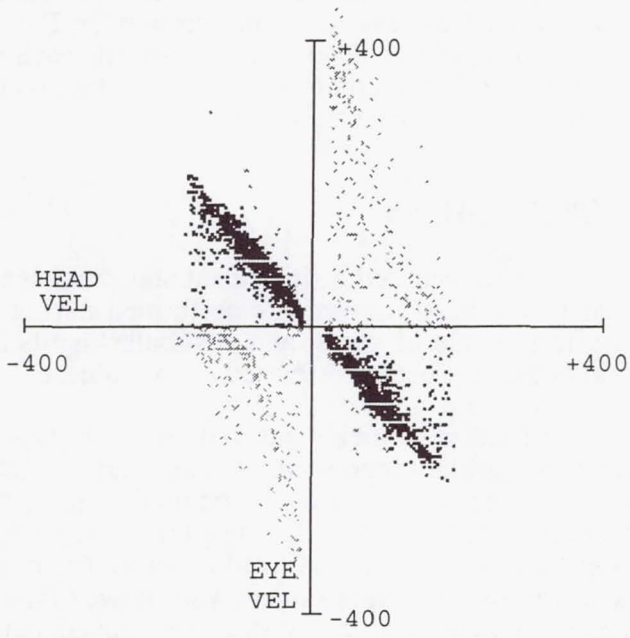

Figure 10. Eye velocity versus head velocity during a gaze refixation task performed after flight.

Combined

Figure 11 combines all results obtained from the 4 test subjects. The number of data points falling in each of sectors 1 to 4 has been expressed as a percentage of the total points for that subject and session, and plotted as a function of time before, during and after flight. A different symbol has been used for each subject, as noted in the figure legend. Almost no data points ever fell in sectors 5 and 6, so these results have not been included.

Although each individual had his own unique style during pre-flight testing, the control results were quite consistent both within and across subjects, with no obvious effect of learning. The majority of data points usually fell in sectors 3 and 4, indicating that the eyes were being stabilized relative to the outside world during most head movements.

The situation changed dramatically on Flight Day 1. When the subjects were compared to the means of their 3 pre-flight trials using the Mann-Whitney Rank Sum Test, there was a significant increase in the number of points in sector 1 (P=0.014), a slightly less significant increase in sector 2 (P=0.029), a statistically insignificant decrease in sector 3 (P=0.100) and a significant decrease in sector 4 (P=0.029). Taken together, this indicates a shift away from stabilizing the eyes relative to the outside world and toward suppression of vestibular reflexes. As anticipated, Subjects 2, 3 and 4 returned to a more normal strategy later in the flight but Subject 1 did not.

Also as expected, the post-landing patterns of all subjects were closely similar to those recorded pre-flight. This was true even for Subject 1, who continued to demonstrate more movements falling in sectors 1 and 2 and fewer in sector 4, indicating consistently lower usage of vestibular stabilization mechanisms.

Motion Sickness

The crewmembers taking part in this experiment were only minimally affected by space motion sickness. Subject 1 reported no specific symptoms but indicated that he felt worse when head "down" on Flight Day 1. Subject 2 was the most affected, experiencing mild cold sweating and malaise and moderate stomach awareness before performing the Torso Rotation Experiment on Flight Day 1. Subject 3 indicated that he developed a headache each time he wore the TRE head unit. On Flight Day 1, however, his discomfort preceded putting on the equipment. Subject 4 did not develop symptoms at any time during the flight.

DISCUSSION AND CONCLUSIONS

The present experiment has demonstrated a significant and consistent increase in gaze slip during spontaneous, self-generated head movements performed during the first day of space flight. This implies a less effective use of visual and vestibular inputs at that time and is not normal behaviour, regardless of the task being performed by the subject.

It is important to note that head velocities measured on Flight Day 1 were mostly below 100°/sec, suggesting a torso-rotation-like suppression of visual and vestibular mechanisms rather than a simple decrease of VOR gain resulting from altered otolith stimulation. In the latter case, visual tracking should have been effective in maintaining gaze on target. It is also significant that all three subjects who demonstrated strong eye stabilization before flight returned to this strategy within seven days of launch, whereas the single subject who showed the most pre-flight slip did not. Furthermore, all subjects reverted to their normal strategies immediately after landing with no need for re-adaptation. Taken together, these facts suggest that the mechanism responsible for the increased gaze slip is behavioral as opposed to a fundamental change in reflex function.

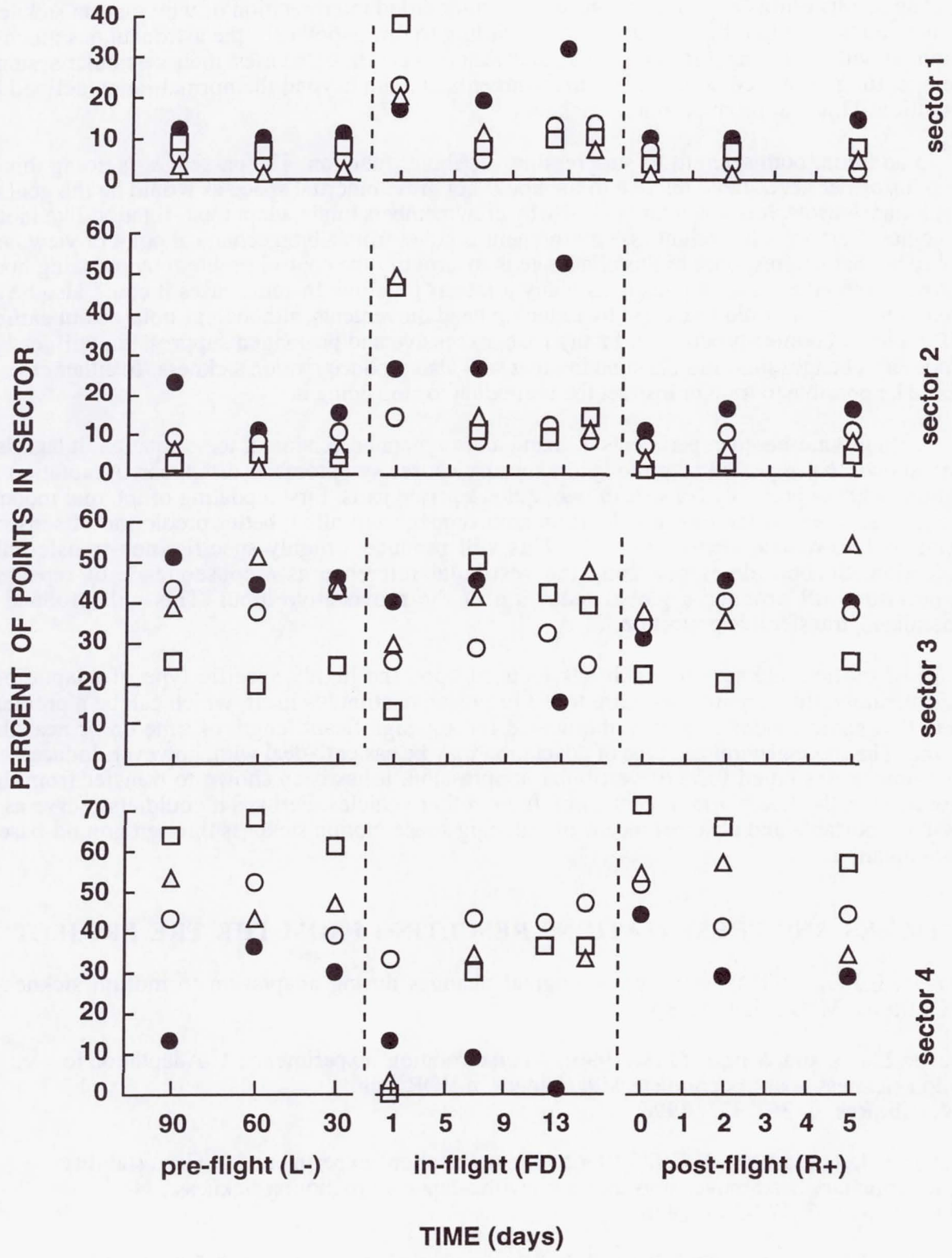

Figure 11. Percentage of data points falling into sectors 1 through 4 as a function of pre-flight, in-flight and post-flight time. Individual subjects have been identified by different symbols: Subject 1 (filled circles), Subject 2 (unfilled circles), Subject 3 (squares), Subject 4 (triangles).

The results of this experiment also support a modified interpretation of why motion sickness occurs and what might be done about it. According to this hypothesis, the astronaut has much in common with a passenger reading in the back seat of a car. In both cases, their vestibular systems are operating in altered acceleration environments that are beyond the normal range defined by evolution. This will produce motion sickness.

In addition, both seem to be suppressing vestibular function. The passenger is doing this to keep his or her gaze stable relative to the book, not gravitoinertial space as would be the goal of vestibular reflexes. It is not entirely clear why crewmembers might adopt torso-rotation-like motor strategies. Certainly the weightless environment is novel from a biomechanical point of view, and it may be that one response to this challenge is to simplify the control problem by reducing body degrees of freedom, i.e. stop using as many joints as possible. In some cases it could also be an attempt to control motion sickness by reducing head movements, although as pointed out earlier, this could be counter-productive. In any case, excessive and prolonged suppression will lead to temporary changes in vestibular function that will also produce motion sickness. In either case, it should be possible to train or instruct the individual to stop doing it.

In ground-based experiments utilizing an exaggerated version of torso rotation, it has also been shown that repeated or prolonged exposure causes symptoms to disappear. Adaptation to motion sickness probably consists of two, quite separate parts. First, updating of internal models as a consequence of the new acceleration environment will allow better prediction of sensory inputs and so reduce sensory conflict. This will produce a highly specific, non-transferable protection. Second, de-emphasizing the vestibular reference as a consequence of repeated suppression will produce a global reduction of the provocative input. This will produce a generalized, transferable protection.

Most motion sickness research has focused upon the highly specific type of adaptation. Unfortunately, this requires exposure to the provocative stimulus itself, which can be a problem when that environment cannot be duplicated for any significant length of time on or near the ground. The more generalized type of adaptation may be easier to deal with, however. Induced by a previously unstudied form of vestibular suppression, it has been shown to transfer from the laboratory to the real world of cars, aircraft and other vehicles. Perhaps it could also serve as a low-cost, portable and efficient means of reducing space motion sickness through ground-based pre-adaptation.

ARTICLES AND PRESENTATIONS RESULTING FROM THE TRE PROJECT

Bouyer, L.J.G. (1995). Neurophysiological changes during adaptation to motion sickness. Ph.D. thesis, McGill University.

Bouyer, L.J.G. and Watt, D.G.D. (1996). "Torso rotation" experiments; 1: Adaptation to motion sickness does not correlate with changes in VOR gain.
J. Vestib. Res. 6: 367-375, 1996.

Bouyer, L.J.G. and Watt, D.G.D. (1996). "Torso rotation" experiments; 2: Gaze stability during voluntary head movements improves with adaptation to motion sickness.
J. Vestib. Res. 6: 377-385, 1996.

Bouyer, L.J.G. and Watt, D.G.D. (1996). "Torso rotation" experiments; 3: Effects of acute changes in vestibular function on the control of voluntary head movements.
J. Vestib. Res. 6: 387-393, 1996.

Bouyer, L.J.G. and Watt, D.G.D. (1997). "Torso rotation" experiments; 4: The role of vision and the cervico-ocular reflex in compensation for a deficient VOR. Submitted, Journal of Vestibular Research.

Watt, D.G.D. (1997). Visual-vestibular weighting and its relationship to space motion sickness. Submitted, Cognitive Brain Research.

Bouyer, L.J.G. and Watt, D.G.D. Effects of acutely altered vestibular function on the control of voluntary head movement. Proceedings, 23rd Annual Meeting, Soc. for Neuroscience, Washington, November, 1993.

Watt, D.G.D. and Oman, C.M. Motion sickness susceptibility testing using torso rotation. Proceedings of Spacebound '94 Symposium, Montreal, May 1994.

Watt, D.G.D. and Bouyer, L.J.G. The "torso rotation" model of motion sickness adaptation: (1) does the loss of symptoms correlate to changes in the VOR? Proceedings, Twenty-Fourth Annual Meeting, Soc. for Neuroscience, Miami Beach, November 1994.

Bouyer, L.J.G. and Watt, D.G.D. The "torso rotation" model of motion sickness adaptation: (2) does the loss of symptoms correlate to changes in overall gaze stability? Proceedings, Twenty-Fourth Annual Meeting, Soc. for Neuroscience, Miami Beach, November 1994.

Bouyer, L.J.G. and Watt, D.G.D. Improvement in gaze stability during adaptation to "Torso Rotation": (1) visual versus non-visual compensatory mechanisms. Proceedings, Twenty-Fifth Annual Meeting, Soc. for Neuroscience, San Diego, November 1995.

Watt, D.G.D. and Bouyer, L.J.G. Improvement in gaze stability during adaptation to "Torso Rotation": (2) cervico-ocular reflex. Proceedings, Twenty-Fifth Annual Meeting, Soc. for Neuroscience, San Diego, November 1995.

Paquet, N. and Watt, D.G.D. The effect of vestibular suppression on the ability of humans to sense linear head displacements in the absence of vision. Proceedings, Congrès des Sciences Neurologiques du Québec, Quebec City, September 1996.

Watt, D.G.D. and Paquet, N. Locomotor errors caused by vestibular suppression. Proceedings, 12th Man in Space Symposium, Washington, June 1997.

Paquet, N. and Watt, D.G.D. Vestibular suppression induced by torso rotation impairs linear locomotion in humans. Proceedings, Twenty-Seventh Annual Meeting, Soc. for Neuroscience, New Orleans, October 1997.

Watt, D.G.D. Torso Rotation Experiment. Life and Microgravity Spacelab Mission, Review of Science Results, Montreal, August 1997.

NON-TECHNICAL SUMMARY

Torso rotation (TR) is a style of moving in which the head is turned by rotating the torso and the eyes move with the head. Continuous TR on the ground usually leads to motion sickness, probably because of excessive suppression of the balance organs (vestibular system). In weightlessness, many individuals also move their heads and upper bodies as a unit. If deliberate TR on the ground causes motion sickness, inadvertent TR in space should have the same effect.

Using equipment attached to the head and upper back, rotational movements of the eyes, head and upper torso were monitored while four astronauts performed other, active tasks. Post-flight analysis demonstrated an abnormally large amount of gaze slip on the first day of flight, indicative of balance organ suppression. A more normal pattern was seen 6 days later.

The results suggest that the astronaut has much in common with the passenger reading in the back seat of a car. In both cases, their balance organs are operating in altered acceleration environments that are beyond the normal range defined by evolution. This will produce motion sickness. In addition, both seem to be suppressing the balance organs. (The passenger is doing this to keep his or her gaze stable relative to the book, not the outside world as would be the goal of inner ear reflexes). Excessive and prolonged suppression will lead to temporary changes in balance organ function that will also produce motion sickness.

Potentially, astronauts could be trained to avoid balance organ suppression, just as car sickness can be reduced by not reading while moving. Alternatively, repeated exposure to exercises that deliberately supress balance organ function on the ground might be used as a means of pre-adapting before flight.

JSC Human Life Sciences Project

E920 - Effect of Weightlessness on Human Single Muscle Fiber Function

Principal Investigator:

Dr. Robert Fitts
Marquette University
Milwaukee, Wisconsin

FINAL REPORT LMS Flight Experiment E920

TITLE: Effect of Weightlessness on Human Single Muscle Fiber Function

Principal Investigator: Robert H. Fitts, Ph.D., Marquette University, Milwaukee, WI

Co-Investigator: D.L. Costill, Ball State University, Muncie, IN

Co-Authors: S.W. Trappe, T.A. Trappe, D.A. Riley, and J.J. Widrick

(1) Experiment Objectives. The primary objectives of this experiment were to: determine the extent to which zero-g alters human performance and skeletal muscle function; study the effects of zero-g on single fiber function to include an evaluation of the physiological and biochemical properties of the individual slow- and fast-twitch fibers of human skeletal muscle; elucidate the cellular mechanisms of the observed zero g-induced alterations in single fiber function; and assess the role of an altered cellular capacity in eliciting the zero g-induced reduction in both skeletal muscle and whole body performance and physical work capacity.

(2) Background. Previous studies on Skylab, Spacelab (SLS-1 and SLS-2), and the Russian Cosmos and Mir missions have documented that weightlessness produces significant muscle wasting particularly in the antigravity muscles. However a comprehensive description of microgravity induced changes in human skeletal muscle structure and function and the underlying cellular mechanisms contributing to the altered function have not been established. Consequently, the prime objectives of this project was to study of the effects of weightlessness on limb skeletal muscle function, and establish the cellular causes of the reduced functional capacity of skeletal muscle.

(3) Methods of Data Acquisition and Analysis.

Subjects. Four male crew members from STS-78 (LMS) were tested as part of this research. The crews average age, height, and weight were 42.8 ± 3.8 yr., 85.7 ± 6.2 kg, and 182.9 ± 7.5 cm, respectively. They were all healthy individuals and participated in moderate physical activities; i.e., running, swimming, or weight lifting. All subjects were informed of the risks and benefits associated with the research and gave their written consent in accordance with the Institutional Review Board's at Ball State University, Marquette University, and National Aeronautical and Space Administration.

Measurement of Oxygen Consumption. Submaximal and maximal exercise was performed on a semi-recumbent electronically resisted cycle ergometer. Two separate incremental exercise protocols were used to study these men. The first was a continuous exercise test to volitional exhaustion (VO_2 max), which consisted of four 3 min stages at 50, 100, 150, and 175 watts(w) followed by 25 w increments every two minutes until exhaustion. The second protocol, a submaximal exercise test, followed the same incremental sequence, but was terminated when the subjects attained a workload that was calculated to demand 85% of the VO_2 max determined during the L-60 testing. The VO_2 max tests were performed on L-60 and L-15, and R+4 and R+8. While the submaximal tests were conducted on L-30, flight days 2, 8, and 13, and R+1 and R+5.

During the ground based testing respiratory exchange was monitored throughout the test using a computer based system that incorporated a low-resistance gas meter, a 3.5 liter mixing chamber, 3.49 cm I.D. hoses, a Hans Rudolph breathing valve (2700 series) and electronic O_2 and CO_2 analyzers. The analyzers were calibrated before each test with gases of known concentrations. Heart rates were measured throughout the tests using radiotelemetry. In-flight testing utilized an on-board computer (LSLE Micro), mass spectrometer (GASMAP), a Hans Ruldolph breathing valve, Fleisch pneumotach #3, 3.5 liter mixing chamber, and 3.49 cm I.D. hoses. The mass spectrometer was calibrated before each test with O_2 and CO_2 of known concentrations. The Haldane transformation was used to calculate respiratory exchange using the predetermined cabin O_2, CO_2, N_2, and H_2O data. Oxygen uptakes and heart rates during the submaximal exercise bouts were used to calculate each crew member's oxygen uptake at maximal heart rate (VO_2@ HRmax). As anticipated, these values were closely related to the subject's measured VO_2 max ($r = 0.98$).

Calf Muscle Testing. Calf muscle performance was determined using a Torque-Velocity Dynamomter (TVD) designed by ESA specifically for the LMS mission. During testing, the subject was in the supine position using a platform/seat and harness to prevent extraneous movement. The lower leg was immobilized at 160 degrees with the foot secured to the foot plate using Velcro straps. The shaft of the dynamometer (Laboratory of Biomechanics, Zurich, Switzerland) was aligned with the axis of rotation about the ankle. The length of the leg restraint lever was adjusted to accommodate different limb lengths.

The right calf muscle of each crew member was tested. The calf muscle strength protocol consisted of three parts: (1) maximal isometric strength at ankle angles of 80, 90, and 100 degrees, (2) force-velocity measurements at 0.52, 1.05, 2.09, 3.14, 4.19, and 5.24 rad/s, and (3) a fatigue test consisting of 30 maximal contractions at 3.14 rad/s. With rest periods included, the total test time was approximately 30 minutes. At each isometric ankle angle, subject's performed two 50% efforts for warm-up followed by one maximal effort lasting 5 seconds. At isokinetic test velocity, a series of four warm-up contractions at approximately 50% effort were performed to familiarize the subjects to the test velocity and movement. Following this warm-up, subjects were asked to perform four maximal plantar flexion contractions at the selected angular velocity. A two-minute rest period occurred between each test velocity. Peak torque was taken as the highest value obtained for each of the four contractions, with the highest value used for analysis. Following a five-minute rest period, subjects performed the 30 maximal contractions without interruption (fatigue test). A contraction was performed at a rate of approximately 1 per s.

Pre-flight testing included four sessions conducted at L-90, L-60, L-30, and L-15. In-flight measurements of calf muscle contractile characteristics were conducted on flight day (FD) 2/3, 8/9, and 12/13. Due to the mission timeline, some crew members performed the TVD protocol on FD 2, while other crew members performed the protocol on FD 3 (the same scenario occurred on FD 8/9 and FD 12/13). These two-day testing sessions were considered together as one session. Post-flight (recovery) TVD testing was conducted on R+2, and R+8.

Cellular Analysis of Single Fiber Function:

(a.) Biopsy Procedure. Muscle biopsy samples were obtained from the gastrocnemius and soleus muscles 45 days before launch (L-45) and within 3 hours after landing. Pre- and post-flight muscle biopsies were placed on saline soaked gauze and divided into several portions. One portion, used for the single fiber functional experiments was immediately submerged in cold skinning solution and shipped overnight at 4°C to Marquette University where upon arrival it was stored at -20°C. A second portion was pinned at a mild stretch and immersion fixed in a 0.1 M cacodylate buffer (pH 7.2) consisting of 4% glutaraldehyde and 2% paraformaldehyde with 5mM calcium chloride. This sample was shipped overnight at 4°C to the Medical College of Wisconsin for osmium post fixation and embedding for electron microscopy.

(b) Single Fiber Functional Experiments. The free Ca^{2+} concentration of the relaxing and activating solutions were pCa 9 (where pCa = -log free [Ca^{2+}]) and pCa 4.5, respectively.
A single fiber segment was isolated from a muscle bundle, transferred to an experimental chamber, and mounted between an isometric force transducer (Cambridge Model 400; Cambridge Technology, Inc., Watertown MA) and a DC position motor (Cambridge Model 300B; Cambridge Technology, Inc.). The experimental apparatus was attached to the stage of an inverted microscope during the experiments. Sarcomere length was adjusted to 2.5 um and the fiber segment length (FL) was

recorded. A Polaroid photograph was taken of the fiber while it was briefly suspended in air and fiber width was measured at three points along the photo. The mean of these measurements was defined as fiber diameter by assuming the fiber takes on a circular cross-section when suspended in air. The fiber was activated by transfer from relaxing solution into an adjacent chamber containing activating solution. These solutions were maintained at 15°C throughout data collection. Output from the force transducer and position motor were directed to a digital storage oscilloscope before being amplified and interfaced to a personal computer. Custom software performed on-line analysis and stored data to disk.

Peak Force. Absolute peak force (in mN) was calculated as the difference between resting force, measured while the fiber was in relaxing solution, and the maximal force obtained during activation at pCa 4.5. Normalized peak force (in kN/m^2) was defined as the absolute peak force divided by the fibers cross-sectional area.

Maximal Shortening Velocity. Maximal shortening velocity (V_o) was determined by the slack test procedure as previously performed in this laboratory. The times required for the redevelopment of force following 5-6 imposed slack steps (each $\leq$ 20% of FL) were plotted against the corresponding slack length and the points fit with a linear least squares regression line. The slope of this line was V_o which was normalized to the length of the fiber and expressed as fiber length/s (FL/s).

Force-Velocity and Force-Power Relationship. To determine the force-velocity relationship, the fiber was fully activated and the position motor stepped to three sub-maximal force loads. After completion of the final step, the fiber was slacked to a length $\leq$ 20% of FL, transferred back into relaxing solution, and re-extended to its original FL. The entire procedure was repeated at various loads in order to produce a total of 15-18 force-velocity data pairs for each fiber. The computer calculated peak force and the average force and shortening velocity over the last half of each isotonic step. The force and velocity data points for an individual fiber were fit with the hyperbolic Hill equation using an iterative curve fitting algorithm.

Fiber Enzyme Analysis. Individual freeze-dried fibers (approx. 2mm long segments) were dissected from the freeze-dried fiber bundles. The fibers were divided into three sections, and used for the enzyme and substrate assays (0.5 ug), and fiber type determination on SDS gels (0.5 ug), respectively. Each segment was weighed on a quartz fiber balance, and the segment used for the enzyme analyses (0.5 ug) was added to 5 ul of a glycerol-KCL-detergent medium under mineral oil. After incubation for 2 hr at room temperature, the samples were transferred to a -80°C freezer and stored under vacuum. Since each assay required only 0.1-0.2 µl of extract, the 5 µl extract provided enough sample for duplicate assays for all enzymes of interest. We used enzymatic methods based on the fluormetric determination of pyridine mucleotides to assay the activity of the glucose handling and/or glycolytic enzymes phosphorylase, hexokinase, glycogen synthase, phosphofructokinase (PFK), and lactate dehydrogenase (LDH), and the oxidative enzymes citrate synthase, and β-hydroxyacyl-CoA dehydrogenase (βOAC). We also assayed the rate limiting enzyme in free fatty acid metabolism CoA-carnitine acyl transferase (CAT). The sensitivity of each reaction was increased by enzymatic cycling

Substrate Assays of ATP, Phosphocreatine (PC), Glycogen, and Lactate. As with the enzyme assays, the selected substrates were assayed using enzyme methods based on the fluormetric determination of pyridine nucleotides, and the sensitivity was increased by enzymatic cycling. The metabolic assays were made on 0.1 N NaOH extracts of each fiber segment. The 0.5 µg fiber sample was extracted in the NaOH for 30 min at 90°C, and the extract stored at 4°C under vacuum. For all substrates 0.1 µl of the

fiber extract was added to the appropriate reaction buffers. In the case of glycogen, ATP, and PC the reagent volume is 1 µl, while for lactate the reagent volume is 0.1 µl.

Fiber Type Determination. Following each experiment, fiber type was determined by myosin heavy chain identification of SDS-PAGE gels. A flat bed scanner with a transparency adapter was used to store an image of each gel on computer disk. Image analysis software (SigmaGel, Jandel Scientific Software) was used to quantify the relative levels of MLC_1, MLC_2, and MLC_3 in each fiber.

Electron Microscopy. Longitudinal and cross thin sections (~ 60 nm) were cut from bundles of fibers and stained with uranyl acetate and lead citrate before examination and photographing in a JEOL 100 CXII electron microscope. Myofilament densities and sarcomere length were determined from cross and longitudinal sections, respectively. Final myofilament density values were adjusted for variations in sarcomere length on an individual subject basis.

Data Analysis. Results are presented as mean ± SE. Data were analyzed using an ANOVA in which the treatment, i.e. the flight effect, was nested within subjects. When a significant treatment effect was observed, pre- to post-flight differences within an individual subject were evaluated with a two-tailed t-test. Statistical significance was accepted at $p < 0.05$.

(4) Flight Results.

Aerobic Capacity. Body weights of the crew averaged 4.1 kg less on R+0 than preflight (L-15). This represents a 4.7% decline in body weight. At R+4 and R+8 the average crew weight was still 2.5% and 1% below the pre-flight value, respectively. Oxygen uptake during submaximal exercise of 50, 100, 150, and 175 watts was similar during tests performed pre-flight, in-flight, and post-flight suggesting that cycling efficiency was unchanged by space flight. Maximal oxygen consumption (VO_2 max) was 10.3% and 4.8% lower on R+4 and R+8 compared to the pre-flight value (Table 1). Although in-flight testing was limited to 85% of VO_2 max, we used the oxygen uptakes and heart rates during the submaximal exercise bouts to calculate each crew member's oxygen uptake at maximal heart rate (VO_2 @ HRmax). As anticipated, these values were closely related to the subject's measured VO_2 max ($r=0.98$). Figure 1 illustrates the means (± SE) for VO_2 @ HRmax before, during, and after the flight. The crew's calculated VO_2 max was significantly lower on FD 8, FD 13, and R+1 compared to the pre-flight value.

TABLE 1. Maximal Oxygen Consumption (VO_2 max)

CREW	L-15	R+4	R+8
A	3.212	2.811	2.949
B	3.795	3.487	3.542
C	3.687	3.386	3.682
D	3.664	3.193	3.450
Mean ± S.D.	3.590 ± 0.258	3.219 ± 0.298	3.406 ± 0.319

FIGURE 1. VO_2 @ Hrmax

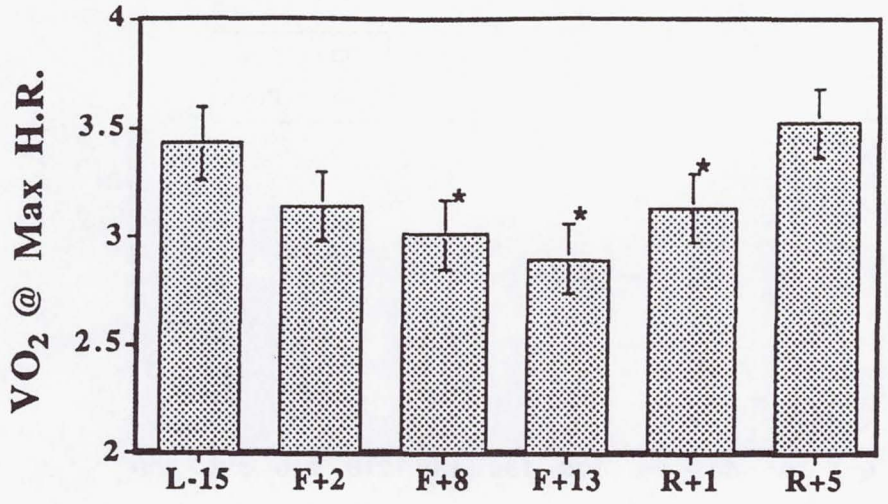

Calf Muscle Testing. Isometric calf strength values are shown in Table 2 The strength measurements on flight day (FD) 2/3 and FD 8/9 were considerably lower than all other testing session. Since the isometric values from FD 12/13 were equal to or slightly greater than pre-flight values, we conclude that technical difficulties with the TVD baseplate were responsible for the subpar performance of muscular strength on FD 2/3 and 8/9. Three of the four crew members had increased isometric strength on flight day 12/13 and R+2, and on R+8 all 4 crew members had isometric strength values that were greater than preflight values. No differences were observed in the torque-velocity relationship during or after the flight, and the pre-to-post relationship shown in figure 2 is representative of all testing sessions.

TABLE 2. Isometric Calf Muscle Strength in Newton·Meters (N·m)

Crew Member	Preflight	FD 2/3	FD 8/9	FD 12/13	R+2	R+8
A	207	99	113	211	230	229
B	193	175	187	201	207	206
C	249	145	221	220	213	270
D	159	102	177	208	171	160
Mean ± SE	202 ± 37	130 ± 37	175 ± 45	210 ± 8	205 ± 25	216 ± 46

FIGURE 2. Calf Torque Velocity Relationship

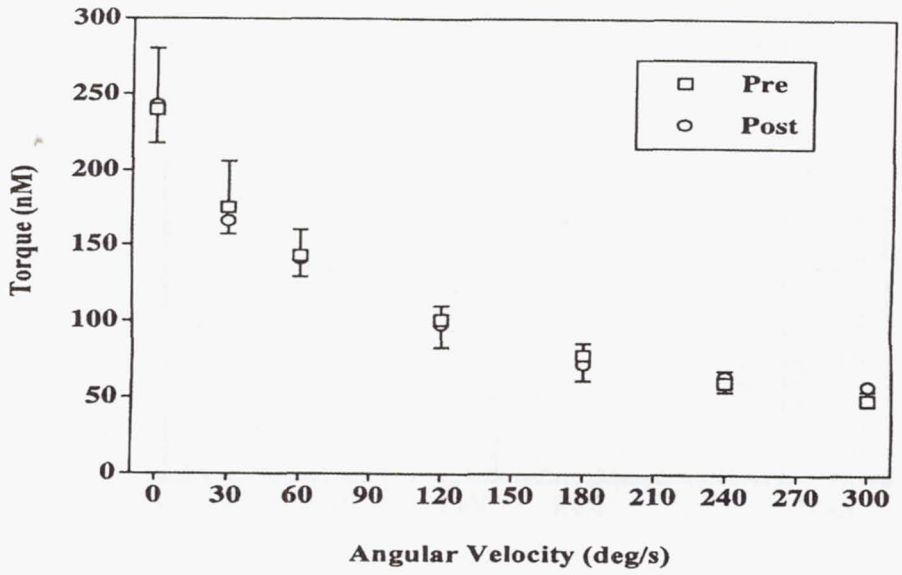

Fiber Type Composition. Enzyme histochemical analysis of the biopsies showed space flight to have no significant effect on the fiber type composition of either the gastrocnemius or the soleus muscles. The composition of the soleus was 85% slow type I and 15% fast type IIa, while the gastrocnemius was 62% type I, 23% type IIa, and 15% fast type IIx. In the fibers isolated for single fiber analysis, we did observe an increase in the percentage of hybrid (fibers containing both slow and fast myosin) and fast type IIa fibers and a decreased percentage of slow type I fibers in the soleus following space flight (Table 3).

Table 3. Myosin Heavy Chain Composition of Pre- and Post-Space Flight Soleus Fibers.

	type I		type I/IIa		type IIa	
subject	pre	post	pre	post	pre	post
A	97% (36)	93% (27)	0%	7% (2)	3% (1)	0%
B	91% (20)	76% (28)	0%	14% (5)	9% (2)	11% (4)
C	88% (37)	65% (24)	0%	0%	12% (5)	35% (13)
D	88% (22)	84% (27)	12% (3)	3% (1)	0%	13% (4)
mean	91% (115)	79% (106)	2% (3)	6% (8)	6% (8)	16% (21)

Values are the percent of the total number of fibers for each individual subject/treatment combination. Number of fibers in parentheses.

Fiber Diameter and Cross-sectional Area. Space flight induced a decline in the mean fiber diameter and cross-sectional area of the slow- and fast-twitch fibers in both the soleus and the gastrocnemius muscles. In 3 of the 4 crew members the decline in the diameter of the soleus slow type I fibers post flight was significant (Table 4). Subject B showed the greatest decline in this variable and in fiber cross-sectional area. In the gastrocnemius muscle, subjects B and D showed a decline in fiber diameter and cross-sectional area for both the slow type I and fast type IIa fibers, while subjects A and C showed either no change or a slight increase in these variables (Table 4).

Table 4. Diameter (μm) of pre- and post-spaceflight single muscle fibers.

	soleus type I			gastrocnemius type I			gastrocnemius type IIa		
subject	pre	post	Δ	pre	post	Δ	pre	post	Δ
A	98 ± 2	95 ± 2	-3	79 ±	84 ± 1	+6	86 ± 2	87 ± 3	+1
B	107 ± 3	87 ± 2	-19 *	90 ±	85 ± 2	-6	103 ± 3	95 ± 2	-8
C	92 ± 2	83 ± 2	-10 *	73 ±	74 ± 3	+1	62 ± 0	71 ± 2	+15
D	93 ± 2	86 ± 2	-8 *	80 ±	70 ± 2	-13	88 ± 1	82 ± 2	-7 *
mean	97 ± 1	88 ± 1		80 ±	79 ± 1		89 ± 2	83 ± 2	
subject	$p < 0.05$			$p < 0.05$			$p < 0.05$		
treatment	$p < 0.05$			$p < 0.05$			$p < 0.05$		

Values are μm (mean ± SE).. Δ indicates percent difference between pre- and post-flight values. p * < 0.05; † 0.10 > p > 0.05.

Peak Force of Individual Fast and Slow Fibers. Space flight induced a 22% and 17% decline in the peak force capacity of the soleus type I and gastrocnemius type IIa fibers. For the slow type I fibers of the soleus, all subjects showed a significant drop in force (Table 5). The primary reason for the decline in peak force (P_o) for the soleus and the gastrocnemius was the reduced fiber size, and for the gastrocnemius muscle the fiber atrophy explained the entire force loss. Consequently, for the gastrocnemius type IIa fibers the force loss was restricted to subjects B and D (Table 5) as these were the only crew to show atrophy of this fiber type (Table 4).

The subject variability in the response to the zero-g induced decline in force is perhaps best observed in Figure 3 which plots the average pre-flight force for each subject and fiber type versus the post-flight value. The figure also clearly shows that the force loss in the slow type I soleus fiber occurred in all 4 subjects, while for the gastrocnemius muscle fibers (type I and IIa) the decline in force was observed in subjects B and D but not A and C.

Table 5. Peak absolute force (mN) of pre- and post-spaceflight single muscle fibers.

	soleus type I			gastrocnemius type I			gastrocnemius type IIa		
subject	pre	post	Δ	pre	post	Δ	pre	post	Δ
A	1.03 ± 0.04	0.91 ± 0.04	-12 *	0.68 ± 0.02	0.74 ± 0.02	+9	0.89 ± 0.04	0.91 ± 0.04	+2
B	1.15 ± 0.05	0.69 ± 0.03	-40 *	0.75 ± 0.02	0.71 ± 0.04	-5	1.13 ± 0.05	0.92 ± 0.04	-19 *
C	0.86 ± 0.04	0.74 ± 0.03	-14 †	0.55 ± 0.04	0.53 ± 0.04	-4	0.45 ± 0.05	0.59 ± 0.02	+31
D	1.02 ± 0.04	0.79 ± 0.03	-23 *	0.74 ± 0.03	0.58 ± 0.02	-22 *	1.01 ± 0.03	0.85 ± 0.04	-16 *
mean	1.00 ± 0.02	0.78 ± 0.02		0.66 ± 0.02	0.66 ± 0.02		0.96 ± 0.04	0.80 ± 0.03	
subject	$p < 0.05$			$p < 0.05$			$p < 0.05$		
treatment	$p < 0.05$			$p < 0.05$			$p < 0.05$		

Values are mN (mean ± SE). Number of fibers per mean same as in Table 1. Δ indicates percent difference between pre- and post-flight values. * $p < 0.05$; † $0.10 > p > 0.05$.

FIGURE 3.

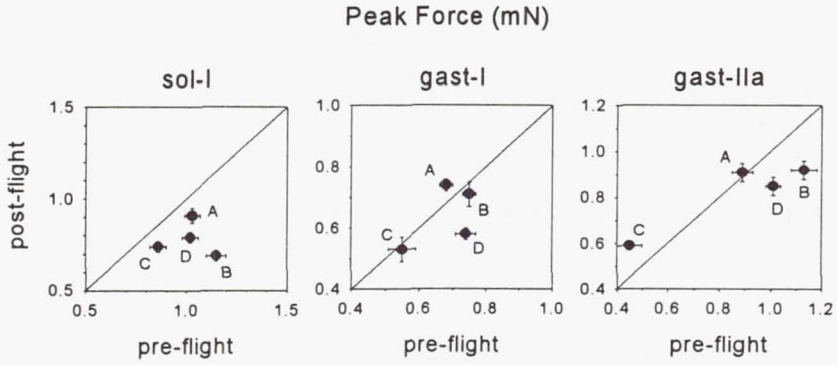

When force was normalized for force per cross-sectional area (kN/m^2) there were no significant changes in the gastrocnemius fibers (slow- or fast-twitch) for any of the four crew members studied. However, for the slow-twitch type I fibers of the soleus, subjects B and D still showed a significant 9% decline in peak force. This indicates that for these subjects the space flight induced decline in peak force of the slow type I fiber could not be explained entirely by the fiber atrophy, but that additional factors most likely a disproportionate loss of contractile protein contributed to the decline.

Maximal Velocity of Fiber Shortening (V_o). Space flight induced an increase in the fiber V_o (fiber lengths/s) in all fiber types in both muscles studied. Furthermore this effect was observed in all 4 crew. This increase is shown in Figure 4 which plots the average pre-flight value for each subject versus their post-flight value. All of the post-flight values are above the line of identity indicating a post-flight increase in V_o for all subjects.

FIGURE 4.

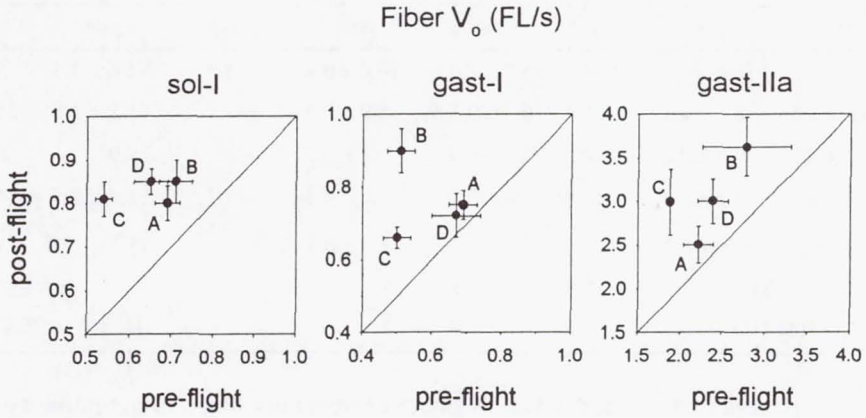

The increased V_o was not caused by an altered myosin heavy or light chain composition (MHC or MLC) as no significant changes were observed in the myosin isozyme pattern. The elevated V_o was associated with an increase in the distance between the actin and myosin filaments. For all subjects, the actin-myosin distance in the slow type I fiber of the soleus increased (Table 6). The increased spacing was caused by a selective loss of actin filaments producing a 25% decrease in the actin density in the A band.

Table 6. Thin and thick myofilament spacing for pre- and post-spaceflight soleus fibers.

	actin-actin distance, nm			myosin-myosin distance, nm			actin-myosin distance, nm		
subject	pre	post	Δ	pre	post	Δ	pre	post	Δ
A	15.0 ± 0.4	17.2 ± 0.2	+15	31.9 ± 0.4	32.0 ± 0.6	0	17.2 ± 0.3	18.6 ± 0.2	+8
B	13.2 ± 0.3	19.2 ± 0.5	+45	35.2 ± 0.5	37.4 ± 1.5	+6	17.6 ± 0.3	21.7 ± 0.2	+23
C	10.9 ± 0.2	16.3 ± 0.3	+50	38.3 ± 1.2	38.1 ± 0.4	0	14.9 ± 0.2	17.7 ± 0.2	+19
D	13.7 ± 0.4	16.9 ± 0.3	+23	39.3 ± 0.7	39.3 ± 1.3	0	16.5 ± 0.3	17.9 ± 0.2	+8
mean	13.2 ± 0.9	17.4 ± 0.6		36.2 ± 0.7	36.0 ± 0.8		16.6 ± 0.6	19.0 ± 0.9	

Values are mean ± SE. Five pre-flight and five post-flight fibers analyzed per subject. Actin-actin distance measured in A band. Δ indicates percent change from pre-flight value.

Peak Power. As a result of the decline in peak force, the peak power of the soleus type I and gastrocnemius type IIa fibers declined with space flight. In the soleus type I fibers the decline was significant for subject B and D, but not A and C (Table 7). This result is consistant with the observation that subjects B and D showed the greatest fall in P_o. In all cases, the post-flight peak power would have been considerably lower had fiber V_o not have increased.

Table 7. Peak power ($\mu N \cdot$fiber length$\cdot s^{-1}$) of pre- and post-spaceflight single muscle fibers.

	soleus type I			gastrocnemius type I			gastrocnemius type IIa		
subject	pre	post	Δ	pre	post	Δ	pre	post	Δ
A	12.2 ± 0.5	12.4 ± 0.5	-2	8.7 ± 0.4	10.0 ± 0.4	+15 *	41.6 ± 2.5	51.1 ± 3.6	+23
B	10.9 ± 0.6	8.2 ± 0.3	-25 *	6.3 ± 0.5	8.9 ± 0.6	+41 *	41.2 ± 3.8	42.1 ± 3.8	+2
C	9.2 ± 0.5	9.6 ± 0.8	+4	7.3 ± 0.8	6.1 ± 0.5	-16	23.9	26.6 ± 2.2	+11
D	11.0 ± 0.6	9.1 ± 0.4	-17 *	8.6 ± 0.7	7.0 ± 0.3	-19 *	51.9 ± 4.5	40.3 ± 1.8	-22 *
mean	10.9 ± 0.3	9.9 ± 0.3		7.9 ± 0.3	8.4 ± 0.3		45.7 ± 2.7	39.6 ± 2.0	
subject	$p < 0.05$			$p < 0.05$			$p < 0.05$		
treatment	$p < 0.05$			$p < 0.05$			$p < 0.05$		

Values are $\mu N \cdot$fiber lengths$\cdot s^{-1}$ (mean ± SE). Number of fibers per mean in parentheses. Δ indicates percent difference between pre- and post-flight values. * $p < 0.05$.

Figure 5 shows the power-force relationship for each subject for the soleus slow type I fiber. From this figure it is clear that all subjects showed a drop in peak force, but only subjects B and D showed a reduced peak power. In the case of subjects A and C, the decline in force was less and the increased shortening velocity compensated, such that peak power was unaltered.

FIGURE 5.

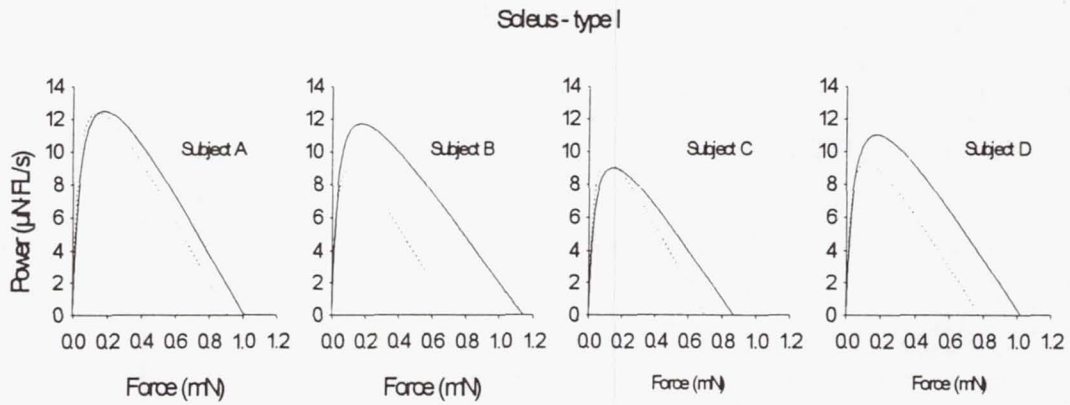

Single Fiber Biochemistry. The experiments analyzing the effects of space flight on muscle enzyme and substrate levels in individual slow- and fast-twitch fibers are still in progress. Consequently, the data presented here are preliminary. The enzyme profile of the slow and fast fibers pre- and post-flight are shown in Table 8.

TABLE 8. Enzymatic Profile of Fast and Slow Fibers

Fiber Type	βOAC	CAT	CS	GP	GS	HK	LDH	PFK
Soleus Type I								
Pre	4.71 ± .36	1.33 ± .17	2.83 ± .22	1.73 ± .24	.269 ± .03	.32 ± .04	6.80 ± .59	.239 ± .03
Post	5.71 ± .48	1.92 ± .17*	3.64 ± .25*	1.85 ± .30	.503 ± .07*	.32 ± .03	6.08 ± .51	.291 ± .04
Gastrocnemius								
Type I								
Pre	3.96 ± .45	1.75 ± .40	3.06 ± .27	1.91 ± .49	.353 ± .05	.39 ± .07	6.19 ± .91	.169 ± .04
Post	4.89 ± .88	3.25 ± .79	3.94 ± .44	1.90 ± .30	.522 ± .10	.47 ± .08	5.98 ± 1.1	.311 ± .08
Type IIa								
Pre	3.29 ± .41	1.53 ± .39	3.10 ± .48	2.18 ± .67	.269 ± .06	.29 ± .05	16.5 ± 1.8	.337 ± .06
Post	2.70 ± .49	1.67 ± .44	4.43 ± .49	3.36 ± .63	.642 ± .19	.53 ± .10	21.5 ± 2.3	.394 ± .07
Type IIx								
Pre	3.37 ± .71	1.12 ± .27	3.53 ± .44	1.34 ± .32	.339 ± .12	.74 ± .27	22.6 ± 3.3	.325 ± .09
Post	2.68 ± .37	1.76 ± .65	2.83 ± .50	3.59 ± 1.3	.612 ± .19	.59 ± .20	25.3 ± 5.3	.487 ± .09

Data are means ± S.E. in mol/kg/hr. Table abbreviations are: GP = glycogen phosphorylase, HK = hexokinase, GS = glycogen synthase PFK = phosphofructokinase, LDH = lactate dehydrogenase, CS = citrate synthase, βOAC = β-hydroxyacyl-CoA dehydrogenase, and CAT = CoA-carnitine acyl transferase. * indicates $P < 0.05$

TABLE 9. Substrate Profile of Single Fast and Slow Fibers (Data Presented as Means ± SE in mol/kg dry wt)

Fiber Type	ATP	PCr	Glycogen	Lactate
Soleus Type I				
Pre	20.3 ± 1.1	71.8 ± 4.4	584 ± 34	21.1 ± 1.8
Post	21.9 ± 1.9	76.1 ± 4.9	637 ± 50	22.3 ± 1.9
Gastrocnemius				
Type I				
Pre	16.8 ± 1.5	62.5 ± 5.9	581 ± 58	18.8 ± 2.9
Post	23.9 ± 3.2	73.2 ± 9.1	795 ± 110	24.5 ± 2.7
Type IIa				
Pre	26.6 ± 3.5	83.6 ± 7.6	678 ± 50	20.1 ± 2.8
Post	25.7 ± 3.2	72.6 ± 6.1	650 ± 65	27.2 ± 4.2
Type IIx				
Pre	20.8 ± 2.9	61.4 ± 5.9	558 ± 105	21.2 ± 6.7
Post	24.5 ± 3.1	75.7 ± 3.4	485 ± 133	14.4 ± 3.8

In slow type I fibers the oxidative and glycolytic enzymes increased with space flight in both the soleus and the gastrocnemius. The only exception was LDH in the soleus and LDH and GP in the gastrocnemius which showed no change. However, the only significant increases occurred in CAT, CS, and GS in the slow fibers of the soleus. The substrate profile for the pre- and post-flight fibers are shown in Table 9. Microgravity had no significant effect on the high energy phosphate profile (ATP and PCr), cell glycogen or lactate in either the fast or the slow fiber types.

Comparison with Ground Based Results. As part of the LMS project, we conducted a 17 day bed rest study designed to duplicate the exact duration and testing sequence of the LMS flight. The studies and assays were identical to those carried out on the LMS crew. The results were for the most part qualitatively similar to the LMS flight results. The bed rest subjects showed a similar decline in VO_2 max, and the whole calf muscle function was essentially unaltered. Similar to flight, the single fiber studies revealed fiber atrophy, and a loss of force. From a quantitative perspective, the cell changes with bed rest were not as great as flight. For example, the soleus type I fibers showed a 5% and 13% decline in fiber size and force, respectively compared to the 10% and 20% change in these parameters following space flight. With bed rest 7 of the 8 subjects showed a significant drop in the peak power of the slow soleus type I fiber, while only 2 of the 4 astronauts showed significant declines in this parameter. With space flight, the large increase in shortening velocity help protect against the loss of power. In both studies, we observed a significant increase in glycogen synthase. The glycogen content of the slow type I fiber of the soleus increased in both studies, however, the increase was small and non-significant in the LMS flight study (Table 9). In contrast, type I cell glycogen increased 66% (from 524 to 875 mol/kg dry wt) with bed rest.

(5) Conclusion

The 17 day LMS space flight resulted in significant decline in the whole body aerobic capacity of the crew, and in the functional performance of individual slow- and fast-twitch fibers. The fiber atrophy and decline in function (force and power) was greatest in the slow type I fibers of the antigravity soleus muscle. Considerable subject variability occurred for example, subject D showed a 40% decline in peak power of the soleus type I fiber, while this parameter was reduced by only 12% in subject A. The reason for the different responsiveness of the crew to microgravity is unknown, but could relate to the degree of exercise countermeasure performed.

Cell atrophy was the primary cause of the decline in fiber force and power as the force per cross-sectional area showed only minimal changes. In the slow type I fibers of the soleus, 2 of the 4 crew members showed a significant drop in peak power. All 4 subjects showed an increased shortening speed, and this partially protected against the loss of power. The increased velocity appears to have resulted from a selective loss of filamentous actin. This increased the actin-myosin filament spacing which in turn allowed a faster cross-bridge cycling rate and increased fiber speed. The structural rearrangement of the filaments represents an important adatation to preserve cell power. One expects that this strategy is considerable more efficient than switching the myosin phenotype from the slow to the fast isozyme. The latter strategy occurs in rats flown in space, and results in a faster but less efficient muscle.

The reduced force and power of the individual fibers of the soleus and gastrocnemius did not result in a compromised calf muscle function. This suggests that the cellular changes were either too small to be detected by the TVD or that the crew compensated for the decline in cell function by altering their motor unit recruitment pattern.

In future studies, it will be important to determine if the deleterious changes in cell function get progressively worse with increasing duration of flight or if a new steady state is obtained. If the latter occurs, we need to know at what point the new steady state is obtained. Animal studies suggest that microgravity induces an altered cell metabolism, such that, skeletal muscle fibers show an increased reliance on carbohydrates and a reduced ability to oxidize fats. In the bed rest study, we observed an increase in the enzymes of carbohydrate metabolism and cell glycogen concentration post bed rest. These data were consistent with an increased reliance on carbohydrate metabolism. In the LMS flight, cell glycogen increased in the slow type I fibers, but the change was not significant. However, data from others indicate that the crew was in negative caloric balance, and this lack of sufficient caloric intake may have reduced the microgravity induced increase in cell glycogen. In future studies, it will be important to determine if fat utilization is inhibited in humans during exercise in space as reliance on cell glycogen and blood glucose will lead to an increased fatigability and reduced physical work capacity. Finally, future studies most rigorously test high resistance exercise as a countermeasure to the microgravity induced cell atrophy.

Non-technical Summary Project E920
Effect of Weightlessness on Human Single Muscle Fiber Function

P.I. Robert H. Fitts
Co-Investigator. David L. Costill
Co-Authors. S.W. Trappe, T.A. Trappe, D.A. Riley, and J.J. Widrick

The 17 day LMS space flight resulted in significant decline in the whole body aerobic capacity of the crew, and in the functional performance of individual slow- and fast-twitch muscle fibers. The reduced cell size and function (force and power) was greatest in the slow type I fibers of the antigravity soleus muscle. Considerable subject variability occurred for example, subject D showed a 40% decline in peak power of the soleus type I fiber, while this parameter was reduced by only 12% in subject A. The reason for the different responsiveness of the crew to microgravity is unknown, but could relate to the degree of exercise countermeasure performed.

The loss of cell size was the primary cause of the decline in fiber force and power as the force per cross-sectional area showed only minimal changes. In the slow type I fibers of the soleus, 2 of the 4 crew members showed a significant drop in peak power. All 4 subjects showed an increased shortening speed, and this partially protected against the loss of power. The increased velocity appears to have resulted from a selective loss of one of the proteins involved in the contractile process. This structural rearrangement of the muscle represents an important adaptation to preserve cell power.

The reduced force and power of the individual fibers of the tested muscles did not result in a compromised calf muscle function. This suggests that the cellular changes were either too small to be detected by the whole leg measurement system or that the crew compensated for the decline in cell function by altering their strategy for muscle activation.

In future studies, it will be important to determine if the deleterious changes in cell function get progressively worse with increasing duration of flight or if a new steady state is obtained. If the latter occurs, we need to know at what point the new steady state is obtained. Animal studies suggest that microgravity induces an altered cell metabolism, such that, skeletal muscle fibers show an increased reliance on carbohydrates and a reduced ability to oxidize fats. In the LMS flight, cell glycogen increased in the slow type I fibers, but the change was not significant. However, data from others indicate that the crew was in negative caloric balance, and this lack of sufficient caloric intake may have reduced the microgravity induced increase in cell glycogen. In future studies, it will be important to determine if fat utilization is inhibited in humans during exercise in space as reliance on cell glycogen and blood glucose and the reduced muscle size will lead to an increased fatigability and reduced physical work capacity. Finally, future studies must rigorously test high resistance exercise as a countermeasure to the microgravity induced loss of muscle mass and physical work capacity.

JSC Human Life Sciences Project

E948 - Human Sleep, Circadian Rhythms and Performance in Space

Principal Investigator:

Dr. Timothy Monk
University of Pittsburgh
Pittsburgh, Pennsylvania

FINAL REPORT OF NASA CONTRACT NAS 9-18404
"Human sleep, circadian rhythms and performance in space"
comprising Experiment E 948 (SACS) of the LMS mission aboard STS-78

SLEEP AND CIRCADIAN RHYTHMS IN FOUR ORBITING ASTRONAUTS

P.I. Timothy H. Monk, PhD, DSc
Co P.I. Daniel J. Buysse, MD

University of Pittsburgh

Pittsburgh Team:
Bart D. Billy MS, Kathy Kennedy BA, Timothy Hoffman MST, Linda Willrich BS, Lynda Rose

Co-I. Claude Gharib, MD
Co-I. Guillemette Gauquelin, PhD

University of Lyon

FINAL REPORT OF NASA CONTRACT NAS 9-18404
"Human sleep, circadian rhythms and performance in space"
comprising Experiment E 948 (SACS) of the LMS mission aboard STS-78

SLEEP AND CIRCADIAN RHYTHMS IN FOUR ORBITING ASTRONAUTS

P.I. Timothy H. Monk, PhD, DSc
Co P.I. Daniel J. Buysse, MD

University of Pittsburgh

Pittsburgh Team:
Bart D. Billy MS, Kathy Kennedy BA, Timothy Hoffman MST, Linda Willrich BS, Lynda Rose

Co-I. Claude Gharib, MD
Co-I. Guillemette Gauquelin, PhD

University of Lyon

Note: the University of Lyon work will be reported separately.

INTRODUCTION

The study of human sleep, circadian rhythms and performance in space has both operational and scientific significance. Operationally, U.S. Spaceflight is moving away from brief missions with durations of less than one week. Most space shuttle missions now last two weeks or more, and future plans involving space stations, lunar bases and interplanetary missions all presume that people will be living away from the gravity and time cues of earth for months at a time. Thus, missions are moving away from situations where astronauts can "tough it out" for an acute limited-time mission, to situations where sleep and circadian disruptions are likely to become chronic, and thus resistant to short term pharmacological or behavioral manipulations. It, thus, becomes imperative that sleep and circadian rhythms in space be understood, so that long term countermeasures can be employed to ensure that crew performance and well-being are not compromised.

As well as the operational significance, there is a strong theoretical imperative for studying the sleep and circadian rhythms of people who are removed from the gravity and time cues of earth. Homo sapiens' development on a planet with a 24h rotation period has had a profound influence on human biology. Like most other organisms on the planet, our species is endowed with a circadian "clock" or pacemaker. This pacemaker is located in the suprachiasmatic nucleus of the hypothalamus (Moore, 1982). It comprises an endogenous, self-sustaining circadian timekeeping system (CTS) which drives circadian rhythms in vital signs, blood chemistry, mood and performance variables . These circadian rhythms "set the stage" for restful sleep at night and active wakefulness during the day. The CTS is entrained to the correct period (24h) and temporal orientation by various time cues ("zeitgebers"), the most powerful of which is the alternation of daylight and darkness. Importantly, the circadian system of our species appears unique in being particularly sensitive to daylight, as compared to the lower light levels characteristic of artificial illumination (Lewy et al., 1980; Wever et al., 1983; Czeisler et al., 1986, but see also Boivin et al., 1996). Thus, in leaving Earth, astronauts are also removing themselves from the prime zeitgeber of their circadian system -- the 24h alternation of daylight and darkness.

Although the present study comprised the first integrated U.S. study of sleep, circadian rhythms and performance in space on more than a single subject, there have been a few investigations of the various components, studied individually. Graeber (1987) gives the best review of sleep in space, drawing upon both the Russian and the American experience. Frost et al. (1976) conducted a series of experiments on Skylab astronauts engaged in long duration missions. Although profound changes in sleep architecture during the mission were not observed, there did appear to be patterns of sleep disruption commensurate with an inappropriately entrained CTS. Moreover, Frost et al.'s subjects noted that in space a given sleep disruption interfered more with "daytime" performance, than would an equivalent sleep disruption on Earth. Santy (1988) reviewed the sleep of 58 crew members from 9 space shuttle flights using a debriefing form and found significant sleep disruptions, especially on dual-shift missions where 50% of subject used a hypnotic in-flight at least once.

Circadian rhythms have also been studied in space. Hanley and Adey (1971) and Gazenko and Ilyin (1987) have studied mammals in various space environments and have shown that there is a tendency in microgravity for the CTS to exhibit aberrant phase relationships and period lengths. It appeared that although circadian rhythms were still generated, entrainment mechanisms did not work as well in the microgravity environment.

Recent support for such a view using human subjects comes from work of Gundel and co-workers (1994) who studied a brief mission of a single German astronaut to the Mir Space Station. This investigation found that the circadian rhythms of rectal temperature and alertness were phase delayed in space, relative to baseline, suggesting a possible transition to free-running. Sleep disruptions were also observed, with shortening and change in architecture during space flight.

The aim of the present study was to test the following 9 hypotheses:

1) Body temperature rhythms would be of lower amplitude in flight than on the ground, and would show further reductions from early flight to late flight;
2) Body temperature phase would be more labile in flight than on the ground, and/or would show changes from early flight to late flight (towards aberrant phases with respect to the sleep wake cycle), perhaps indicating free-running;
3) Circadian rhythms in urinary free cortisol and melatonin sulphate would be of lower amplitude and would be more phase labile in-flight than on the ground;
4) Sleep (as assessed both polygraphically and by diary) would be more disrupted in flight than on the ground, showing less SWS and aberrant patterns of REM sleep (e.g. short REM latencies); particularly late flight.
5) Sleep in the late flight block would be worse than that in the early flight block.
6) Hypnotic use would be more prevalent late flight than early flight.
7) Daily levels of mood, activation and objective performance would be influenced by sleep disruption and circadian dysfunction, taking the form of a deterioration from early flight to late flight;
8) End of shift questionnaires would reflect an increase in subjective fatigue and required effort as the flight progressed.
9) Ambient light levels as detected by the Actillume 8 would be lower in flight than on the ground.

METHODS

The Space Mission

Strenuous efforts were made to ensure that the timing and trajectory of the mission was as least disruptive as possible to the astronauts' circadian rhythms. Lift-off was in daylight (10:50 EDT), requiring

only a slightly earlier than usual waketime (05:50 EDT). For operational reasons, there were changes in bedtime and waketime (and thus the whole routine) throughout the flight, but these were distributed equally throughout the mission leading to a phase advance of 25 minutes per day for all but one day of the mission. Thus, for most of the mission, the astronauts lived, essentially on a 23.58h day. Strict rules ("Appendix K") governed the astronaut's time availability for work. An eight hour sleep opportunity was mandated for each day, as well as rest times at either end of the sleep period and time off for meals. For the present experiment, time was set aside during the work shift to "pay back" for time spent in EEG wiring etc close to the sleep episode.

Subjects

The subjects were four of the seven astronauts aboard the mission. All were males, ages ranged from 38y to 47y (mean= 42.5y). Two of the subjects were members of the NASA astronaut corps, two were payload specialists recruited specifically for this mission. All were extremely healthy with no reported sleep abnormalities. Arbitrary subject code numbers (S1 through S4) will be used throughout this report. The study was approved by both University of Pittsburgh and NASA Internal Review Boards for the ethical treatment of human subjects.

Measurement Block

The experiment was structured in terms of 72h measurement blocks within which all sleep, circadian rhythm, mood and performance measures were taken. There was one measurement block before the mission "pre-flight" (starting 7d before launch), one after the mission "post-flight" (starting 18d after landing), and two in-flight. The two in-flight measurement blocks were towards the beginning "early flight" (starting 2d after launch) and towards the end "late flight" (starting 12d after launch) of the 17-day mission. Each measurement block ran for exactly 72h. In-flight measurement blocks started and ended at the beginning of the workday, pre-flight and post-flight measurement blocks started and ended at the end of the workday.

Core Body Temperature

For the duration of each 72h measurement block, each subject wore a rectal thermistor connected to a Minilogger 8 beltpack recorder. Probes were only removed for defecation. Rectal temperature was sampled automatically every six minutes around the clock, allowing 3-cycle circadian temperature rhythms to be plotted.

Urinary Variables

Urine samples were collected and urine volumes measured throughout each 72h measurement blocks. Samples were assayed for melatonin sulphate and free cortisol. Using the volume measure of each void, the assay results were then expressed as a rate per hour of melatonin or cortisol production, considering the bladder as an integrator. Also plotted was the volume of urine generated (water) per minute.

Objective Sleep Recording

Each sleep during the 72h measurement block was recorded using the Medilog Sleep Research

Recorder (MSRR) system. Electrodes recording EEG, EOG, and EMG were positioned on the subject's head using a cap-based system with extra disposable electrodes. Signals were recorded onto magnetic tape. After recovery, the tapes were played back in order to: 1) visually score each minute of sleep into conventionally defined sleep stages (0, 1, 2, 3, 4 and REM); and 2) run the signals through a computer-based analysis system allowing the measurement of: a) a count of delta waves, and b) a count of eye movements. These procedures allowed a detailed characterization of the duration, depth and architecture of each sleep episode.

Subjective Sleep Diary

After each sleep episode during the 72h measurement block, each subject completed a modified computer-based version of the Pittsburgh Sleep Diary (PghSD) (Monk et al., 1994). This brief instrument assesses the estimated timings of sleep onset and offset, records the number and nature of within-night awakenings, the use of space motion sickness and hypnotic medications, and concludes with visual analogue scale ratings of: 1) subjective sleep quality, 2) mood on awakening (tense vs. relaxed), and 3) alertness on awakening (sleepy vs. alert). The Pittsburgh Sleep Diary has been used in our laboratory for more than 7 years in well over 700 different subjects and patients and has been shown to be a useful adjunct to objective sleep recording.

Actillumes 8

For the duration of each 72h measurement block, each subject wore an Actillume 8 on the non-dominant arm. Actigraphy involves wearing an electronic device which counts the number of arm movements per minute recording each minute's total individually in a memory chip. In the Actillume 8 device, this is supplemented by the simultaneous recording of ambient light levels. At the end of the study, the data from the device is dumped into a computer for subsequent analysis and storage.

Mood and Alertness

Five times per day (within each measurement block) spread throughout the waking interval, a very brief computer-based visual analogue scale technique (Monk 1989) was used to measure subjective alertness (global vigor) and overall mood (global affect). These ratings were used to create daily mean levels of mood and alertness.

Performance Tests

At three times per day (within each measurement block), before breakfast, lunch and dinner, each subject completed a 6-minute performance battery using the computer. The battery has been used in our laboratories for more than 12 years and is described in Monk et al. (1985). The two component tests (the speed and accuracy of which are evaluated) comprise 32 trials of a simple serial search task (searching for the letter "E" in 30 random uppercase letters) and 32 trials of a modified form of the Baddeley (1968) reasoning test (determining the truth or falsity of statements such as "M IS NOT BEFORE C - CM"). Results of these tests were used to create: 1) time of day functions in performance, and 2) mean daily levels, for each of the two tasks.

End-of-Shift Questionnaire

At the end of each work shift in the 72h measurement block, subjects completed a brief questionnaire regarding stresses such as EVAs, equipment malfunction and changes in procedure, as well as ratings of how long the shift lasted and how satisfied the subjects were with their work on it.

Data Analysis

Circadian rhythms in core temperature, urinary variables and subjective alertness were analyzed by sinusoidal technique involving the fitting of both a 24h fundamental and a 12h harmonic (Monk and Fort 1983) in order to derive an estimate of phase (time of fitted minimum), amplitude (fitted maximum minus fitted minimum, divided by two) and mean level for each subject within each 72h measurement block. Sleep variables were likewise reduced to conventional measures of objective sleep quality and architecture for each sleep "night." Sleep diary and end-of-shift questionnaires variables were used both as measures in their own right, and also as modifiers of the other sleep indices (e.g., "tagging" nights that may have been influenced by space motion sickness or hypnotic medications, or excessive work load).

RESULTS

Deviations from protocol

By and large, the quality of data collection was extremely good, especially inflight. Ground measurement blocks often suffered from competing demands upon the astronauts' time which occasionally lead to lost data. Battery problems meant that all pre-flight Actillume 8 data were lost. Technical problems with electrodes and/or tapes meant that three partial subject-nights of sleep were lost in the pre-flight measurement block, but some of these were made up with additional recordings. Similar technical problems meant that late flight and post-flight polysomnographic data were not available for one astronaut. There were fairly long gaps in the temperature record for one subject pre-flight. Two of the astronauts finished the post-flight measurement block 12h early. Occasional missing mood and performance sessions also occurred, but not enough to compromise the ability to test hypotheses.

Hypothesis 1 ("Body temperature amplitude will be reduced")

The mean rectal temperature rhythms of the four astronauts (expressing each datum a deviation from that subject's 72h mean) with standard errors is plotted in Figure 1 using the same axes throughout. Apart from a slight change in rhythm shape (discussed below), temperature rhythms under flight and ground conditions differed little. In particular, the similarity of amplitude between the four curves was quite striking. Figure 2 further illustrates this with comparisons between pre-flight and early flight (upper panel), and between early flight and late flight (lower panel), with appropriate changes of the abscissa to represent differences in wake time. Even when individual curves were compared separately for each subject (Figure 3), there was a fairly striking similarity between early flight and late flight curves, with no evidence of a diminution of temperature rhythm amplitude which would have occurred had the circadian pacemaker moved out of phase with the imposed routine. Table 1 also reveals that when amplitude measures (half-range) were calculated using 24h and 12h sinusoidal fits to each time series separately, the mean temperature rhythm amplitudes for the four measurement blocks showed only a slight diminution in-flight (pre-flight: 0.57, early flight 0.43, late flight 0.47, post-flight 0.52 deg.C). Clearly, there was no general confirmation of Hypothesis 1.

Hypothesis 2 ("Body temperature phase will be labile and/or indicate free-running")

As stated in the introduction, a feature of space flight is that it frees astronauts from the shackles of earth time. The depth of this freedom only became really apparent to the authors when they monitored the mission at the Science Monitoring Area at Johnson Space Center, Houston. All activities connected

with the flight were timed according to "Mission Elapsed Time" (MET). MET is a notional "time zone" that starts at day 0, 00:00 at the moment of lift-off (whenever that happens to be). There were two clocks in the Science Monitoring Area, one on MET the other on Greenwich Mean Time. Further, as described above, for operational reasons, each bedtime and waketime was advanced by 25 minutes per day during the mission. This made defining phase markers for the circadian rhythms difficult. For this reason we chose the most powerful earth zeitgeber the astronauts experienced, namely the playing of loud music from Huntsville to wake them up each morning (referred to here as "Reveille"). Arbitrarily we defined reveille on the first morning of the measurement block as "zero time", measuring phases from this temporal marker for all three circadian cycles. In terms of GMT, reveille was at 09:29 on 1996/6/22 for the early flight measurement block, and 05:39 on 1996/7/2 for the late flight block. For simplicity, we ignored the fact that actual day length (as measured by the sleep/wake cycle) was 23.58h rather than 24h (re-doing the analyses at a T of 23.58 made no difference to the general conclusions but prevented the use of clock time in reporting results). Unfortunately, there was no equivalent powerful zeitgeber for the ground baselines. For these we simply took the scheduled waketime on Day 1. Because of this, in flight versus ground differences in phase are best considered suspect.

The circadian phase marker was taken as the time of fitted (24h + 12h) minimum. On the ground, in healthy day workers, this typically occurs 2 to 4h before waketime (Czeisler et al, 1992; Monk et al, 1995). As is clear from Figure 2, there was no apparent difference in temperature curves between early flight and late flight measurement blocks, with both inflight blocks showing the same sort of phase relationships normally observed on the ground. Thus, the sinusoidal analysis (Table 1), revealed average minimum phase timings of 3.13h before reveille early flight, and 2.68h before reveille late flight. Two subjects showed a slight phase advance, two a slight phase delay (Table 1), but in no case was the phase difference more than 85 minutes, despite a delay of almost ten calendar days between the start of each 72h block. Thus there was no evidence to support Hypothesis 2.

Hypothesis 3 ("Urinary circadian rhythms will be disrupted in flight")

Figures 4, 5 and 6 plot the circadian rhythms (averaged across the three days of a measurement block) for each subject separately for water (urine volume), melatonin sulphate and free cortisol. These data were, as expected quite noisy, rendering it difficult to properly test Hypothesis 3. However, in melatonin sulphate, the two subjects showing a clear "standard" pattern on the ground (with a melatonin onset about 12h-15h after waking), also showed the same pattern in-flight. Thus, what evidence there was favored rejection of Hypothesis 3.

Hypothesis 4 ("Sleep will be more disrupted in-flight than on the ground")

For operational reasons, the pre-flight baseline sleeps took place within the week before the flight. This was an extremely busy and stressful time for the astronauts, rendering it unsuitable as a true "on ground" comparison. In the three subjects (S1,S2,S4) for whom, this was possible, the post-flight baseline, two weeks after the end of the mission was used as a comparison, for the fourth subject (S3), comparisons were made with the pre-flight baseline. In all cases, summary statistics were obtained from the average of nights 2 and 3 of each 72h block.

Statistics from polysomnography are given in Table 2 and Figures 7 - 10. Two main findings emerged from the data: 1) Time spent asleep was reduced from an average of 392 mins. in baseline to an average of 362 mins. in-flight, with three of the four subjects showing a reduction; and 2) Slow wave sleep (from both hand-scored and automated measures) was markedly reduced in flight (Stages 3&4: baseline= 37 mins., in-flight= 11 mins.), with all four subjects showing a reduction. Measures of sleep continuity and those connected with REM sleep failed to show any consistent pattern.

These findings were broadly confirmed by the diary findings (Table 2). Reported time in bed was reduced for all four subjects. It should be noted that the diary study did not reveal any major sleep disruption as a function of space flight. Rather, the extent to which Hypothesis 4 was confirmed appeared to be limited to reduced sleep durations and a suppression of delta sleep.

Hypothesis 5 ("Sleep will deteriorate from early flight to late flight")

As is illustrated in Figures 7 - 10, there was no consistent trend for sleep late flight to be inferior to early flight, or to have a different sleep architecture. Hypothesis 4 was thus not confirmed.

Hypothesis 6 ("More hypnotic use in flight")

No hypnotics (or anti-space adaptation sickness medications) were reported as being used in space, so Hypothesis 5 was not confirmed.

Hypothesis 7 ("Mood and performance more impaired late flight than early flight")

Because the mechanics of actually doing the performance tasks are very different in microgravity, performance comparisons could only be made between the two in flight measurement blocks, whereas all four measurement blocks could be used in the assessment of mood and activation. Unfortunately there were still residual practice effects which made the interpretation of the performance data difficult. The main consistent finding was that subjective alertness did show a decline from early flight to late flight in all four subjects, suggesting some confirmation of Hypothesis 7. However, some of this apparent deterioration may have been simply that the early flight readings were artificially inflated from the initial exhilaration of being up in space

Hypothesis 8 ("More effort needed late flight than early flight")

The in flight end of shift questionnaire data indicated that 88% of astronaut-shifts (21/24) were reported as having passed "very quickly" or "fairly quickly". One subject reported himself as being tired both at the beginning and end of shifts both early flight and late flight, the other three showed no particular trend. Features of the shift that affected astronauts were: equipment problems (7/24), timeline problems (6/24), physically strenuous work (5/24), and space motion sickness (1/24). Hypothesis 7 was not confirmed; three of the four subjects reported themselves as requiring less effort to carry out their work late flight than early flight.

Hypothesis 9 ("Less light exposure in flight")

Hypothesis 8 was confirmed, light levels averaged 70 Lux in flight versus 350 Lux post-flight. Actigraphy revealed no systematic change in sleep restlessness when comparing early flight to late flight.

DISCUSSION

While some of the present results speak to the resiliency of the human circadian system, even when faced with something as profound as orbiting the Earth in a weightless environment, there were some major effects observed, particularly in the various stages of sleep observed, and in the duration and depth of sleep actually obtained. Considering first the circadian temperature rhythm findings, it should

again be emphasized that this mission was unique in attempting to minimize any "mission operations" causes of circadian desynchrony. Thus, this was a single shift mission which took off in daylight, and which followed a trajectory that minimized the required phase shift between take off and landing. Further, instead of accomplishing this phase shift in abrupt one-hour shifts (as is often done), the required phase advance was instead trickled in at a rate of 25 minutes per day. This yielded a day length of 23.58h, which appeared to be well within the circadian range of entrainment of the present subjects. Without doubt, had a mission with a less benign schedule been studied, the much greater disruptions may have been observed. Having noted this, however, the authors must admit surprise that the human circadian system appears to be remarkably resilient to something as profound as that of orbiting the earth at 17,198 miles per hour, with no gravity, and sunrises and sunsets appearing every 90 minutes. Certainly, when designing the experiment we fully expected at the very least reduced rhythm amplitude and increased phase lability, with perhaps, even, evidence of free-running. The absence of such effects in the present data confirm the conclusions of Boivin et al., (1996) that daylight/darkness cycles are not a prerequisite for circadian entrainment, and also recent animal work suggesting that non-photic zeitgebers may be important (Mrosovsky, 1988).

Although the circadian temperature rhythm changes we observed were not as profound as we had expected, there were baseline versus in-flight differences in circadian temperature rhythm shape that were of interest. In particular, the rhythm took more of a "saw tooth" shape, than the more usual "tilted inverted U" shaped function usually observed on earth. Interestingly, this parallels findings made by Fuller and colleagues in orbiting monkeys. It is noteworthy that this saw tooth pattern is not the same rhythm shape as is observed in 6 deg. head-down tilt bedrest, a model of microgravity that mimics many of the fluid shift and cardiovascular effects. As we have demonstrated in a recent 17d bedrest study incorporating many of the experiments flown in the present LMS mission, bedrest appears to lead to a reduction in rhythm amplitude, and delay in phase (timing), but all within a rhythm shape that remains essentially sinusoidal.

The urinary circadian measures broadly confirmed the story given by the temperature rhythms, though with much less clarity. In the subjects showing clear rhythms on the ground (e.g., S1 and S2 in melatonin sulphate), there was a continuation of such well-ordered rhythms in both early flight and late flight measurement blocks.

Time of day effects in mood and performance efficiency were sometimes hard to interpret because of the strong practice ("learning curve") effect that was still observed in performance. Also, performance while floating in microgravity was undoubtedly very different to that while seated comfortably at a desk on Earth. For that reason, performance comparisons within the mission, are probably more justified than those comparing in-flight to ground. Here however, there was no compelling case for a build up in performance decrements as indicated by late flight versus early flight comparisons. Indeed (probably due to practice effects), performance appeared to be, if anything, better late flight than early flight. This appeared to part of a general trend, observable in other measures such as sleep diaries, end of shift questionnaires, polysmonography and nocturnal actigraph counts, which all failed to show increasing disruptions in either sleep or daytime performance as the flight progressed. Indeed, the only measure to show an early flight superiority was subjective alertness (global vigor) where the effect may have been simply due to an elevation of early flight readings above baseline levels.

The end-of-shift questionnaire data was useful in giving an insight into some of the features of space flight that might lead to a difficult workday in space. In the present mission, only one of our subjects reported experiencing space motion sickness, and that for only one day (the first in our early flight measurement block). Thus, the main challenges appeared to be those related to equipment malfunction and time-line (schedule) over-runs which are perennial problems in manned space flight. Having made that point, however, it would appear that the careful timeline planning constraints that are in place to protect the astronauts ("Appendix K") did their job in ensuring that excessive fatigue did not build up,

even towards the end of the mission.

With regard to sleep, it is clear that when scheduling is careful to avoid circadian disruptions, sleep in space need not be a major problem. This confirms the early findings of Frost et al. from the Skylab missions in the 1970s. What is clear from the present findings, however, is that without doubt, sleep is shorter and shallower in space than it is on the ground. As Table 1 reveals, actual sleep durations in our study averaged 5.9h early flight 6.3h late flight, compared with 7.0h post-flight (pre-flight sleeps were too close to the mission (L-7d) to be undisrupted). Our overall in-flight average figure of 6.1h of total sleep obtained (Stages 1-4 plus REM) is very close to the figure of 6.03h reported by Santy from retrospective reports. Using PSG on selected nights, Frost reported a figure of 6.00h and 6.30h for the 28d and 59 day Skylab studies, and 6.69h for the 84 day mission, although the figure fell to 5.87h when only the first 19 days of the 84 day mission were considered. While this figure may be acceptable for certain individuals, and for missions lasting less than three weeks, it would certainly seem to be problematical if much longer missions, involving a manned space station or a trip to Mars are involved, which would require people to live in space for months or years at a time.

When considerations of sleep depth are added, the effect becomes much more profound. All four of our subjects showed a quite dramatic diminution in delta sleep, as measured either by hand scored or automated techniques (Table 2, Figures 7 - 10). Since delta sleep represents the stages of sleep considered to be the deepest and most restorative (Horne, 1988), this flight-related effect is clearly of great concern. Since the circadian disruption of the flight was shown to be minimal, we must conclude that the delta sleep effect is not a function of the circadian system, but, rather an effect of the microgravity per se. Future experiments should focus upon this effect, which in many ways mimics the decline in delta sleep observed in advancing age (Reynolds, et al., 1991).

The lack of inappropriate phasing of the astronauts' circadian timekeeping systems was confirmed by the normal distribution of REM sleep over the night, and by the fairly normal REM latencies (52 minutes) shown in space relative to the same subjects' REM latencies on the ground (59 minutes). Again, these findings did not appear to differ when early flight and late flight measurement blocks were compared.

Although the sleep diary findings broadly confirmed the objective PSG data with regard to sleep timing and WASO, it failed to reflect the decrease in sleep depth evidenced by the delta sleep disruptions. Indeed, there was no evidence of a general decrease of subjective sleep quality when in-flight sleeps were compared with ground baselines, or when early flight and late flight sleeps were compared. The sleep diary was useful in providing insights into what factors typically disrupt sleep in space. The diary questions were developed in consultation with the astronauts, whose colleagues with flight experience interacted with them, thus rendering the questions appropriate. Again, one should note the caveats that this was a single shift mission specifically designed to minimize circadian disruptions, but it appeared that neither sleep medications (hypnotics) nor space adaptation sickness medications were used in flight, thus avoiding this potential confound. The main sources of sleep disruption appeared to be ambient temperature and noise.

CONCLUSIONS

When careful steps are taken to ensure that the astronauts' work/rest schedule does not lead to circadian desynchrony, there is no evidence that microgravity per se will disrupt the human circadian timekeeping system, or that such rhythms will degrade over a 17d mission. In particular, there was no evidence of amplitude reduction, phase lability or "free-running" behavior. Despite the astronauts' circadian rhythms being intact, there were some effects on sleep, notably a reduction in sleep duration, and a suppression of the deepest stages of sleep (Stages 3 and 4). However, there were no other

consistent effects of flight in sleep architecture. The only systematic effect on mood and performance appeared to be an increase in alertness in the early flight measurement block. End of shift questionnaires revealed timeline problems and equipment malfunction to be the major impacts on the astronauts' work.

PAO SUMMARY

The aims of this experiment are to find out how the human biological clock reacts to weightlessness and the removal of earth-based time cues such as sunrise and sunset, and how sleep and daytime mood and performance are affected by these changes. Fours astronauts recorded daily rhythms in their body temperature, wrist movements, and urinary constituents, recorded their sleep by electrodes placed on their head, and completed computer-based diaries and tests of mood, activation and performance. These measurements were all taken in four 72-hour measurement blocks, one before and one well after the mission, and two during the space flight itself (one towards the beginning, and one towards the end). In order to get a relatively "pure" idea of what effects were due directly to space flight, rather than to changes in routine, the space shuttle mission was especially designed to take off during daylight, to avoid shift work, and to minimize the changes in work/rest schedule required by the flight.

When we plotted the daily ("circadian") rhythms collected by the astronauts in variables such as body temperature, we found the rhythms in orbit to be very similar to the ones we measured from the astronauts when on the ground. Also, there was no change in rhythms collected early on in the flight, as compared with those collected towards the end of the flight. In all cases, the rhythms indicated that the biological clock was successfully doing its job of preparing the body for sleep at "night" and wakefulness during the "day". This success was also reflected in mood, activation and performance scores, which showed no deterioration during the flight. However, there were some reliable changes in the sleep of the astronauts. Although the patterning or "architecture" of the various stages and depths of sleep was normal in space, there was less of the deepest stages of sleep (called "delta" sleep). Also, the total amount of sleep obtained (an average of 5.9 hours early in the flight, 6.3 hours later on in the flight) was below what is considered to be adequate (and below the average of 7 hours obtained well after the flight was over). The results of this experiment are important in telling us how we should schedule work and rest in future space missions, and in identifying a sleep problem that must be solved before we embark on long duration missions associated with Space Station and Manned Mars Missions.

LITERATURE CITED

Baddeley, A.D. (1968). A three-minute reasoning test based on grammatical transformation. *Psychonomic Science, 10,* 341

Boivin, D.B., Duffy, J.F., Kronauer, R.E., Czeisler, C.A. (1996). Dose-response relationships for resetting of human circadian clock by light. *Nature* 379:540-542.

Czeisler, C.A., Dumont, M., Duffy, J.F., Steinberg, J.D., Richardson, G.S., Brown, E.N., Sanchez, R., Rios, C.D., Ronda, J.M. (1992). Association of sleep-wake habits in older people with changes in output of circadian pacemaker. *Lancet* 340:933-936.

Czeisler, C.A., Allan, J.S., Strogatz, S.H., Ronda, J.M., Sanchez, R., Rios, C.D., Freitag, W.D., Richardson, G.S., & Kronauer, R.E. (1986). Bright light resets the human circadian pacemaker independent of the timing of the sleep-wake cycle. *Science, 233,* 667-671.

Frost, J.D., Shumate, W.H., Salamy, J.G., & Booher, C.R. (1976). Sleep monitoring: The second manned Skylab mission. *Aviation, Space, and Environmental Medicine, 47(4),* 372-382.

Gazenko, O.G., & Ilyin, E.A. (1987). Physiological investigations of primates onboard Biosatellites COSMOS-1514 and COSMOS-1667. *The Physiologist, 30(1),* S31-S35.

Graeber, R.C. (1987). Sleep in space. In NASA Ames Research Center (Ed.), *Sleep and it's applications for the military (Proceedings of the XXVII NATO DRG Seminar).* (pp. 16-17). Moffett Field, CA: Aerospace Human Factors Research Division.

Gundel, A., Nalishiti, V., Reucher, E., Vejvoda, M., & Zulley, J. (1994). Sleep and circadian rhythm during a short space mission. *The Clinical Investigator, 71(9),* 718-724.

Hanley, J., & Adey, W.R. (1971). Sleep and wake states in the Biosatellite III monkey; Visual and computer analysis of telemetered electroencephalographic data from earth orbital flight. *Aerospace Medicine, 42,* 204-313.

Horne, J.A. (1988). *Why we sleep: the functions of sleep in humans and other mammals.* Oxford University Press, Oxford.

Lewy, A.J., Wehr, T.A., Goodwin, F.K., Newsome, D.A., & Markey, S.P. (1980). Light suppresses melatonin secretion in humans. *Science, 210,* 1267-1269.

Monk, T.H. (1989). A visual analogue scale technique to measure Global Vigor and Affect (GVA). *Psychiatry Research, 27,* 89-99.

Monk, T.H., Buysse, D.J., Reynolds, C.F., Kupfer, D.J., Houck, P.R.(1995). Circadian temperature rhythms of older people. *Experimental Gerontology* 30:455-474.

Monk, T.H., Fookson, J.E., Kream, J., Moline, M.L., Pollak, C.P., & Weitzman, M.B. (1985). Circadian factors during sustained performance: Background and methodology. *Behavior Research Methods,Instruments and Computers, 17,* 19-26.

Monk, T.H., & Fort, A. (1983). COSINA - A cosine curve fitting program suitable for small computers. *International Journal of Chronobiology, 8,* 193-222.

Monk, T.H., Reynolds, C.F.I., Kupfer, D.J., Buysse, D.J., Coble, P.A., Hayes, A.J., Machen, M.A., Petrie, S.R., & Ritenour, A.M. (1994). The Pittsburgh Sleep Diary (PsgSD). *Journal of Sleep Research, 3,* 111-120.

Moore, R.Y. (1982). The suprachiasmatic nucleus and the organization of a circadian system. *Trends in Neurosciences, 5(11),* 404-407.

Mrosovsky, N. (1988). Phase response curves for social entrainment. *J Comp Phys A* 162:35-46.

Reynolds, C.F., Monk, T.H, Hoch, C.C., Jennings, J.R., Buysse, D.J., Houck, P.R., Jarrett, D.B., Kupfer, D.J. (1991). EEG sleep in the healthy "Old Old": A comparison with the "Young Old" in visually scored and automated (period) measures. *J Gerontol* 46:M39-M46.

Santy, P.A. (1988). Analysis of sleep on shuttle missions. *Aviation,Space and Environmental Medicine, 59,* 1094-1097.

Wever, R.A., Poiasek, J., & Wildgruber, C.M. (1983). Bright light affects human circadian rhythms. *Pfulgers Archiv European Journal of Physiology, 396,* 85-87.

PUBLICATIONS RESULTING FROM CONTRACT

There are currently no papers resulting directly from the LMS flight. However, the following manuscript is under review:

Monk, T.H. Buysse, D.J. Billy, B.D. Kennedy, K.S. & Kupfer, D.J.(under review). The effects on human sleep and circadian rhythms of 17 days of continuous bedrest in the absence of daylight. *Sleep.*

In addition the following list of papers cite support from the NAS 9 - 18404 contract:

Alward, R.R. & Monk, T.H. (1993). *The nurses shiftwork handbook.* Washington,D.C.:American Nurses Publishing.

Carrier,J. And Monk, T.H. (1997) Estimating the endogenous circadian temperatue rhythm without keeping people awake. *Journal of Biological Rhythms, 12,* 266-277.

Monk, T.H.(ed.) (1991). *Sleep, sleepiness and performance.* Chichester and New York:John Wiley & Sons Ltd.

Monk, T.H. & Carrier, J. (In press). Speed of mental processing in the middle of the night. *Sleep, 20.*

Monk, T.H., Buysse, D.J, Reynolds, C.F.III, Kupfer, D.J. & Houck, P.R. (1995) Circadian temperature rhythms of older people. *Experimental Gerontology,* 30(5), 455-474.

Monk, T.H., Folkard, S. & Wedderburn, A.I. (1996) Maintaining safety and high performance on shiftwork.

Applied Ergonomics, 27(1), 17-23.

Monk, T.H., Petrie, S.R., Hayes, A.J. & Kupfer, D.J. (1994). Regularity of daily life in relation to personality, age, gender, sleep quality and circadian rhythms. *Journal of Sleep Research,* 3:196-205.

Monk, T.H., Reynolds, C.F.III, Kupfer, D.J., Buysse, D.J., Coble, P.A., Hayes, A.J., Machen, M.A., Petrie, S.R. & Ritenour, A.M. (1994). The Pittsburgh Sleep Diary (PsgSD). *Journal of Sleep Research*, 3, 111-120.

Monk, T.H., Buysse, D.J., Reynolds, C.F., Berga, S.L., Jarrett, D.B., Begley, A.E., and Kupfer, D.J. (1997). Circadian Rhythms in human performance and mood under constant conditions. *Journal of Sleep Research, 6, 9 - 18.*

TABLE 1
Results of sinusoidal analyses of body temperature data

		Pre-flight	Early flight	Late flight	Post-flight
Amplitude	S1	0.68	0.47	0.51	0.56
	S2	0.61	0.56	0.71	0.58
	S3	N/A	0.31	0.23	0.54
	S4	0.42	0.39	0.44	0.39
	Mean	0.57	0.43	0.47	0.52
Phase	S1	1.10	3.00	2.10	1.00
	S2	2.70	3.00	3.20	3.60
	S3	N/A	3.70	2.30	2.30
	S4	3.10	2.80	3.10	3.20
	Mean	2.30	3.13	2.68	2.53
Mean Level EC	S1	36.84	36.80	36.91	36.95
	S2	37.03	36.89	36.97	36.99
	S3	N/A	36.74	36.73	36.89
	S4	36.81	36.51	36.54	36.90
	Mean	36.83	36.73	36.79	36.93
Percent Rhythm	S1	84.42	67.60	82.62	68.39
	S2	67.45	81.11	84.69	77.63
	S3	N/A	75.36	57.96	79.55
	S4	73.31	71.51	80.29	56.13
	Mean	75.06	73.89	76.39	70.42

TABLE 2
Results from PSG sleep recording.
All data are in minutes except Average delta counts per minute

		Baseline	Early flight	Late flight
Time Spent Asleep	S1	364	396	390
	S2	411	345	366
	S3	312	322	–
	S4	480	347	369
	Mean	392	353	375
Delta	S1	49	11	2
	S2	25	6	19
	S3	64	42	–
	S4	8	0	0
	Mean	37	15	7
REM	S1	68	103	110
	S2	144	97	81
	S3	70	63	–
	S4	118	99	81
	Mean	100	91	91
REM Latency	S1	61	40	50
	S2	40	37	40
	S3	76	70	–
	S4	57	53	59
	Mean	59	50	50
Average Delta Counts	S1	15.30	9.73	11.23

S2	15.90	15.92	13.15
S3	26.67	15.63	—
S4	9.20	3.18	3.01
Mean	16.77	11.12	9.13

TABLE 3
Sleep Diary Results

		Baseline	Early flight	Late flight
Estimated Time Asleep	S1	293	385	352
	S2	427	402	400
	S3	438	395	425
	S4	497	368	372
	Mean	414	388	387
Estimated Sleep Latency	S1	32	22	15
	S2	2	5	6
	S3	13	7	12
	S4	12	12	5
	Mean	15	12	10
Estimated WASO	S1	37	20	12
	S2	3	3	5
	S3	7	8	10
	S4	0	0	0
	Mean	12	8	7
Sleep Quality	S1	33	56	56
	S2	89	90	89
	S3	68	79	69
	S4	86	95	89
	Mean	69	80	76
Alert	S1	46	42	48
	S2	73	88	66
	S3	48	48	30
	S4	25	41	16

	Mean	48	55	40
Mood	S1	58	49	85
	S2	87	90	61
	S3	73	79	72
	S4	91	92	94
	Mean	77	78	78

FIGURE CAPTIONS

Figure 1

Mean core body temperatures (n=4) expressed as deviation from each subject's 72h mean. Mean +/- one s.e.m. is plotted as a function of time into 72h measurement block for each of the four measurement blocks. Pre-flight and post-flight measurement blocks started in the evening, in-flight measurement blocks in the subjective "morning".

Figure 2

Mean core body temperature (n=4) expressed as a deviation from each subject's 72h mean and plotted as a function of time. Upper panel: pre-flight baseline versus early flight, with the abscissa changed to line up to subjective "morning" (see text). Lower panel: early flight versus late flight measurement blocks, with both plotted simply as a function of hours into measurement block.

Figure 3

Core body temperature plotted as a 24h curve averaged across the three cycles comprising each measurement block. In all cases the abscissa is expressed as time from wake time on day 1 of the measurement block, and the ordinate uses the same size of scale for temperature.

Figure 4

Urinary water volume (mls per minute) regarding the bladder as an integrator. The data are plotted as a 24h curve averaged across the three cycles comprising each measurement block separately for each subject in each measurement block. In all cases the abscissa is expressed as time from wake time on day 1 of the measurement block, and the ordinate uses the same size of scale for volume.

Figure 5

Urinary melatonin sulphate excretion (ng per minute) regarding the bladder as an integrator. The data are plotted as a 24h curve averaged across the three cycles comprising each measurement block separately for each subject in each measurement block. In all cases the abscissa is expressed as time from wake time on day 1 of the measurement block, and the ordinate uses the same size of scale for melatonin sulphate.

Figure 6

Urinary free cortisol excretion (ug per minute) regarding the bladder as an integrator. The data are plotted as a 24h curve averaged across the three cycles comprising each measurement block separately for each subject in each measurement block. In all cases the abscissa is expressed as time from wake time on day 1 of the measurement block, and the ordinate uses the same size of scale for free cortisol.

Figure 7

Astronaut S1: Sleep architecture from baseline (post-flight), early flight and late flight measurement blocks. Plotted is the average of nights 2 and 3.

Figure 8

Astronaut S2: Sleep architecture from baseline (post-flight), early flight and late flight measurement blocks. Plotted is the average of nights 2 and 3.

Figure 9

Astronaut S3: Sleep architecture from baseline (pre-flight) and early flight measurement blocks (technical problems led to the loss of late flight and post-flight data). Plotted is the average of nights 2 and 3.

Figure 10

Astronaut S4: Sleep architecture from baseline (post-flight), early flight and late flight measurement blocks. Plotted is the average of nights 2 and 3.

Figure 1

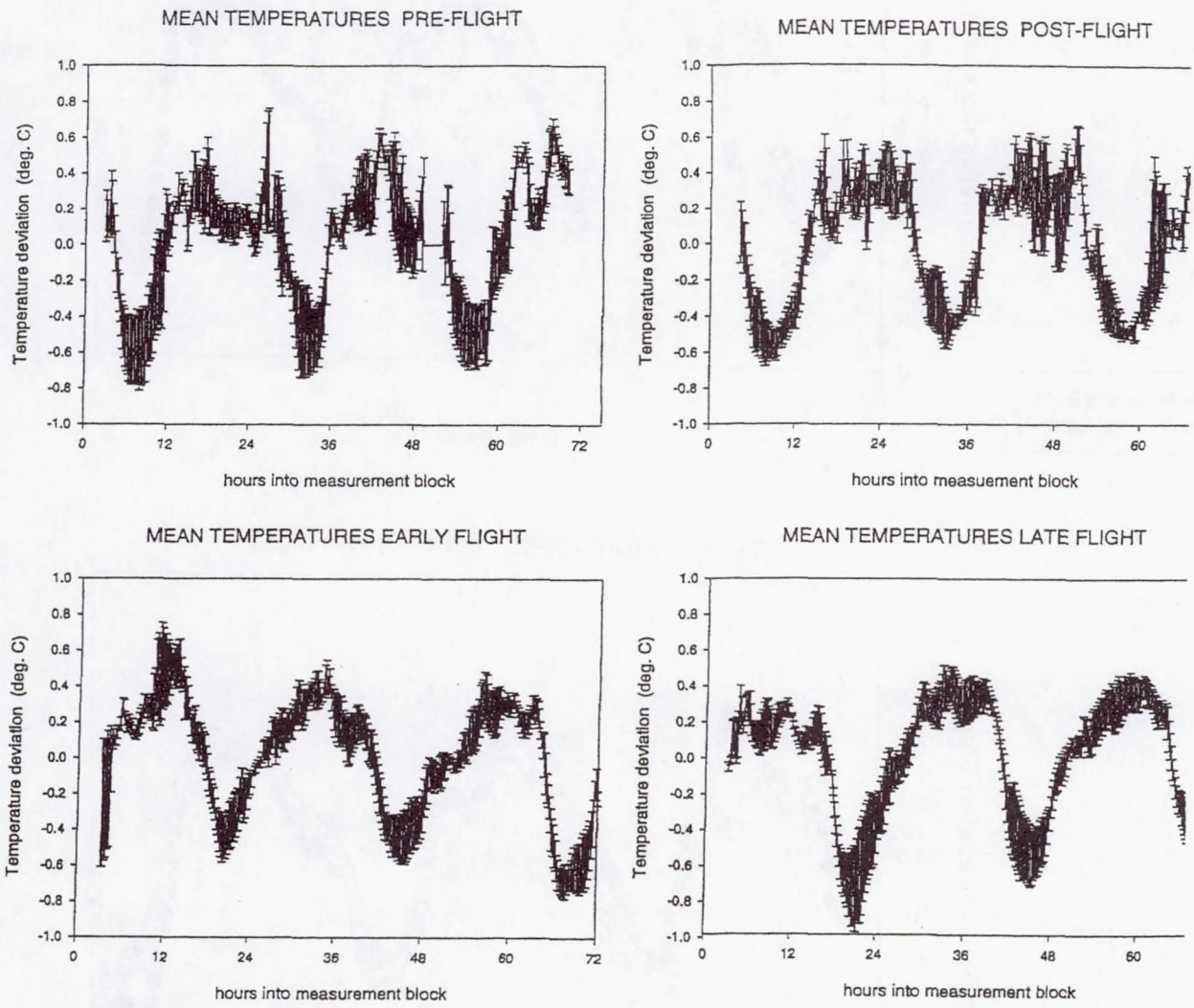
MEAN TEMPERATURES PRE-FLIGHT
Temperature deviation (deg. C)
1.0
0.8
0.6
0.4
0.2
0.0
-0.2
-0.4
-0.6
-0.8
-1.0
0
12
24
36
48
60
72
hours into measurement block
MEAN TEMPERATURES POST-FLIGHT
Temperature deviation (deg. C)
hours into measuement block
MEAN TEMPERATURES EARLY FLIGHT
Temperature deviation (deg. C)
hours into measurement block
MEAN TEMPERATURES LATE FLIGHT
Temperature deviation (deg. C)
hours into measurement block

Figure 2

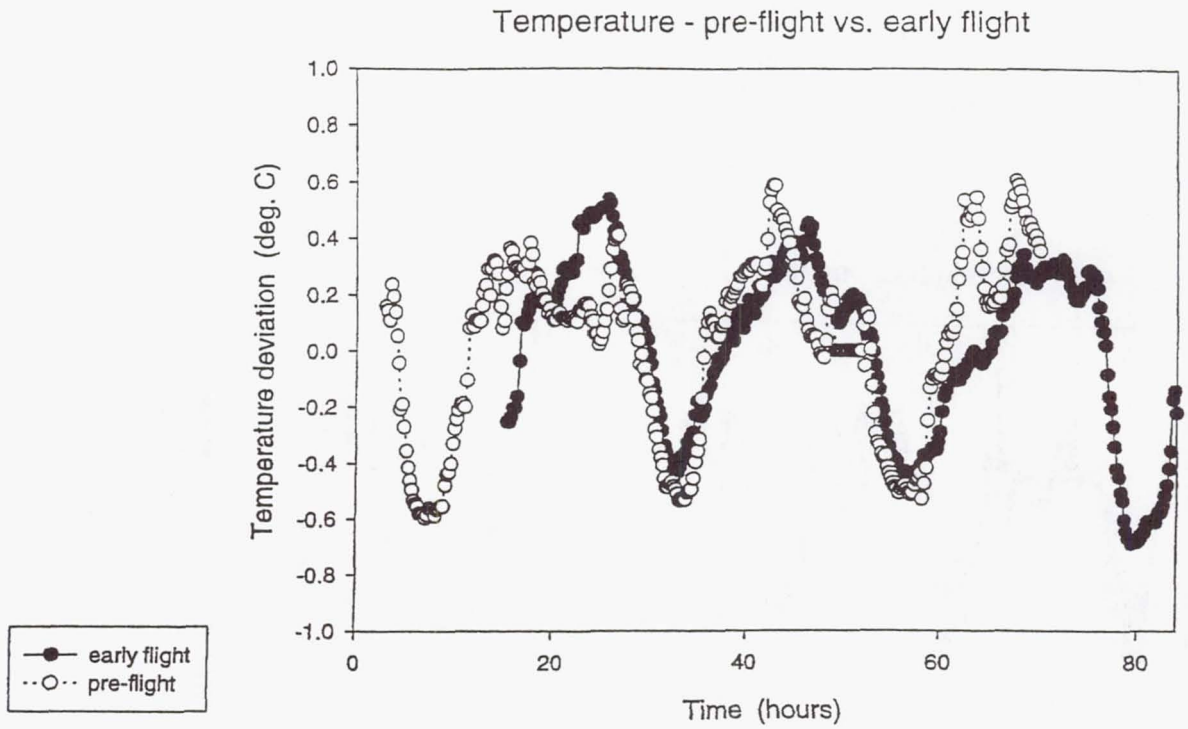
Temperature - pre-flight vs. early flight
Temperature deviation (deg. C)
1.0
0.8
0.6
0.4
0.2
0.0
-0.2
-0.4
-0.6
-0.8
-1.0
0
20
40
60
80
Time (hours)
early flight
pre-flight

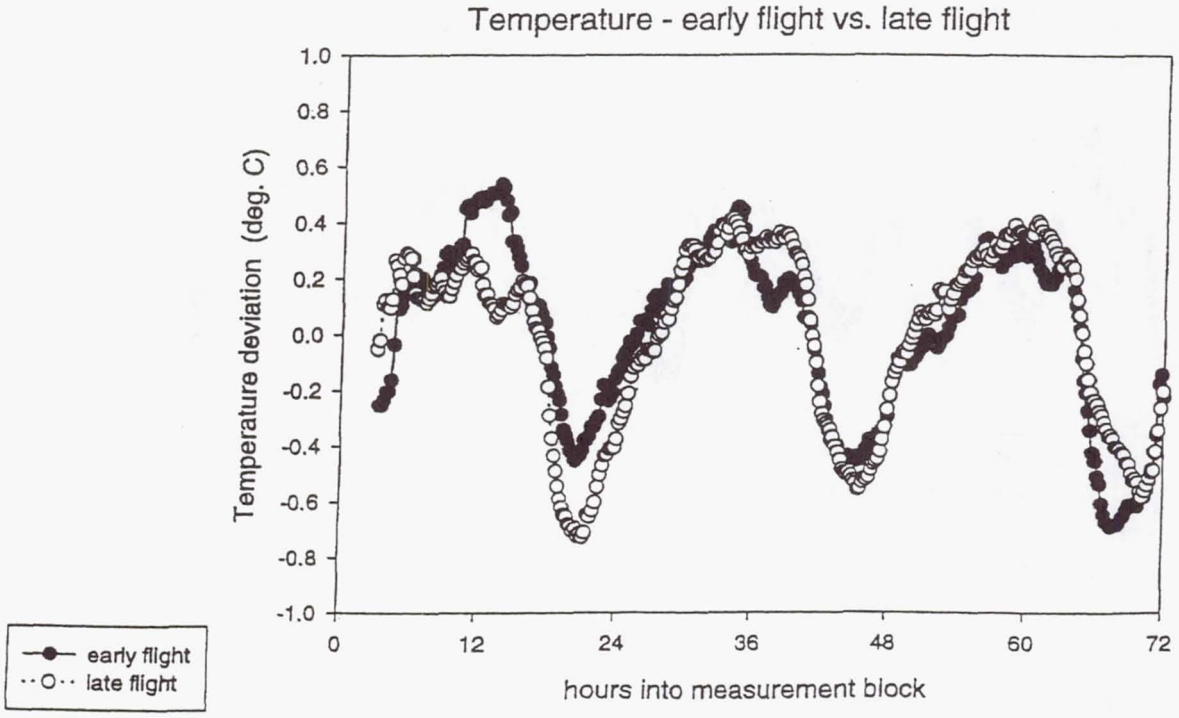
Temperature - early flight vs. late flight
Temperature deviation (deg. C)
1.0
0.8
0.6
0.4
0.2
0.0
-0.2
-0.4
-0.6
-0.8
-1.0
0
12
24
36
48
60
72
hours into measurement block
early flight
late flight

Figure 3

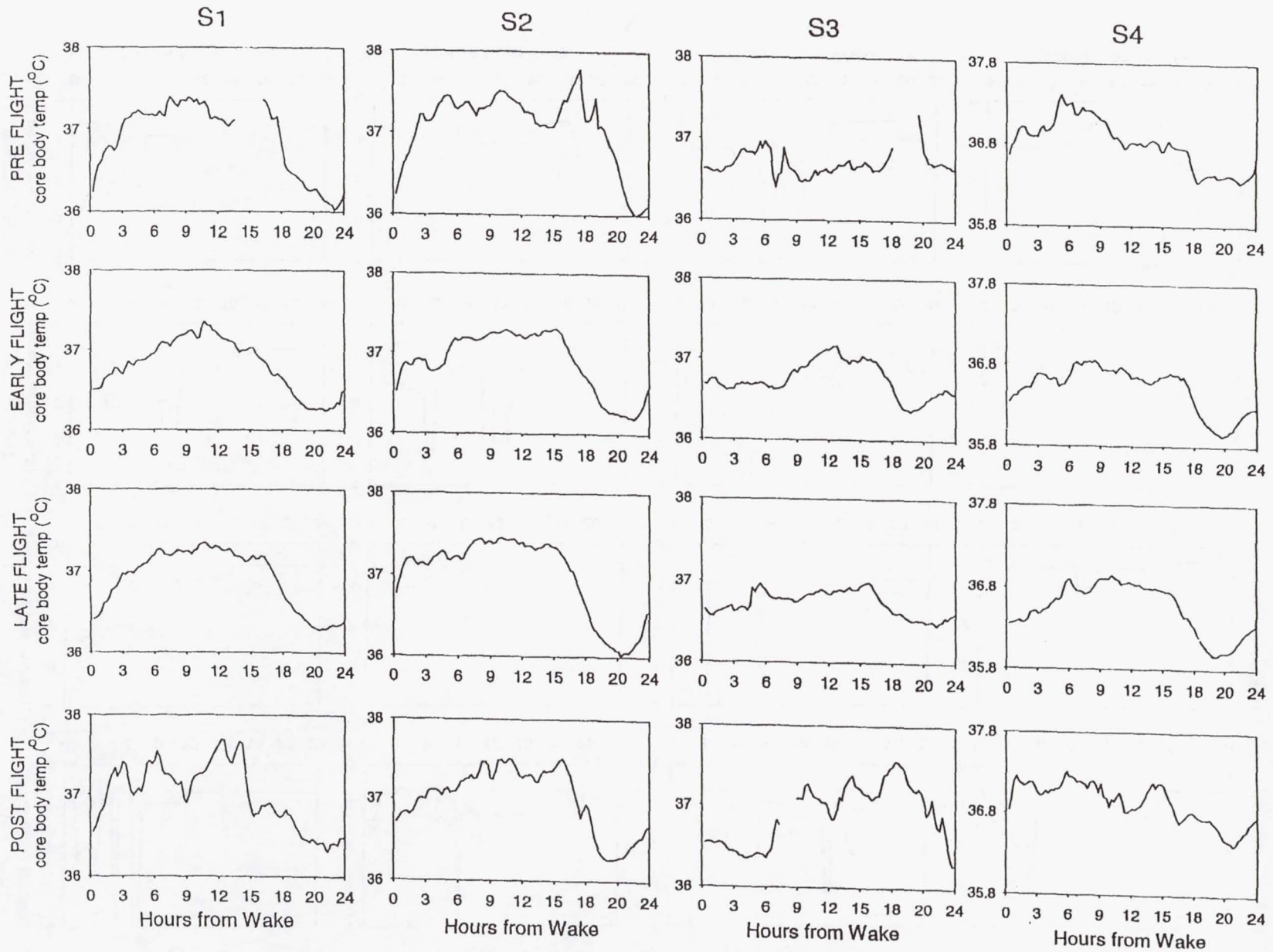
S1
S2
S3
S4
PRE FLIGHT
EARLY FLIGHT
LATE FLIGHT
POST FLIGHT
core body temp (°C)
38
37
36
37.8
36.8
35.8
0 3 6 9 12 15 18 20 24
Hours from Wake

Figure 4

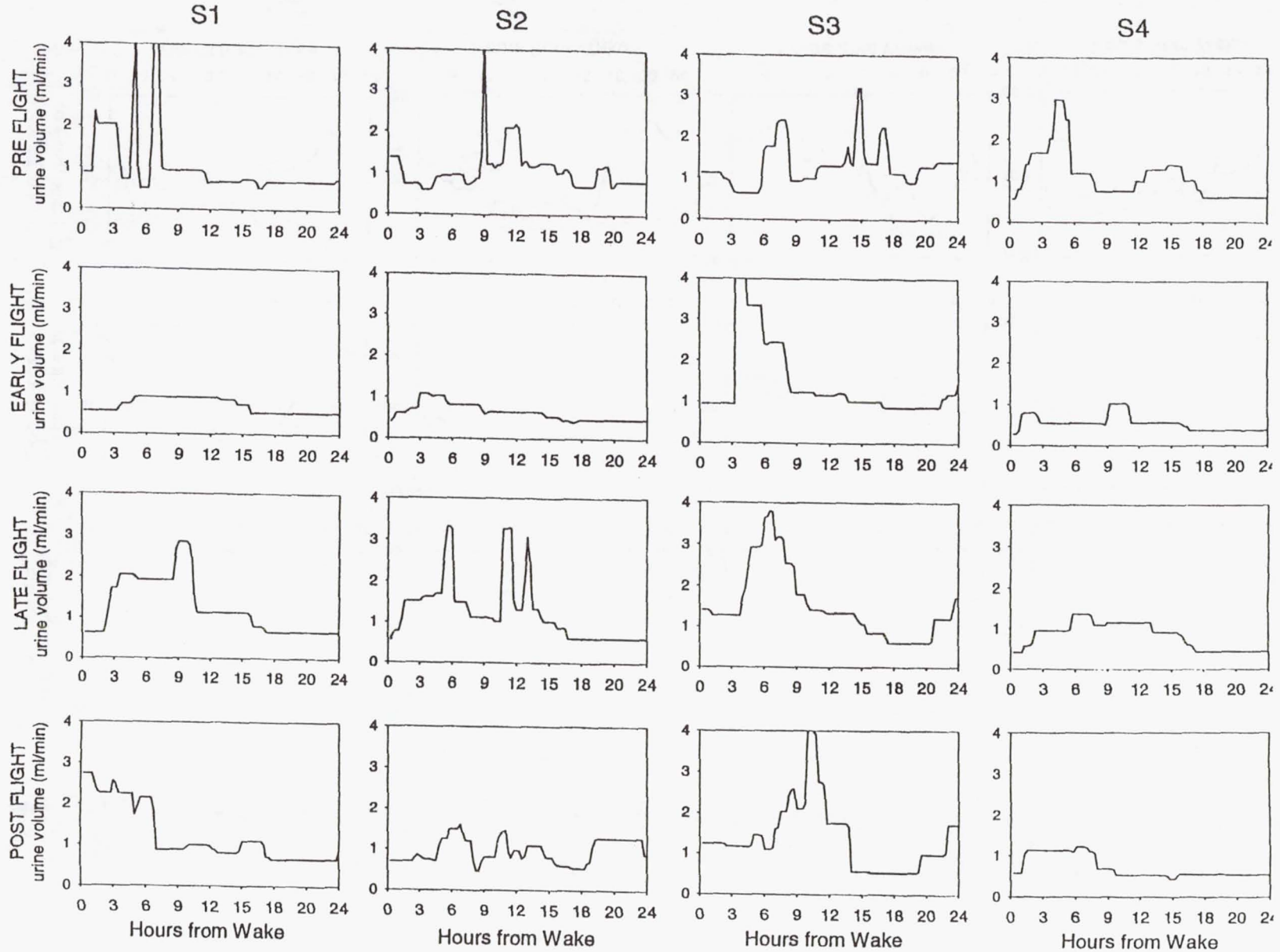
S1
S2
S3
S4
PRE FLIGHT
EARLY FLIGHT
LATE FLIGHT
POST FLIGHT
urine volume (ml/min)
0 1 2 3 4
0 3 6 9 12 15 18 20 24
Hours from Wake

Figure 5

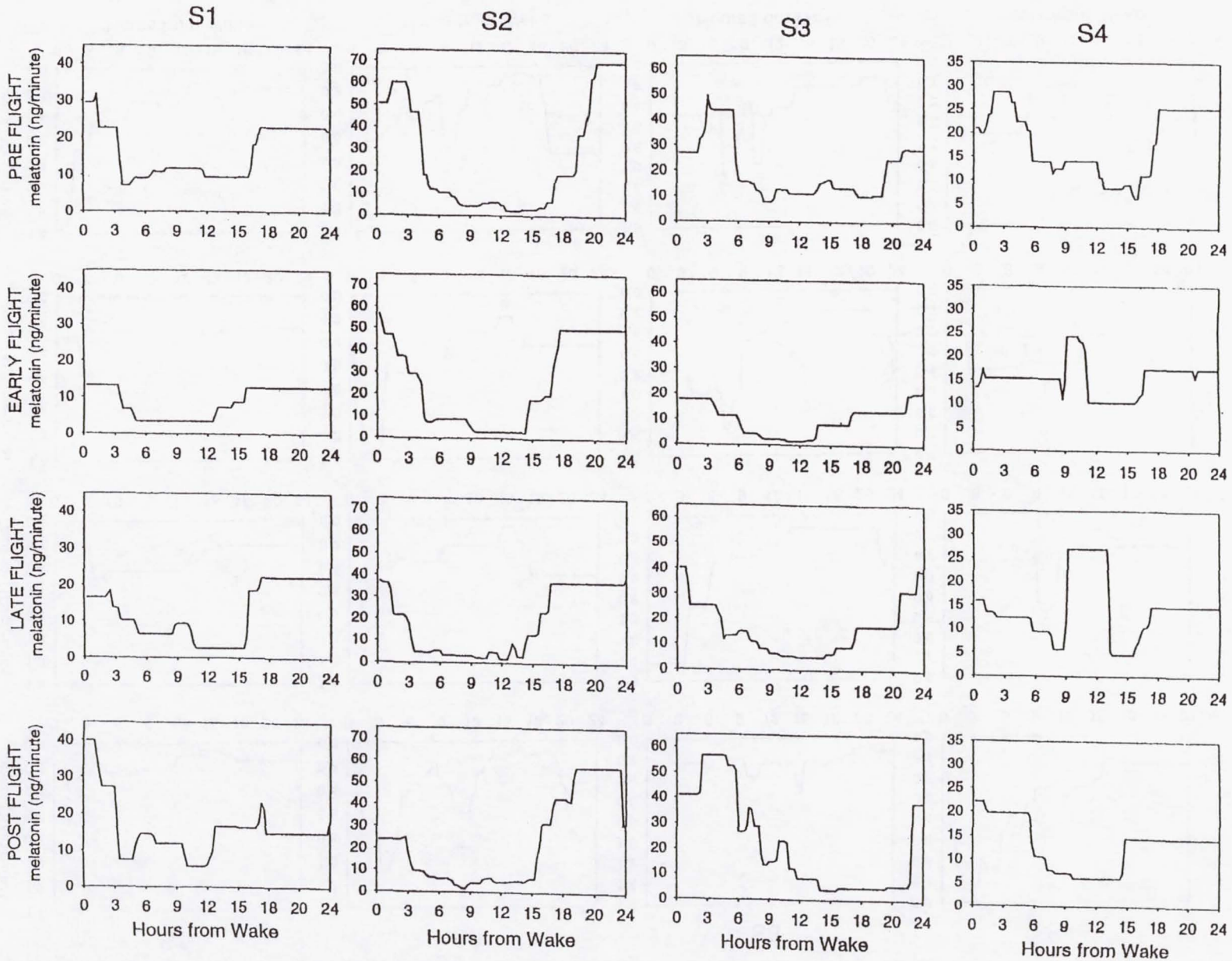
S1
S2
S3
S4
PRE FLIGHT
EARLY FLIGHT
LATE FLIGHT
POST FLIGHT
melatonin (ng/minute)
Hours from Wake

Figure 6

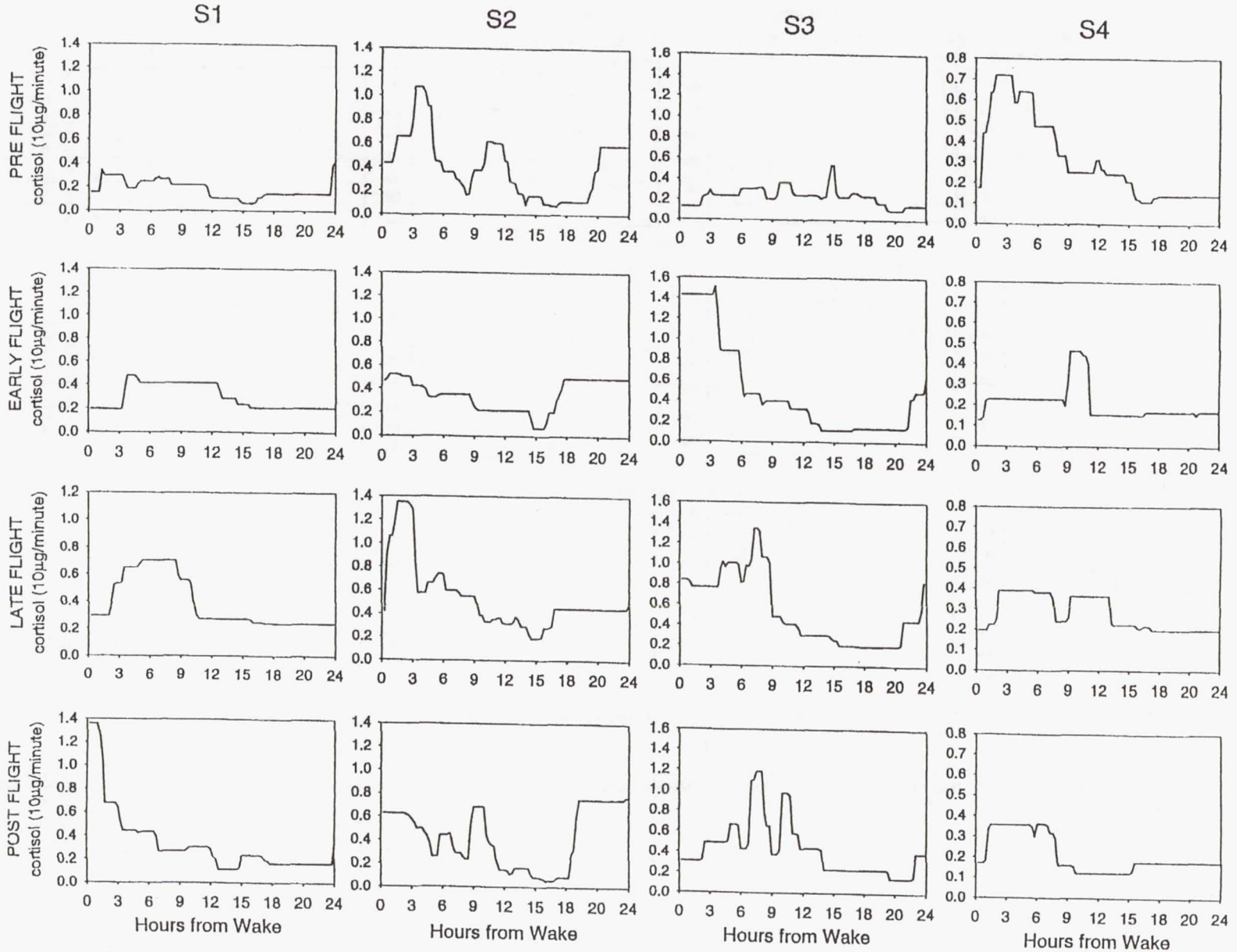
S1
S2
S3
S4
PRE FLIGHT
EARLY FLIGHT
LATE FLIGHT
POST FLIGHT
cortisol (10µg/minute)
Hours from Wake

Figure 7

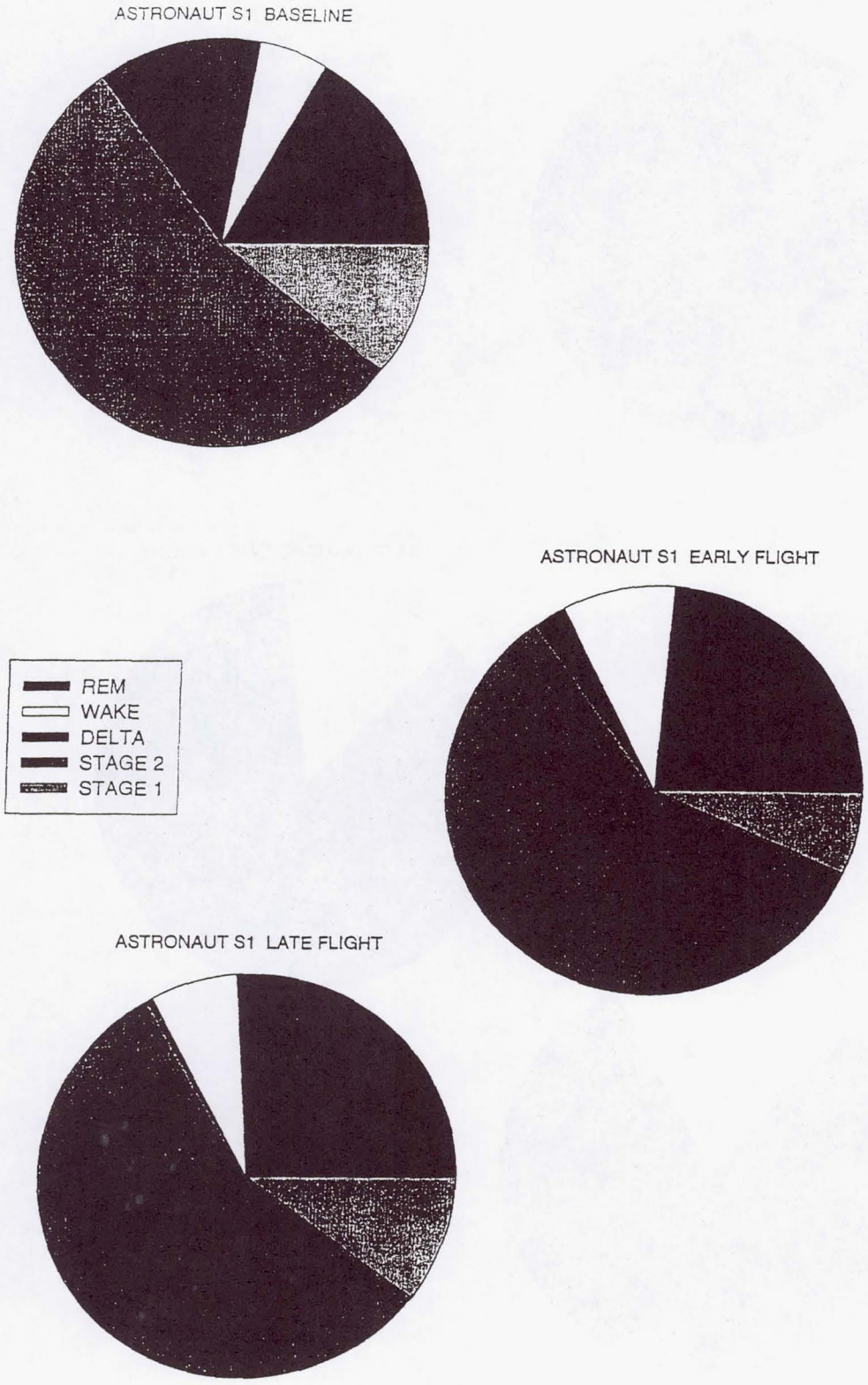
ASTRONAUT S1 BASELINE
ASTRONAUT S1 EARLY FLIGHT
ASTRONAUT S1 LATE FLIGHT
REM
WAKE
DELTA
STAGE 2
STAGE 1

Figure 8

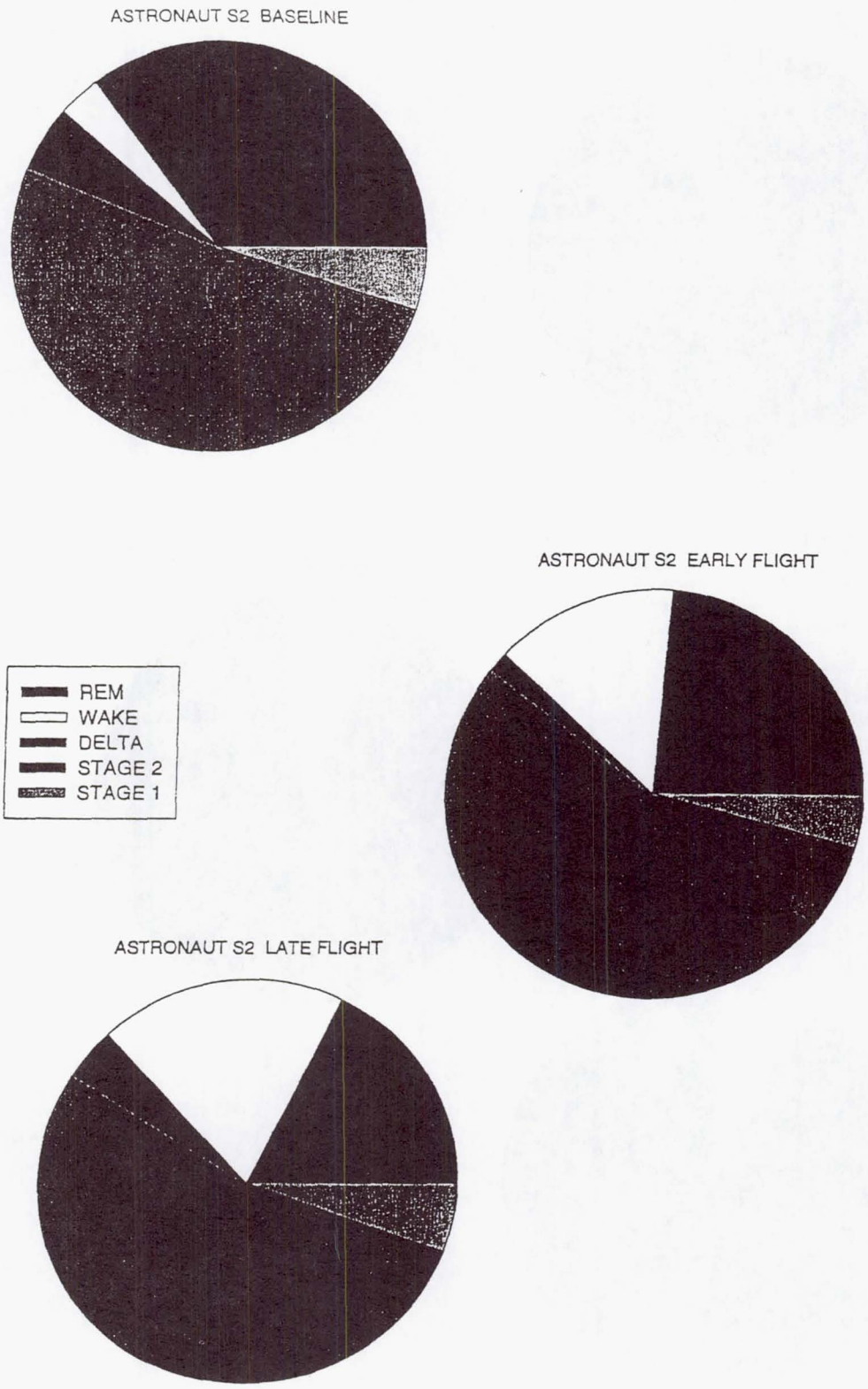
ASTRONAUT S2 BASELINE
ASTRONAUT S2 EARLY FLIGHT
ASTRONAUT S2 LATE FLIGHT
REM
WAKE
DELTA
STAGE 2
STAGE 1

Figure 9

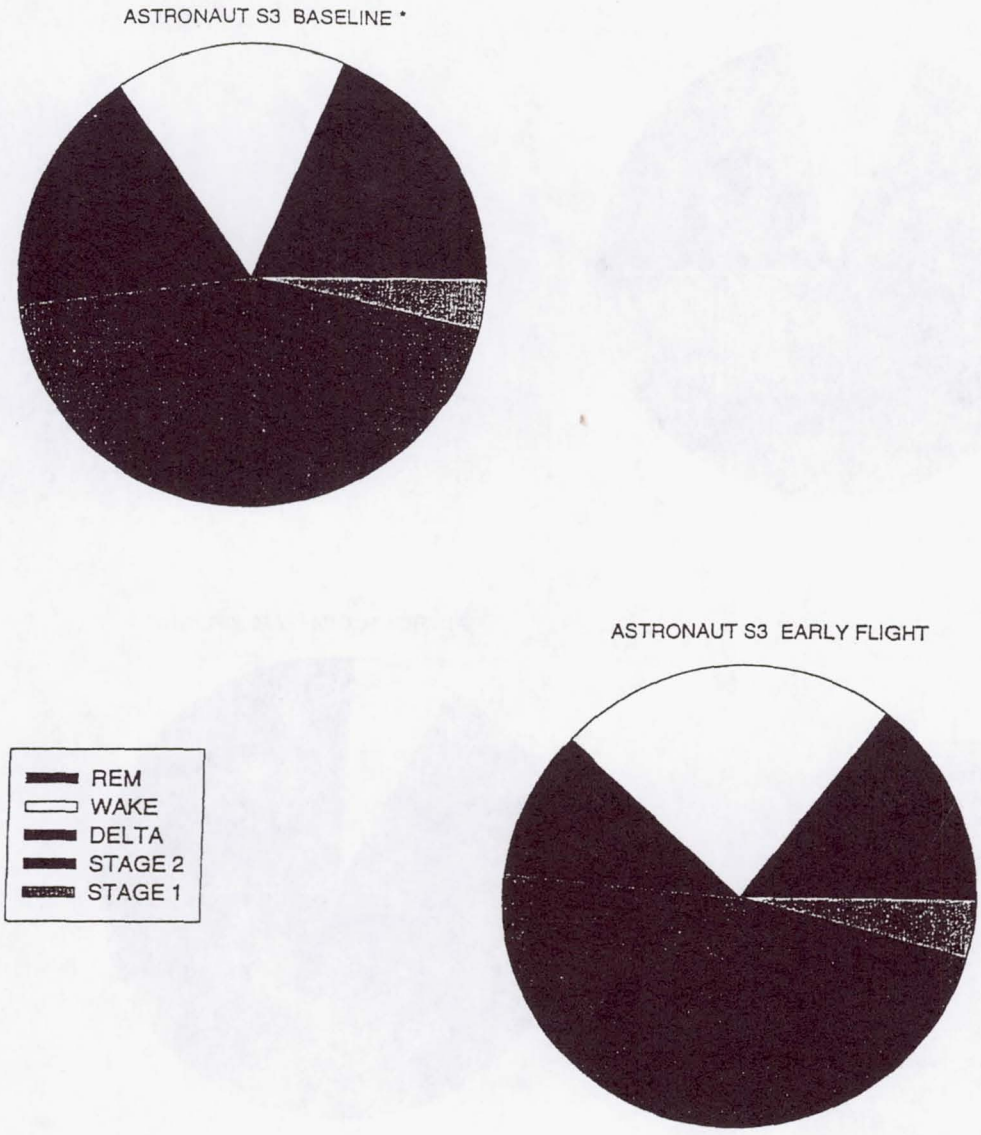
ASTRONAUT S3 BASELINE *
ASTRONAUT S3 EARLY FLIGHT
REM
WAKE
DELTA
STAGE 2
STAGE 1

Figure 10

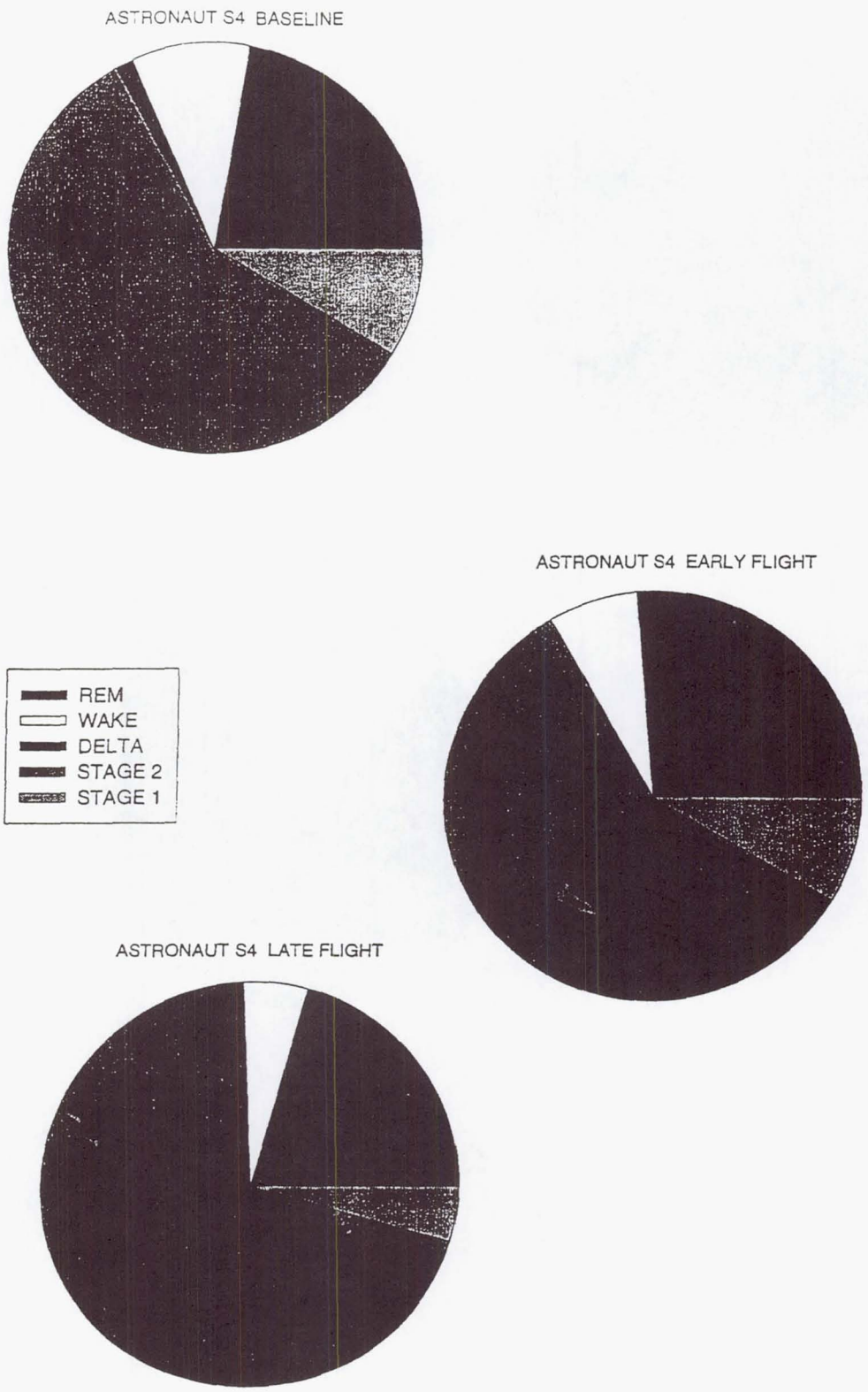
ASTRONAUT S4 BASELINE
ASTRONAUT S4 EARLY FLIGHT
ASTRONAUT S4 LATE FLIGHT
REM
WAKE
DELTA
STAGE 2
STAGE 1

JSC Human Life Sciences Project

E963 - Microgravity Effects on Standardized Cognitive Performance Measures

Principal Investigator:

Dr. Sam Schiflett
USAF Armstrong Lab
Brooks Air Force Base, Texas

LMS-PAWS

Microgravity Effects on Standardized Cognitive Performance Measures

Principal Investigator:
Samuel G. Schiflett
USAF Armstrong Laboratory
Brooks AFB Texas, USA

Co-Investigators:
Douglas Eddy, NTI, Incorporated
Robert E. Schlegel, University of Oklahoma
Randa Shehab, University of Oklahoma

OBJECTIVE

The objective of this experiment was to determine the effects of microgravity upon cognitive skills critical to the success of operational tasks in short-term space flight.

BACKGROUND

Previous In-orbit Research

Astronauts are subject to a variety of stresses during space flight. These stresses include microgravity, physical isolation, confinement, lack of privacy, fatigue, and changing work/rest cycles [1]. Any one or a combination of these stressors could degrade the cognitive skills required to perform tasks essential to the success of a mission. Of these potential stressors, fatigue and changing work/rest cycles are known to cause deterioration in astronaut productivity [2]. However, over the past 20 years, only limited attempts have been made to systematically determine the effects of space flight on cognitive skills [3, 4, 5, 6].

In a previous cooperative USAF/NASA experiment [7,8], the Performance Assessment Workstation (PAWS) was flown as part of the payload for the Second International Microgravity Laboratory (IML-2) on-board the Space Shuttle Columbia (STS-65) in July 1994. The experiment studied the interactive effects of microgravity and fatigue on cognitive functioning of three astronauts for 13 days on a dual-shift mission. The same PAWS battery of performance tests used on the IML-2 flight was reflown on LMS. The tests measured short-term memory, spatial processing, attention, tracking, and dual task timesharing. All three astronauts completed 40, 20-minute sessions of the PAWS battery containing 6 cognitive performance tests and 2 subjective scales (mood and fatigue) on a laptop computer. Twenty-four sessions were preflight, 13 sessions were in-orbit, and 3 sessions were postflight.

In general, performance patterns of the astronauts in-orbit and during ground-based periods were comparable after learning of the task had stabilized, with the exception of Continuous Recognition and Attention Switching-Manikin. One subject showed an improvement in both tasks and the other two subjects each had a decrement in rate of responding (time/item) and reaction time for a single task. The remaining decrements in performance found in-orbit compared to ground-based learning predictions of modeled performance occurred in only one subject for Attention Switching-Mathematical Processing, Unstable Tracking (lambda) and Dual Tracking (control losses). The results showing deviations from single-subject predicted performance levels occurred mainly during the first and last few days in space related to adaptation and accumulative fatigue, respectively. These trends of early and late performance decrements, especially in Tracking Tasks, are similar to the findings in Manzey, *et al.* [5].

Even if one considers the converging evidence from all of the Shuttle and MIR in-flight experiments reviewed, the currently available database about human performance in space is still too small to warrant final conclusions about cognition and visuomotor performance while living and working in microgravity. Also, isolation of microgravity as the single stressor causing in-orbit performance deterioration cannot be fully determined from the results as reported to date. Therefore, additional ground-based control research studies

and more in-orbit subjects are required before these results can be generalized to future space travelers. This LMS mission was flown to add to the performance database and gain additional insights into the cognitive functioning of astronauts in space.

Performance Test Selection Criteria

The Performance Assessment Workstation was assembled from tests contained within the Unified Tri-Service Cognitive Performance Assessment Battery (UTC-PAB) [9]. Upon examination of past payload and mission specialists' tasks and insights gained at NASA workshops held at Johnson Space Center on Human Factors requirements, several functional task areas potentially affected by microgravity were identified. Of these, spatial information-processing, fine motor control, directed attention, and time-sharing play a disproportionately important role in the success of a variety of Spacelab and Space Station tasks. An additional test selection criterion was the information provided by a specific test should aid in identifying the locus of the performance decrement potentially affected by living and working in microgravity.

METHODS

Data Aquisition

Subjects. The four male astronaut subjects were members of the seven person crew on Columbia Space Shuttle flight STS-78. Two of the astronauts had previous flight experience. Subject anonymity in data collection, analysis, and reporting of results was protected by randomly assigning subject numbers to the four astronauts. During the recovery phase all debriefing sessions of results were done on an individual basis.

Equipment. The Performance Assessment Workstation consists of a NASA modified IBM ThinkPad 755C laptop computer with a color display and a NASA 2" trackball (MSI Model 622).

Description of Tests and Subjective Scales. The performance tests are described in the order of presentation to the subjects. Unless otherwise noted the dependent measures for each test included: the percentage of correct responses, the mean correct reaction-time, and throughput. The duration of each test was three minutes unless stated otherwise. More detailed descriptions of all the PAWS tests and subjective scales as related to the ground-based reference group training schedules, test reliability and differential stability can be found in Schlegel, Shehab, Gilliland, Eddy, and Schiflett[10].

Visual Analogue Mood Scale. This scale samples the subject's mood using eight descriptors: alert, sad, tense, level of effort, happy, weary, calm, and sleepy. The subject indicates on a horizontal line how much each mood descriptor applies to him/her by placing a cursor between end points labeled "very little" and "very much" [11].

Unstable Tracking. This test, requires the subject to maintain a target (vertical line) in the center between two vertical lines on the left and right of the screen. A forcing function of increasing difficulty (lambda level) is used to displace the target. The subject must manipulate a control device, trackball, to null this input disturbance. The dependent measure was the mean of the difficulty level (lambda) the subject was capable of achieving before each control loss during a two-minute session.

Matrix Rotation. The Matrix test developed by Damos and Lyall [12] was used to assess spatial processing. This 90 second test displays a series of patterns. Each pattern is a 5 by 5 matrix with five illuminated cells that have been selected at random. The subject indicates whether successive matrices are similar or different with key responses. For "same" responses, the two patterns are never presented in exactly the same orientation; the second pattern is always rotated either 90 degrees clockwise or counter clockwise relative to the preceding pattern.

Sternberg Memory Search. The short-term memory test paradigm requires subjects to recognize visually presented letters and respond as rapidly and accurately as possible. At the beginning of the test, a set of four letters drawn randomly from a restricted alphabet is presented to the subject for memorization. Individual letters are presented next. If the presented letter matches one of the letters in the previously memorized set, the subject responds with a key press indicating "same" otherwise "different."

Continuous Recognition. In this working memory test, the subject is presented with two numbers, one above the other. The first task is to remember the bottom number. When the next two numbers appear, the subject determines if the new top number is the same as the previous bottom number. However, before responding, one must note the new bottom number because as soon as a response is made, the numbers are replaced by a new pair.

Directed Attention--Manikin and Mathematical Processing. In this four minute test, the subject has two distinct and discrete tasks to perform. One task is spatially-based and the other is mathematically-based. Both appear side-by-side in every display. An indicator shows which task is "active" (i.e., must be responded to) and each task has separate response keys. The switching from task to task is random (within constraints). The first key press for either task is taken as the response. Reaction times after a switch are recorded separately. The spatial processing task, manikin, appears on the left, the mathematical processing task is on the right of the display. A manikin "stick figure" is presented facing either forward or backward, upright or upside-down. The figure stands on a box and inside the box is either a rectangle or a circle symbol. Each of the figure's hands contains one of the symbols. The subject's task is to indicate which hand, left or right, holds the matching symbol. The mathematical processing task presents three single-digit numbers that must be added or subtracted. The subject indicates if the answer is greater or less than five with different response keys.

Dual Task. This test combines the Unstable Tracking and Sternberg Memory Search tests into a single time sharing task. In this implementation, the tracking task is presented in the center of the screen and the letters of the memory search task appear in a fixed location directly above the center null point. The tracking task was individually adapted after the first nine training trials and presented in the subcritical mode, with a "fixed lambda" empirically determined using the results of the single Unstable Tracking test. The dependent measure for tracking was the number of control losses during the trial.

Fatigue Scale. The subject keys a number from one to seven indicating which of seven statements best describes his momentary fatigue state. The statements range from fully alert (1) to completely exhausted (7).

Experimental Procedure. An orientation session provided subjects with background information about the experiment and a demonstration of the PAWS approximately one year prior to launch. Data were collected from each subject over a period of approximately two months. All four astronauts took the tests on roughly the same schedule. They completed 37 sessions that consisted of 24 sessions preflight (8 training ses-sions over 2 days and 16 practice sessions over approximately 3 weeks), 9 sessions approximately every other day in-orbit, and 4 sessions postflight every other day. After each test battery was completed the subjects wrote down or voiced into a micro-cassette recorder a data summary display containing 11 measures.

With the exception of the Dual Task, all task parameters remained constant throughout the experiment. Initially, the tracking component of the Dual Task was fixed at a constant lambda (difficulty level) of 2.0 for all subjects. However, the lambda value was individualized for each subject at a specific point during practice in order to equate task difficulty among subjects with different tracking abilities. The final lambda value for each subject was set at 70% of the mean of the maximum lambda values for the Unstable Tracking test on training Trials 7 and 8. The first exposure to the individualized fixed lambda level for each subject was at Trial 10. After being individualized, the lambda value remained constant for the Dual Task for the remaining practice, in-orbit, and recovery periods.

Analysis

Approach. Hypothesis testing is usually performed with standard statistical tests that require 8 to 12 subjects per group or test condition. On the LMS mission, normal inferential statistics for repeated measures would be woefully under powered to find significant effects with only four subjects. Therefore, single-subject analyses were used and the findings are only applicable to the actual subjects tested. The approach used with these data was a variation on the one presented at the 66th Annual Meeting of the Aerospace Medical Association [7] in conjunction with the results of IML-2.

Previous research by Newell and Rosenbloom enables the development of mathematical models of learning for each subject's performance data [13]. Once the "best" model is identified, appropriate transforms can be used to linearize both the model and data thus allowing standard regression predictions with known confidence limits. The predictions of the learning equations serve as "the baseline" for comparing the in-orbit data. This "baseline" contains the expected improvement (learning) that occurs with each administration.

Modeling Procedure. Three families of mathematical equations were fit to each subject's preflight data. They were power, hyperbolic, and exponential. These nonlinear equations have been shown to provide good fits to cognitive performance measures in controlled environments [13]. The following PAWS data measures were selected for modeling from each subject: Mean Lambda (1), Throughput (5), Mean Correct Reaction Time (RT) (5), Switching Time (2), and Control Losses (1). The number in parentheses is the number of measures of that type. Only the training and practice data (Trials 1 through 24) were used to determine the models of learning. The generalized models and their equations follow:

Power	$Y = A + B(X+E)^C$	(1)
Hyperbolic	$Y = A + B/(X+E)$	(2)
Exponential	$Y = A + Be^{CX}$	(3)

Y is the dependent measure of interest, for example, the number of tracking control losses. X is the trial or session number. A is the asymptote for the curve. E is the number of sessions that were theoretically missed before data collection commenced. B and C are parameters related to the rate of learning or growth of the function. The A and E values are occasionally zero giving the simpler forms of the equations. Each subject was allowed to have their own model family for each dependent measure. A common best model was not selected for all subjects. All data manipulation and statistical procedures were accomplished with the SAS Statistical Package, Version 6.1.

To make predictions from the models and estimate the confidence interval for their predictions, the data and estimates had to be linearized. This was accomplished with a log/log transform in the case of the power and hyperbolic functions and a log transform in the case of the exponential function. A linear regression was performed on the linearized data (session number and dependent measure). The statistic was the difference between the means of the predicted points and the mean of the actual in-orbit data values divided by the standard deviation for the regression of the baseline values. This approach tests for a shift in the mean of the in-orbit data from the mean of the data predicted by the model.

The approach was validated on the data of 96 ground-based subjects [10] who should not have had any "in-orbit" effect. The statistical test gave from three to eight significant effects out of the 96 subjects with alpha set at 0.05. Most dependent measures were best fit by a mixture of models: 40-50% exponential, 30-50% power, and 10-15% hyperbolic. In summary, the learning models allowed the assessment of the in-orbit effects while removing the expected, small effects of continued performance improvement with each testing session.

Single Subject Modeling Analyses

The results of modeling each astronaut's baseline data are shown in the table. Each test is listed with its measures. The mean R^2 is listed summarizing the model fits for **all** subjects.

LMS Statistical Results by Task

Task/Dep. Measure	Mean R^2	Significant* In-orbit Effects
Tracking		
Mean Lambda	0.73	1°
Matrix		
Time/Item	0.78	0
Mean RT	0.80	1
Memory Search		
Time/Item	0.71	0
Mean RT	0.79	0
Continuous Recognition		
Time/Item	0.87	0
Mean RT	0.88	0
Directed Attention - Manikin		
Time/Item	0.92	0
Mean RT	0.84	0
Switching time	0.88	0
Directed Attention - Math. Processing		
Time/Item	0.85	1
Mean RT	0.81	2
Switching time	0.62	2
Dual		
Control Losses	0.32	0

* $p < 0.05$ ° performance exceeded model predictions

Comparison of In-orbit Performance with Learning Model Projections

The table summarizes the statistically significant in-orbit effects for each dependent measure. The number in the last column indicates how many subjects of the four showed a significant effect ($p<0.05$). Using this single-subject, modeling approach, the performance measures of most tests were not significantly affected in-orbit. No subject's mean in-orbit performance showed a significant deviation from model projections for the following tests: Memory Search, Continous Recognition, Manikin, and Dual. Each test showing a significant effect is discussed and graphically illustrated with the subject's data in the following subsections. All the models were based on the first 24 trials and projected through the in-orbit and postflight trials. All significant effects were confined to the same two subjects designated as one (1) and two (2).

Critical Tracking Test. The most unexpected in-orbit effect was found for the Tracking test. Based on a generalized exponential model of preflight performance, Subject 1 showed improved in-orbit performance, t(4)

= -2.99, p =.041. The dependent variable was Lambda, the difficulty level of the unstable element that the subject was able to tolerate before loosing control. Figure 1 shows the reciprocal of his Lambda ($1/\lambda$) plotted against trials. Apparently this subject found a better strategy for tracking in the last two sessions prior to launch and continued to use the approach thereafter.

Matrix Test. Figure 2 shows the second subject's RT for the Matrix Test improving until the fourth session after launch, Trial 28. Thereafter, RT appears to level off until recovery where it slows to a level comparable to pre-launch. The difference between the predicted RT and the actual was 143 msec, $t(4) = 3.17$. This subject's percentage of correct responses fluctuated from 84-97% during practice making the throughput measure difficult to model and it did not show a statistically significant effect. The one very slow RT on Trial 28 was unexplained.

Directed Attention Test. Performance on the mathematical portion of the Directed Attention Test showed significant degradation for two subjects. Figure 3 shows the RT measure from the mathematical processing task for the same two subjects shown in earlier figures. Actual RT and model predictions are plotted against trials on the left axis. Figure 3a also shows the subjective fatigue ratings of Subject 1 plotted against the right axis. For Subject 1, there was a pronounced increase in RT latency starting on the first session after launch, Trial 25, that was associated with his highest fatigue rating in-orbit. The difference between the predicted mean RT for all in-orbit sessions and the actual was 207 msec, $t(4) = 3.62$. This effect persisted through 7 days of recovery in which four postflight testing sessions were recorded. As shown in the figure, this subject gave another high fatigue rating on the first session of recovery, Trial 34. Dr. Lawrence Young, an astronaut selectee, commented at the 12th IAA Man in Space Symposium presentation of these data that the subject appears to have a new and reduced performance level resulting from the in-orbit experience.

In Figure 3b, Subject 2 appears to be responding slower starting on Trial 30 and never regains his speed even after recovery. Recall that the Matrix task showed this trend beginning on Trial 28 for this subject. The difference between the predicted mean RT and the actual was 129 msec, $t(4) = 2.98$.

Figure 4 shows the time per item measure for Subject 1 in the mathematical processing task. Again, starting on the first in-orbit testing session, Mission Day 2, performance was significantly degraded. Performance was highly variable on succeeding in-orbit days. The difference between the mean predicted time per item values and the actual was 220 msec, $t(4) = 2.85$. The time per item measure is the reciprocal of throughput, a combined measure of speed and accuracy. This subject appears to improve performance in the last three testing sessions after recovery; however, his best performance remains two sessions before launch.

Switching time is the reaction time for the mathematical processing task after responding to the manikin task in a previous display. It requires the subject to change cognitive processing from a spatial context to a logical symbol manipulation context. Figure 5 shows mean switching time and the model predicted values plotted against trials for the two significantly affected subjects. It appears for these two subjects that, in orbit, it was more difficult to transition from manikin to math than it was preflight. Figure 5a shows a switching time increase of nearly 400 msec when comparing performance pre-launch baseline with the first in-orbit testing session. A corresponding fatigue rating from 2 to 5 may explain some of the performance decrement. This performance level is equivalent to that of Trial 6 in early training. The difference between the predicted in-orbit mean switching time and the actual was 166 msec, $t(4) = 3.11$. In Figure 5b, Subject 2 appears to be having trouble as early as Trial 27 or 28 on this measure. The difference between the predicted mean switching time and the actual was also 166 msec, $t(4) = 3.05$. Seven days after recovery this subject had not yet recovered his speed on this task.

The statistical approach taken in this paper is very conservative. However, Subject 1 showed non-signifi-cant degradation in Manikin, Continuous Recognition and Matrix. Subject 2 showed non-significant degradation in Manikin, Continuous Recognition and the Dual Task. For a third subject with high variability, his data showed degradation in the plots of all tasks accept the Tracking and Dual tests, but none were statistically

significant. The fourth subject showed non significant reduced performance in plots of Memory Search and Manikin, but actually showed improvement in the mathematical processing task.

CONCLUSIONS

Significance

With only four subjects it is not possible to generalize results to a population of future space travelers. However, if one confines their analysis and interpretation to the four subjects tested in this 16-day mis-sion, some tentative conclusions can be drawn. Generally, in-orbit subjects were able to respond to the tests without significant impairment. The mathematical processing task, a part of the Directed Attention Test, showed significantly degraded performance in two out of the four subjects. The Matrix test perform-ance was degraded in one subject. The improvement seen in the Tracking test for one subject appeared to be the result of an improved tracking strategy developed in the last two practice sessions prior to launch.

The current available database on human performance in space is too small to warrant final definitive conclusions about specific processes of cognition and psychomotor performance affected by living and working in microgravity. However, the data from this flight support the following preliminary conclusions.

1. Cognitive and psychomotor performance can be reliably measured in the microgravity.
2. Performance measures are sensitive to the combined stressor effects of the microgravity environment.
3. Predicted performance levels based on preflight data were not achieved in-orbit for mathemati-cal processing for two-out-of-four subjects. The same was true of one subject on the Matrix Test.
4. A single stressor, such as microgravity or fatigue causing the in-orbit performance deterioration on the two tests cannot be fully determined from these results.

Future Plans

More research controlling other variables that are confounded with these results is needed. Some of the other variables include: experience (number of previous flights), work shift (red or blue), sleep quality and quantity, medications, fatigue, and subject motivation. A research proposal is currently under review at NASA that proposes a shuttle mission simulation that could remove many of the potential confounded causes of performance degradation observed in orbit.

The data from LMS will be combined with those from IML-2 for a future publication. Although there were many differences between the experiments on the two missions, the modeling approach taken with these data will permit a combined analysis with conclusions based on all seven subjects.

REFERENCES

1. J. Christensen and J. Talbot, Review of psychological aspects of space flight. *Aviation, Space and Environmental Medicine* **57**, 203-212 (1986).

2. A. Gundel, V. Nalishiti, E. Reucher, M. Vejvoda and J. Zulley, Sleep and circadian rhythm during a short space mission. Clinical Investigator 71, 718-721 (1993).

3. D.J. Newman, B.K. Lichtenberg and H.L. Alexander, Mental workload and performance experiment. NASA-JSC Grant No. NAG9-125, Unpublished final science review, New Orleans, April 8 (1993).

4. T. Benke, O. Koserenko, N.V. Watson and F. Gerstenbrand, Space and cognition: The measurement of behavioral functions during a 6-day space mission. Aviation, Space and Environmental Medicine 64, 376-379 (1993).

5. D. Manzey, B. Lorenz, A. Schiewe, G. Finell and G. Thiele, Behavioral aspects of human adaptation to space: Analysis of cognitive and psychomotor performance in space during an 8-day space mission. Clinical Investigator 71, 725-731 (1993).

6. D. Manzey, B. Lorenz, V. Nalishiti, Y. Spatenko and G. Finell, Human performance during a long-term stay in space. Proceedings 11th IAA Man in Space for Science and Technology Development, Toulouse-Labege, France, 27-31 March (1995).

7. D.R. Eddy, In-orbit cognitive performance compared to model predictions based on preflight baseline learning. Aerospace Medical Association Abstracts, No. 504, 66th Annual Meeting, Anaheim, CA, May 7-11 (1995).

8. S.G. Schiflett, D.R. Eddy, R.E. Schlegel, J. French & R.L. Shehab, Astronaut performance during preflight, in-orbit, and recovery. Aerospace Medical Association Abstracts No. 503, 66th Annual Meeting, Anaheim, CA, May 7-11 (1995).

9. W. A. Perez, P.J. Masline, F.R. Ramsey & K.E. Urban, Unified tri-services cognitive performance assessment battery: review and methodology, AAMRL-TR-87-007, Wright-Patterson AFB, OH (1987).

10. R. E. Schlegel, R.L. Shehab, K. Gilliland, D.R. Eddy and S.G. Schiflett, Microgravity effects on cognitive performance measures: Practice schedules to acquire and maintain performance stability, AL/CF-TR-94-0040, Brooks AFB, TX (1995).

11. T.H. Monk, J.E. Fookson, J. Kream, M.L. Moline, C.P. Pollack and E.D. Weitzman, Circadian factors during sustained performance: Background and methodology. *Behavior Research Methods, Instruments, and Computers*, 17, 19-26 (1985).

12. D.L. Damos and E.A. Lyall, The effect of asymmetric transfer on dual-task assessment of voice technology. Proceedings of the 28th Annual Meeting of the Human Factors Society, Santa Monica, CA, Human Factors Society (1984).

13. A. Newell and P.S. Rosenbloom, Mechanisms of skill acquisition and the law of practice. In J.R. Anderson (Ed), Cognitive skills and their acquisition, pp. 1-56. Lawrence Erlbaum Assoc., New Jersey (1981).

BIBLIOGRAPHY RELATED TO LMS

D.R. Eddy, S.G. Schiflett, R.E. Schlegel and R. Shehab, Cognitive performance aboard the Life and Microgravity Spacelab. Submitted for publication to Acta Astronautica.

D.R. Eddy, S.G. Schiflett, R.E. Schlegel and R. Shehab, Cognitive performance aboard the Life and Microgravity Spacelab. 12th Man in Space Symposium: The Future of Humans in Space, pp. 106, Washington, D.C., June 8-13, 1997.

R.E. Schlegel, R. Shehab, S.G. Schiflett & D.R. Eddy, The NASA performance assessment workstation: Cognitive performance during head-down bed rest. 12th Man in Space Symposium: The Future of Humans in Space, pp. 107, Washington, D.C., June 8-13, 1997.

R. Shehab, R.E. Schlegel, S.G. Schiflett & D.R. Eddy, The NASA performance assessment workstation: Cognitive performance during head-down bed rest. Submitted for publication to Acta Astronautica.

ABSTRACT

The impact of microgravity and other stressors on cognitive performance need to be quantified before long duration space flights are planned or attempted since countermeasures may be required. Four astronauts completed 38 sessions of a 20-minute battery of six cognitive performance tests on a laptop computer. Twenty-four sessions were preflight, 9 sessions were in-orbit, and 5 sessions were postflight. Mathematical models of learning were fit to each subject's preflight data for each of 14 dependent variables. Assuming continued improvement, expected values were generated from the models for in-orbit comparison. Using single subject designs, two subjects showed statistically significant in-orbit effects. One subject was degraded in two tests, the other was degraded in one test and exceeded performance expectations in another. Other subjects showed no statistically significant effects on the tests. The factors causing the deterioration in the two subjects can not be determined without appropriate ground-based control groups.

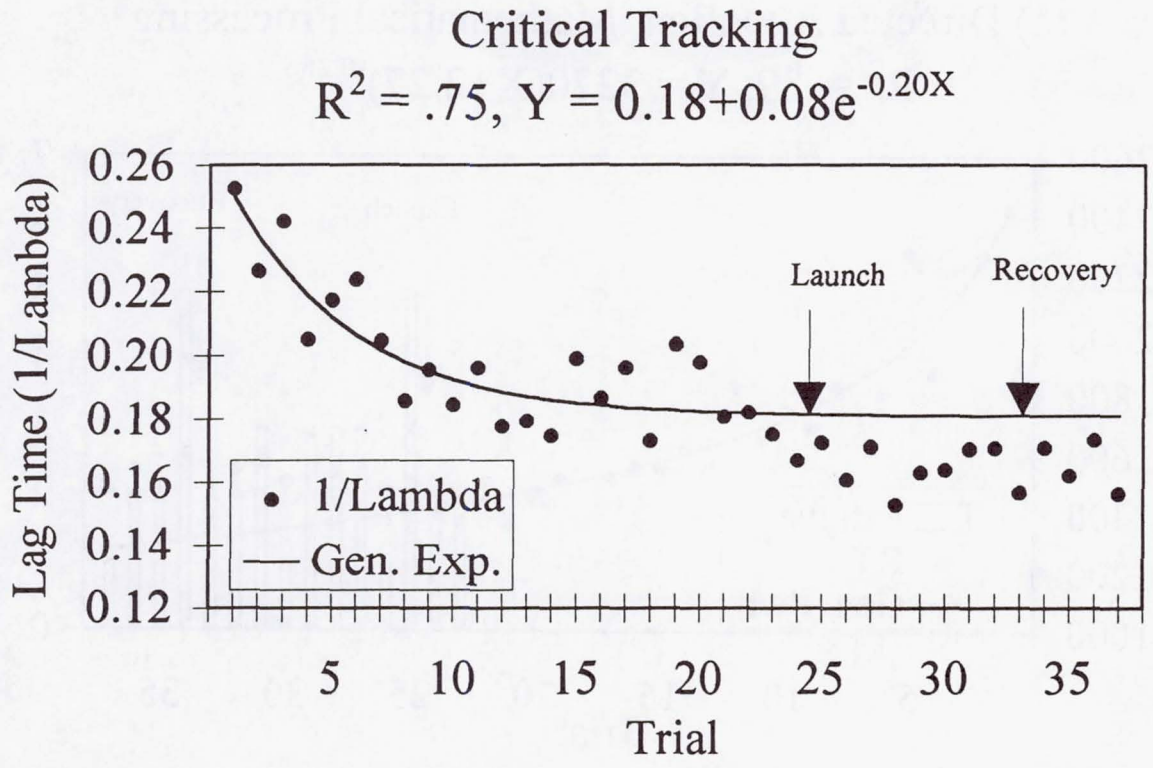

Figure 1. Lag time (1/Lambda) is plotted against trials for Subject 1. The solid line shows the generalized exponential model predictions; the circles are the data values.

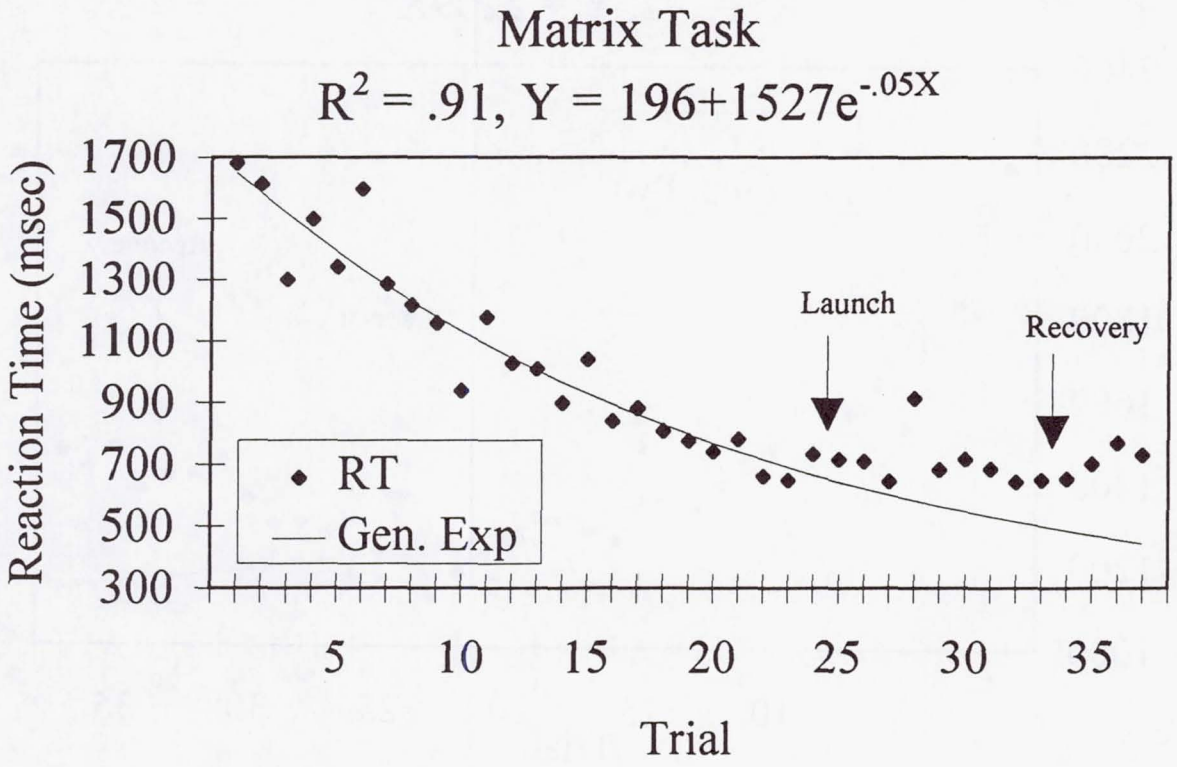

Figure 2. Mean correct RT plotted against trials for Subject 2 showing performance degradation in-orbit. The diamonds show actual data values.

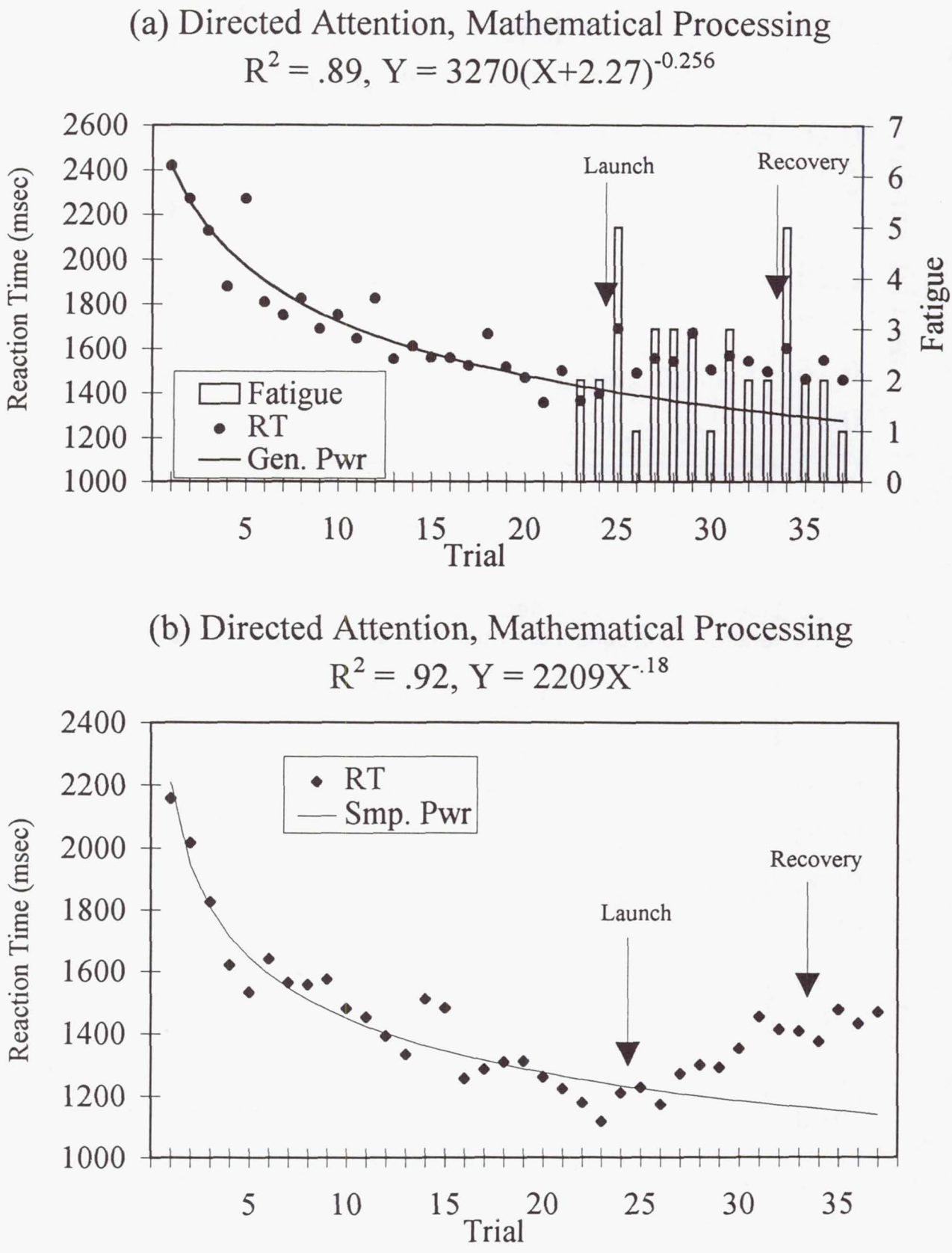

Figure 3. Mean correct RT plotted against trials. (a) Fatigue ratings for Subject 1 start two trials before launch, (b) data from Subject 2.

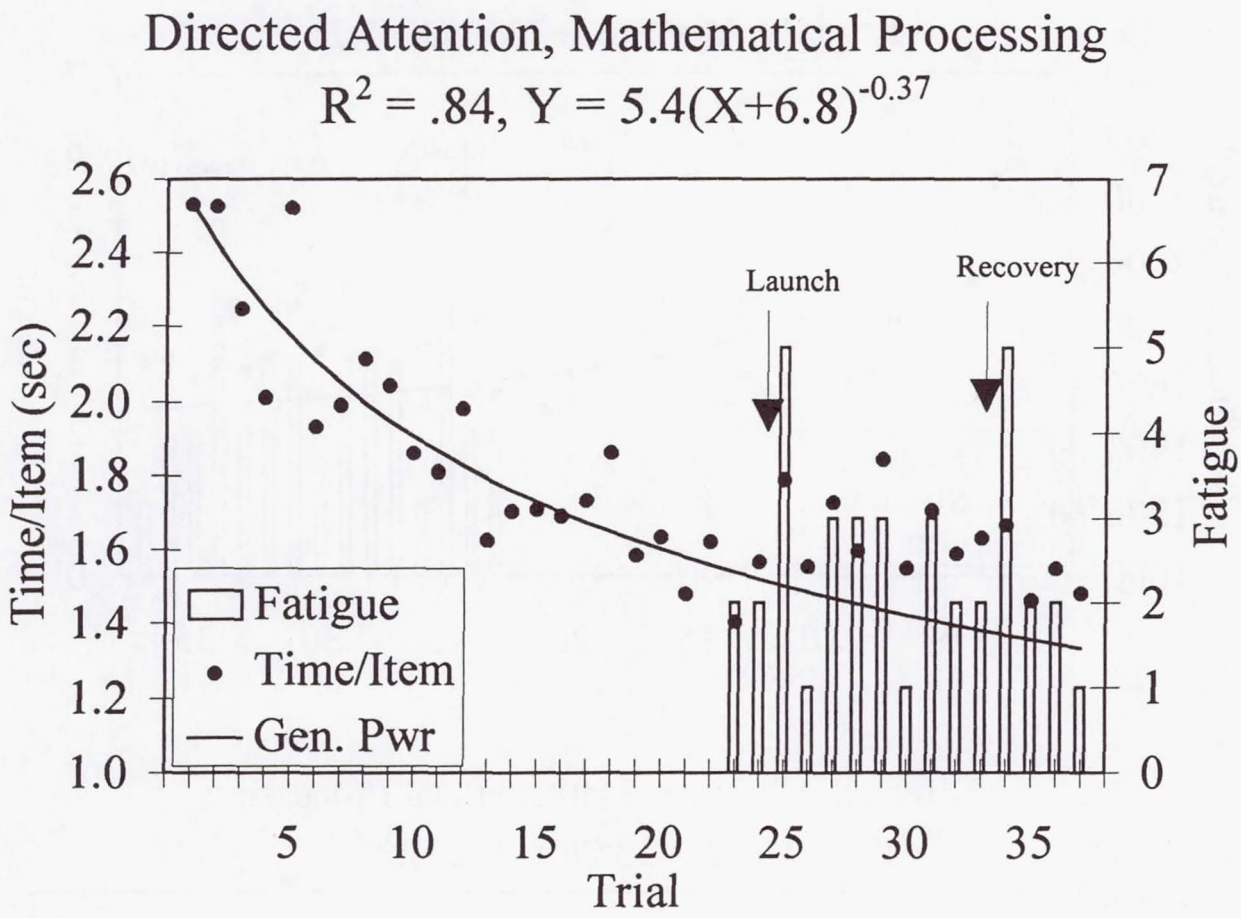

Figure 4. Time-per-item plotted against trials for Subject 1. Fatigue ratings are shown in the histogram plotted against the right axis starting two trials before launch.

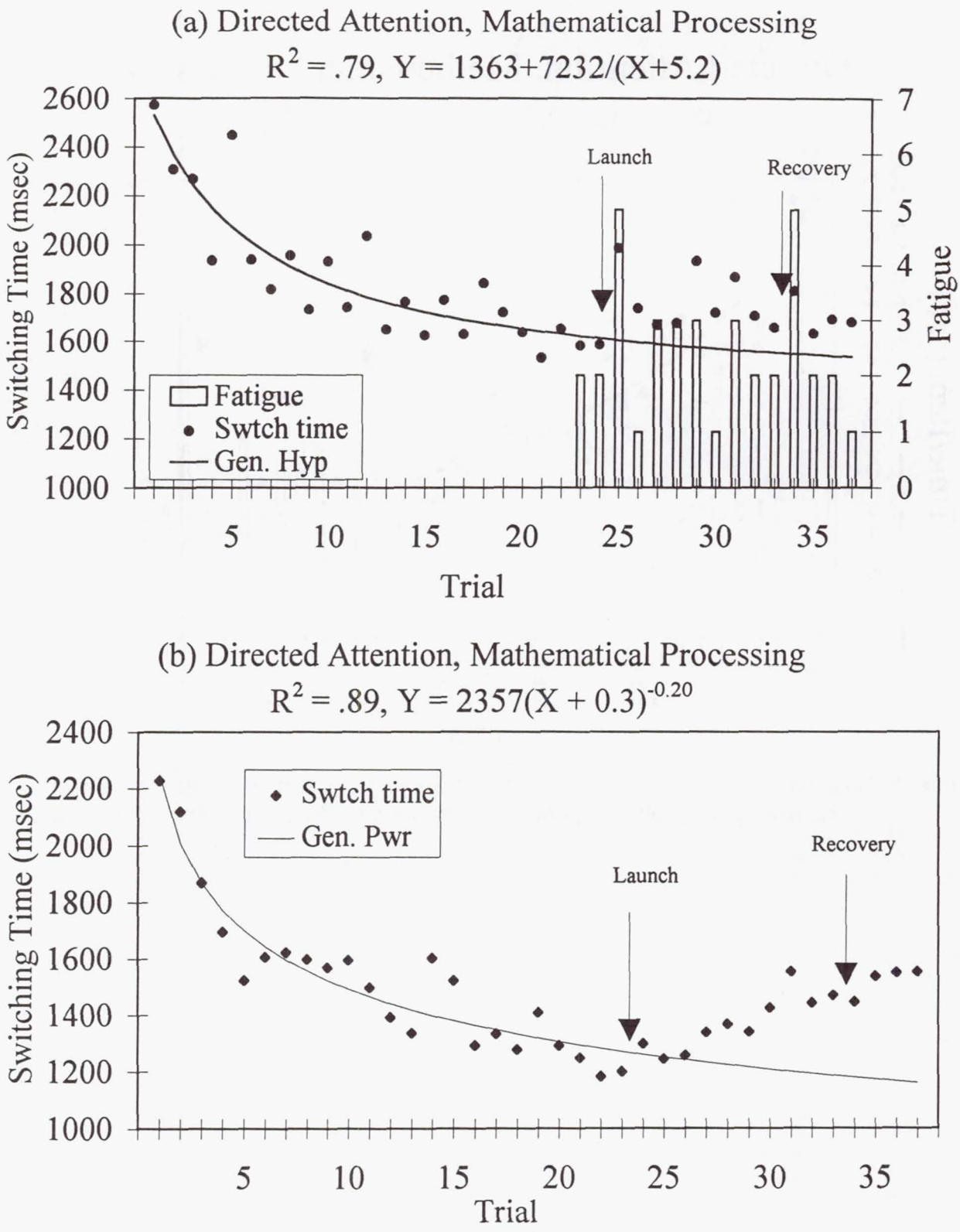

Figure 5. Mean switching time plotted against trials. Model predictions are shown with solid lines, (a) data from Subject 1 including Fatigue ratings, (b) data from Subject 2.

JSC Human Life Sciences Project

E971 - Measurement of Energy Expenditures During Spaceflight Using the Doubly Labeled Water Method

Principal Investigator:

Dr. Peter Stein
University of Medicine and Dentisty of New Jersey
Stratford, New Jersey

E971. MEASUREMENT OF ENERGY EXPENDITURE DURING SPACE FLIGHTUSING THE DOUBLY LABELED WATER (DLW) METHOD

T.P. Stein, PhD, PI
University of Medicine and Dentistry of New Jersey
Stratford, NJ 08084

M.D. Schluter, BS, Experiment Mgr.
University of Medicine and Dentistry of New Jersey
Stratford, NJ 08084

H.W. Lane, PhD, Co-I
NASA LBJ Space Center
Houston, TX 77058

R.J. Gretebeck, PhD, Co-I
Purdue University
West Lafayette, IN 47907

R.W. Hoyt, PhD, Co-I
US Army Institute for Environmental Medicine
Natick MA 01760

M.J. Leskiw, BS, Res. Assoc.
University of Medicine and Dentistry of New Jersey
Stratford, NJ 08084

A. SPECIFIC AIMS

1. To measure human energy expenditure during flight on the space shuttle by using the doubly labeled water method for measuring energy expenditure.

2. To determine whether astronauts are in negative energy balance during space flight on the shuttle.

3. To compare energy expenditure during spaceflight against that found with bedrest.

B. BACKGROUND

Human spaceflight is associated with a loss of body protein. Studies of nitrogen balance during spaceflight have reported a persistent negative nitrogen balance (5,18,24). Specific changes include a loss of lean body mass, decreased muscle mass in the calves, and decreased muscle strength (5,10,22). The major muscle loss is believed to be associated with the anti-gravity (postural) muscles.

The problem of protein wasting is of considerable practical importance because it may result in 'impaired performance during flight' (14). On the ground, chronic protein wasting has serious consequences. Apart from decreased physical performance, there is progressively increasing susceptibility to infection (1,23). Other processes that are compromised include wound healing, which may be a problem if injury ever occurs during spaceflight. It is interesting to note that decreased immunocompetence during spaceflight has been reported (6,7).

As yet, the mechanism of protein wasting during space flight is unknown and the protein wasting persists in being a problem particularly with long term missions. There are a number of viable hypotheses based on ground control analogies which can account for the muscle atrophy and protein loss. The principal ones are:

(1) Muscle atrophy secondary to disuse. Muscle atrophy can occur from less work being required of certain muscles at '0' g.- e.g. the postural muscles. The corresponding ground based analogy is bed rest (13).

(2) A stress response. A characteristic response to a metabolic stress (e.g. trauma) is a transient protein loss, which is usually self limiting (12,25). Conceivably the body responds to the acute change to '0' g as a stress. As part of the response to stress, protein turnover is increased with the increase in protein breakdown being greater than the increase in protein synthesis, hence the protein loss. Stress hormone levels (glucocorticoids, catecholamines) were found to be increased in the Skylab missions (9). We have shown on the SLS1 and SLS2 missions that a metabolic stress response is a factor in at least the early protein loss on the shuttle (18,19,20).

(3) An energy deficit. A characteristic response at '1' g to an energy deficit is a loss of body protein. An energy deficit can occur either from decreased intake or increased energy expenditure. An energy deficit was a factor in the muscle loss found on the Skylab missions. By using the dietary intake, nitrogen excretion, body composition data and computer modeling, the Skylab investigators concluded that the crew were in an energy deficit state for most of the flight (11,15).

The primary objective of this study was to determine if the payload crew were in energ balance. A secondary objective was to address the question of whether human energy expenditure is increased or decreased in flight for comparable activity. This is issue was addressed by comparing the inflight energy expenditure and balance measurements against those obtained on the ground from the LMS bed rest study.

C. APPROACH TO PROBLEM

Energy expenditure for both studies was determined by the doubly labeled water (DLW, $^{2}H_{2}{}^{18}O$) method. Energy intake was measured by dietary monitoring and energy balance from the difference betweeen intake and expenditure.

The doubly labeled water method is a highly accurate means of measuring energy expenditure in a safe, non-invasive, time-efficient manner using only urine or saliva specimens for

analysis. The accuracy is better than 5% and the reproducibility between repeat studies on the same subject is about 9%. T he method consists of giving water labeled with the stable (non-radioactive) isotopes deuterium (^2H) and ^{18}O. The two isotopes leave the body water at different rates. Deuterium leaves as water, mainly as urine, whereas ^{18}O leaves as both water and exhaled CO_2. The difference in loss rates is therefore equal to the rate of CO_2 production. The CO_2 production rate is directly related to the rate of energy expenditure.

The principal requirements from the subject is that he/she drink water labeled with the non-radioactive, naturally occurring isotopes ^{18}O and ^2H and the body water sampled at suitable time intervals (~3 - 20d, 2,17). The body water can be sampled either as blood, urine or saliva. We used saliva. Other measurements necessary to achieve these objectives included dietary intake, nitrogen balance, 3-methyl histidine excretion and body composition.

We measured energy expenditure and body composition before flight, inflight and postflight. Energy expenditure and balance were measured over blocks of 6 days. There were two consecutive 6 day blocks preflight (days L-15 to L-9 and L-9 to L-3), two similar consecutive 6 day blocks inflight (days FD-3 to FD-9 and FD-9 to FD-15) and a similar schedule postflight (R+3 to R+6 and R+9 to R+15). L-X refers to launch day minus X days, FD-X, flight day X and R+X to return + X days. Using such a block scheme increases the sensitivity of the measurements by allowing for duplicate measurements on each subject, an important factor when the number of test subjects is small. The space flight study was restricted to the four payload crew.

Table 1. PERIODS FOR MEASUREMENT OF ENERGY EXPENDITURE

PREFLIGHT	INFLIGHT	POSTFLIGHT
BLOCK 1 PRE L-15 to L-9	BLOCK 3 IN FD-3 to FD-9	BLOCK 5 POST R+3 to R+9
BLOCK 2 PRE L-9 to L-3	BLOCK 4 IN FD-9 to FD-15	BLOCK 6 POST R+9 to R+15

Figure 1. Energy expenditure was measured during the six time blocks shown above. For the fligght experiment the blocks are space flight, preflight, inflight and post flight. For the bed rest study the blocks are pre-bed rest, bed rest and recovery.

In order to compare the flight results with that of the ground based LMS bed rest study we used the same protocol to study the bed rest subjects. Eight subjects were studied i the bed rest phase of this program. An important point about the bed rest study is that it included the full complement of exercise testing that was done on the payload crew. By doing so enables us to compare (bed rest + exercise) against (space flight + exercise + working in space) thereby providing an estimate of the energy costs of working in space.

A 17 day bedrest with 6° head down tilt was conducted in the Clinical research Center of the NASA-AMES Research Center. 8 healthy adult males were recruited from the local community.

The study was divided into three phases, a 15 day pre bedrest ambulatory period followed by 17 days of bedrest and ending with a fifteen day recovery period. During the 47 days of the study the subjects received all their nutrition from the research center. An attempt was made to provide the subjects with a 'controlled' ad libidum diet. Twelve daily menus were made up comprising of 2500 kcal/d and 90 g protein/d. In addition subjects were allowed access to a snack basket which contained fruit, cookies, some candy and granola bars. An accurate record of dietary intake was kept for the entire period. Urines were collected continuously for the 47 day period.

D-1. RESULTS: BED REST EXPERIMENT.

The combination of providing the subjects with access to a snack basket and not compelling them to eat all the food offered introduced enough latitude for them to adjust their intake needs to the situation. The difference was primarily in the two ambulatory phases where the subjects made more extensive use of the snack basket, although food items were also declined from the set menus. There was a significant decrease in intake for the bedrest phase (table 2). It is interesting to note that this intake value (33 kcal. $kg^{-1}.d^{-1}$) is higher than the energy expenditure reported for bedrest without activity (24 kcal. $kg^{-1}.d^{-1}$, 4) but about the same as that found for minimal activity (confined to a GCRC, 30 kcal. $kg^{-1}.d^{-1}$, 3). Since the subjects in this study had several days of quite intensive exercise one would expect their energy expenditure value to be above that of bedrest alone.

As expected, the subjects were in negative nitrogen balance during the bedrest phase of the experiment. Closer inspection of the N balance data shows that N balance on bedrest days 13-14 was significantly less than on any of the other bedrest days. These two days encompassed the last of the pulmonary function tests/exercise protocols (21). One possible explanation is that some of the muscles had been weakened by the bedrest to such an extent that the imposition of a strenuous exercise regimen caused some actual muscle damage.

PERIOD	CONTROL	BED REST	RECOVERY
n =	7	7	6
Energy intake, kcal. $kg^{-1}.d^{-1}$	35.9 $\pm$ 2.0*	32.8 $\pm$ 1.6	36.3 $\pm$ 2.0*
N intake, mg N. $kg^{-1}.d^{-1}$	181.8 $\pm$ 9.6	177.9 $\pm$ 8.8	186.5 $\pm$ 10.4
N balance, mg N. $kg^{-1}.d^{-1}$	21.8 $\pm$ 3.0	1.1 $\pm$ 4.6*	27.2 $\pm$ 4.8

Table 2. Data from the NASA-LMS bed rest study. * $p<0.05$ vs control period.

The 3-MeH data from the bed rest study enabled us to close an important gap in our SLS1/2 studies. Specifically it permitted the comparison of 3-MeH excretion from two Life Sciences Shuttle missions (duration 9.5 and 16 d, n=9) against 17 days of bed rest (n=7) with 6° head down tilt against the pre-existing Skylab data. The Skylab studies had shown a marked elevation of 3-MeH excretion in flight; we found no increase on SLS1/2 and most bed rest studies did not show an increase. However no bed rest study except for the present bed rest study incorporated an exercise component specifically designed to emulate a shuttle flight. 3-MeH excretion was unchanged with either bed rest, (pre bed rest 5.30 $\pm$ 0.29 (7) vs bed rest 5.71 $\pm$ 0.30 (7) μmol 3-MeH $kg^{-1}.d^{-1}$, p=ns) or spaceflight, (preflight 4.98 $\pm$ 0.37 (9) vs 4.59 $\pm$ 0.39 (9) μmol 3-MeH $kg^{-1}.d^{-1}$ inflight p=ns). From these comparisons we concluded: (i) 3-MeH excretion was unaffected by spaceflight on the

Shuttle or bed rest plus exercise. (ii) Since protein breakdown (elevated 3-MeH) was increased on Skylab but not on Shuttle, it follows that muscle protein breakdown is not an inevitable consequence of space flight (21).

At time of writing we have completed all of the ^{18}O measurements and this enables us to calculate the total body water values. The ^{2}H measurements are in progress. The total body water data is summarized in table 3. The values look reasonable. However close inspection of the data indicates a potential problem. The body water tracked the body weight changes body weight. The mean change in TBW was -0.03 $\pm$ 0.21 liters and the decrease in body weight was -0.63 $\pm$ 0.22. kg.

PERIOD/SUBJECT	1	2	3	4	5	6	MEAN	SEM
CONTROL, C-1	44.17	45.11	41.04	44.34	49.49	48.31	45.41	1.25
CONTROL, C-6	42.91	46.18	41.01	46.00	51.11	50.83	46.34	1.67
BEDREST, BR-4	44.02	45.61	39.76	44.75	49.88	49.95	45.66	1.58
BEDREST, BR-10	44.02	46.62	41.56	44.65	49.34	49.88	46.01	1.32
RECOVERY, R+5	43.69	46.66	41.13	45.98	50.61	50.85	46.48	1.56
RECOVERY, R+10	45.63	44.56	45.23	47.56	51.90	52.28	47.86	1.40
BED REST CHANGE	0.48	0.47	-0.36	-0.47	-0.69	0.35	-0.04	0.22
RECOVERY CHANGE	1.12	-0.03	2.15	1.60	0.95	2.00	1.30	0.33

Table 3. Summary of the total body water changes with bed rest. Bed rest change is the difference between the bed rest values and the pre bed rest values; recovery changes is the difference between recovery and bed rest.

D-2. RESULTS: FLIGHT EXPERIMENT

The flight analyses are at present only partially completed. The principal result that we have to date is determination of the energy expenditure rates and hence energy balance for the two inflight periods. These are summarized in table 4. While this data is still in preliminary form some conclusions can be drawn. Firstly energy intake was very low on this mission. The level is the same as that expended by a subject at complete rest. Energy expenditure was about where we had predicted it would be (20). It as apparent that the subjects were in marked negative energy balance throughout the mission.

INFLIGHT PERIOD	Days 3-9	Days 9-16
Energy intake (kcal. $kg^{-1}.d^{-1}$.)	22.8 $\pm$ 1.8	24.4 $\pm$ 3.0
Energy expenditure (kcal. $kg^{-1}.d^{-1}$.)	28.7 $\pm$ 1.4*	28.5 $\pm$ 2.0*
Energy balance (kcal. $kg^{-1}.d^{-1}$.)	-6.4 $\pm$ 0.6#	-5.0 $\pm$ 2.0#

Table 4. Inflight energy intake, expenditure and balance for the four payload crew members. * $p<0.05$ vs intake or # balance.

This negative energy balance led to a substantial loss of N in the urine. Because energy balance was so negative in flight it make the comparison of the bed rest data against the flight data

somewhat problematic because during bed rest the subjects were not in energy balance. While we have considerably more data than is presented here, we feel that it would be premature to comment on it further in print at this point.

F. REFERENCES

1. Chandra RK. 1990 McCollum award lecture. Nutrition and Immunity: lessons from the past and new insights into the future. Am. J. Clin. Nutr. 53:1087-1101, 1991.
2. Coward WA and Prentice AM. Isotope method for the measurement of carbon dioxide production rate in man. Am. J. Clin. Nutr. 41:659-61, 1985.
3. Goran MI, Poehlman ET and Danforth E. Jr. Experimental reliability of the doubly labeled water technique. Am J Physiol 266: E510-E515, 1994.
4. Gretebeck RJ, Schoeller DA, Gibson EK and Lane HW. Energy expenditure during antiorthostatic bedrest (simulated microgravity). J. Appl. Physiol. 78: 2207-2211, 1995.
5. Grigoriev AI and Egorov AD. General mechanisms of the effect of weightlessness on the human body. Advances in Space Biology and Medicine. Ed. S.J. Bonting. 2:1-43, 1992.
6. Gmunder FK, Konstantinova I, Cogoli A, Lesnyak A, Bogulov W and Grachov AW. Cellular immunity in cosmonauts during long duration spaceflight on board the orbital MIR station. Aviat. Space and Environ. Med. 65:419-423, 1994.
7. Hughes-Fulford MH. Altered cell function in microgravity. Exp. Gerontol. 26: 247-256, 1991
8. Leach CS, Rambaut PC and Di Ferrante N. Amino aciduria in weighlessness. Acta Aeronautica. 6:1323-1333, 1979.
9. Leach CS, Altschuler SI and Cintron NM. The endocrine and metabolic response to space flight. Med. Sci. Sports, Exer. 15: 432-440, 1982
10. Leblanc A, Rowe R, Schneider V, Evans H and Hedrick T. Regional muscle loss after short duration spaceflight. Aviat. Space and Environ. Med. 66:1151-1154, 1995.
11. Leonard JI, CS Leach, and PC Rambaut. Quantitation of tissue loss during prolonged space flight. Am. J. Clin. Nutr. 38:667-679, 1983.
12. Lowry SF. Modulating the metabolic response to infection. Proc. Nutr. Soc.51:267-277, 1992.
13. Nicogossian AE, Sawin CF and Grigoriev AI. Countermeasures to Space Deconditioning. In: Space Medicine and Physiology, 3rd Ed. Ed AE Nicogossian, CL Huntoon and SL Pool, Lea and Febiger, Philadelphia, PA. chapter 26, pp 447-467, 1994.
14. Nicogossian AE. Overall Physiological Response to Space Flight. In Space Medicine and Physiology, 3rd ed. Ed. A.E. Nicogossian, C.L. Huntoon and S.L. Pool. Chapter 11, pp 213-227, Lea and Febiger, Philadelphia, PA, 1994.
15. Rambaut PC, Leach CS and Leonard JI. Observations in energy balance in man during space flight. Am. J. Physiol. 233:R208-R212, 1977.
16. Rennie MJ. Muscle protein turnover and the wasting due to injury and disease. Br. Med. Bull. 41:257-264, 1985.
17. Schoeller DA and Rosenberg IH. Precision of the $^{2}H_{2}{}^{18}O$ method for measuring energy expenditure in humans: Effect of dose and metabolic period. Am.J. Clin. Nutr. 37:698-704, 1983.
18. Stein TP, Leskiw MJ, Schluter MD. The effect of spaceflight on human protein metabolism. Am J Physiol. 264:E824-E828, 1993.
19. Stein TP, Schluter MD. Excretion of IL6 by astronauts during spaceflight. Am. J. Physiol. 266:E448-E452, 1994.

20. Stein, TP, Leskiw MJ and Schluter MD. Diet and Nitrogen Metabolism during Spaceflight on the Shuttle. J. Appl. Physiol. 81: 82-97, 1996
21. Stein TP and Schluter MD. Human skeletal muscle protein breakdown during space flight. Am. J. Physiol. 272: E688-E695, 1997.
22. Thornton WE and JA Rummel. Muscular deconditioning and its prevention in space flight. In: Biomedical results from Skylab (NASA SP-377), edited by RS Johnston and LF Dietlein. U.S. Government Printing Office, Washington, DC, 191-197, 1977.
23. Waterlow JC. Whole-body protein turnover in humans-past, present and future. Ann. Rev. Nutr. 15:57-92, 1995.
24. Whedon GD, L Lutwak, Rambaut PC et al. Mineral and nitrogen metabolic studies, Experiment MO71. In: Biomedical results from Skylab (NASA SP-377), edited by RS Johnston and LF Dietlein. U.S. Government Printing Office, Washington, DC, 164-174, 1977.
25. Wolfe RR, F Jahoor and WH Hartl. Protein and amino acid metabolism after injury. Diabetes/Metabolism Rev. 5: 149-164, 1989.

E. PUBLICATIONS

Stein TP and Schluter MD. Human skeletal muscle protein breakdown during space flight. Am. J. Physiol. 272: E688-E695, 1997.

Plant Growth Facility (PGF)

Compression Wood Formation in a Microgravity Environment

Principal Investigator:

Dr. Norman Lewis
Washington State University
Pullman, Washington

Compression Wood Formation in a Microgravity Environment

Mi Chang[1], Diana L. Bedgar[1], William C. Piastuch[2], Laurence B. Davin[1] and Norman G. Lewis[1]

[1]Institute of Biological Chemistry, 467 Clark Hall, Washington State University, Pullman, WA 99164

[2]Plant Space Biology, Dynamac Corporation, Mail Code DYN-3, Hangar L, Kennedy Space Center, FL 32899

Abstract

In a microgravity environment aboard the Space Shuttle Columbia Life and Microgravity Mission STS-78, compression wood formation and hence altered lignin deposition and cell wall structure, was induced upon mechanically bending the stems of the woody gymnosperms, Douglas fir (*Pseudotsuga menziesii*) and loblolly pine (*Pinus taeda*). Although there was significant degradation of many of the plant specimens in space-flight due to unusually high temperatures experienced during the mission, it seems evident that gravity had little or no effect on compression wood formation upon bending even in microgravity. Instead, it apparently results from alterations in the stress gradient experienced by the plant itself during bending under these conditions. This preliminary study now sets the stage for long-term plant growth experiments to determine whether compression wood formation can be induced in microgravity during phototropic-guided realignment of growing woody plant specimens, in the absence of any externally provided stress and strain.

Introduction

The woody gymnosperms, loblolly pine (*Pinus taeda*) and Douglas fir (*Pseudotsuga menziesii*) represent two very important commercial plant species used today in pulp and paper manufacture and for lumber applications. Understanding how to optimize both the quality and the texture of their woods (secondary xylem) is an important biotechnological goal, particularly with the trends towards moving to 'fast-growing' plantations as sources of fiber and wood (*1*). A very deleterious feature in woody plant development, however, occurs when their stems are displaced from a vertical alignment (2). This results in such plants realigning their growth

processes, *via* some presumed gravitactic response, in order to restore vertical alignment to the photosynthetic canopy. This is attained by specific cells in the stem, which were originally programmed to form 'normal' xylem, being induced to undergo formation of a specialized reinforcement tissue trivially known as reaction wood (compression wood in gymnosperms). Formed only in woody plants, it buttresses the stem which results in a concomitant, yet slow, vertical realignment of the photosynthetic canopy as growth continues. Gymnosperm reaction wood consists of two distinct regions, namely compression wood formed at the underside of leaning stems and branches, and opposite wood formed at the upperside, respectively. In compression wood, such as in loblolly pine (*Pinus taeda*), tracheids are shorter than normal (10-40% less), and have rounded outlines with frequently distorted tips and thicker cell walls, which results in a specific gravity approximately twice that of normal wood (2). From an anatomical viewpoint, these differ from normal tracheids as follows: The S_1 layer of compression wood is thicker than 'normal' wood, the S_2 layer is deeply fissured, and there is no S_3 layer (Figure 1). Further, compression wood has a cellulose with a lower degree of polymerization and which is less crystalline, whereas its lignin is both significantly higher in amount and with a large increase in its *p*-coumaryl alcohol content. Significant differences in cellulose microfibril angles are also observed, strongly indicating that the microtubule assembly/orientation is also affected, *i.e.*, from 35.1° to 22.8° depending upon whether the tissue is 'normal' or 'compression' wood. Opposite wood, on the other hand, has longer tracheids of a squared or rectangular shape, with the S_2 layers being unusually thick with transverse helical patterns. In opposite wood, the relative proportions of the plant cell wall polymers (lignin, cellulose and hemicelluloses) appear to be unchanged with respect to 'normal' wood.

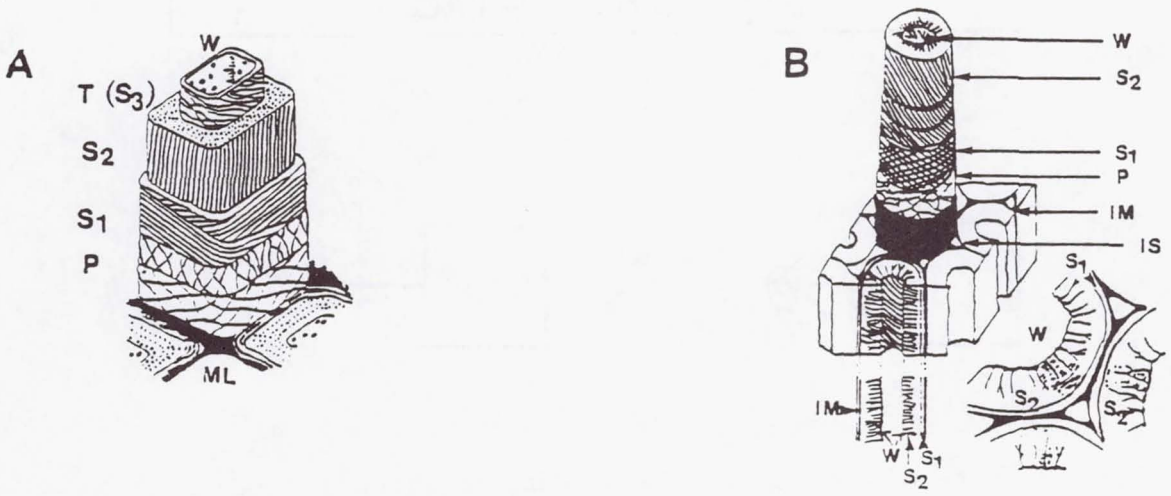

Figure 1. Schematic model of the cell wall structure of A: softwood tracheids and hardwood libriform fibers and B: typical compression wood tracheids (redrawn from references *3* and *2*, respectively).

ML: Middle lamella; P: Primary cell wall; S_1: Secondary wall 1; S_2: Secondary wall 2; $T(S_3)$: Tertiary wall; W: Warty layer; IS: Intercellular space; IM: Intercellular material.

Results and Discussion

In the first objective of LMS Mission on STS-78, we wished to establish whether compression wood formation, which is believed to result as a consequence of alterations in the perceived gravitational vector acting on the entire plant, is formed in microgravity. With the proposed STS-78 mission (June-July 1996) planned for 17 days, several ground-based base-line experiments were first carried out prior to embarking upon the space-flight experiment. These included: (i) establishing that compression wood formed within the time-frame of the proposed flight duration and (ii) definition of experimental protocols for initiating experiments, when the Shuttle was in orbit, that would normally result in compression wood formation at 1 *g*. As described below, this involved a very comprehensive series of experiments (with corresponding controls) at the preflight stage.

In the context of the preferred experimental design to test whether compression wood formation occurs in microgravity, the best approach would be to grow woody plants horizontally, relative to the light source, in microgravity. Then, some months later, when reorientation of the stem and photosynthetic canopy had occurred, to examine the resulting xylem cells for compression wood formation. In such an experiment, there would be no imposed external stress on the plants (*e.g.*, by mechanical means due to bending), and hence it would be the ideal experiment (Figure 2).

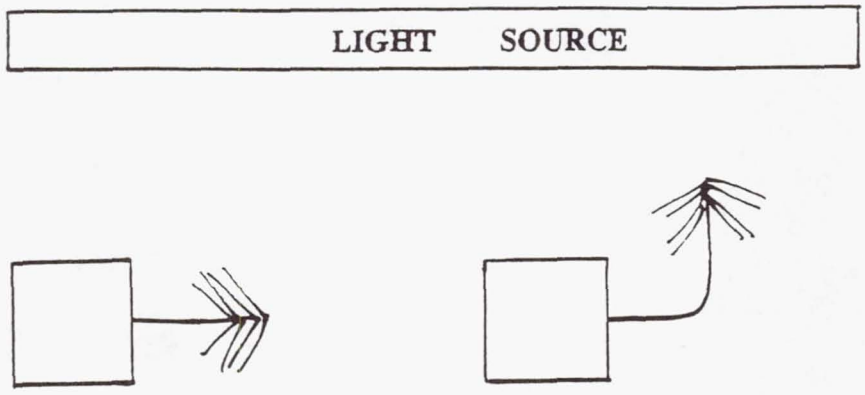

Figure 2. Preferred conformation for studying compression wood formation in microgravity.

But such an experiment is not possible until the onset of Space Station Alpha, since the time-frame required (number of months) for such reorientations to occur is too short for Shuttle Flight experiments. Consequently, we developed an alternative system for examining whether compression wood formation could be engendered in microgravity over the STS-78 flight duration (17 days).

This involved bending (at both 45° and 90°) loblolly pine and Douglas fir plants (see Figure 3) at 1 *g* for different time intervals (1, 3, 5, 7 and 14 days). After these different time periods, the plants were restored to a vertical alignment, and after a total of 14 days were analyzed for the onset and development of compression wood formation. Under these conditions, it was established that for both loblolly pine and Douglas fir, compression wood formation could readily be detected after 3 days of initial bending and an additional 4 days of further growth when restored to an upright position (Figure 4).

The next technical development required was to be able to grow the plants in the NASA supplied plant growth chambers (PGC's), whose light, temperature, and nutrient provision abilities are quite limited. For example, temperatures can only be *raised* if they fall below the ambient temperature of the Space Shuttle cabin, *i.e.*, they lack cooling capability. Moreover, nutrients and water cannot be supplied during flight, a technical difficulty that NASA is still trying to overcome. Nevertheless, we devised conditions for the satisfactory growth of both loblolly pine and Douglas fir plants in the PGC, using Nutrient Packs (agar gels containing requisite water and nutrients) developed previously in my laboratory for space-flight studies. As shown in Figure 5, this enabled the facile growth of the plants under the light, temperature and humidity levels typical of Shuttle flights.

Following about 10 months of developing the necessary protocols, the basic experimental approach had, therefore, been devised to explore whether compression wood formation could be formed in microgravity.

With progress to this point in hand, two major technical hurdles needed still to be resolved. The first included conducting a Payload Verification Test (PVT) by transporting the plants to Kennedy Space Center, and then growing the plants under conditions expected for the Shuttle flight. These experiments were conducted over 18 days with plants orientated at 45° after 2 days, then harvested, sectioned and chemically fixed (2.5% glutaraldehyde, 2% paraformaldehyde) on days 11 and 17. Each sectioned tissue was then subjected to subsequent light microscopy examination. The results obtained are illustrated in Figure 6.

Next, the astronauts, Jean-Jacques Favier and Susan Helms were shown how to put specific loblolly pine and Douglas fir plants into the correct (45°) orientation, this being ultimately planned to occur following 2 days of growth in orbit in microgravity. Selected plants were harvested and sectioned (both upright vertical controls and oriented specimens, at days 10 and 13, respectively) under shuttle flight laboratory conditions, in preparation for light microscopy analyses.

With all preparations satisfactorily completed, Shuttle Columbia (STS-78) was launched on June 22, 1996, from Kennedy Space Center. The space flight experiment, while answering the question of whether compression wood formation occurred under such conditions, was not without difficulty. The Shuttle cabin temperatures were higher than any recorded previously (> 29°C), this having a deleterious effect on the growth of several specimens. Nevertheless, those still in obviously good conditions (*i.e.*, containing new growth) were harvested, sectioned and fixed both in space (at days 10 and 13), with the remainder harvested, sectioned and fixed upon recovery after the 17 day flight. The results obtained are shown in Figure 7. As can be seen, under the conditions employed, both sets of plants (*i.e.*, microgravity and 1 *g* grown) were essentially identical, all forming compression wood when orientated at 45°. On the other hand, compression wood formation did not occur when either plants were placed in a vertical configuration (Figure 8). Note also that the experiments had to be repeated several times post-flight (under flight conditions) to verify that the difficulties experienced were, in fact, due to the

temperatures experienced. This was established to be the case (data not shown), and a future publication will describe the entire preparations and space-flight experiment and its results in full detail (*4*).

Many authorities would have expected compression wood not to be formed if the gravitational vector was removed. Thus, to account for its formation in space, either the microgravity influence is still high enough to ensure that the organisms can still respond to it, or much more likely, the effect of mechanical loading (by harnessing as shown in Figures 9 and 10) overrides the gravitactic responses (*i.e.*, due to overlapping signal transduction, perception and response mechanisms). Put in another way, even in microgravity, the plants can make appropriate corrections to alleviate the stress gradient introduced by bending, thereby hence forming compression wood. Indeed, this is why the next experiment on Space Station Alpha now needs to be conducted, *i.e.*, where the plants can reorientate over longer periods, but without introduced mechanical stresses such as by bending.

Work is also currently in progress, using a freeze-fracture approach, to examine the cellulose microfibril orientation of the space flight plant tissues, in order to determine if the effects on cell wall organization were altered in microgravity in either the newly formed compression wood or normal xylem cells.

Concluding Remarks

It is now established that woody gymnosperm plants, such as Douglas fir, when placed in off-vertical configuration in microgravity, relative to the light source, respond by forming compression wood. This is proposed to be due to the influences of an internal stress gradient within the plant. It now needs to be established if woody angiosperm would form comparable reaction wood under these conditions. This adds to the steadily growing body of knowledge associated with general phenylpropanoid metabolism and cell wall development (*5- 36*). It also needs to be proven whether reaction (compression) wood would result if plants were able to realign their stems without the influence of harnessing *e.g.*, by phototropic responses over longer time periods (months, years). This will be an important experiment to conduct in Space Station Alpha.

Acknowledgments

The authors wish to thank NASA (NAG10-0164) for generous financial support of this study, and to Deborah Vordermark and Rina Thompson for excellent technical assistance. Special thanks are also expressed to astronauts, Jean-Jacques Favier and Susan Helms, for their participation in this study.

References

1. Lewis, N.G. and Davin, L.B. 1994 Evolution of Lignan and Neolignan Biochemical Pathways. *In* "Evolution of Natural Products" (Nes, W.D., Ed.), ACS Symp. Ser. **562:** 202-246.

2. Timell, T.E. 1986 Compression Wood in Gymnosperms, Springer-Verlag, Berlin, Heidelberg, Volumes 1-3, pp 2150.

3. Fengel, D. and Wegener, G. 1984 Wood: Chemistry, Ultrastructure, Reactions, Walter de Gruyter, Berlin, New York, pp 613.

4. Chang, M. Bedgar, D.L. Piastuch, W.C., Davin, L.B. and Lewis, N.G. (manuscript in preparation).

5. Lewis, N.G., Yamamoto, E., Wooten, J.B., Just, G., Ohashi, H. and Towers, G.H.N. 1987 Monitoring Biosynthesis of Cell Wall Phenylpropanoids *in Situ*. Science **237**:1344-1346.

6. Lewis, N.G., Razal, R.A., Dhara, K.P., Yamamoto, E., Bokelman, G.H. and Wooten, J.B. 1988 Incorporation of [2-^{13}C]Ferulic Acid, a Lignin Precursor, into *Leucaena leucocephala* and its Analysis by Solid State ^{13}C N.M.R. J. Chem. Soc. Chem. Commun. 1626-1628.

7. Lewis, N.G., Razal, R.A., Yamamoto, E., Wooten, J.B. and Bokelman, G.H. 1989 Carbon-13 Specific Labeling of Lignin in Intact Plants. *In* "Biosynthesis and Biodegradation of Plant Cell Wall Polymers" (Lewis, N.G. and Paice, M.G., Eds.), ACS Symp. Ser. **399**:169-181.

8. Yamamoto, E., Bokelman, G.H. and Lewis, N.G. 1989 Phenylpropanoid Metabolism in Plant Cell Walls. *In* "Biosynthesis and Biodegradation of Plant Cell Wall Polymers" (Lewis, N.G. and Paice, M.G., Eds.), ACS Symp. Ser. **399**:68-88.

9. Lewis, N.G. and Yamamoto, E. 1990 Lignins: Occurrence, Biosynthesis and Biodegradation. Annu. Rev. Plant Phys. Plant Mol. Biol. **41**:455-497.

10. Umezawa, T., Davin, L.B. and Lewis, N.G. 1991 Formation of Lignans, (-)-Secoisolariciresinol and (-)-Matairesinol with *Forsythia intermedia* Cell-free Extracts. J. Biol. Chem. **266**:10210-10217.

11. Davin, L.B., Umezawa, T. and Lewis, N.G. 1991 Enantioselective Separations in Phytochemistry, Modern Phytochemical Methods (Stafford, H.A. and Fischer, K., Eds.), Plenum Press, NY, Rec. Adv. in Phytochem. **25**:75-112.

12. Lewis, N.G. and Davin, L.B. 1992 Phenylpropanoid Metabolism: Biosynthesis of Monolignols, Lignans, Lignins and Suberins. *In* "Recent Advances in Phytochemistry" (Stafford, H.A., Ed.), **26**:325-375, Plenum Press, New York.

13. Lewis, N.G. and Davin, L.B. 1992 Stereoselectivity in Polyphenol Biosynthesis. *In* "Plant Polyphenols: Synthesis, Properties and Significance" (Hemingway, R.W. and Laks, P.E., Eds.), Plenum Press, New York, pp. 73-95.

14. Davin, L.B., Bedgar, D. Katayama, T. and Lewis, N.G. 1992 On the Stereoselective Synthesis of (+)-Pinoresinol in *Forsythia suspensa* from Its Achiral Precursor, Coniferyl Alcohol. Phytochemistry **31**:3869-3874.

15. Bernards, M. and Lewis, N.G. 1992 Alkyl Ferulates in Wound Healing Potato Tubers. Phytochemistry **31**:3409-3412.

16. Lewis, N.G. and Ryan, C.A. 1992 Microgravity in Plant Biological Systems: Realizing the Potential of Microgravity Research in Molecular Biology. AIAA **92**:13-34.

17. Lewis, N.G. 1993 Plant Phenolics. *In* "Antioxidants in Higher Plants" (Hess, J.L. and Alscher, R., Eds.), CRC Press, 135-169.

18. Eberhardt, T.L., Bernards, M., Davin, L.B., Yamamoto, E., Wooten, J.B. and Lewis, N.G. 1993 Lignification in Cell Suspension Cultures of *Pinus taeda* During Early Stages of Cell Wall Thickening. J. Biol. Chem. **268**:21088-21096.

19. Chu, A., Dinkova, A., Davin, L.B., Bedgar, D., and Lewis, N.G. 1993 Stereospecificity of Benzylic Aryl Ether Reductions in Lignan Formation: Reduction of (+)-Pinoresinol and (+)-Lariciresinol. J. Biol. Chem. **268**:27026-27033.

20. Lewis, N.G. and Davin, L.B. 1994 Evolution of Lignan and Neolignan Biochemical Pathways (Nes, W.D., ed.). ACS Symp. Ser. **562**:202-246.

21. Paré, P.W., Wang, H.-B., Davin, L.B. and Lewis, N.G. 1994 (+)-Pinoresinol Synthase: A Stereoselective Oxidase Catalysing 8,8'-Lignan Formation in *Forsythia intermedia*. Tetrahedron Lett. **35**(27):4731-4734.

22. Lewis, N.G., Kato, M., Lopes, N. and Davin, L.B. 1995 Lignans: Diversity, Biosynthesis and Function. ACS Symp. Ser. **588**:135-167.

23. Bernards, M.A., Lopez, M.L., Zajicek, J. and Lewis, N.G. 1995 Hydroxycinnamate Polymers Constitute the Aromatic Domain of Suberin. J. Biol. Chem. **270**:7382-7386.

24. Nose, M., Bernards, M.A., M., Zacijek, J., Eberhardt, T.L. and Lewis, N.G. 1995 Towards the Specification of Consecutive Steps in Macromolecular Lignin Assembly. Phytochemistry **39**(1):71-79.

25. Razal, R.A., Ellis, S., Lewis, N.G. and Towers, G.H.N. 1996 Nitrogen Recycling During Phenylpropanoid Metabolism. Phytochemistry **41:**31-35.

26. Bernards, M.A. and Lewis, N.G. 1996 Suberin: An Hydroxycinnamic Acid-Derived Polymer. Polyphenols Actualités **14:**4-6.

27. Van Heerden, P., Towers, G.H.N. and Lewis, N.G. 1996 Nitrogen Metabolism in Lignifying *Pinus taeda* Cell Cultures. J. Biol. Chem. **271:**12350-12355.

28. Dinkova-Kostova, A.T., Gang, D.R., Davin, L.B., Bedgar, D.L., Chu, A. and Lewis, N.G. 1996 (+)-Pinoresinol/(+)-Lariciresinol Reductase from *Forsythia intermedia*: Cloning, Expression and Comparison with Isoflavone Reductase. J. Biol. Chem. **271:**29473-29482.

29. Davin, L.B., Wang, H.-B., Crowell, A.L., Bedgar, D.L., Martin, D.M., Sarkanen, S. and Lewis, N.G. 1997 Stereoselective Bimolecular Phenoxy Radical Coupling by an Auxiliary (Dirigent) Protein without an Active Center. Science **275:**362-366.

30. Gang, D.R., Dinkova-Kostova, A.T., Davin, L.B. and Lewis, N.G. 1997 Phylogenetic Links in Plant Defense Systems: Lignans, Isoflavonoids and Their Reductases. *In* "Phytochemical Pest Control Agents" (Hedin, P., ed.), ACS Symposium Series **658**, American Chemical Society, Washington, DC, pp. 58-89.

31. Marchand, P.A., Zajicek, J. and Lewis, N.G. 1997 Oxygen Insertion in *Sesamum indicum* Furanofuran Lignans. Diastereoselective Syntheses of Enzyme Substrate Analogues. Can. J. Chem. **75**:840-849.

32. Towers, G.H.N., Singh, S., Van Heerden, P., Zuiches, J., and Lewis, N.G. 1997 Integrating Nitrogen and Phenylpropanoid Metabolic Pathways in Plants and Fungi, ACS Symp. Ser. (Lewis, N.G. and Sarkanen, S., eds.), Lignin and Lignan Biogenesis, Washington, D.C. (XXXX, in press).

33. Bernards, M.A. and Lewis, N.G. 1997 The Aromatic Domain of Suberin. Phytochemistry (in press).

34. Pearce, G.A., Marchand, P.A., Griswold, J., Lewis, N.G. and Ryan, C.A. 1997 Accumulation of Feruloyltyramine and *p*-Coumaryltyramine in Tomato Leaves in Response to Wounding. Phytochemistry (in press).

35. Marchand, P.A., Kato, M.J. and Lewis, N.G. 1997. Oxygen Insertion in *Sesamum indicum* Furanofuran Lignans: Isolation and Hemisynthesis of (+)Sesamone. J. Nat. Products (in press).

36. Singh, S., Lewis, N.G. and Towers, G.H.N. 1997. Nitrogen Recycling during Phenylpropanoid Metabolism in Sweet Potato Tubers. J. Plant Physiol. (submitted).

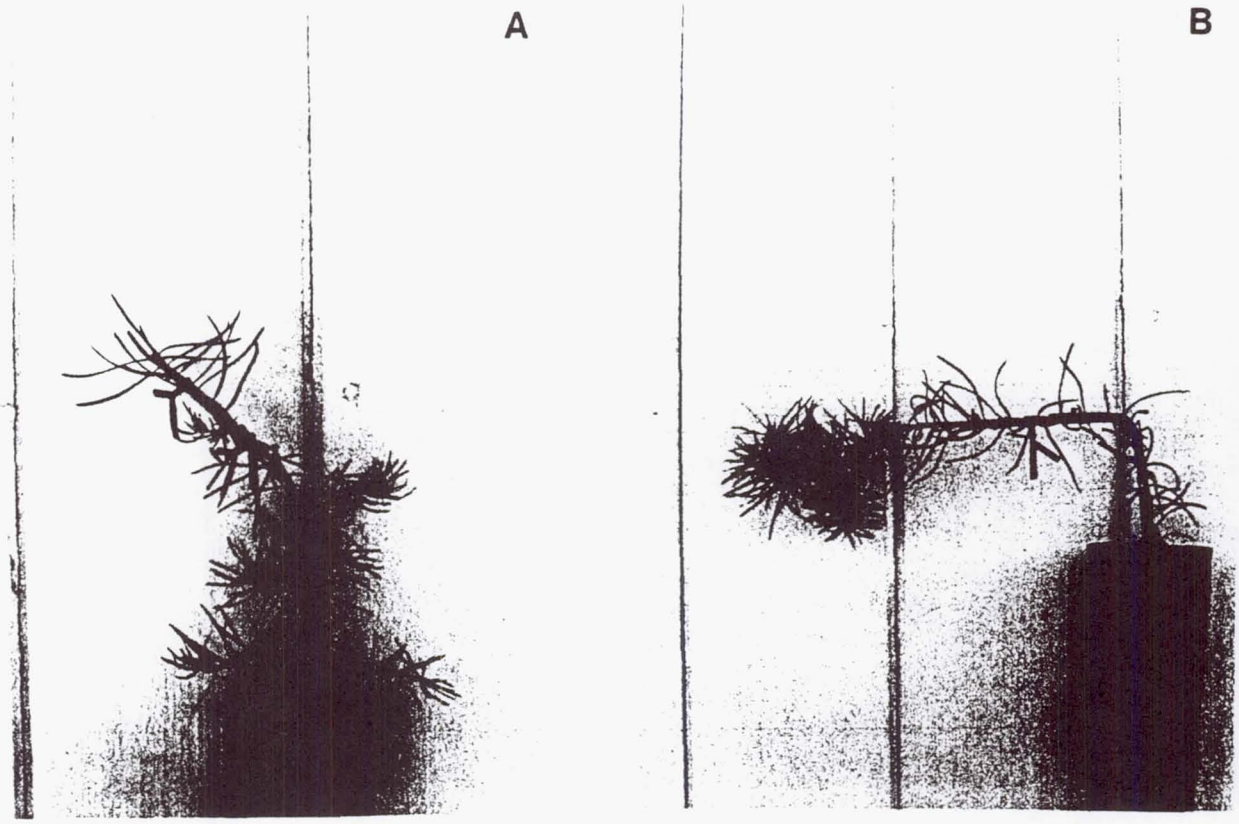

Figure 3. Douglas fir (*Pseudotsuga menziesii*) seedlings grown at **A:** 45° and **B:** 90°.

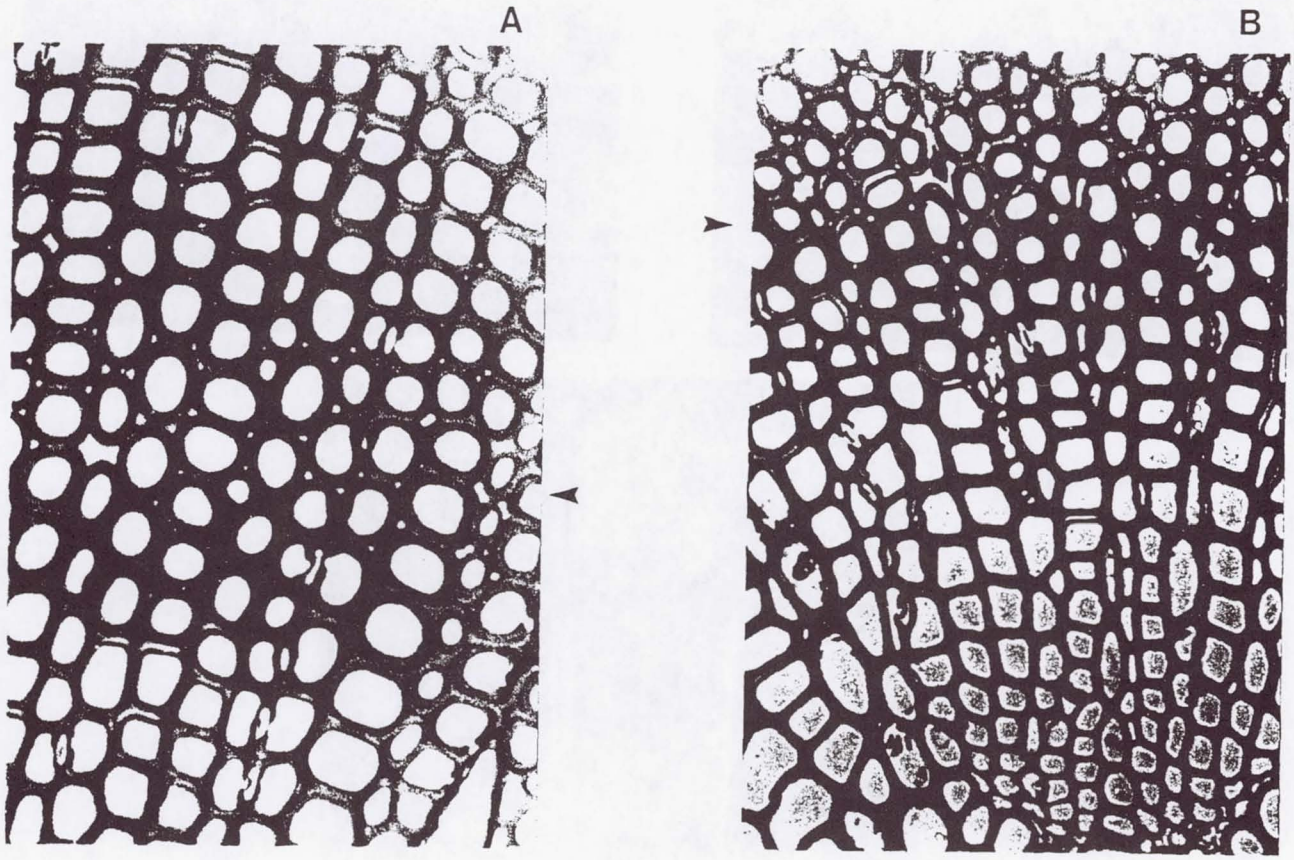

Figure 4. Light microscopy cross-sections of Douglas fir (*Pseudotsuga menziesii*) seedlings bent for 3 days, then allowed to further grow for an additional 4 days in an upright position. **A:** 45° orientation and **A:** 90° orientation. Arrow shows compression wood.

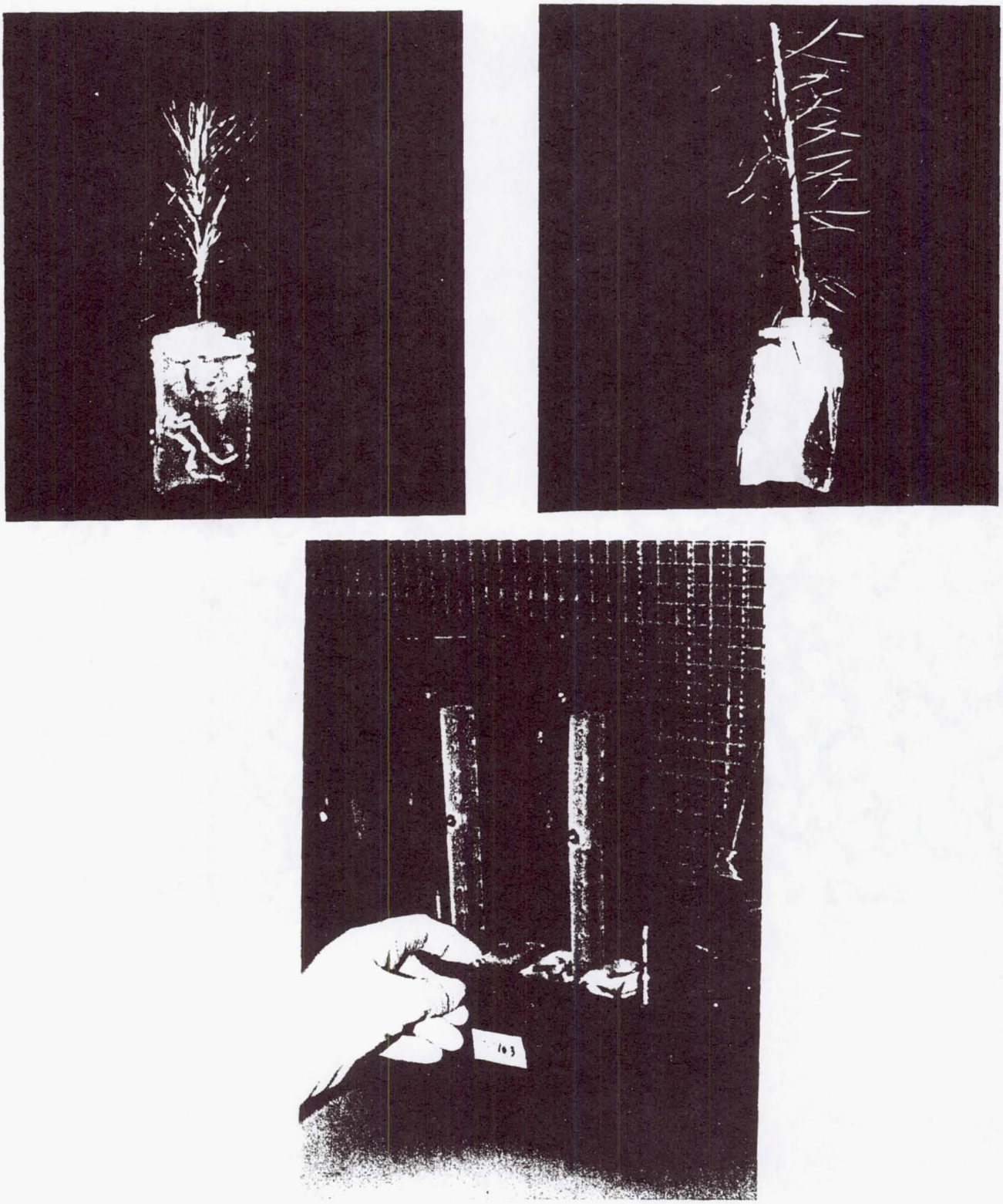

Figure 5. Nutrient pack and PGC.

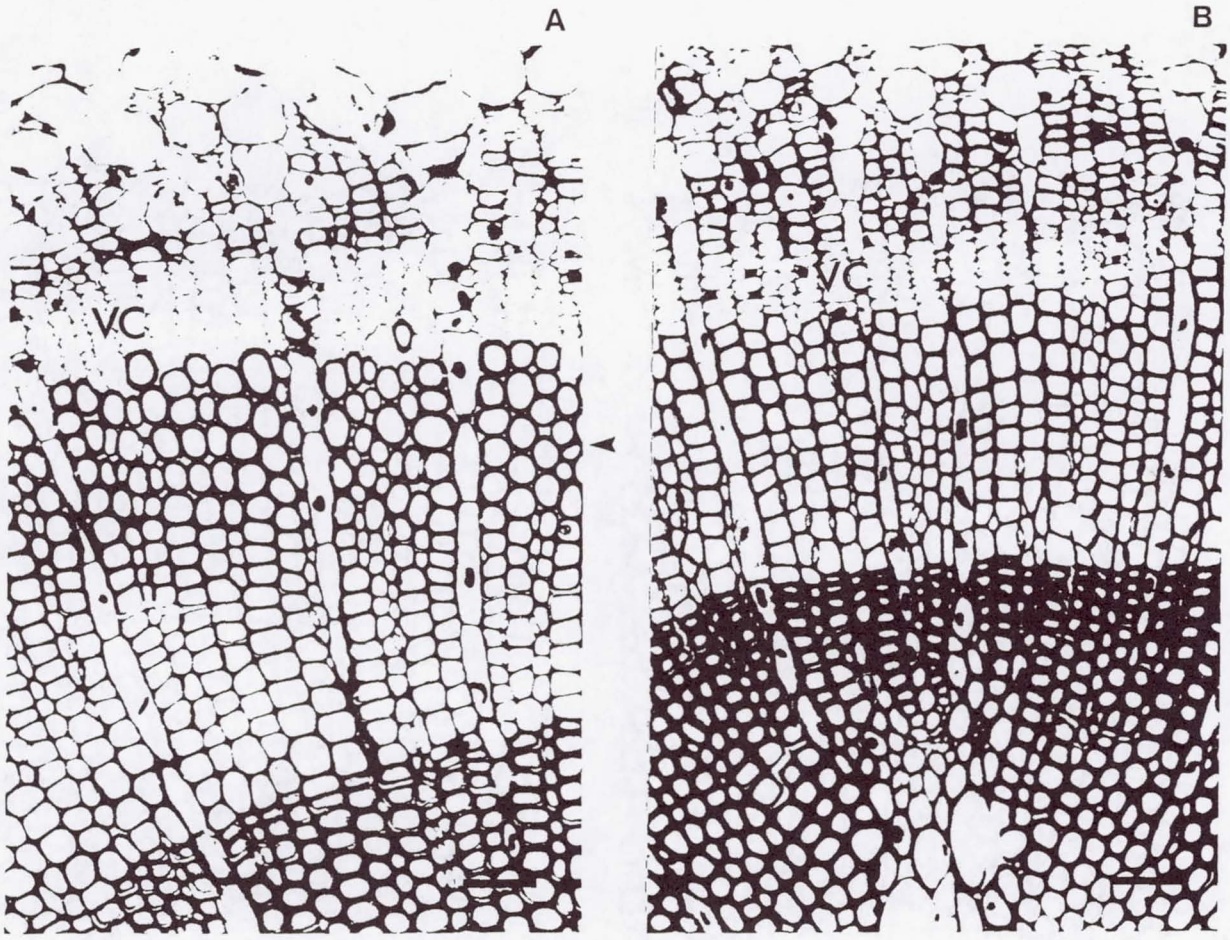

Figure 6. Light microscopy cross-sections (310X) of Douglas fir (*Pseudotsuga menziesii*) seedlings. Payload Verification Test; 15 days; 45° orientation. **A:** Reaction wood and **B:** Opposite Wood. Arrow shows compression wood.

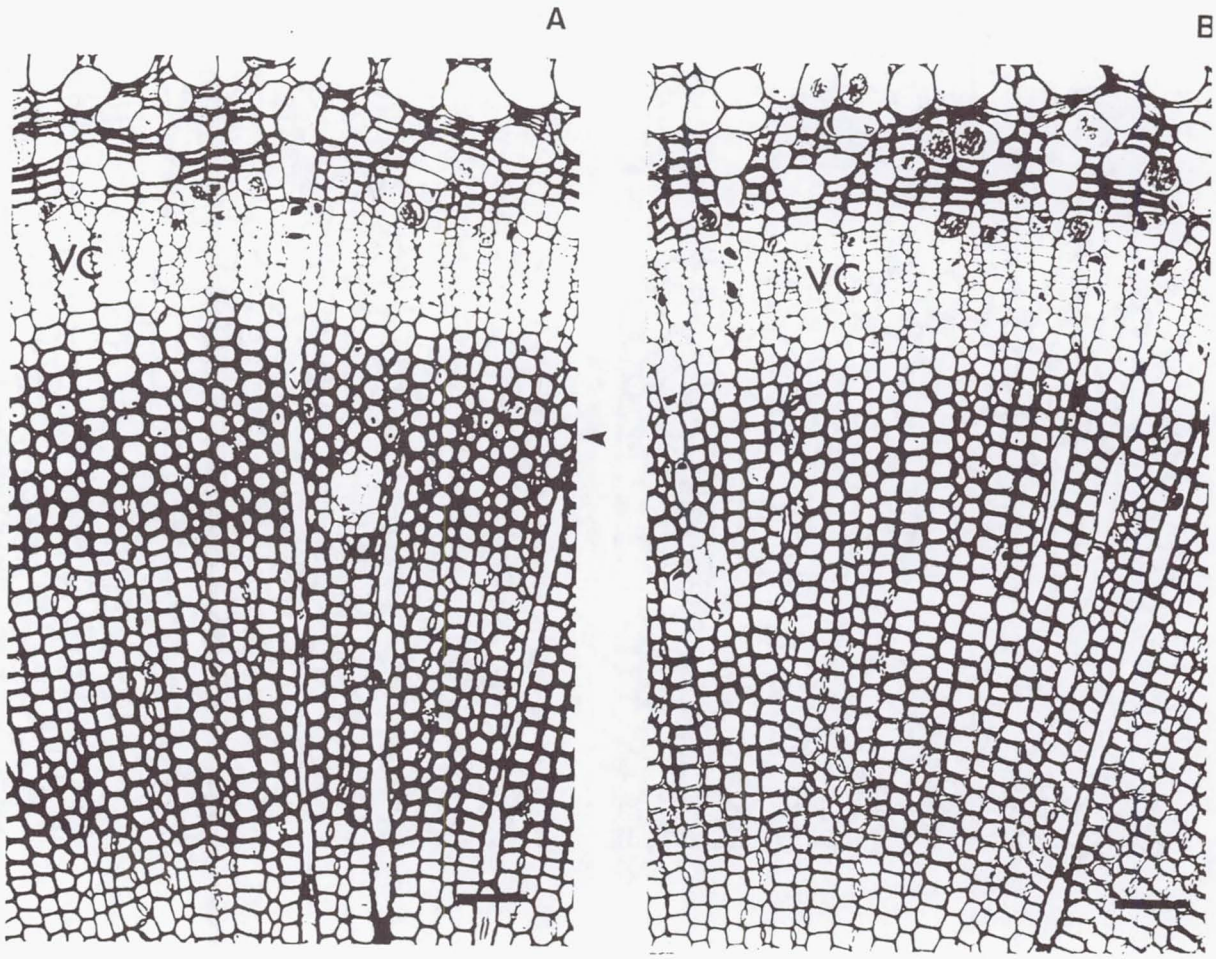

Figure 7. Light microscopy cross-sections (310X) of Douglas fir (*Pseudotsuga menziesii*) seedlings. STS-78; flight; 16 days; 45° orientation. **A:** Reaction wood and **B:** Opposite Wood. Arrow shows compression wood.

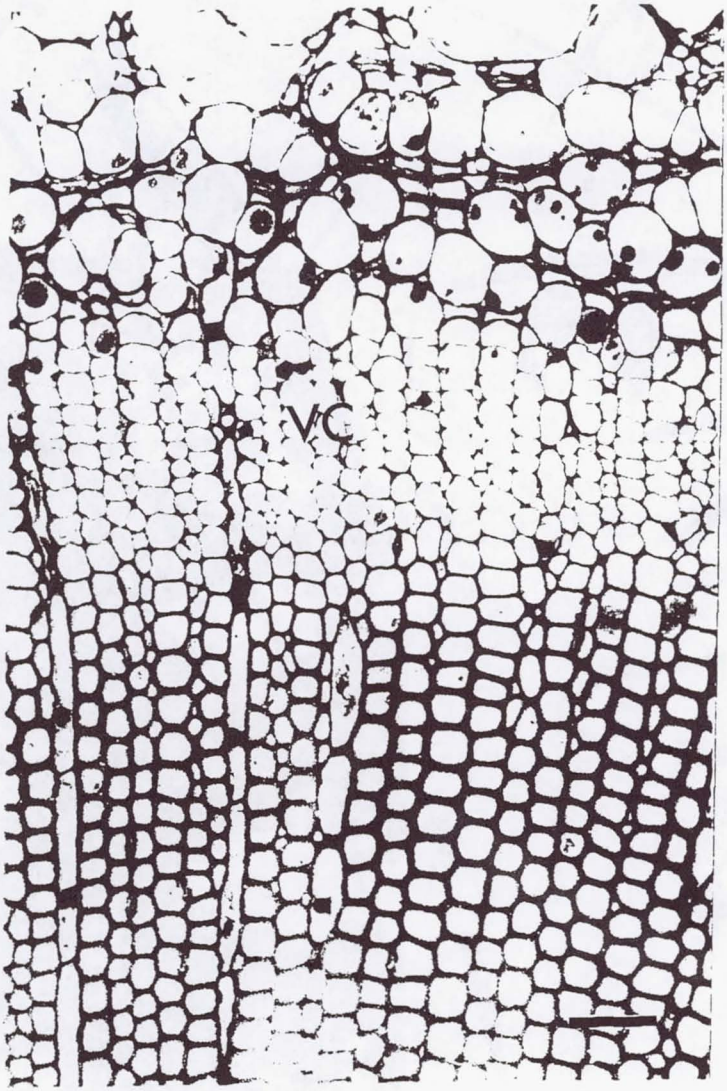

Figure 8. Light microscopy cross-sections (310X) of Douglas fir (*Pseudotsuga menziesii*) seedlings. STS-78; flight; 16 days; vertical orientation.

Figure 9. Harness used to keep the seedlings at a 45° angle

Figure 10. Plant Growth Chamber.

Space Tissue Loss Configuration B (STL-B)

Development of the Fish Medaka in Microgravity

Principal Investigator:

Dr. Debra Wolgemuth
Columbia College of Physicians and Surgeons
New York, New York

FINAL SCIENCE REPORT - LMS

Principal Investigators

Debra J. Wolgemuth, Ph.D.
Columbia University College of Physicians and Surgeons

Carey R. Phillips, Ph.D.
Bowdoin College

(1) Objectives:

The goal of these experiments was to determine the effect of microgravity on the early development of the fish medaka. There were two objectives for this flight series. The primary objective was to assess the effects of microgravity on different stages of development and to ascertain whether the relevant developmental questions can be addressed at the gross morphological level or if the issues involve more subtle questions about regulation at the molecular and cellular levels. The secondary objective was the assessment of the utility of flight hardware with the capabilities to perform embryological studies.

We have been able to take advantage of the flight testing phase of the STL-B hardware to also study the effects of microgravity on the early development of the fish, Medaka. Our initial studies involved monitoring the early Medaka development and raising flight embryos for breeding. Images of the developing embryos were collected either via video which was either taken by the astronauts or broadcast to Earth. Sample video images were digitized and stored on a hard drive resident within the on-board STL-B unit. Embryos were fixed at specific intervals, returned to Earth and are being analyzed for the timing and location of molecular events associated with controlling the morphological pattern for the onset of adult structures.

(2) Background:

Initial embryological studies on the effects of microgravity of any organism will involve similar questions and thus require, at least in the past, common technical capabilities. The first obvious question is whether the organism will survive through all stages of development and reproduce, either while in microgravity or after having been exposed to microgravity through a significant period of its development. The second level of questions involve the timing to and between different developmental stages and examination for subtle perturbations in the developmental physiology. Experiments addressing timing issues require continuous observation, a high degree of temperature

control, and the ability to fix embryos at the desired developmental stages. Temperature control is a particularly important problem in space research because the lack of gravity diminishes convection. The lack of convection causes uneven heating of the experimental environment which can lead to false interpretation of the data. The third level of experimentation often involves the ability to change media or add chemical compounds to the developing embryos at defined stages. Lastly, the ability to fix embryos at precise times to perform various molecular analyses becomes highly desirable. The STL-B has been engineered to provide all of these capabilities for small aquatic embryos.

Previous experiments using frog embryos in space (Black, S., Larkin, K., Jacqmotte, N., Wassersug, R., Pronych, S., and Souza, K. 1996. Advances in Space Research 17:209-217) indicate that morphologically normal tadpoles will develop in microgravity, even though some of the early developmental stages show subtle differences from Earth-grown embryos. It appeared that amphibian embryos have the ability to regulate for some variations in developmental pattern when subjected to a microgravity environment. This is an especially curious finding since these same developmental variations have not been observed on Earth. Therefore, our second and third flight experiments focused on gathering more precise information on the developmental morphology of the embryos in microgravity and ground-based studies involved the analysis of molecular events associated with pattern formation. Embryos were fixed during early gastrula through late neurula and are currently being assayed for a variety of gene expression patterns.

There are a number of reasons for the selection of the fish medaka for these experiments (Wolgemuth et al., 1997). The medaka represents an excellent model for vertebrate development. There are a number of laboratories around the world creating libraries of developmental mutants. There are an increasing number of molecular probes being generated, including studies from Dr. Wolgemuth's group (G. Herrada, D.A. Crotty, X.Wang, and D.J. Wolgemuth, in preparation), which will greatly enhance the analysis of regulation events during early development at the molecular and cellular levels. The embryos of medaka are clear and therefore amenable to digital video recordings of the development of internal as well as external organs. Of great importance for the particular studies was the fact that the developmental rate of the embryos can be experimentally controlled through the use of temperature. Finally, it is important to note that the medaka was also selected for a series of studies by Japanese Space Science investigators, thereby increasing the body of information which will ultimately be available to the scientific community.

(3) Methods of Data Acquisition and Analysis:

a) Overview: These studies were undertaken in collaboration with Dr. William Weismann and colleagues at WRAIR. The development of flight certified scientific hardware necessary to address the initial questions being asked by embryologists on the

effects of microgravity on embryonic development has been reported elsewhere (Wiesmann, W.P., L.A., Pranger, E.S., Delaplaine, and T. Cannon. 1994. A1AA Conference on Space Life Sciences. September 1994.). In short, initial embryological studies require gross morphological visual observations over the entire developmental time course, the ability to control the environment of the embryos in terms of oxygen, media flow, and temperature, and the ability to fix embryos at appropriate times for subsequent sectioning and more detailed analysis.

Thirty-six medaka embryos were flown on a modified STL-B hardware system. Embryos were collected within one half hour after fertilization, cleaned of chorionic hairs, transferred to both flight and ground control STL-B growth chambers. The embryos were held at 11.5-12.0°C until one half hour after reaching microgravity, at which time the temperature was raised to 17.5-18.5°C. Embryos in all chambers were monitored by video which was either broadcast to Earth, stored on videotape, or stored as digitized images. The six chambers of the STL-B were fixed with Bouins fixative at pre-programmed times and the embryos returned to Earth for detailed morphologcial and molecular analysis. Digital images and real-time video sequences were taken of the flight, synchronous ground and non-synchronous ground embryos under identical conditions except for the flight environment (acceleration into orbit and microgravity). Embryos were intended to be fixed at the following intervals: Orbit plus 24, 48, 72, 96, 142 and 166 hours. A hardware malfunction led to the fixation pre-flight of chamber #4 (72 hrs.) and the Orbit plus 142 and 166 hour embryos not being fixed until the shuttle landed back on Earth. This was later traced by the STL-B team to intermittent contact on the wiring to the pump board assembly and the flowpath pumps. The wiring was most likely compromised during the exchange prior to NASA turnover. The pumps were checked and functioning properly at the time of turnover. The remaining fixative was injected to the flowpaths during ground processing. The embryos had not reached the hatching phase at this time. Media and gas exchange to the two flowpaths was affected by the intermittent wiring. The effects of the intermittent nature of pumping on the embryos was investigated in the first of three post-flight tests conducted at Bowdoin College (C.R. Phillips).

All of the embryos, both flight and control, have been embedded and sectioned. No gross morphological abnormalities were observed between the flight and control embryos or between flight or control animals and comparably staged untreated embryos. Analysis of the video and digital data is still under examination. However, some conclusions can be drawn, the most important being that overt development was normal.

b) Selection of Fixation Protocols: Our preliminary histological evaluations from STS 70 suggested that 4% paraformaldehyde in the spaceflight condition yielded adequate but not optimal fixation for histological observations. While 4% paraformaldehyde is the fixative of choice for use in fixing tissues for subsequent *in situ* hybridixation analysis, it does not appear to be the best fixative for morphological integrity of medaka embryos, particularly when fixed through the chorion. Since Bouin's fixative had been used by one of us (C.R. Phillips) in an extensive series of studies and was found to yield both optimal

morphological preservation and adequate detection of at least certain cellular proteins by immunohistochemistry, this was the fixative of choice for STS 78.

c) Video Analysis of Medaka Development in Control and Flight Environments: Medaka fish embryos are optically clear, allowing direct observation of embryonic development by video-microscopy. Such instrumentation has been developed by our colleagues from Walter Reed as part of the STL-B hardware. The STL-B hardware has flown experiments on the shuttle on three separate occasions. The first, STS 59, was considered a hardware flight test and was not supported by NASA. Medaka embryos were flown on this mission and all systems checked out in terms of biocompatibility. The second and third flights, STS 70 and 78, provided the opportunity for a series of video observations and fixation of embryos for subsequent histological examinations on the effects microgravity on the development of the medaka at various stages.

The first video sequence served as a reference for fish development. There is normally a rotation of the animal pole upwards, relative to gravity, and active cytoplasmic rearrangement towards the animal pole following fertilization. Cytoplasmic components are localized to the animal pole as mitosis begins to partition the egg into cells. It is during the early stages of cell division shown here that the dorsal/ventral and right/left axes are determined. All of the major body organs are spatially determined during gastrulation.

The primary on-orbit activities conducted by the crew was to provide the on-orbit reference to the system at 7 hours after launch and to re-program the embryo positions to accommodate any shifting resulting from launch and orbit. This reprogramming optimized the digital image storage and the on-board recordings by centering embryos in the viewfield. Once the embryos were correctly positioned and the video cables set up, it became possible to receive an earlier than planned, additional downlink. This downlink verified embryo viability and positioning. The first planned downlink was operated by Commander Tom Hendricks, who provided us with a much longer than scheduled downlink. During this downlink, each of the six embryo chambers were reviewed and observed. This proved to provide a good baseline for system operation, performance, and status of the embryos. Subsequent downlinks and on-board recordings were conducted automatically by ground commmanding of the shuttle systems. In many cases the downlinks were longer than originally scheduled, and on-board recordings were more frequent than scheduled. The landing preparation reference was provided following our final scheduled downlink and the termination of the last samples.

Following the mission, ground and flight digital images were decompressed and recorded onto compact disks. Copies of these disks have been provided to one of us (C.R. Phillips) for analysis.

d) Studies of Complete Life Cycle of Medaka Embryos Which Were Allowed to Hatch Upon Return to the Earth Environment: Although not formally part of LMS, the following observations from STS 70 are relevant to the overall scientific mission. Two of the culture chambers containing embryos in the experiments flown in STS 70 were returned to earth unfixed. These embryos and one chamber of control embryos were held at KCS for 9 days at 18°C. They were then shipped to Columbia University in a container to maintain the 18°C temperature. Upon receipt on 7/25/95, they were placed in a controlled temperature environment of 21-25°C, average temperature was 23°C. The lighting regimen in the culture incubator was 12 hours light: 12 hours dark from 7/25/95 to 8/17/95. After 8/25/95, the light/dark cycle was changed 16 hours light: 8 hours dark. The average hatching time, in days post arrival at Columbia University, was 30 days for the flight animals (two groups of six embryos each) and 40 days for the control (one group of 6 embryos). Both series are considerably longer than the typical hatching time for medaka of 10-14 days total at 25°C. This delayed hatching in embryos in the culture chamber is potentially interesting and should be investigated further; however, the numbers in the present study were too small to be evaluated statistically.

Upon hatching, the fry were allowed to develop into adulthood. Over a 4 month-period, 3 control animals and 5 experimental animals survived and began to reproduce. The two females and one male of the control group produced 8 eggs that were recovered but then stopped reproducing, no doubt due to the small number of animals in the tank. In contrast, the space flight animals consistently yielded batches of fertilized embryos from 11-10-95 through 7-16-96. This result demonstrated that animals exposed to microgravity during embryogenesis could reproduce. A sample of the embryos yielded from the flight animals were then removed to a separate culture environment and allowed to develop to adulthood. Upon reaching sexual maturity, these animals began to mate as well. Thus, the progeny of the space flight animals are also fertile.

4) Flight Results Compared with Ground Results:

a) Use of Reduced Temperatures in Studies of Early Embryogenesis in the Microgravity Environment: One of the reasons for selecting the fish medaka as an ideal model for studying vertebrate development in space is its ability to tolerate reduced temperatures during early embryogenesis. This has permitted us to slow down early embryogenesis until the embryos were exposed to microgravity. A series of temperature shift trials have been run to determine the appropriate temperatures in which to hold medaka embryos so that a minimal amount of development has occurred prior to arrival in microgravity. The length of time the embryos are held in a slow developing state depends on the flight hardward turnover time established for each particular flight. In STS-78, temperatures were held at 12°C during loading of the embryos and in the STL-B hardware unit until orbit was achieved. Once in orbit, the system raised the temperature in the chambers to 17.5°C, which allowed development to proceed at a faster rate. The

temperature was monitored throughout the flight and held to within 1°C. An example of the temperature tracking is shown in Fig. 1.

One important consequence of the previous flight experiments was the preliminary observation that flight embryos might develop at slightly different rates than do the ground controls. Analysis of developmental rate differences in fish embryos will be highly dependent on controlling and monitoring the temperature during both the flight and control samples. As noted above, the STL-B can maintain temperatures with a one degree centigrade accuracy. Therefore, in order to study the effects that microgravity might have on rates of development, it is important to understand the effects of small temperature changes, up or down, on the developmental rates between specific stages of embryonic development. We have done extensive studies on the effects of temperatures at 14° C, 15° C, and 16° C, concentrating on the period of development encompassing gastrulation. Interestingly, embryos raised at 14° C appear to develop faster during the initiation of movements at gastrulation than do embryos raised at either 15° or 16° C. (Fig. 2). By mid-gastrulation, the developmental rates are equivalent between embryos raised at these three temperatures. Time lapse video analysis is currently being done to determine the cause and mechanisms involved in these differences during early gastrulation.

Comparison of both developmental heterogeneity within a clutch of embryos and developmental rates between ground control and flight embryos is highly sensitive to temperature fluctuations. The STL-B was designed to minimize the temperature differentials within the growth chamber. This was accomplished by minimizing the volume and replacing the media with new media at the appropriate temperature. The volume of each of the six chambers was 70 microliters and the media was changed 10 times per hour. Ground-based tests indicate that this rate of flow provides adequate oxygenated media and waste removal for normal development.

b) Analysis of Gene Expression in Medaka Embryos: We have begun to analyze the expression of the medaka *Hoxa-4* gene as a marker of embryonic development for analyzing the effect of microgravity on pattern formation and embryonic segmentation. To this end, we are currently determining the expression pattern of medaka *Hoxa-4* during embryogenesis, under normal conditions. Our Northern blot analysis of total RNA isolated from embryos pooled at various stages of development revealed the expression of a major transcript of ~1.7 kb, first detected at stage 21, when the medaka embryos have six to eight somites. Our next experiments will extend this analysis to sections of embryos at various stages of development by *in situ* hybridization on histologically sectioned embryos. This will be critical for studies on the expression of specific genes in flight embryos, as multiple genes could be assayed in the same embryo. We have concomitantly successfully obtained whole mount *in situ* hybridizations with medaka embryos, but feel it is critical to develop the use of sectioned material to maximize data return. An example of whole mount *in situ* hybridization of the homeobox gene *Hoxa-4* is shown in Fig. 3.

c) Effects of Retinoic Acid on Developing Medaka Embryos: Retinoic acid had been shown to be an important regulator of vertebrate development, in both the fish and mouse. In concurrent studies in our lab, we have shown that some Hox genes in the mouse, particularly *Hoxa-4* (Alan Packer and D. J. Wolgemuth, unpublished observations), are regulated at least in part by the administration of all-trans retinoic to pregnant females. Although no retinoic acid binding element has yet been identified in the upstream region of medaka *Hoxa-4*, we wanted to know if this mode of regulation of the expression of this gene in mouse could be conserved through other species. Medaka embryos at various stages prior or at the begining of *Hoxa-4* expression (see above) were treated with all-trans retinoic acid for two hours in the dark. Embryos treated with 1uM did not show any specific phenotype, although none of them were allowed to develop further than stage 27. Embryos treated with 10 uM retinoic acid died at stage 20-21, with a typical curly tail, proving that the normal pattern of body development was strongly affected at that concentration. Whole-mount analysis of treated embryos showed that, at both concentrations, *Hoxa-4* expression in the neural tube was shifted more anteriorly, and that the amplitude of the shift could be affected by the concentration of retinoic acid. Interestingly, the shift observed at stage 25 exhibited two bands of expression, more anterior than the normal limit of *Hoxa-4* expression and very similar to what we have observed in the mouse (A. Packer and D.J. Wolgemuth, unpublished observations).

(5) Conclusions Including Significance and Future Plans:

Earlier flight experiments produced embryos showing truncation of anterior structures. However, analysis of the temperature profile indicated that a temperature spike to near 32°C occurred during the early stages of the flight. We have grown embryos at 32°C in 1 g, both for long durations and for short bursts of time during gastrulation and have not seen the kinds of anterior truncations observed in these early flight experiments. However, we can not rule out that the combination of stresses due to higher temperature and microgravity, in combination might lead to the observed anterior truncations. The temperature problems for the STL-B were corrected and a second flight experiment (STS 70) where the temperature control responded correctly produced normal embryos which subsequently were bred and produced live young. Therefore, the possibility of the combined stress of microgravity and temperature has not been addressed.

Sections of flight and control embryos would ultimately provide detailed information about developmental morphology and molecular events controlling development. However, fish embryos are small and difficult to orient when embedding. Therefore, sectioned embryos tend to lay at various orientations, making it difficult to compare subtle differences in morphology between embryos. We have been working on a method of digitally reconstructing sectioned embryos to make comparisons easier. Digital sections can be used to make 3-D reconstructions or they can be used to make movies of simultaneous "flights" through the embryo. Movies of both flight and ground control embryos can be compared simultaneously as a means of detecting more subtle

morphological differences. Eventually, three dimensional reconstructions of each organ within the embryos will be made and animated through all of the developmental stages which have been fixed in flight and sectioned here on earth. An additional observation that merits future study is the extended hatching time that was observed in both control and experimental medaka embryos flown on STS 70.

(6) Bibliographic Citations of Articles/Presentations Resulting from the Flight (to date)

Wolgemuth, D.J., G. Herrada, S. Kiss, T. Cannon, C. Forsstrom, L.A. Pranger, W.P. Weismann, L. Pearce, B. Whalon, C.R. Phillips. (1997). Vertebrate Development in the Environment of Space: Models, Mechanisms, and Use of the Medaka. **The ASGSB Bulletin**, in press.

(7) Non-technical Summary

In the flight experiment on LMS, June 20, 1996, thirty-six medaka embryos were flown on a modified STL-B hardware system. Digital images and real-time video sequences were taken of the flight, synchronous ground and non-synchronous ground embryos under identical conditions except for the flight environment (acceleration into orbit and microgravity). In addition, ground-based studies have been performed on the use of reduced temperatures to study early embryogenesis, on developing alternative fixation protocols, on gene expression in medaka embryos, and on the effects of retinoic acid on embryogenesis in developing medaka.

FIGURE LEGENDS

Figure 1. The embryo temperatures from the flight unit on STS-78 were kept at 12°C (lower boundary) once loaded into the STL-B. Approximately 9 hours after orbit, the temperature was gradually raised to 17.5°C, where it remained for the duration of the mission. Data points on this graph are instantaneous, not averaged, values which were recorded every 5 minutes.

Figure 2. Effects of reduced temperatures on rates of medaka development.

(2a). Ten embryos each from one clutch were incubated at temperatures of 14.5, 15.5, and 16.5°C. At varying intervals, the embryos were staged according to Kirchen and West (1976). The embryos were monitored from the beginning of gastrulation at approximately 11 hours of development through 72 hours of development at the three temperatures depicted above. The development of embryos at 25°C is shown from a second clutch of embryos. All embryos within a clutch developed synchronously at a given temperature.

(2b). Embryos at the lower temperature appear to develop faster during early to mid-gastrula stages, as shown in Figure 2a. A second clutch of embryos were incubated at 14.5, 15.5, and 16.5°C during the early to late stages of gastrulation. Embryos from this clutch also exhibited increased rates of development at 14.5°C than embryos grown at 15.5 or 16.5°C.

Figure 3. Expression of the medaka homeobox-containing gene Hoxa-4 at specific developmental stages. Embryos were cultured, harvested at specified stages, and subjected to whole mount *in situ* hybridization (D.A. Crotty, G. Herrada, X. Wang, and D.J. Wolgemuth, in preparation). The stages of embryonic development are assigned according to the criteria described by T. Iwamatsu (Zool. Sci., 11: 825-839, 1994).

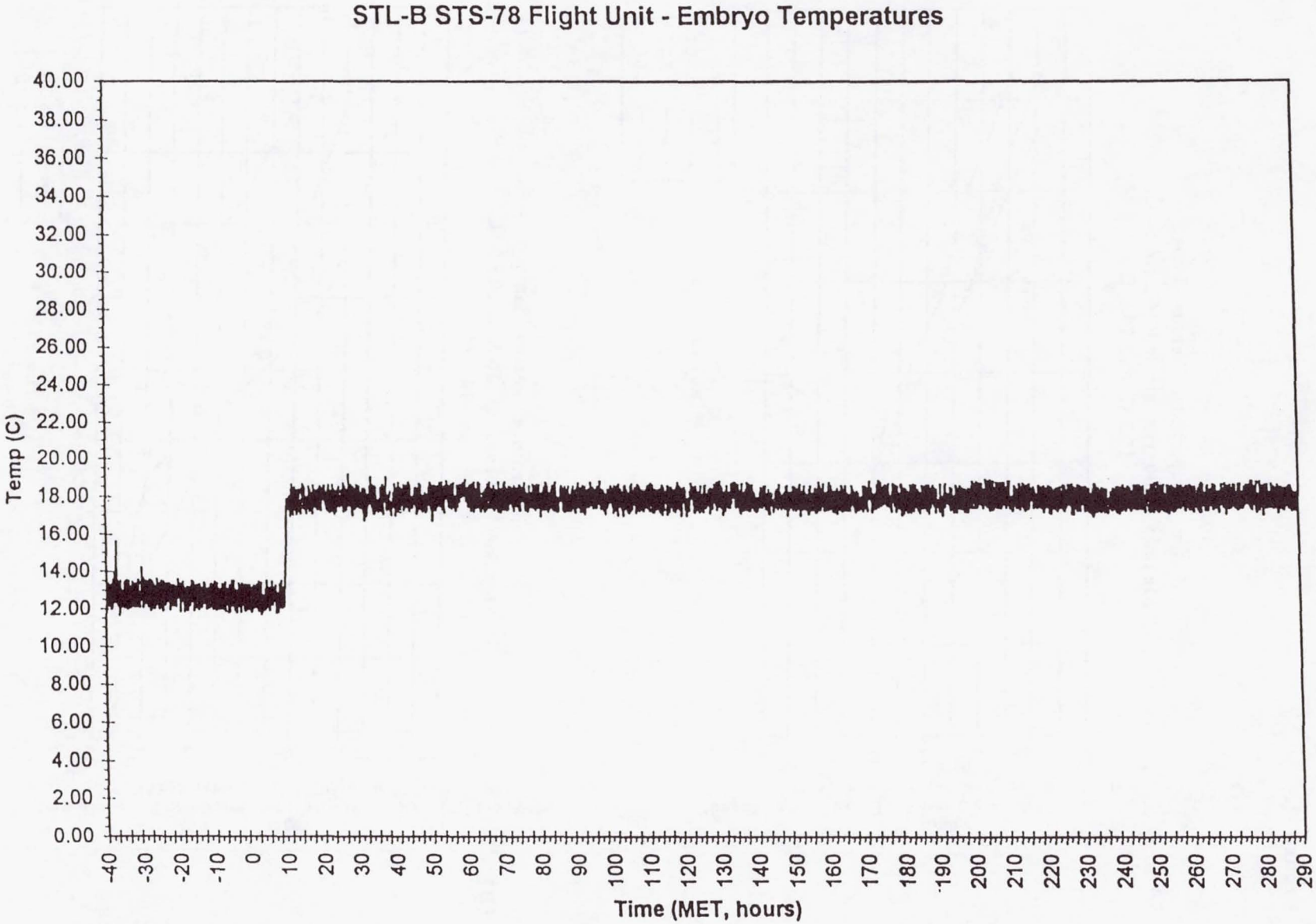
STL-B STS-78 Flight Unit - Embryo Temperatures
Temp (C)
40.00
38.00
36.00
34.00
32.00
30.00
28.00
26.00
24.00
22.00
20.00
18.00
16.00
14.00
12.00
10.00
8.00
6.00
4.00
2.00
0.00
-40
-30
-20
-10
0
10
20
30
40
50
60
70
80
90
100
110
120
130
140
150
160
170
180
190
200
210
220
230
240
250
260
270
280
290
Time (MET, hours)

Figure 1.

Figure 2.

[A]

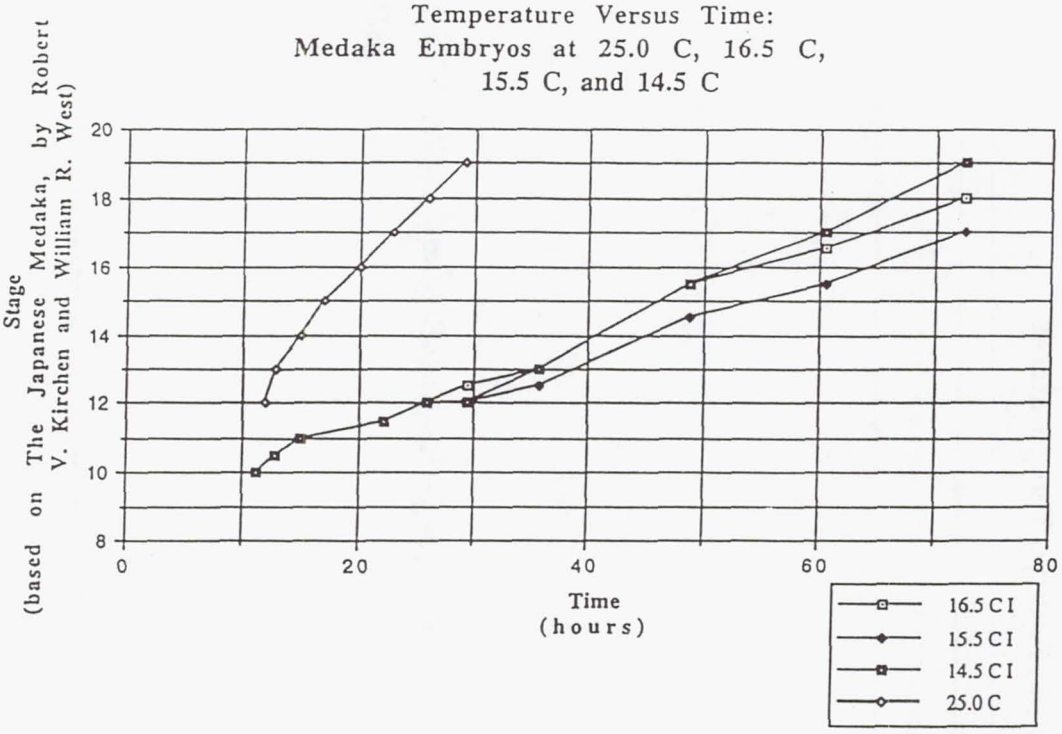
Temperature Versus Time:
Medaka Embryos at 25.0 C, 16.5 C,
15.5 C, and 14.5 C
Stage
(based on The Japanese Medaka, by Robert V. Kirchen and William R. West)
20
18
16
14
12
10
8
0
20
40
60
80
Time
(hours)
16.5 C I
15.5 C I
14.5 C I
25.0 C

[B]

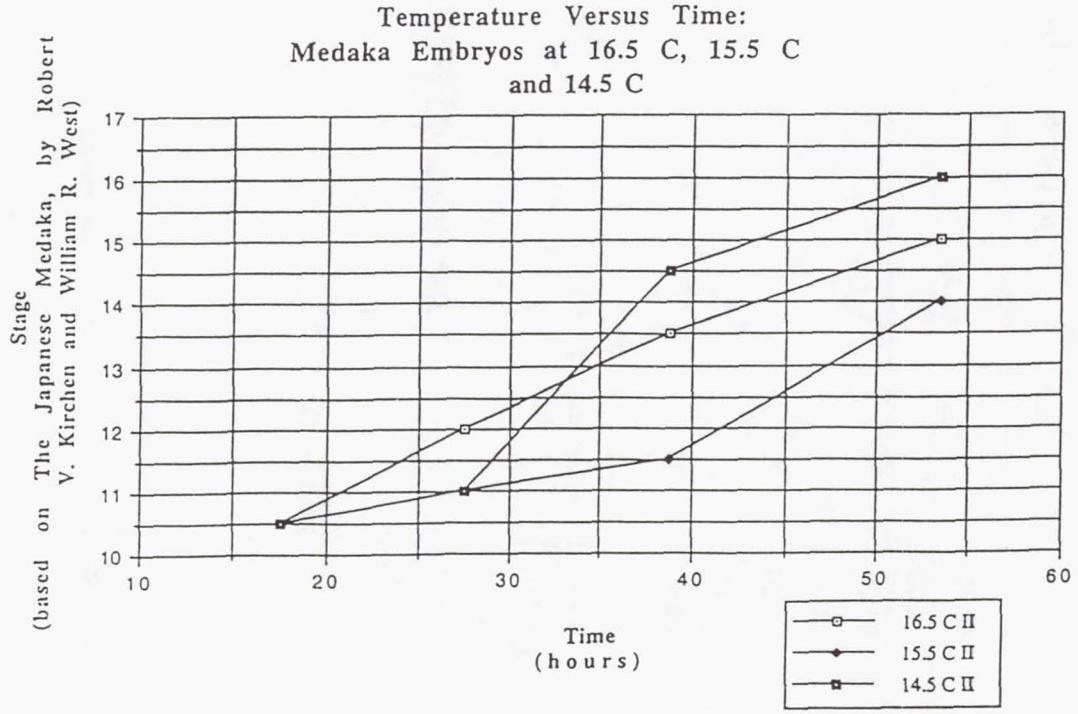
Temperature Versus Time:
Medaka Embryos at 16.5 C, 15.5 C
and 14.5 C
Stage
(based on The Japanese Medaka, by Robert V. Kirchen and William R. West)
17
16
15
14
13
12
11
10
10
20
30
40
50
60
Time
(hours)
16.5 C II
15.5 C II
14.5 C II

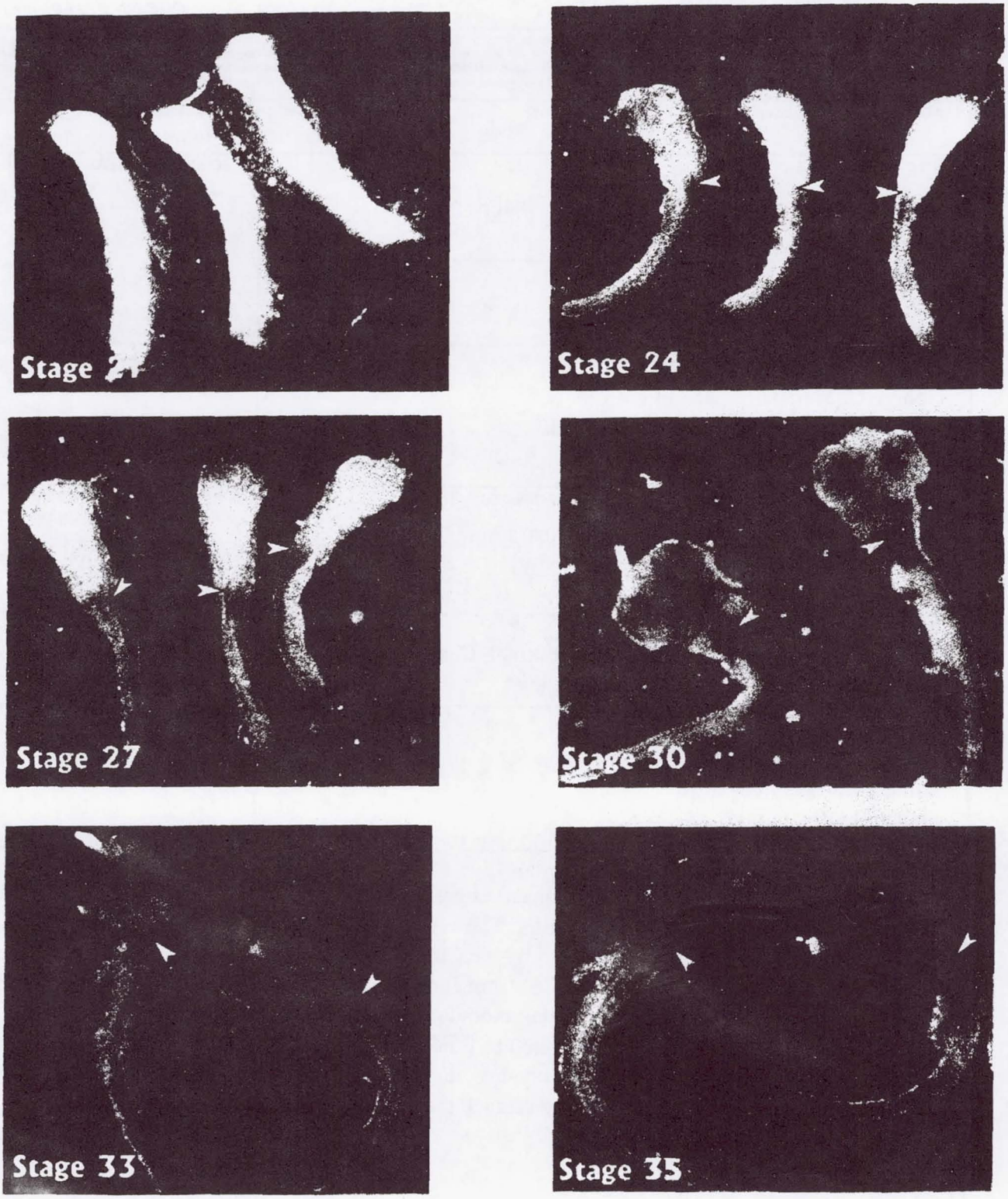

Figure 3.
Expression of Hoxa-4 in different stages of Medaka Embryonic Development
(arrowheads show anterior boundary)

REPORT DOCUMENTATION PAGE

Form Approved
OMB No. 0704-0188

Public reporting burden for this collection of information is estimated to average 1 hour per response, including the time for reviewing instructions, searching existing data sources, gathering and maintaining the data needed, and completing and reviewing the collection of information. Send comments regarding this burden estimate or any other aspect of this collection of information, including suggestions for reducing this burden, to Washington Headquarters Services, Directorate for Information Operation and Reports, 1215 Jefferson Davis Highway, Suite 1204, Arlington, VA 22202-4302, and to the Office of Management and Budget, Paperwork Reduction Project (0704-0188), Washington, DC 20503

1. AGENCY USE ONLY *(Leave Blank)*	2. REPORT DATE	3. REPORT TYPE AND DATES COVERED
	February 1998	Conference Publication

4. TITLE AND SUBTITLE

Life and Microgravity Spacelab (LMS) Final Report

5. FUNDING NUMBERS

6. AUTHORS

J.P. Downey, Compiler

7. PERFORMING ORGANIZATION NAMES(S) AND ADDRESS(ES)

George C. Marshall Space Flight Center
Marshall Space Flight Center, AL 35812

8. PERFORMING ORGANIZATION REPORT NUMBER

M–854

9. SPONSORING/MONITORING AGENCY NAME(S) AND ADDRESS(ES)

National Aeronautics and Space Administration
Washington, DC 20546

10. SPONSORING/MONITORING AGENCY REPORT NUMBER

NASA/CP—1998–206960

11. SUPPLEMENTARY NOTES

Proceedings of a conference held in Montreal, Canada, on August 20–21, 1997. The conference was hosted by the Canadian Space Agency.

12a. DISTRIBUTION/AVAILABILITY STATEMENT

Unclassified–Unlimited
Subject Category 88
Standard Distribution

12b. DISTRIBUTION CODE

13. ABSTRACT *(Maximum 200 words)*

This document reports the results and analyses presented at the Life and Microgravity Spacelab (LMS) One Year Science Review meeting. The science conference was held in Montreal, Canada, on August 20–21, 1997, and was hosted by the Canadian Space Agency. The LMS payload flew on the Space Shuttle Columbia (STS–78) from June 20–July 7, 1996. The LMS investigations were performed in a pressurized Spacelab module and the Shuttle middeck. Forty scientific experiments were performed in fields such as fluid physics, solidification of metals, alloys, and semiconductors, the growth of protein crystals, and animal, human, and plant life sciences. The results demonstrate the range of quality science that can be conducted utilizing orbital laboratories in microgravity.

14. SUBJECT TERMS

LMS, Spacelab, microgravity research, life sciences, materials science, biotechnology, space biology, human physiology, protein crystal growth

15. NUMBER OF PAGES

624

16. PRICE CODE

A99

17. SECURITY CLASSIFICATION OF REPORT	18. SECURITY CLASSIFICATION OF THIS PAGE	19. SECURITY CLASSIFICATION OF ABSTRACT	20. LIMITATION OF ABSTRACT
Unclassified	Unclassified	Unclassified	Unlimited

NSN 7540-01-280-5500

Standard Form 298 (Rev. 2-89)
Prescribed by ANSI Std. 239-18
298-102